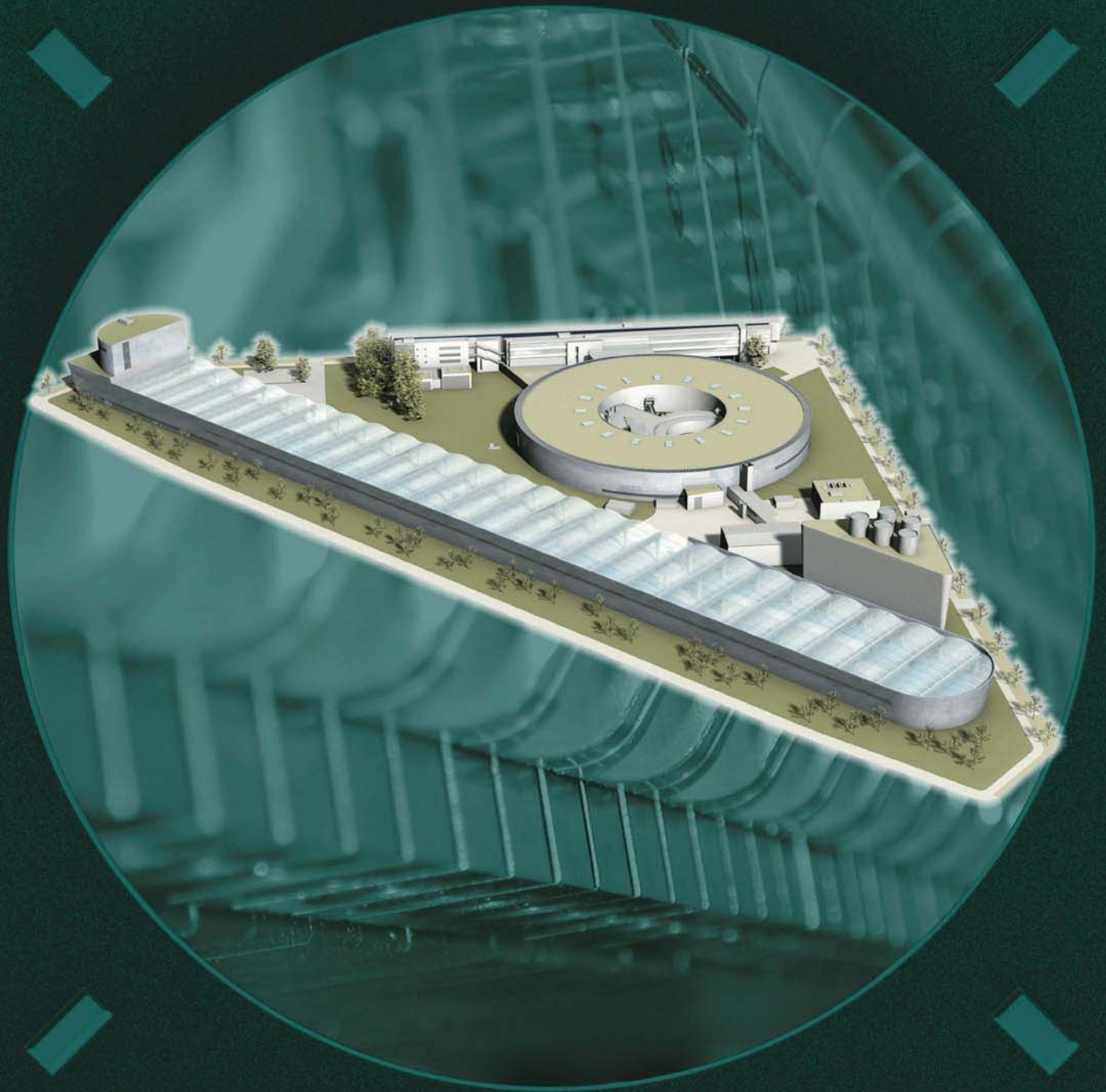




The BESSY Soft X-ray Free Electron Laser

Technical Design Report

March 2004



**Publisher**

Berliner Elektronenspeicherring-Gesellschaft
für Synchrotronstrahlung (BESSY) m.b.H.

Albert-Einstein-Straße 15
12489 Berlin
Germany
Tel: +49-(0)30-6392-2999
Fax: +49-(0)30-6392-2990
www.bessy.de
fel@bessy.de

BESSY is a member of the Leibniz-Association



Leibniz
Gemeinschaft

**Cover**

Graphilox, Josch Politt, Berlin

**Printing**

Pinguin Druck GmbH, Berlin

**Editors**

D. Krämer, E. Jaeschke, W. Eberhardt

ISSN xxx-xxx-xxx-xx

Copyright by BESSY GmbH, Berlin 2004

Preamble

Research with synchrotron radiation in Berlin has been an unparalleled success story for more than 20 years. From the start-up of the first German dedicated synchrotron radiation source, BESSY I, thousands of researchers from Germany and abroad, from universities, research centers, and industry, have beaten a path to Berlin. The most recent highlight is the BESSY II third-generation facility at the WISTA in Berlin-Adlershof, which initiated user operation in 1999 and surpassed its predecessor in brilliance by many orders of magnitude. The quest for even higher brilliance, and in addition extreme time resolution in the regime of femtoseconds, is continuing, pushing technology into the micro- and nanoworlds of the 21st century. The instrument of choice is a Free Electron Laser (FEL) optimized for the user community and covering their specific needs from the vacuum ultraviolet to the soft X-ray radiation.

The Berliner Elektronenspeicherring-Gesellschaft für Synchrotronstrahlung therefore presents this Technical Design Report (TDR) proposing to build a Soft X-ray FEL user facility in the photon energy range 24 eV to 1000 eV, based on the High-Gain-Harmonic Generation (HG HG) principle, whereby external femtosecond seed pulses from UV lasers are used to control the FEL process. This facility is able to deliver reproducible radiation pulses controlled to only a few femtoseconds in duration, opening the way to the attosecond pulses. The external seed lasers serve as a master clock for the synchronization of pump-probe experiments over the whole wavelength range from the UV to hard X-ray photons.

The wide field of research accessible through the utmost brilliance and extreme time resolution of the new instrument has been described previously and is continuously expanded in an ongoing series of workshops. It ranges from studies of dynamical processes, in femtochemistry, magnetic information storage, and plasma physics all the way to the life sciences including proteins and living cells. The possibility of synchronizing the FEL pulses with external lasers will enable hitherto inconceivable pump-probe experiments. The high FEL output power in the gigawatt range opens up the field for investigations of dilute systems such as individual mass-selected clusters or aerosol particles and processes relevant for the chemistry in the upper atmosphere to basic studies of nonlinear processes in atoms, molecules, and solids at photon energies in the soft X-ray range. The coherent photons create possibilities for new imaging techniques in microscopy and holography on samples from micro- and nanotechnology, environmental characterization and remediation, to cell biology. The extreme brilliance of the FEL will convert directly into spectral, spatial, and time resolution in spectroscopic and structural investigations unattainable up to now.

The BESSY FEL design group has benefited greatly from discussions, comments and suggestions made by colleagues from Germany (DESY, MBI, TU-Darmstadt, TU-Dresden) as well as from abroad (ALS, APS, BNL, Cornell, ELETTRA, ESRF, INFN Milano, JLab, Maxlab, MIT Bates, CEA Saclay, SLAC, IPN Orsay and UCLA). Their contributions were invaluable for the completion of this TDR.

Special thanks are to the 'Zukunftsfonds des Landes Berlin' and the 'Bundesministerium für Bildung und Forschung' (BMBF) for funding this study.

Overview

Preceding the detailed technical description of the proposed facility, *chapter 1* is an **Executive Summary** outlining the scientific case, the performance characteristics and the general layout of the facility. Here one will also find estimates of the personnel and capital cost.

Chapter 2 is a short introduction to the presently discussed FEL schemes, including the motivation to propose a second-generation FEL based on the externally seeded **cascaded HGHG-scheme**. Advantages in terms of photon beam-power stability, reproducibility and the unique possibility to generate intense well-formed fs-pulses are discussed. The **simulation results** for the seeded HGHG-FEL radiation sources in the VUV to soft X-ray regime are presented in *chapter 3*. The unique features of the seeding schemes are explained, emphasizing the variable and ultra-short femtosecond-pulse duration capabilities of the BESSY design. *Chapter 4* is on the most important aspect of **seed laser and synchronization of lasers**.

In *chapters 5 to 9* the central systems such as the **photoinjector**, the **CW linac**, **bunch compressors**, and **undulators** are discussed, demonstrating that the requirements for the BESSY FEL components, although demanding, are based on a proven technology available today.

The planning for the **beamlines**, **instrumentation** and **experimental end-stations** is described in *chapters 10 and 11*, while *chapters 12 to 16* deal with special aspects, such as **beam diagnostics**, **control system**, **safety issues**, and **conventional facilities**.

Finally, the **project budget and the time schedule** are presented in **chapter 17**, giving an overview on the detailed cost estimates and the assumptions that had to be made to quantify the financial and personnel requirements. Particular care was taken to make certain that these estimates are on a sound basis, both for the total investment and the manpower required. The goal of this project is to build the facility outlined in this Technical Design Report on time and in budget.

The BESSY FEL Design Study Group

BESSY

M. Abo-Bakr, W. Anders, J. Bahrtdt, R. Bakker*, K. Bürkmann, G. Bisoffi[♥], P. Budz, O. Dreßler, H. Dürr, V. Dürr, W. Eberhardt, S. Eisebitt, J. Feikes, R. Follath, A. Gaupp, K. Goldammer, M. v. Hartrott, S. Heßler, K. Holldack, E. Jaeschke, T. Kamps, S. Khan, J. Knobloch, B. Kuske, P. Kuske, D. Krämer, F. Marhauser, A. Meseck, G. Mishra[§], R. Mitzner, R. Müller, A. Neumann, M. Neeb, K. Ott, W. Peatman, D. Pflückhahn, H. Prange, T. Quast, M. Scheer, T. Schroeter, F. Senf, G. Wüstefeld, Y. Xiang⁺

Max-Born-Institut Berlin

I.V. Hertel, F. Noack, W. Sandner, M. Schnürer, P. Tzankow, I. Will

Forschungszentrum Rossendorf

D. Janssen, P. Michel, J. Teichert

TU Dresden

G. Bartlock, Ch. Haberstroh, A. Kutzschbach, H. Quack

*now Sincrotrone Trieste, § DAVV Indore, India, + now GSI Darmstadt, ♥INFN Laboratori Nazionali di Legnaro

Table of Contents

Preamble	I
Overview	III
1 Executive Summary	1
1.1 Introduction	1
1.2 Scientific Goals	5
1.3 Selection of Major System Parameters	13
1.4 The Layout of the BESSY Soft X-Ray FEL User Facility	14
1.5 Main Performance Parameters	16
1.6 The BESSY FEL in the International Context	17
1.7 The Phase I Normal-Conducting Injector	19
1.8 The Phase II Superconducting Injector	21
1.9 The Linac Modules	23
1.10 Electron Acceleration and Bunch Compression	25
1.11 The Undulators	27
1.12 Beamlines and End-Station	29
1.13 Conventional Facilities and Buildings	32
1.14 Cost and Schedule	34
References	36
2 The Quest for Brilliance and Extreme Time Resolution	39
2.1 Introduction to FELs	39
2.2 The SASE Principle	41
2.3 Seeded FELs	42
2.4 The Cascaded HGHG-FEL	44
References	46
3 Simulation of the BESSY HGHG-FEL	49
3.1 The High-Gain-Harmonic Generation	49
3.1.1 Working Principles of a Multi-Stage HGHG-FEL	50
3.1.2 Layout of the HGHG Undulator Section	51
3.1.3 Optimization of Undulator Parameters	53

3.1.4	Optimization of the HHG Stages Using Genesis	54
3.2	Performance Calculations	56
3.3	Future HHG-Laser-Seeded FELs	71
3.4	Tolerance Studies	73
3.4.1	Sensitivity towards Electron Beam Parameters	74
3.4.1.1	Beam Energy Spread	74
3.4.1.2	Beam Emittance	76
3.4.1.3	Beam Current	76
3.4.1.4	Seed-Laser Power	79
3.4.1.5	Correlated and Uncorrelated Undulator Errors	81
	References	85
4	Gun, Seed, and Experiment Lasers: Concept and Synchronization	87
4.1	Introduction	87
4.2	Seed and Experiment Lasers	88
4.2.1	Seed Lasers	88
4.2.1.1	Description of the Individual Components of the Seed Laser	88
4.2.1.2	Alternative Solutions	92
4.2.1.3	Summary	93
4.2.2	Experiment Lasers	94
4.3	Future Prospects: HHG Seeding at Shorter Wavelengths	96
4.3.1	HHG Frequency Conversion	97
4.3.2	Stability	98
4.3.3	Tunable Spectra, Spatial Beam Profile	98
4.3.4	Temporal and Spectral Pulse Profile	98
4.3.5	Feasibility	99
4.4	Synchronization of Seed and Experiment Lasers	100
	References	104
5	The High-Brilliance Electron Injector	107
5.1	Room-Temperature RF Photoinjector Guns	107
5.1.1	General Layout	107
5.1.2	Emittance Conservation	108
5.2	The PITZ Collaboration RF Photoinjector	111

5.3	The BESSY Normal-Conducting Injector	113
5.3.1	The High-Duty Cycle, High-Power Injector Cavity	113
5.3.2	Working Point and Magnetic Field	116
5.3.3	RF Phase at Injection	117
5.3.4	The First Linac Section	119
5.3.5	The Third-Harmonic Cavity	122
5.4	Injector RF System	124
5.4.1	Klystron Requirements	124
5.4.2	Modulator Requirements	124
5.4.3	Fast Amplitude Control Loop	126
5.5	The Photocathode Laser	128
5.5.1	The Photocathode Laser, Parameters, and Influence on the Emittance	128
5.5.2	The Photocathode Laser for the BESSY FEL	130
5.5.2.1	Basic Layout of a Diode-Pumped UV Laser	130
5.5.2.2	Suitable Laser Materials	131
5.5.2.3	Layout of the Photocathode Laser	133
5.5.3	Components of the Laser	134
5.5.3.1	The Laser Oscillator	134
5.5.3.2	Pulse Shaper	135
5.5.3.3	The Regenerative Amplifier	136
5.5.3.4	Equalizing Pockels Cell ("Micro-Pulse Equalizer")	137
5.5.3.5	The Double-Pass Booster Amplifier	138
5.5.3.6	Wavelength Conversion Stage	138
5.5.3.7	Control of Micro-Pulse Shape	138
5.5.4	Comparison with Existing Photocathode Lasers at TTF and PITZ	139
5.5.5	Conclusions and Summary	139
5.6	A Future Superconducting Photoinjector	140
5.6.1	The FZR Rossendorf-BESSY-DESY-MBI Photoinjector	140
5.6.2	Photoinjectors Based on Multicell Superconducting Cavities	143
5.6.2.1	Main Challenge	143
5.6.2.2	Simulations	144

5.6.2.3	Emittance Conservation in a Booster Linac	146
5.6.2.4	Niobium Photocathode	148
	References	149
6	The Superconducting CW Accelerator	151
6.1	Linac Design	151
6.2	Accelerator Modules	152
6.2.1	Cavities and Cryostat	153
6.2.2	Input Coupler	157
6.2.3	Cavity Tuner	158
6.3	Considerations for BESSY FEL CW Operation	159
6.3.1	Cavity Field	161
6.3.1.1	Cost Analysis	161
6.3.1.2	Feasibility of Field	162
6.3.2	Bath Temperature	163
6.3.3	Dynamic Heat Load	165
6.3.4	CW Module Design	166
6.3.4.1	JT Valve	167
6.3.4.2	Heat Transfer in Helium II	167
6.3.4.3	Heat Conduction and Mass Flow in the Two-Phase Line and GRP	170
6.3.5	Impact of Microphonics on CW Operation	175
6.3.5.1	Optimum Input Coupling	178
6.3.6	Beam Loading	180
6.3.7	Higher-Order-Mode Power	182
6.4	High-Power RF System	183
6.4.1	RF-Power Tubes	184
6.4.2	RF Transmitter Power Supplies.	187
6.5	Low-Level RF Control	188
6.5.1	Motivation for Low-Level RF Control	188
6.5.2	Layout of the Low-Level Control System	188
6.5.3	Energy- and Time-Jitter Requirements.	190
6.5.4	Error Sources	191
6.5.5	RF Control Simulations	192

6.5.5.1	Choice of Gain	192
6.5.5.2	Simulation Results	192
6.5.6	Piezo Compensation	197
6.6	HoBiCaT—a Test Facility for Superconducting Cavities	198
6.6.1	HoBiCaT Cryostat and Refrigeration	199
6.6.1.1	Cryostat	199
6.6.1.2	Refrigeration	201
6.6.2	RF Transmitter for HoBiCaT	203
6.6.3	HoBiCaT Cavity Units	203
	References	205
7	Bunch Compression	209
7.1	Principle of Bunch Compression	209
7.2	Bunch Compression Scheme for the BESSY FEL	213
7.2.1	Basic Layout Considerations	213
7.2.2	Injector Beam Parameters	215
7.2.3	Layout of BC1	216
7.2.4	Layout of BC2	217
7.3	The 180 Degree Arc	218
7.4	Electron Beam Extraction	220
7.5	Start-to-End Simulations	222
	References	228
8	Beam Distribution System	229
8.1	The Linac Optics	229
8.2	Beam Distribution Kickers and Pulsers	232
8.2.1	Stability Requirements for the Kickers	232
8.2.2	A Semiconductor-Based Pulsar for the Kicker	233
8.2.3	First Results from the Test Pulsar	234
8.3	Standard ‘Warm’ Vacuum System	236
8.3.1	Materials	237
8.3.2	Vacuum Pressure	237
8.4	Beam-Transport Elements	239
8.4.1	Conventional Magnet Designs	241

8.4.2	Power Converters	245
	References	247
9	Undulators for the BESSY Soft X-Ray FEL	249
9.1	Magnetic Design	250
9.1.1	Choice of the Undulator Design	250
9.1.2	The Modified APPLE II Design	253
9.1.3	Selection of Magnetic Material for the Undulators	255
9.1.4	Parameters of the Undulators	257
9.1.5	The Endpole Structure	260
9.2.	Transverse Field Distribution and Focusing	262
9.3	Undulator Tolerances	266
9.3.1	Tolerance Estimates from 1-D Theory	266
9.4	Field Optimization	268
9.4.1	Characterization of Magnets	268
9.4.2	Sorting	269
9.4.3	Shimming	270
9.5	The Phase Shifters	272
9.6	The Mechanical Layout	276
9.6.1	The Magnetic Structure	276
9.6.2	The Support and Drive System	278
9.7	Manufacturing of the Undulator Modules	279
9.7.1	R & D Studies	279
9.7.2	Fabrication and Logistics	280
9.8	Drive and Control System	281
9.8.1	Specifications	281
9.8.2	The Axis Controller and Interfaces	282
9.8.3	Computer Hard- and Software	282
9.9	Beam Collimation at the Undulator Sections	283
9.9.1	Boundary Conditions	284
9.9.2	General Layout of the Collimator	284
9.9.3	Transverse Collimation	285
9.9.4	Energy Collimation	287

9.9.5	Diagnostics	288
9.9.6	Further Studies	288
9.10	Wakefield Effects in the Undulator Section	289
9.11	The Intersection Regions	295
9.12	The Undulator Vacuum Chamber	296
	References	298
10	Beamlines for the BESSY FEL	303
10.1	Introduction	303
10.2	General Considerations	303
10.2.1	Photon-Induced Damages	305
10.2.2	Mirrors	306
10.2.2.1	Total External Reflection	306
10.2.2.2	Coatings	308
10.2.2.3	Thermal Properties	310
10.2.2.4	Surface Quality	312
10.3	Diffractive X-Ray Optics	313
10.3.1	Beam Shaping	315
10.3.2	Timing	315
10.3.3	Raytracing	317
10.4	General Layout	317
10.5	Frontends	319
10.5.1	Diagnostics	322
10.6	Beamlines for the Low-Energy FEL	323
10.6.1	Beamline for High-Energy Resolution	323
10.6.2	Beamline for Short Pulses	329
10.6.3	Focused Direct Beam	334
10.7	Beamlines for the Medium-Energy and High-Energy FELs	335
10.7.1	Beamline for High-Energy Resolution	335
10.7.2	Beamline for Short Pulses	341
10.7.3	Focused Direct Beam	345
10.8	Beamlines for Spontaneous Radiation	347
	References	348

11 Experiments and End-Stations	349
11.1 X-Ray Microscopy and Holography – Single-Shot Experiments	351
11.1.1 Transmission X-Ray Optics for nm Focusing of FEL Radiation	352
11.1.2 Full-Field Microscope for fs X-Ray Imaging	353
11.1.3 Single Shot X-Ray Holography with Coherent FEL Radiation	356
11.2 Coherent X-Ray Scattering	359
11.2.1 Experimental Techniques	360
11.2.2 Experimental Setup	362
11.2.3 Single-Shot Experiments: Intensity Considerations	365
11.2.4 Single-Shot Experiments: Signal Detection	367
11.3 Resonant Inelastic X-Ray Scattering	367
11.4 Cluster and Atomic/Molecular Beam Instrumentation	371
11.5 Very High-Energy-Resolution Photoemission	377
11.6 High Temporal Resolution Photoemission: Spectroscopy and Microscopy	379
11.7 Summary	381
References	382
12 Electron and Photon Beam Diagnostics	387
12.1 Distribution of Diagnostics	387
12.2 Electron Beam Diagnostics in the Accelerator	389
12.2.1 Energy and Energy Spread	389
12.2.2 Charge	390
12.2.3 Bunch length	392
12.2.3.1 Cavity Bunch-Length Monitor	392
12.2.3.2 Zero-Phasing Technique	394
12.2.3.3 Streak Camera	394
12.2.3.4 Coherent Synchrotron Radiation	394
12.2.4 Beam Position	397
12.2.4.1 Pickup BPMs in the Bunch Compressors and the ARC	398
12.2.4.2 Stripline BPMs in the Undulator Intersections	399
12.2.4.3 Cold BPMs	399
12.2.5 Phase	399
12.2.6 Profile and Transverse Emittance	401

12.2.6.1	Viewscreens and Optical Transition Radiation	402
12.3	Electron and Photon Beam Diagnostics in the HGHG Sections	405
12.3.1	Visible-Light Imaging of Synchrotron Radiation	405
12.3.2	X-Ray Imaging of SR	407
12.3.3	Transverse Overlap of the Electron and Photon Beams	408
12.3.4	Longitudinal Overlap of Electron and Photon Beam	409
12.3.5	Emittance and Phase Matching in Undulators	411
12.4	Photon Beam Diagnostics at the Experiments	414
12.4.1	Flux Monitors: Giant Ionization Chambers (GIC)	414
12.4.2	FEL Pulse-Length Diagnostics	415
12.4.2.1	FEL Pulse Autocorrelation	415
12.4.2.2	FEL Optical Sideband Generation	419
12.4.2.3	Two-Photon Photoemission	419
12.4.2.4	Photon-In Photon-Out Sum-Frequency Generation	422
	References	424
13	Control System	427
13.1	Common Controls Environment	427
13.2	Architecture	427
13.2.1	Vertical Structure	427
13.2.2	Horizontal Topology	429
13.3	Data Model: Devices, Device Classes	430
13.3.1	Goal: Complete Control-System Model	430
13.3.2	Starting Point: Consistent Data Model	431
13.3.3	I/O Requirements: Device Classes	431
13.3.4	Sub-Systems	432
13.4	Control System Applications	432
13.4.1	Generic Applications	432
13.4.2	Beam Steering and Shaping	433
13.5	New Challenges	434
13.5.1	Process Tuning	434
13.5.2	Machine Protection	434
13.5.3	Diagnostics	435

References	436
14 Alignment	439
14.1 Surveying and Alignment	439
14.1.1 The Geodetic Reference Frame	439
14.1.2 Alignment Coordinate System	440
14.1.3 Fiducialization	440
14.2 Beam-Based Alignment	441
References	444
15 Conventional Facilities	445
15.1 Civil Construction: Site and Buildings	445
15.1.1 Site Selection	445
15.1.2 Ground Stability at the BESSY FEL Site	446
15.1.3 Buildings for the FEL Facility	448
15.2 Supply Installations	452
15.2.1 Electric Power Supply	452
15.2.2 Cooling Installations and Ventilation Equipment	454
15.2.2.1 Cooling Installation	454
15.2.2.2 Air Conditioning and Ventilation	454
15.3 Cryogenics	454
15.3.1 Cryogenic Supply Network: Cryostats, Modules, Sections	455
15.3.2 Choice of Refrigerator Size	456
15.3.3 Technology of Large Helium Refrigerators	457
15.3.4 Helium Storage	457
15.3.5 Model Refrigerator	459
15.3.6 Model Refrigerator Flow Diagram	459
References	462
16 Beam Loss, Radiation Protection, and Environmental Safety Considerations	463
16.1 Machine Protection	463
16.2 Dose Monitoring in the Undulator Section	465
16.2.1 Optical Fibers for Cherenkov Radiation	465
16.2.2 Thermo-Luminescence Dosimeters	466

16.3	Electron Losses, Types of Radiation Produced, Radiation Areas	467
16.3.1	Gamma Radiation	467
16.3.2	Neutron Radiation	467
16.3.3	Proton Radiation	467
16.3.4	Myon Radiation	468
16.3.5	The Linac Tunnel	468
16.3.6	Technical Areas	468
16.3.7	Experimental Areas	468
16.3.8	Beam Dump	468
16.4	Activation	470
16.4.1	Activation of Cooling Water	470
16.4.2	Activation of Soil and Ground Water	471
16.4.3	Activation of Air	471
	References	472
17	Cost, Time Schedule, and Operation	473
17.1	Project Cost	474
17.1.1	Cost Evaluation for the Linear Accelerator	474
17.1.2	Cost Evaluation for the FEL Lines	475
17.1.3	Civil Engineering	475
17.1.4	Additional Infrastructure	475
17.2	Time Schedule	476
17.3	Operation	478
	References	479
18	Parameter List	481

1 Executive Summary

1.1 Introduction

With this Technical Design Report (TDR), the Berliner Elektronenspeicherring-Gesellschaft für Synchrotronstrahlung (BESSY) proposes to build a Soft X-ray Free Electron Laser (FEL) user facility in the photon energy range 24 eV to 1000 eV, based on the High-Gain-Harmonic Generation (HGHH) principle. This project will be carried out in collaboration with the Deutsches Elektronen-Synchrotron (DESY), the Max-Born-Institut (MBI) and the Technische Universität Dresden (TU Dresden).

The HGHH approach offers the only possibility of generating photon pulses of variable femtosecond duration, gigawatt peak power, full shot-to-shot pulse reproducibility and full transverse and longitudinal coherence. Figure 1.1 shows, as an example, the pulse characteristics of the low-energy FEL line of the BESSY Soft X-ray FEL in comparison to a SASE solution. It is obvious, that only a HGHH 2nd generation FEL will be able to fulfill the crucial requirements of the user community: Crucial in terms of pulse length, pulse shape, reproducibility, synchronization, and pulse peak power.

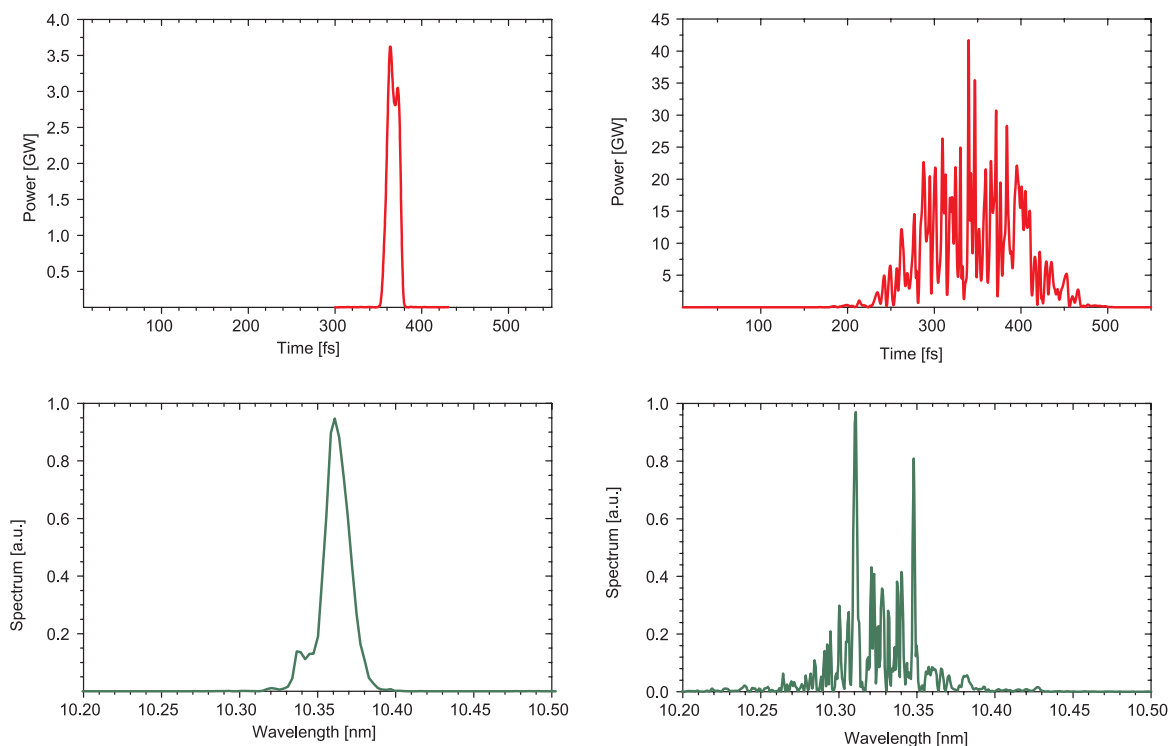


Fig. 1.1: Time-resolved power distribution (top) and spectral power distribution (bottom) calculated for the low-energy HGHH-FEL line at $\lambda = 10.3$ nm (left) in comparison to a SASE-FEL of the same wavelength (right).

BESSY had presented the Scientific Case for its FEL in 2001 to the German Science Council [1]. The “Science Council Working Group on Large-Scale Facilities for Fundamental Scientific Research” stated in July 2002:

The planned scientific program of the Soft X-ray FEL is extremely strong and well defined. It is complementary to the scientific program of the TESLA X-FEL. Both programs are at the forefront of international research and will certainly have a strong impact on basic as well as applied science.

The technical features of the proposed VUV and Soft X-ray FEL at BESSY will be a tremendous improvement of current facilities like SR storage rings and conventional lasers. It will extend existing techniques to ultra-short time resolution for investigations of the electronic structure of matter. ... Concerning the scientific program and the technical characteristics of the laser beam, the TESLA X-FEL as well as the Soft X-ray-FEL will be unique in Europe. Both facilities will open up new domains in coherent radiation, time resolution, wavelengths and intensity and allow for a broad interdisciplinary research that certainly extends current X-ray science.

The BESSY Soft X-ray FEL will utilize a **superconducting CW-linac** to produce **flexible pulse patterns** of mono-energetic soft X-ray pulses of variable femtosecond duration at extremely **high peak brightness** and **full transverse and longitudinal coherence**. The use of an external seed in this cascaded HGHG-FEL provides **full control on** the output photon pulse in terms of **pulse duration** and **pulse shape**. More than that, as a strong seed field is driving the electron beam spatial modulation, the coherent emission is free from statistical properties in contrast to the photon beam characteristic of SASE-FELs. In consequence this leads to significant advantages in **output-power stability**, negligible power fluctuations during the pulse, and a shot-to-shot reproducible **non-spiky spectral power distribution**. The BESSY Soft X-ray FEL will first operate with **3 independently tunable FEL-lines** at a **pulse repetition rate of 1 kHz each** in parallel with a later possibility to increase the number **from 3 to 5 FEL lines** and the pulse repetition rate to 25 kHz.

These properties and expected performance characteristics at this FEL user facility, a 2nd generation, post-SASE-FEL, are summarized in figure 1.2 and table 1.1.

In figure 1.2 the calculated **peak brilliance and peak power** of the BESSY Soft X-ray FEL is compared to 3rd generation synchrotron light sources as BESSY II, the present DESY VUV-FEL under construction, the proposed European X-FEL laboratory and the Linac Coherent Light Source (LCLS) at SLAC. Performance data of modern laser systems are given for completeness. Compared to storage-ring based synchrotron light sources, the gain in peak brilliance of the FEL is more than **9 orders of magnitude**. The BESSY FEL covers BESSY’s very own VUV to XUV spectral range: 24 eV to 1000 eV photon energy with unprecedented, reproducible, short (< 20 fs) pulses in a quality not available anywhere else today.

Table 1.1: Performance parameters for the three FEL lines of the BESSY Soft X-ray FEL with a normal-conducting injector. Data are for a 20 fs seed-pulse duration and 1 kHz pulse-repetition rate.

		LE-FEL	ME-FEL	HE-FEL	Unit
Photon energy range	$h\nu$	24 - 120	100-600	500-1000	eV
Pulse duration	Δt	20	20	20	fs
Peak power	P_p	14 - 3.5	9 - 1.5	1.5	GW
Peak brilliance	B_p	0.6 - 1.6	3 - 6	5 - 13	10^{30*}
Average brilliance	B_a	0.3 - 0.8	1.2 - 2.9	2.7 - 6.8	10^{20*}
Spectral bandwidth (fwhm)	$\Delta\lambda/\lambda \times 100$	0.40 - 0.14	0.16 - 0.04	0.16 - 0.20	
Effective source size (fwhm)	σ	60 - 120	16 - 45	30 - 60	μm

* Photons/s/mm²/mrad²/0.1% bw

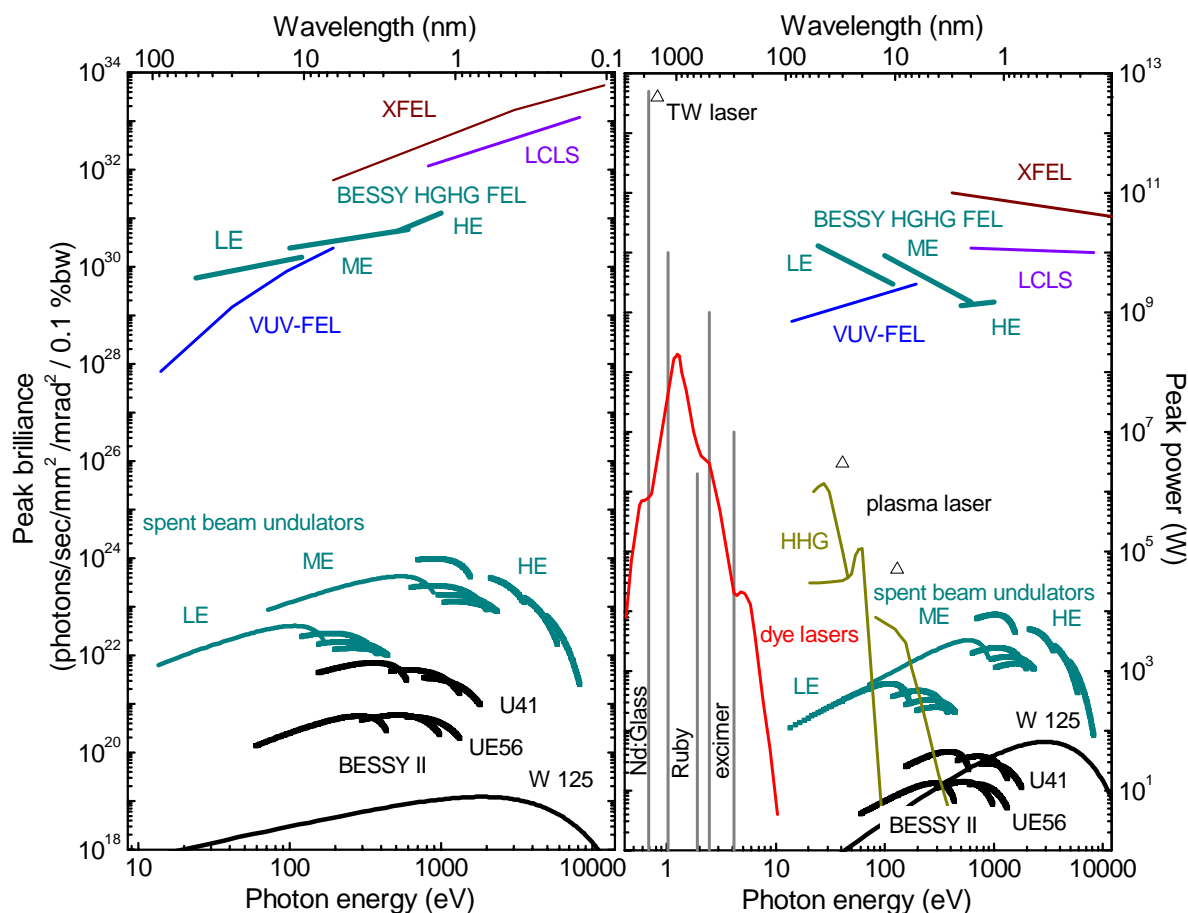


Fig. 1.2: Peak brilliance (left) and peak power (right) of the BESSY Soft X-ray FEL and additional undulators using the spent electron beam. The performance of the BESSY II synchrotron radiation source in single-bunch mode (10 mA, $\Delta\lambda/\lambda = 0.1\%$) the DESY VUV-FEL, the X-FEL, and the Stanford LCLS are shown for comparison.

The BESSY Soft X-ray FEL project will be realized in two phases. The present design (**phase I**) is based on solid technologies available today; a **phase II** will see besides the installation of **additional undulators and beamlines** the replacement of the normal-conducting (n.c.) injector by a **superconducting (s.c.) CW RF photo gun**, increasing the average output by more than one order of magnitude and allowing one to operate at freely selectable pulse patterns fitting the experimental requirements. This drastic improvement of performance, enabling the experimenter to choose the desired pulse sequence at will, can be seen in figure 1.3. Furthermore, the conventional undulators which use the spent electron beam after the final amplifiers of the HGHG-FEL will double the number of experimental stations. They give sub-ps pulses at a peak brilliance exceeding existing storage rings by orders of magnitude. These pulses are intrinsically synchronized with the FEL pulses, thus enabling pump-probe experiments throughout the energy range from eV up to multi keV.

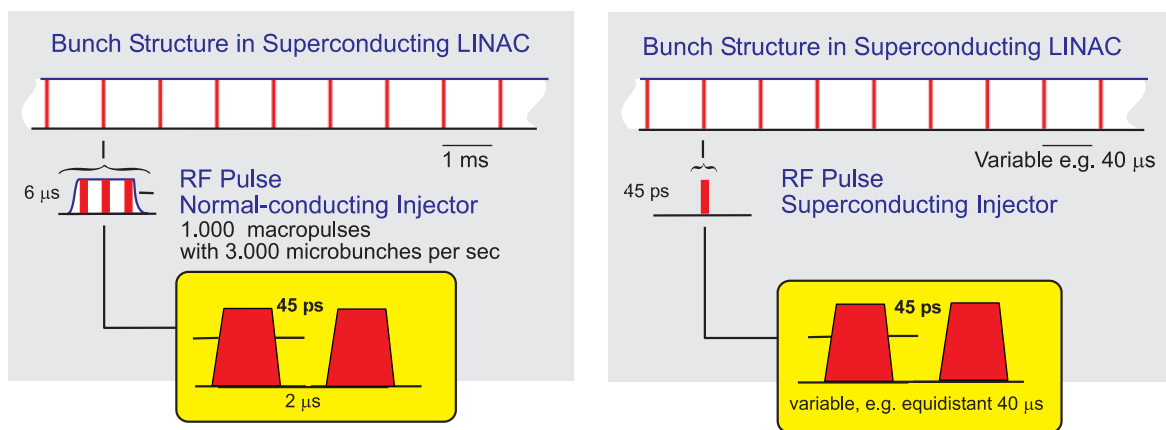


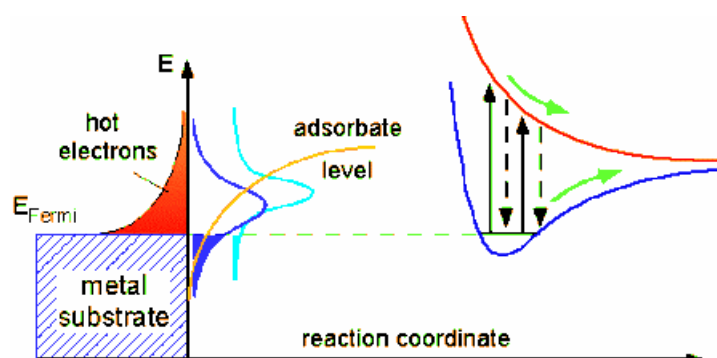
Fig. 1.3: Bunch patterns generated by the n.c. and s.c. photoinjector, respectively. The physical limits of the bunch structure are set only by the maximum design beam power and the maximum beam loading that the RF sources of the linac can handle.

The rapid progress in the field of conventional high-intensity short wavelength lasers is expected to open up an option in the future where suitable **HHG seed lasers** can be used to decrease the number of stages of the proposed cascaded HGHG scheme and thus improve the quality of FEL photon beam. Reducing the already **ultra-short photon pulses** even further to the range of only a few femtoseconds (fs), or possibly to the atto-second (as) range seems feasible. The ultimate physical limits of the scheme given by the Fourier transform limit and the undulator bandwidth show that photon pulses generated from the BESSY FEL at a wavelength below 10 nm may be significantly shorter than 1 fs.

1.2 Scientific Goals

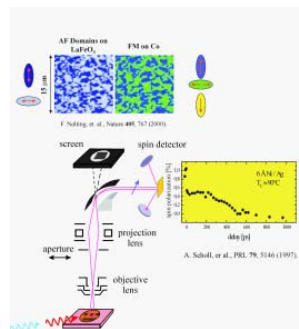
The scientific case for the BESSY Soft X-ray FEL was presented in the “Visions of Science: The BESSY SASE-FEL in Berlin-Adlershof” [1] in 2001 as a final document of a series of workshops. The “Visions of Science” established a solid scientific program that pushed the development of the new source. Below the comprehensive summary is recalled to identify the various fields of scientific applications therein.

The BESSY Soft X-ray FEL will open the unique possibility to explore and resolve **ultra-fast dynamical processes**. The control of the pulse duration down to a few femtoseconds is inherent to the HGHG seeding scheme. This opens up the possibilities for unprecedented studies on structural and electron dynamics of systems including the femtochemistry field. Due to the fact that the time structure is determined by the seed pulse it will be possible for the first time to synchronize the FEL pulse with pulses from external lasers to perform **pump-probe experiments** involving soft X-rays.



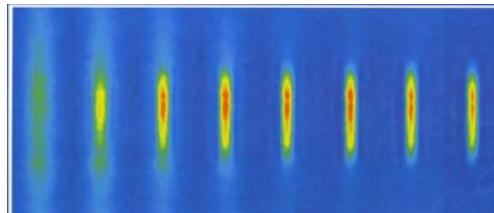
- **Femtochemistry - Understanding the dynamics and formation of a chemical bond**

On the fs time scale the nuclei in a molecule or solid are "standing still". Typical vibration periods are between 20 and several 100 fs. Therefore spectroscopy with fs time resolution allows one to observe the effects of the motion of the nuclei on the electronic structure in a molecule, a solid, or adsorbate on a surface. In pump-probe experiments the development of the electronic states in a dissociating or desorbing molecule can be followed, yielding insights into the transition states and the nature of barriers determining the pathways for chemical reactions. This extends the pioneering work of A.H. Zewail who was awarded the Nobel Prize in chemistry in 1999 for his work in "femtochemistry" using lasers, to higher photon energies. Thus the dynamics of the complete electronic structure can be observed using photoemission as a tool.



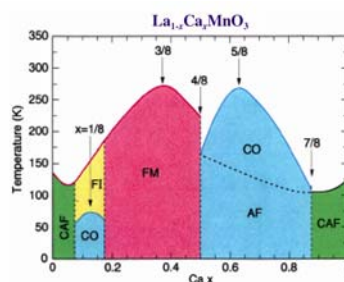
- **Magnetization dynamics of nanostructures on the fs time scale**

Magnetic data storage is continuously increasing in density and speed. In order to explore and expand the limits of this important technology the BESSY FEL will enable studies of the magnetization dynamics of small magnetic nanostructures and clusters on the fs time scale in conjunction with nm spatial resolution. Dichroic effects in the soft X-ray regime are an ideal probe to monitor the magnetic moments with elemental specificity in space and time. P. Carra, G. van der Laan, and G. Schütz were awarded the Agilent Technologies Europhysics Prize 2000 for the development of this important experimental technique exploiting the circular polarization of synchrotron radiation.



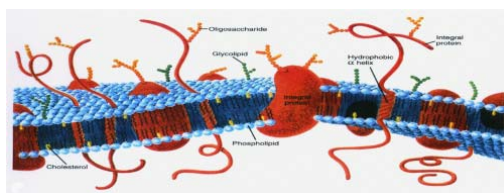
- **Atoms and molecules - New fundamental limits**

Novel exotic states of matter can be prepared by Bose condensation of atoms in electrodynamic and optical traps (Nobel Prizes in Physics 1997 awarded to S. Chu, C. Cohen-Tannoudji, and W. D. Phillips and 2001 to E. A. Cornell, W. Ketterle, and C. E. Wieman). The BESSY FEL offers unique possibilities for spectroscopy and selective preparation or excitation of dilute assemblies and condensates of atoms in various traps. Thus, elementary steps for the experimental realization of quantum computers may be explored. Furthermore, linear and non-linear interaction of radiation with atoms and molecules serves to test very basic theoretical models with the highest possible precision.



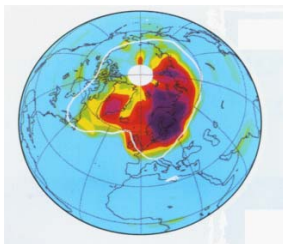
- **The nature of complex solids**

For the discovery of the superconducting oxides K. Bednorz and A. Müller received the Nobel Prize in physics in 1987. Even now the mechanism of superconductivity in these highly correlated materials is not yet understood and accordingly studies on them are at the forefront of research in solid state physics. In general, these oxidic materials exhibit a wealth of phenomena. Apart from the high temperature superconductivity of the cuprates this includes also the colossal magnetoresistance phenomenon of the manganates. These materials exhibit complex phase diagrams with interesting stationary and dynamic phases. Resonant inelastic soft X-ray scattering, which can be carried out also in the presence of magnetic fields, as well as electron spectroscopy with ultimate energy and momentum resolution, hold the promise to furnish decisive data to resolve some of these mysteries of modern physics. With the FEL the resolution capabilities for electron spectroscopy and soft X-ray scattering will be enhanced by orders of magnitude in the spectral and spatial domain.



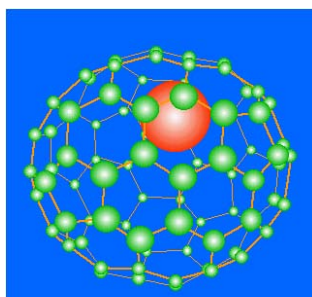
- **Dynamics in biological systems**

The BESSY Soft X-ray FEL opens the unique possibility to combine microscopy with a resolution in the nanometer range, spectroscopy with high-energy resolution and accordingly high chemical selectivity, and a superb time resolution in the fs range in investigations of biological systems in their natural wet environment. This will open a new route to an understanding of functional systems such as ion channels, molecular motors, and pumps embedded in cellular membranes. Furthermore, the dynamics of various steps in biological functional cycles in photosynthesis or in enzymatic reactions may be followed and resolved in real time. Radiation damage is a concern. However, this may be alleviated by the fact that sufficient signal may be recorded within the time frame of a single FEL pulse, faster than the fragmentation processes that are occurring.



•Chemistry of radicals

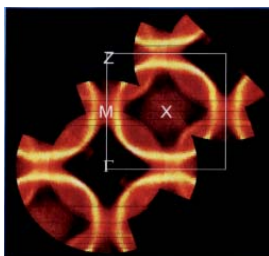
Understanding the factors and key processes influencing the global change in climate is one of the most important scientific problems of present times. P.J. Crutzen, M.J. Molina, and S.F. Rowland were awarded the Nobel Prize in chemistry in 1995 for their discovery of the molecular reaction cycles leading to the build-up and destruction of the ozone layer in the upper atmosphere. The chemistry of radicals as well as of photophysical reactions on the surfaces of suspended nanoparticles play an important role in understanding the processes and interactions in the upper atmosphere. The FEL, possibly in conjunction with an ion storage device, will furnish a new spectroscopic tool to study these processes, reaction pathways, cross sections and the formation of elusive chemical species in an unprecedented fashion. Furthermore, the FEL offers fascinating prospects for the study and the simulation of the processes and reactions occurring in interstellar clouds in the presence of intense VUV and X-ray radiation.



•Clusters as new materials

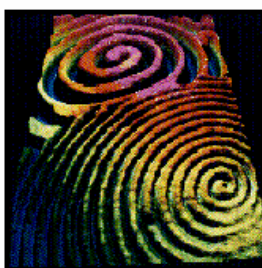
Clusters of almost any element of the periodic table may be assembled with an exactly defined number of atoms thus preparing the way to the development of new materials tailored with unprecedented precision. The fullerenes are presently the best known example of such cluster materials. In 1996 R.F. Curl, H.W. Kroto, and R.E. Smalley received the Nobel prize in chemistry for their discovery. Upon condensation, the fullerenes form a semiconducting solid, the third modification of carbon apart from graphite and diamond. Because of their low density, mass-resolved clusters can in general only be produced and studied in molecular beams using lasers. Consequently, with a few exceptions, for individual clusters neither the atomic geometry nor the electronic structure has been determined. The FEL with a photon energy in the VUV and soft X-ray range and pulse energy

comparable to present day lasers will be a unique tool for the characterization of these exciting new materials.



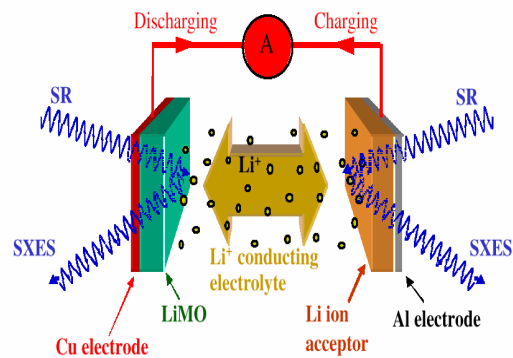
- **Ultrahigh resolution spectroscopy**

The dramatic increase in brightness of the FEL opens up the possibility to perform investigations of the electronic structure of atoms and molecules, solids and surfaces with a resolution comparable to the thermal energy scale (K). This allows one to investigate energy gaps in superconductors, phase transitions, Kondo resonances, and other many-body phenomena with unprecedented spectroscopic precision.



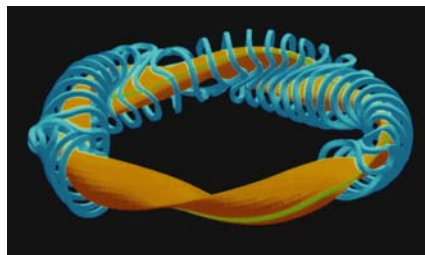
- **New perspectives on catalysis**

Spectroscopy of catalysts under 'real conditions', i.e. under a gaseous atmosphere or submerged in a liquid is one of the visions to advance research in catalysis from the study of model systems towards real catalysts. Photons are able to penetrate this environment and to carry spectroscopic information. Using sum frequency generation (IR + VUV), for example, a specific vibration mode can be detected originating at a specific atom selectable via the chemical shift of its core electrons. Resonant inelastic X-ray scattering is another probe with a high potential for impact on industrial technology. It allows one to distinguish the electronic structure at atomic centers according to their chemical environment, promising new insights into local electronic interactions at the reaction centers in this complex environment.



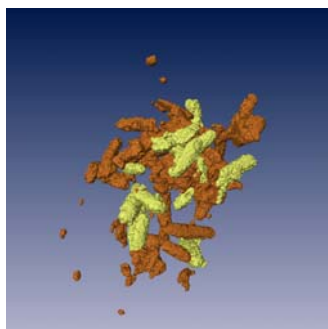
- **Materials and processes observed under technologically relevant conditions**

Electrochemical reactions, thin film growth, corrosion, and friction are, apart from catalysis, technologically and economically highly relevant processes, where surfaces are in contact with a gas or a liquid. The FEL photons have sufficient intensity to penetrate this liquid or gaseous environment. This opens the field for spectroscopic investigations of these surfaces under process conditions using the methods of resonant inelastic soft X-ray scattering for the investigation of the electronic structure with not only elemental but even chemical specificity.



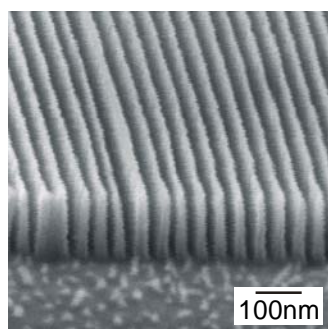
- **Characterization of fusion plasmas**

The diagnostics of elementary processes in fusion reactors relies on the analysis of the characteristic radiation emerging from the reactor. Important parameters for these diagnostics are absolute cross sections and lifetimes of highly excited states of multiply charged ions, which currently are only partially known. Using the FEL a reliable database may be established in studies of dilute plasmas or on ion beams to provide a better understanding and diagnostics for the development of this future energy source.



- **Environmental chemistry and analysis**

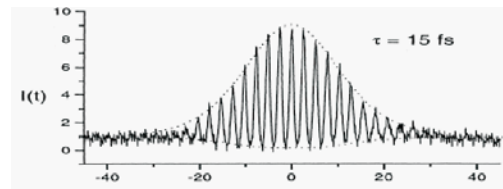
Chemical and biological processes occurring at the complex interfaces between organic and inorganic matter, aqueous solutions, and gases control the composition of the environment and determine the migration and toxicity of pollutants in the biosphere. Understanding these processes and their dynamics at the molecular size scale in their natural environment is a key factor for the development of better models for the spreading of pollutants and to develop better strategies for environmental remediation. soft X-rays from the FEL uniquely enable a characterization of these systems and processes in their natural state with nanometer spatial and sub-picosecond time resolution.



- **Nanofabrication of materials using soft X-rays**

Materials with a structural size on the nm size scale offer unprecedented possibilities for atomic scale engineering of materials which is synonymous with tailoring the electronic, optical, magnetic, chemical or even mechanical properties to specific needs. Already today, thin film systems, where one dimension is reduced to the nanometer-size scale, form the basis of the high-tech electronics and information industries with revenues in the multibillion dollar range. These systems have an impact on everybody's daily life. Laterally or even 3-D structured materials with controlled features in the nm range are still largely a challenge for the future. At the BESSY FEL, feature sizes may be realized much smaller than envisioned for the next step in industrial applications of EUV lithography (at 13.5 nm), corresponding to a wavelength limit as short as 1.2 nm. The FEL, where

the high power is concentrated in an extremely narrow spectral range, is an ideal source for nanolithography.



- **Time resolved spectroscopy - reaching the attosecond range**

Intrinsically a SASE-FEL has pulses of about 200 fs in length. Advanced seeding concepts which are the basis of the HGHG design of the BESSY FEL presented here, will be implemented in close collaboration with scientists from the Max-Born-Institute. This design holds the promise to reach pulse lengths shorter than 20 fs. Ultimately for soft X-ray pulses the time resolution could be pushed into the attosecond region, far beyond the limits of lasers at photon energies in the visible optical spectrum.



- **New frontiers in photon-related spectroscopies and coherence**

The FEL offers a fully transverse coherent beam with about 10^9 degenerate photons within the coherence volume. Exploiting the coherence opens the pathway for new 'imaging' techniques, where the individual rather than the statistical properties of the sample can be probed in time resolved single shot experiments in life, environmental, materials and chemical sciences. Furthermore, photons are able to penetrate through solids, liquids, and gases. Thus resonant (inelastic) scattering offers a unique, element and chemical environment selective probe of the electronic structure.

1.3 Selection of Major System Parameters

The main system parameters of the proposed FEL, such as the electron energy, beam current, emittance, and the undulator parameters, are the result of extensive multi-dimensional simulations, using various codes to generate a most realistic picture on the performance (chapter 3). The theoretically well understood FEL physics, however, provides a good insight already in a simple one-dimensional (1-D) model. This model is used for a first system parameter definition on the basis of the requirements of the future users for the BESSY FEL:

Three overlapping, independently tunable FEL lines fully cover the VUV to soft X-ray spectral range (24 eV to 1 keV). A highly flexible linac with the lowest necessary electron energy assures a compact radiation source delivering high-quality photon beams with variable polarization, freely selectable pulse widths ($\Delta t < 20$ fs), and peak power in the GW range. The potential is there to reach even the attosecond range in the future.

For example, when selecting the tuning range for the high-energy FEL (500 to 1000 eV) and assuming a reasonable set of parameters for the electron beam (table 1.2), all basic parameters of the FEL such as output power, e-folding gain length and the required electron-beam energy can be estimated from the 1-D model.

A simple 1-D-parameter scan immediately shows that the final stage of a seeded HGHG scheme requires a beam energy of 2.0 to 2.5 GeV to keep the gain length within limits. Covering the photon energy range 500 to 1000 eV by gap drive - assuming the minimum gap does not fall below 10 mm - indicates that an undulator period length $\lambda_u < 35$ mm is required to achieve a peak output power in the GW range. On the other hand, the undulator period length cannot be much larger than 35 mm if it is to cover the requested photon energy range. These 1-D estimates are confirmed in the simulation. Thus, the electron beam energies and undulator layout necessary for the 3 FEL lines that can be seen in table 1.2 were selected as a compromise between linac length and FEL performance.

Table 1.2: Electron Beam and Undulator parameters for the three FEL lines of the BESSY Soft X-ray FEL for 1.5π mm mrad normalized slice emittance.

		LE-FEL	ME-FEL	HE-FEL	Unit
Electron beam energy	E	1.02	2.3	1.6 - 2.3	GeV
Peak electron current	I_p	1750	1750	1750	A
Undulator period length ⁺	λ_u	50	50	28.5	mm
Undulator length [§]	L_u	≤ 8.1	≤ 20	≤ 18	m

⁺ only final amplifier, [§] L_u depends on wavelength λ

For the user of the FEL facility, a CW injector complementing the CW linac, thus allowing for any arbitrary pulse pattern, will be the ultimate solution. Because of the significant progress in the R&D of superconducting (s.c.) RF photoinjectors with low-emittance high-brightness electron beams, such devices can be expected to replace the state-of-the-art normal conducting injector technology in a phase II of the project. Thus, the repetition frequency to generate bunch trains from the gun is limited for the time being by the duty cycle of the normal conducting gun cavity to a value of 1 kHz.

1.4 The Layout of the BESSY Soft X-Ray FEL User Facility

The BESSY Soft X-ray FEL is designed to operate as a seeded FEL, e.g. an external laser field will determine the FEL output rather than statistical shot noise which is the case for a SASE-FEL. Thus, the FEL output is characterized by a stable clear spectrum, transversely and longitudinally fully coherent with a smooth temporal shape determined by the external seed. To start the seeded FEL process, a tunable titanium sapphire (Ti:Sa) laser will generate pulses of ~500 MW peak power of ~20 fs duration at wavelengths tunable from 460 to 230 nm. This seed is frequency multiplied in a cascade of a HGHG-FEL that operates in the 3rd and/or 5th harmonic of the seed frequency. The 2-stage HGHG-LE-FEL converts the 258 nm seed to 51 and to 10 nm radiation which finally drives the electron beam in the final amplifier undulator to saturation, i.e. 3 GW peak power. The time duration of the FEL photon pulse is essentially determined by the initial seed pulse modified by the phase slip within the first modulator. Similarly the ME-FEL uses a 3 stage cascade converting the 230 nm to 46, 9 and 3 nm. For the BESSY HE-FEL, a 4-stage HGHG cascade is planned. Together with the LE-FEL and the ME-FEL it will be possible to cover without gaps the photon energy ranges 24 to 120, 100 to 600, and 500 to 1000 eV. Table 1.3 gives the main parameters for the seed laser, the tuning range and the resulting photon output.

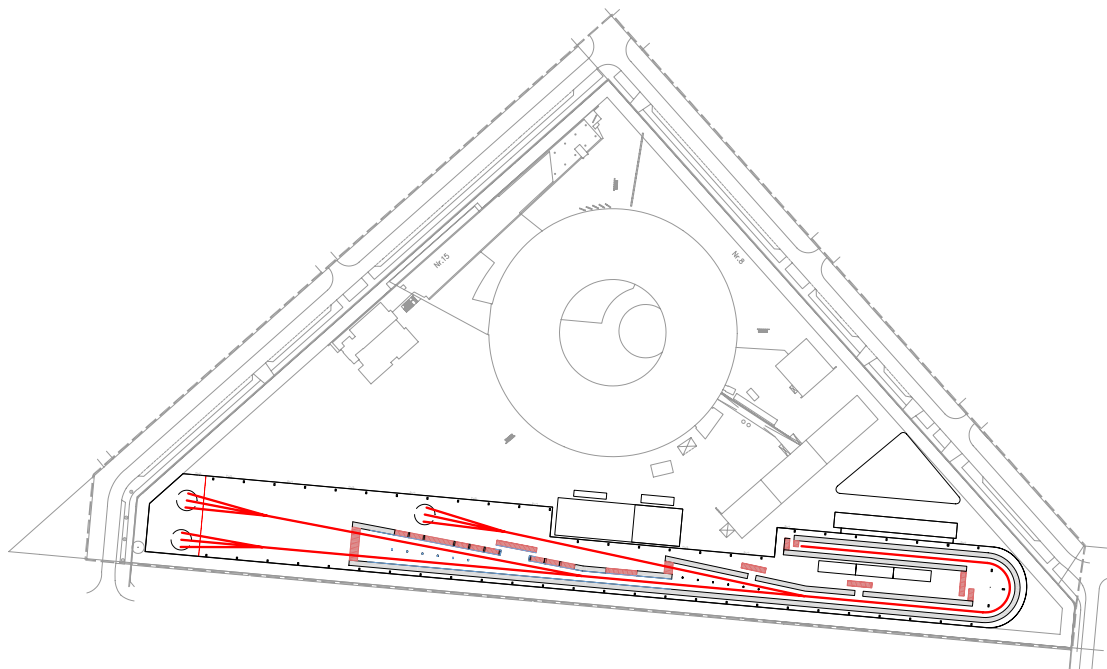
Once the laser developments have made sufficient progress to obtain pulses derived from a High-Harmonic-Generation (HHG) scheme powerful enough (500 MW) for seeding the HE-FEL, even shorter FEL pulses can be achieved.

The concept of the facility, figure 1.4 depicts an overall view, allows for future expansion to 5 FELs. This is achieved by locating the FEL facility close to the southern border of the site, leaving space for further expansion in the direction of the existing BESSY II light-source building.

The growing field of free electron lasers bears surprises for new and clever ideas. This situation was taken into account by a most flexible use of the building, e.g. by making the radiation protection tunnel in major parts from moveable blocks, rather than to cast it completely in solid concrete. The central building is a most simple industrial hall with all relevant systems built in a house-in-house approach to be able to respond to new developments.

Table 1.3: Wavelength and power output of the various stages of the FEL lines.

FEL		LE-FEL	ME-FEL	HE-FEL	Unit
	Photon energy	24 - 120	100 - 600	500 - 1000	eV
	Wavelength range	51.66 - 10.33	12.4 - 2.07	2.48 - 1.24	nm
1. Stage	Seed λ	460 - 258	380 - 230	385 - 230	nm
	Seed power	500	500	500	MW
	Power	6000	1600	4500	MW
2. Stage	λ output	155 - 51.8	110 - 46	66.96 - 55.9	nm
	Power	7500	950	1800	MW
3. Stage	λ output	51.8 - 10.33	37.0 - 9.2	22.32 - 11.16	nm
	Power		240	1900	MW
4. Stage	λ output		12.4 - 2.0	7.44 - 3.73	nm
	Power			130	MW
Final amplifier	λ output			2.48 - 1.24	nm
	Power	14 - 3.5	9 - 1.5	1.5	GW
	λ output	51.66 - 10.33	12.4 - 2.07	2.48 - 1.24	nm

**Fig. 1.4: Overview on the FEL facility with the 3 cascaded FEL lines. Beamlines and end-stations are indicated. The shaded area is a footprint of the new building.**

1.5 Main Performance Parameters

An overview on the main parameters of the BESSY Soft X-ray FEL is given in table 1.4. The performance data predicted are the outcome of elaborate studies using 3-D time-resolved simulations based on a start-to-end approach.

Table 1.4: Main performance parameters of the BESSY Soft X-ray FEL.

Parameter	Value	Unit
Number of FEL lines	3	
Number of beamlines	9 (15) [#]	
Electron beam energy	2.3	GeV
Electron beam emittance	1.5	π mm mrad
Electron bunch length [†]	290	μ m
Electron peak current	1.75	kA
Total beam power	18* (150)	kW
Wavelength range	51 - 1.24	nm
Photon beam peak power	1.5 - 14	GW
Photon beam average power	0.260 - 0.016 * (2.0 - 0.12)	W
Photon beam size (fwhm)	14 - 160	μ m
Photon beam divergence (fwhm)	37 - 140	μ rad
Photon beam spec. bandwidth	\sim 0.001	
Photon beam pulse duration	\leq 20	fs
Min. pulse separation	2	μ s
No. of pulses in a train	3 * (1) [§]	
Repetition rate	1000* (>25000)	Hz
Number of photons per pulse	$2 \cdot 10^{11}$ - $7 \cdot 10^{13}$	
Average flux of photons	$2 \cdot 10^{14}$ - $7 \cdot 10^{16}$	
Peak brilliance	$6.4 \cdot 10^{29}$ - $1.3 \cdot 10^{31}$	ph/(s·mrad ² ·mm ² ·0.1% bw)

† Value at the entrance to the undulator section

§ Freely selectable taking into account the beam power

* n.c. injector, values in brackets for s.c. injector # Phase II

The numbers quoted are based on hardware specifications that are achievable and have been demonstrated with present-day technology for phase I, e.g. the injector, where a standard room temperature PITZ-type gun cavity is assumed. Replacement of this injec-

tor with a superconducting gun cavity (phase II) will permit an increase of the average photon flux by a factor of about 10. The option to enlarge the number of FEL lines to 5 with potentially different photon energy ranges is not included in the above data.

1.6 The BESSY FEL in the International Context

The work in the field of free electron lasers during the last decades has resulted in a deep theoretical understanding of the underlying physical processes [2 - 5] and in a growing interest to use the Self-Amplified Spontaneous Emission (SASE) principle and more sophisticated FEL schemes for most powerful new radiation sources in the short wavelength regime of VUV and hard X-rays. Figure 1.5 illustrates the development over the years including the presently proposed projects.

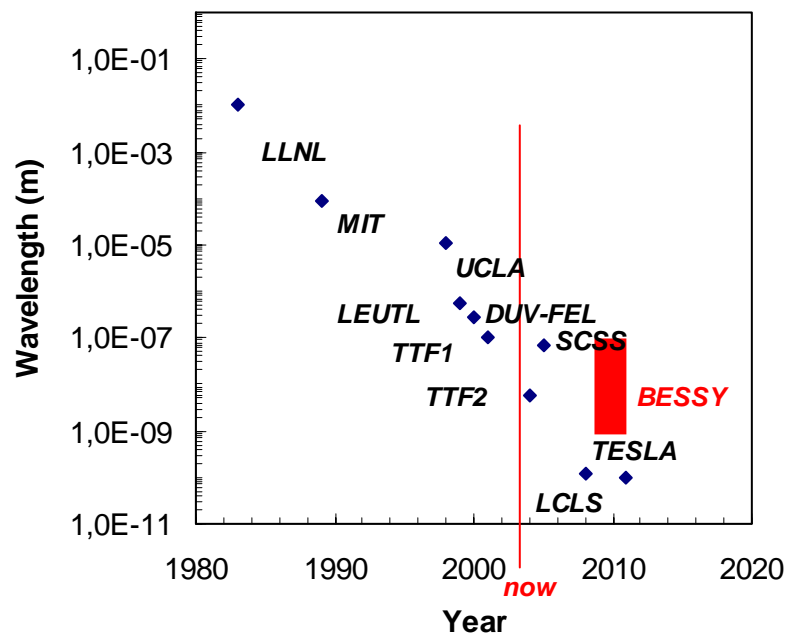


Fig. 1.5: Photon wavelength of existing and proposed projects.

The success of the proof-of-principle experiments at UCLA, APS, DESY, and BNL initiated a number of proposals for these new light sources, with the DESY TTF II and SLAC LCLS already in the realization phase and the DESY X-FEL as a European project well on the way.

In the VUV-XUV spectral range the 4GLS and the SPARC projects have already received funds to start R&D programs, whereas ELETTRA and MAX-Lab applications for funding are pending. In the USA, MIT Bates and LBNL issued requests to fund conceptual design work.

The driving force for almost all of these projects is the wish for a gain in peak brilliance of more than 10 orders in magnitude compared to present 3rd generation light sources, and for the possibility to generate short photon pulses - especially the variable fs-pulses in the HGHG approach - opening hitherto inaccessible fields in science.

Table 1.5: List of short wavelength FELs operational, under construction, or proposed.

Project	Type	Location	Country	Beam energy (GeV)	λ photon (nm)	Status
LEUTL	SASE	APS	USA	0.22	660 - 130	since 2001
TTF I	SASE	DESY	D	0.3	125 - 85	since 2002
DUV-FEL	HGGH	BNL/NSLS	USA	0.145	400 - 100	since 2002
SCSS	SASE	SPring8	J	0.230	40	in 2005
TTF II	SASE*	DESY	D	1.0	6	in 2004
X-FEL	SASE	DESY	D	25	0.1	in 2011
LCLS	SASE	SLAC	USA	15	0.15	in 2008
Soft X-ray FEL	HGGH	BESSY	D	2.3	64 - 1.2	proposal
SPARC	SASE	ENEA,INFN	I	0.15	VUV	in 2005
SPARX	SASE	ENEA,INFN	I	2.5	1.5	proposal
VXFEL	SASE*	ELETTRA	I	1.0		proposal
FERMI	SASE	ELETTRA	I	3.0	1.2	proposal
4GLS	ERL	Daresbury	GB	0.6	VUV-XUV	proposal
	HGGH	MIT Bates	USA	3.0	VUV-XUV	proposal
LUX	ERL*	LBL	USA	3.0		proposal
	ERL	Cornell	USA	5 - 7		proposal
ARC-EN CIEL	ERL*		F	0.7		proposal
MAX IV*		Max Lab	S	3.0		proposal

* incl. seeding schemes

For the design work presented in this report extensive use of the start-to-end approach was made, e.g. simulating the electron beam right from the cathode following the phase space development through the linac up to the undulator exit. Additionally the photon pulses are traced through the beamlines all the way to the experiments. This gives confidence in the predicted design and calculated performance data (chapters 3, 5, 7, 9, 10).

Even if new ideas allow one to improve the FEL performance further, the present BESSY FEL design is flexible and is based on well established principles. The results from tolerance studies (chapter 3) show that the proposed FEL user facility is feasible as it is carefully designed.

The simulations and the associated work on the technical design was done in parallel following two routes: Searching for the best light source for the users and strictly improving the performance compared to a SASE-type FEL. The understanding that an externally seeded FEL is the key for the generation of reproducible pulses with variable (short) duration, grew steadily. This concept offers substantial advantages over the SASE-FEL concerning spectral purity, pulse power stability, temporal pulse stability and reproducibility. The price for the smooth, non-statistical performance of a seeded FEL compared to the SASE-FEL is a slightly reduced peak power and technically a more complex machine. In this report the status of the major subsystems is summarized. The following chapters outline how BESSY is preparing for the science of the future.

1.7 The Phase I Normal-Conducting Injector

The photoinjector for the BESSY Soft X-ray FEL is *the* essential system to produce trains of high-quality high-intensity electron bunches of 45 ps bunch length at a peak current of 65 A with a projected normalized emittance as small as $\varepsilon_n \cong 2 \cdot 10^{-6} \pi$ mm mrad. After acceleration, electrons are fed to the three HGHG-FEL lines in parallel at a repetition frequency of 1 kHz or more. The emittance, or to be precise, the slice emittance, should be as small as possible, since at the shortest wavelength the beam emittance has to fulfill the relation

$$\varepsilon_n \leq \frac{\lambda}{4\pi} \gamma \quad (1.1)$$

where γ is the relativistic factor and λ the photon wavelength.

Furthermore, the emittance of the electron beam has a strong influence on the general layout of the FEL with respect to the total length of undulator sections and electron energy. Knowing the importance of a high beam-quality injector, BESSY joined the **PITZ collaboration** [6]. Here BESSY is involved in the development and optimization of RF photo guns, focusing on the diagnostics of the low-energy high-brightness electron beams.

The present PITZ photoinjector (figure 1.6) is a safe basis for the design of the injector for the phase I BESSY Soft X-ray FEL. Based on this design and employing the same emittance compensation scheme [7], an injector was modeled to deliver 1000 bunch trains per second with 3 bunches each.



Fig. 1.6: The PITZ collaboration photoinjector at DESY Zeuthen.

Present-day photoinjectors operate at a duty cycle of a few percent as the ultimate achievable emittance is strongly determined by the field at the cathode. The higher the field, the smaller the emittance [8]. For the BESSY injector, a **moderate 40 MV/m** field in the gun cavity is sufficient to assure stable and reliable operation. However, the RF input power to the room-temperature gun sets a limit due to the thermal capabilities of the cavity cooling. At the PITZ photo gun a field of 40 MV/m has been achieved for an 800 μs long pulse at 10 Hz repetition frequency [9]. Using an **improved cooling** scheme, finite element simulations show that a 25 μs long pulse can be achieved at a **repetition frequency of 1 kHz**, the design goal for the BESSY FEL injector. Based on these simulations, the technical design of the new gun-cavity is currently under way. The **high duty-cycle gun-cavity** will be manufactured by BESSY and tested within the PITZ collaboration.

Systematic studies of the photo gun were performed with standard codes as PAR-MELA [10] and ASTRA [11] with an optimized pulse form of the photocathode laser to derive parameters for the electron pulse of approximately 45 ps, 65 A peak current, and 2.5 nC bunch charge. Short rise and decay times with a “flat-top” intensity profile turned out to be essential. Tracking the beam through the gun and the first accelerator modules (figure 1.7) shows that a **normalized slice emittance of $1.5 \pi \text{ mm mrad}$** can be achieved as required for the operation of the BESSY FEL.

Thus, a PITZ-type photoinjector modified to a 1 kHz repetition rate is a safe technical starting point for the BESSY FEL injector.

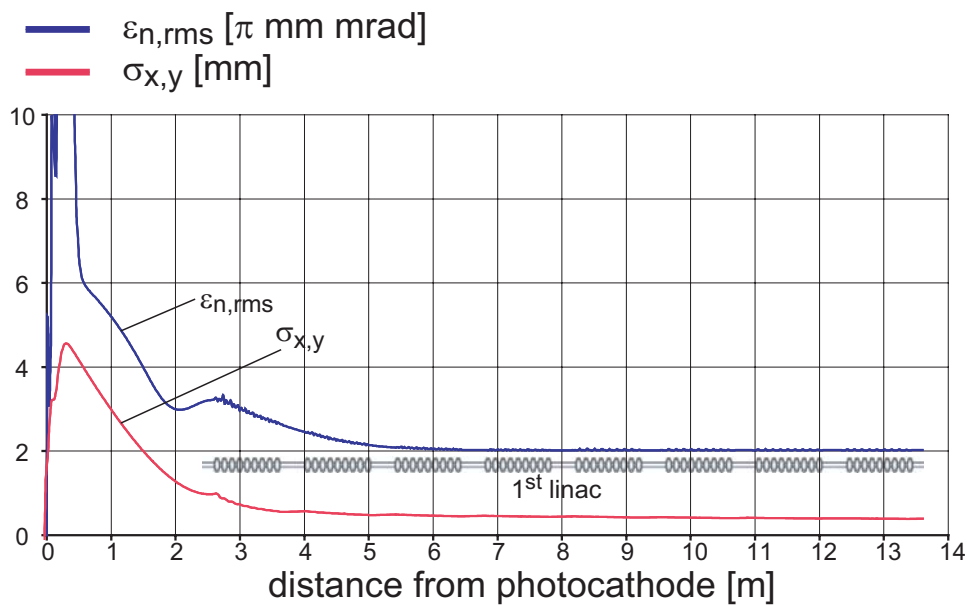


Fig. 1.7: Evolution of beam emittance (blue line) and beam size (red line) from the photo-injector to the end of the first superconducting accelerator module. A 45 ps long electron pulse of 65 A peak current (2.5 nC) is tracked. Applying the standard emittance conservation scheme [12], the normalized slice emittance is calculated to 1.5 π mm mrad.

1.8 The Phase II Superconducting Injector

The normal-conducting photoinjector allows for significant flexibility within the 1 kHz bunch train repetition frequency. The limitation is given by the maximum possible duty cycle of the gun cavity. However, only with a superconducting CW gun cavity it is possible to fully exploit the potential of a CW-linac and to generate freely selectable bunch patterns according to the needs of the individual user. In this case only the maximum permissible beam power and the linac RF power sources will set a limit to the inter-bunch spacing of 2 μ s.

The presently discussed FEL and ERL light sources gave a push to the development of CW electron sources [13, 14]. Nevertheless, there is the problem that the successful emittance compensation scheme [7, 12, 15] cannot be applied to an s.c. gun cavity directly, as in this case the high magnetic field of the solenoid would immediately destroy the superconductivity of the cavity. Various ideas were considered to overcome the problem [16]. However, until recently [17] no convincing **emittance compensation scheme for an s.c.**

gun cavity had been published. An updated version of a possible s.c. injector including emittance compensation is depicted in figure 1.8, showing that emittance of a 1 nC beam is conserved with the new design, very comparable to n.c. photo guns.

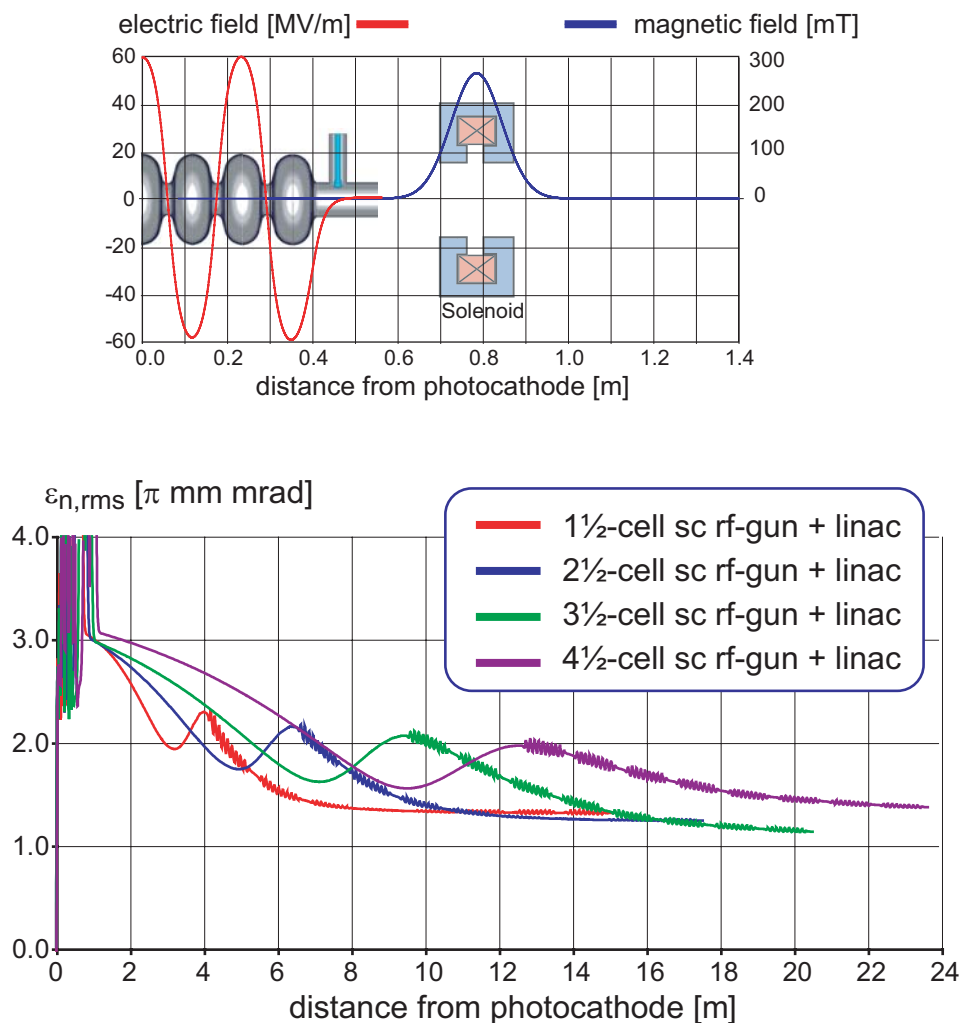


Fig. 1.8: Upper graph: Geometry of the superconducting gun as used in the simulation. Lower graph: Development of transversal emittance in the gun and in the first acceleration module for different gun-cavity geometries: 1½ to 4½ cells.

The emittance compensation solenoids are located far from the s.c. cavity. By proper selection of system parameters the scheme can be made compatible with a zero magnetic field in the cavity without emittance dilution. These results, which have been obtained with simulations at BESSY, are an essential step for the realization of a CW injector. Furthermore, the **Forschungszentrum Rossendorf (FZR)** together with **BESSY**, **DESY**, and

MBI formed a **collaboration** to build a full-scale **dedicated s.c. gun** (figure 1.9). An engineering model has been worked out, ancillary components have been specified and the production has started.

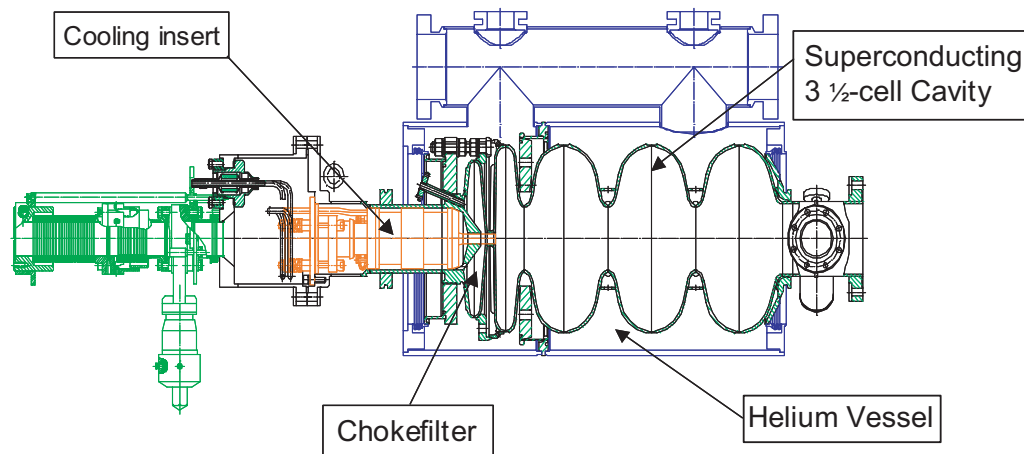


Fig. 1.9: Assembly drawing for the 3½ cell superconducting gun ready to be built by the FZR, DESY, MBI, BESSY collaboration.

1.9 The Linac Modules

Superconducting RF technology as developed for the TESLA linear collider [18] will be the basis for the CW linear accelerator of the BESSY FEL. This choice is driven by the mature technology that has already demonstrated reliable operation offering the only possibility for CW operation of the linac; any conventional, pulsed normal conducting linac cannot in principle offer the required flexibility for the experiments.

The **TESLA modules** consist of eight niobium 9-cell cavities, each module being 12.2 m long. In careful investigations on the long-term economic operating conditions in CW-mode a field of about 15 – 20 MV/m was found to be the optimum. This is why 18 modules operating at **fields of ~ 16 MV/m CW** will be used to accelerate the electron beam to an energy of 2.3 GeV.

Only minor modifications are required to adapt the (pulsed) TESLA technology for CW operation. The details and consequences of the increased He-flux from the cavities and in the two-phase He supply line are discussed in Chapter 6.3. No technical risk is anticipated with the modifications for CW operation. Figure 1.10 depicts a TESLA module as used at DESY TTF.



Fig. 1.10: A TESLA cryo-module as will be the basis of the BESSY FEL linac.

To confirm the basis for a reliable CW operation, BESSY has started an intensive qualification program. Tests of couplers and tuners and important studies of cryogenic parameters as optimum bath temperatures required for a safe and economic CW operation are being performed. A **Horizontal Bi-Cavity Test** facility (named **HoBiCaT**) has been set up for this purpose, figure. 1.11.

Furthermore, the HoBiCaT will allow for extensive tests of new concepts of damping microphonics - not an issue for the TESLA operation parameters – and will as well give an excellent test bed for RF source R&D, allowing for a cost-optimized specification when a total of 144 1.3 GHz-power sources have to be procured.

The test stand is supplied with 4.4 K liquid helium from a **TCF 50 cryoplant**, available since 2003 for supplying various superconducting devices in the BESSY II storage ring. Two niobium cavities were delivered at the end of 2003 so that the training and test program of HoBiCaT can start in 2004.



Fig. 1.11: The BESSY horizontal cavity test bench HoBiCaT.

1.10 Electron Acceleration and Bunch Compression

The electron bunches from the injector are about 9 mm (fwhm) in length at a peak current of 65 A. For high gain of the FEL process in the undulators they have to be compressed in length by a factor of about 30 resulting in a peak current of $I_p = 1.75$ kA without diluting the beam brightness. The space-charge forces, non-linearities in the RF acceleration, and coherent synchrotron radiation generated in the compressor magnets (mainly in the IR spectral range) prohibit the compression in only one step. Bunch compression is therefore done in two successive steps at beam energies of 219 and 753 MeV. Using non-standard, sophisticated 6- and 8-magnet chicane arrangements respectively, a solution was found for the BESSY FEL that conserves the normalized electron emittance.

All optimizations for the FEL were based on start-to-end simulations. The evolution of the electron beam quality was simulated using the codes ASTRA and PARMELA for the injector, while the beam dynamics in the linac and in the sections in-between was simulated using the ELEGANT program. The details in the undulators were calculated with the GENESIS code time resolved (references for the various codes are given in chapters 3, 5 and 7). This approach is essential to obtain a state-of-the-art realistic picture of the beam dynamics of the FEL. The result is the layout of the machine as depicted in figure 1.12.

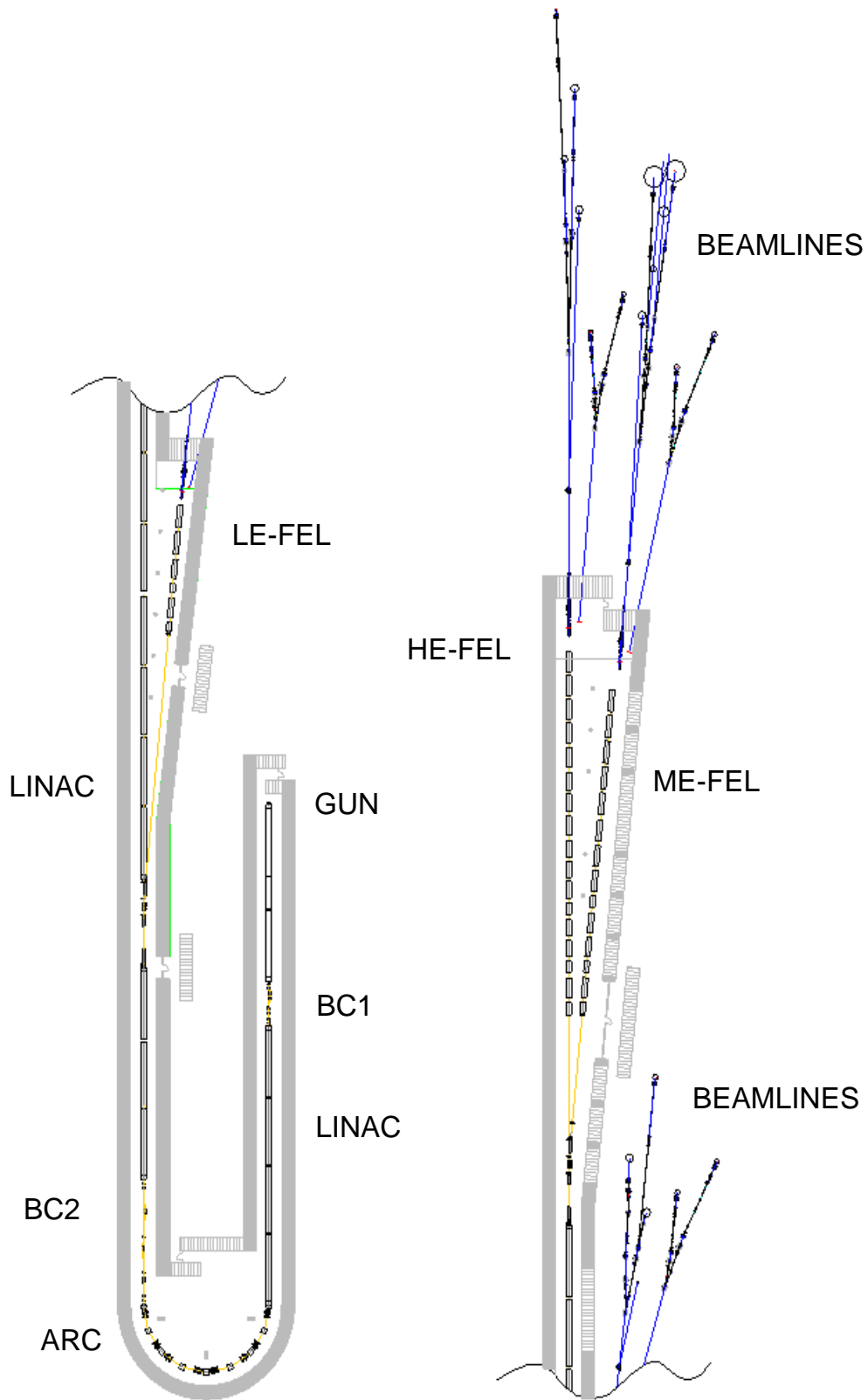


Fig.1.12: Layout of the BESSY Soft X-ray FEL.

Different sources of emittance dilution have been considered such as wakefields in the acceleration modules and CSR in the 180 degree arc and in the compressor chicanes. Adequate chirping of the beam at low energies by a third-harmonic cavity allows for proper shaping of the energy distribution in the bunch. However, the overall sensitivity in obtaining the optimized beam parameters clearly shows that the FEL requires excellent diagnostics to measure and verify or re-optimize the beam parameters at any strategic location of the machine. Developing adequate sensors for the electron beam - and equally true for the photon beam - are key issues for reliable and reproducible operation of a user facility. Fortunately BESSY in conjunction with the construction of BESSY II has had an extensive diagnostics program both on electron beam and on photon beam characteristics since the early 1990's. Now these programs are concentrated on the specific requirements of the FEL. The BESSY femtosecond slicing project [19] as well as PITZ and TTF at DESY will serve as test beds for these developments.

1.11 The Undulators

For the proposed three individually tunable FEL lines a variety of very specialized undulators (total length ~120 m) is needed for the cascaded HGHG-FELs. The list of table 1.6 refers to the various systems that have to be supplied. Essential for the users is the fact that all long undulators of the final amplifier stages will be of the elliptical type. These devices will be of a modified APPLE II kind utilizing a new magnet configuration, allowing for 1.5 times higher K-values than conventional APPLE II insertion devices (figure 1.13). Thus, all FELs will produce variably-polarized light, the photon polarization to be determined by the user himself according to the experiment being performed.

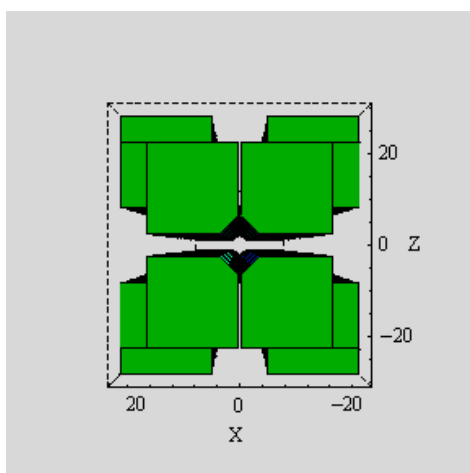


Fig. 1.13: Schematics of the new magnetic structure for high K parameter elliptical undulators.



Fig. 1.14: Photo of the APPLE II UE 46 operating in the BESSY II storage ring.

Detailed analysis of the undulators shows that the present-day shimming technology is sufficient to fulfill the tolerances required for FEL operation. BESSY is well prepared for that; 38 m of undulators - planar and elliptical devices - have been designed and built in-house for the BESSY II storage ring as well as for other third generation light sources such as the SLS. Figure 1.14 shows one of the various insertion devices in routine user operation.

Table 1.6: Period length and total length for the undulators for the various HGHG-stages. All undulators are planar devices except for the final amplifiers.

FEL		LE-FEL	ME-FEL	HE-FEL	Unit
Photon energy range		24 - 120	100 - 600	500 - 1000	eV
1. Stage	Modulator λ_u	80	122	122	mm
	Modular length	1.600	2.196	2.196	m
	Radiator λ_u	62	92	92	mm
	Radiator length	3.472	3.680	3.680	m
2. Stage	Modulator λ_u	62	92	92	mm
	Modular length	1.612	2.024	2.024	m
	Radiator λ_u	50	70	70	mm
	Radiator length	3.450	7.280	6.020	m
3. Stage	Modulator λ_u		70	70	mm
	Modular length		2.100	2.100	m
	Radiator λ_u		50	50	mm
	Radiator length		11.550	9.000	m
4. Stage	Modulator λ_u			50	mm
	Modular length			3.450	m
	Radiator λ_u			28.5	mm
	Radiator length			6.413	m
Final Amplifier	λ_u	50	50	28.5	mm
	Fin. ampl. length	8.100	19.650	17.955	m

Though the FEL undulators will be segmented to a length of typically 3.5 m, similar to the 4 m devices for BESSY II, the volume of production calls for an optimized logistics to meet the time schedule for procurement of less than 3.5 years in total. The major part of the work will be with the suppliers. Final quality assurance and shimming of the sections will remain within the BESSY undulator laboratory.

Special attention has been paid to the undulator vacuum chamber. The wakefield induced by the electron beam has been analyzed. A smooth copper surface with a roughness < 100 nm rms will be “seen” by the electron beam. A tentative chamber layout was worked out. More difficult than the chambers are the intersections between the undulator modules. These intersections will be ~ 0.95 m long and contain various electron-beam diagnostic elements, phase shifters, quadrupole and steering magnets, as well as vacuum pumps. A description of the undulator layouts with all relevant details is presented in chapter 9.

1.12 Beamlines and End-Stations

The scientific areas identified in the “Visions of Science” [1] can be covered by three FEL lines. For each line two types of beamlines have been designed: one type optimized for ultra-high energy resolution, the second type for ultra-short pulse conservation. The design study shows that for the latter type pulse prolongation by the beamline can be kept to between 10 and 20 fs. For experiments requiring ultra-high energy resolution resolving powers up to 270,000 can be achieved. Switching between both types of beamlines installed at each FEL is accomplished by moveable mirror units similar to the ones realized at the BESSY II storage ring light source. Additionally, stations where the FEL pulse can be used directly without a monochromator are provided for.

Figure 1.15 gives a sketch of a possible layout of the experimental area with the short pulse beamline, the high resolution line and beamlines to guide the focused direct FEL beam to the experiment for all three FEL lines. Furthermore, as the electron beam is still of high quality after having passed the FEL undulators, it can be sent through a conventional undulator to generate sub-ps-short pulses of spontaneous radiation. Space will be kept free in the tunnel for later installation of the undulators between the electron beam dump and the end of the FEL undulators. Here a switching toroidal mirror will also allow for the use of a double beamline. Thus, up to 9 end-stations (15 in phase II) can be made available for the users.

The performance of the beamlines at the low-energy FEL is shown in the following graphs. Special care has been taken in order to preserve the superb time structure of the FEL pulses. At low energies this is accomplished by a double grating monochromator design, whereas at high energies the temporal lengthening of the pulse can be controlled by varying the illumination of the grating. Additionally at low energies an excellent resolution for a monochromator of $E/\Delta E = 270,000$ results in an energy spread of $90 \mu\text{eV}$ at 24 eV photon energy. The graphs in figures 1.16 and 1.17 and the tables 1.7 and 1.8 are given as examples of the two beamlines at the LE-FEL. More details for the ME- and HE-FEL are given in chapter 10.

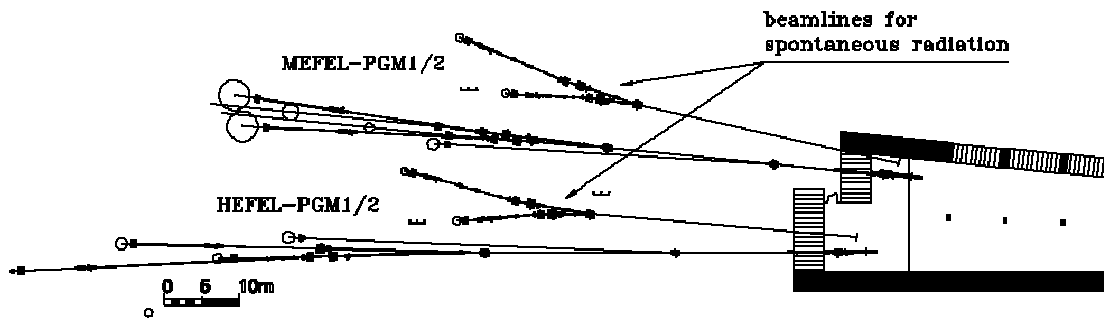


Fig. 1.15: Possible layout for end-stations at the BESSY FEL lines with beamlines for short pulses, high resolution, direct beam, and spontaneous radiation.

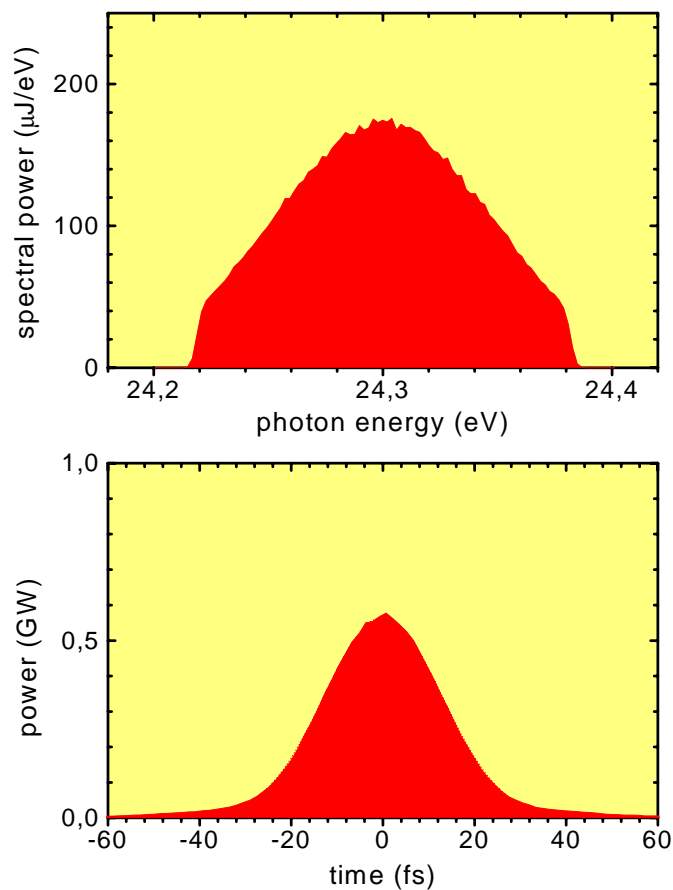


Fig. 1.16: Bandwidth and pulse shape for a 1 mm slit setting of the short-pulse beamline at the LE-FEL. The Gaussian shape of the energy distribution reflects the spectral distribution of the incident light, which is assumed to be Gaussian with a width given in table 1.7. With this slit setting almost the complete bandwidth of the FEL pulse is transmitted through the beamline.

Table 1.7: Performance of the short-pulse beamline on the LE-FEL. Bandwidth, pulse length and spot size are given as fwhm values.

Photon energy	24	120	eV	
Exit slit size	100	1000	10	100 μm
Bandwidth	16	160	50	160 meV
Photons per pulse	$7.2 \cdot 10^{11}$	$4.9 \cdot 10^{12}$	$1.3 \cdot 10^9$	$1.1 \cdot 10^{10}$
Pulse length	210	30	170	35 fs
Spot size (hor. x vert.)	120 x 55	110 x 50	85 x 21	80 x 20 μm^2

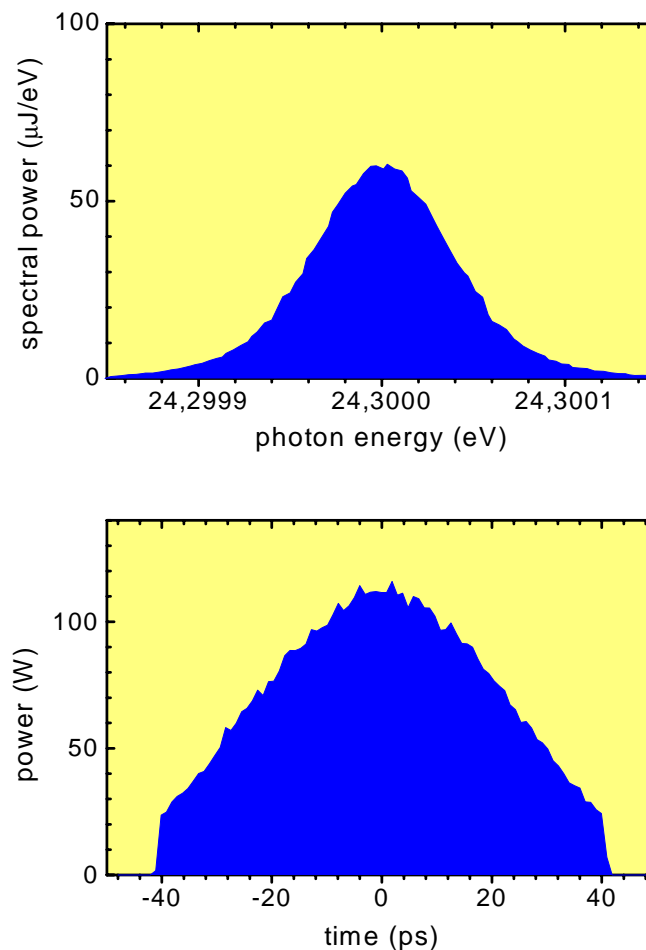


Fig. 1.17: Bandwidth and pulse shape for a 10 μm slit setting of the high-energy-resolution beamline at the LE-FEL. The bandwidth corresponds to a resolving power of 270,000. This is close to the diffraction limit due to the illuminated grating length (336,000).

Table 1.8: The performance of the high-energy resolution beamline on the LE-FEL. The values for bandwidth, pulse length, and spot size are given as fwhm values.

Photon energy	24		120		eV
Exit slit size	10	100	10	100	μm
Bandwidth	90	470	800	6000	μeV
Photons per pulse	$1.6 \cdot 10^9$	$1.6 \cdot 10^{10}$	$1.2 \cdot 10^8$	$1.2 \cdot 10^9$	
Pulse length	80	80	5	5	ps
Spot size (hor.x vert.)	60 x 16	60 x 13	60 x 7	60 x 9	μm^2

For experiments and end stations various proposals have been worked out for as presented in more detail in chapter 11:

- X-ray microscope with single-shot capability to investigate time-resolved dynamical biological and plasma processes.
- Transmission X-ray optics for nanometer focusing.
- A full-field X-ray microscope for holography.
- X-ray photon correlation spectroscopy.
- Resonant inelastic X-ray scattering (RIXS).
- Cluster and molecular beam instrumentation.
- X-ray pump - X-ray probe experiments.
- Laser-pump - X-ray probe experiments.
- Very-high-energy resolution photoemission.
- High-temporal resolution photoemission, spectroscopy and microscopy.

1.13 Conventional Facilities and Buildings

BESSY was in the fortunate position to involve the “Bauabteilung” (Department III - Construction and Engineering) of its major shareholder, the Max-Planck-Gesellschaft, in the preparation of the TDR. A detailed report on the building concept of the FEL user facility, based on the spatial and technical requirements for the project has been worked out, demonstrating the feasibility of the project on the BESSY site and deriving a sound cost basis [20].

The central element of the buildings (figure 1.18) is a 20,000 m² hall following industrial standards, giving space to the folded accelerator and the experimental areas. Major parts

of the hall will be only moderately temperature controlled, as the hall serves more as a shelter to the installation, constructed as a house-in-house architecture, rather than stabilizing the whole 100,000 m³ volume. Linac and undulator sections are behind the heavily shielded radiation protection tunnel. It is this tunnel volume that is equipped with an appropriate air conditioning. The same holds for the experimental areas. All sensitive equipment will be housed locally in hutches. Control rooms and laboratories for operation of the accelerator, lasers and experiments will be realized in fixed locations. The space in the northern part in the experimental hall, allocated to future expansion, will serve as (temporary) office space and additional rooms for the staff and guest experimenters during the start-up phase, to be relocated whenever needed.

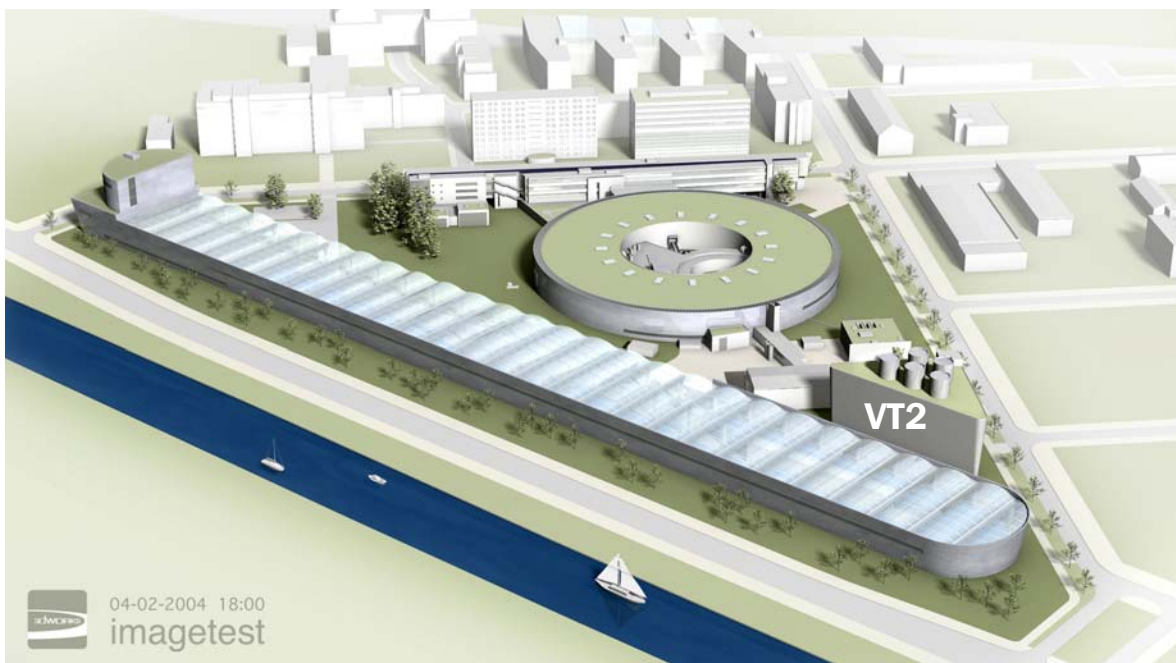


Fig. 1.18: Bird's eye view of the BESSY site with the BESSY II light source and the main building for the accelerator and the FEL experimental hall, left-hand side. The building between the injector area and the BESSY building (VT2) houses all essential infrastructure, including the LHe cryoplant.

The foundation of the building benefits from a special vibration damping. To avoid transmission of vibrations caused by the traffic from the nearby Ernst-Ruska-Ufer that would have deteriorated the BESSY II operation, a special foundation for the street had been employed all along the 500 m wide southern border of the BESSY site.

A central part of the infrastructure of the facility is the cryogenic plant delivering 3.5 kW super-fluid He-II at a temperature of 1.8 K. The cryohall will occupy significant

space in the VT2 block with compressors and the gaseous He purifier columns. The He storage capabilities will be installed in the open next to the building, whereas cold box and the intermediate storage dewar are located in the main building close to the linac tunnel. A cross-section of the linac tunnel is shown in figure 1.19.

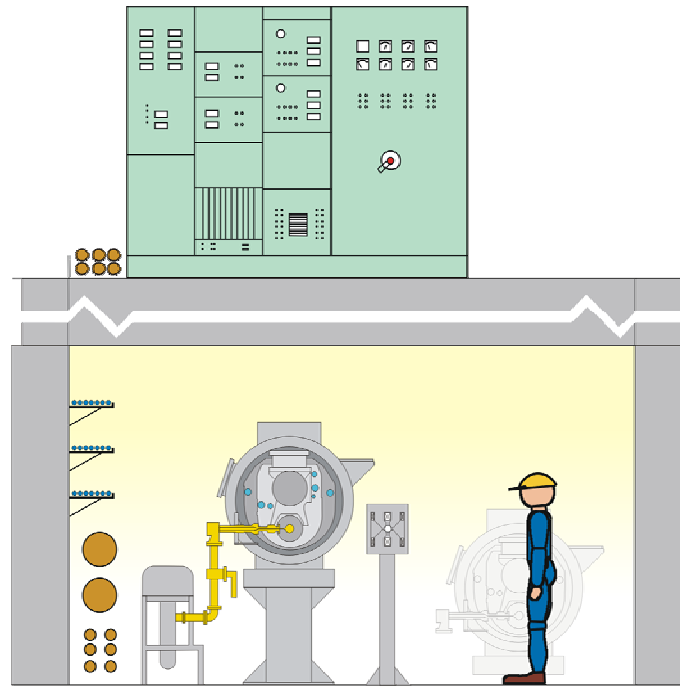


Fig. 1.19: Cross section of the inner linac tunnel.

1.14 Cost and Schedule

The project costs of the BESSY soft X-ray user facility were analyzed taking into account the synergies of the existing BESSY laboratory on site, e.g. infrastructure and expertise of BESSY personnel during the planning and construction period. A detailed realistic study of the investment costs of subsystems was made with frequent reference to industrial sources. While the costs of most hardware elements of accelerator and experimental instrumentation can be evaluated to a high level of confidence, the investment for the accelerating modules depends heavily on the conditions of fabrication. There is a significant benefit in price if the DESY X-FEL cryomodules are produced at the same time, so an effective synchronization of BESSY's and DESY's procurement phases is mandatory. This has been accounted for in the present cost estimate.

The building costs have been evaluated by the Bauabteilung of the Max-Planck-Gesellschaft in close collaboration with architects from DGI Bauwerk (Berlin) and engineers from IB Krone (Berlin), IB Müller/Bleher (Radolfzell), and Ebert Ingenieure (München). A detailed study on the buildings and infrastructure has been worked out [20].

Figure 1.20 gives the distribution of costs relative to the total investment within the project.

The construction time for the BESSY Soft X-ray FEL is four years, starting with the beginning of civil construction, assuming a two-year precursory detail planning phase.

Taking into account the manpower during the design, procurement, assembly installation, and commissioning phases of 150 FTEs, the total cost for the BESSY Soft X-ray FEL has been estimated at **198.2 million €**.

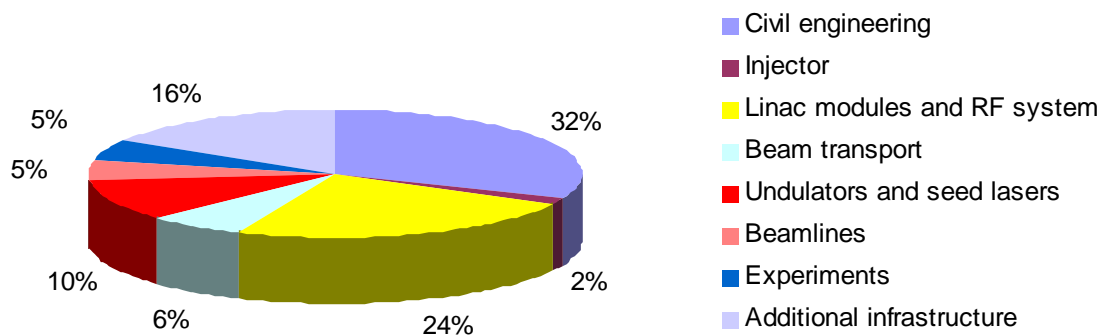


Fig. 1.20: Relative distribution of the costs for the BESSY Soft X-ray-FEL.

References

- [1] Visions of Science, BESSY Berlin-Adlershof (2001):
<http://www.bessy.de/publications/01.felscientific/files/sc.pdf> .
- [2] E. L. Saldin, E. A. Schneidmiller, M. V. Yurkov, "The Physics of Free Electron Lasers", (Advanced Texts in Physics), Springer-Verlag Berlin Heidelberg (2000).
- [3] G. Dattoli, A. Marino, A. Renieri, F. Romanelli, *IEEE J. Quant. Elec.* **17/8** (1981) 1371.
- [4] R. Bonifacio, C. Pellegrini, L. M. Narducci, *Opt. Comm.* **50/6** (1984) 373.
- [5] K.-J. Kim, *Nucl. Instrum. and Meth. A* **250/1-2** (1986) 396.
- [6] F. Stephan, I. Bohnet, J. Bähr, U. Gensch, H. J. Grabosch, D. Lipka, A. Oppelt, R. Bakker, E. Jaeschke, D. Krämer, M. v. Hartrott, Z. Li, J.-P. Carneiro, K. Flöttmann, Ph. Piot, J. Rossbach, S. Schreiber, V. Djordjadze, P. Michelato, C. Pagani, D. Sertore, V. Miltchev, I. Tsakov, A. Liero, H. Redlin, W. Sandner, R. Schumann, I. Will, R. Cee, M. Krassilnikov, S. Setzer, T. Weiland, K. Abrahamyan, B. Petrossyan, *Proc. of the 8th EPAC* (2002) 1813.
- [7] L. Serafini, J. B. Rosenzweig, *Phys. Rev.* **55/6** (1997) 7565.
- [8] M. Ferrario, K. Flöttmann, B. Grigoryan, T. Limberg, Ph. Piot, TESLA Report FEL-Report 2001-03, DESY (2001).
- [9] M. Krasilnikov, K. Abrahamyan, J. Bähr, I. Bohnet, J.-P. Carneiro, K. Flöttmann, U. Gensch, H.J. Grabosch, J.H. Han, V. Miltchev, A. Oppelt, B. Petrossyan, J. Rossbach, S. Schreiber, F. Stephan, M.v. Hartrott, E. Jaeschke, D. Krämer, D. Lipka, P. Michelato, C. Pagani, D. Sertore, I. Tsakov, H. Redlin, W. Sandner, R. Schumann, I. Will, R. Cee, S. Setzer, T. Weiland, *Proc. of the 2003 PAC* (2003) 2114.
- [10] L. M. Young, "PARMELA", Los Alamos National Laboratory Report LA-UR-96-1835 (Revised April 22, 2003):
<http://laacg1.lanl.gov/laacg/services/parmela.html> .
- [11] K. Flöttmann, "ASTRA, A Space Charge Tracking Algorithm":
<http://www.desy.de/~mpyflo> .
- [12] B. E. Carlston, *Nucl. Instrum. and Meth. A* **285/1-2** (1989) 313.
- [13] T. Srinivasan-Rao, I. Ben-Zvi, A. Burriell, G. Citver, A. Hershcovisch, D. Pate, A. Reuter, J. Scaduto, Q. Zhao, Y. Zhao, H. Bluem, M. Cole, A. Favale, J. W. Rathke, T. J. Schultheiss, J. Delayen, P. Kneisel, *Proc. of the 2003 PAC* (2003) 92.
- [14] D. Janssen, P. v. Stein, A. Bushuev, M. Karliner, S. Konstantinov, J. Kruchov, V. Petrov, I. Sedlyarov, A. Tribendis, V. Volkow, *Proc. of the 1997 PAC* (1997) 2838.

- [15] M. Ferrario, J. E. Clendenin, D. T. Palmer, J. B. Rosenzweig, L. Serafini, SLAC-PUB-8400 (2000).
- [16] V. Volkov, D. Janssen, *Nucl. Instrum. and Meth. A* **452**/1-2 (2000) 34.
- [17] D. Janssen, H. Büttig, P. Evtushenko, U. Lehnert, P. Michel, K. Möller, Ch. Schneider, J. Stephan, J. Teichert, S. Kruchkov, O. Myskin, A. Tribendis, V. Volkov, W. Sandner, I. Will, T. Quast, K. Goldammer, F. Marhauser, P. Ylä-Oijala, *Nucl. Instrum. and Meth. A* (2004), article in press.
- [18] R. Brinkmann, K. Flöttmann, J. Roßbach, P. Schmüser, N. Walker, H. Weise, (editors), TESLA Technical Design Report, Part II - The Accelerator, DESY-2001-011 (2001).
- [19] S. Khan, H.-H. Bäcker, J. Bahrtdt, H. A. Dürr, V. Dürr, W. Eberhardt, A. Gaupp, K. Holldack, E. Jaeschke, D. Krämer, H.-C. Mertins, W. B. Peatman, T. Quast, G. Reichardt, M. Scheer, F. Senf, G. Wüstefeld, I. Hertel, F. Noack, W. Sandner, I. Will, N. Zhavoronkov, *Proc. of the 2003 PAC* (2003) 836.
- [20] Gutachten – Gebäude und haustechnische Ausrüstung des Projekts Freie Elektronen Laser BESSY FEL der Berliner Elektronenspeicherringgesellschaft für Synchrotronstrahlung BESSY G.m.b.H., Bauabteilung der Max-Planck-Gesellschaft z.F.d.W. e.V. in cooperation with H. Machleidt (Machleidt & Partner), C. Huboi (DGI – Bauwerk), M. Hamann (Ing. Büro Krone, Berlin), H. Bleher (Müller & Bleher, Radolfzell), G. Engelbrecht (Ebert Ingenieure, München), (2004).

2 The Quest for Brilliance and Extreme Time Resolution

2.1 Introduction to FELs

Electromagnetic radiation ranging from radio waves to hard γ -rays is one of the most important tools in physics; this wavelength range includes infrared radiation, visible light, ultraviolet radiation as well as soft, and hard X-rays.

Delivering peak brilliance of 15 orders of magnitude higher than the original X-ray tube of C.W. Röntgen, today's synchrotron radiation sources have expanded the possible applications of this radiation covering now continuously the spectral range from the far infrared up to hard X-rays.

However, in electron storage ring based synchrotron radiation sources the electrons emit the electromagnetic radiation incoherently, i.e. without a fixed phase relation, whereas in a free electron laser the interaction between the electrons and the radiation field introduces a phase relation, giving rise to coherent emission. As a consequence of the large number of electrons involved, on the order of 10^{10} , the peak brilliance, which scales proportionally to the square of the number of electrons, is dramatically increased.

The work on coherently emitting electron beam devices goes back to the development of microwave tubes delivering high power in the centimeter region. In 1951 H. Motz showed that high power and high coherence of radiation can be emitted by a bunched electron beam traveling through an undulator [1]. The first FEL, then named differently, was a Philips microwave tube from 1960 [2]. In the early 1960s and 1970s much theoretical work was performed on the FEL principle [3, 4, 5]. Finally it was J.M.J. Madey who recognized that coherent electromagnetic radiation is generated and amplified by stimulated emission of bremsstrahlung, when relativistic electrons propagate co-linearly with the radiation field in a periodic magnet array of an undulator [6]. His successful demonstration of this device operating at a wavelength of $10\ \mu\text{m}$ [7] triggered further developments of the optical klystron and its close relative, the undulator.

In the FEL, similar to insertion devices in modern synchrotron radiation sources, the radiated wavelength λ is related to the energy of the electron beam E or the relativistic factor γ and the magnetic properties of the undulator

$$\lambda = \frac{1}{2\gamma^2} \lambda_u (1 + K^2). \quad (2.1)$$

where λ_u and K denote the undulator period and the K -parameter which is proportional to the magnet field strength.

Unlike conventional laser systems, the FEL can be tuned to any desired wavelength and - compared to synchrotron radiation sources - has the advantage of:

- High peak power, typically up to nine orders of magnitude higher;
- High peak brilliance, up to ten orders of magnitude higher;
- Full transverse and partially longitudinal coherence of the output radiation.

With these assets the advantages of an FEL are clear and many laboratories around the world have successfully demonstrated the feasibility of the FEL, both as research objects and as user-facilities for tunable coherent radiation. An overview of activities in the field was given in [8]. Figure 2.1 displays the steep increase in brilliance from the various light sources in the last century to the novel FEL sources proposed.

Until recently the operation of the FEL has been limited to the far infrared, visible and near UV spectral range. At shorter wavelength, e.g. $\lambda < 100$ nm, the multi-pass optical cavity based FEL suffers from the lack of high-quality mirrors [9].

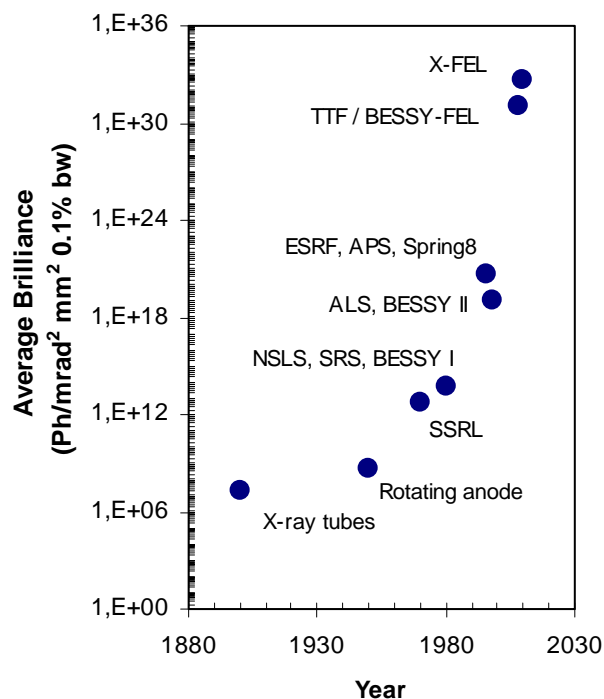


Fig. 2.1: Average brilliance of electromagnetic radiation from various sources vs. time in a semi-log plot. Note: Brilliance for FELs is peak brilliance. The log-scale is spanning 36 orders of magnitude.

An alternative approach, achieving lasing without an optical cavity, i.e. self-amplified spontaneous emission (SASE) of radiation from an electron bunch in a single pass through an undulator, was suggested first by A.M. Kondratenko and E.L. Saldin [10]. In this scheme an electron beam with high current density is passed through an undulator, stimulated to emit coherently, amplifying its own spontaneous radiation by several orders of magnitude in a single pass. A recent series of experiments at UCLA [11], ANL [12], DESY [13] and BNL [14] have demonstrated the validity of the theory as well as the potential of the SASE-FEL as a light source for the VUV to hard X-ray spectral range.

2.2 The SASE Principle

In a SASE-FEL (figure 2.2), electrons traveling through an undulator initially emit spontaneous radiation as in a storage ring undulator. Due to the large number of electrons the radiation field generated is strong and increases rapidly. Electrons interacting with this electromagnetic field within the same undulator are either decelerated or accelerated depending on their relative phase with respect to the radiation, e.g. the electrons are modulated in energy.

On their way through the magnet structure this energy modulation is transformed into a longitudinal density modulation, called micro-bunching. The bunch separates into equidistant slices of micro-bunches corresponding in length to the radiation wavelength λ . The micro-bunches emit coherently amplifying the radiation field. More and more electrons radiate in phase which results in a coherent superposition of the radiation emitted. The higher the intensity of the radiated electromagnetic field, the more pronounced is the spatial density modulation. The power of spontaneous radiation at the start of the process is proportional to the number of electrons in the bunch. It is converted ideally into the total power emitted which scales with the number of electrons squared. This is why the FEL peak output power exceeds that of modern synchrotron light sources by 10 to 11 orders of magnitude. However, a limitation due to the random noise buildup is the poor temporal coherence since the coherence time is much less than the pulse duration.

The two most prominent examples on successful demonstration of the idea of SASE at VUV wavelengths are the Low Energy Undulator Test Line (LEUTL) at ANL [12] and the TESLA Test Facility (TTF) at DESY [13].

The FEL at Argonne has demonstrated the ability to deliver sustained operation over a tunable wavelength range from 660 to 120 nm. This laser was the first SASE-FEL to reach saturation, proving the feasibility of such devices and underscoring their promise of achieving laser-like operation well into the X-ray spectrum.

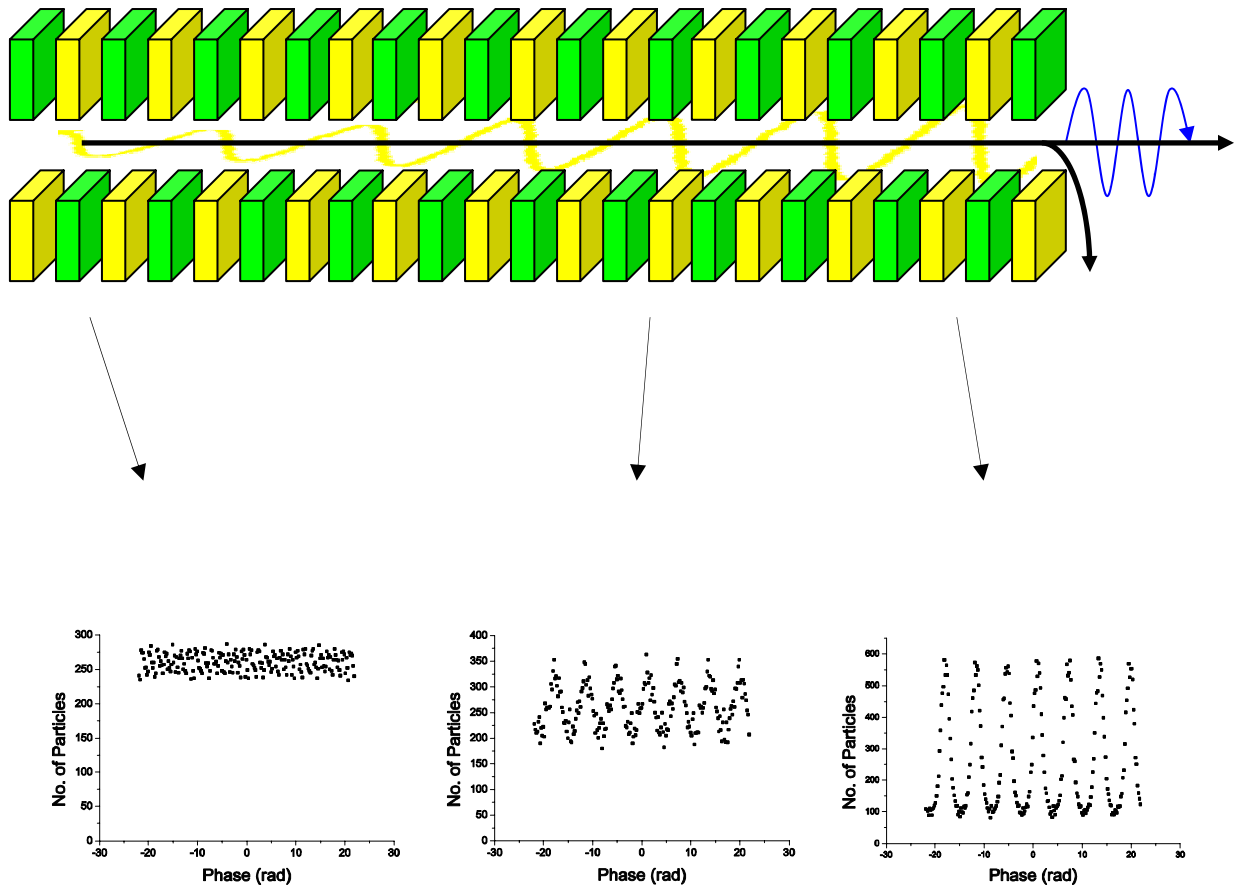


Fig. 2.2: Spatial density distribution at the beginning, mid of the undulator, and when the SASE-process has reached saturation. Figures were derived with the code Genesis [15] for a scenario as described in [16].

The TESLA Test Facility at DESY [13] proved the principle of SASE-FEL at VUV photon wavelength from 80 to 180 nm [17]. First lasing was achieved in February 2000, since then the device has been used for further linear accelerator R&D and user experiments. The upgrade of the FEL to a wavelength down to 6 nm and the conversion into a user facility (VUV FEL) [18] is under preparation at the time of writing, expected to start operation in 2004.

2.3 Seeded FELs

It was soon recognized that the performance of SASE-FELs had to be improved. To avoid the consequences originating from the statistical nature of starting up the lasing

process, in particular the uncontrollable spiky nature of the output, different and more sophisticated magnetic and optical configurations have been proposed: regenerative amplification [19], two stage SASE-FEL [20], side band seeded FELs [21] and pulse compression [22], to name a few.

An alternative single-pass FEL approach is the High Gain Harmonic Generation scheme (HGFG) pioneered and successfully demonstrated at BNL by L.H. Yu and co-workers [23, 24]. The underlying idea is to overlap the electron bunch with the field of an external seed laser in a short undulator. In this magnet structure, called the modulator, the seed field interacts with the electron beam introducing a small energy modulation. It should be emphasized that this energy modulation is induced by the high-peak power of the high-quality seed. The energy-modulated electron beam then passes through a dispersive section, e.g. a three dipole chicane, where the energy modulation is converted into spatial modulation. Figures 2.3 and 2.4 illustrate the longitudinal phase space distribution after the modulator and the density distribution after the dispersive section respectively.

Due to the high seed peak power the phase information of the seed laser is impressed onto the density modulated electron beam as it dominates the noise from spontaneous emission. Abundant harmonics exist in the modulated beam which thereafter enters a second undulator, called the radiator. The radiator is set to be resonant to a higher harmonic of the seed laser frequency λ_s , e.g. at $\lambda_s/3$ or $\lambda_s/5$. Coherent emission at this higher harmonic is produced and is exponentially amplified until saturation is achieved. Ideally the HGFG output radiation is Fourier-transform-limited since it is completely longitudinally coherent. In case of a Gaussian pulse of time duration Δt_{fwhm} the relative bandwidth is given by:

$$(\Delta\lambda / \lambda)_{\text{fwhm}} = \frac{2 \ln(2)}{\pi} \frac{\lambda}{c \Delta t_{\text{fwhm}}} \quad (2.2)$$

with c denoting the speed of light and λ the central wavelength.

The major advantage of the HGFG-FEL is that the properties of the output radiation at the harmonic wavelength are a map of the characteristics of the high-quality fundamental seed laser field. This includes a high degree of stability, the bandwidth, the output power, the shape, and the duration of the output pulse. As the seed pulse can be made shorter than the electron bunch the output pulse duration is no longer determined by the length of the bunch but by the seed laser pulse. This in fact is the most important feature compared to SASE-type FELs where the output pulse duration is determined by the electron bunch length. Thus, the HGFG-FEL is flexible within the parameter field of high-power seed lasers. Furthermore, uncontrollable statistical fluctuations of the startup signal, which is shot noise, reflects the temporal characteristics of the SASE output. Consequently

the SASE output is not longitudinally coherent but is a superposition of the many wave trains with random phases emitted from the many slices in the beam which are of the length of a cooperation length. A HGHG-FEL, however, delivers an almost Fourier-transform-limited “smooth” pulse.

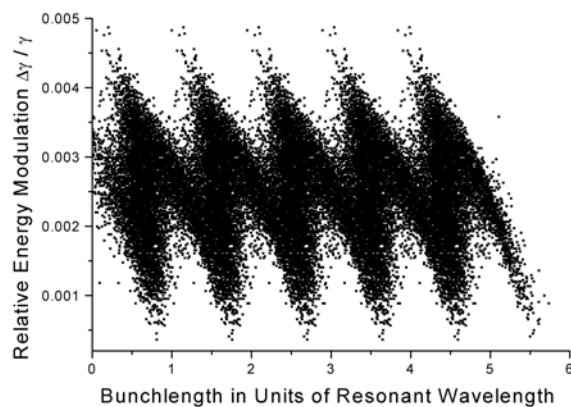


Fig 2.3: Longitudinal phase space distribution after the modulator.

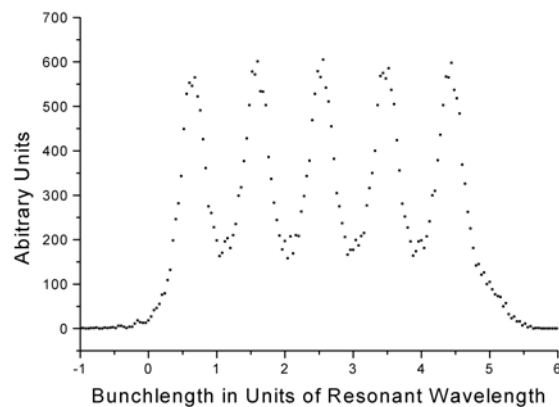


Fig. 2.4: Longitudinal density distribution after the dispersive section.

This concept has been experimentally verified at the DUV-FEL at Brookhaven National Laboratory (BNL) [25].

The DUV-FEL operates with a fundamental at 266 nm and a third harmonic at 89 nm. The fundamental has an output of 0.1 mJ in a 200 fs pulse and the third harmonic has an output energy of 1 μ J with a similar pulse length. The output radiation has the full longitudinal and transverse coherence and stability of the seed laser.

2.4 The Cascaded HGHG-FEL

The HGHG output itself can be used as a seed to drive a second HGHG-FEL. Hence one can use multiple stages, e.g. cascading the HGHG-FEL, in order to reach a final wavelength of around 1 nm with a 4 stage device. The cascade starts with a conventional fs-

laser and a start seed of wavelength 375 nm which is then up-converted by harmonic generation of $N=5 \cdot 5 \cdot 5 \cdot 3=375$.

To achieve the best efficiency of up-conversion in a HGHG stage it is mandatory to have a fresh part of the electron bunch interact with the seed field, e.g. use a relatively long bunch and introduce a delay between electron bunch and seed to avoid interaction of seed and already disturbed electron beam. This “fresh bunch” technique has been proposed by Ben-Zvi, Yang and Yu [26].

Figure 2.5 is a schematic of the cascaded HGHG-FEL for the case of 2 stages as will be used for the BESSY low-energy (LE-)FEL line.

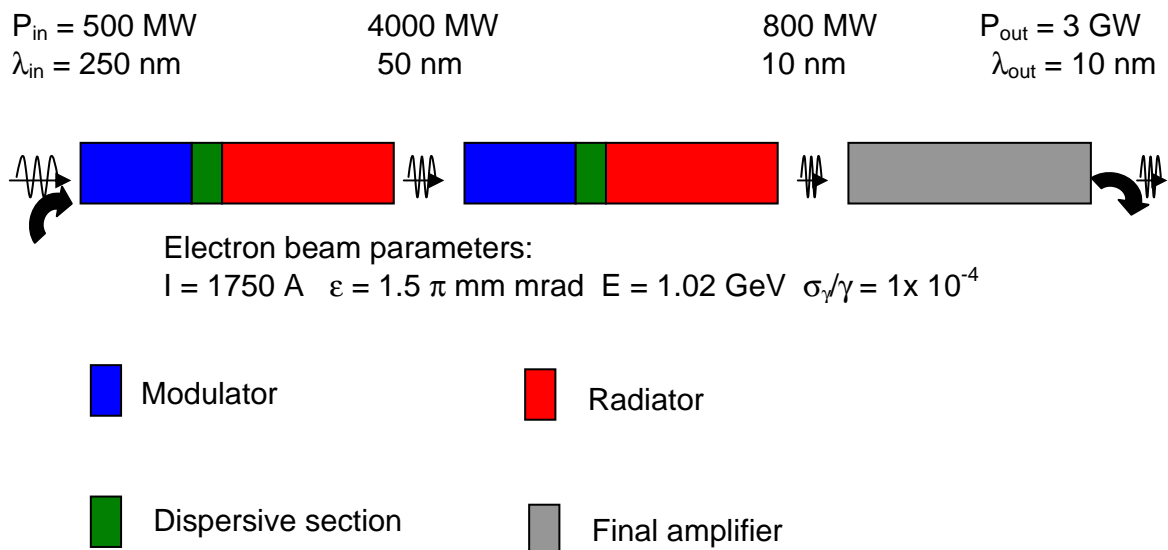


Fig. 2.5: Schematic of a 2-stage cascaded HGHG-FEL. P_{in} and λ_{in} denote the power and wavelength of the external seed laser, P_{out} and λ_{out} the FEL output pulse power and wavelength. Up-conversion is from 250 to 10 nm.

References

- [1] H. Motz, *J. Appl. Phys.* **22** (1951) 527.
- [2] R. M. Philips, *IRE Trans. Electron Devices* **7** (1960) 231.
- [3] R. V. Palmer, *J. Appl. Phys.* **43** (1972) 3014.
- [4] K. W. Robinson, *Nucl. Instrum. and Meth. A* **239** (1985) 111.
- [5] P. Csonka, *Part. Acc.* **8** (1978) 225.
- [6] J. M. J. Madey, *J. Appl. Phys.* **42** (1971) 1906.
- [7] D. A. G. Deacon, L. R. Elias, J. M. J. Madey, G. J. Ramian, H. A. Schwettman, T. I. Smith, *Phys. Rev. Lett.* **38** (1977) 892.
- [8] W.B. Colson, *Nucl. Instrum. and Meth. A* **475** (2000) 397.
- [9] B. L. Henke, E. M. Gullikson, J. C. Davis, *At. Data Nucl. Data Tables* **54** (1993) 181.
- [10] A. M. Kondratenko, E. L. Saldin, *Part. Acc.* **10** (1980) 207.
- [11] A. Tremaine, J. B. Rosenzweig, S. Anderson, P. Frigola, M. Hogan, A. Murokh, C. Pellegrini, D. C. Nguyen, R. L. Sheffield, *Phys. Rev. Lett.* **81/26** (1998) 5816.
- [12] S. V. Milton, E. Gluskin, S. G. Biedron, R. J. Dejus, P. K. Den Hartog, J. N. Galayda, K.-J. Kim, J. W. Lewellen, E. R. Moog, V. Sajaev, N. S. Sereno, G. Travish, N. A. Vinokurov, N. D. Arnold, C. Benson, W. Berg, J. A. Biggs, M. Borland, J. A. Carwardine, Y.-C. Chae, G. Decker, B. N. Deriy, M. J. Erdmann, H. Friedsam, C. Gold, A. E. Grelick, M. W. Hahne, K. C. Harkay, Z. Huang, E. S. Lessner, R. M. Lill, A. H. Lumpkin, O. A. Makarov, G. M. Markovich, D. Meyer, A. Nassiri, J. R. Noonan, S. J. Pasky, G. Pile, T. L. Smith, R. Soliday, B. J. Tieman, E. M. Trakhtenberg, G. F. Trento, I. B. Vasserman, D. R. Walters, X. J. Wang, G. Wiemerslage, S. Xu, B.-X. Yang, *Phys. Rev. Lett.* **85/5** (2000) 988.
- [13] J. Andruszkow, B. Aune, V. Ayvazyan, N. Baboi, R. Bakker, V. Balakin, D. Barni, A. Bazhan, M. Bernard, A. Bosotti, J. C. Bourdon, W. Brefeld, R. Brinkmann, S. Buhler, J.-P. Carneiro, M. Castellano, P. Castro, L. Catani, S. Chel, Y. Cho, S. Chorooba, E. R. Colby, W. Decking, P. Den Hartog, M. Desmons, M. Dohlus, D. Edwards, H. T. Edwards, B. Faatz, J. Feldhaus, M. Ferrario, M. J. Fitch, K. Flöttmann, M. Fouaidy, A. Gamp, T. Garvey, C. Gerth, M. Geitz, E. Gluskin, V. Gretchko, U. Hahn, W. H. Hartung, D. Huber, M. Hünng, R. Ischebek, M. Jablonka, J. M. Joly, M. Juillard, T. Junquera, P. Jurkiewicz, A. Kabel, J. Kahl, H. Kaiser, T. Kamps, V. V. Katelev, J. L. Kirchgessner, M. Körfel, L. Kravchuk, G. Kreps, J. Krzywinski, T. Lokajczyk, R. Lange, B. Leblond, M. Leenen, J. Lesrel, M. Liepe, A. Liero, T. Limberg, R. Lorenz, Lu Hui Hua, Lu Fu Hai, C. Magne, M. Maslov, G. Materlik, A. Matheisen, J. Menzel, P. Michelato, W.-D. Möller, A. Mosnier, U. C. Müller, O. Napoly, A.

- Novokhatski, M. Omeich, H. S. Padamsee, C. Pagani, F. Peters, B. Petersen, P. Pierini, J. Pflüger, P. Piot, B. Phung Ngoc, L. Plucinski, D. Proch, K. Rehlich, S. Reiche, D. Reschke, I. Reyzel, J. Rosenzweig, J. Rossbach, S. Roth, E. L. Saldin, W. Sandner, Z. Sanok, H. Schlarb, G. Schmidt, P. Schmüser, J. R. Schneider, E. A. Schneidmiller, H.-J. Schreiber, S. Schreiber, P. Schütt, J. Sekutowicz, L. Serafini, D. Sertore, D. Sertore, S. Setzer, S. Simrock, B. Sonntag, B. Sparr, F. Stephan, V. A. Sytchev, S. Tazzari, F. Tazzioli, M. Tigner, M. Timm, M. Tonutti, E. Trakhtenberg, I. R. Treusch, D. Trines, V. Verzilov, T. Vielitz, V. Vogel, G.v. Walter, R. Wanzenberg, T. Weiland, H. Weise, J. Weisend, M. Wendt, M. Werner, M. M. White, I. Will, S. Wolff, M. V. Yurkov, K. Zapfe, P. Zhogolev, F. Zhou, *Phys. Rev. Lett.* **85/18** (2000) 3825.
- [14] A. Murokh, R. Agustsson, P. Frigola, C. Pellegrini, S. Reiche, J. Rosenzweig, A. Tremaine, M. Babzien, I. Ben-Zvi, E. Johnson, R. Malone, G. Rakowsky, J. Skaritka, X. J. Wang, K. A. van Bibber, L. Bertolini, J. M. Hill, G. P. Le Sage, M. Libkind, A. Toor, R. Carr, M. Cornacchia, L. Klaisner, H.-D. Nuhn, R. Ruland, *Proc. of the 2001 PAC* (2001) 2748.
- [15] S. Reiche, *Nucl. Instrum. and Meth. A* **429** (1999), 243.
- [16] A. Meseck, M. Abo-Bakr, D. Krämer, B. Kuske, S. Reiche, *Proc. of the 25th FEL conf.* (2003), to be published in *Nucl. Instrum. and Meth. A*.
- [17] J. Rossbach, V. Ayvazyan, N. Baboi, R. Brinkmann, M. Castellano, P. Castro, W. Decking, M. Dohlus, H. T. Edwards, B. Faatz, A. Fateev, J. Feldhaus, K. Flöttmann, A. Gamp, T. Garvey, C. Girth, E. Gluskin, V. Gretchko, U. Hahn, K. Honkavaara, M. Hüning, R. Ischebeck, M. Jablonka, T. Kamps, M. Körfer, J. Krzywinski, J. Lezellen, M. Liepe, A. Liero, T. Limberg, T. Lokajczyk, C. Magne, G. Materlik, J. Menzel, P. Michelato, A. Mosnier, A. Novokhatski, C. Pagani, F. Peters, J. Pflüger, P. Piot, L. Plucinski, K. Rehlich, S. Reiche, I. Reyzl, S. Roth, E. L. Saldin, W. Sandner, H. Schlarb, G. Schmidt, P. Schmüser, J. R. Schneider, E. A. Schneidmiller, H. J. Schreiber, S. Schreiber, D. Sertore, S. Simrock, B. Sonntag, F. Stephan, K. Sytchev, M. Timm, M. Tonutti, E. Trakhtenberg, R. Treusch, D. Trines, V. Verzilov, R. Wanzenberg, T. Weiland, H. Weise, M. M. White, I. Will, K. Wittenburg, M. V. Yurkov, K. Zapfe, *Nucl. Instrum. and Meth. A* **475** (2001) 13.
- [18] SASE FEL at the TESLA Facility, Phase 2, TESLA-FEL note 2002-01 DESY (2002).
- [19] B. Faatz, J. Feldhaus, J. Krzywinski, E. L. Saldin, E. A. Schneidmiller, M. V. Yurkov, *Nucl. Instrum. and Meth. A* **429** (1999) 424.
- [20] J. Feldhaus, E. L. Saldin, J. R. Schneider, E. A. Schneidmiller, M. V. Yurkov, *Opt. Commun.* **140** (1997) 341.

- [21] W. Brefeld, B. Faatz, J. Feldhaus, M. Körfer, J. Krzywinski, T. Möller, J. Pflüger, J. Rossbach, E. L. Saldin, E. A. Schneidmiller, S. Schreiber, M. V. Yurkov, *Nucl. Instrum. and Meth. A* **483**/1-2 (2002) 62.
- [22] C. Pellegrini, *Nucl. Instrum. and Meth. A* **445** (2000) 124.
- [23] I. Ben-Zvi, L. F. Di Mauro, S. Krinsky, M. White, L. H. Yu, *Nucl. Instrum. and Meth. A* **304** (1991) 181.
- [24] L.H. Yu, *Phys. Rev. A* **44**/8 (1991) 5178.
- [25] L. DiMauro, A. Doyuran, W. Graves, R. Heese, E.D. Johnson, S. Krinsky, H. Loos, J. B. Murphy, G. Rakowsky, J. Rose, T. Shaftan, B. Sheehy, J. Skaritka, X. J. Wang, L. H. Yu, *Nucl. Instrum. and Meth. A* **507** (2003) 15.
- [26] I. Ben-Zvi, K. M. Yang, L. H. Yu, *Nucl. Instrum. and Meth. A* **318** (1992) 726 and L. H. Yu, I. Ben-Zvi, *Nucl. Instrum. and Meth. A* **393** (1997) 96.

3 Simulation of the BESSY HGHG-FEL

Ultra-short pulses from single-pass free electron lasers are *the tools* for future time-resolved experiments. Whereas the SASE approach produces short wavelength light at high peak power and excellent spatial mode, the poor temporal coherence and the intrinsic chaotic shot-to-shot variations of the process made the development of alternative approaches mandatory. In the High-Gain-Harmonic Generation (HG HG)-FEL [1], the light output is derived from a coherent subharmonic “seed” field. Consequently, the optical properties of the output reflect the high-quality characteristics of the seed. The benefit is a pulse with selectable short duration, a high degree of stability, and control of the central wavelength and bandwidth. The laser frequency is up-converted by a cascade of up to four HG HG-stages to reach the required photon energies [1, 2]. The so-called “fresh-bunch” technique [3] is employed to prevent the electron beam from heating effects of FEL interaction in the upstream stages leading to a reduction of the final output power and spectral quality.

All calculations have been performed with the time-dependent 3-D-simulation code GENESIS [4], modified to allow for seeding and the treatment of the higher harmonics [5].

3.1 The High-Gain-Harmonic Generation

HG HG cascades are required to convert the seed laser wavelength (tunable Ti:Sa laser) to the desired spectral range. Each stage consists of an undulator - dispersion - undulator structure. In the first undulator, the so-called modulator, the interaction of the electron beam with the radiation field from the external laser (later on with the radiation of the preceding stages) leads to an energy modulation of the electron beam with a period length equal to the seeding wavelength. The following dispersive section converts this energy modulation into a spatial modulation or bunching, which includes bunching on higher harmonics of the seed frequency. The fundamental of the second undulator, the so-called radiator, is set in resonance with a chosen harmonic of the modulator. The bunched beam then radiates at the harmonic wavelength with high efficiency. The radiator output is used as the seed for the next stage. The “final amplifier” follows the last radiator. It is seeded at the desired wavelength and the amplification process is brought to saturation.

The optimization of an HG HG line includes the proper choice of the harmonic cascade, the undulator parameters and the strength of the dispersive sections. In the following the steps taken during the optimization process are described.

3.1.1 Working Principles of a Multi-Stage HGHG-FEL

In a cascaded HGHG scheme the necessary seeding power for each stage is produced by adjusting the output power of the previous stage. The output power of the radiator is proportional to the square of the bunching factor b_n of the electron beam [1]:

$$p_{out} \sim b_n^2. \quad (3.1)$$

The bunching factor for the n^{th} harmonic is given by:

$$\begin{aligned} b_n &= \langle \exp(in\theta_i) \rangle = \exp\left(\frac{-1}{2}n^2\sigma_\gamma^2\left(\frac{d\theta}{d\gamma}\right)^2\right) J_n\left(n\Delta\gamma\frac{d\theta}{d\gamma}\right) \\ &= \exp\left(\frac{-1}{2}\sigma_\gamma^2\left(\frac{d\psi}{d\gamma}\right)^2\right) J_n\left(\Delta\gamma\frac{d\psi}{d\gamma}\right), \end{aligned} \quad (3.2)$$

where θ is the ponderomotive phase of the electron beam in the modulator, $\psi=n\theta$ the phase in the radiator, $\Delta\gamma$ the maximum energy modulation generated in the modulator, σ_γ the energy spread of the electron beam, $d\theta/d\gamma$ the strength of the dispersive section, and J_n the n^{th} order Bessel function.

Large bunching factors can be achieved, when the energy modulation impressed by the seed dominates the energy spread of the electron beam. Hence, for an optimum performance of an HGHG stage the energy modulation induced by the seed should fulfill the following inequality [3]:

$$\Delta\gamma \geq n\sigma_\gamma. \quad (3.3)$$

When the radiation parameters at the entrance of the modulator and the transverse size of the electron beam are matched, the energy modulation of the electron beam scales with the seed power p_{seed} , seed wavelength λ_s , the modulator length L_{mod} , the electron beam energy γ , and the undulator parameter K as:

$$\Delta\gamma \sim \frac{K}{\gamma} L_{mod} \sqrt{\frac{p_{seed}}{\lambda_s}}. \quad (3.4)$$

The modulator length should not exceed twice its power gain length in order to avoid an increase in electron beam energy spread due to spontaneous radiation. For a given electron beam energy, seed wavelength, and a fixed modulator length, the energy modulation $\Delta\gamma$ can be controlled by the undulator parameter or the seed power, both of which have technical limits. The dispersive section has to be adjusted according to the energy modulation reached in the modulator, taking into account the effective dispersion in the modulator and radiator. The total dispersive strength is given by [1, 2]:

$$\frac{d\psi}{d\gamma} \approx -\frac{n2\pi L_{mod}}{\lambda_{um}\gamma} + \left(\frac{d\psi}{d\gamma}\right)_{dis.sec.} - \frac{4\pi L_{rad}}{\lambda_{ur}\gamma}, \quad (3.5)$$

where λ_{um} and λ_{ur} are the modulator and radiator period length, and L_{rad} is the length of the radiator.

Due to the interaction of the electron beam with the seed, the total energy spread $\sigma_{\gamma,tot}$ of the electron beam entering the radiator is given by

$$\sigma_{\gamma,tot} = \sqrt{\sigma_{\gamma}^2 + \frac{(\Delta\gamma)^2}{2}}. \quad (3.6)$$

An increased energy spread causes an enhanced gain length and therefore extends the length of the radiator. The fresh-bunch technique is employed to limit the growth of energy spread from stage to stage in a cascaded HGHG-FEL. In this approach the seed pulse is significantly shorter than the electron bunch. As a result the harmonic generation process and the enlargement of the energy spread applies only to a fraction of the bunch. After passing the first HGHG-stage the resulting radiation is shifted to a fresh part of the electron bunch which has not been affected by the seed.

3.1.2 Layout of the HGHG Undulator Section

The BESSY HGHG multi-user FEL facility will consist of three undulator lines to cover the photon energy range from 24 eV to 1 keV ($51 \text{ nm} \geq \lambda \geq 1.2 \text{ nm}$). Each line is seeded by a tuneable fs-laser covering the spectral range 230 nm to 460 nm. The pulses are of Gaussian profile, the peak power is 500 MW and the rms pulse duration is about 15 fs. For more details see chapter 4. Out of the several combinations of harmonics that can be used to provide the desired wavelength range in each HGHG line, the one requiring the minimal number of stages is chosen.

The accessible harmonic content in the bunching drops off with rising harmonic numbers and photon energies limiting the usable harmonics to the first five. The fifth harmonic is used in the early stages where adequate power and thus bunching is obtained within acceptably short modulator and radiator lengths. Later stages use the third harmonics. The harmonic combination may be altered when the undulator gap, and thus the resonant wavelength, is varied to span the full wavelength range of interest.

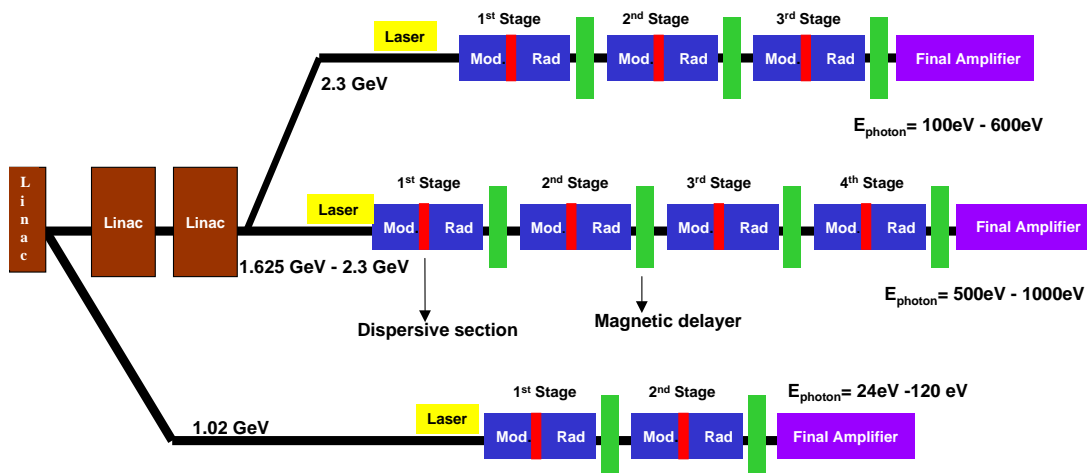


Fig. 3.1: The BESSY HGHG multi-user FEL-facility consists of three HGHG lines to cover the target wavelength range.

The “low-energy” (LE-)HGHG-FEL consists of two stages operating at a beam energy of 1.02 GeV and delivers photons in a spectral range of 24 eV to 120 eV. An energy of 2.30 GeV is chosen for the “medium-energy” (ME-) HGHG-FEL. A cascade of three stages covers the energy range of 100 eV to 600 eV. The “high-energy” (HE-)HGHG-FEL operates at variable electron beam energies of 1.625 GeV to 2.30 GeV. After four stages it delivers photon energies in the range from 500 eV to 1000 eV. Figure 3.1 shows a schematic view of the BESSY HGHG multi-user FEL facility.

Between each HGHG stage space is provided for magnetic chicanes which delay the electron bunch with respect to the radiation field to ensure that the radiation field always interacts with an unperturbed fresh part of the bunch in the next modulator. Furthermore, space is kept available for quadrupole magnets, steerers, diagnostic devices and phase shifters. Some of the larger radiators and the final amplifiers include magnetic elements between undulator-segments to focus the electron beam.

3.1.3 Optimization of Undulator Parameters

The resulting resonant wavelength of the FEL λ at the n^{th} harmonic depends on the undulator period length λ_u , the K-value, and the electron beam energy γ (in units of the electron's rest mass):

$$\lambda = \frac{1}{2\gamma^2 n} \lambda_u (1 + K^2). \quad (3.7)$$

The maximum achievable K-value is limited by the permanent magnet undulator technology. The minimal (nominal) gap is set to 10 mm according to impedance considerations. The minimum acceptable K-value is set to 0.8 as the interaction between the radiation field and the electron beam will suffer otherwise. Figure 3.2 shows the saturation length and power as functions of the K-value for the final amplifier of the medium-energy HGHG-FEL. The steep decline of FEL performance with decreasing K-parameter is obvious for $K < 0.8$.

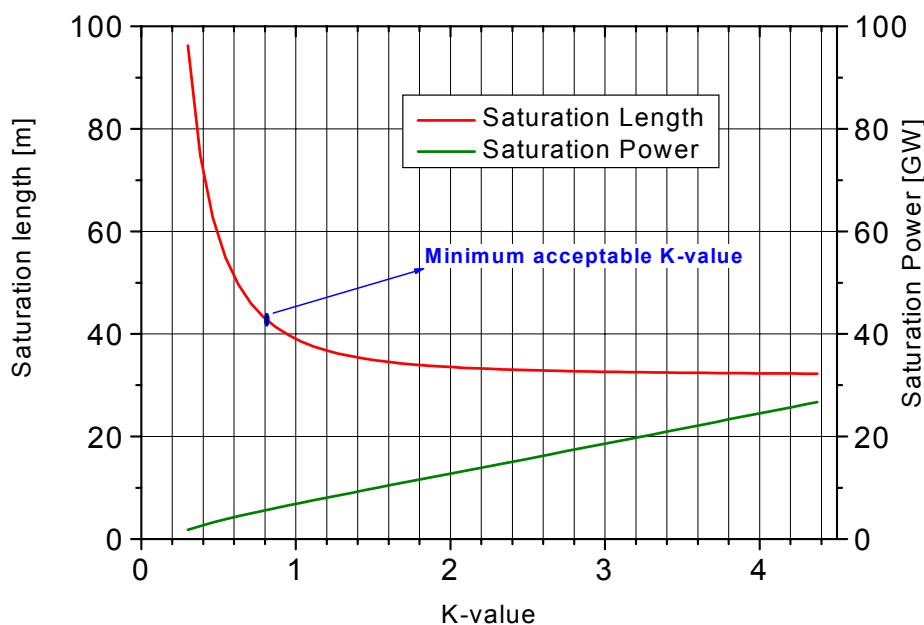


Fig. 3.2: Saturation length and power as functions of the K-value for the final amplifier of the medium-energy HGHG-FEL. The FEL performance declines with decreasing K-value.

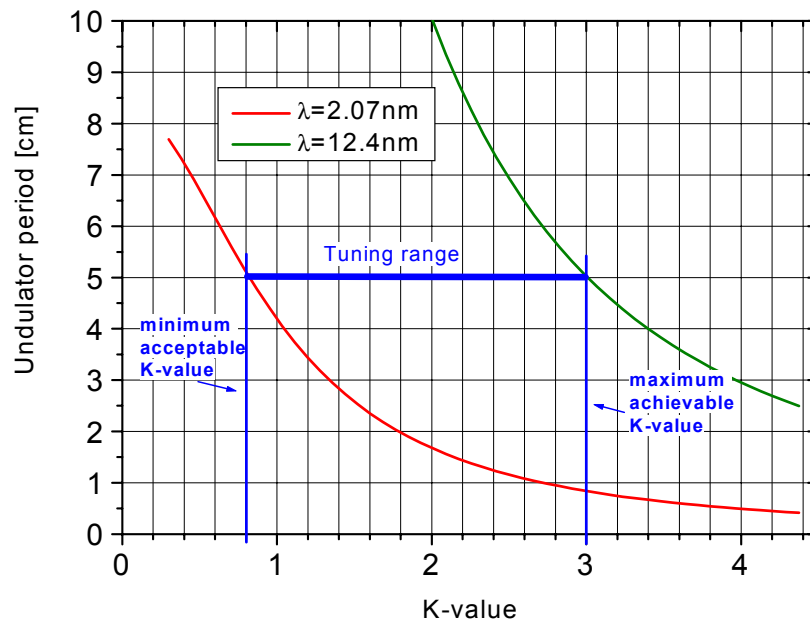


Fig. 3.3: The undulator period as function of K-value for the final amplifier of the medium-energy HGHG-FEL. The tuning range is limited by the minimum acceptable and maximum achievable K-value. With an undulator period of 5 cm the desired wavelength range can be covered by gap variation.

The undulator period length is chosen to permit spanning the desired wavelength range completely within the given range of K-parameter. Figure 3.3 shows the tuning range for the medium-energy HGHG-FEL as an example. Selecting the undulator period $\lambda_u \approx 5$ cm the desired wavelength range is fully covered. Once the period length λ_u is fixed the resonant wavelength can be altered by adjusting the gap of the undulator.

3.1.4 Optimization of the HGHG Stages Using Genesis

The 3-D FEL-code GENESIS is used to calculate the interaction between the electrons and the radiation field along the undulator. In the time-independent mode the program assumes an infinitely long, unstructured electron bunch and radiation field. In the time-dependent mode, the bunch is split into slices and the evolution of each slice interacting with the radiation field is calculated. This way, the power, the radiation spectrum, and the bandwidth are generated. The distribution of the particles in each slice and the radiation field are extracted at the end of each undulator. The extracted particle distribution includes the higher harmonics in the density modulation as well. GENESIS calculates the increase in the energy spread along the stages and allows one to simulate the dispersive

sections between the modulator and radiator. Using these features, extended simulation studies were carried out to determine the optimal lengths of the modulators and radiators and the strengths of the dispersive sections for the HGHG lines. Optimization criteria are: the modulator has to be long enough to achieve the necessary energy modulation according to equation (3.4); the strength of the dispersion has to be adjusted according to the energy modulation with respect to the total dispersive strength given in equation (3.5); the radiator length has to be suitably chosen to deliver the required power for the next stage, where the total energy spread generated in the modulator determines the efficiency of the radiator.

The main parameters of the undulators and dispersive sections for each HGHG line are listed in tables 3.1, 3.2 and 3.3. Listed are the undulator period length λ_u , the number of periods N, and the undulator length L.

Table 3.1: High-energy HGHG-FEL.

Stage	Modulator			Radiator		
	λ_u (mm)	N	L (m)	λ_u (mm)	N	L (m)
1	122	18	2.2	92	40	3.7
2	92	22	2.0	70	86	6.0
3	70	30	2.1	50	180	9.0
4	50	69	3.5	28.5	225	6.4
Final				28.5	630	18.0

Table 3.2: Medium-energy HGHG-FEL.

Stage	Modulator			Radiator		
	λ_u (mm)	N	L (m)	λ_u (mm)	N	L (m)
1	122	18	2.2	92	40	3.7
2	92	22	2.0	70	104	7.3
3	70	30	2.1	50	231	11.6
Final				50	393	19.7

Table 3.3: Low-energy HGHG-FEL.

Stage	Modulator			Radiator		
	λ_u (mm)	N	L (m)	λ_u (mm)	N	L (m)
1	80	20	1.6	62	56	3.5
2	62	26	1.6	50	69	3.5
Final				50	162	8.1

3.2 Performance Calculations

Modelling the amplification process in an HGHG line starts with defining the initial conditions of the electron bunch and the seed pulse that enter the first modulator. Using the results from the start-to-end simulations of the beam transport as described in chapter 7, the electron beam at the entrance to the HGHG lines is characterized by a normalized transverse slice emittance of 1.5π mm mrad, a relative energy spread of less than 0.02%, and a current of 1.75 kA at the “flat top”. The duration of the flat top is 730 fs. For the calculation an electron bunch with transverse Gaussian distribution is assumed. The nominal values of the electron beam parameters are listed in table 3.4.

Table 3.4: Electron beam parameters used in the simulations for the different BESSY FEL-lines.

Parameter	HE-FEL	ME-FEL	LE-FEL	Unit
Emittance ε_n	1.5	1.5	1.5	π mm mrad
Peak current I_{peak}	1.75	1.75	1.75	kA
Beam energy E	1.63-2.3	2.3	1.02	GeV
Rel. energy spread σ_E/E	0.01-0.014	0.01	0.02	%
Pulse width Δt	730	730	730	fs

A proper modeling of the seed radiation in the time domain is necessary in order to calculate correctly the pulse length and shape, as well as the spectrum and bandwidth of the output radiation. As described in section 3.1.1, the energy modulation of the beam is induced by the seed, and scales with the seed power and the seed wavelength. Contrary to a continuous seed pulse as used for the DUV-FEL [6, 7], in the case of a short Gaussian-shaped pulse the electrons do not experience the full peak-seed power during the entire

transition through the modulator. Since the integrated power experienced by electrons should be in the same order of magnitude to induce the same amount of bunching, the Gaussian-shaped seed pulse requires a higher peak power. For example, the 30 MW continuous power (wavelength of 800 nm) used for the DUV-FEL, with a modulator of 10 periods, corresponds - according to equation (3.4) - to a seed power of 90 MW for a seed wavelength of 266 nm for the same number of modulator periods. A Gaussian-shaped seed with 266 nm wavelength and 15 fs rms pulse length requires a peak power of 1.3 GW in an 10 period modulator to induce the same bunching. Since the modulator can be chosen longer for the 266 nm seed radiation, using a proper modulator of 18 periods a peak power of 400 MW is sufficient. Thus, for the simulations a radiation pulse with transverse and longitudinal Gaussian profile, 500 MW peak power, and 15 fs pulse length (rms) was used. The actual wavelength of the seed radiation provided by the laser is deduced from the desired final wavelength and the harmonic cascade. The laser seed profile in the time domain is generated with a modified version of the GENESIS output routine.

In spite of the short length of the modulators and radiators, see tables 3.1 - 3.3, the degradation of the unseeded fresh part of the bunch due to the emission of incoherent radiation cannot be neglected. The resulting increase of the energy spread and decrease in the central energy from stage to stage are shown in figure 3.4 for the high-energy case. The relative increase of the energy spread at the entrance of the second modulator is only 0.2% but increases to 4% at the fourth modulator.

The loss in the central energy at the entrance of the fourth modulator is about 0.45% which is larger than the bandwidth of about 0.2% of the fourth radiator and the final amplifier. This means that the following radiator and amplifier have to be readjusted to meet the resonance condition for the lower central energy. Note that the estimated coherent energy modulations of the bunches by wakefields (see also chapter 9) are a factor of 10 smaller than the incoherent synchrotron radiation effects. The loss of the electron beam quality causes a reduction in the maximum bunching and dilutes the spectral properties of the output radiation.

Figure 3.5 shows a comparison of the simplified approach, to start each stage with the initial electron parameters, and the more realistic approach of tracking the electrons through all the previous undulators. The degradation of the spectral radiation properties from stage to stage as well as the decrease of the maximum bunching are clearly visible. In the case of the last two stages, where the difference in maximum bunching is up to 30%, the higher bunching leads to a markedly higher total energy spread at the radiator entrance. This reduces the increase of the radiator output power in spite of the higher initial bunching as shown in figure 3.5 bottom left. The output power of the final amplifier calculated within the simple approach is a factor of three higher than the output power of the more realistic approach, as displayed in figure 3.6. This example demonstrates the clear necessity to calculate the FEL performance as realistically as possible. Therefore, for

the performance calculations of the BESSY FEL, the more realistic approach of tracking the electrons through all the previous undulators was used.

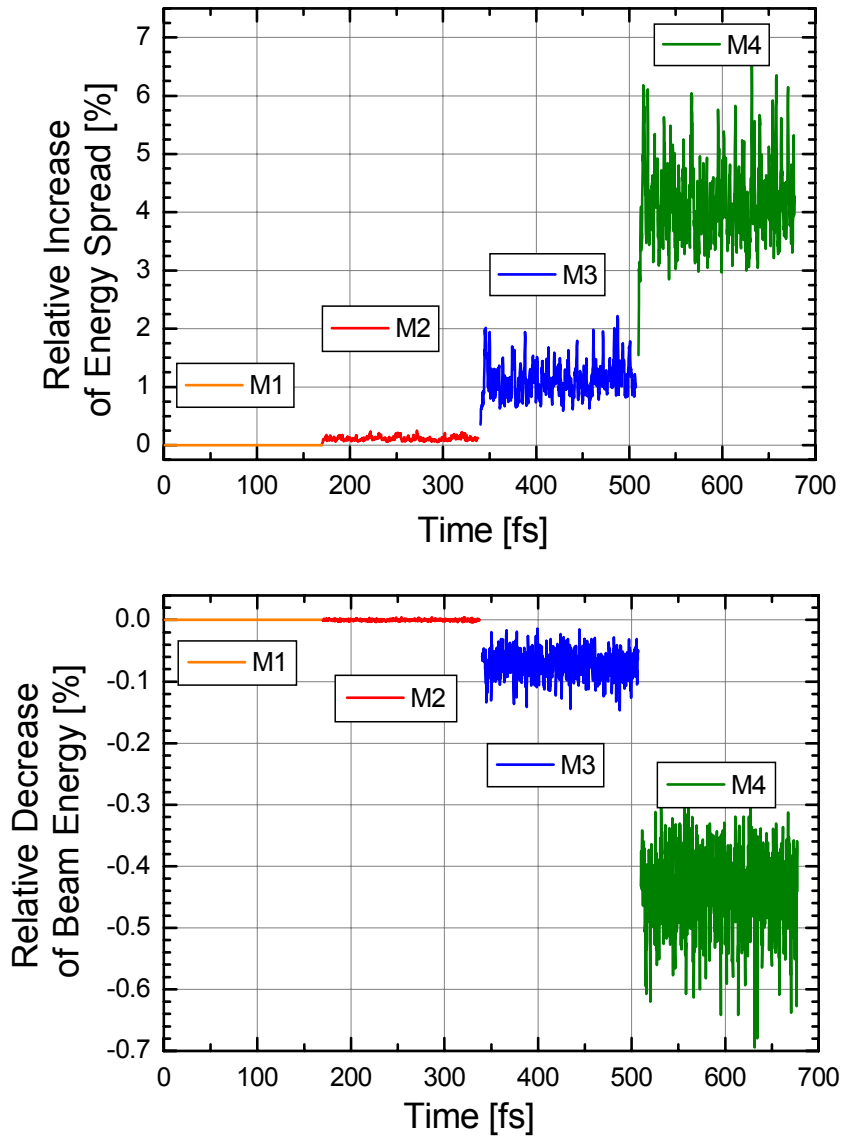


Fig. 3.4: Degradation of the unseeded part of the bunch for the high-energy HGHG-FEL. The relative changes in energy spread (top) and the central energy (bottom) are depicted at the entrance of modulators, M1 to M4.

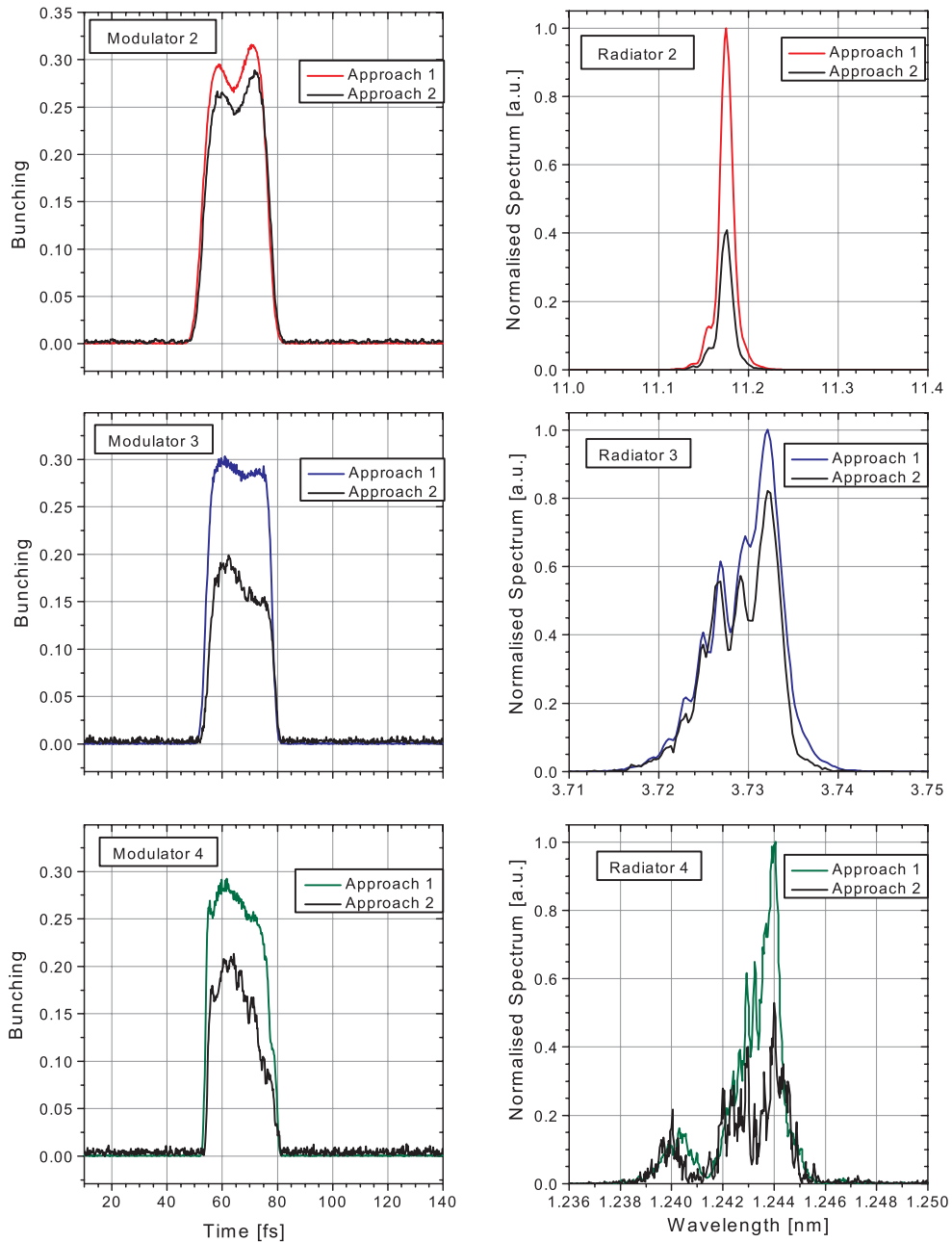


Fig. 3.5: A comparison of the simplified *Approach 1*, starting in each stage with the initial electron parameters, and *Approach 2*, tracking the electrons through all previous undulators; the bunching after the dispersion section and the spectrum of the radiation in each stage are shown.

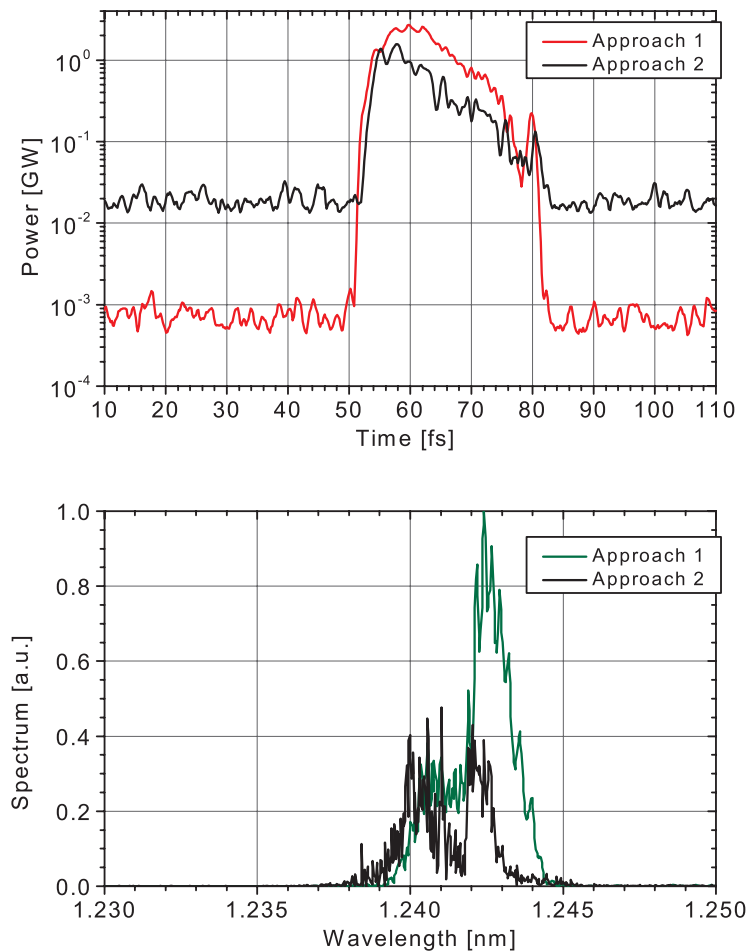


Fig. 3.6: A comparison of the simplified *Approach 1* and the realistic *Approach 2*; time-resolved power distribution (top) and the spectral power distribution (bottom).

For the optimization of the HGHG-FEL performance, the adjustment of the bunching, by setting the modulator length and the dispersion strength, is of major importance. The laser seed interacts with electrons at the trailing part of the flat top. Due to the slippage effect only a part of the interacting electrons experience the full power of the Gaussian-shaped seed as mentioned before. Optimizing the modulator length and dispersive section to a somewhat reduced power-level, the output of the following radiator can be maximized. In this case, the electrons at the centre of the bunch, experiencing the full power sufficiently long, are somewhat overbunched.

Figure 3.7 shows the bunching after the first dispersion section for the high-energy HGHG-FEL. The overbunching causes a power dip in the radiation pulse provided by the first radiator, as shown in figure 3.8a. Figure 3.8b shows the corresponding radiation spectrum. The overbunched electrons perform synchrotron oscillations in the ponderomotive bucket. The resulting modulation of the emitted radiation frequency generates sidebands [8]. The more electrons are overbunched, the stronger is the growth of the sidebands. This effect repeats itself in the following stages, where the slippage shifts the sidebands to one side. In this way the number of sidebands in the spectrum adds up from stage to stage. The higher the harmonic numbers in the cascade, the stronger are the sidebands. For example in the case of the medium-energy HGHG-FEL the sidebands for $\lambda = 2.07$ nm with harmonic numbers 5·5·5, figure 3.13, are much stronger than for $\lambda = 12.4$ nm with harmonic numbers 3·3·3, figure 3.12. The sidebands can be avoided by optimizing the stages for the seed peak power. In this case, the output of the following radiator is reduced and the bunching distribution is of more Gaussian shape. An example of such a case optimized for spectral purity is shown in figure 3.9, where the power and spectral distributions of a purity optimized and a power optimized case are displayed in the same graph for comparison. The sidebands of the purity optimized case are only half of those of the power optimized case.

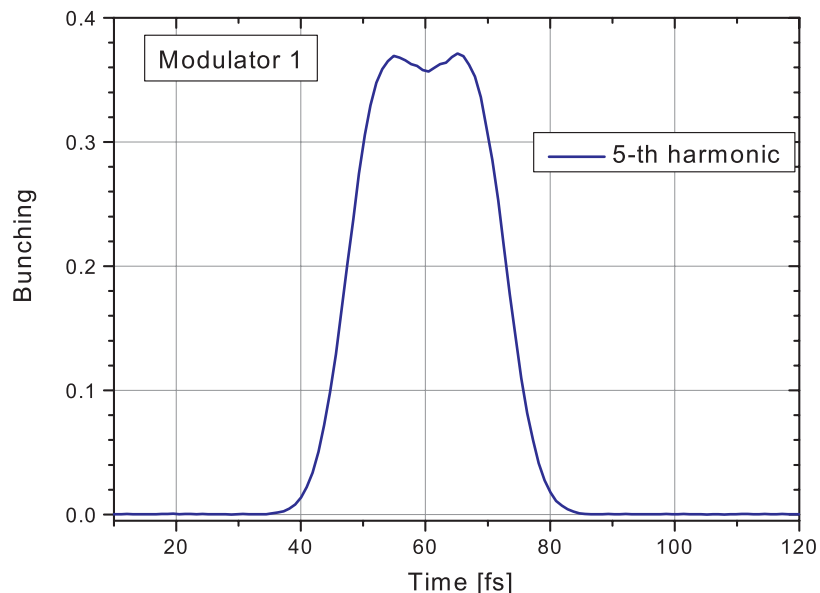


Fig. 3.7: Bunching on the fifth harmonic after the first dispersion section for the high-energy HGHG-FEL.

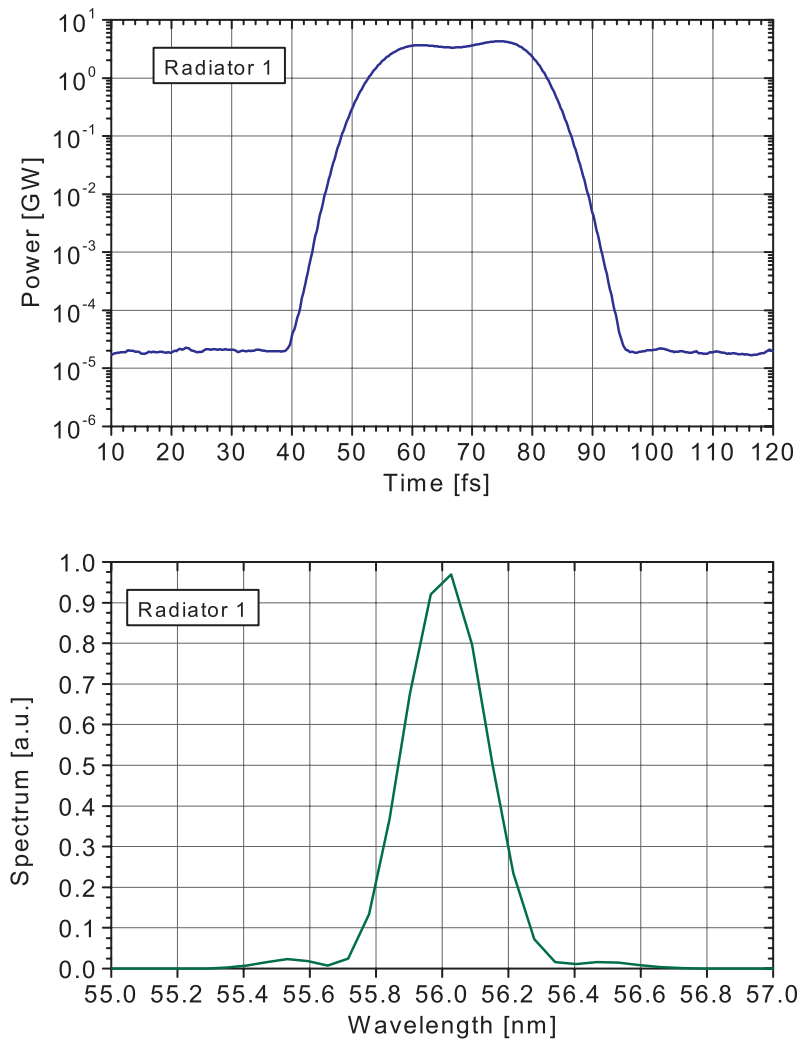


Fig. 3.8: Simulation results for the first radiator of the high-energy HGHG-FEL: a) time resolved power distribution (top) and b) spectral power distribution (bottom).

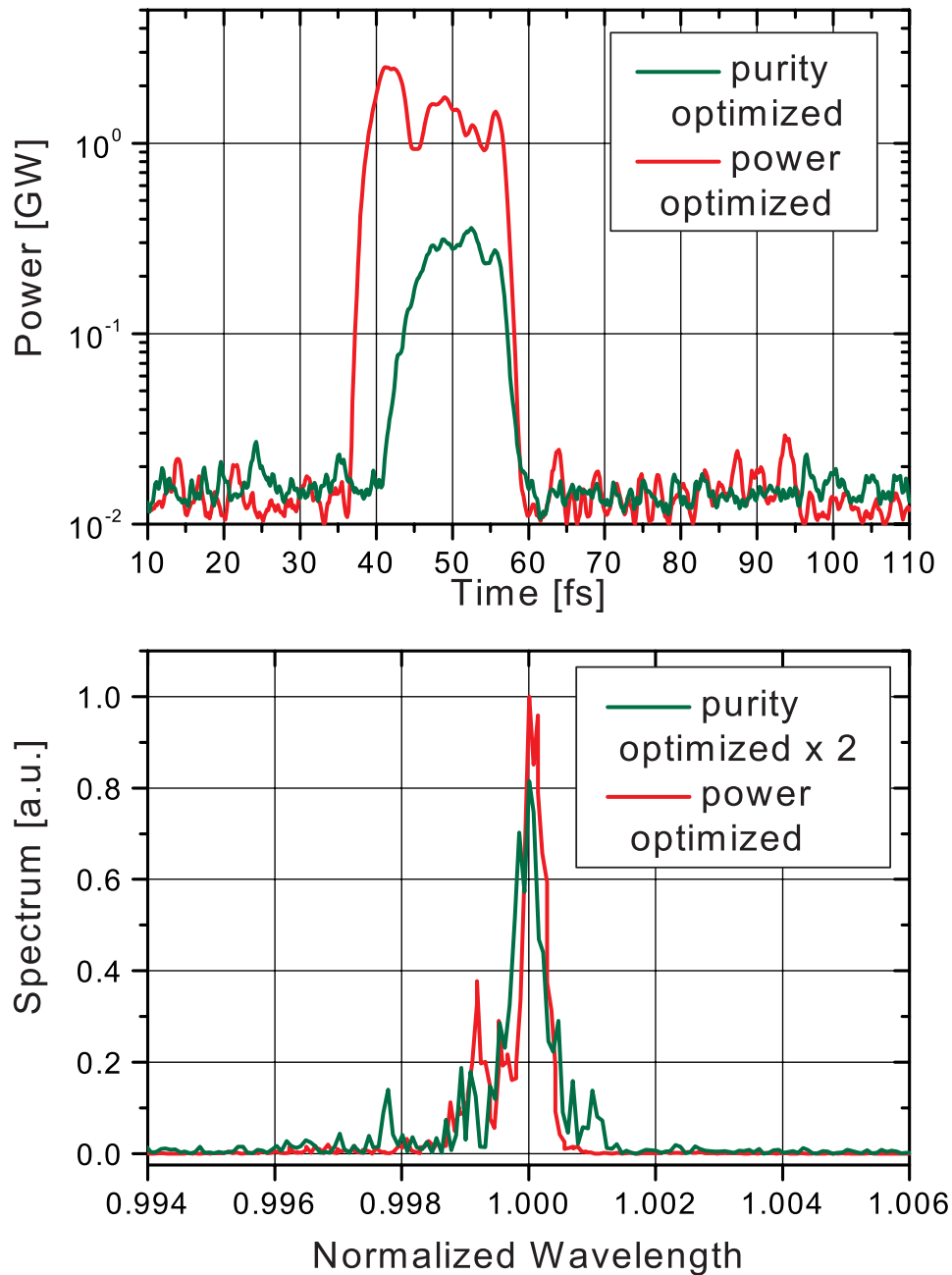


Fig. 3.9: Simulation results for the medium-energy HGHG-FEL, power and spectral distributions of a purity-optimized case, and a power-optimized case. The sidebands of the purity optimized case are only half of those of the power optimized case.

The details of the cascades for the boundary wavelengths of each HGHG line are summarized in the tables 3.5 to 3.10. Figures 3.10 to 3.14 display the simulation results for the corresponding final amplifiers. All these examples were optimized with respect to maximum output power.

Table 3.5: High-energy HGHG-FEL at an output wavelength of 1.24 nm, beam energy 2.3 GeV. Listed are the seed laser wavelength λ_{seed} , harmonic number, radiator output wavelength λ_{rad} and output power.

Stage	Modulator		Radiator	
	λ_{seed} (nm)	harm. no.	λ_{rad} (nm)	Power (GW)
1	297.50	5	55.90	4.5
2	55.90	5	11.18	1.8
3	11.18	3	3.73	1.9
4	3.73	3	1.24	0.1
Final			1.24	1.5

Table 3.6: High-energy HGHG-FEL at an output wavelength of 2.48 nm, beam energy 1.63 GeV

Stage	Modulator		Radiator	
	λ_{seed} (nm)	harm. no.	λ_{rad} (nm)	Power (GW)
1	334.80	5	66.96	3.9
2	66.96	3	22.32	4.0
3	22.32	3	7.44	0.5
4	7.44	3	2.48	0.1
Final			2.48	1.3

Table 3.7: Medium-energy HGHG-FEL at an output wavelength of 2 nm, beam energy 2.3 GeV

Stage	Modulator		Radiator	
	λ_{seed} (nm)	harm. no.	λ_{rad} (nm)	Power (GW)
1	258.25	5	51.65	1.6
2	51.65	5	10.33	1.0
3	10.33	5	2.07	0.2
Final			2.07	1.5

Table 3.8: Medium-energy HGHG-FEL at an output wavelength of 12.4 nm, beam energy 2.3 GeV.

Stage	Modulator		Radiator	
	λ_{seed} (nm)	harm. no.	λ_{rad} (nm)	Power (GW)
1	334.80	3	111.60	5.5
2	111.60	3	37.20	2.7
3	37.20	3	12.40	1.5
Final			12.40	9.0

Table 3.9: Low-energy HGHG-FEL at an output wavelength of 10.3 nm, beam energy 1.02 GeV.

Stage	Modulator		Radiator	
	λ_{seed} (nm)	harm. no.	λ_{rad} (nm)	Power (GW)
1	258.25	5	51.65	2.5
2	51.65	5	10.33	0.6
Final			10.33	3.5

Table 3.10: Low-energy HGHG-FEL at an output wavelength of 51 nm, beam energy 1.02 GeV.

Stage	Modulator		Radiator	
	λ_{seed} (nm)	harm. no.	λ_{rad} (nm)	Power (GW)
1	459.00	5	153.00	6.0
2	153.00	5	51.00	7.5
Final			51.00	14.0

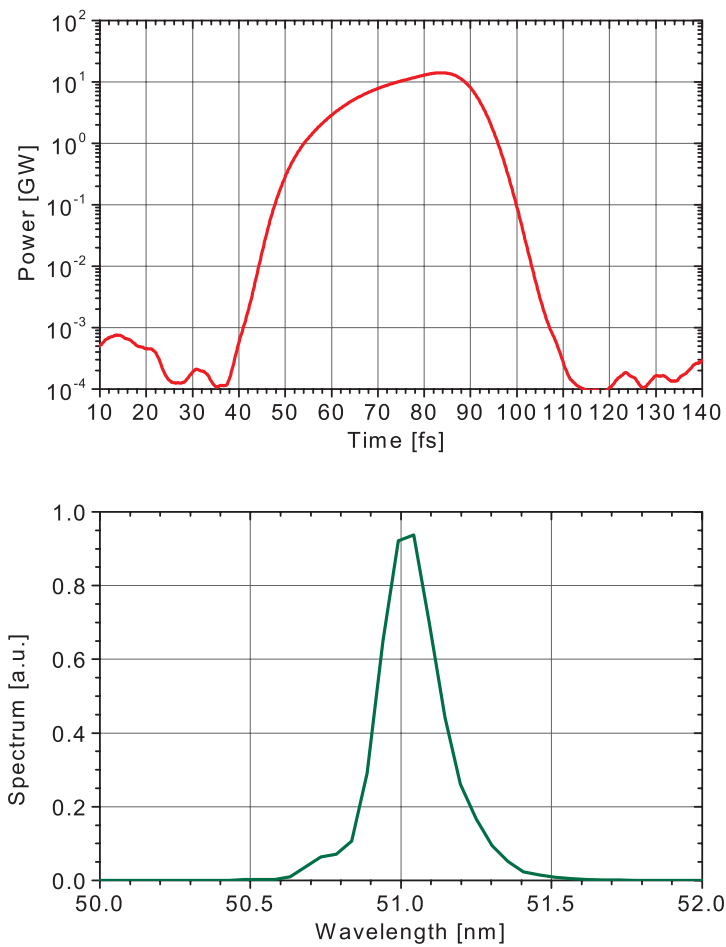


Fig. 3.10: Simulation results for the low-energy HGHG-FEL at an output wavelength of $\lambda = 51$ nm. Calculated are the time resolved power distribution (top) and the spectral power distribution (bottom).

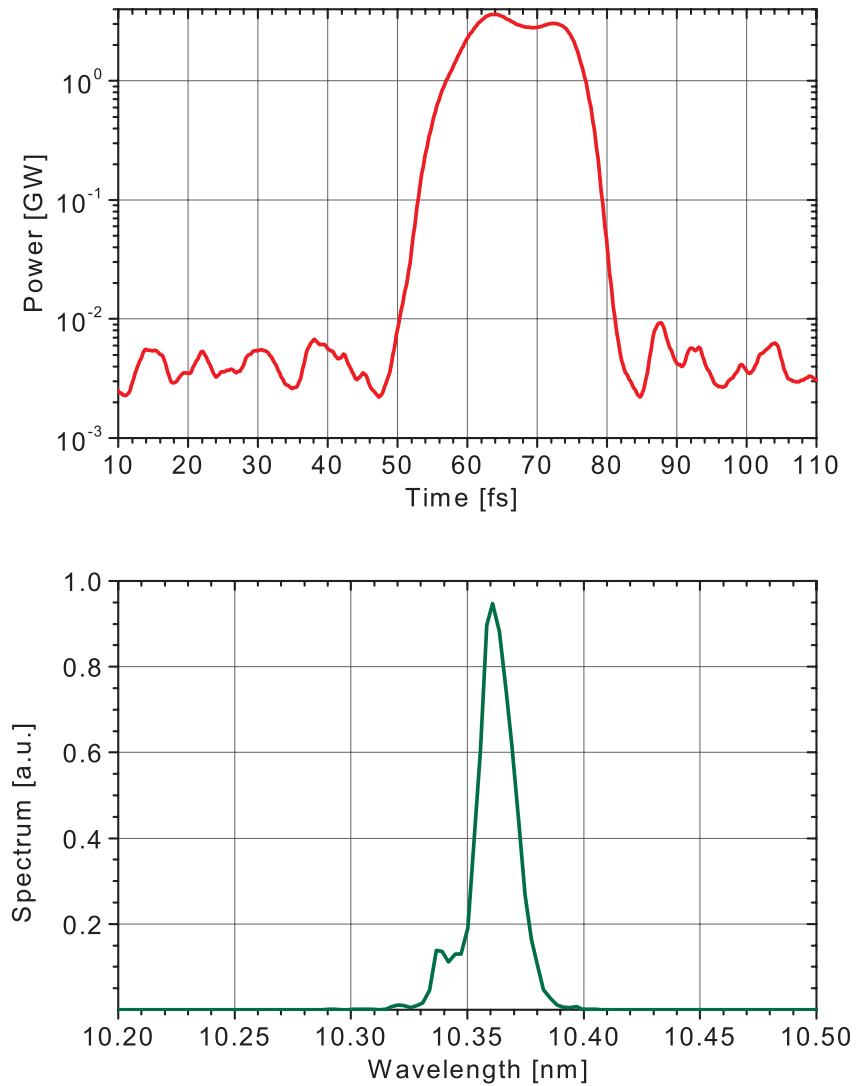


Fig. 3.11: Simulation results for the low-energy HGHG-FEL at an output wavelength of $\lambda = 10.3$ nm. Calculated are the time resolved power distribution (top) and the spectral power distribution (bottom).

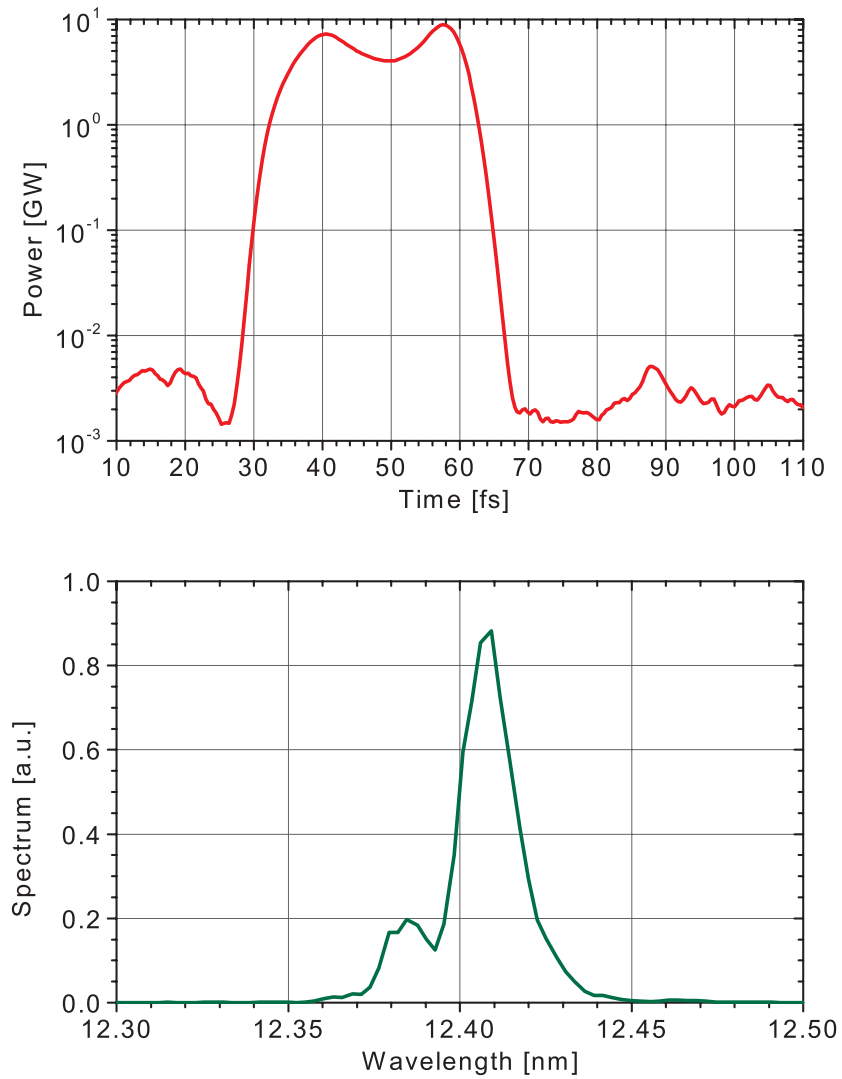


Fig. 3.12: Simulation results for the medium-energy HGHG-FEL at an output wavelength of $\lambda = 12.4$ nm. Calculated are the time resolved power distribution (top) and the spectral power distribution (bottom).

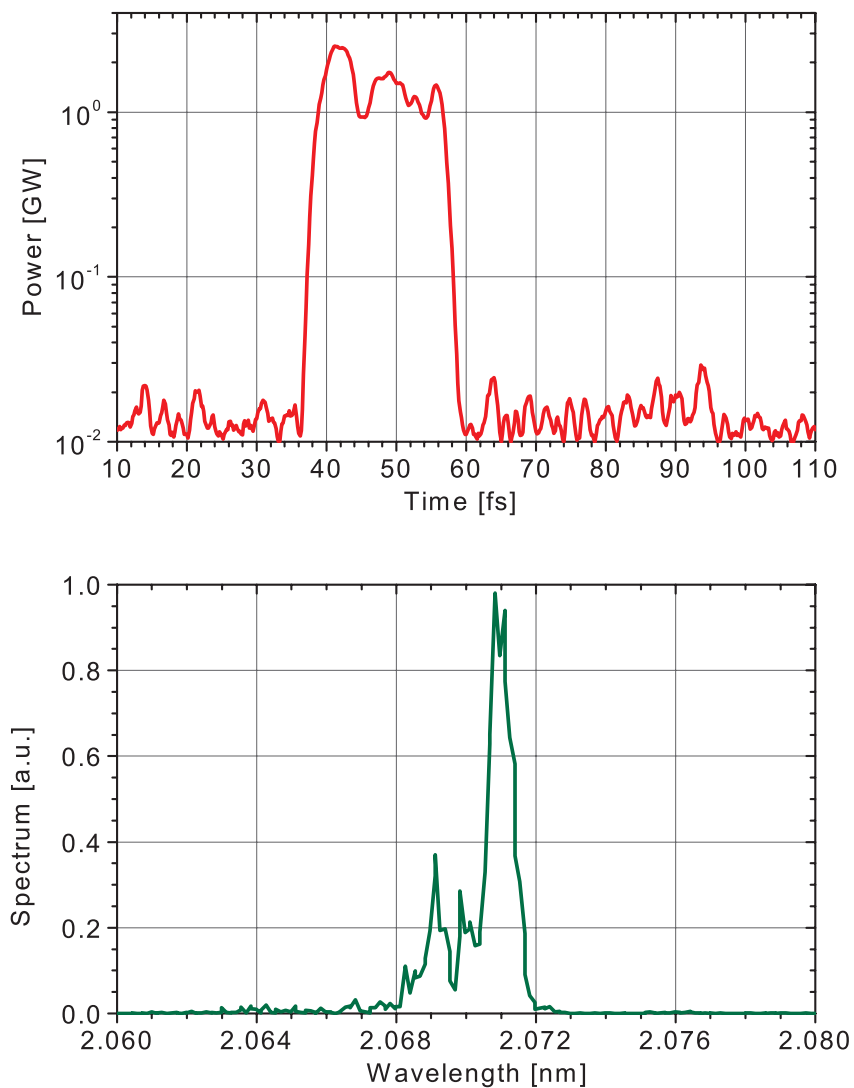


Fig. 3.13: Simulation results for the medium-energy HGHG-FEL at an output wavelength of $\lambda = 2.07$ nm. Calculated are the time resolved power distribution (top) and the spectral power distribution (bottom).

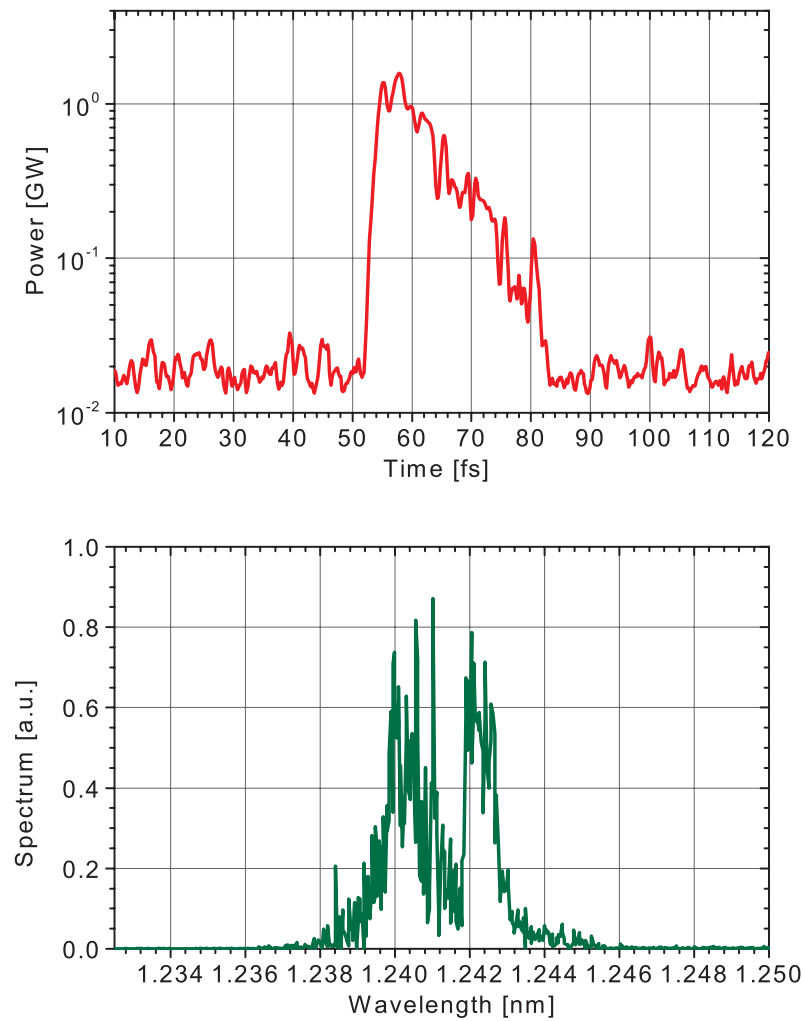


Fig. 3.14: Simulation results for the high-energy HGHG-FEL at an output wavelength of $\lambda = 1.24$ nm. Calculated are the time resolved power distribution (top) and the spectral power distribution (bottom).

These simulations for the BESSY FEL clearly show the expected advantages of the HGHG scheme. The output pulse lengths of about 30 fs fwhm correspond to the seed pulse lengths. Compared to SASE-FEL outputs the spectra are pure. The bandwidth is determined by the bandwidth of the final amplifier as expected for the 15 fs rms seed pulse length. All performance calculations so far have been performed without tapering the undulators. It is expected that the HE-FEL power output in particular will benefit from tapering the long final amplifier. The HGHG scheme presented here will undergo still further improvements and optimizations to be done in the detailing R&D phase of the project.

3.3 Future HHG-Laser-Seeded FELs

In a cascaded multi-stage HGHG-FEL, the loss of electron beam quality and the accumulation of the sidebands as described, lead to a decline of the radiation output quality with increasing number of stages. The properties of the output radiation, however, can be further optimized by decreasing the number of stages using shorter seed wavelengths.

Present-day High-Harmonic-Generation (HHG) laser techniques deliver wavelengths of a few ten nanometers [9]. Considering the work in progress [10] it is realistic to assume adequate high-peak power HHG-seed lasers in the future. The layout of the BESSY HGHG-FEL is designed in such a way that an HHG-seed laser can be included easily once suitable HHG lasers are available.

An example for an HHG-seeded HGHG-FEL is shown in figure 3.15. A 31 nm HHG-seed with a peak power of 300 MW and fwhm pulse length of 6 fs in a cascade of two stages leads to an output wavelength of 1.24 nm. The improved purity of the spectral power distribution is clearly visible.

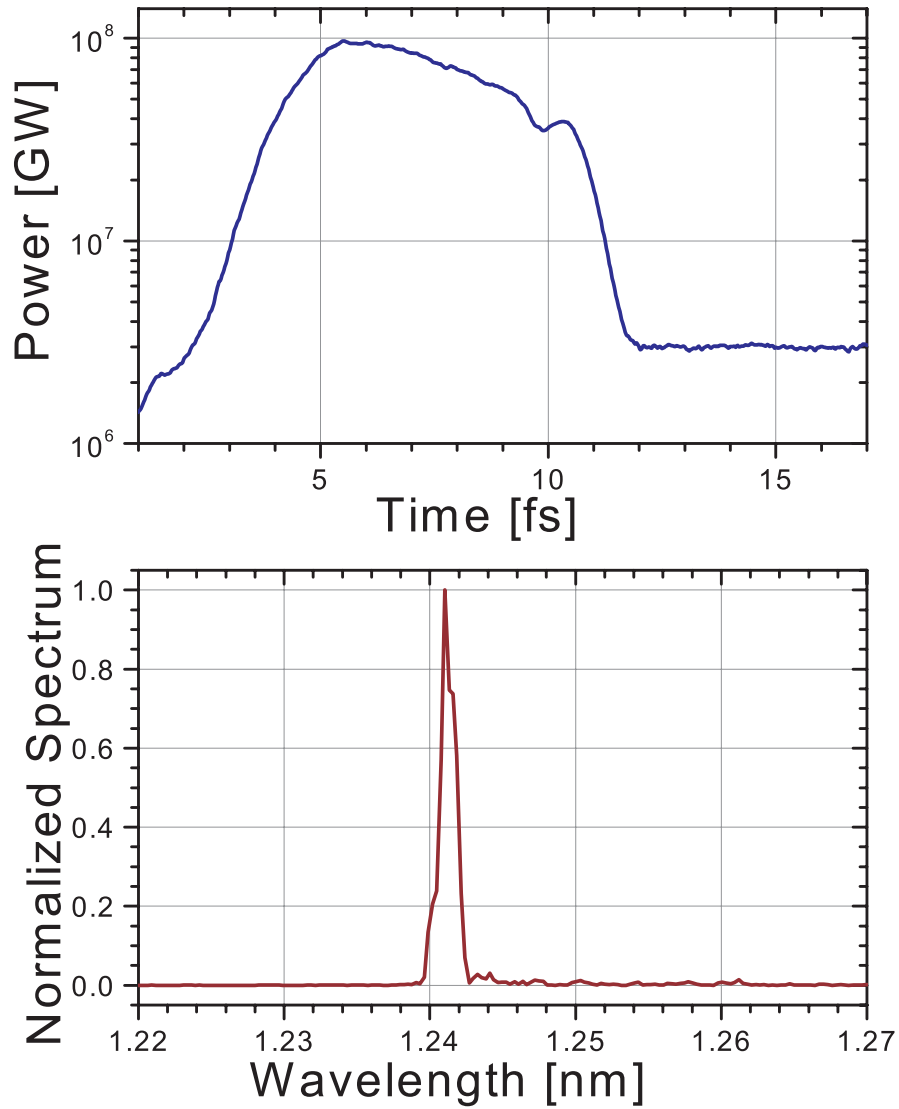


Fig. 3.15: Simulation results for a HG-seeded two stage high-energy HGHG-FEL, output wavelength is $\lambda_s = 1.24$ nm. The time resolved power distribution (top) and the spectral power distribution (bottom) are calculated for a 31 nm HHG-seed with a peak power of 300 MW and an fwhm pulse length of 6 fs.

3.4 Tolerance Studies

Tolerance studies for the BESSY HGHG-FEL with respect to undulator errors and electron beam parameter variations have been performed. These simulation studies, as well as the simulations in [1, 11] show, that the properties of an HGHG-FEL strongly depend on the details of the specific layout, rather than follow the simplified analytical expressions derived from 1-D FEL theory [2, 12].

The allowable tolerances were studied using the code GENESIS in the time-dependent mode. In this mode simulation runs of cascaded structures take days on multi-processor platforms. Thus, systematic parameter scans or statistical investigations were extremely time-consuming. The studies were restricted to representative cases, which indicate that the required tolerances can be met for the BESSY FEL.

Calculations for the two-stage, low-energy BESSY HGHG-FEL were carried out varying beam emittance, energy spread, peak current and seed power by typically 10% as compared to the design values. Simulations assuming correlated and uncorrelated undulator field errors have been performed to illuminate the required hardware tolerances and to quantify the sensitivity of the solutions presented.

At this point, it is worthwhile to stress the difference between time independent errors and pulse-to-pulse fluctuations of the parameters. While steady state offsets generally can be counteracted, e.g. by retuning the dispersion strength, parameters varying on a shot-to-shot basis can only be compensated for by intelligent feed-forward systems.

To a certain extent, earlier results from tolerance studies on SASE-FELs can be transferred to the HGHG final amplifiers (FA), as the amplification reaches the exponential regime, contrary to the modulators and radiators which are operating in the linear regime. In the SASE process the bunching builds up slowly and is easily disturbed by fluctuations in the electron beam parameters. In the HGHG-FEL, however, the initial bunching is generated by the seed field. In this respect the FA is relatively insensitive to electron beam fluctuations. On the other hand, the output power of the FA does also depend on the electron beam parameters and is reduced when the beam parameters are not well matched. For similar reasons the FA should be tolerant to undulator field errors. But again, this has to be correlated to the reduced quality of the seed spectrum taking into account that all effects depend on the actual wavelength under consideration.

The concept of saturation length is less applicable to an HGHG design, as different parts of the bunch saturate at largely diverging lengths due to the fresh bunch technique and the seeding. The final amplifiers are relatively short (< 20 m for the BESSY FEL) so that the possibility of opening gaps of undulator segments in order to meet the optimum is usually too crude. However, all results presented here are taken at the end of the planned devices, thus, the simulations are more likely to show pessimistic results.

3.4.1 Sensitivity towards Electron Beam Parameters

3.4.1.1 Beam Energy Spread

The energy spread of the electron beam is modified during the passage through the undulators due to the emission of spontaneous synchrotron radiation. Furthermore, an additional energy modulation is induced in the beam by the interaction with the seed field. The imprinted modulation depth, $\Delta\gamma$, has to fulfill the relation $\Delta\gamma \geq n\sigma_\gamma$, with n the harmonic number. Therefore, the larger the beam energy spread, σ_γ , the harder it is to modulate the beam at the seeding frequency. A smaller energy spread in the radiator supports the amplification process, as more particles fulfill the resonance condition.

GENESIS runs of the low-energy HGHG-FEL have been performed using the nominal energy spread $\sigma_\gamma = 0.2$ MeV and with a 10% reduced energy spread. The results are displayed in figure 3.16. The smaller energy spread leads to a slightly higher bunching rate at the 5th harmonic in modulator 1. As a consequence, radiator 1 delivers more power which in turn supports the bunching in modulator 2. The gain in spectral power in radiator 2 is less than that in radiator 1. Part of the power is shifted to the two sidebands. The particles at the center of the prebunched part of the beam are already overbunched and enhance the sidebands. The particles at the edges of the bunch face optimal conditions and start to radiate at the central frequency. The same effect repeats itself in the final amplifier. The total power emitted from the final amplifier in both cases is practically the same since the FA reaches saturation in both cases. By reducing the strength of the dispersion in modulator 1 and 2, the power in the sidebands could be shifted to the central peak adding more power to the central peak of the spectrum.

Thus, changes in the energy spread of the order of a few percent will not severely affect the performance of this HGHG line.

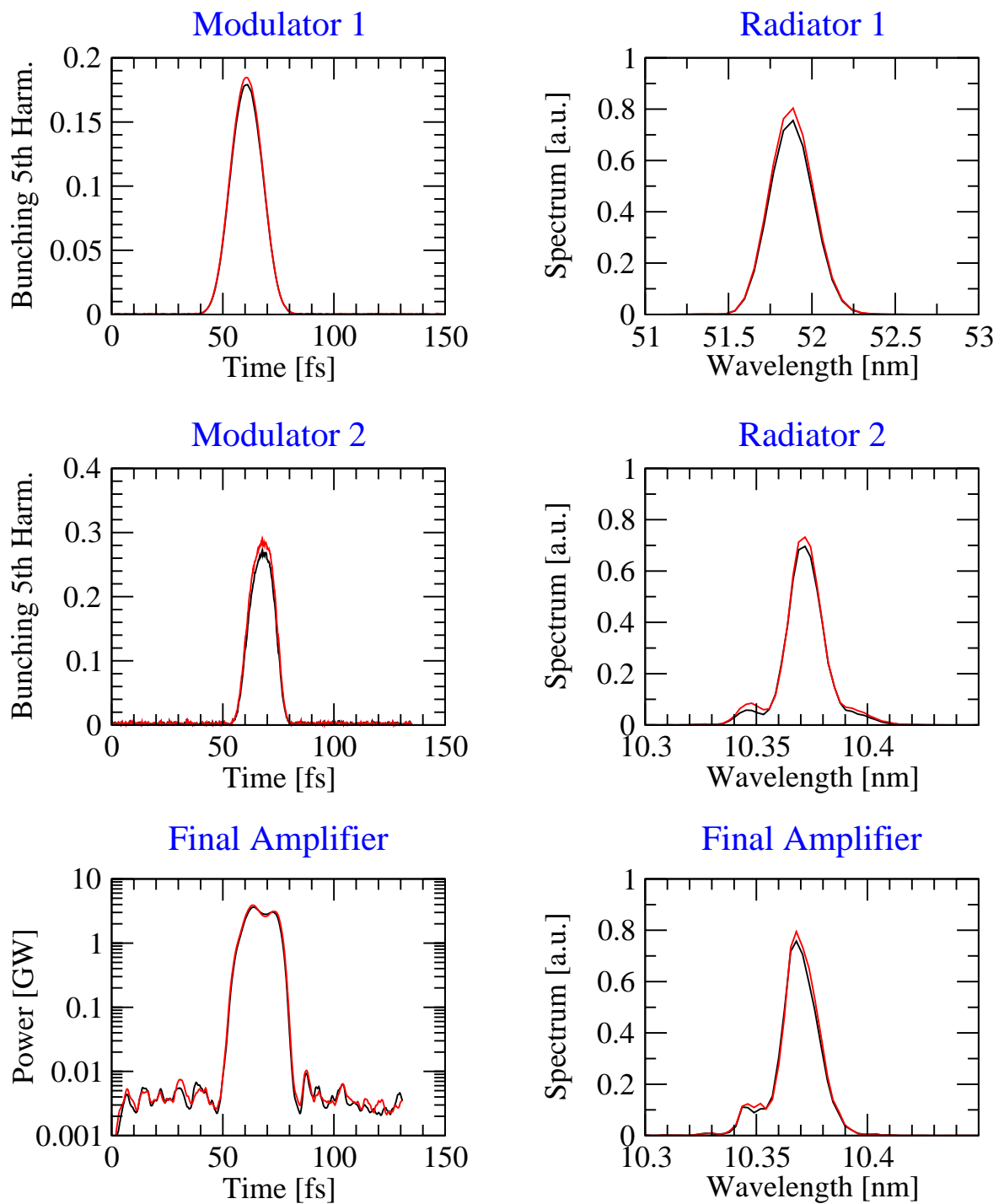


Fig. 3.16: Evolution of bunching and radiation in the low-energy HGHG line for two beams with different energy spread, $\sigma_\gamma = 0.2$ MeV (black) and $\sigma_\gamma = 0.18$ MeV (red).

3.4.1.2 Beam Emittance

A decrease in the transverse beam emittance causes a decrease in the effective energy spread induced to the beam during its passage through the undulator. The effect depends on ε_n/λ , where ε_n is the normalized emittance, and λ is the resonant wavelength. In addition, the amplification process in the radiator profits from the reduced emittance, as the power on-axis is increased due to the smaller beam dimensions.

Figure 3.17 shows the results of GENESIS calculations of the low-energy FEL line, for the design slice emittance of $\varepsilon_n=1.5 \pi$ mm mrad, and for an emittance reduction of 10%. While the difference in emittance is not large enough to change the bunching in the first modulator, the output of the adjacent radiator is enhanced by 6%. Modulator 2 is seeded with higher power and, thus, its bunching rate increases. Radiator 2 starts with a higher bunching rate and additionally profits from the smaller emittance. This adds up to an increase in spectral power by nearly 30%. However, the enhancement of the sidebands in the spectrum of radiator 2 indicates that the electrons are overbunched in modulator 2. As mentioned above, this could be counteracted by reducing the strength of the dispersive section. Despite the fact that the amplification process in the final amplifier profits from the reduced emittance, only a third of the surplus in seeding power is conserved through the amplifier, and enhances the spectral power by only 10%. In the amplifier the high gain region is reached, and other parameters, such as the total energy spread, dominate the process. The increase in spectral power is comparable to the reduction in emittance in this HGHG-FEL line.

3.4.1.3 Beam Current

Figure 3.18 shows the results of simulations, increasing the electron beam current by 10% compared to the design value. An enhanced beam current increases the spontaneous modulator radiation and, thus, the bunching rate in the first modulator, as can be seen in the upper left graph of Figure 3.18. The output of the following radiator is enhanced by nearly 40%, also supported by the higher current. However, this leads to a strong overbunching in modulator 2 that can be identified by the flattened top of the red curve, and by the fact that the surplus in bunching does not increase, in spite of the additional seeding power. The sidebands are strongly enhanced in the spectrum of radiator 2 and the peak power is reduced. In the final amplifier the advantage of the power concentration on-axis dominates and there is a minor improvement in spectral power.

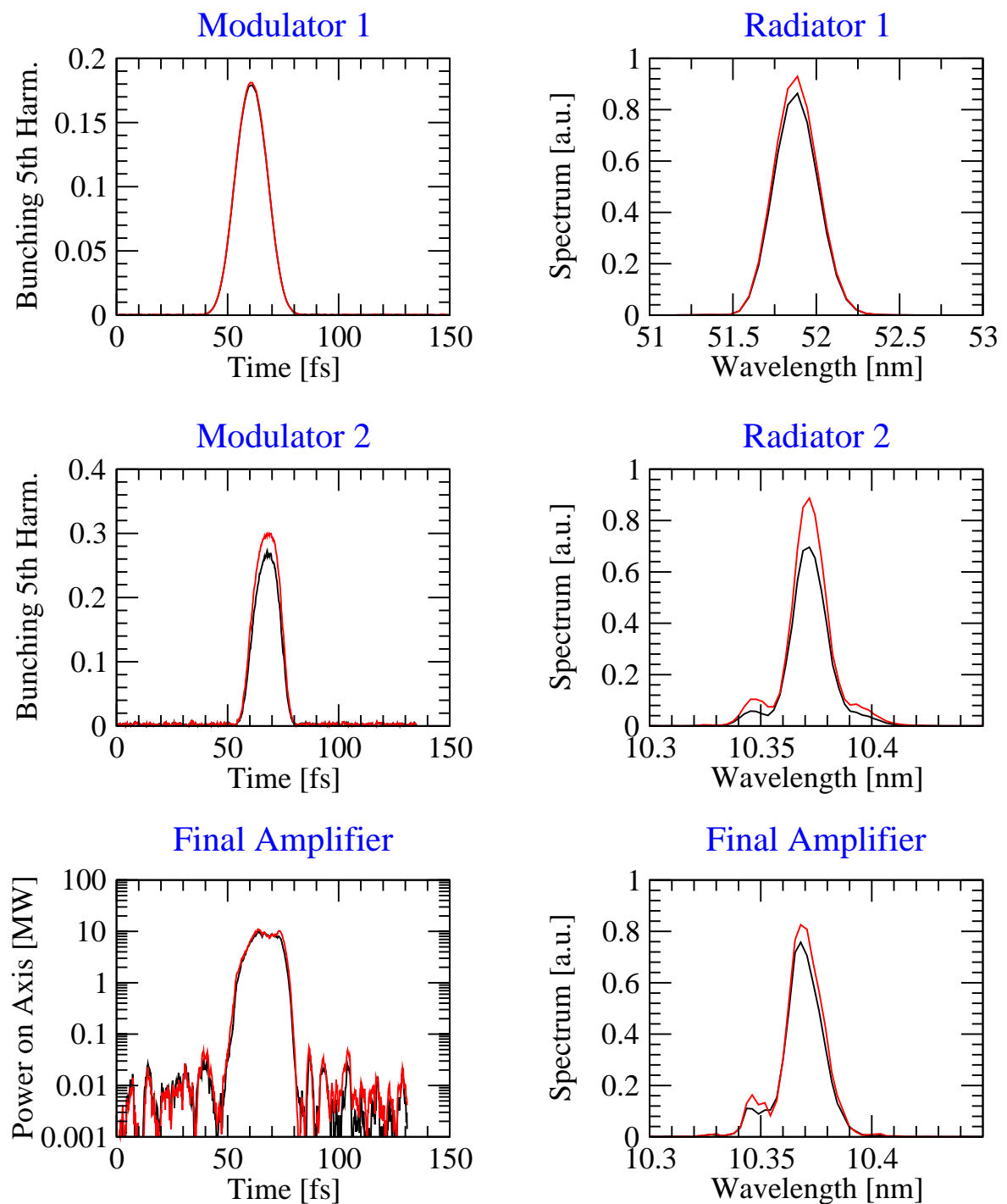


Fig. 3.17: Evolution of bunching and radiation in the low-energy HGHG line for beam emittances of 1.5π mm mrad (black) and 1.35π mm mrad (red).

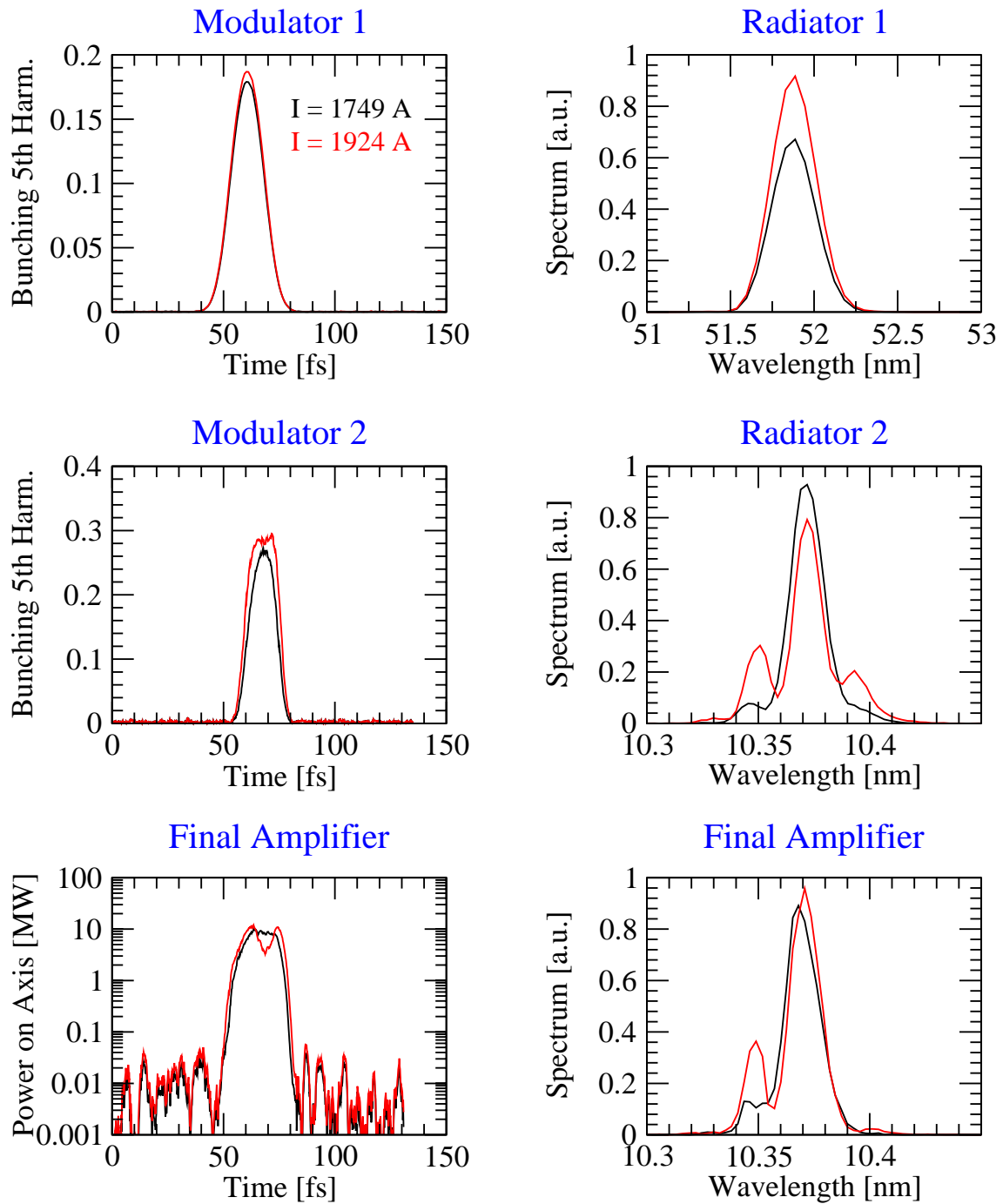


Fig. 3.18: Evolution of bunching and radiation in the low-energy HGHG line for beams with peak currents differing by 10%

3.4.1.4 Seed-Laser Power

The effect of power fluctuations in the seed laser has been calculated using seed laser powers differing by $\pm 10\%$ from the nominal value. The 10% difference in seed power gives rise to a 30% stronger bunching rate in the first modulator, figure 3.19, and to a 40% increase in the power emitted from radiator 1. This increase is not repeated in the second stage. The energy modulation achieved in a modulator is a function of the square root of the seed power, the modulator length, and the K-value. Although the difference in seed power grows, the K-value of the second modulator is less than half of the K-value of modulator 1. The remaining excess in bunching on the 5th harmonic gets lost due to the strong overbunching at the center of the stimulated part of the bunch. Thus, the difference in the output is small enough not to make much of a change in radiator 2. The dip in the power spectrum for the + 10% case results from the dip in the bunching distribution. For the - 10% case the same dip develops in radiator 2. The final amplifier emits less power in the case of the stronger seeding power, although the power on-axis is of comparable strength. The green curve in the power spectrum displays the result for the reference seed. Without readjusting the dispersion section after modulator 2, a surplus in seed power is more damaging than a reduction in this case.

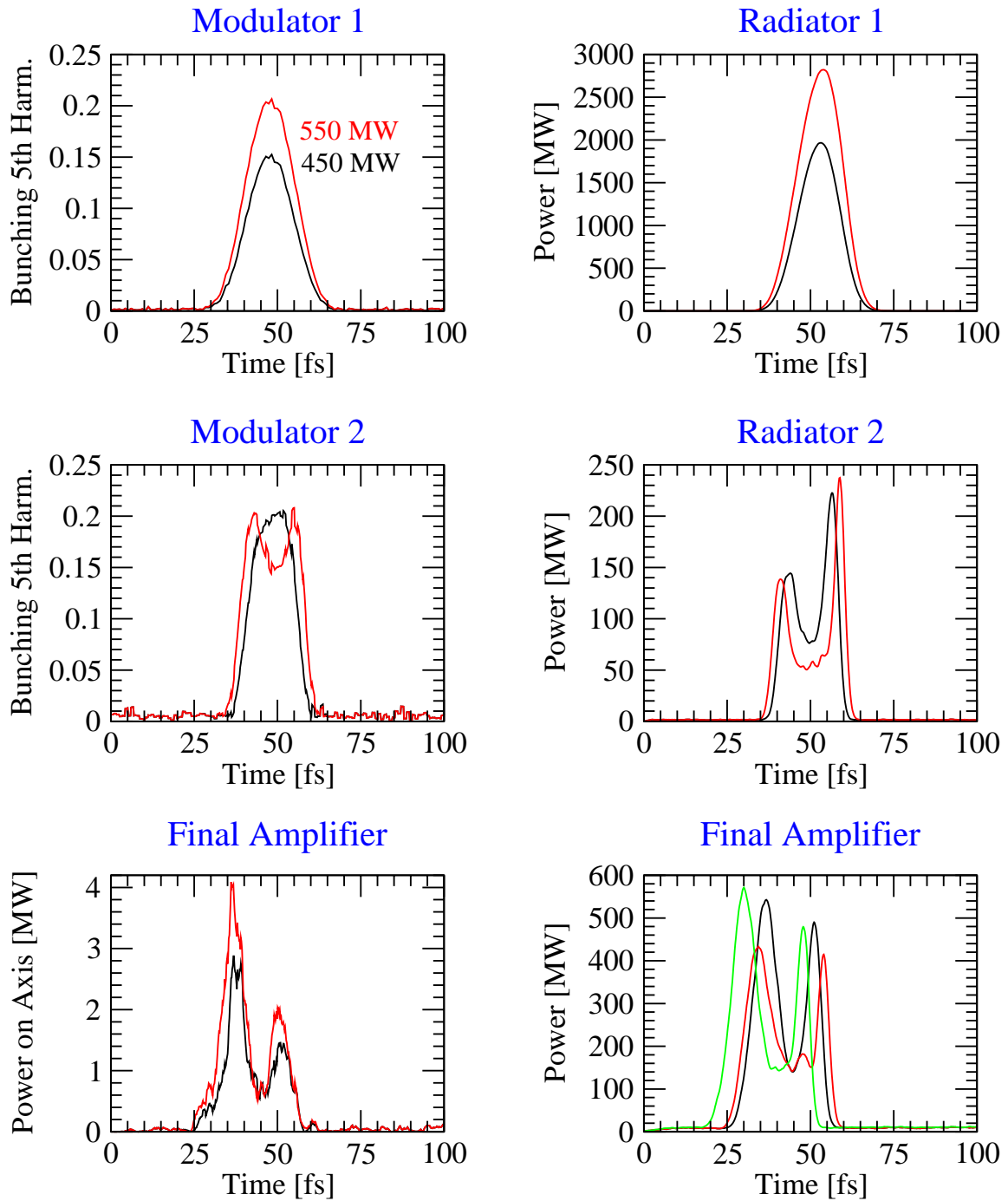


Fig. 3.19: Evolution of bunching and radiation in the low-energy HGHG line when the seed power is varied by $\pm 10\%$.

3.4.1.5 Correlated and Uncorrelated Undulator Errors

Besides variations in the beam parameters and in the seed power, the HGHG process can be disturbed by imperfections in the undulator modules, such as correlated field errors, that still retain the vanishing first and second field integral and cause phase errors, uncorrelated field errors causing trajectory deviations, gap errors, and phase mismatch between the modules. Results of the first two effects are presented in the following section.

Uncorrelated field errors cause a trajectory offset inside the undulators and reduce the overlap between the electron beam and the radiation. Optical elements to realign the beam are arranged for between each of the stages and in the intersections between the FA modules. In a first set of calculations, Gaussian distributed uncorrelated field errors of $2 \cdot 10^{-4}$ rms were applied to the undulators of the low-energy HGHG line and no trajectory correction was applied. The results for two different error distributions are presented in figure 3.20. The graphs show the bunching at the 5th harmonic in the two modulators, and the spectral output power in the radiators and the final amplifier. Without realignment the rms trajectory offset, or beam wander, rises from $7 \cdot 10^{-6}$ m in radiator 1, to $2 \cdot 10^{-5}$ m in radiator 2, up to $6 \cdot 10^{-5}$ m in the final amplifier. Due to these trajectory offsets, almost 50% of the spectral power is lost in the second radiator, an effect easily counteracted by corrector magnets. The blue curve in the lower right graph of figure 3.20 shows the effect of a single steerer in front of the final amplifier directing the beam back onto the axis. This steerer reduces the rms beam wander in the final amplifier significantly and restores 80% of the original spectral power.

In case of correlated errors, the high-energy FEL line has been simulated. Gaussian-distributed errors with an rms value of $2 \cdot 10^{-3}$ have been applied to all undulators, keeping the first and second field integral zero, to eliminate global trajectory offset and restricting the error mechanism to phase errors between the electron and the radiation phases. Figure 3.21 shows the results for the first 3 stages. Already modulator 1 shows a reduction in the bunching on the 5th harmonic, which leads to a reduction in spectral power in radiator 1. The bunching process in the following modulator suffers from the reduced seeding power as well as from the field errors. The process enhances itself from stage to stage, the driving mechanism being the reduced bunching on the harmonics in the modulators.

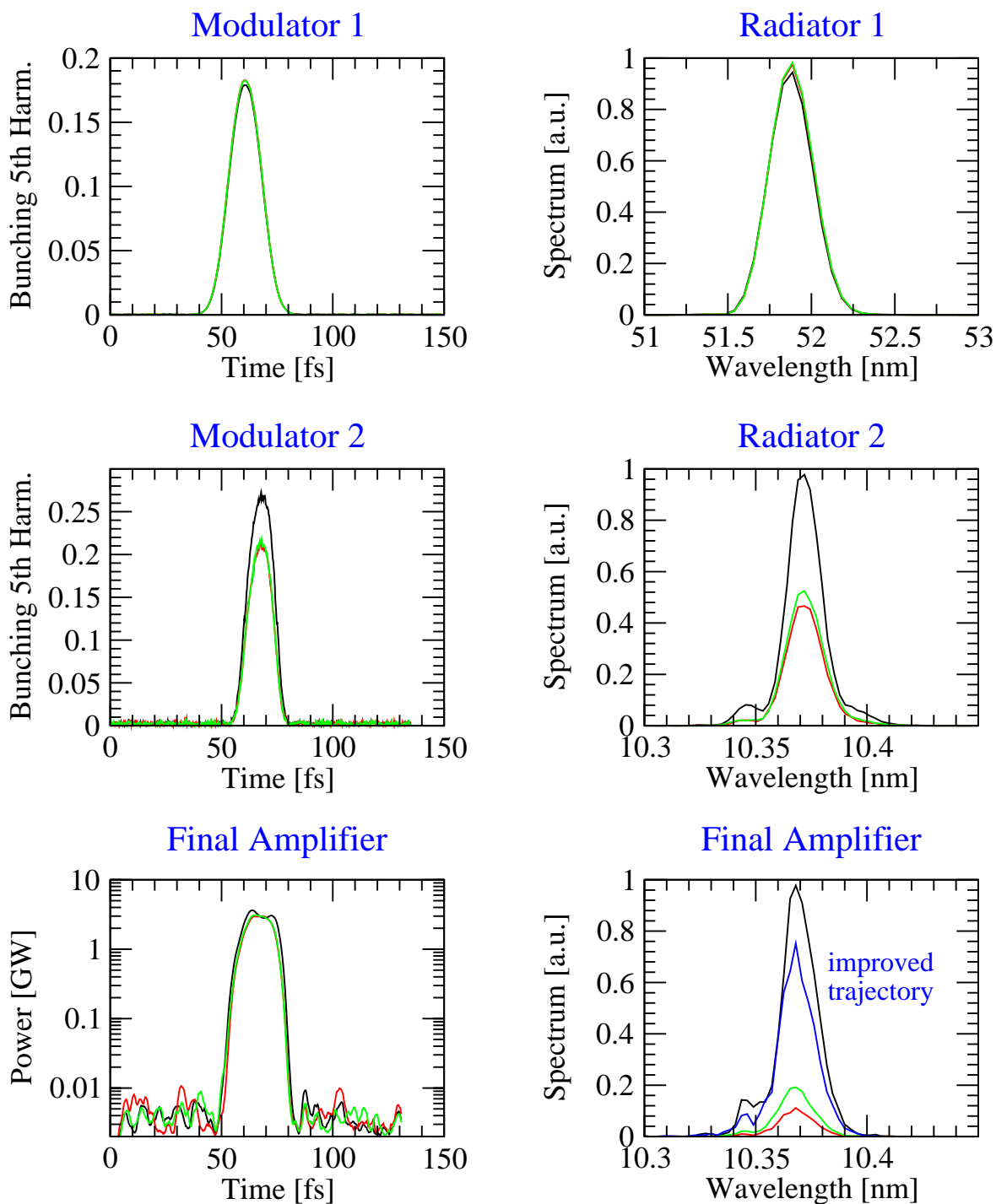


Fig. 3.20: Evolution of bunching and radiation in the low-energy HGHG line, when two sets of uncorrelated undulator field errors of $2 \cdot 10^{-4}$ rms are applied to all undulators. The trajectory has not been corrected. The blue curve in the lower right graph shows the effect of a single corrector in the front of the FA. The black curve represents the undisturbed curve.

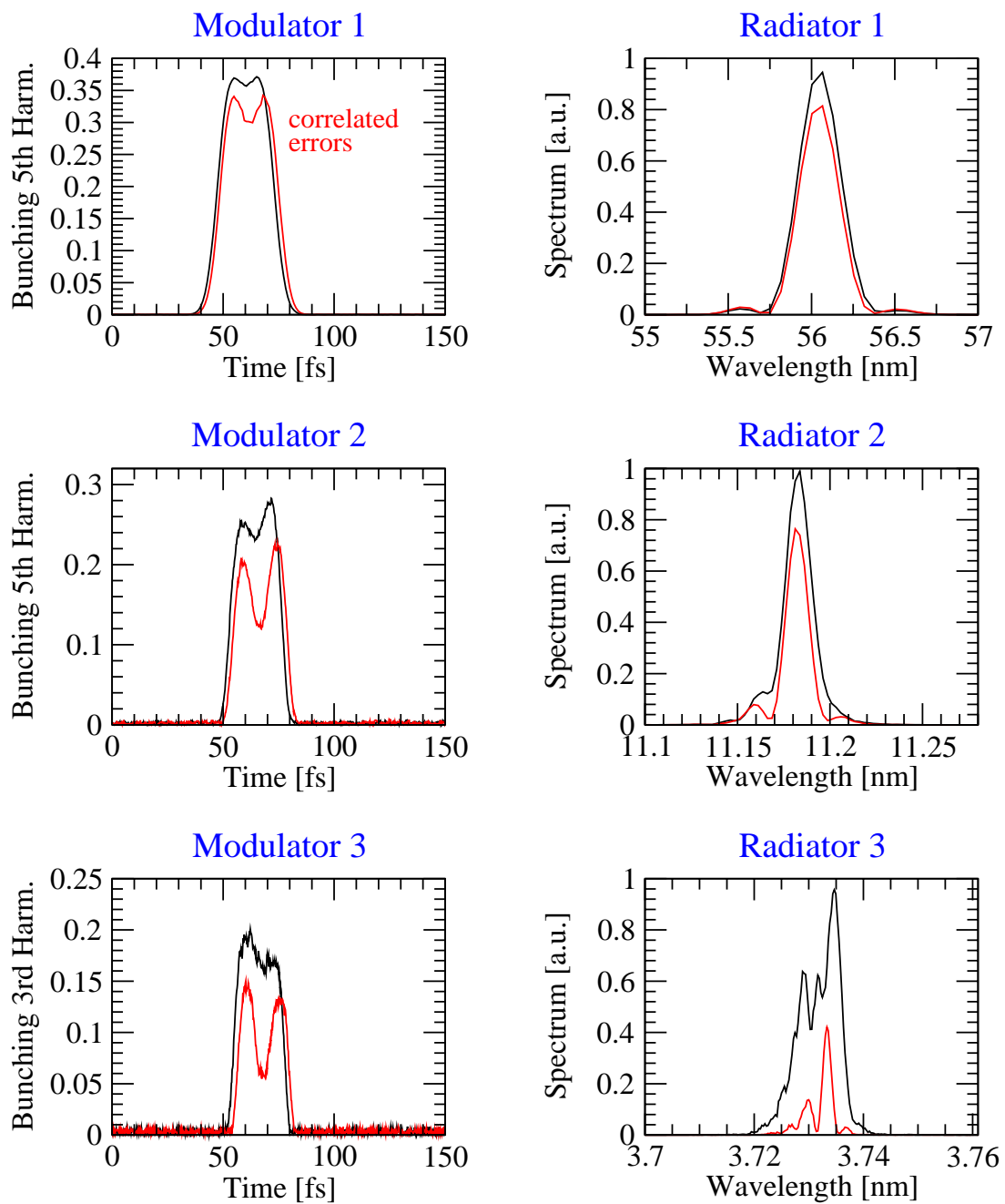


Fig. 3.21: Evolution of the bunching and radiation in the first 3 stages of the high-energy HGHG line, when correlated errors of $2 \cdot 10^{-3}$ rms are applied to the all undulators. The black curve represents the undisturbed curve.

Figure 3.22 illuminates the process in the first modulator. The solid lines display the bunching on the different harmonics for the undisturbed case, whereas the dotted lines display the results with correlated field errors. The slight shift along the bunch is explained by the elongation of the trajectory due to the errors. The electrons are delayed and the radiation interacts with an earlier part of the bunch. The achieved bunching rate on the fundamental is slightly increased due to the errors. With a higher harmonic number, the losses in the bunching rate grow. The dash-dotted green line (5th harmonic) shows the results for a different error distribution. It demonstrates the same principle behavior. Minor fluctuations in the electron phases seem to have a considerable impact when the energy modulation is converted to spatial bunching in the dispersive section. This effect has to be studied in more detail to develop proper means of reducing its impact on the final amplifier output.

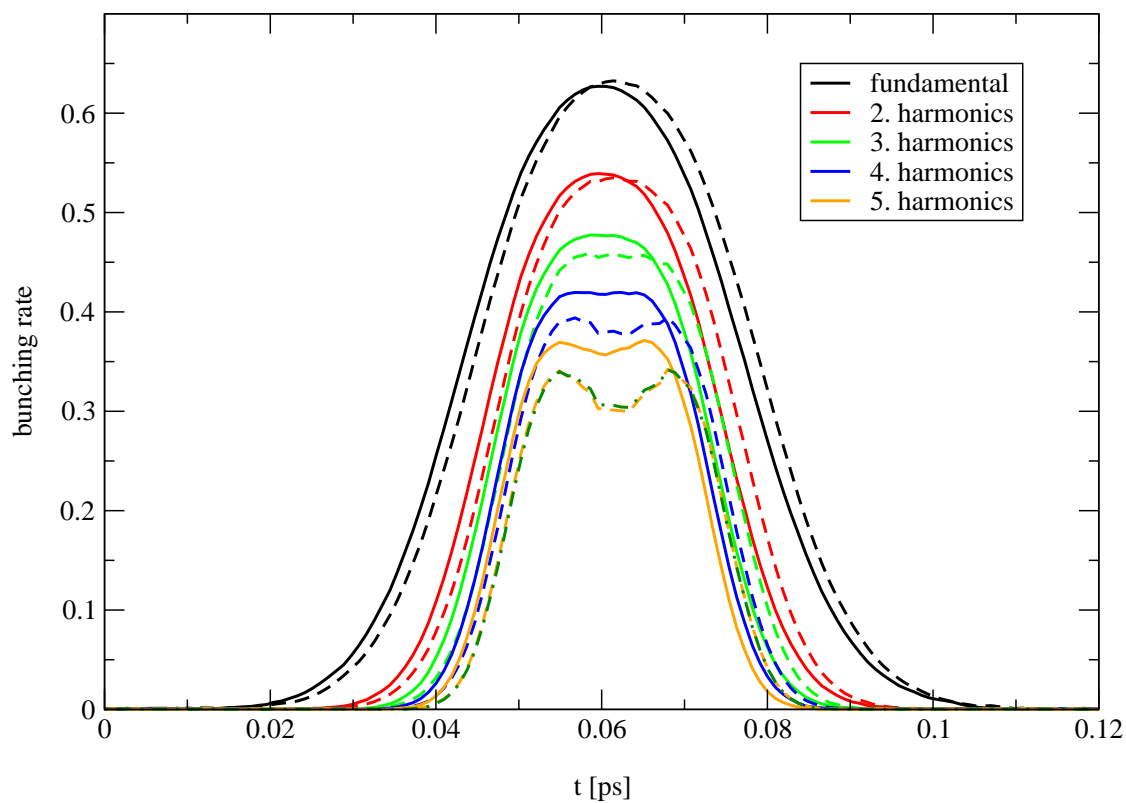


Fig. 3.22: Reduction of bunching with higher harmonics due to correlated field errors in modulator 1. The solid lines display the no-error case. The dash-dotted green line shows the results for a second error distribution on 5th harmonic.

References

- [1] L. H. Yu, J. Wu, *Nucl. Instrum. and Meth. A* **483** (2002) 493.
- [2] J. Wu, Thesis, May 2002.
- [3] L. H. Yu, I. Ben-Zvi, *Nucl. Instrum. and Meth A* **393** (1997) 96.
- [4] S. Reiche, *Nucl. Instrum. and Meth A* **429** (1999) 243.
- [5] A. Meseck, M. Abo-Bakr, D. Krämer, B. Kuske, S. Reiche, *Proc. of the 25th FEL conf.* (2003), to be published in *Nucl. Instrum. and Meth A*.
- [6] L. H. Yu, L. DiMauro, A. Doyuran, W. S. Graves, R. Heese, E. D. Johnson, S. Krinsky, H. Loos, J. B. Murphy, G. Rakowsky, J. Rose, T. Shaftan, B. Sheehy, J. Skaritka, X. J. Wang, Z. Wang, *Phys. Rev. Lett.* **91** (2003) 074801.
- [7] A. Doyuran, L. DiMauro, W. S. Graves, R. Heese, E. D. Johnson, S. Krinsky, H. Loos, J. B. Murphy, G. Rakowsky, J. Rose, T. Shaftan, B. Sheehy, Y. Shen, J. Skaritka, X. J. Wang, Z. Wang, L. H. Yu, *Proc. of the 2003 PAC* (2003) 217.
- [8] E. L. Saldin, E. A. Schneidmiller, M. V. Yurkov, "The Physics of Free Electron Lasers", (Advanced Texts in Physics), Springer-Verlag Berlin Heidelberg (2000).
- [9] M. Schnürer, Z. Cheng, M. Hentschel, G. Tempea, P. Kálmán, T. Brabec, F. Krausz, *Phys. Rev. Lett.* **83** (1999) 722.
- [10] E. Takahashi, Y. Nabekawa, T. Otsuka, M. Obara, K. Midorikawa, *Phys. Rev. A* **66** (2002) 21802(R).
- [11] W. M. Fawley, W. A. Barletta, J. N. Corlett, A. Zholents, *Proc. of the 2003 PAC* (2003) 923.
- [12] E. L. Saldin, E. A. Schneidmiller, M. V. Yurkov, *Opt. Commun.* **202** (2002) 169.

4 Gun, Seed, and Experiment Lasers: Concept and Synchronization

4.1 Introduction

The correct functioning of a cascaded HGHG-FEL must be ensured by an accurate timing of a number of different processes. The electron production in the photo gun, the overlap of the electron bunch at the first modulator with the seed laser as well as the correct overlap of light and electrons in the following stages, and finally the congruence of the FEL photon pulses with short-pulse experiment lasers must be synchronized with fs accuracy. The cascaded BESSY HGHG-FEL requires that the electron bunch is long enough so that the seed pulses of the external fs-seed laser and all additional HGHG stages are in temporal overlap with the electron distribution. This is schematically shown in figure 4.1. Analyzing the sources for the arrival jitter of the electron bunch at the entrance to the HGHG cascade values of 150 fs have been estimated as a pessimistic parameter setting (see also chapter 6), while a jitter of < 30 fs is expected to be within reach. Similar values are expected for the synchronization accuracy. Until recently standard techniques in accelerator technology allowed electronic synchronization in the sub-picosecond range (0.5 ps) typically and research concentrated on reaching 100 - 200 fs. Recent developments for synchronizing two fs-lasers are much ahead of these results reaching an accuracy down to 0.3 fs [1]. The latter result is important since synchronization of the HGHG-FEL photon pulses with pump-probe lasers at the experiments has to be done with respect to the seed laser rather than to the electron bunch.

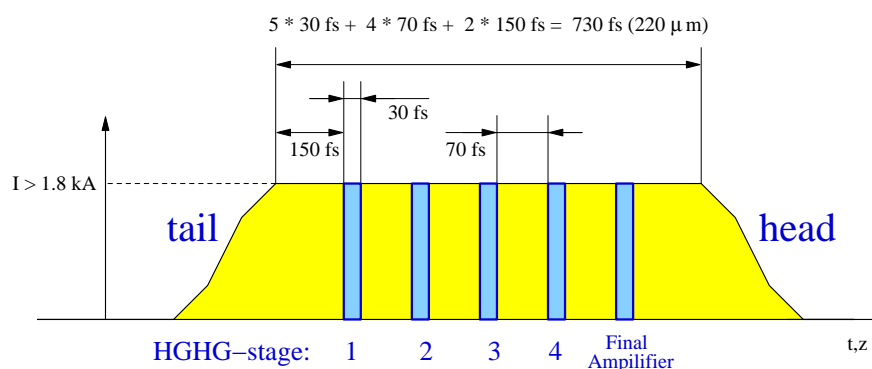


Fig. 4.1: Timing requirements for seeding of an FEL electron bunch (yellow) with an fs laser pulse (blue). Assuming a timing jitter of 150 fs between the two, the laser should hit the electron bunch about 150 fs before the tail of the electron bunch in the first HGHG stage. The temporal width of the seeded slice corresponds to the fs-laser pulse length (30 fs). For a four-stage HGHG-FEL the electron bunch needs to be sufficiently long to incorporate four additional seeded slices (blue).

4.2 Seed and Experiment Lasers

External fs laser systems will be used for seeding and delivering pump-probe pulses to experiments. The heart of such a laser system is a titanium-sapphire (Ti:Sa) oscillator with one or more Ti:Sa multipass amplifier stages delivering typically 20 – 30 fs pulses of 1-10 mJ pulse energy at 1 kHz repetition rate. Depending on the purpose different frequency conversion stages will be used. In the following we will only briefly describe the design of experiment lasers and concentrate on that of seed lasers since they are essential for the operation of HGHG-FELs.

4.2.1 Seed Lasers

A seed laser system optimized to match the HGHG process must provide short, synchronized pulses of 20 - 30 fs duration, tunable between 230 and 460 nm wavelength with a pulse energy larger than 10 μ J. The pulses should be produced with 1 kHz repetition rate.

From the laser point of view such design parameters are compatible with today's technology. This leads to the assessment that a seed laser with the above specifications is an essential tool for the BESSY FEL. Nevertheless, a number of alternative solutions have been investigated for this report. The solution presented in section 4.2.1.1 was chosen for reasons of balancing performance, reliability and proven compliance with today's state-of-the-art laser technology. Some alternative solutions presented in section 4.2.1.2 open the potential to go well beyond the present design parameters, even if in some cases additional research and development may be necessary to achieve the same balanced overall performance. It should be stressed, however, that the rate of progress in laser research towards shorter pulses and shorter wavelengths leaves little doubt that the above design parameters may well be exceeded in only a few years. This provides substantial future potential for the BESSY FEL.

4.2.1.1 Description of the Individual Components of the Seed Laser

The seed laser system will contain the following building blocks which are schematically shown in figure 4.2:

1. A femtosecond titanium:sapphire pump laser (Ti:Sa).
2. A Traveling-Wave Parametric Amplifier (e.g. TOPAS®).
3. A White-Light Continuum Generator (WLG).
4. A Non-collinear Optical Parametric Amplifier (NOPA).
5. A Prism Pulse Compressor.
6. A Second-Harmonic Generation (SHG) stage for the output pulses of the NOPA.

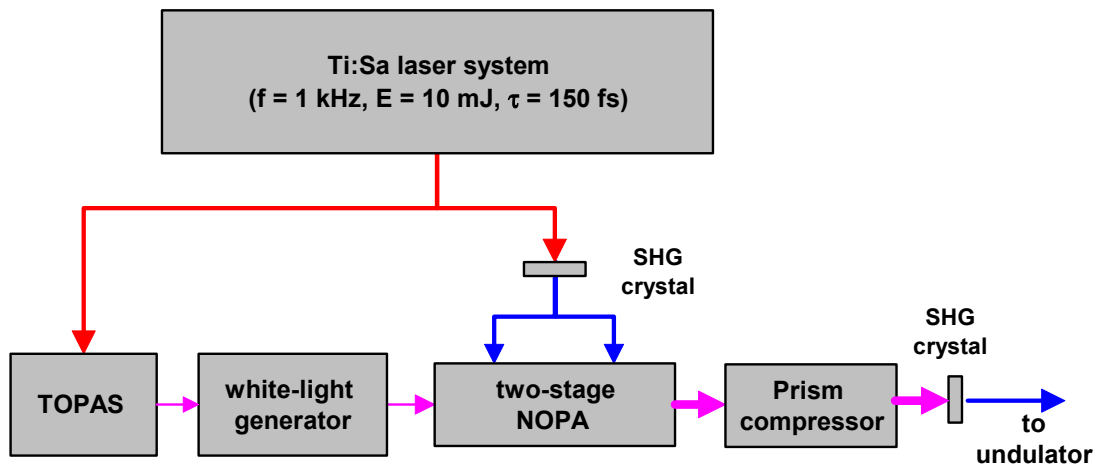


Fig. 4.2: Main building blocks of the seed laser for the BESSY FEL.

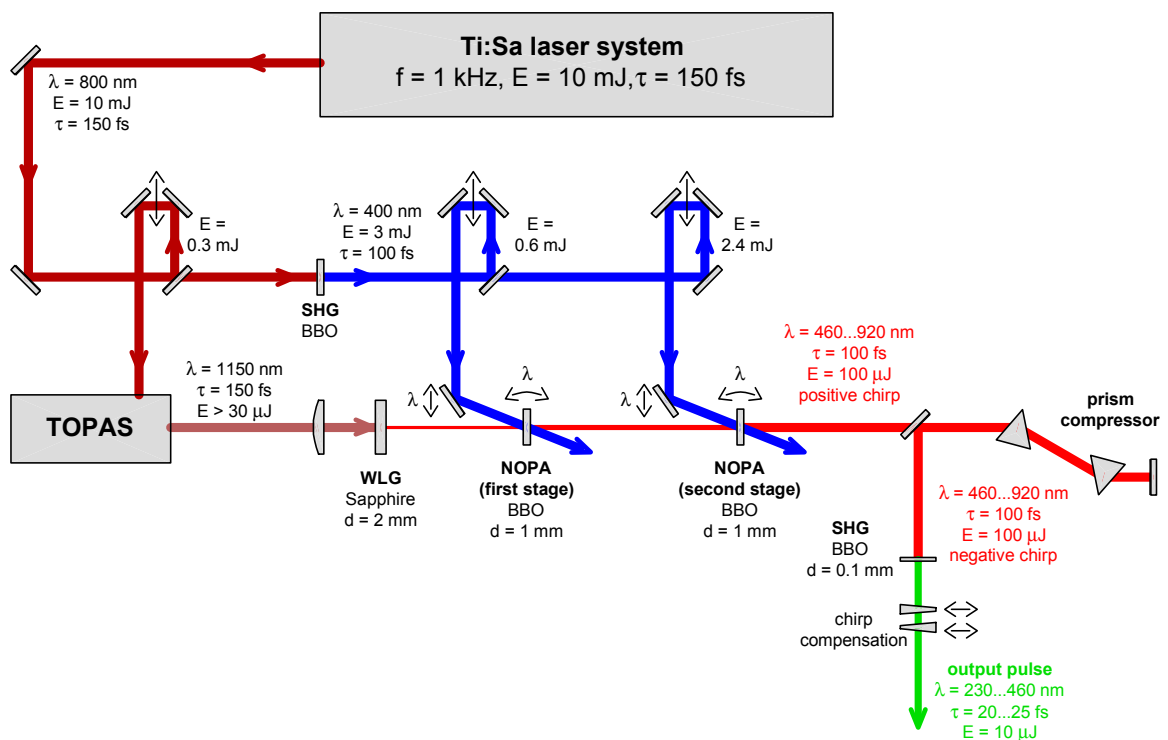


Fig. 4.3: Optical layout of the proposed seed laser.

An overview of the optical layout is shown in figure 4.3. The individual components are described in the following:

The Ti:Sa pump laser

The Ti:Sa pump laser generates the pump pulses for both the Traveling-Wave Parametric Amplifier (TOPAS[®]) and the two-stage Non-Collinear Optical Parametric Amplifier (NOPA). The laser should produce pulses of 10 mJ energy and 150 fs duration. Shorter pulses are not beneficial for the proposed optical setup leading to the required 25 fs pulse length at the output of the system. Shorter pump pulses would lead to additional complication of the NOPA system for preserving the high conversion efficiency, i.e. introducing angular dispersion of the pump beam. The combination of 10 mJ pulse energy, 150 fs pulse duration and 1 kHz repetition rate is well within today's state-of-the-art Ti:Sa technology.

The Traveling Wave Optical Parametric Amplifier (TOPAS[®])

The Traveling Wave Optical Parametric Amplifier consists of an OPG (Optical Parametric Generator) and a two-stage OPA (Optical Parametric Amplifier) [2] and is commercially available, e.g. as a TOPAS[®] system (Light Conversion, Vilnius, Lithuania). All components are operated in a collinear geometry in order to achieve optimum beam quality.

The TOPAS[®] generates pulses of $E > 20 \mu\text{J}$ energy at 1150 nm wavelength. These pulses are then used for generation of a white-light continuum. Although other methods for generation of pulses with 1150 nm wavelength could be taken into account, the TOPAS[®] provides the best beam quality and the best pulse-to-pulse energy stability. This ensures both highest stability and beam quality of pulses produced by the following white-light continuum generator.

The White-Light Continuum Generator (WLG)

The pulses from the TOPAS[®] are tightly focused into a sapphire plate and generate a white-light continuum [3] in a single filament. Although the spectrum of the generated white light exhibits strong modulations near the wavelength of the input pulse, i.e. between 1000 and 1300 nm, it turns out to be flat at wavelengths of 460...920 nm. Furthermore, an optimum energy stability of the produced pulses is obtained between 460 and 920 nm which is mainly determined by the beam quality and the pulse-to-pulse energy stability of the 1150 nm input pulses.

The Non-Collinear Optical Parametric Amplifier (NOPA)

The NOPA amplifies the seed pulses from the WLG in a two-stage arrangement. In the first stage the main part of the parametric amplification occurs. In the second stage the parametric amplification is only by a factor of 5-10 and exhibits slight energy saturation of the output pulses which is needed for optimal energy stability and beam quality.

The center wavelength of the pulses is determined by the three parameters [4]:

- Mutual delay between seed and pump pulses.
- Tuning angle of the NOPA crystals.
- Angle between pump and signal.

For proper operation of the NOPA, these parameters have to be tuned by a computer-controlled system using pre-configured look-up tables.

Special care has to be taken to achieve the required pulse duration which is of the order of 20 fs: In the spectral range 460 - 750 nm the bandwidth of the NOPA output pulses will be determined by both the duration of the pump pulses and the chirp of the white-light continuum. On the other hand, the required phase matching condition in the Beta Barium Borate (BBO) crystals is expected to limit the pulse bandwidth in the spectral range 750 - 920 nm. Consequently, the thickness of the BBO crystals has to be carefully optimized. The estimated optimum thickness of the NOPA crystals is between 1 and 2 mm.

The pulse compressor

The pulse compressor utilizes two prisms to control the chirp of the output pulses of the NOPA. In contrast to the standard alignment, this compressor is aligned to over-compensate the negative chirp of the input pulses thereby forming pulses with a negative chirp and with approx. 100 fs duration. As an additional option, a slightly more sophisticated adaptive pulse compressor [5] may be used instead of the simple prism compressor. This adaptive shaper would enable one to tune the phase of the spectral components by means of a computer-controlled LCD array. Both the duration and the shape of the generated output pulses can be manipulated this way in order to adapt them to the real requirements of the FEL.

The Second Harmonic Generation (SHG) stage

A 50 - 100 μm thick BBO crystal converts the pulses into the second harmonic. The intensity in the crystal should be optimized between 50 and 200 GW/cm^2 for best conversion efficiency and beam quality. Under proper operating conditions, the conversion process reaches an efficiency on the order of 10%.

The negative chirp of the NOPA pulses introduced by the pulse compressor is required in order to avoid significant self-phase modulation in the SHG crystal. This chirp also leads to an improvement of the conversion efficiency and the spectral width of the converted pulses by avoiding spectral narrowing in the second harmonic generation process [6]. Lenses made from fused silica or CaF_2 should be used for focusing and collimation of the UV pulses. Since the negative chirp is transferred to the SHG pulses, a chirp compensation system consisting of two adjustable quartz wedges is required at the output of the system. These quartz plates compress the output pulses to their final duration of 20 - 25 fs.

Tuning of both the quartz plates and the prism compressor requires on-line measurement of the duration of the output pulses. At present, a specially designed SPIDER [6-8] seems to be the most suitable device for this purpose.

4.2.1.2 Alternative Solutions

The following alternative solutions for a seed laser for the BESSY FEL have been considered. All of these alternative schemes contain a high-power Ti:Sa laser as the primary source of ultra-short pulses. Subsequently, these pulses are transferred to the desired wavelength range of 230...460 nm by different optical setups which utilize different nonlinear processes:

1. *Sum-frequency generation between pulses from a Ti:Sa laser ($\lambda \sim 800$ nm) and pulses from a high power NOPA*

This technique would provide both an improved pulse-to-pulse energy stability [9] and an improved beam quality. The pump energy required is reduced with respect to the proposed NOPA system. Unfortunately, the tuning range of this setup is limited to 290...460 nm. Although tuning between 214 and 290 nm can be accomplished by an additional mixing channel, this would significantly increase the complexity of the overall system. Tuning over the required wavelength range would require switching between two output channels. This results in a much more complicated tuning process than that proposed here.

2. *Self-phase modulation, induced phase modulation or spectral broadening in impulsively Raman excited media in a hollow waveguide at 400 nm and/or 266 nm wavelength*

This technique is capable of producing extremely short, sub-femtosecond pulses. Although only preliminary demonstration experiments at 400 nm wavelength have been performed [10 - 12], theoretical calculations clearly show the feasibility of this technique [13].

The most severe limitation of this technique with regard to the seed-pulse laser for the BESSY FEL is the limited tuning range in wavelength. Eventually, the appropriate wavelength could be obtained by selecting portions of the broadband pulses by spectral filtering.

Regarding the produced output pulses, strong spectral modulations but exceptional beam quality (ideal Bessel beams from the hollow waveguides) are expected. There is a restriction to the energy of the driving Ti:Sa laser since the intensity in the hollow waveguide must be below 10^{14} W/cm² to avoid ionization.

3. *Broadband harmonic generation and sum frequency generation in crystals with angular dispersed beams (tilted-pulse fronts)*

This technique has the potential to circumvent the spectral restriction of the $\chi^{(2)}$ nonlinear frequency conversion of fs-broadband pulses implied by the phase matching condition [14, 15]. Although the usefulness of tilted pulse fronts has been demonstrated, the generated pulses have never been used in experiments. The biggest problem of this technique seems to be the reliable control of the outgoing phase front, in particular of the angular chirp of the generated pulses.

4. *Novel solid-state materials for frequency-doubling of the output pulses of the proposed NOPA*

New solid-state nonlinear materials especially for periodically poled structures [16, 17] would allow for higher efficiency, broader phase-matching conditions, and simultaneous compression for the SHG from NOPA [18]. The UV pulses could be shortened, thus reducing the requirement for high energies from the Ti:Sa pump laser. These novel materials are expected to appear on the market during the next five to ten years. The use of these materials in the frequency conversion stage of the proposed setup has to be taken into account depending upon the real schedule for setting up the seed laser.

5. *Four wave mixing in a gas-filled hollow wave-guide between pulses from a high power NOPA and harmonics of Ti:Sa laser*

For this application, the NOPA should reach a pulse energy of 100-200 μJ at a wavelength tunable between 460 and 700 nm wavelength and a pulse duration of $t < 30$ fs. The mixing technique in hollow wave-guides exhibits straightforward tuneability and has the potential for sub-10-fs pulses. Although there are some preliminary results in third harmonic generation of 800 nm pulses [19], the complete mixing technique has not yet been realized at the desired energy level. Typically for the hollow waveguide based techniques one expects exceptional beam quality (ideal Bessel beams). On the other hand, the energy requirement of the driving Ti:Sa laser is very high due to the low nonlinearity of the gas in the waveguide.

4.2.1.3 Summary

At the present stage of development, the techniques discussed in section 4.2.1.1 have been chosen as the most promising, stable and reliable scheme for generation of the ultra-short optical seed pulses for the BESSY FEL. As mentioned above, future developments may certainly lead to a re-assessment of the alternatives described in section 4.2.1.2 at a later stage and may open new possibilities for the BESSY FEL.

4.2.2 Experiment Lasers

Ti:Sa laser systems are nowadays widely used for optical pump-probe experiments. Such laser systems provide pulse durations down to a few 10 fs and a pulse energy of several mJ with repetition rates of typically several kHz [20, 21]. Such lasers are, therefore, also ideally suited to provide pump pulses in optical pump-FEL probe experiments.

Table 4.1 summarizes typical values of the relevant output parameters for commercially available Ti:Sa laser systems. The laser output at the fundamental frequency can be frequency doubled (SHG) and tripled (THG). SHG and THG stages will routinely provide pulse energies > 0.2 mJ (> 0.1 mJ) at 400 nm (267 nm) wavelength in a 30 fs pulse.

In contrast to the seed laser system described above experiment lasers should provide output in the wavelength range from the far infrared to the UV region. This can be achieved by an optical parametric amplifier (OPA) being pumped by the amplified 800 nm beam [22]. The proposed setup of the laser system is shown schematically in figure 4.4. Values of the achievable output parameters are summarized in table 4.2.

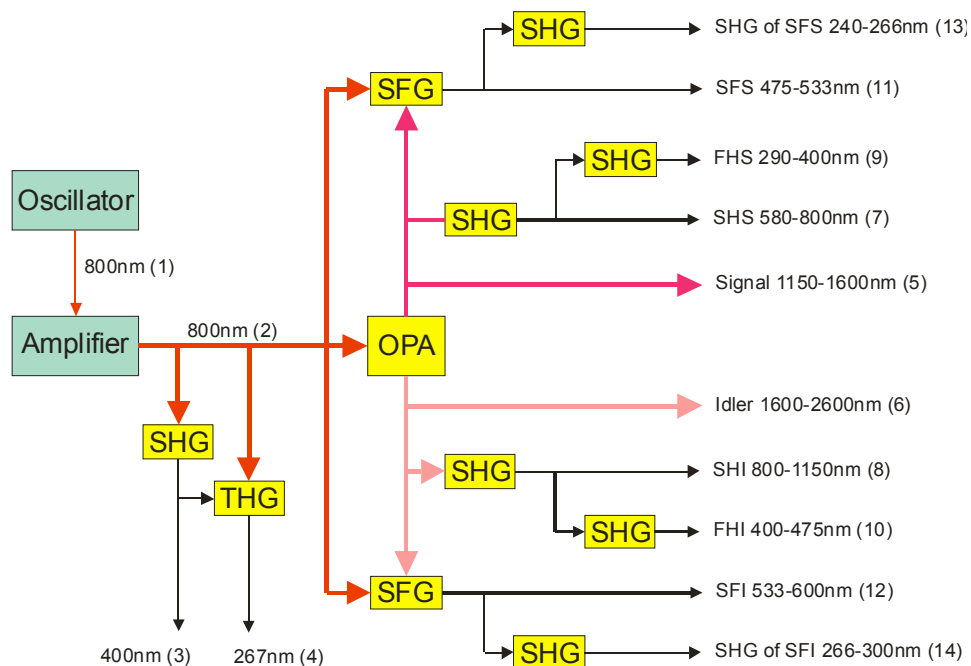


Fig. 4.4: Scheme of the experimental laser system. A large variety of different wavelengths is available by combining an optical parametric amplifier (OPA) with several second harmonic (SHG) and sum frequency (SFG) stages. See also tables 4.1 and 4.2.

Table 4.1: Parameters of the experimental laser system with SHG and THG stages. For the numbers listed in the second table column see figure 4.4.

	Number	Pulse energy	Wavelength	Pulse duration
Oscillator	(1)	5 nJ	780 – 800 nm	20 fs
Amplifier	(2)	>1.5 mJ	780 – 800 nm	30 fs
SHG	(3)	> 0.4 mJ	400 nm	30 fs
THG	(4)	> 50 μ J	267 nm	30 fs

Table 4.2: The output wavelength and energy of the OPA. For the numbers listed in the second table column see figure 4.4.

	Number	Tuning range	Pulse energy (at peak)
Signal/Idler (S/I)	(5),(6)	1150-2600 nm	> 100 μ J (375 μ J)
SHG from Signal/Idler (SHS/SHI)	(7),(8)	580-1150 nm	> 20 μ J (60 μ J)
Pump + Signal (SFS)	(11)	475-533 nm	> 30 (100 μ J)
Pump + Idler (SFI)	(12)	533-600 nm	> 20 (75 μ J)
FHG of S/I (FHS/FHI)	(9),(10)	290-475 nm	> 3 (7 μ J)
SHG of SFS/SFI	(13),(14)	240-300 nm	> 1 μ J (7 μ J)

The signal and idler wave in the near infrared will give a tunable range from 1150 nm to 2600 nm with a pulse energy > 100 μ J. By frequency doubling of the signal (SHS) and idler (SHI) respectively and by frequency mixing of the pump beam with the signal (SFS) and idler (SFI) respectively, a wavelength range from 475 nm to 1150 nm will be accessible with a pulse energy of approximately 50 μ J. The UV from 240 nm to 475 nm can be accessed by again frequency doubling of the prior described beams. Namely these are the fourth harmonic (FHG) of signal and idler (FHS and FHI) and the SHG of the SFS and SFI beams.

4.3 Future Prospects: HHG Seeding at Shorter Wavelengths

The present BESSY FEL technical design is based on the HGHG-FEL concept, using optical laser seed pulses in the spectral range of 230 - 460 nm.

Seed pulses in this spectral range cannot be obtained through direct optical laser action: although lasers, in particular dye lasers, are known to operate in this region, their stability, pulse duration and output power are not suited for the present application. Hence, the seed pulses are obtained by nonlinear frequency conversion from a primary pump laser, in the present case a Ti:Sa laser operating around 800 nm. Physically, the frequency schemes discussed above can be explained in terms of second and higher order corrections to the dielectric susceptibility, i.e. in terms of bulk material constants.

In principle, the BESSY HGHG-FEL concept can be modified to incorporate shorter seed wavelengths, thereby reducing the number of frequency conversion stages and possibly even supporting shorter FEL pulse lengths. Thus, the frequency conversion problem is partially shifted from the FEL undulator towards the optical seed laser. If higher (n-th) order harmonic generation again is based on n-th order dielectric susceptibility their efficiency would decrease with the n-th power of the input intensity.

Fortunately, a different, much more efficient physical conversion process is known, called High-Harmonic-Generation (HHG). The process usually sets in around the 10th harmonic (~80 nm) and exhibits for any given target gas an efficiency “plateau” up to very high frequencies (the “cut-off”), limited mainly by the input intensity of the pump laser. The physics of HHG may be explained in terms of temporary ionization, energy gain and recombination of an atomic valence electron [23]. It thus is restricted to gaseous media and high – but not too high – pump intensities.

If considered as a frequency conversion scheme for a seed laser several properties of HHG have to be investigated: the conversion efficiency, the stability, the tuneability and the spatial, temporal, and spectral beam quality. Finally, the power requirements and the projected feasibility of a HHG-based optical seed laser need to be discussed. This is briefly done in the following sub-section.

Extensive calculations and numerical simulations of the FEL process, performed at BESSY, resulted in the following pulse parameter requirements for HHG seeding: Seeding wavelength 31-51 nm (roughly 25th through 40th harmonics of the Ti:Sa fundamental):

- Pulse duration ~ 6 fs.
- Peak power 250 MW, resulting in 1.5 μJ pulse energy.
- Synchronization accuracy: 100 fs.
- Long-term (8h) power stability: 10%.

4.3.1 HHG Frequency Conversion

The generated photon number in the VUV is determined by the conversion efficiency $\eta = E_{\text{HHV}}/E_{\text{Laser}}$, the ratio between the emitted VUV energy per harmonic bandwidth E_{HHV} and the incident optical energy E_{Laser} per pulse. It strongly depends on the incident intensity, focus or wave-guide geometry, phase matching conditions, and on the target gas. Generally, the efficiency exhibits a plateau for each target gas, with a high-energy cut-off determined by the target gas and the laser intensity. Generally, gases with higher cut-off have an overall lower efficiency, which results in an overall decrease of the efficiency as a function of VUV energy, irrespective of the target gas.

This behavior is depicted in figure 4.5, in which optimized experimental results obtained during the last four years are summarized. Guided by the eye one can recognize a scaling power law to the efficiency envelope, covering all gases. It turns out that the envelope roughly scales with $\eta \sim \lambda^{4.3}$, giving an upper limit to the conversion efficiency at any desired VUV output energy. This reflects the fact that shorter wavelength generation requires higher laser intensities which have to be propagated in media with higher ionization potential but lower effective recombination probability (from Xe via Ar, Ne to He).

The points in figure 4.5 show already the result of a quasi-phase-matched high harmonic generation in the VUV-absorption limit of the converting gaseous medium, using different target capillaries and phase matching mechanisms [29, 30], and laser pulse shapes. Despite considerable efforts there are no schemes in sight, experimental or theoretical, which suggest the feasibility of significantly higher conversion efficiencies.

The pulse energy efficiency in the relevant region (30 – 50 nm) for BESSY FEL HHG seeding is between $1 \cdot 10^{-5}$ and $5 \cdot 10^{-5}$. Therefore, if micro-Joule pulse energies are necessary for HHG-seeding in the 30 to 50 nm wavelength band, an optical pump laser delivering short (20 – 60) fs pulses with about 100 mJ pulse energy is necessary.

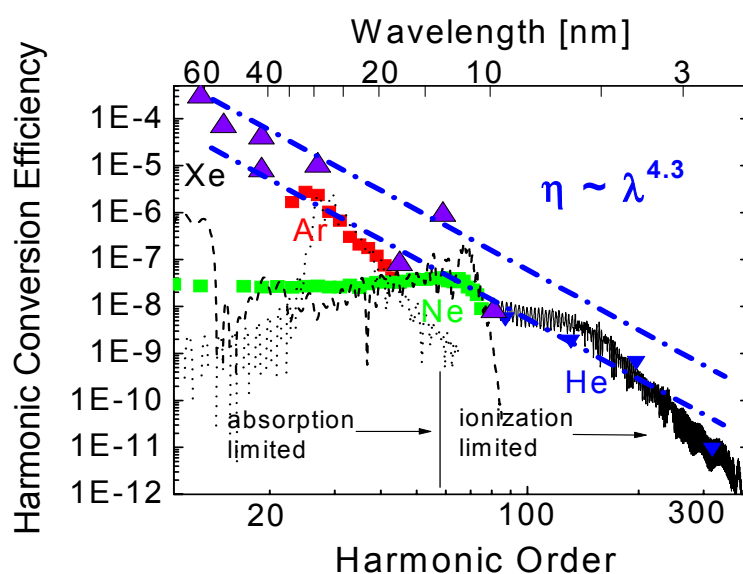


Fig. 4.5: Efficiencies of generated high harmonic energies in relation to incident optical pulse energy obtained during recent years. The data around the lower blue line are from few cycle optical pulses using tighter focusing due to available pulse energies [24], the upper blue line is along recently obtained maximum values [25-28] (purple triangles) using loose focusing and higher laser pulse energies.

4.3.2 Stability

Up to now little information has been published concerning the high harmonics (HH)-signal fluctuation statistics. Data from single-shot acquisition spectrographs [31] enable preliminary estimates of signal fluctuations in a range of 10% to 20% to be made [32], when no special methods of driver laser control and target control are applied, a rather moderate value considering the high degree of non-linearity in the process. Thus, a signal fluctuation of only a few percent should be within the reach of an advanced stabilized laser and target system. An actively stabilized Ti:Sa-laser system in combination with quasi-static gas cells with a definite gas throughput should be used. Alternatively, gas-filled hollow fibers can be used, but the laser input-coupling, already at material ablating intensities, could be more critical here.

4.3.3 Tunable Spectra, Spatial Beam Profile

The spectrum of high harmonics consists of the odd orders of the incident-fundamental optical frequency and extends up to the cut-off, characteristic for each target gas and incident intensity. The desired FEL seed-pulse would contain one HH with the required seed-frequency; this HH has to be filtered out. Spectral filtering usually comes with an increase in pulse width; thus eventually re-compression methods will have to be used if few fs or even sub-fs HH are required. In order to have full access to the spectral region, e.g. between 10 nm and 50 nm wavelength, the Ti:Sa laser should be variable between 740 nm and 820 nm approximately. The fluorescence and spectral amplification curve of Ti:Sa is sufficiently broad for this demand.

The beam profile of the HH-beam is directly related to the optical laser beam profile and homogeneous profiles of HH-beams with a divergence corresponding to the frequency ratios. If the HH seed-beam should propagate on the order of 10 m and the overlay cross-section with the electron-beam is on the order of some millimeters, VUV-optical elements are necessary for collimation of the HH-beam which typically have a divergence between 0.1 and 1 mrad.

4.3.4 Temporal and Spectral Pulse Profile

High harmonic generation, by the very nature of the underlying physical process, leads to periodic structures both in frequency and time, i.e. a temporal pulse train of very short (sub-fs) pulses or, in frequency space, a comb of equidistant spectral lines separated by twice the pump frequency. Both are not ideally suited for HHG seeding, where single, smooth pulses of a few fs duration are required. Generally, this requires spectral pulse selection combined with temporal pulse stretching after the initial HHG process. Both

appear generally feasible today, even if it almost certainly comes at a reduction in the overall conversion efficiency.

An elegant way of selecting single pulses instead of pulse trains is to select the pump intensity such that the desired HHG output frequency lies at the high-energy-cutoff of the frequency comb. Physically, only one cycle of the driver laser contributes to this process, leading to a very short sub-fs output pulse. Subsequent temporal stretching can, in principle, be performed in dispersive media, whereby gases, e.g. argon, may be suitable. Since argon may also be used for the primary HHG process in this region it is not inconceivable that a rather simple experimental setup may be found to perform both tasks simultaneously. It should be mentioned, however, that this or any other temporal and spectral pulse shaping scheme still requires substantial research efforts for the proof-of-principle and optimization, even though it appears principally feasible.

4.3.5 Feasibility

When comparing the above HHG properties with the calculated pulse requirements for BESSY FEL seeding with HHG pulses, the following assessment can be made:

- The spectral range of 30 - 50 nm is well within reach of established HHG schemes. In fact, it can be covered with efficient heavy rare gases as conversion media. Tuneability can, in principle, be achieved by tuning of the primary pump.
- Stability and spatial beam quality appear to be within technical reach, although some development regarding stability will be needed.
- The temporal and spectral beam profile of the seed pulse needs to be shaped after the initial HHG process in order to fulfill the seeding requirements of a spectrally smooth pulse of a few fs duration. Pulse shaping at these frequencies requires considerable proof-of-principle and subsequent optimization research, although it should be principally feasible.
- An estimate of the power requirement for a HHG seed pulse pump laser indicates that at least 100 mJ input power is necessary, provided that the pulse shaping schemes are sufficiently efficient. At 1 kHz repetition rate this results in an average power of 100 Watt for a short-pulse (~ 20 fs) driver laser. Such a laser is about a factor of 10 above current fs-laser technology, but should be available within the foreseeable future. There are no known technological bottlenecks that would prevent the development of such a laser.
- Scaling of the HHG process towards input pulse energies in the 100 mJ region at 1 kHz repetition rate has not yet been demonstrated, due to the lack of suitable driver lasers. The complexity of the conversion process, in particular, the sensitivity with respect to phase matching, makes scaling of the existing schemes rather

difficult, especially when small capillaries are involved. On the other hand, there are no known physical reasons why scaling to such parameters should not be possible at the present conversion efficiency numbers.

In summary, HHG as a frequency conversion scheme to yield shorter wavelengths and shorter pulse durations for FEL seed pulses has several attractive features and appears to be physically feasible, but requires substantial research and technological development to serve as a base for a reliable engineering design. The attractive features are the relatively high conversion efficiency, when compared to “classical” high-order non-linear optics, and the intrinsic pulse shortening with respect to the pump lasers. The critical parts for the present applications would be the spectral and temporal pulse shaping, and the scaling of the conversion process towards very high average powers of the driver laser, of the order of 100 W or above.

If it had to be realized tomorrow, HHG seeding would represent a critical part with some risk for the overall design of the BESSY FEL. Given a few years of additional R&D such a scheme could turn out to be attractive for future modifications, especially with regard to shorter pulse durations of the FEL.

4.4 Synchronization of Seed and Experiment Lasers

For a seeded FEL the timing of the seed pulse is a crucial topic. This is true especially for a multi-stage HGHG setup. From calculations on the allowable timing jitter between the electron bunch and the seed laser (see chapters 3 and 6) it turns out that one has to aim for a relative jitter of about 70 fs (rms). A larger jitter for the synchronization of the photocathode laser can be tolerated since it will be reduced by the bunch compression along the linac. The situation is shown schematically in figure 4.6.

Both the photocathode laser and the seed laser will be synchronized to the RF master oscillator that has to provide a stable reference with a low phase noise. The synchronization of the experiment lasers (not shown in figure 4.6) should be better than the FEL pulse duration. Since the additional jitter picked up by the electron bunch traversing the subsequent HGHG stages should be smaller than the FEL pulse duration this task is reduced to synchronizing two fs laser systems. A straightforward way could be the use of a single Ti:Sa master oscillator synchronized to the electron bunches. As shown in figure 4.7 the output pulses can be transported to amplifier/frequency-converter stages closer to the first HGHG-FEL and experiments, respectively. Due to the large distances that can be involved it will be necessary to transport the fs pulses in vacuum tubes to avoid wavefront and pulse shape distortion in air. In addition optical path length changes induced by temperature variations can be minimized via control of the environmental conditions.

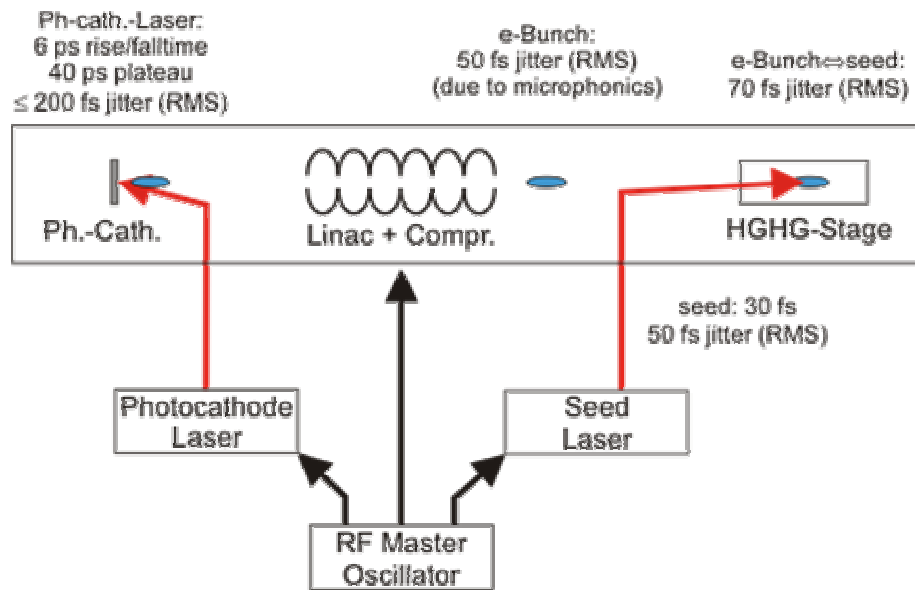


Fig. 4.6: Jitter requirements at the different stages of the FEL.

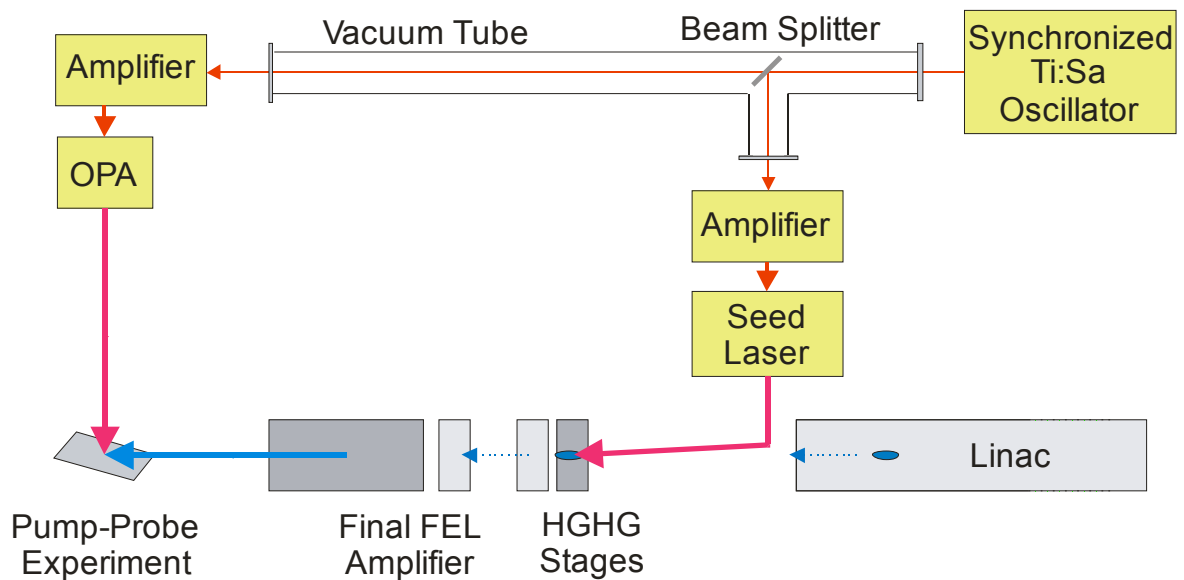


Fig. 4.7: To obtain an optimal synchronization accuracy in a pump-probe experimental setup the same pulse from a synchronized Ti:Sa oscillator will be used to drive the FEL seed and the experimental laser. For minimum jitter the optical laser pulse will run in a vacuum tube parallel to the FEL stages.

The modular character of both seed and experiment lasers implies that only the first module, i.e. a Ti:Sa master oscillator (figure 4.7), needs to be synchronized to the RF master oscillator. The general scheme of a timing synchronization is described in figure 4.8.

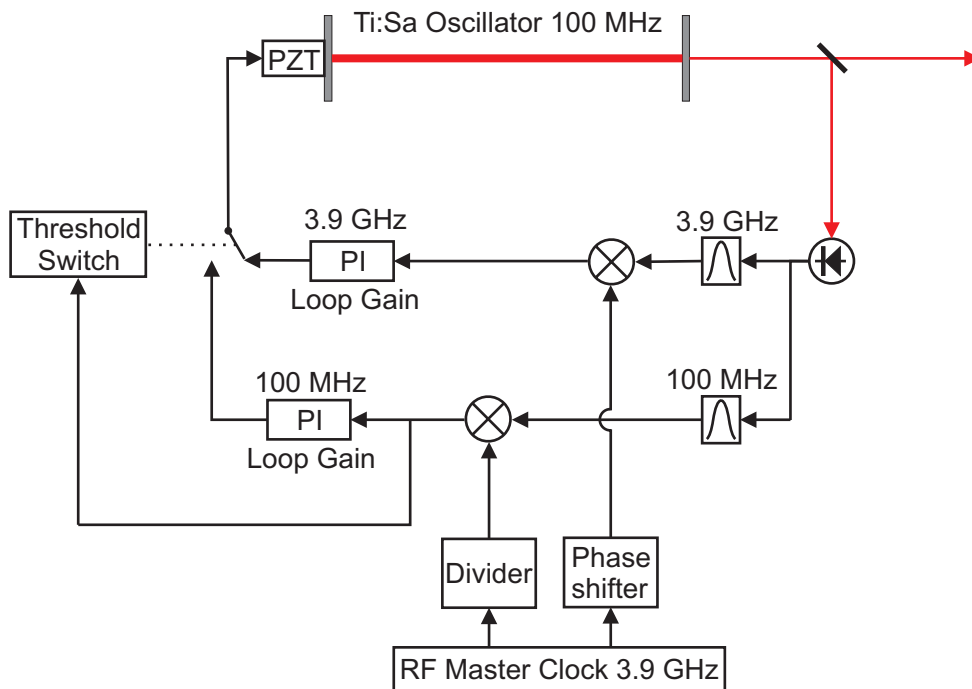


Fig. 4.8: Schematic of the timing synchronization of a Ti:Sa oscillator. By synchronizing to the fundamental frequency at startup, the correct phase relative to the 100 MHz signal is ensured. To achieve the final accuracy the RF-mixer runs at a higher harmonic of the fundamental laser repetition frequency. Switching between the two loops is controlled by the output signal of the 100 MHz mixer.

The signal from a fast photodiode pickup provides the repetition frequency of the laser cavity. Together with the reference RF signal from the master oscillator it is fed into an analog mixing circuit. Provided that the frequency of the RF and the laser are the same, the output of the mixer gives a voltage corresponding to the relative phase of both signals. This output, acting as an error signal, is fed back to the laser cavity via a loop filter and a piezo-mirror. The laser synchronization circuit therefore forms a phase-locked loop (PLL). The loop filter can be considered as the main item of the synchronization loop. It contains a specially designed proportional and integral circuit and has to account for resonances in the piezo-drives. The piezo with the attached mirror is optimized to have a high resonance frequency (~ 50 kHz). To get higher synchronization accuracy the phase mixing is performed at a higher harmonic of the laser repetition frequency. This will increase the sensitivity of the mixer and therefore result in an enhanced signal-to-noise ratio in the

phase detection [33]. An rms-timing jitter of only 1.75 fs was reported for two independent 100 MHz Ti:Sa lasers being synchronized to a 14 GHz RF reference frequency [34].

With phase detection at a harmonic of the oscillator repetition frequency one has multiple possible timing positions at which the lower repeating laser can lock to the higher reference frequency. To overcome this problem one uses a second PLL working at the fundamental of the round trip frequency of the laser. At startup only the low frequency loop will be in operation providing a coarse synchronization. By monitoring the phase error signal of the 100 MHz mixer one knows when the loop has reached a stability level that allows switching over to the high frequency loop without jumping to a neighbor phase position. During operation one will switch back to the slow feedback loop, whenever the output of the 100 MHz mixer has reached a certain threshold indicating that the fast feedback has jumped to a different position.

In summary, amazingly small values for the rms-jitter that are well below 10 fs have reached the necessary accuracy in laser synchronization in the past few years [34, 35, 36]. In these studies a Ti:Sa oscillator was synchronized directly, or indirectly via a second Ti:Sa oscillator, to an external RF master oscillator. The technology of synchronization therefore seems to be established and capable of providing synchronization to an external RF frequency at a level of 10 fs on a day-to-day basis. In fact a synchronized laser shows less fast phase noise above a certain frequency than the RF master oscillator [36] and the synchronization accuracy seems to be limited to the practical range of the microwave technology. Hence, the lowest timing jitter was reached by locking two independent lasers to stable common optical oscillator [37].

References

- [1] T. R. Schibli, J. Kim, O. Kuzucu, J. T. Gopinath, S. N. Tandon, G. S. Petrich, L. A. Kolodziejski, J. G. Fujimoto, E. P. Ippen, F. X. Kaertner, *Opt. Lett.* **28**/11 (2003) 947; F. X. Kaertner: http://mitbates.mit.edu/xfel/Talks/kaertner_seeding.ppt
- [2] M. Nisoli, S. De Silvestri, V. Magni, O. Svelto, R. Danielius, A. Piskarskas, G. Valiulis, A. Varanavicius, *Opt. Lett.* **19**/23 (1994) 1973.
- [3] M. K. Reed, M. K. Steiner-Shepard, D. K. Negus, *IEEE J. Quant. Elec.* **31**/9 (1995) 1614.
- [4] E. Riedle, M. Beutter, S. Lochbrunner, J. Piel, S. Schenkl, S. Spörlein, W. Zinth, *Appl. Phys. B* **71**/3 (2000) 457.
- [5] A. Baltuška, T. Fuji, T. Kobayashi, *Opt. Lett.* **27**/5 (2002) 306.
- [6] P. Baum, S. Lochbrunner, E. Riedle, *Opt. Lett.* **29**/2 (2004) 210.
- [7] M. Zavelani-Rossi, D. Polli, G. Cerullo, S. De Silvestri, L. Gallmann, G. Steinmeyer, U. Keller, *Appl. Phys. B* **74**/S1 (2002) 245.
- [8] W. Kornelis, J. Biegert, J. W. G. Tisch, M. Nisoli, G. Sansone, C. Vozzi, S. De Silvestri, U. Keller, *Opt. Lett.* **28**/4 (2003) 281.
- [9] A. Kummrow, M. Wittmann, F. Tschirschwitz, G. Korn, E. T. J. Nibbering, *Appl. Phys. B* **71**/6 (2000) 885.
- [10] E. T. J. Nibbering, O. Dühr, G. Korn, *Opt. Lett.* **22**/17 (1997) 1335.
- [11] O. Dühr, E. T. J. Nibbering, G. Korn, G. Tempea, F. Krausz, *Opt. Lett.* **24**/1 (1999) 34.
- [12] N. Zhavoronkov, G. Korn, *Phys. Rev. Lett.* **88**/20 (2002) 2039011.
- [13] V. P. Kalosha, J. Herrmann, *Phys. Rev. A* **67**/3 (2003) 031801(R).
- [14] B. A. Richman, S. E. Bisson, R. Trebino, E. Sidick, A. Jacobson, *Appl. Opt.* **38**/15 (1999) 3316.
- [15] Y. Nabekawa, K. Midorikawa, *Opt. Exp.* **11**/4 (2003) 324.
- [16] Y.-H. Chen, J.-H. Yao, B.-X. Yan, H.-L. Deng, Y.-F. Kong, S.-L. Chen, J.-J. Xu, G.-Y. Zhang, *Opt. Commun.* **224**/1-3 (2003) 149.
- [17] S. C. Buchter, T. Y. Fan, V. Liberman, J. J. Zayhowski, M. Rothschild, E. J. Mason, A. Cassanho, H. P. Jenssen, J. H. Burnett *Opt. Lett.* **26**/21 (2001) 1693.
- [18] L. Gallmann, G. Steinmeyer, U. Keller, G. Imeshev, M. M. Fejer, J.-P. Meyn, *Opt. Lett.* **26**/9 (2001) 614.

- [19] C. G. Durfee III, S. Backus, M. M. Murnane, H. C. Kapteyn, *Opt. Lett.* **22/20** (1997) 1565.
- [20] S. Backus, C. G. Durfee III, M. M. Murnane, H. C. Kapteyn, *Rev. Sci. Instrum.* **69/3** (1998) 1207.
- [21] S. Backus, R. Bartels, S. Thompson, R. Dollinger, H. C. Kapteyn, M. M. Murnane, *Opt. Lett.* **26/7** (2001) 465.
- [22] K. R. Wilson, V. V. Yakovlev, *J. Opt. Soc. Am. B* **14/2** (1997) 444.
- [23] P. B. Corkum, *Phys. Rev. Lett.* **71/13** (1993) 1994.
- [24] M. Schnürer, Z. Cheng, M. Hentschel, G. Tempea, P. Kálmán, T. Brabec, F. Krausz, *Phys. Rev. Lett.* **83/4** (1999) 722.
- [25] J.-F. Hergott, M. Kovacev, H. Merdji, C. Hubert, Y. Mairesse, E. Jean, P. Breger, P. Agostini, B. Carré, P. Salières, *Phys. Rev. A* **66/2** (2002) 021801(R).
- [26] V. Tosa, E. Takahashi, Y. Nabekawa, K. Midorikawa, *Phys. Rev. A* **67/6** (2003) 063817.
- [27] E. Takahashi, Y. Nabekawa, K. Midorikawa, *Opt. Lett.* **27/21** (2002) 1920.
- [28] E. Takahashi, Y. Nabekawa, K. Midorikawa, Applications of high field and short wavelength sources X, Biarritz Oct. 2003, Technical Digest, to be published in *Appl. Phys. B* (2004).
- [29] A. Rundquist, C. G. Durfee III, Z. Cheng, C. Herne, S. Backus, M. M. Murnane, H. C. Kapteyn, *Science* **280** (1998) 1412.
- [30] E. A. Gibson, A. Paul, N. Wagner, R. Tobey, D. Gaudiosi, S. Backus, I. P. Christov, A. Aquila, E. M. Gullikson, D. T. Attwood, M. M. Murnane, H. C. Kapteyn, *Science* **302** (2003) 95.
- [31] M. Nisoli, G. Sansone, S. Stargira, S. De Silvestri, C. Vozzi, M. Pascolini, L. Poletto, P. Villorresi, G. Tondello: Applications of high field and short wavelength sources X, Biarritz Oct. 2003, Technical Digest, to be published in *Appl. Phys. B* (2004).
- [32] P. Villorresi, Milano: private communication.
- [33] D. J. Jones, E. O. Potma, J.-X. Cheng, B. Burfeindt, Y. Pang, J. Ye, X. S. Xie, *Rev. Sci. Instrum.* **73/8** (2002) 2843.
- [34] R. K. Shelton, S. M. Foreman, L.-S. Ma, J. L. Hall, H. C. Kapteyn, M. M. Murnane, M. Notcutt, J. Ye, *Opt. Lett.* **27/5** (2002) 312.
- [35] R. K. Shelton, L. S. Ma, H. C. Kapteyn, M. M. Murnane, J. L. Hall, J. Ye, *Journal of Modern Optics* **49/3** (2002) 401.

- [36] L.-S. Ma, R. K. Shelton, H. C. Kapteyn, M. M. Murnane, J. Ye, *Phys. Rev. A*, **64**/2 (2001) 021802(R).
- [37] A. Bartels, S. A. Diddams, T. M. Ramond, L. Hollberg, *Opt. Lett.* **28**/8 (2003) 663.

5 The High-Brilliance Electron Injector

The electron injector is a central system for any FEL that has to deliver high brightness electron beams as the beam emittance and beam current directly influence the photon beam characteristics and determine the parameters of the undulator section as well. For the BESSY HGHG-FELs electron bunches of 2.5 to 3 nC with a pulse duration of 40 to 60 ps from the injector are required at a slice emittance of typically 1.5π mm mrad to achieve a trapezoidal charge distribution with an approximately 750 fs long flat top and a bunch profile with 1.75 kA peak current after bunch compression at the entrance to the undulator section.

For the first years of operation it is planned to use a well-established room temperature normal-conducting (n.c.) photoinjector RF gun. At a later stage this gun will be replaced by a superconducting (s.c.) RF gun. The latter is favored as it allows generating bunch patterns of extreme flexibility according to the needs of the experiments by fully exploiting the capabilities of the superconducting CW linear accelerator.

This chapter explains the following aspects of the injector: Working scheme of an RF photoinjector (section 5.1); the achievements that have been demonstrated by the PITZ collaboration (section 5.2); the simulations for a PITZ-type injector with a 1 kHz high-duty-cycle gun cavity as is required for the operation of the BESSY FEL (section 5.3); the RF system and the photo-cathode laser for the BESSY injector (sections 5.4 and 5.5). Finally, some ideas of a superconducting injector are presented in section 5.6.

5.1 Room-Temperature RF Photoinjector Guns

5.1.1 General Layout

Present-day electron gun technology is based on RF photoinjectors producing low-emittance high-current electron beams [1-3]. The basic idea is to generate high intensity beams on a cold photocathode when shining a short-pulse high-power laser onto the cathode, minimizing contributions to the emittance from hot surfaces as is the case with dispenser cathodes. The photocathode is located in a high-field cavity structure for immediate acceleration of the electrons to as high an energy as possible, minimizing the effects of high repulsive space charge forces. Furthermore, coherent momentum modulation along the bunch arising from the space charge is compensated by applying a suitable external magnetic field which compensates for emittance dilution at a certain position downstream from the cathode. A subsequent linac section provides further acceleration to ultra-relativistic energies, “freezing” the normalized emittance.

Figure 5.1 shows a sketch of the layout of the RF photocathode injector as it will be used for the BESSY Soft X-ray FEL. The RF gun, to begin with, is based on a $1\frac{1}{2}$ cell copper cavity [4]. The RF power is transmitted through a rectangular waveguide matched with a “doorknob” transition to a coaxial input power coupler exciting a TM_{010} -like π -mode at 1.3 GHz used for acceleration. The laser beam is guided via a mirror system through the hollow inner coaxial conductor to illuminate the photocathode. A main solenoid provides for beam focusing. A bucking coil behind the gun compensates for non-zero magnetic fields at the cathode which would lead to a significant deterioration of the emittance during the emission process [5].

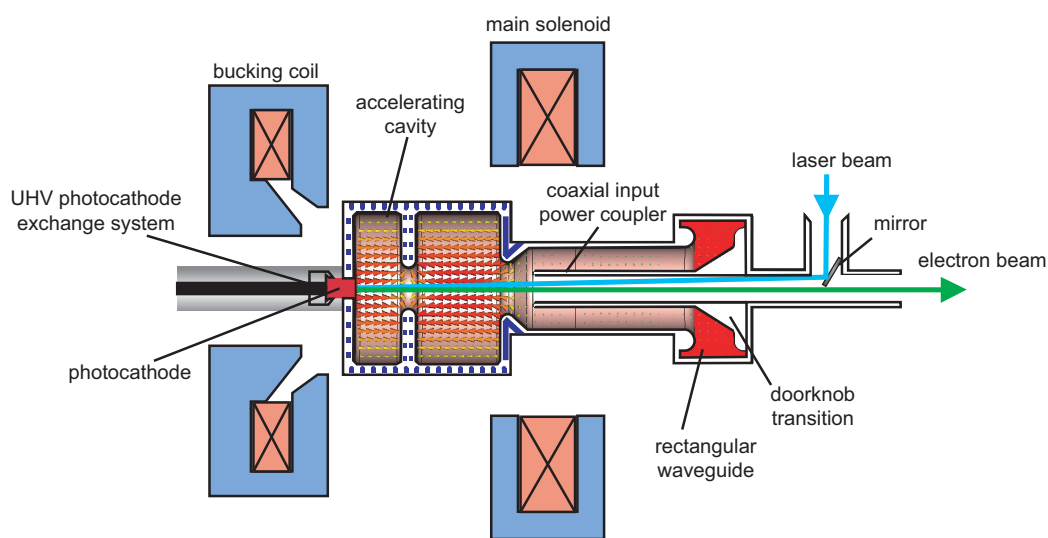


Fig. 5.1: Schematic view of a $1\frac{1}{2}$ -cell laser driven n.c. photoinjector RF gun showing the coaxial input coupler and solenoids for emittance compensation.

5.1.2 Emittance Conservation

During the emission process at the cathode the transverse emittance deteriorates considerably by linear and nonlinear space-charge forces. The bunch center experiences a much larger space-charge field than the head or tail of the bunch, the projected initial emittance increases since different longitudinal slices in the bunch are not well aligned to each other any more, i.e. they possess different radial momenta. This correlation can be compensated for by a counteracting static magnetic field produced by an external solenoid lens. Consequently, a considerable reduction of the projected emittance can be achieved after a drift space behind the gun. This so-called emittance compensation process was originally proposed by Carlston [6] and has been verified experimentally [7]. Figure 5.2 illustrates this compensation process, whereby the injected particle distribution is

tracked through the RF gun and a subsequent drift space using the ASTRA code [8]. The evolution of the projected normalized transverse rms emittance $\epsilon_{n,rms}$ and the transverse rms beam size σ is illustrated.

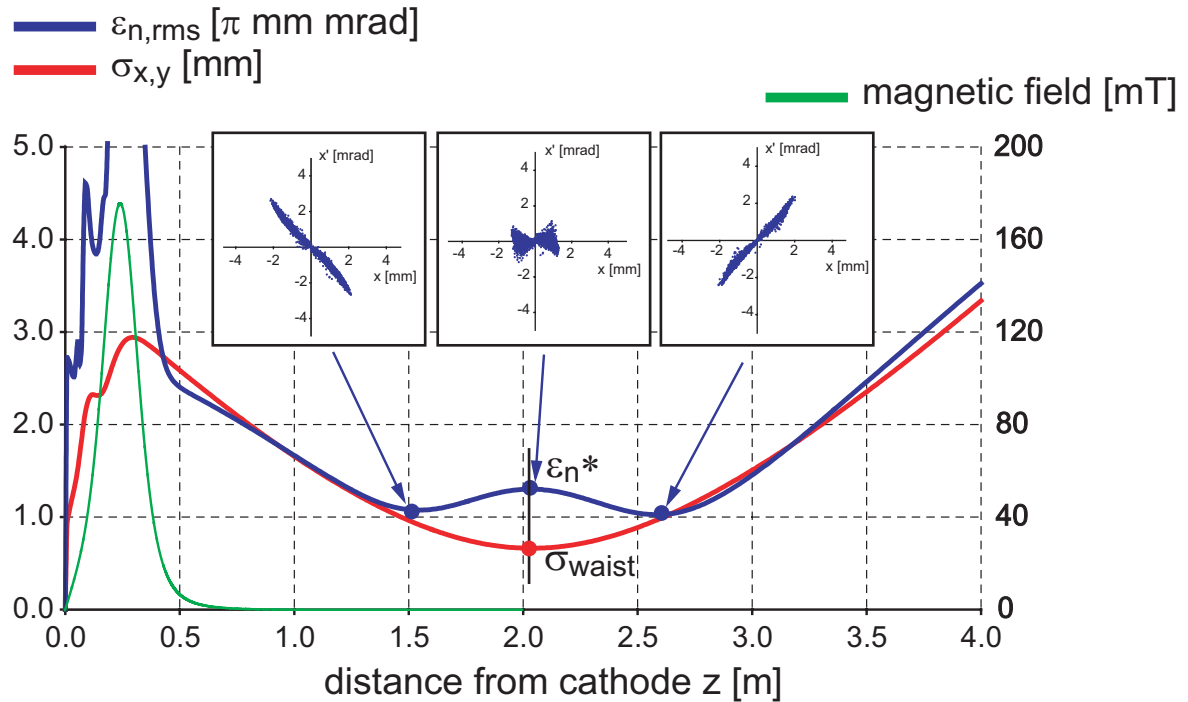


Fig. 5.2: Emittance compensation process in the drift space behind the RF gun ($z = 0$: position of cathode). Red is the beam radial rms size, blue the normalized projected transverse rms beam emittance, the corresponding phase space ellipses are shown. Green is the on-axis solenoid field profile. ASTRA simulation with a peak field in the gun of $E_{peak} = 40$ MV/m, bunch charge $Q_B = 1$ nC and a solenoid magnet located 24 cm behind the photocathode.

The beam is focused by the applied magnetic field into a beam waist σ_{waist} after a certain drift space. In the subsequent drift space the beam diverges again under the influence of space charge forces. A similar behavior is true for the normalized emittance $\epsilon_{n,rms}$. However, the RF-induced energy spread gives rise to chromatic effects in the solenoid causing the bunch slices to oscillate with different frequencies in the transverse phase space. Hence, a local emittance maximum ϵ_n^* evolves in the drift space. Actually, the slice emittances are better aligned to each other in the adjacent minima as depicted in figure 5.2 by the transverse phase space distribution shown in the insert. At the first minimum all slice emittances are convergent; at the second minimum they are divergent. In between, the projected emittance is at a relative maximum. The magnetic field strength in general can be optimized so that the local emittance maximum is located at the same position as the

beam waist shown in figure 5.2. This dedicated position z^* is an efficient “working point” to place the entrance of the following accelerating section [9]. As a result, the slice oscillations can be damped such that the second emittance minimum of the beam is formed further downstream within the accelerator and at higher energies, where space-charge forces play a minor role. Thus $\varepsilon_{n,rms}$ is frozen at a lower level. The adiabatic damping due to the acceleration finally determines the geometrical emittance. The complete process is illustrated in figure 5.3 where a single booster linac (9-cell TESLA cavity) has been placed at the working point position z^* for the example given above.

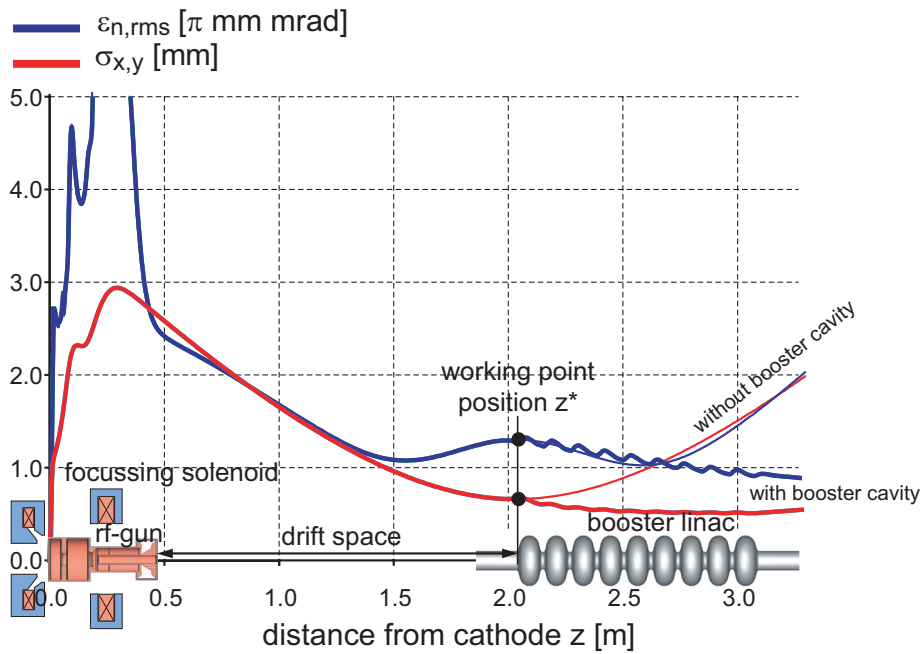


Fig. 5.3: Evolution of the normalized projected transverse emittance (blue) and beam size (red) with a booster linac placed at the working point. The increase in beam size and emittance without the booster is indicated in thinner lines.

The optimum position z^* largely depends on the given solenoid position and corresponding strength, which on the other hand determines the beam size at the waist position σ_{waist} . To properly match the beam to the linac the field in the booster cavity has to be chosen according to the “invariant envelope” matching criterion [10]

$$\gamma' = \frac{2}{\sigma_{waist}} \sqrt{\frac{I_{peak}}{3I_0\gamma}}, \quad (5.1)$$

whereby γ denotes the normalized beam energy at the entrance of the booster, γ' the normalized accelerating gradient in the booster linac, I_{peak} the peak current normalized by the Alfvén current $I_0 = ec/r_e \approx 17\text{kA}$. Following this line normalized projected emittances below $2.0 \pi \text{ mm mrad}$ and corresponding slice emittances below $1.5 \pi \text{ mm mrad}$ respectively are achieved in the simulations for beams of total charge up to 2.5 nC .

5.2 The PITZ Collaboration RF Photoinjector

In a collaboration of DESY, MBI, TU Darmstadt and BESSY a RF photoinjector development suitable for FELs and linear colliders was started in 2000 [2]. The injector has been steadily improved since first beam was achieved in December 2001. Figure 5.4 shows a photo of the Photoinjector Test facility (PITZ) at DESY Zeuthen. The achievements in terms of beam quality are already suitable for the BESSY FEL. Table 5.1 summarizes the major performance data.

Table 5.1: Major performance data achieved by the PITZ collaboration photoinjector.

Parameter	Unit
Bunch charge	1 nC
Projected emittance	1.7 $\pi \text{ mm mrad}$
Peak input power	2.93 MW
Length of bunch train	800 μs
Repetition frequency	10 Hz
Duty cycle	0.8 %
Peak field at cathode	42 MV/m
Average RF power	23.4 kW

The RF gun has been operated up to a mean power level of 23.4 kW limited by vacuum interlock events [11]. Once the gun has been conditioned no problems are expected to fulfill the TTF II specifications of 26.4 kW corresponding to a duty cycle of 0.9% (10 Hz , $900 \mu\text{s}$). When compared to the BESSY FEL design goals, it is the repetition rate and the length of the macro-bunch that have to be adapted to a $1000 \text{ Hz} \cdot 25 \mu\text{s}$ pulse operation, i.e. a duty cycle of 2.5% to be realized with an improved cooling scheme. The work on this high duty cycle cavity is described in the next paragraph. Table 5.2 summarizes the system parameters required for the BESSY FEL injector.



Fig. 5.4: The PITZ photoinjector as in late 2003. The two solenoids (main solenoid and bucking coil in blue are clearly visible with the RF cavity herein). In the foreground is the cathode exchange system.

Table 5.2: BESSY FEL operational parameters of the n.c. RF gun cavity.

Parameter		Unit
Resonant frequency	1.3 (TM ₀₁₀ - π mode)	GHz
Number of cells	1½	
Unloaded quality factor (95% of calculated)	~ 22000	
Coupling factor ($Q_0 \approx Q_{ext}$)	~ 1	
Field rise time (99.85% of full amplitude)	17.5	μ s
Length of bunch train	6	μ s
Repetition frequency	1000	Hz
Duty cycle	~2.5	%
Peak field at cathode	40	MV/m
Peak input power	3.0	MW
Average RF power	75	kW
Max. surface heat flux	53	W/cm ²
Max. beam energy at exit	4.2	MeV

5.3 The BESSY Normal-Conducting Injector

5.3.1 The High-Duty Cycle, High-Power Injector Cavity

During operation a constant resonance frequency of the cavity has to be guaranteed to avoid RF phase and amplitude mismatch. Hence thermal frequency drifts must be minimized, which necessitates a well optimized cooling scheme. At PITZ a stable operation of the RF gun at a peak field of 40 MV/m and a mean power of up to 23.4 kW has been demonstrated. In figure 5.5 the cooling channel layout is shown for the present PITZ RF gun. Thermal sensors in the cavity are located at dedicated positions for diagnosis.

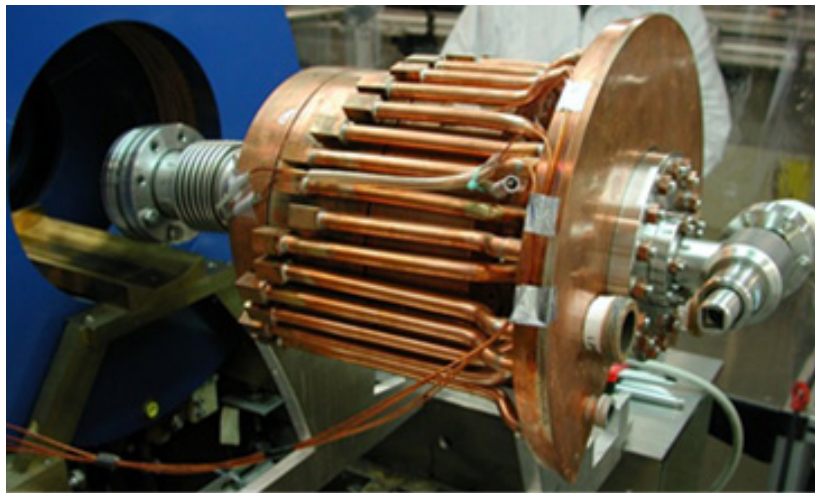


Fig. 5.5: The actual n.c. PITZ RF gun.

A thermal detuning of the cavity can be compensated in principle by changing the inlet water temperature (~ 20 kHz/ $^{\circ}$ C), while the water temperature is stabilized with a precision of 0.1° C during operation. No mechanical tuner at the cavity wall is to be incorporated since this would lead to field distortions and thus to beam emittance dilution [11]. For the BESSY FEL a design peak field of 40 MV/m has been chosen. Consequently an average wall power loss of 75 kW has to be taken into account due to an operation at a duty cycle of 2.5%. As the cooling scheme of the present PITZ cavity does not allow operation at a mean input power of 75 kW, an improved cooling scheme has been developed to lower the thermal gradients in the cavity walls. Additional cooling channels have been included in the front, the end plate and the iris. Water inlets and outlets have been realistically modeled. Thermal and structural analyses have been carried out using the multi-physics package of the ANSYS code [12].

Figure 5.6 illustrates the numerical procedure applied to calculate the temperature distribution in the cavity wall in a realistic way. A 3D cavity model has been created including the water cooling channels (figure 5.6a). Once the mesh and the electric boundary conditions are defined (figure 5.6b) the electromagnetic field distribution of the accelerating TM_{010} -like π -mode is calculated. The ohmic wall power loss P_{loss} , induced by the surface magnetic fields H (figure 5.6c), is calculated by integrating H over the entire cavity surface A , i.e.

$$P_{\text{loss}} = \frac{R_s}{2} \cdot \oint \! \! \! \oint dA \cdot H = \frac{1}{2} \sqrt{\frac{\mu_0 \pi f}{\sigma}} \cdot \oint \! \! \! \oint dA \cdot H \quad , \quad (5.2)$$

where R_s denotes the surface resistance, f the resonance frequency and σ the electric conductivity. The heat flux at each boundary element is determined (figure 5.6d) [13]. The maximum heat flux has been calculated to be $53\text{W}/\text{cm}^2$ at $P_{\text{loss}}=75\text{ kW}$ located at the iris plane. In a next step the cavity wall is meshed, and the heat flux distribution is transferred to the corresponding elements as a realistic heat source (figure 5.6e). Convection loads are applied to the water channels to simulate the cooling water flow (figure 5.6f).

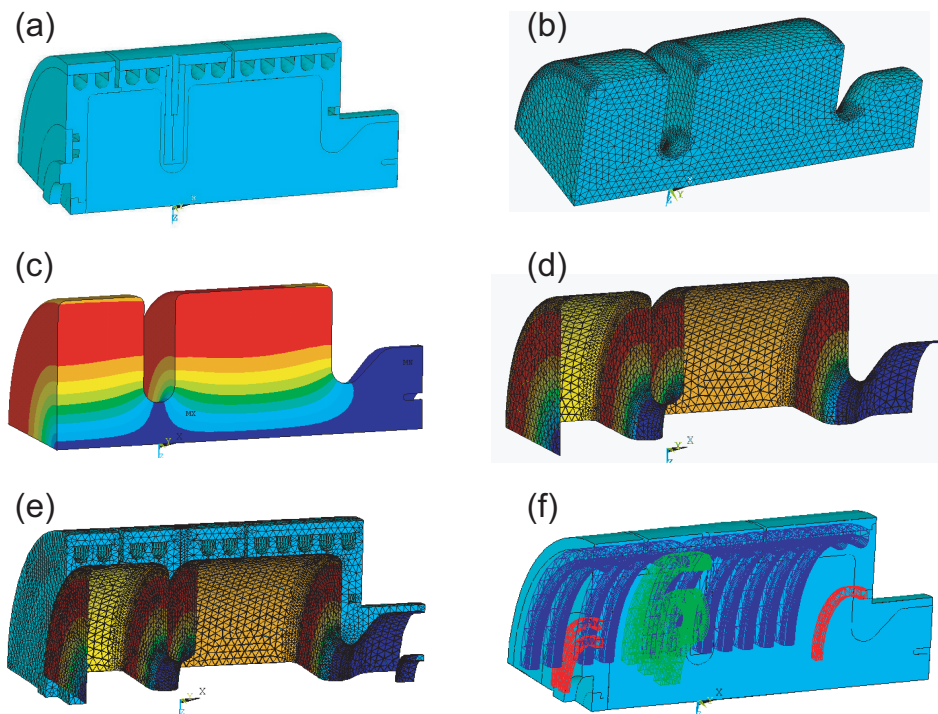


Fig. 5.6: ANSYS procedure to calculate the thermal distribution in the cavity wall.

Using the heat flux as heat-generation source and the water convection as a heat sink, the temperature distribution in the cavity walls can be calculated. The corresponding thermal plot at $P_{\text{loss}}=75$ kW is shown in figure 5.7. The outline of the non-deformed cavity is depicted as well to indicate the thermal expansion (arbitrarily scaled).

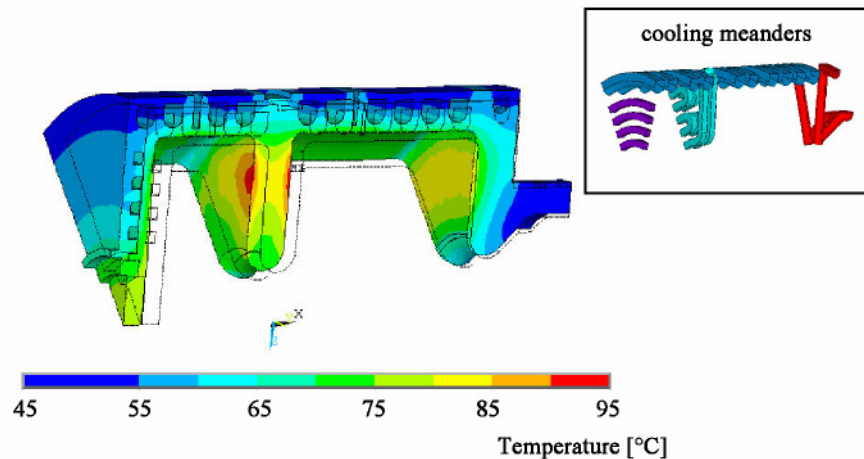


Fig. 5.7: Thermal distribution at $P_{\text{loss}}=75$ kW for an improved cooling scheme (42°C bulk water temperature, water flow velocity 2 m/s).

The average temperature in the cavity body is $\sim 20^\circ\text{C}$ above the bulk water temperature assumed to be 42°C in the calculations. At the cathode the temperature is about 75°C which is low enough to yield no degradation of the quantum efficiency of a Cesium Telluride (Cs_2Te) photocathode [14]. The hottest spot of 93°C is located at the iris, where the necessary water inlet and outlet disrupt the angular water flow. The thermal load causes wall distortions typically in the range of several ten microns, which gives rise to internal wall stresses. Figure 5.8 depicts the von Mises stresses in the cavity taking the vacuum load into account. Main stresses are at a level well below the 0.2% proof stress of copper (124 MPa) preventing inelastic deformations.

The frequency shift of the cavity, caused by the thermal expansion and the vacuum load, have been evaluated using SUPERFISH [15]. The main thermal and structural results are summarized in table 5.3. The total frequency shift has to be considered for fabrication as only small frequency drifts (~ 22 kHz/ $^\circ\text{C}$) can be compensated by changing the inlet temperature of the cooling water. Since no mechanical tuner is provided to avoid perturbation of the accelerating field, tuning will be done by plastic deformation of the end-plates and iris. Work is still in progress to further improve the cooling concept and to lower the internal stresses.

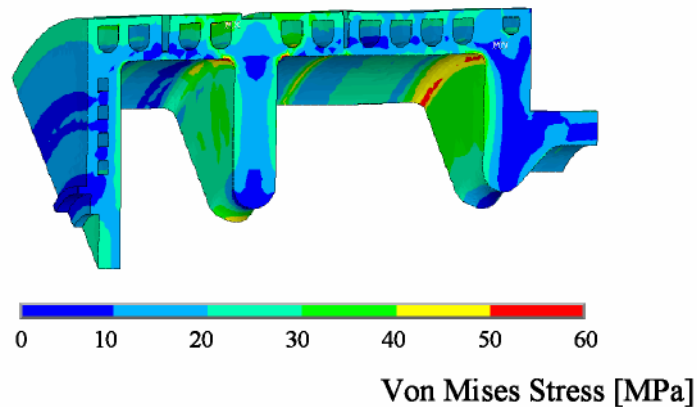


Fig. 5.8: Von Mises stresses due to the thermal expansion at $P_{\text{loss}}=75$ kW (42°C bulk water temperature, water flow velocity 2m/s).

Table 5.3. Thermal and structural results for the n.c. RF gun operating at 75 kW average wall power loss (bulk water temperature 42°C, water flow rate 2m/s).

Parameter		Unit
Max. temperature rise	51	°C
Max. spot temperature	93	°C
Average temperature	61.3	°C
Max. wall displacement	180	μm
Max. von Mises stress	60	MPa
Water tuning range	22	kHz/°C
Frequency shift by thermal load	-0.9	MHz
Frequency shift by vacuum load	+0.4	MHz

5.3.2 Working Point and Magnetic Field

The optimum parameter settings for the BESSY injector are a compromise between the theoretical emittance minimum and the space requirements for cryogenic and diagnostics in the drift space behind the gun. Usually more drift space can be gained by placing the main focusing solenoid and therefore the working-point-position booster entrance further downstream at the expense of a transverse emittance increase. Optimization studies have been done using different solenoid positions resulting in different magnetic peak field locations as shown in figure 5.9 [16].

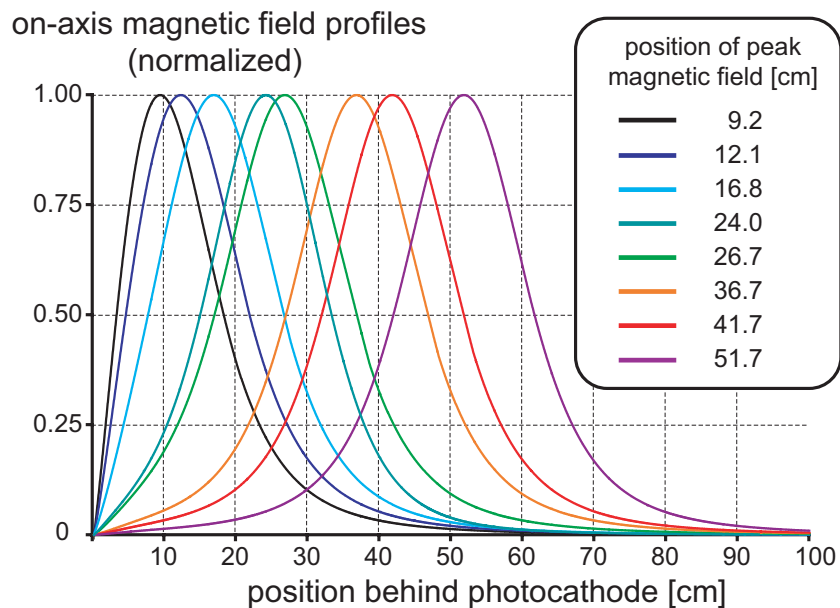


Fig. 5.9: Normalized on-axis magnetic field profiles with zero field at the cathode ($z = 0$) for various positions of the main solenoid, i.e. peak-field locations as listed in the legend.

With these field profiles the beam parameters ε_n^* and σ_{waist} at the working-point position z^* have been calculated varying the solenoid strength. Results are shown in figure 5.10 on the left side. Equal positions of ε_n^* and σ_{waist} correspond to an ideal working point z^* indicated by the diagonal line. In this example simulations are presented for a bunch charge of 1 nC. However, the working point position z^* does not vary significantly with the bunch charge as a result of the to-first-order frequency-independent slice envelope oscillations on the charge density [10].

The plot on the right side of figure 5.10 depicts the steady increase of z^* with the solenoid location. The corresponding emittances ε_n^* are listed as well. A peak field located at 27 cm behind the cathode is well suited for the BESSY FEL delivering a sufficiently long drift space up to the linac entrance with transverse emittances at a sufficiently low level.

5.3.3 RF Phase at Injection

The injection phase φ_{rf} of the electrons with respect to the RF voltage (launch phase) impacts all essential beam parameters. A typical dependence of the emittance ε_n^* , beam size σ_{waist} , working point position z^* and corresponding magnetic flux density B on the launch phase φ_{rf} is shown in figure 5.11, whereby φ_{rf} is related to the phase of maximum energy gain ($\varphi_{\text{rf}} \equiv 0^\circ$). The minimum emittance ε_n^* can be produced, when $\varphi_{\text{rf}} = -1.5^\circ$ as illustrated in figure 5.10 on the left side which is due to an improved balance of RF-focusing and defocusing effects in the gun. With decreasing φ_{rf} the magnetic field strength

has to be reduced to produce an ideal working point. Hence due to the diminished focusing strength the beam size σ_{waist} is enlarged shifting the working point further downstream at the same time. This behavior is depicted in figure 5.11 on the right side.

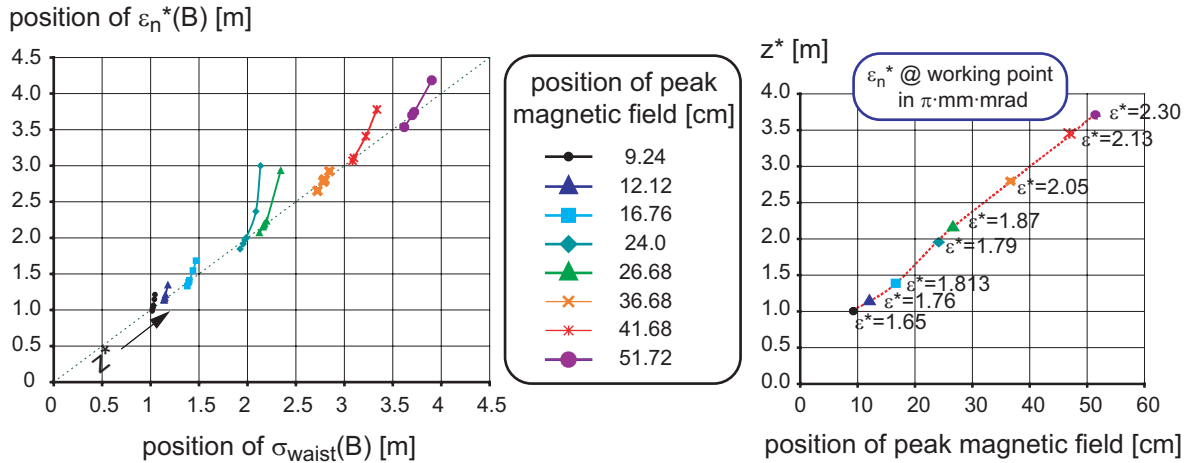


Fig. 5.10: Optimization of the working-point position z^* with varying magnetic flux density B of the solenoid for different magnetic field profiles (left) and corresponding optimum z^* and ϵ_n^* (right) as listed in the legend. ASTRA simulations with $E_{\text{peak}}=40\text{MV/m}$ and $Q_B=1\text{nC}$.

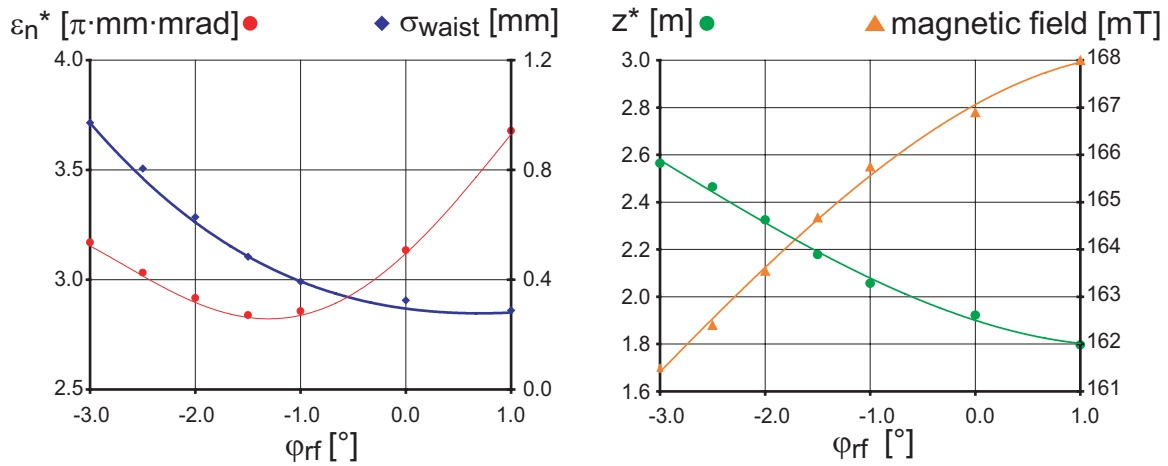


Fig. 5.11: Left: Projected transverse emittance ϵ_n^* and rms beam size σ_{waist} at the working point for different launch phases ϕ_{rf} . Right: Corresponding working point z^* and magnetic flux density. ASTRA simulations with $E_{\text{peak}}=40\text{ MV/m}$, $Q_B=2.5\text{nC}$, $t_r = 38\text{ ps}$, 4 ps rise/fall time, $\varnothing_{\text{laser}} = 3\text{mm}$, peak magnetic field at 26.7 cm behind the cathode, thermal emittance included.

According to equation (5.1), the beam size σ_{waist} is proportional to the optimum accelerating gradient at a given peak current. In fact for a launch phase $\varphi_{\text{rf}} = -1.5^\circ$, the corresponding booster field exceeds the typical operation field of 15.6 MV/m considerably. Thus a launch phase of $\varphi_{\text{rf}} = -3^\circ$ has been chosen, which lowers the optimum booster field. In fact a comparably low transverse emittance after the linac exit is achieved as in case of $\varphi_{\text{rf}} = -1.5^\circ$.

5.3.4 The First Linac Section

The first linac section consists of eight standard 9-cell TESLA-cavities housed in a single cryostat (cryomodule). The parameter setting of the linac has been optimized with regard to the invariant envelope condition. In figure 5.12 the essential outcome for the transverse phase space is shown by means of the evolution of the projected normalized transverse emittance $\varepsilon_{n,\text{rms}}$ and beam size σ . The minimum of both values has been shifted to the linac exit freezing the emittance at $\varepsilon_{n,\text{rms}} = 2.0 \pi \text{ mm mrad}$ at a beam size of $\sigma = 0.4 \text{ mm}$.

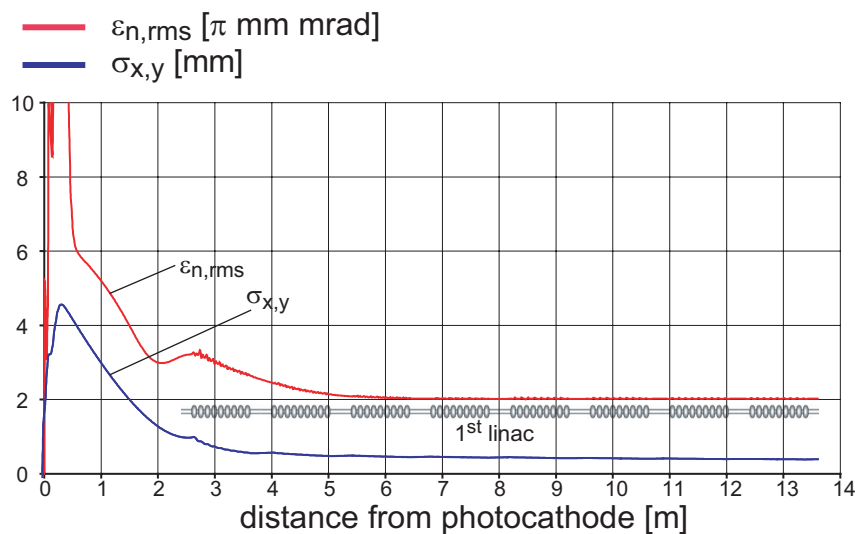


Fig. 5.12: Evolution of the projected normalized transverse rms emittance $\varepsilon_{n,\text{rms}}$ (red), and beam size $\sigma_{x,y}$ (blue), up to the exit of the 1st linac cryomodule, consisting of eight 9-cell superconducting cavities. ASTRA simulations with $E_{\text{peak}}=40 \text{ MV/m}$ (gun), $Q_B=2.5 \text{ nC}$, $t_F = 38 \text{ ps}$, 4 ps rise/fall time, $\varnothing_{\text{laser}} = 3 \text{ mm}$, $B_z=161.5 \text{ mT}$ at 26.7 cm behind cathode, $E_{\text{acc}} = 12.5 \text{ MV/m}$ (cav. #1-4), $E_{\text{acc}} = 15.6 \text{ MV/m}$ (cav. #5-8), thermal emittance included.

The effect of a thermal emittance is already included. The emittances averaged over different longitudinal bunch slices amount to 1.5π mm mrad, fulfilling the need of the BESSY FEL.

The main results in longitudinal phase space are presented in figure 5.13 depicting the beam energy E_{kin} , the projected longitudinal emittance $\varepsilon_{z,\text{rms}}$, the rms energy spread ΔE_{rms} and the longitudinal beam size σ_z . With respect to the matching condition equation (5.1) the first four cavities operate at a lower field, whereas the last four cavities are operating at the maximum possible field to maximize the beam energy at the exit.

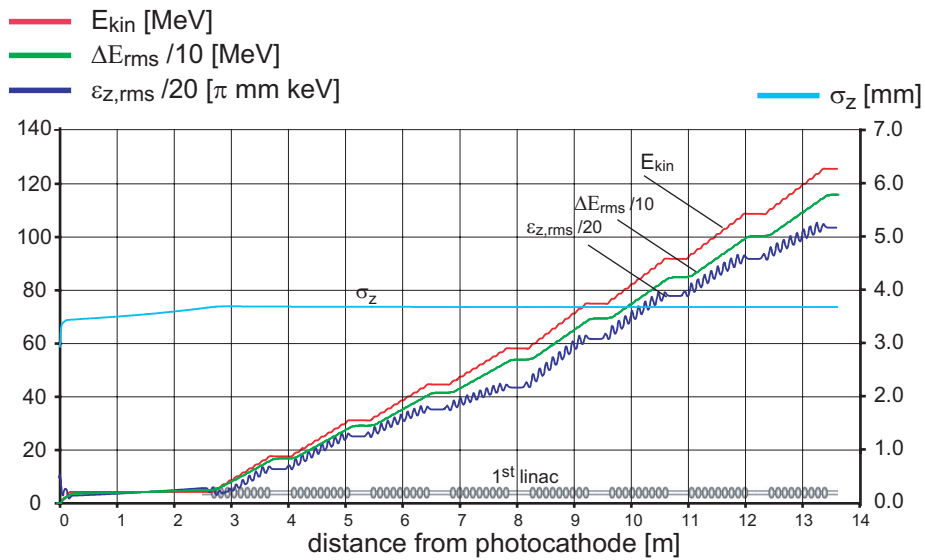


Fig. 5.13: Evolution of the average kinetic energy E_{kin} (red), rms energy spread ΔE_{rms} (green), the projected normalized longitudinal rms emittance $\varepsilon_{z,\text{rms}}$ (blue) and the longitudinal beam size σ_z up to the exit of the 1st linac cryomodule for the optimum parameter settings.

Table 5.4 summarizes the optimum parameter settings of the RF gun, solenoid and first linac section. The launch phases in the linac cavities are chosen to introduce a certain energy chirp with respect to the needs of the first bunch compressor stage located after the second linac module.

The basic beam parameters after the first linac are listed in table 5.5.

Table 5.4: Parameter settings for the RF-gun, solenoid and first linac module.

Parameter	Unit	
Normal conducting RF gun cavity		
Mode of operation	TM ₀₁₀ – π mode	
Total bunch charge	2.5	nC
Resonant frequency	1.3	GHz
Peak field	40	MV/m
Relative injection phase (0°= max. energy gain)	-3	degree
Focusing solenoid		
Peak field position behind cathode	267	mm
Peak magnetic field	161	mT
Superconducting linac module		
Mode of operation	TM ₀₁₀ – π mode	
Resonant frequency	1.3	GHz
Cavities # 1-4		
Effective field	12.5	MV/m
Relative injection phase (0°= max. energy gain)	-7.5	degree
Cavities # 5-8		
Effective field	15.6	MV/m
Relative injection phase (0°= max. energy gain)	-7.5	degree

Table 5.5: Electron beam parameters (rms values) after the first linac module.

Parameter	Unit	
Transverse phase space		
Normalized transverse emittance (Including thermal emittance)	2.0	π mm mrad
Average slice emittance	1.5	π mm mrad
Transverse beam size	0.4	mm
Longitudinal phase space		
Average kinetic energy	126	MeV
Energy spread	1040	keV
Normalized longitudinal emittance	2300	π keV mm
Longitudinal beam size	3.7	mm

5.3.5 The Third-Harmonic Cavity

Short bunches as needed for the BESSY FEL cannot be produced directly by the injector since space-charge effects result in intolerable high transverse emittances. Bunch compression is mandatory to produce high peak currents at energy levels where space charge forces play a minor role. For the BESSY FEL, a staged bunch-compression scheme is envisioned utilizing the energy-dependent path lengths in magnetic dipole chicanes. The first bunch compressor will be placed behind the second linac module. The bunch compressor works most effectively, when the longitudinal phase space exhibits a linearized energy spread (chirp). However, during acceleration the bunch has gathered an inevitable non-linear phase space distortion due to the cosine-like nature of the RF voltage in the linac cavities. A third-harmonic system consisting of 3.9 GHz superconducting cavities will be used to linearize these correlated distortions. The cavity design is based on a scaled 9-cell TESLA cavity currently under development at Fermilab National Laboratory [17]. The on-axis cavity field of the FNAL design is shown in figure 5.14.

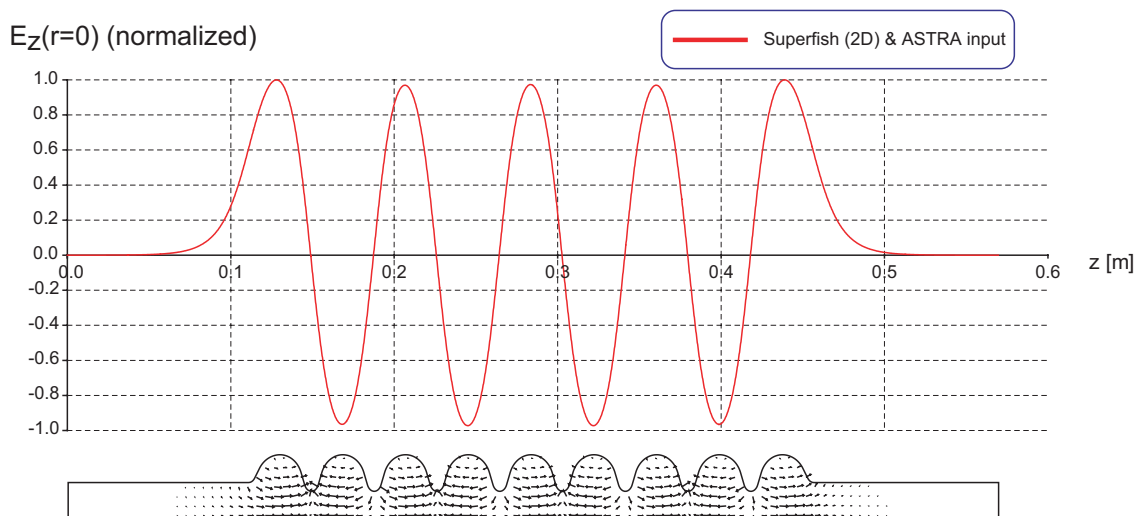


Fig. 5.14: On-axis electric field of the accelerating mode in the 3.9 GHz s.c. 9-cell cavity (top) and vector plot of the TM_{010} -like π -mode (bottom).

The cavity voltage needed to compensate for the distortions is determined by the particle energy already gained in the linac. The main goal is to achieve a linear voltage sum over the bunch length by choosing a proper amplitude and phase of $V_{\text{harm}}(t)$ with respect to $V_{\text{acc}}(t)$. Assuming an on-crest acceleration within the linac for simplification and substituting $t=s/c$ (bunch coordinate s), the sum of all voltages is given by

$$V_{sum}(s) = \hat{V}_{acc} \cdot \cos\left(\omega_0 \frac{s}{c}\right) + \hat{V}_{harm} \left(\cos(\Delta\varphi) \cdot \cos\left(\omega_{harm} \frac{s}{c}\right) - \sin(\Delta\varphi) \cdot \sin\left(\omega_{harm} \frac{s}{c}\right) \right) \quad (5.3)$$

with the center of the bunch at $s = 0$.

Using a Taylor expansion at $s = 0$ one can simplify this expression;

$$V_{sum}(s) \approx \hat{V}_{acc} + \hat{V}_{harm} \cos(\Delta\varphi) - \hat{V}_{harm} \frac{3\omega_{harm}s \sin(\Delta\varphi)}{c} - \frac{1}{2} \left(\omega_0 \frac{s}{c} \right)^2 \left(\hat{V}_{acc} + 9\hat{V}_{harm} \cos(\Delta\varphi) \right). \quad (5.4)$$

For a constant voltage across the whole bunch length, the linear and quadratic terms in equation (5.4) have to be eliminated, thus

$$\hat{V}_{harm}(s) = - \left(\frac{\omega_0}{\omega_{harm}} \right)^2 \frac{\hat{V}_{acc}}{\cos \Delta\varphi} \quad \text{and} \quad \Delta\varphi = -180^\circ \quad (5.5 \text{ a,b})$$

respectively. Consequently the harmonic cavity decelerates the beam ($\Delta\varphi = -180^\circ$) and $1/9^{\text{th}}$ of the linac voltage is required, as determined by the frequency ratio of both systems. However, for the bunch compressor a certain energy spread must be provided. Therefore, the beam is accelerated off-crest. The simplified description in equation (5.5a,b) does not fully hold in practice but is sufficient to estimate the required voltage. The necessary voltage of the harmonic cavity system will be 28.2 MV. As the active length of a single cavity is 0.3459 m, eight cavities need to be installed with a moderate field of up to 13 MV/m per cavity. The operating mode parameters (TM₀₁₀- π mode) of the third harmonic cavities are summarized in table 5.6.

Table 5.6: Basic parameters of the third harmonic cavity system.

Parameter	Unit	
Resonant frequency f_0	3.9	(TM_{010} - π mode) (GHz)
Number of cells	9	
Active length	0.3459	m
R_{eff}/Q_0	373	
Effective field (max.)	13	MV/m
Number of cavities	8	
Peak-to-effective electric field ratio	2.3	
Peak-to-effective magnetic field ratio	4.9	mT/(MV/m)

5.4 Injector RF System

The injector RF system requires a pulsed RF power source with a repetition rate of 1 kHz. A pulsed modulator power supply will feed a klystron. The RF power will be transferred by a waveguide and a circulator to the injector gun cavity. A fast amplitude feedback loop will reduce the filling time of the cavity and will provide a stable flat top.

5.4.1 Klystron Requirements

The requirements for the klystron remain well within reasonable technological limits. Units have been built for higher and lower frequency bands with substantially higher output powers. The choice of L-band klystrons is nevertheless limited. 3 MW are needed to achieve a peak field of 40 MV/m in the injector gun cavity. More power enables shorter fill times of the cavity. The required pulse length is 25 μ s (total). The TH2104 U klystron is a perfect match for the demands of the injector RF system. The parameters are listed in table 5.7, a photo of the device is shown in figure 5.15.

5.4.2 Modulator Requirements

The requirements for the modulator are moderate with respect to the peak power and the pulse length, but the high repetition rate of 1 kHz as well as the high average power exceeds the values achieved by existing modulators. In a study the technical solutions were investigated jointly with component manufacturers.



Fig. 5.15: Klystron TH2104 U for use in the gun modulator and in the high power processing transmitter.

Table 5.7: Data of the klystron for the gun modulator.

Data of klystron TH2104 U		Unit
Frequency	1.3	GHz
Peak RF output power	10	MW
Average RF output power	250	kW
Peak drive power	320	W
Maximal duration of output pulse	250	μ s
Bandwidth (-1 dB)	8	MHz
Gain	50	dB
Efficiency	45	%
DC voltage	185	kV
DC current	68	A
Physical height	2.04	m
BESSY injector RF system parameters		
Peak RF output power	10	MW
Duration of output pulse	25	μ s
Repetition rate	1	kHz

Three different approaches were investigated: A line-type modulator, a hard-tube modulator using a pulse transformer, and a directly switched modulator. The hard-tube modulator is the favored solution with respect to flexibility, technical aspects as well as costs. The circuit is shown in figure 5.16. One 15 kV power supply charges a bank of capacitors. A part of the energy is transferred by an on/off IGBT switch to a pulse transformer feeding the klystron with a 165 kV pulse. The pulse length is variable. It can be controlled by the length of the trigger pulse of the switch allowing the pulse length to be optimized without changing any hardware.

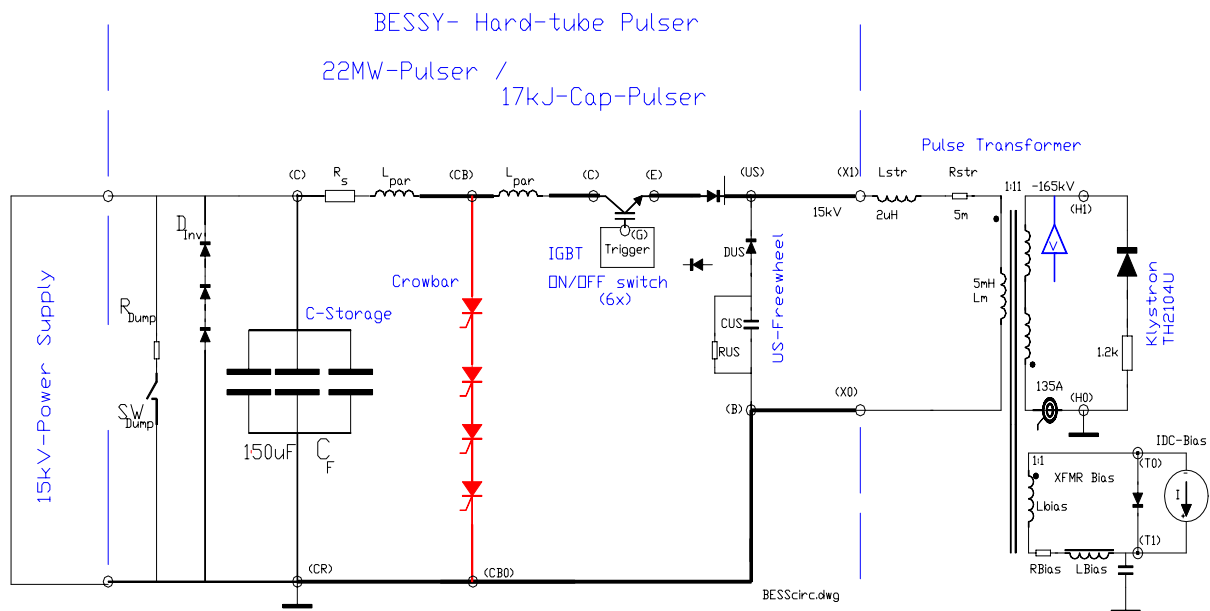


Fig. 5.16: Hard-tube modulator for the n.c. gun cavity.

5.4.3 Fast Amplitude Control Loop

The most sensitive device of the injector is the highly loaded gun cavity. By introducing a fast amplitude control loop the RF pulse can be stabilized and the filling time can be minimized. In this way the heating of the cavity can be reduced and stability requirements of the modulator can be relaxed. The amplitude loop with a bandwidth of several MHz has a fixed set-point for the duration of the RF pulse. After the electron bunches have been accelerated, the stored energy in the gun cavity is removed actively by revers-

ing the drive phase. To demonstrate the concept a low-power prototype of this loop was tested using a 1.5 GHz normal-conducting Landau cavity of BESSY II with $Q_0=22,000$ and loaded Q - value of 11,000. The results are shown in figure 5.17 giving a flat top of 20 μs out of a 25 μs pulse.

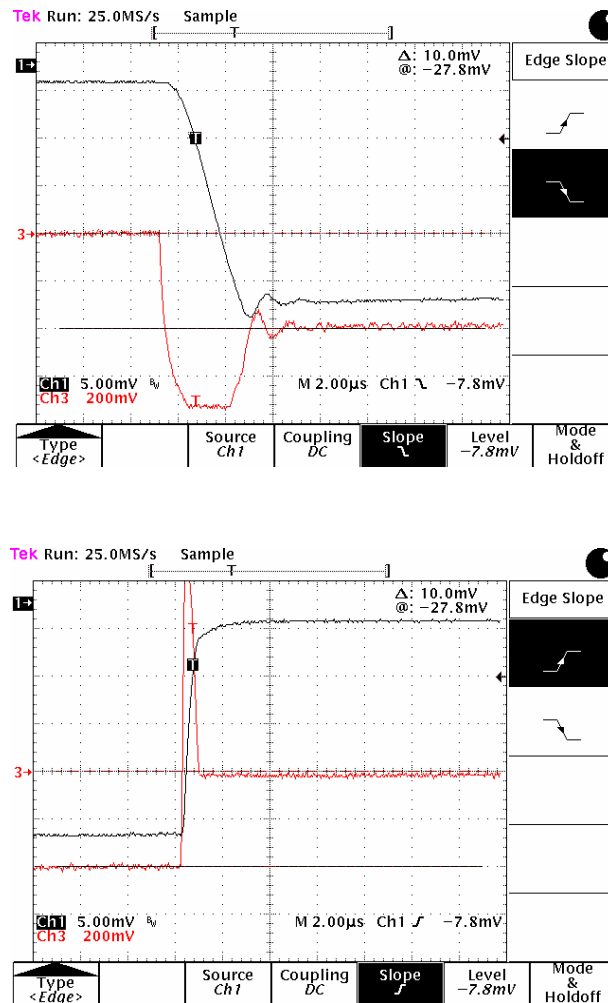


Fig. 5.17: Rise and fall time of a low-level fast amplitude loop. Measurements are taken using a copper 1.5 GHz cavity with a loaded Q value of 11,000. The red and black curves are the drive power and cavity voltage, respectively. Display is set to negative voltage.

5.5 The Photocathode Laser

5.5.1 The Photocathode Laser, Parameters, and Influence on the Emittance

Picosecond electron pulses at a charge of several nC are generated by illuminating the photocathode with a laser beam. The initial laser settings have to be chosen mainly with regard to

- The space-charge-dominated transverse emittance and
- The thermal emittance.

The thermal emittance is the initial emittance generated at the cathode depending on the local cathode temperature at the laser spot. The energy, energy spread and angular distribution of the emitted electrons depend on the cathode material and the photon energy of the laser. Consequently, the thermal emittance yields a lower limit of the achievable emittance in a photoinjector. For a cesium telluride Cs₂Te cathode the normalized thermal emittance can be expressed by [14]:

$$\epsilon_{n,rms}^{th} = \frac{\sigma_{rms}}{\sqrt{3}} \sqrt{\frac{2E_{kin}}{m_0c^2}} \quad (5.6)$$

where σ_{rms} denotes the rms laser spot size at the cathode and E_{kin} the mean free energy of the emitted electrons, which is 0.55 eV for UV photons at an energy of 4.72 eV ($\lambda = 263$ nm). While small spot sizes are preferred to reduce the emittance, one can find a better setting for both the projected and reduced space charge dominated transverse emittance (removing linear and quadratic correlations of the electrons in r , p_r and z within the bunch) for a special laser spot size and pulse length, which also depend on the RF launch phase [18]. A laser providing a homogeneous electron charge density in both longitudinal and radial direction is advantageous to minimize non-linear space charge forces that can not be removed by the emittance compensation process. A flat-top laser pulse with rise and fall times as small as possible is required.

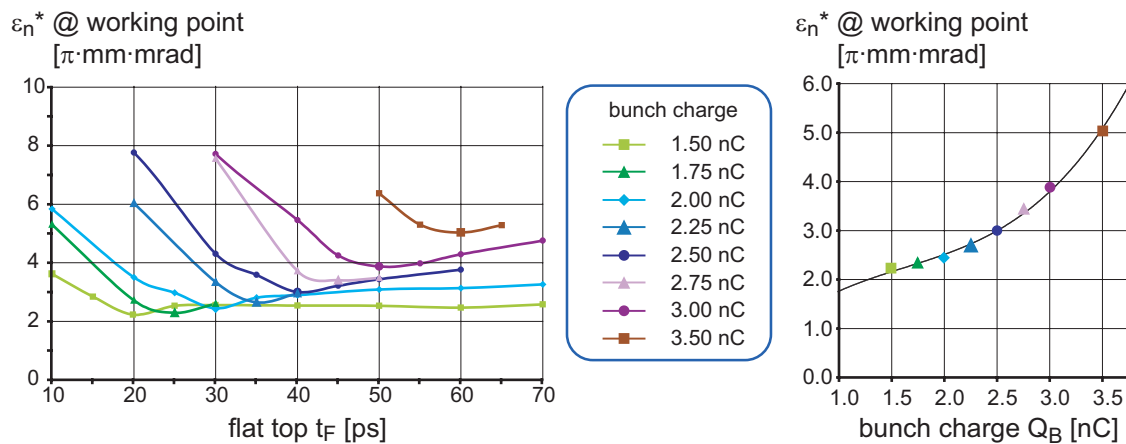


Fig. 5.18: Left: Normalized projected transverse emittance ϵ_n^* at the working point for different flat top laser pulse lengths t_F and various bunch charge values. Right: Corresponding minimum emittance ϵ_n^* as a function of the bunch charge (ASTRA simulations with $E_{\text{peak}}=40$ MV/m, 4 ps rise/fall time, laser spot size $\varnothing_{\text{laser}} = 3$ mm at cathode, peak magnetic field at 26.7 cm behind the cathode).

As a result of space-charge forces the laser pulse length not only impacts the longitudinal but also the transverse phase space. Furthermore, the optimum pulse shape largely depends on the bunch charge. In figure 5.18 ASTRA results are plotted showing the ideal position of working points z^* for various laser settings providing different bunch charges Q_B within 1.5-3.5 nC and flat-top pulses $t_F = 10 - 70$ ps. A finite laser rise and fall time of 4 ps was taken into account. For each bunch charge which is shown in figure 5.18, the normalized transverse emittance ϵ_n^* at the working point initially decreases steeply with an increase of the pulse length as a result of diminished space-charge forces. On the other hand, a pulse length which is too long degrades the emittance compensation, and thus a minimum of ϵ_n^* results. A higher Q_B causes additional space-charge forces to be compensated by an increase of the optimum laser-pulse length (~ 20 ps/nC within the considered bunch-charge range). However, with an increase of Q_B , a significant increase of the minimum emittance has to be considered as illustrated in figure 5.18 on the right side. When fulfilling the invariant envelope condition the final projected emittance at the exit of the gun is generally much lower than ϵ_n^* . For HGHG operation, a bunch charge of $Q = 2.5$ nC has been chosen resulting in an optimum flat-top pulse length of $t_F = 38$ ps with a rise and fall time of 4 ps. The main parameters of the drive-laser system are listed in table 5.8 assuming a stable quantum efficiency (QE) in long-term operation of $\text{QE} = 0.6\%$ for a Cs_2Te cathodes [19].

Table 5.8 Parameters of photocathode drive laser.

Parameter	Unit	
Material of photocathode	Cs ₂ Te	
Laser wavelength/photon energy	263/4.72	nm/eV
Quantum efficiency	~0.6	%
Bunch charge	2.5	nC
Electrons per bunch	1.56·10 ¹⁰	
Laser energy per bunch	2.0	μJ
Laser energy per bunch train	6.0	μJ
Average power (1kHz rep. rate)	6.0	mW
Laser pulse length (fwhm)	42	ps
Rise/fall time	4	ps
Laser spot size	3	mm
Normalized thermal emittance	0.63	π mm mrad

5.5.2 The Photocathode Laser for the BESSY FEL

This chapter deals with the photocathode laser optimized for the BESSY FEL RF gun. According to the requirements, the laser should generate short trains (macro-pulses) of picosecond pulses. The individual picosecond pulses in the train must be trapezoidal.

The parameters of these pulse trains are summarized in table 5.9.

A suitable laser with the pulse parameters listed in the above table is currently not commercially available. It can be developed on the basis of the existing technology of diode-pumped solid-state lasers.

5.5.2.1 Basic Layout of a Diode-Pumped UV Laser

The existing lasers do not permit the generation of synchronized picosecond pulses in the UV directly. That is the reason why one often starts with the generation of picosecond pulses by means of solid-state lasers, where lasing takes place at a wavelength near 1 μm. In a second step the infrared radiation (IR) emitted by the laser is converted to the ultra-violet (UV) in a two-stage conversion system. This conversion process typically reaches efficiencies on the order of 15%.

Table 5.9: Design parameters of the laser pulses.

Parameter	Value
Wavelength	$\lambda \approx 0.26 \mu\text{m}$
Pulse structure	Macro-pulses (bursts) containing 1, 3, 6 micro-pulses (variable)
Repetition rate of the macro-pulses	$f_{\text{macro}} = 0.5 \text{ Hz} \dots 1 \text{ kHz}$ (variable)
Energy of the micro-pulse (UV)	$E \geq 10 \mu\text{J}$ (for up to 10 nC bunch charge)
Maximum average power of the laser (at 1 kHz repetition rate and 3 micro-pulses per bunch)	$P_{\text{UV}} = 90 \text{ mW}$
Spacing of the micro-pulses within the macro pulses	1...4 microseconds (variable)
Pulse shape	flat top (trapezoidal)
Width of the flat-top pulse (fwhm)	$\lambda = 20 \dots 60 \text{ ps}$ (variable)
Rising and falling edges of the micro-pulses	4...8 ps (dependent on laser material)
Synchronization accuracy of the micro-pulses to an external RF master oscillator	< 1 ps

5.5.2.2 Suitable Laser Materials

Photocathode lasers require a very high reliability and a good long-term stability of the pulse parameters. These requirements can most likely be fulfilled by a diode-pumped, all solid-state laser system.

For the photocathode laser of the BESSY FEL the following laser materials, which can be pumped by semiconductor laser diodes, are considered:

- Neodymium-doped yttrium-lithium-fluoride (**Nd:YLF**),
- Neodymium-doped yttrium-vanadate (**Nd:YVO₄**),
- Neodymium-doped lanthanum scandium borate (**Nd:LSB**),
- Ytterbium-doped tungstates.

The photocathode lasers developed at the MBI presently use **Nd:YLF** as active material. The main advantage of this material is a very small thermal lens. A disadvantage is

the relatively small thermal conductivity. This, however, is not a critical limitation for the application at the BESSY FEL even for the case with the highest repetition rate and the highest number of pulses in the train: An average power in the UV of $P_{UV} = 60$ mW (1 kHz repetition rate, 6 micro-pulses per bunch) requires a laser power of 0.4...0.6 W in the IR which can be reached with Nd:YLF. A more severe limitation of Nd:YLF may consist in the fluorescence bandwidth of the material, which is in the order of 2 nm. This bandwidth limits the slope of the edges of the micro-pulses in practice to 4...6 ps length (10 - 90% value for the pulses converted to the UV).

If individual parameters of the laser should be enhanced, three other materials may be considered:

- Neodymium-doped yttrium vanadate (Nd:YVO₄) would allow one to increase the pulse energy and the average power of the laser by more than one order of magnitude. Unfortunately, this material has a much stronger thermal lens than Nd:YLiF and would require the compensation of the thermally induced wavefront errors if the average power (i.e. repetition rate or/and pulse energy) is markedly changed during operation of the laser.
- Neodymium-doped lanthanum-scandium-borate (Nd:LSB) is a very efficient laser material which would allow for steeper edges of the flat-top pulse in the order of 3...4 ps because of a two times higher fluorescence bandwidth compared to Nd:YLF. However, the gain reached with this material at comparable pumping conditions is significantly smaller. Furthermore, it exhibits a much stronger thermal lens. These properties require a more complicated layout of the laser. Hence, Nd:LSB should only be considered if the rising and falling edges of 4...6 ps reached with Nd:YLF are too long for the photocathode laser of the BESSY FEL.
- Ytterbium-doped tungstates are another class of laser materials, which are very promising for the use in a photocathode laser of the BESSY FEL. With these materials the generation of pulses with sharp edges (approximately 2 ps) is possible. However, the very low gain reached by these materials requires a more complicated layout of the laser. Consequently, the costs would increase and the reliability of the laser may be somewhat reduced. Nevertheless, these materials are an interesting alternative and the progress in the application of these materials should be taken into account in a final decision.

In summary, Nd:YLF fulfils all the requirements of the photocathode laser for the BESSY FEL. The only important restriction for this application arises from the limited fluorescence bandwidth that results in a slope of the edges of the micro-pulses of 4 - 6 ps. Nd:YLF is a technically advanced laser material. Its main advantage is a low thermal lens, which permits stable laser operation at variable power levels and it can be pumped by semiconductor diodes.

5.5.2.3 Layout of the Photocathode Laser

Figure 5.19 shows a sketch of the main building blocks of the laser. An overview of the proposed optical layout is shown in figure 5.20. This layout uses to a large degree the components, which have already been designed in the framework of the development of the photocathode lasers for the TTF and PITZ at DESY Zeuthen.

The proposed laser system contains the following building blocks:

- i. A **mode-locked oscillator** which generates the initial picosecond pulses;
- ii. A **grating pulse shaper** to shape the desired flat-top pulses from the initial pulses of Gaussian shape;
- iii. A regenerative amplifier ;
- iv. A programmable micro-pulse equalizer, i.e. a Pockels cell which equalizes the pulse energy of the individual micro-pulses;
- v. A **double-pass amplifier** which amplifies the pulses to about 100 μJ ;

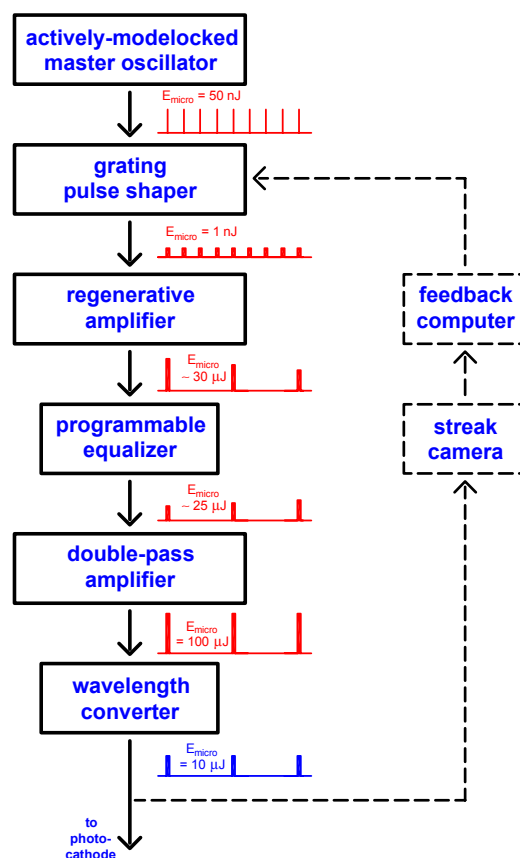


Fig. 5.19: Building blocks of the photocathode laser system.

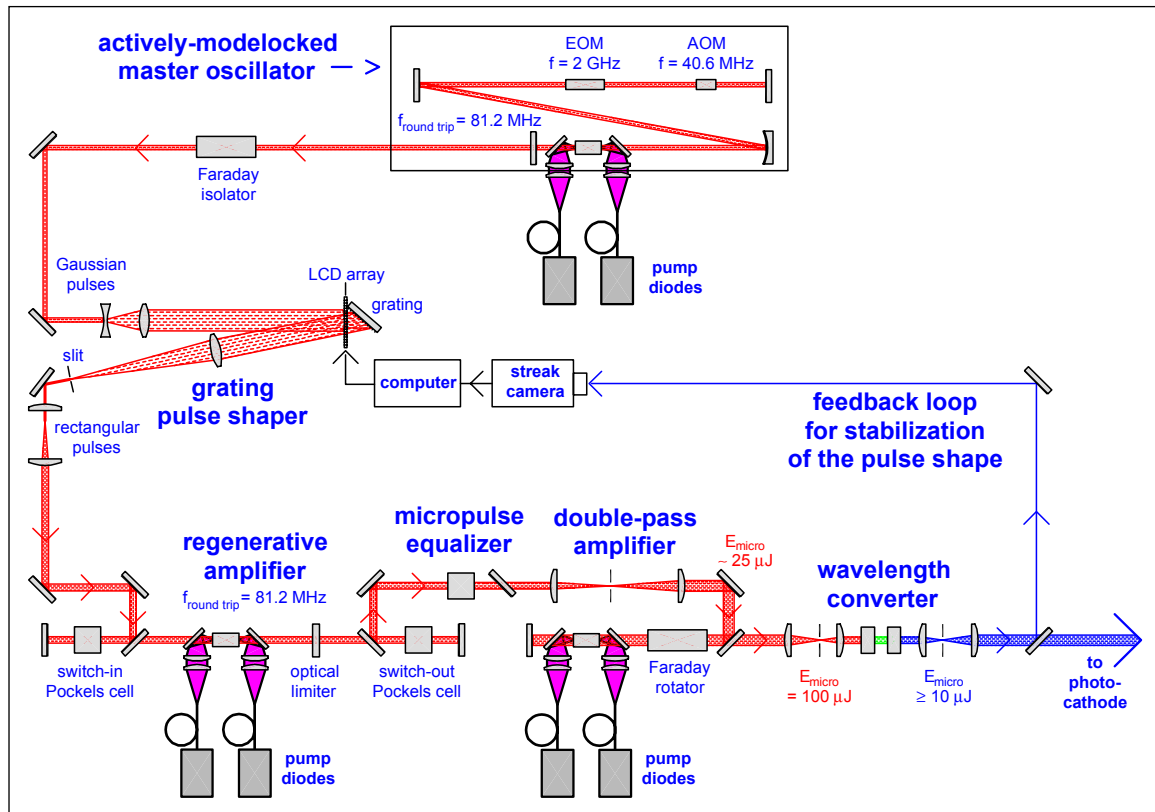


Fig. 5.20: Optical layout of the proposed laser.

- vi. A **wavelength converter** for conversion of the infrared laser pulses to the ultraviolet;
- vii. A **feedback system** for continuous measurement and control of the **shape** of the **micro-pulses**.

Both function and construction of the individual components are discussed in more detail in section 5.5.3.

5.5.3 Components of the Laser

5.5.3.1 The Laser Oscillator

The diode-pumped laser oscillator generates the initial laser pulses with 81.25 MHz repetition rate (16^{th} subharmonic of 1300 MHz). A combination of two active mode-lockers is used for shortening the pulses produced to several picoseconds. Since both mode-lockers are driven by RF signals originating from the electronic master oscillator, the laser operates in tight synchronization ($\sigma < 1$ ps) with the photoinjector.

The proposed type of oscillator has been extensively tested in the photocathode lasers installed at the TESLA Test Facility and PITZ. The oscillator presently emits trains of picosecond pulses with 7...8 ps duration which are well suited for the generation of flat-top pulses with rising and falling edges of 4...6 ps.

5.5.3.2 Pulse Shaper

We propose a so-called Direct-Space-to-Time (DST) pulse shaper for shaping of the flat-top pulses. The major element of this shaper is a grating in connection with a liquid crystal array (LCD array). The latter will be used to precisely control the shape of the output pulses of the laser by electronic means.

A preliminary and simplified version of the pulse shaper has been tested at the MBI (figure 5.21; these measurements have been carried out in the framework of the development of the PITZ photocathode laser). The measured output pulses from the shaper have been recorded with a synchroscan streak camera (figure 5.22). From this measurement we conclude that the proposed type of pulse shaper is well suited for the generation of flat-top micro-pulses with 20...60 ps duration and 5...8 ps edges.

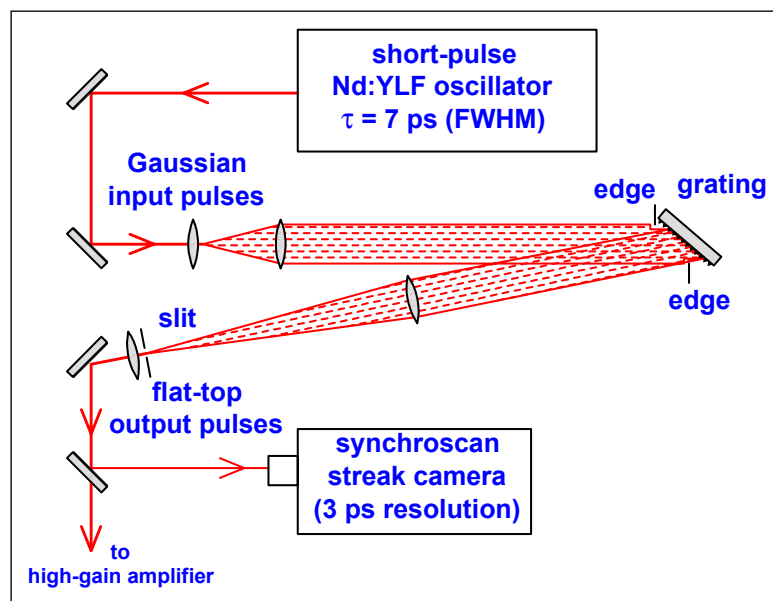


Fig. 5.21: Optical layout of the tested DST shaper.

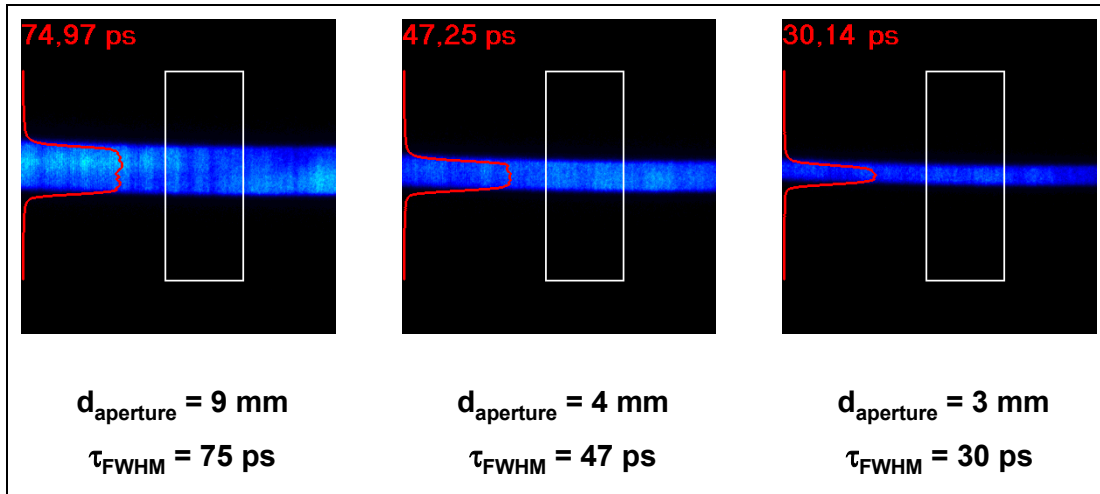


Fig. 5.22: Streak camera records of flat-top pulses of different duration produced by the DST shaper.

5.5.3.3 The Regenerative Amplifier

The regenerative amplifier should provide a total amplification on the order of 10^5 . Assuming a single-pass gain of the medium of 2.0, approximately 10 round trips are required to reach this amplification. The operational mode of the regenerative amplifier is characterized by the following numbers:

- The regenerative amplifier is designed for 30 μJ output energy.
- The resonator is laid out for approximately 0.7 mm beam diameter in the active medium, which results in a peak intensity of 0.4 GW/cm^2 for the shortest pulses of 20 ps length. This value is well below the damage threshold of the optical components of the amplifier. However, a relatively large margin is chosen for suitable long-term stability of the system.
- The energy density for 0.7 mm beam diameter is $8 \cdot 10^{-3} \text{ J}/\text{cm}^2$. This value is 135-times smaller than the saturation energy of Nd:YLF $E_{\text{sat}} = h \cdot c / (\sigma \cdot \lambda) = 1.05 \text{ J}/\text{cm}^2$. Therefore, the amplifier is operated in small-signal (non-saturated) mode. Additional measures are essential to stabilize the pulse energy and to protect the amplifier from damage in case of unfortunate timing or misalignment of the pulse shaper. We propose inserting an optical limiter in the cavity for this purpose. A suitable limiter consists of an SHG crystal that partially converts the IR radiation into green light, which will simply be discarded in the cavity. Besides limiting the energy of the pulses being amplified in the regenerative amplifier, the fast limiter will significantly contribute to the formation of the flat-top pulse shape.

Each individual micro-pulse of the train removes about one percent of the energy stored in the laser rods of the regenerative amplifier and the final linear booster during the pump-up phase. Since this causes a corresponding drop in amplification of the medium, the energy of the micro-pulse at the output of the laser system will tend to successively drop towards the end of the pulse train.

One can partially compensate for this effect by appropriately changing the trigger time of the switch-in Pockels cell of the regenerative amplifier while simultaneously keeping the timing of the switch-out cell constant. The number of round trips in the regenerative amplifier is tuned this way in order to stabilize the output energy of the individual micro-pulses in the train. An appropriate lookup table in the control system of the laser will be used for optimum adjustment of the trigger.

In order to simplify timing, the regenerative amplifier and the oscillator have an identical round-trip frequency of $f_{\text{round_trip}} = 81.2$ MHz. Consequently, the duration of the complete amplification process during ten round trips amounts to $0.12 \mu\text{s}$, which is much smaller than the minimum spacing between successive micro-pulses in the train of $T_{\text{min}} = 1.0 \mu\text{s}$ at $f_{\text{max}} = 1$ MHz repetition rate. This means that the gain of 2.0 provides sufficient overhead for safe operation of the regenerative amplifier.

5.5.3.4 Equalizing Pockels Cell ("Micro-Pulse Equalizer")

Although the major part of the drop in amplification during the pulse train will be compensated by varying the number of round trips in the regenerative amplifier, an additional possibility for fine-tuning will be required.

Despite of the optical limiter in the regenerative amplifier, the energy of the micro-pulses will still drop towards the end of the pulse train. This effect is less pronounced for short pulse trains, which contain only few micro-pulses. Nevertheless, the drop in output energy of the individual micro pulses cannot be completely avoided, since each individual micro-pulse removes a certain amount of the energy stored in the laser rod during the pump-up phase.

A dynamically controlled Pockels cell in the optical path is provided for this adjustment. This Pockels cell should be progressively opened during the pulse train. The real-time control computer can perform the optimization of high-voltage control signal to be supplied to the Pockels cell.

5.5.3.5 The Double-Pass Booster Amplifier

The pulse energy in the regenerative amplifier is intensity-limited to approximately 30 μJ due to the beam diameter given by the resonator design. Therefore the final booster amplifier, which operates with a larger 1.5 mm beam diameter is needed. A double-pass geometry has been chosen which easily provides a total gain of $g = 4$. This amplifier is designed for a micro-pulse energy of $E_{\text{micro}} = 100 \mu\text{J}$ resulting in a peak intensity of 0.4 GW/cm^2 for 20 ps pulses. This intensity again provides a sufficient safety margin in particular for the case of misalignment of the pulse shaper.

The progressive drop in power of the individual micro-pulses of the train due to energy extraction from the laser medium will be pre-compensated by appropriately tuning the number of round trips in the regenerative amplifier and by the equalizing Pockels cell.

5.5.3.6 Wavelength Conversion Stage

In order to reach a suitable quantum efficiency of the cesium telluride photocathode, the infrared radiation of the laser has to be converted into the ultraviolet at the end of the laser system. Two nonlinear crystals (LBO and BBO) will accomplish this. This type of wavelength conversion has been intensively tested in the photocathode lasers at TTF and PITZ and is well suited for the expected energy level of the pulses. A desirable side effect is the observed reduction of the rising and falling edges from 6...8 ps (IR) to 4...6 ps (UV) due to the nonlinearity of the conversion process.

5.5.3.7 Control of Micro-Pulse Shape

There are at least two possibilities to record the shape of the micro-pulses:

- An appropriate streak camera. Since this camera would operate in special and well-defined conditions, it can be much more compact than a typical commercial camera for universal application.
- An optical sampling system, which samples the longer flat-top pulse by difference-frequency mixing with the shorter laser pulses emitted from the laser oscillator.

The electronic signal from this measurement system is transferred to a control computer. This computer modifies the control signal of the liquid crystal array of the pulse shaper. In this way a continuous correction of the shape of the micro-pulses is achieved.

5.5.4 Comparison with Existing Photocathode Lasers at TTF and PITZ

The basic Master Oscillator-Power Amplifier (MOPA) layout of the laser with an added wavelength-conversion system corresponds to the photocathode lasers developed for TTF and PITZ. There are, however, significant differences, which result from different parameters of the pulse trains:

- The maximum repetition rate in the pulse train of 1 MHz is an order of magnitude lower than for TTF and PITZ (max. 9 MHz repetition rate in the train). This allows for amplification of the micro-pulses in a regenerative amplifier, which is more compact than a linear amplifier chain with comparable amplification.
- The number of micro pulses per train is much smaller (≤ 6 micro pulses) than the design parameters for TTF and PITZ (up to 7200 micro pulses). The energy-storage capabilities of the laser medium can be utilized if additional measures are taken. In particular, the extraction of energy from the laser media by each micro-pulse causes a progressive drop of the gain during the pulse train in this operational mode. Tuning the number of round trips in a regenerative amplifier compensates for this. Additional fine-tuning of the micro-pulse energy is carried out by a Pockels cell, which is controlled by the control computer of the laser system.
- The BESSY FEL requires a repetition rate of the pulse trains of up to 1 kHz. To reach this, an appropriate cooling system and a strongly optimized pump layout are needed.
- The maximum pulse duration required is three times longer than at TTF and PITZ. In addition, it should be variable. This requires a different layout of the pulse shaper compared to the one used at PITZ. A complex feedback system is needed to maintain flatness of the flat-top region of these long pulses.

In summary, the reduced number of micro-pulses in the train at BESSY enables one to build a somewhat more compact amplifier than at PITZ and TTF. On the other hand, the larger ratio between duration of flat-top pulses and their edges requires a more complicated feedback system, which should measure the pulse shape and control the pulse shaper to maintain flatness of the micro-pulses.

5.5.5 Conclusions and Summary

On the basis of the experience of the MBI with the photocathode lasers at TTF and PITZ, the proposed laser system can be developed at the MBI at low risk. The main challenge of the laser consists of the generation of flat-top micro-pulses with short rising and

falling edges. This is accomplished by means of a grating pulse shaper with a computer-controlled liquid crystal array. A streak camera at the output of the laser system permanently monitors the shape of the micro-pulses. This camera is part of a feedback system, which continuously controls and optimizes the shape of the micro-pulses.

The generation of trains of picosecond pulses is achieved by implementing special measures. In particular, the extraction of energy from the laser media by each micro-pulse causes a progressive drop of the gain during the pulse train. This is compensated for by tuning the number of round trips in a regenerative amplifier. Additional fine-tuning of the micro pulse energy is carried out by a Pockels cell, which is dynamically controlled by the main computer of the laser system.

We propose Nd:YLF as the laser material. It supports the generation of flat-top micro-pulses with 4...6 ps long edges. Shorter edges require other materials, i.e. Nd:LSB or ytterbium-doped tungstates. However, the lower gain and the stronger thermal lensing of these materials would increase the complexity and the cost of the laser. The proposed Nd:YLF laser design allows to vary the repetition rate, the number of micro-pulses in the train, and the duration of the flat-top micro-pulses. It also contains sufficient overhead in pulse energy to reach a high reliability of the laser and a suitable long-term stability of the pulse parameters.

The development of this laser would be an important milestone towards a reliable, easy-to-use photocathode laser, optimized for driving high-brightness photoinjectors.

5.6 A Future Superconducting Photoinjector

5.6.1 The FZR Rossendorf-BESSY-DESY-MBI Photoinjector

For the BESSY Soft X-ray FEL (phase II) a photoinjector with an s.c. gun cavity is the ideal choice to exploit the full capabilities of the superconducting CW linear accelerator. Such an s.c. cavity gives the potential to operate with flexible bunch patterns.

The first stable operation of an s.c. photoinjector has been demonstrated in 2002 at the Forschungszentrum Rossendorf (FZR) [20]. The design was based on a $\frac{1}{2}$ cell L-Band cavity made from niobium using a normal conducting Cs₂Te cathode (figure 5.23). An operating field of 22 MV/m near the cathode has been achieved corresponding to a beam energy of 900 keV at the gun exit. Bunch charges of up to 20 pC could be extracted. The main challenge of operating an n.c. cathode at cryogenic temperatures has been demonstrated successfully without a significant deterioration of the cavity quality factor, i.e. $Q_0 = 2 \cdot 10^8$ at 4.2 K. Lower temperatures could not be reached due to constraints of the cryogenic system.

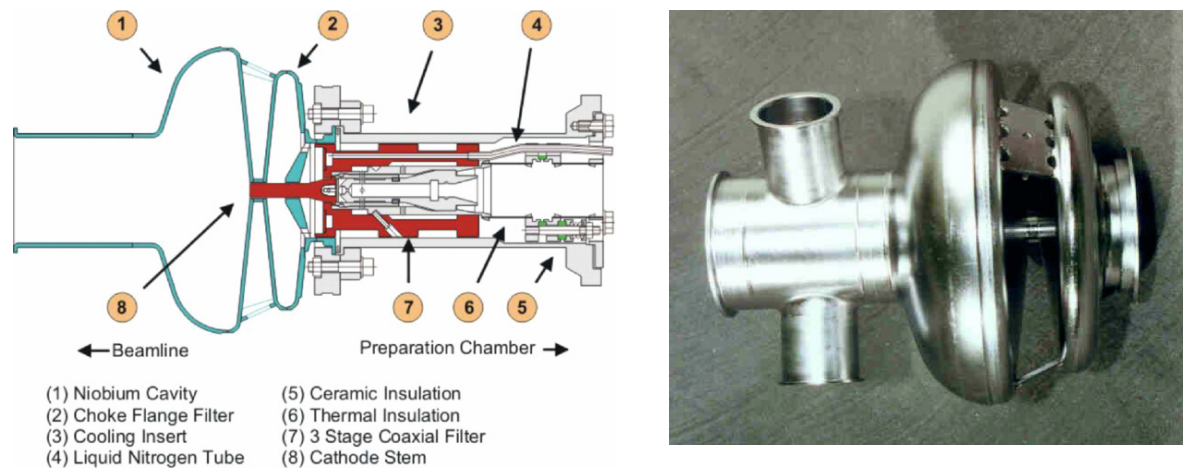


Fig. 5.23: The first s.c. gun cavity operated with a Cs_2Te cathode at the FZR Rossendorf [20]. A choke cavity is used to reject the fundamental mode from propagating in the coaxial line of the photocathode.

Based on experience, an improved $3\frac{1}{2}$ cell L-Band cavity has been proposed in a joint project of FZR Rossendorf, BESSY, DESY, and MBI, with the aim of accelerating highly charged bunches to a beam energy of 10 MeV. Figure 5.24 illustrates the cavity outline. The geometry near the cathode is shown in detail on the left side indicating the electric field lines. The shape of the cavity is based on an optimized half cell geometry and three standard TESLA cells. It makes use of an RF focusing scheme, whereby the cathode is curved and pulled outside of the cavity behind the back plane to create radial components of the electric field able to focus the beam [21]. A full schematic of the proposed s.c. injector in its helium tank is presented in figure 5.25.

The main challenge of the joint photoinjector project is to demonstrate a CW gun operation at high fields minimizing the transverse emittance down to a level of $1 - 2 \pi \text{ mm mrad}$ for bunch charges up to 1 nC. Questions on synchronization and stability of the cathode drive laser, lifetime and quantum efficiency of the cathode, beam dynamics and diagnosis will be addressed as well.

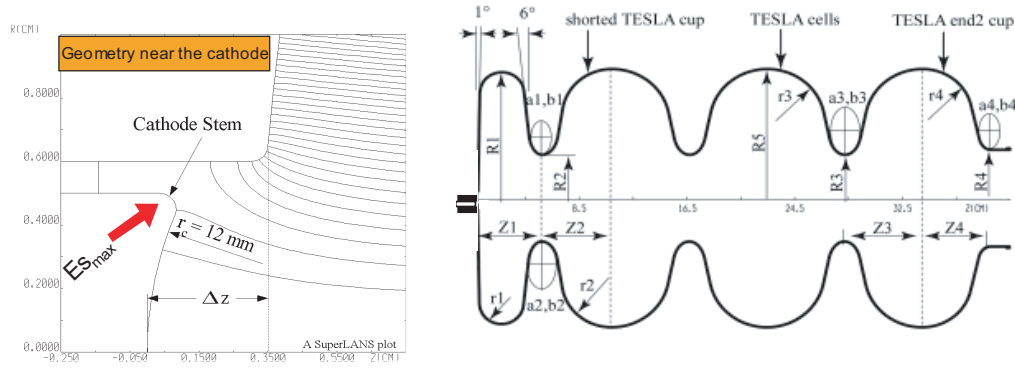


Fig. 5.24: Outline of the FZR-BESSY-DESY-MBI $3\frac{1}{2}$ cell s.c. cavity showing the cathode in more detail on the left side.

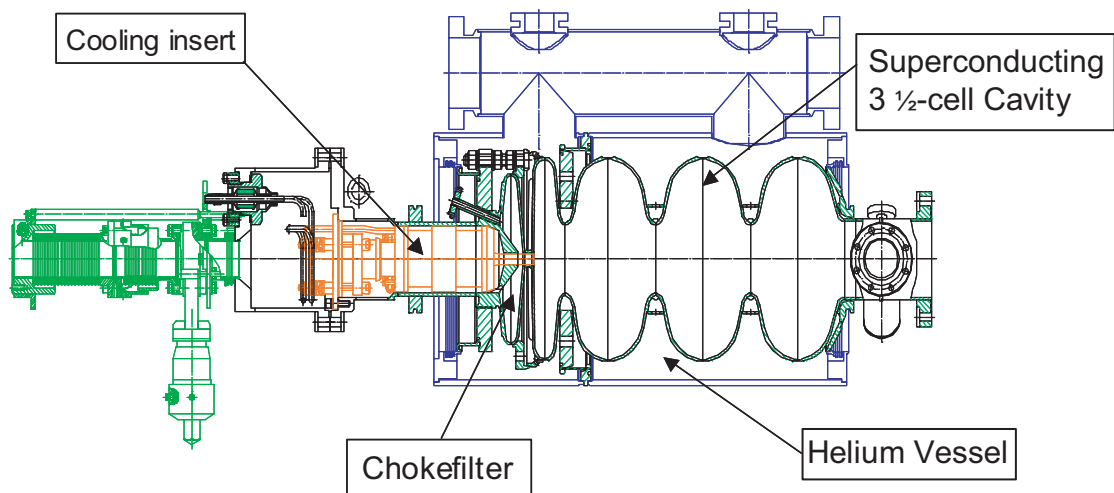


Fig. 5.25: Cut drawing of the FZR-BESSY-DESY-MBI $3\frac{1}{2}$ cell s.c. cavity.

5.6.2 Photoinjectors Based on Multicell Superconducting Cavities

5.6.2.1 Main Challenge

Besides the joint FZR–BESSY–DESY–MBI project, a new approach of a split photoinjector concept, i.e. accelerating and subsequent focusing by a solenoid as in case of n.c. RF guns, has been developed recently, giving the potential to simplify the cavity design since the complex RF focusing scheme would become superfluous. The main idea of such a concept is depicted in figure 5.26, e.g. with a $3\frac{1}{2}$ cell gun cavity. Due to superconductivity the niobium walls of the cavity cannot be exposed to magnetic fields. Hence, the use of an external focusing magnet sufficiently far away from the cavity surface is proposed. However, with a solenoid placed far away from the cathode, emittance compensation is applied at a very late stage, so that space charge induced emittance growth in the intermediate drift space is compensated for less efficiently. To reduce this effect as far as possible operation at a high field is mandatory. Consequently, the main problem to overcome with this idea arises from the limitation of the accelerating, which is related to the surface magnetic field at the inner cavity wall. For a typical niobium L-Band cavity based on the geometry of a TESLA cavity, the peak magnetic field is restricted by the superheating field of 200 - 240 mT corresponding to accelerating fields as high as 50-60 MV/m. The latter would require an unloaded quality factor Q_0 in a range of 10^{10} [22].

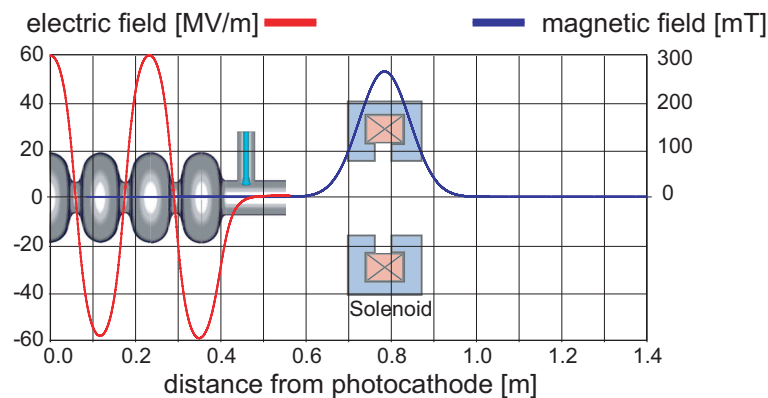


Fig. 5.26: Layout of a split $3\frac{1}{2}$ cell s.c. photoinjector with a solenoid placed far behind the cavity to prevent trapped magnetic dc fields in the niobium surface. The on-axis electric and magnetic fields are indicated.

Essential to achieving such high-quality factors is operation at a cryogenic temperature of about 2 K. Besides the temperature-dependent surface resistance ($\sim 15 \text{ n}\Omega$ @ 2 K) a residual surface resistance of a few $\text{n}\Omega$ has to be taken into account, depending upon mate-

rial impurities as well as on trapped magnetic flux lines. Weak magnetic dc fields can be trapped in the surface when cooling down the cavity, leading to a surface resistance of $3.5 \text{ n}\Omega/\mu\text{T}$ at 1.3 GHz [22]. When using a split photoinjector scheme, the position of the solenoid should be chosen to prevent from trapped magnetic fluxes which would lead to a breakdown of the superconducting state. In each case, the magnetic field has to be switched on after cooling down the cavity. A safe limit for the remaining magnetic flux density at the cavity surface B_s caused by a focusing solenoid can be derived from

$$B_s = \frac{G}{3.5 \text{ n}\Omega/\mu\text{T}} \times \frac{1}{Q_0}, \quad (5.7)$$

where G denotes the geometry factor of the cavity. For standard TESLA cells with $G = 270 \Omega$ this leads to a maximum permissible external dc field of $3.8 \mu\text{T}$ in order to achieve a quality factor of $Q_0 = 2 \cdot 10^{10}$ necessary for a high-gradient operation.

5.6.2.2 Simulations

Investigations have started to study the feasibility of the split photoinjector concept with four different multi-cell cavities as shown in figure 5.27 using a standard TESLA cell geometry. Calculations for the beginning were based on a 20 ps long flat top laser pulse (no rise/fall time), a homogeneous laser spot size of 3 mm at the cathode and 1 nC of total bunch charge. The focusing field used for simplicity is of Gaussian profile ($\sigma = 8 \text{ cm}$). An accelerating field of 30 MV/m was assumed, as already demonstrated for a large series of TESLA 9-cell cavities. The corresponding maximum energy gain in the different cavities is listed in the legend of figure 5.27.

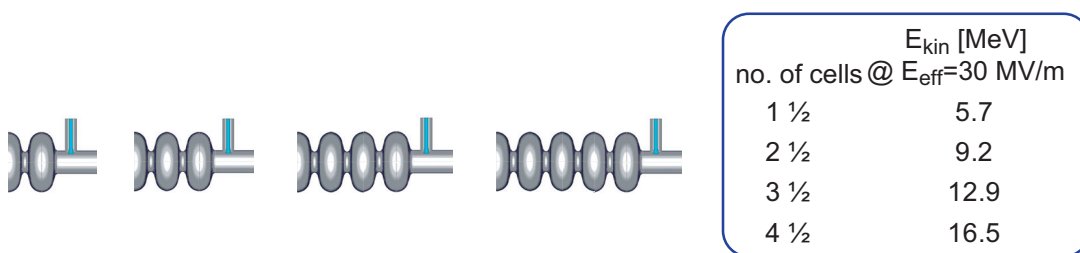


Fig. 5.27: Multi-cell cavities under investigation based on standard TESLA cavities. Coaxial power couplers are situated at the exit of the gun as indicated. The table insert gives electron energies at an effective acceleration field of 30 MV/m.

In figure 5.28, the optimized projected transverse emittance ε_n^* at the ideal working point and the appropriate magnetic flux density are shown as a function of the peak magnetic field location. The position of the individual cavity cells is illustrated as well.

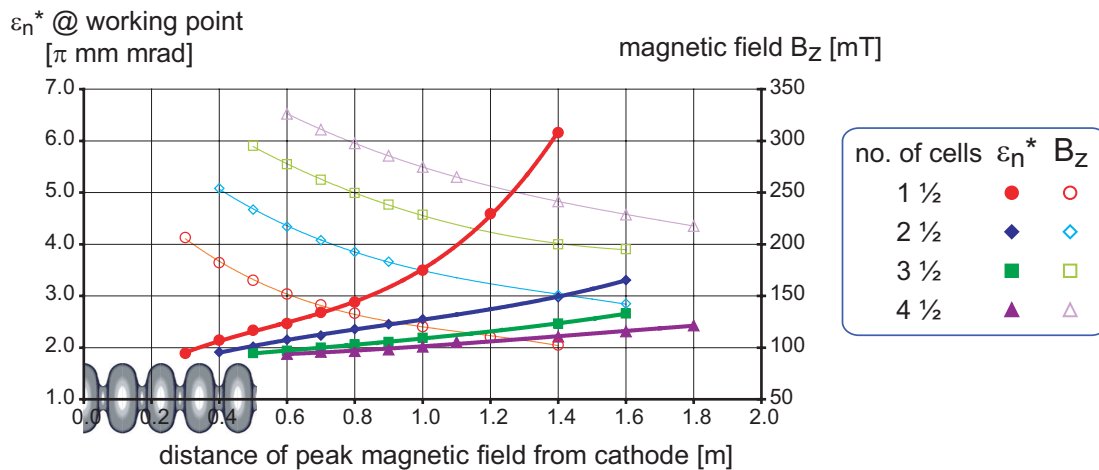


Fig. 5.28: The projected normalized transverse emittance ε_n^* at the working point position and corresponding magnetic-flux density B_z as a function of the location of the peak magnetic field. ASTRA simulations with $E_{\text{eff}}=30\text{MV/m}$, $Q=1\text{ nC}$, $t_f = 20\text{ ps}$ (no rise/fall time), $\varnothing_{\text{laser}} = 3\text{ mm}$.

The essential result obtained for all different multi-cell cavities is that a solenoid should be placed as close as possible to the cavity surface to reduce the transverse emittance ε_n^* as far as possible. By the use of a subsequent booster linac, transverse emittances well below $1.5\pi\text{ mm mrad}$ suitable for the BESSY FEL would be achieved. When increasing the number of cells and therefore the beam energy, space-charge effects are reduced so that at any fixed peak-field location the minimum transverse emittance ε_n^* is achieved for the $4\frac{1}{2}$ cell RF gun. At a lower beam energy, i.e. for the $1\frac{1}{2}$ cell cavity, the emittance is affected most strongly by the change of the solenoid position. The focusing strength has to be increased appropriately at higher beam energies, i.e. to operate at the same Q_0 -level the solenoid has to be placed slightly further away from the gun exit when increasing the number of cavity cells.

This behavior is illustrated in figure 5.29. The maximum allowable magnetic flux density B_s has been evaluated using equation (5.7) as a function of the quality factor by parameterizing the distance-dependent optimum peak magnetic flux density as calculated with ASTRA. From this the closest possible location of the peak field to the cavity surface Δz has been derived using the waveguide iris at the exit of each cavity as the reference plane. For a $Q_0 = 2 \cdot 10^{10}$ the distance Δz and consequently the absolute position of the peak magnetic field z_{peak} behind the photocathode has been evaluated as listed in the legend of

figure 5.29. Herein the closest peak magnetic-field location to the reference plane (Δz) and to the photocathode (z_{peak}) have been derived. Results are based on a Gaussian shaped magnetic field profile with $\sigma = 8$ cm.

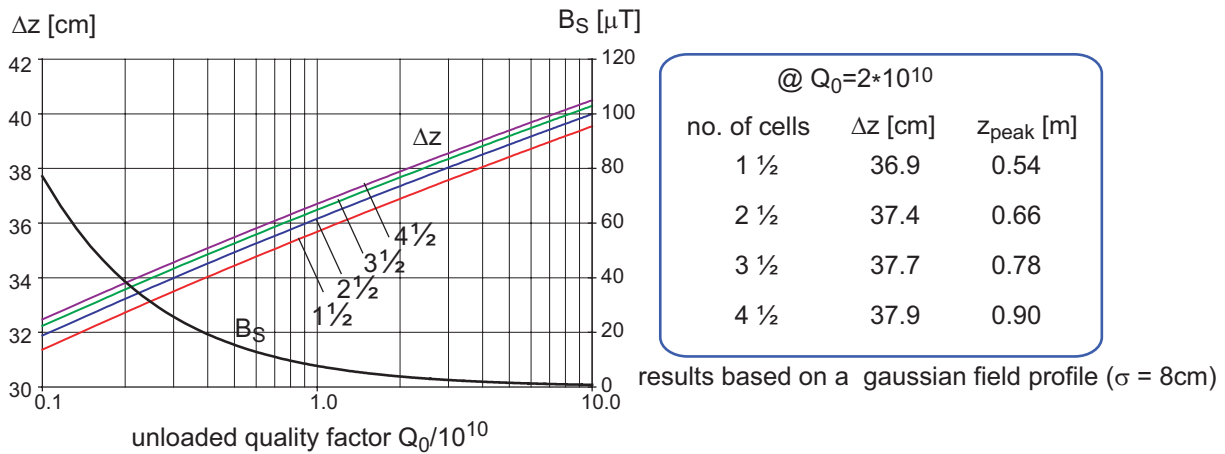


Fig. 5.29: The closest distance Δz of the peak magnetic field to the cavity exit (reference: iris plane at gun exit) for a 1½-cell up to a 4½-cell cavity (colored lines) and upper limit of the surface magnetic flux density B_s (black line) as a function of the unloaded quality factor Q_0 to be operated at.

5.6.2.3 Emittance Conservation in a Booster Linac

Using a 1½-, 2½-, 3½ and 4½ cell RF gun geometry, matching the beam to a subsequent s.c. module (booster linac) has been investigated. The evolution of projected transverse emittance $\epsilon_{n,\text{rms}}$ and beam size $\sigma_{x,y}$ up to the linac exit are shown in figure 5.30 and figure 5.31 respectively. The obvious blowup of beam size in the RF gun due to space charge forces is reduced by a higher beam energy, i.e. when increasing the number of cavity cells. At higher beam energies, however, a stronger focusing field is required and the working point is shifted further downstream.

For each gun cavity model the projected normalized transverse emittance $\epsilon_{n,\text{rms}}$ is reduced to a level below 1.5π mm mrad, a very promising result considering that no further optimization of the RF gun models has been performed so far.

In fact, after a steady reduction of the emittance with cell number, the final emittance achieved with a 4½ cell cavity is larger compared to the other geometries. As a compromise, a 1½ or 2½ cell cavity seems to be the optimum choice. A more detailed analysis is under way including simulations at a higher bunch charge (2.5 nC) as required for the BESSY FEL. Technical issues such as the optimization of the cavity cell shape, especially

for the first half cell, and the realization of an adequate confinement and shielding of the focusing magnetic field near the niobium surface will be addressed.

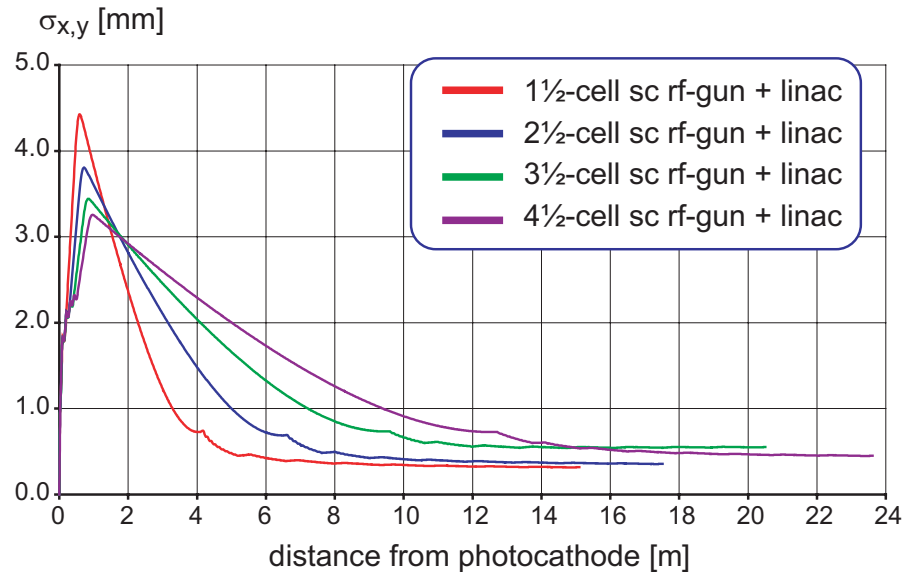


Fig. 5.30: Evolution of the transverse beam size $\sigma_{x,y}$ for the different gun cavities up to the exit of a first linac module. ASTRA simulations with $E_{\text{acc}}=60$ MV/m, $Q_B=1.0$ nC, $t_f = 20$ ps (no rise/fall time), $\varnothing_{\text{laser}} = 3$ mm.

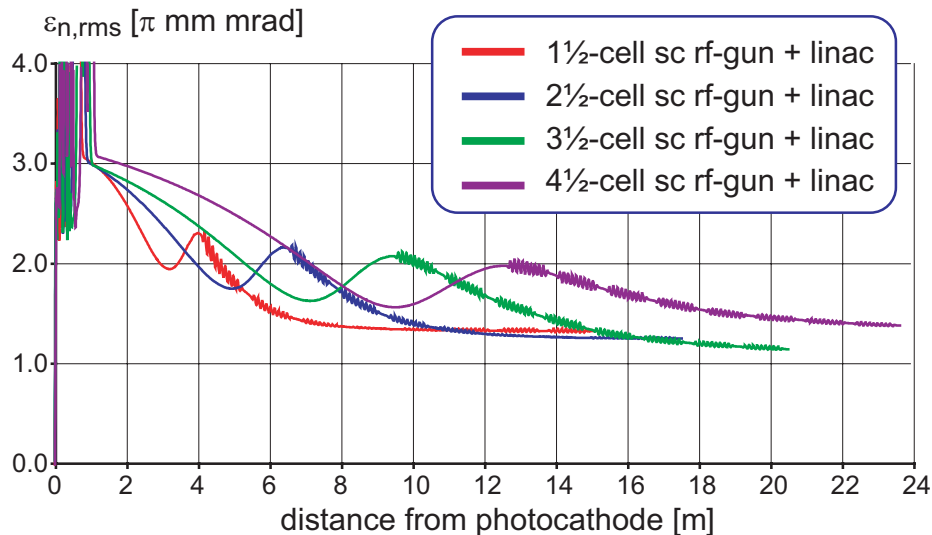


Fig. 5.31: Evolution of the projected normalized transverse rms emittance $\epsilon_{n,rms}$ corresponding to figure 5.30.

5.6.2.4 Niobium Photocathode

A niobium cathode would be a natural choice for an s.c. split photoinjector simplifying the cavity design and reducing the possibility of quality-degrading effects by contamination of the niobium with cathode material.



Fig.5.32: The all-niobium BNL s.c. gun cavity design (photograph taken from [23]).

One of the main challenges is to increase the poor quantum efficiency (QE) of the niobium. R&D programs on this field are progressing in the “all-niobium RF gun project” at the Brookhaven National Laboratory (BNL). At BNL a $\frac{1}{2}$ cell L-Band s.c. cavity has already been built utilizing niobium as cathode material. The photocathode is simply the end wall of the cavity as shown in figure 5.32. Input coupler and pickup probes are placed at the exit waveguide. Using in-situ laser cleaning procedures at room temperature [24], the quantum efficiency could be enhanced by about two orders of magnitude from initially $QE = 10^{-7}$ to about $QE = 5 \cdot 10^{-5}$. These tests were performed at low dc-voltage. Since the QE efficiency increases with the applied field, an extrapolation of the measured data yields an optimistic $QE = 10^{-4}$ for peak fields of 35MV/m. This must be verified in the RF gun at cryogenic temperatures.

References

- [1] J. Clendenin, L. Rinolfi, K. Takata, D.J. Warner, *Proc. of the XVIII Int. Linac Conf.* (1996) 298.
- [2] F. Stephan for the PITZ Collaboration Team, *Proc. of the 2003 PAC* (2003) 2114.
- [3] J.-P. Carneiro, R. A. Carrigan, M. S. Champion, P. L. Colestock, H. T. Edwards, J. D. Fuerst, W. H. Hartung, K. P. Koepke, M. Kuchnir, J. K. Santucci, L. K. Spentzouris, M. J. Fitch, A. C. Melissinos, P. Michelato, C. Pagani, D. Sertore, N. Barov, J. B. Rosenzweig, *Proc. of the 1999 PAC* (1999) 2027.
- [4] B. Dwersteg, K. Flöttmann, J. Sekutowicz, Ch. Stolzenburg, *Nucl. Instrum. and Meth. A* **393** (1997) 93.
- [5] I. Bohnet, K. Flöttmann, Q. Zhao, „Magnetic Field Investigations of the Solenoid Arrangement for PITZ”, PITZ Note, Oct. 2002.
- [6] B. E. Carlston, *Nucl. Instr. and Meth. A* **285** (1989) 313.
- [7] X. Qiu, K. Batchelor, I. Ben-Zvi, X-J. Wang, *Phys. Rev. Lett.* **76/20** (1996) 3723.
- [8] K. Flöttmann, “ASTRA, A Space Charge Tracking Algorithm”: <http://www.desy.de/~mpyflo> .
- [9] M. Ferrario, J. E. Clendenin, D. T. Palmer, J. B. Rosenzweig, L. Serafini, SLAC-PUB-8400, LCLS-TN-00-04, LNF-00/004 (2000)
- [10] L. Serafini, J. B. Rosenzweig, *Phys. Rev. E* **55/6** (1997) 7565.
- [11] J. Baehr, I. Bohnet, J.-P. Carneiro, K. Floettmann, M.v. Hartrott, O. Krebs, D. Lipka, F. Marhauser, V. Miltchev, A. Oppelt, B. Petrossyan, S. Schreiber, F. Stephan, “Behaviour of the TTF2 RF Gun with Long Pulses and High Repetition Rates”, to be published as TESLA Report.
- [12] ANSYS Version 7.1: <http://www.ansys.com>.
- [13] N. Hartman, R. Rimmer, *Proc. of the 2001 PAC* (2001) 912.
- [14] K. Flöttmann, TESLA Report, TESLA-FEL 97-01.
- [15] K. Halbach, R.F. Holsinger, Poisson Superfish, distributed by the Los Alamos Accelerator Code Group (LAACG), *Particle Accelerators* **7/4** (1976) 213, <http://laacg1.lanl.gov/laacg/services/possup.html>
- [16] F. Marhauser, BESSY Technical Report Nr. 224/03 (2003) 31.
- [17] N. Solyak, H. Edwards, M. Foley, I. Gonin, T. Khabiboulline, D. Mitchell, J. Reid, L.Simmons, *Proc. of the 2003 PAC* (2003) 1213.

- [18] M. Ferrario, K. Flöttmann, B. Grigoryan, T. Limberg, Ph. Piot, TESLA-FEL Report 2002-03 (2001).
- [19] S. Schreiber, P. Michelato, L. Monaco, D. Sertore, *Proc. of the 2003 PAC* (2003) 2071.
- [20] D. Janssen, Bushuev, M. Karliner, S. Konstantinov, J. Kruchkov, O. Myskin, V. Petrov, I. Sedlyarov, A. Tribendis, V. Volkov, P. vom Stein, H. Vogel, A. Matheisen, M. Pekeler, W. Sander, I. Will, *Proc. of the 1999 PAC* (1999) 2033.
- [21] V. Volkov, D. Janssen, *Nucl. Instrum. and Meth. A* **452/21** (2000) 34.
- [22] B. Aune, R. Bandelmann, D. Bloess, B. Bonin, A. Bosotti, M. Champion, C. Crawford, G. Deppe, B. Dwersteg, D. A. Edwards, H. T. Edwards, M. Ferrario, M. Fouaidy, P.-D. Gall, A. Gamp, A. Gössel, J. Graber, D. Hubert, M. Hüning, M. Juillard, T. Junquera, H. Kaiser, G. Kreps, M. Kuchnir, R. Lange, M. Leenen, M. Liepe, L. Lilje, A. Matheisen, W.-D. Möller, A. Mosnier, H. Padamsee, C. Pagani, M. Pekeler, H.-B. Peters, O. Peters, D. Proch, K. Rehlich, D. Reschke, H. Safa, T. Schilcher, P. Schmüser, J. Sekutowicz, S. Simrock, W. Singer, M. Tigner, D. Trines, K. Twarowski, G. Weichert, J. Weisend, J. Wojtkiewicz, S. Wolff, K. Zapfe, *Phys. Rev. ST Accel. Beams* **3** (2000) 092001.
- [23] T. Srinivasan-Rao, I. Ben-Zvi, A. Burrill, G. Citver, A. Hershcovitch, D. Pate, A. Reuter, J. Scaduto, Q. Zhao, Y. Zhao, H. Bluem, M. Cole, A. Favale, J.W. Rathke, T.J. Schultheiss, J. Delayen, *Proc. of the 2003 PAC* (2003) 92.
- [24] Q. Zhao, M. Cole, *Proc. of the 2003 PAC* (2003) 2047.

In the first two linac sections the bunches are accelerated off crest to generate a correlated energy spread which is used for bunch compression. Since quadratic terms in the RF voltage (as well as even higher-order terms) reduce the efficacy of the bunch compressors, they will be compensated for by decelerating the beam in third-harmonic cavities (3.9 GHz). A total decelerating voltage of 36 MV is required. Further details are provided in chapters 5 and 7.

Table 6.1: Linac sections of the BESSY FEL.

Component	Acceleration phase	Exit energy
RF gun	0°	4 MeV
Linac 0 (booster)	-13.3°	131 MeV
3 rd harmonic cavity	177°	95 MeV
Linac 1	-13.3°	219 MeV
Bunch compressor 1		
Linac 2	-5°	753 MeV
Arc + bunch compressor 2		
Linac 3	0°	1020 MeV
Extraction for FEL 1	0	
Linac 4	0°	2300 MeV
FEL 2 + FEL 3		

6.2 Accelerator Modules

Superconducting RF technology, originally developed for the TESLA linear collider [1], has been adopted for beam acceleration. The choice is driven by the fact that it is mature technology whose reliable operation has already been demonstrated at the TESLA Test Facility (TTF) [2]. Only relatively minor modifications are required to adapt TESLA technology for CW BESSY FEL operation, these being discussed in section 6.3.

Furthermore, the production and preparation methods of a number of the main components have already been transferred to industrial partners, a step that is necessary for the large-scale production of linac modules. The use of TESLA technology therefore translates directly into a significant development-time and cost savings, both during the design and the production phases.

What follows is a short overview of the TESLA technology, more details being presented in [1]. Section 6.3 then discusses the proposed modifications to adapt this for BESSY FEL operation.

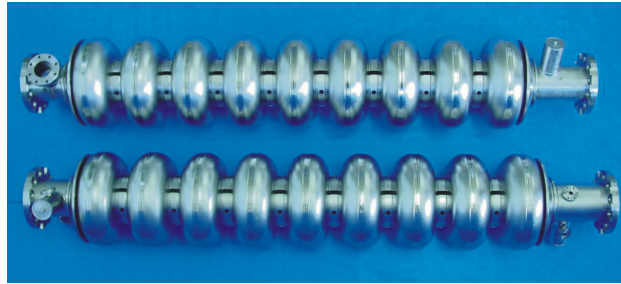


Fig. 6.2: Two 9-cell, 1.3 GHz TESLA cavities produced for BESSY.

6.2.1 Cavities and Cryostat

The TESLA technology is based on 1.3 GHz superconducting niobium cavities [3] as depicted in figure 6.2, the main parameters being summarized in table 6.2. These cavities are welded in a titanium helium tank as shown in figure 6.3. Each cavity is also equipped with a high-power input coupler and a tuner (discussed in sections 6.2.2 and 6.2.3).

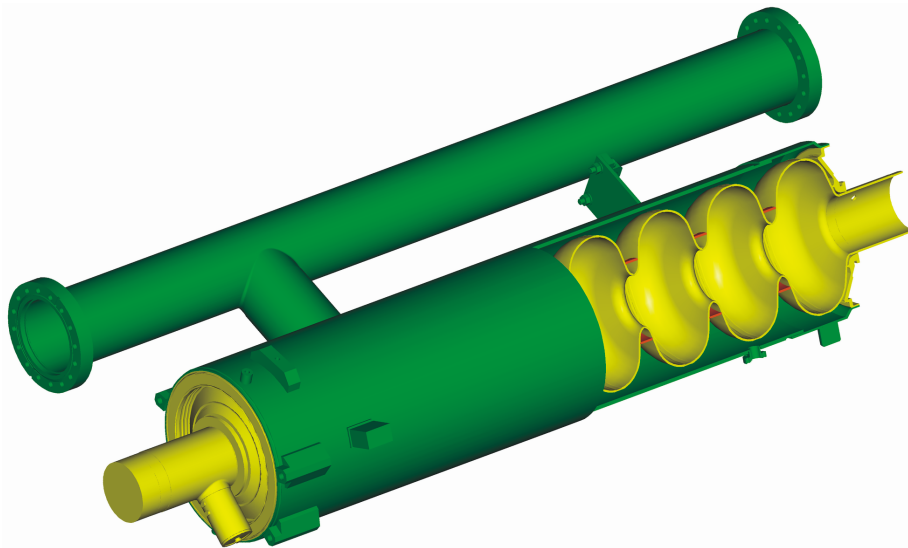
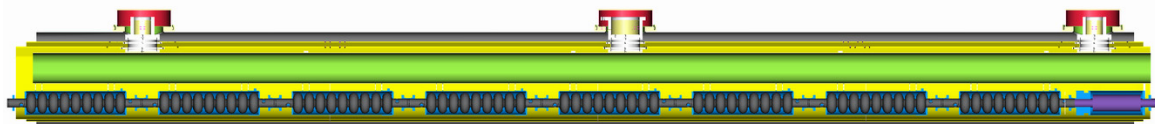


Fig. 6.3: A TESLA cavity integrated into a liquid helium tank.

For TTF (and the BESSY FEL), altogether eight cavity units are integrated in one, 12 m long, cryostat as shown in figure 6.4. In the TESLA proposal a module comprises 12 cavities, rather than eight. A 4.5 K superconducting quadrupole, a beam-position monitor and steerers at the end of the module complete the design. Currently, a beam-tube higher-order-mode load is also being designed, which will connect to the last cavity.



(a)



(b)

Fig. 6.4: a) Longitudinal cross section and b) photo of a type-III module as is installed in TTF II.

Three cryostat generations have been developed so far, the most recent being the type-III module now being installed in the TTF II accelerator [4 - 6]. This design has also been adopted by BESSY.

Table 6.2: Properties of TESLA cavities.

Parameter	Value
Accelerating mode	TM ₀₁₀
Frequency	1.3 GHz
Quality factor (Q ₀)	2 · 10 ¹⁰ at 1.8 K
Number of cells	9
Accelerating length	1.038 m
Shunt impedance (R/Q)	1041 Ω
E _{pk} /E _{acc}	2
B _{pk} /E _{acc}	4.26 mT/(MV/m)
Δf /ΔL	315 kHz/mm
Δf /ΔP	20 Hz/mbar
Lorentz force detuning constant (K _L)	1 Hz/(MV/m) ²

The transverse cross section and flow scheme in figure 6.5 illustrates the cryogenic layout of the module. The cavities are cooled by 2.0 K superfluid helium. A 1.2 bar, 2.2 K supply line expands liquid through a Joule-Thompson (JT) valve into a 2-phase line spanning several modules. It supplies each helium-vessel via a “chimney” with 2.0 K liquid. Accumulated boil-off gas in the two-phase line is transferred to a 300 mm diameter line which returns the gas to the refrigeration plant. This gas-return pipe (GRP) forms the “backbone” of the module, serving as the reference and support for all other components. It is suspended in the vacuum vessel by three posts.

In the TESLA proposal, about 10 modules (each with 12 cavities) are connected in series to form a “cryogenic string” without any warm transitions in between [7]. A feed and an end box terminate the strings, several of which are grouped together to form one cryogenic unit. The 2.2 K cryogen supply line and the GRP span the entire cryogenic unit, whereas the two-phase line is terminated at the end of each string.

At the beginning of each string the JT valve supplies superfluid helium to the two-phase line. At the end of the string, the two-phase line ends in a reservoir containing a level meter for level control and a heater to balance dynamic-load changes in the string. In each module a connection between the two-phase line and the GRP allows the evaporated

helium to enter the return stream to the refrigeration plant. Additional lines span the cryogenic units to cool two aluminum radiation shields at 40 - 80 K and 4 - 8 K. The latter loop also cools the quadrupoles.

Static losses for a 12 cavity module are 1.74 W at 2.0 K. The dynamic losses are on the order of 12.8 W for TESLA operation. Thus a cryostrung dissipates almost 150 W, which has to be cooled by the JT valve and the two-phase line. A complete cryounit comprising up to 16 strings must then be able to handle heat loads of order 2800 W for TESLA 500 operation. For TESLA 800, the heat load roughly doubles.

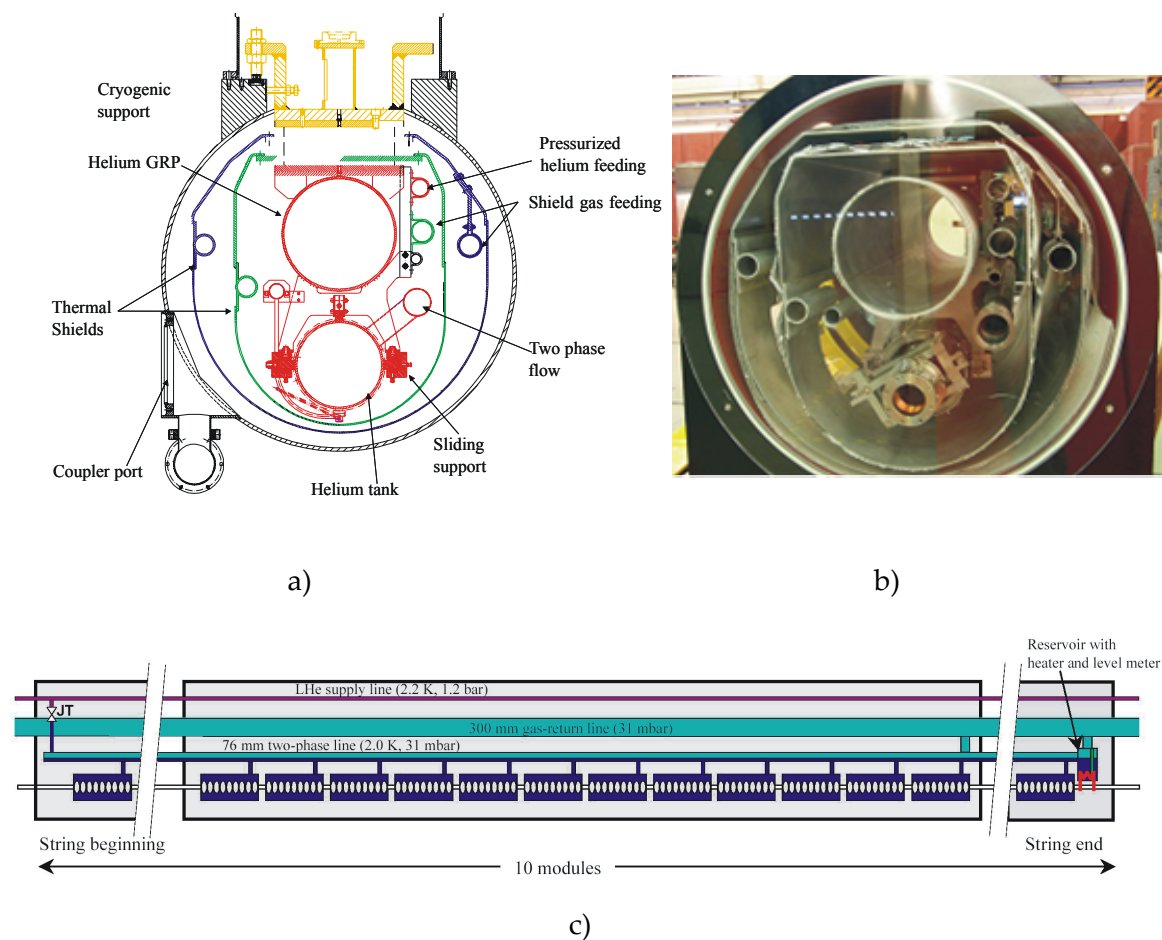


Fig. 6.5: a) Transverse cross section of a type-III module as it is installed in TTF II. b) Picture of a model cryostat. c) Cryogenic flow scheme of one "string" for TESLA.

Further details on the cryomodule design are available in the TESLA TDR [1] and numerous papers [4 - 6].

6.2.2 Input Coupler

The TTF III input coupler [8] is depicted in figure 6.6. This coaxial system connects to the cavity beam tube through the side of the vacuum vessel. It has cylindrical warm and cold TiN-coated ceramic windows and a coax-to-waveguide transition. Two heat intercepts, one at 70 K and one at 4.5 K reduce the static losses to the helium bath to less than 0.1 W [1]. Bellows allow the penetration of the inner conductor into the beam tube to be varied, thereby adjusting the coupling factor.

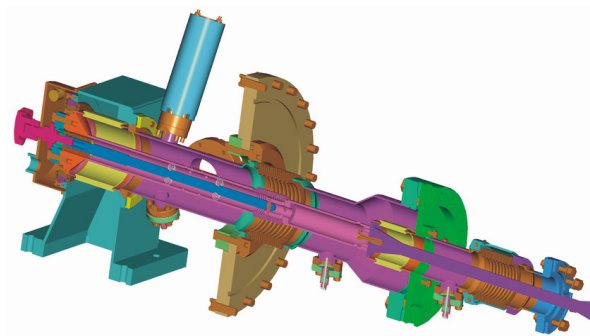


Fig. 6.6: High-power input coupler.

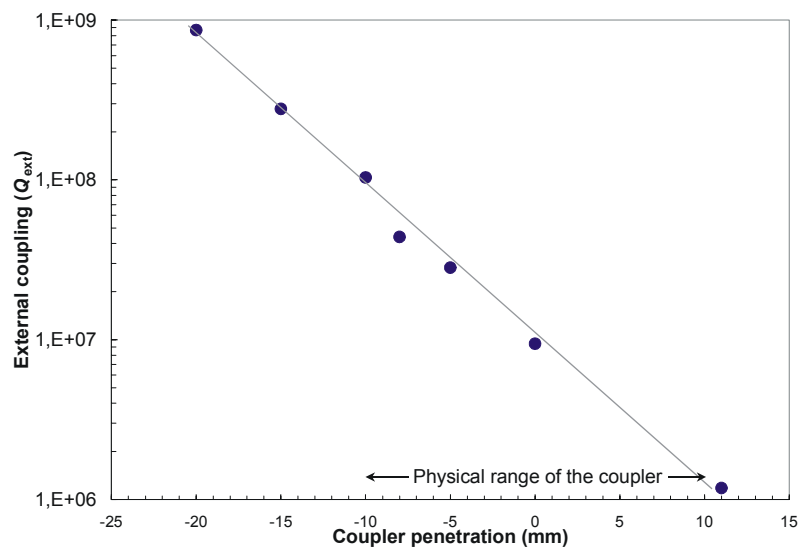


Fig. 6.7: External coupling as a function of penetration of the inner conductor into the cavity beam tube for the TTF III input coupler.

Figure 6.7 depicts a CST MICROWAVE STUDIO® calculation of the external quality (Q_{ext}) as a function of beam-tube penetration by the inner conductor (Computer Simulation Technology GmbH, Darmstadt, www.cst.com). A slight modification of the adjustment spindle has increased the stroke from 1.5 cm to 2 cm. Thus the coupling factor can be adjusted by nearly two decades. Weak coupling of order $3 \cdot 10^7$ is necessary for normal BESSY FEL operation because the beam loading is small (< 1.5 kW) when compared to the TESLA proposal (230 kW). On the other hand, strong coupling of order 10^6 will be required if cavities need to be conditioned by high-peak-power processing (HPP) [9]. This technique has been found to be very useful in recovering cavities after, for example, a vacuum accident, thereby avoiding a costly and time consuming disassembly of the module. For that reason a coupling range of a factor of 100 is very desirable. If this has to be extended further still, a three-stub tuner in the waveguide section can be used.

The TTF III coupler is designed for high-power pulsed operation (230 kW for 1.3 ms). Thus arcing and multipacting will not be an issue for the relatively low-power BESSY FEL operation (up to 15 kW). Room-temperature and cold tests with 1 MW, 2 Hz and 1.3 ms traveling-wave RF pulses, yielding an average power of 2.6 kW, have been performed successfully [10, 11]. Tests with the previous design generation (TTF II), which is very similar to the TTF III system, even have achieved 4.7 kW average power [11].

The BESSY FEL requires an average standing-wave power of up to 5 kW. Estimates suggest that the coupler can withstand this much standing-wave power [12], although the warm inner conductor may require additional cooling at the bellows. More precise simulations with ANSYS are currently under way to determine the power limit. A test series in collaboration with Cornell University, FZR Rossendorf, and ACCEL Instruments has also been initiated to measure the CW standing-wave-power limit of the coupler.

6.2.3 Cavity Tuner

Two options are currently being considered for the cavity tuning mechanism: One as installed in TTF (figure 6.8a) [2], and the newer “blade tuner” that was originally developed for the TESLA superstructure (figure 6.8b) [13]. Both attach to the helium vessel and adjust the cavity frequency by compressing the cavity. The frequency changes by approximately 0.32 Hz per nm cavity-length change [3]. The TTF tuner attaches to the end of the helium vessel and grabs the cavity beam tube directly whereas the blade tuner is mounted coaxially on the helium vessel and acts on the cavity via the vessel. Lateral motion is achieved by rotating the center ring thereby twisting the blades which, in turn, either contracts or expands the gap between the outer rings.

Measurements in the HoBiCaT test facility (section 6.6) will analyze the performance of the two systems. In particular, the stiffness and the resolution are of importance.

The stiffness impacts the mechanical resonances of the cavity system, which determines how well mechanical vibrations couple to the cavity field. As discussed in section 6.3.5, this is a critical issue for the CW operation of cavities with little beam loading.

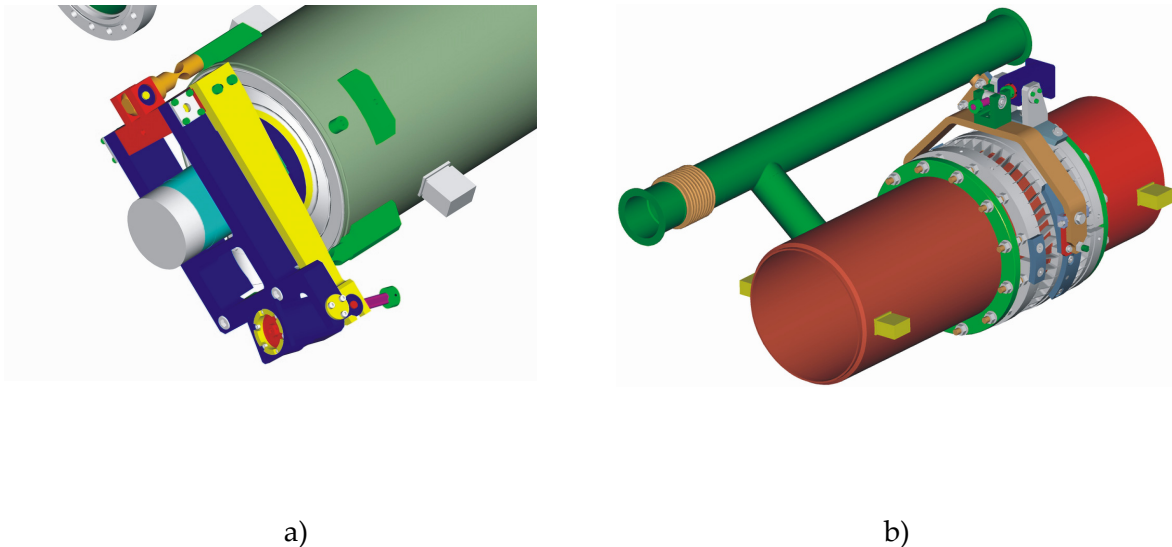


Fig. 6.8: a) Turner system as installed in TTF, and b) “blade tuner” originally developed for the TESLA superstructure.

The resolution is also of importance, because the BESSY FEL cavities will operate with a bandwidth in the tens of Hz range and a high tuner resolution is critical. The TTF tuner achieves a value of 0.74 Hz/step, while the blade tuner is almost twice as good at 0.38 Hz/step [13].

6.3 Considerations for BESSY FEL CW Operation

The TESLA technology was developed for pulsed operation with a 1% duty factor. Although most of the system is equally suited for CW operation, there are a number of issues that must be considered. In some cases, relatively minor modifications of subsystems are needed. BESSY’s approach has been to try maintain the TESLA design “philosophy” and only make changes where necessary for reliable CW operation, and/or if significant cost savings can be realized.

The following issues are to be considered:

- **Cavity field:** TESLA was originally designed to operate at 23.4 MV/m (pulsed). CW operation at this level would require a prohibitive 10 kW refrigeration power for the BESSY FEL. In fact, as discussed in section 6.3.1, a lower gradient reduces the overall cost of the machine while improving its reliability.
- **Bath temperature:** In the BESSY FEL linac the dynamic cavity losses constitute almost the entire refrigeration budget. 2.0 K operation, as for TESLA, therefore does not necessarily represent an optimum. Since the BCS resistance of niobium drops exponentially with temperature, a lower bath temperature in fact reduces the capital and operating cost of the refrigeration system (section 6.3.2).
- **Helium heat transfer:** The dynamic cryogenic load per module is of the order of 20 times higher for BESSY FEL modules than for TESLA. Slight modifications of the module are required to avoid unstable operating conditions. Details are given in section 6.3.4.
- **Microphonics and cavity tuning:** The average beam loading in BESSY FEL cavities is low. To match the cavity to the klystron, ideally weak input coupling should be used and thus the cavity bandwidth is small (order 5 Hz). Consequently, the cavity is very susceptible to microphonic detuning of the resonance and the RF power budget is driven almost entirely by the microphonics, rather than the beam loading. The level of microphonics, their sources, and means of reducing these must be understood. See section 6.3.5 for details.
- **Beam loading:** The *average* beam loading in the BESSY FEL cavities is less than 1.5 kW. Still, there is a demand in the synchrotron user community for variable bunch spacing and bunch trains, thereby driving up the *peak* beam loading. The klystron power per cavity has to be optimized to satisfy these needs while still maintaining a reasonable cost (section 6.3.6).
- **RF control:** The RF control of very-narrow-bandwidth cavities requires a high-gain feedback system. It must be demonstrated that the achievable beam energy and phase jitter does not exceed the acceptance of the HGHG FEL. Rapidly varying beam loading conditions due to bunch-train operation also requires the implementation of a feed-forward system. Details are discussed in section 6.5.
- **Input coupler:** TTF III couplers were developed for high-peak-power and low-average-power operation, whereas the BESSY FEL will run almost always at low peak power and moderate average power. The CW power limit of the coupler must be determined.

6.3.1 Cavity Field

6.3.1.1 Cost Analysis

The BESSY FEL needs up to 18 accelerator modules (144 cavities). For a total acceleration of 2.3 GeV, the cavities must be operated at 15.4 MV/m or more on average. Fewer cavities can be used if the field is increased. The cost scaling of the linac installation, as well as the performance of the cavities at higher gradients impact the choice of operating field. As discussed subsequently, neither favor a significantly higher field.

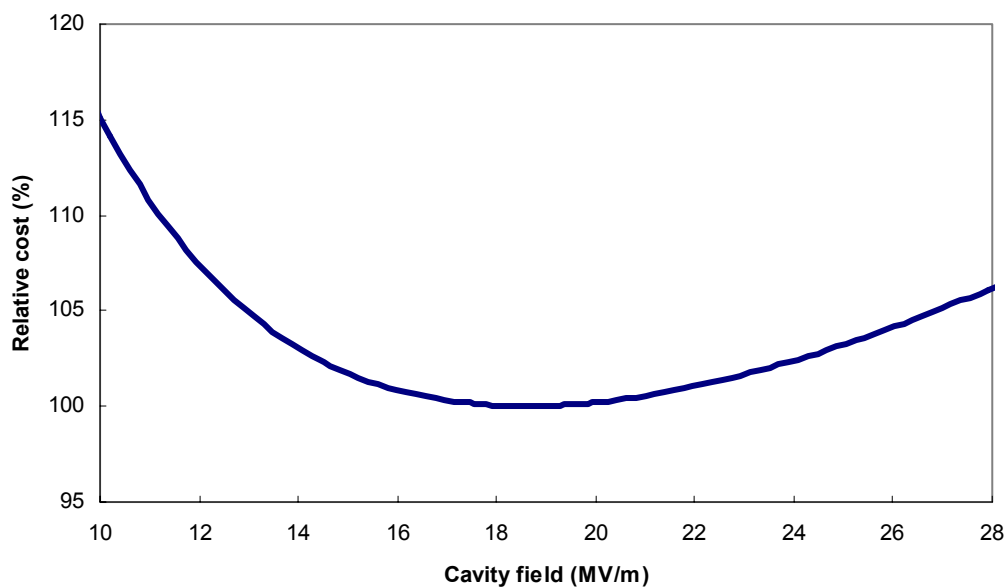


Fig. 6.9: Relative capital plus 10 year AC power operating cost of the accelerating modules, RF power, and refrigeration plant.

The number of cavity units (and hence, to first order, the capital cost) decreases as $1/E_{\text{acc}}$, E_{acc} being the accelerating field. On the other hand, both the refrigeration load and RF power per cavity increase with E_{acc}^2 . See also section 6.3.5 for details. Thus there exists an optimum field that minimizes the total installation cost of the cryomodules, RF system, and refrigeration system. The cost of wall-plug power for the entire installation also increases with field so that the inclusion of AC operating costs tends to favor lower values.

Figure 6.9 depicts the (relative) total capital cost of the RF system, cryomodules, and the refrigeration plant as well as the 10 year AC operating cost for these systems (assuming 6000 hours of up-time per year). A broad minimum exists near 18 MV/m. The location of the minimum will shift depending on the assumptions made (cost of refrigeration and klystrons, cavity quality factors, increase in cavity preparation costs as the field is raised

etc.) but because it is shallow its exact location has little bearing on the overall cost of the BESSY FEL. The choice of the operating field is therefore relatively unconstrained and other aspects, such as reliability of the linac, can drive the selection of the field.

6.3.1.2 Feasibility of Field

Accelerating fields of 15 MV/m and higher are routinely achieved in vertical cavity tests [14]. More importantly, though, TTF operation of TESLA accelerating modules (including all ancillary devices) have demonstrated that fields up to 20 MV/m can be achieved without significant Q degradation, as illustrated in figure 6.10. Above 20 MV/m the quality factor Q does begin to deteriorate, thereby increasing the refrigeration load which makes CW operation impractical.

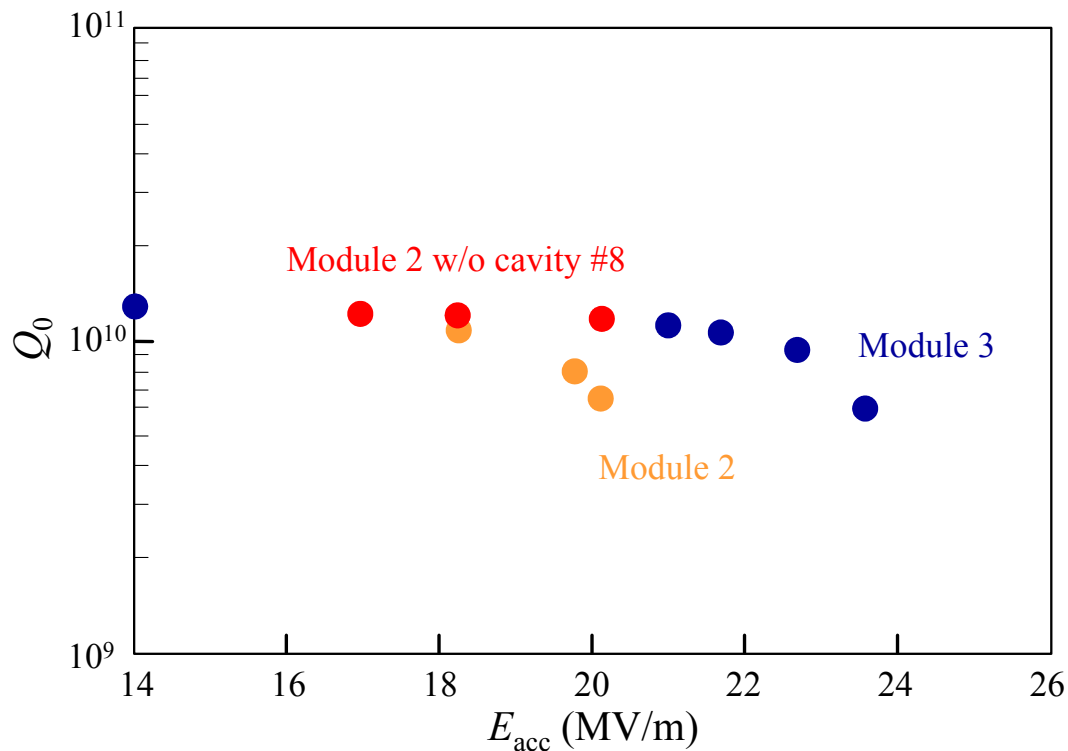


Fig. 6.10: Cavity quality factor Q versus accelerating field of the TTF modules 3 and 4. The average over all eight cavities in a module is depicted. In the case of module 3, one cavity was degraded. When this was detuned, the average Q of the remaining seven cavities was significantly higher. Measurements were made at 2.0 K, with 10 Hz pulsed operation, 800 μ s flat top RF pulse [15].

Accelerating fields above 20 MV/m without any degradation of the unloaded quality have been achieved, albeit in vertical tests [14] without ancillary devices mounted. But a costly high-temperature heat treatment is needed to safeguard against thermal breakdown and the cavity has to be electropolished to prevent the Q degradation. By choosing a field of less than 20 MV/m for the BESSY FEL, these steps can be avoided, thereby reducing the cost of cavity production. In that case, the cavity treatment only includes the well-established procedures of chemical polishing [16] with buffered chemical polish (BCP), high-pressure rinsing [17], and an 800 °C heat treatment to avoid any hydrogen contamination of the niobium and the resultant “Q disease” [18]. Should field-emission limit the cavity performance at the operating field, high-power processing [9] with the spare 10 MW injector klystron will be used to condition the cavity.

Importantly, operation at 15.4 MV/m offers an additional safeguard against cavity failures due to, for example, coupler problems. A failed cavity can then be detuned and the other seven are able to make up for the lost voltage by operating at 17.6 MV/m - considerably less than the 20 MV/m limit when the post-production heat treatment becomes necessary. This significantly improves the overall reliability and availability of the BESSY FEL.

6.3.2 Bath Temperature

The dynamic heat load in TTF and TESLA is only a fraction of the overall refrigeration budget and therefore cavity operation at 2.0 K represents an optimum choice. The temperature is sufficiently far below the helium lambda point to guarantee stable operation, while not unnecessarily low to incur a heavy Carnot-efficiency penalty.

With CW operation, the dynamic losses make up almost the entire refrigeration budget. Since the BCS surface resistance of niobium drops exponentially with temperature, a lower operating point potentially can reduce the capital and operating cost of the refrigeration plant.

Anomalous (temperature independent) losses due to field emission, trapped magnetic flux, and other residual losses limit the gain in Q as the temperature is reduced [19]. Also the complexity of the cryoplant increases with decreasing temperature so that the optimum temperature is likely to be around 1.8 K. Operation at even lower temperatures becomes increasingly difficult because the volume of boil-off helium gas at low pressure increases dramatically, and the TESLA module pipe dimensions are insufficient to handle this. A significant redesign of the module would then become necessary.

Figure 6.11 a) depicts an example of Q measurements as a function of temperature performed in a vertical test cryostat at TTF. Clearly, even at 1.5 K the quality factor has not yet saturated. These Q values were obtained at low field, but a sample Q versus E_{acc} curve

at 1.8 K (figure 6.11 b) illustrates, that this quality factor can be maintained out to the operating field of the BESSY FEL.

The Q at 1.8 K was $2.4 \cdot 10^{10}$, 50% more than that at 2.0 K. Even though the Carnot efficiency is 10% less, the Q improvement reduces the 2.0 K equivalent refrigeration power. However, the operating pressure would drop from 31 mbar to 16 mbar and it must be shown that the increased flow rate can be handled by the TESLA modules. An analysis of the system is discussed in section 6.3.4.3.

Horizontal measurements of the cavity quality *at the operating field* as a function of temperature are still lacking for cavities with all ancillary components, such as the input coupler, attached. It is likely that the improvement versus temperature is less dramatic than that shown in figure 6.11. BESSY intends to perform such measurements in the near future to optimize the layout of the cryoplant (section 6.6). These tests should also provide insight into whether residual losses can be reduced by improving the magnetic shielding, or if other loss mechanisms dominate.

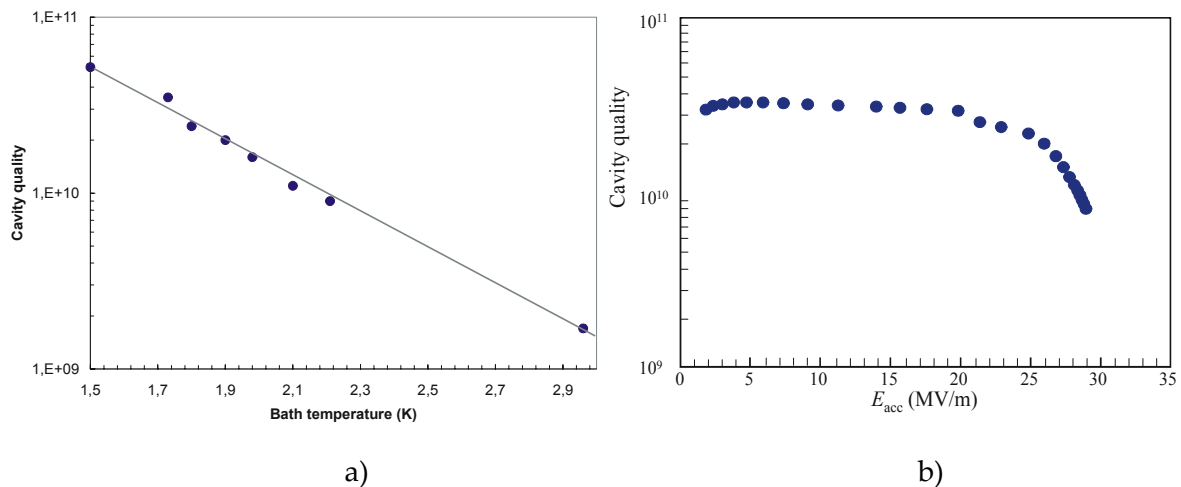


Fig. 6.11: a) Quality factor as a function of temperature measured on the TTF vertical test stand with cavity C 21. Tests were performed after various treatments and on different days, and the 1.8 K result represents an average value; b) Cavity quality as a function of field at 1.8 K.

6.3.3 Dynamic Heat Load

Given an 18 module linac and fixed energies at the bunch compressor and beam-extraction points (figure 6.1), table 6.3 lists the fields and power dissipation in the cavities for the individual linac sections. It is assumed that the cavity performance shown in figure 6.10 is achieved. In all likelihood, better Q values can be realized at lower temperature, so that the quoted values represent a conservative estimate.

At most, each cavity will therefore dissipate 21 W and each module 166 W for a total linac load of nearly 3 kW. For reliable linac operation, however, the modules and cryogenic systems should be designed such that the shut-down of one cavity in a module can be compensated by the remaining seven. In this case the losses increase to 27 W per cavity and 216 W per module.

Table 6.3: Cavity fields and cavity power dissipation in the individual linac sections of the BESSY FEL. A conservative value of $1.3 \cdot 10^{10}$ based on the 2.0 K measurements in figure 6.10 was assumed, but improvements at 1.8 K are expected.

Linac	Number of modules	Field (MV/m)	Cavity loss (W)	
			Per module	Per section
Booster	1	15.7	157	294
3 rd harm. cavities	63 cells	14.9	20*	20*
Linac 1	1	15.3	150	150
Bunch compressor 1				
Linac 2	4	16.1	166	664
Arc + bunch compressor 2				
Linac 3	2	16.1	165	329
FEL 1				
Linac 4	10	15.4	151	1513
FEL 2 + FEL 3				
Total power dissipation in the cavities				2833

* To estimate the losses of the third-harmonic cavities the 1.3 GHz cavity geometry was simply scaled to 3.9 GHz.

6.3.4 CW Module Design

A number of issues must be examined to ensure that TESLA-like modules can be operated with high CW dynamic losses:

1. Capacity of the JT valve; its throughput must be sufficient to provide the cooling for one module.
2. The capacity of the helium tank to transfer the dynamic load to the chimney without inducing boiling.
3. The capacity of the chimney to exhaust the heat from the helium tank without boiling.
4. The stability of two-phase He II flow in the two-phase supply line.
5. Mass flow and pressure drop in the gas-return pipe to the refrigeration plant.

Note that a single cryogenic string in the TESLA design, which is supplied by one JT valve, dissipates 150 W. Provided each CW module is equipped with its own JT valve, then this is approximately equivalent to one TESLA cryogenic string, except that there are more connections between the two-phase line and the GRP in the TESLA case.

Also, in the TESLA design the helium boil off from one cryounit (approximately 2.8 kW) is handled by the GRP. Similar values apply to the entire BESSY FEL.

Thus these general considerations suggest that TESLA modules can indeed be used for BESSY-FEL CW operation with only minor modifications. This has been confirmed by calculations and simulations, as discussed below.

Figure 6.12 depicts the proposed modified layout of the TESLA modules for CW operation. Each module will be equipped with its own JT valve. There is no connection of the two-phase lines between neighboring modules, in contrast to the TESLA layout. If this were not the case, “cross talk” from one module to the next would complicate the liquid-level control in the two-phase lines.

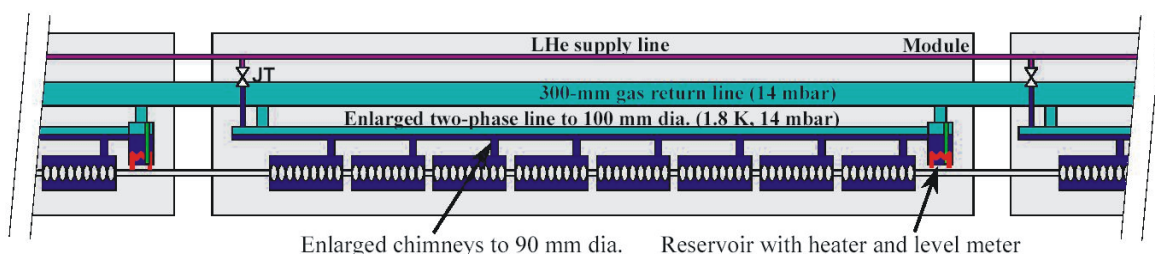


Fig. 6.12: Schematic of the BESSY-FEL module for CW operation.

The diameter of the two-phase line has been increased to 100 mm to improve the mass-flow conditions. The larger size can be accommodated if minor modifications to the quadrupole's helium supply are made.

An additional connection between the two-phase line and the GRP was also incorporated in each module. One connection is situated near the JT valve to effectively remove flash gas. The other is located close to the reservoir to exhaust the gas that is produced by the compensation heater. The diameter of these connections was scaled to 90 mm although this is not necessary as the pressure drop in this region was found to be negligible.

As discussed in section 6.3.4.3 the pressure drop in the GRP is small, even in CW operation, so its size (300 mm) needs not be increased. This fact is important because any changes to the critical GRP would impact the overall design of the cryomodule significantly.

6.3.4.1 JT Valve

The 1.8 K He II is obtained by expanding 2.2 K, 1.2 bar helium through the JT valve to a pressure of 16 mbar. To provide a cooling capacity of 200 W at 1.8 K, at least 8.7 g/s liquid He II is needed. If a safety factor of 1.5 is included, the JT valve must provide 13.1 g/s He II in each cryomodule. In the expansion process, about 1.9 g/s of flash gas is generated, which also is injected into the two-phase line. Thus the JT valve must have a total capacity of at least 15.0 g/s helium. JT valves with this capacity are commercially available (for example, WEKA's P-TEV/875/6-10-15.0) so that this will not limit BESSY FEL operation.

6.3.4.2 Heat Transfer in Helium II

As with ordinary materials, heat transport in He II produces a temperature gradient [20]. However, the heat-transport capacity of He II is larger by orders of magnitude for the same temperature gradient. Even with such unique and excellent heat-transfer characteristics, vapor formation within the bulk of He II is still possible when high heat loads must be removed. Any boiling in He II may increase the microphonic detuning of the cavities and can impact the stable cryogenic operation adversely. Boiling in He II may occur when the pressure and temperature within the liquid are close to the saturated liquid line. Additional heat flow can then drive the system locally into saturation resulting in the formation of bubbles [20].

In a column of He II, a heat source at the bottom will establish a temperature gradient, the resultant temperature difference between the top and the bottom being greater the taller the tube. But at the same time, the hydrostatic pressure (and hence the saturation temperature) increases with the depth of the liquid. For the levels of heat flux being considered here ($\approx 0.5 \text{ W/cm}^2$) these two effects roughly cancel, so that the critical flux (\dot{Q}_{crit}) at

which boiling occurs is nearly independent of the tube length [21]. A conservative value for \dot{Q}_{crit} is 1 W/cm^2 . The dimensions of the helium tank and chimney must be such that this value is not exceeded during CW operation of the cavities.

Figure 6.13 depicts the longitudinal and transverse cross sections of the helium tank. Within the tank itself, the largest heat flux is expected in the narrow annular regions between the cavity equator and the tank wall (area = 66 cm^2). For BESSY FEL operation the maximum flux will therefore be 0.5 W/cm^2 or less. This produces a temperature gradient of less than 0.11 mK/cm at 1.8 K [20].

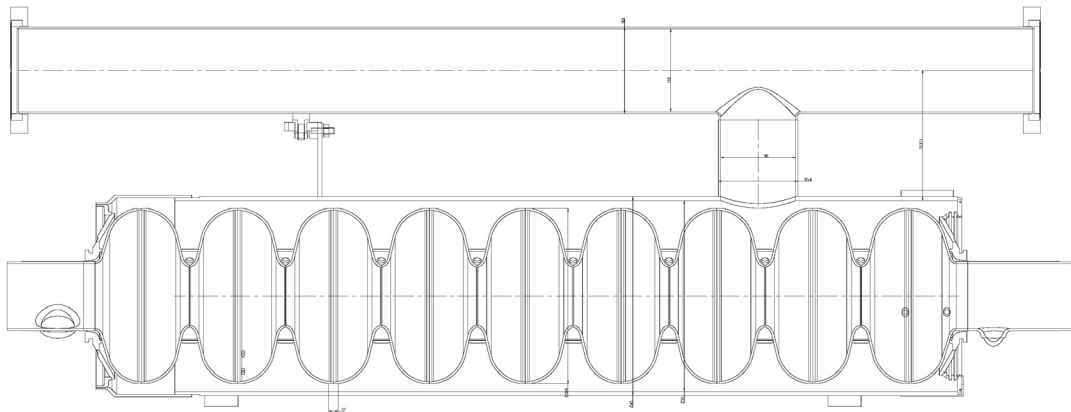
The chimney must be able to conduct the full cavity losses. Its diameter in the TESLA design is 54 mm yielding a cross section of 23 cm^2 , which is insufficient for CW operation. For the BESSY FEL modules, its diameter has been enlarged to 90 mm to ensure that the heat flux in this region is also less than 0.5 W/cm^2 .

In figure 6.13 b) the three critical points where boiling is most likely to occur are marked B, C, and D. Table 6.4 summarizes the local hydrostatic pressures and resultant saturation temperatures at these points if the pressure at point A is maintained at 1638 Pa .

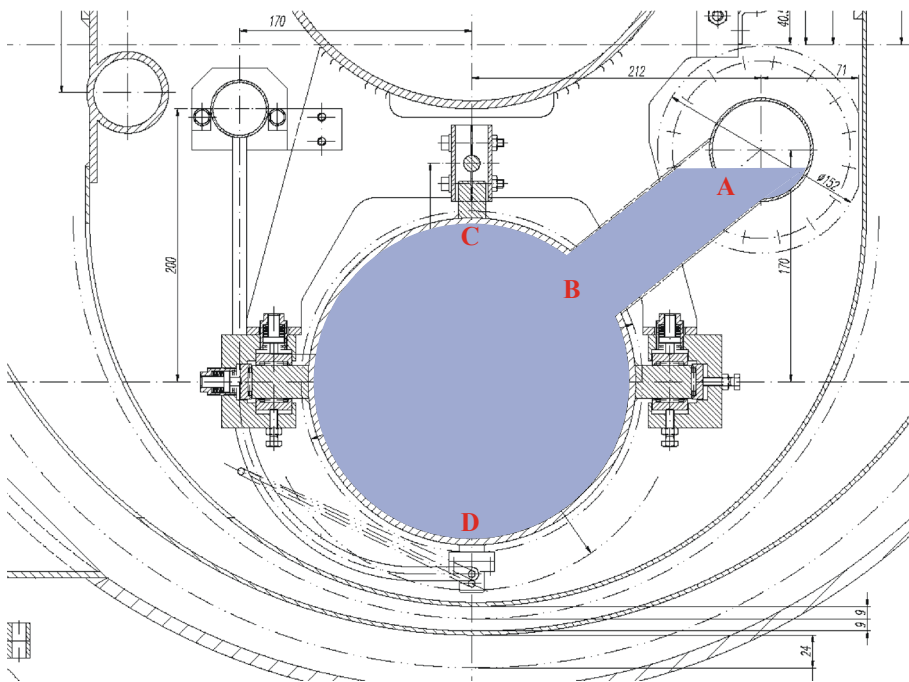
Given a chimney length of 16 cm , the temperature at point B therefore is 1.802 K for a heat flux of 0.5 W/cm^2 . The heat-transfer analysis for positions C and D is more complicated because of the three-dimensional configuration. As a rough but safe estimation we assume the heat flux along these two annular sections also equals the full 0.5 W/cm^2 . Hence the temperature difference between position C and B over the arc length of 10 cm is 1.1 mK . Similarly, D and B are separated by 26 cm resulting in a temperature difference of 2.9 mK . The temperatures at positions C and D are therefore 1.803 K and 1.805 K , respectively, as summarized in table 6.4. Clearly, the temperatures at B, C, and D are all significantly lower than the local saturation temperature so that boiling is unlikely to occur. Tests in the HoBiCaT facility (section 6.6) will be used to confirm this conclusion.

Table 6.4: Pressure and saturation temperature at the four positions marked in Figure 6.13 b). Also listed is the expected maximum temperature at these points (see text).

Pos.	Depth w.r.t. A cm	Local pressure Pa	Local saturation temp. K	Actual temp. K
A	0	1638	1.800	1.800
B	10	1780.6	1.824	1.802
C	5.5	1716.5	1.813	1.803
D	28.5	2044.5	1.864	1.805



a)



b)

Fig. 6.13: a) Longitudinal and b) transverse cross section of the helium tank. In b) the cavity is not shown.

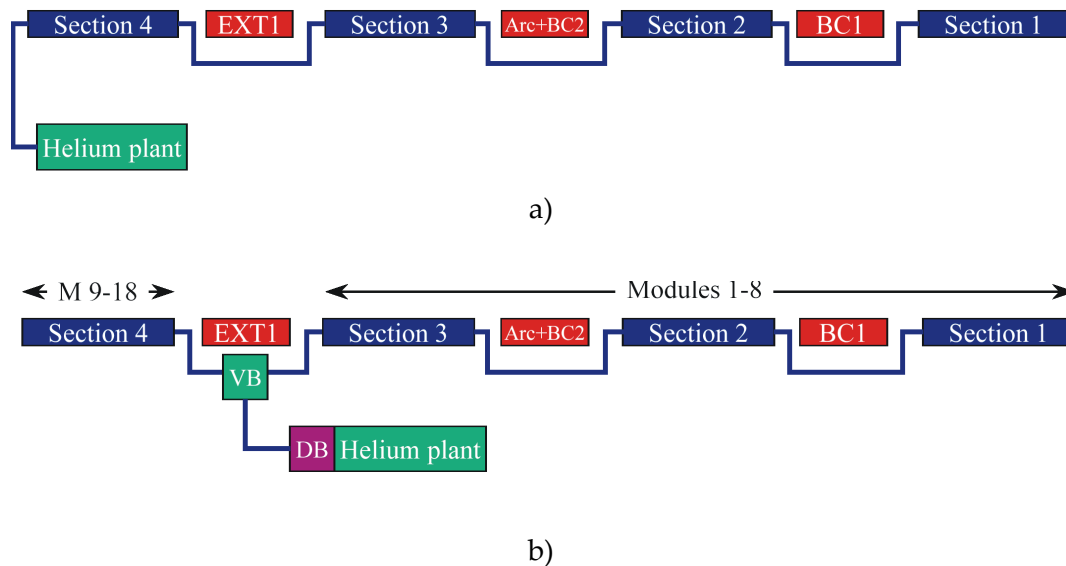


Fig. 6.14.: Two possible cryogenic layouts of the linac. a) The plant supplies all sections in series, b) two, roughly equal parts of the linac are supplied in parallel. Bypasses circumvent the warm sections of the linac (DB = distribution box, VB = valve box).

6.3.4.3 Heat Conduction and Mass Flow in the Two-Phase Line and GRP

Special attention has to be paid to the large mass-flow in the two-phase line and the GRP. Here both two-phase and superfluid flow must be considered. Stratified flow must be maintained in the two-phase line to avoid excessive waves or even plugs which cause microphonics and unstable cryogenic operation. The mass flow in the GRP also determines the pressure drop along the linac and ultimately the cavity operating temperature.

As shown in figure 6.1, the linac is divided into four cold sections. Figure 6.14 depicts two possible schemes for the cryogenic distribution, more details being given in chapter 15. In the first scheme, the entire linac is supplied in series by the cryoplant. Hence boil-off gas from section 1 must travel through the entire linac in the GRP before it is returned to the cryoplant. In the alternative scheme, the linac is split roughly in half at the first beam-extraction point, creating two parallel paths of 8 and 10 modules, respectively. This layout reduces the total pressure drop in the linac. As an added benefit, the second scheme would permit the cryogenic operation or commissioning of one half of the linac while the other is at room temperature.

Given the complexity of the system, simulations of the heat and mass flow in the two-phase line and GRP must be performed for the entire linac to gain a better understanding

of the tolerable heat load. Details of the program for these studies are described in [22] and [23]. The simulations, as discussed below, yield information on the pressure drop in the linac and the helium-flow pattern in the two-phase line. They have demonstrated that stable operating conditions exist for the BESSY FEL with an ample safety margin.

The module and cryogenic layouts in figures 6.12 and 6.14, respectively, were used as the basis for the simulations. Cryogenic bypasses for the warm sections (beam extraction points, bunch compressors, and arc) were included to account for any pressure drop in these segments. Vapor produced by the flash gas after the JT valve (13%) was also included in the calculations. The liquid level in the two-phase line at the reservoirs, where the level meter is located, was fixed at 1/3 of the pipe diameter. An evenly distributed heat load of 250 W per module was assumed even though, on average, the BESSY FEL modules will dissipate only 2/3 of this value. This provides for a substantial safety margin. To further investigate the operation of a hypothetical under-performing module, an extreme heat load of 400 W in a single module was also included in the simulations. This value corresponds to all cavities operating at 22 MV/m with $Q_0 = 10^{10}$.

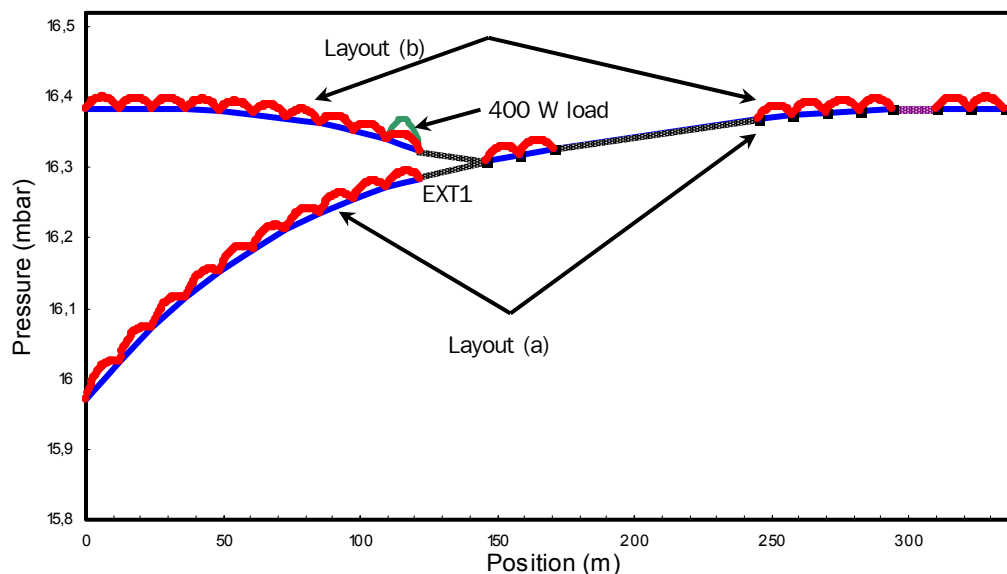


Fig. 6.15: Two-phase-flow simulation results for the BESSY FEL, but with cryogenic losses 1.5 times those expected during normal operation. The pressure in the GRP is depicted in blue, that in the two-phase lines of the individual modules in red, and that in the warm-section bypasses in black. Results for both configurations in Figure 6.14 are shown. The green curve represents the pressure in the module following beam extraction if its cryogenic load is increased to 400 W.

Figure 6.15 depicts the gas pressure in the GRP and the two-phase lines of the individual modules for both linac configurations. Also shown are the results if the cryogenic load of one module is increased to 400 W (green). Obviously, the pressure drop over the linac

is greater for configuration a), this amounting to less than 0.5 mbar. The temperature difference between the two linac ends will then be about 9 mK, which does not limit the cavity operation. For configuration b) the pressure drop is improved further by a factor of 5.

The vapor velocity in the two-phase line of some of the individual modules is shown in figure 6.16. The flow is bidirectional because of the two connections between the two-phase line and the GRP at the ends of each module. The symmetry about the module center is not maintained for the modules closest to the pumps because the pressure gradient in the GRP increases. This is due to the fact that the gas from all previous modules also has to be transported by the GRP. Thus, in the two phase line, more gas flows towards the downstream chimney than towards the upstream one.

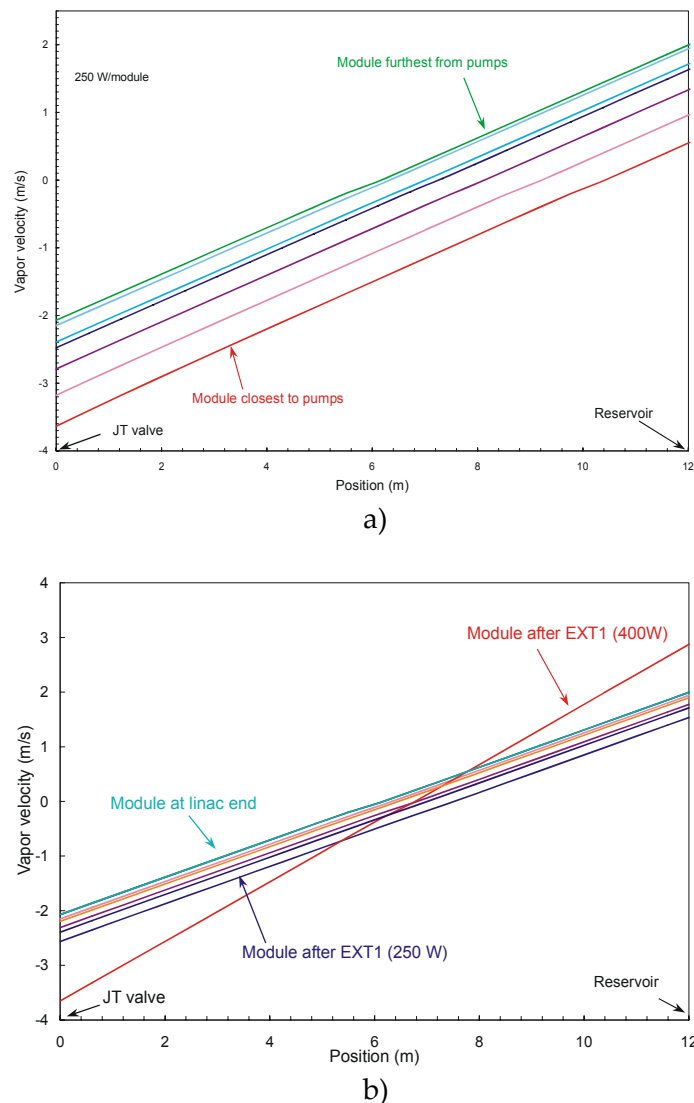


Fig. 6.16: Vapor velocity in the two-phase lines of some modules for the two configurations in figure 6.14, respectively.

Importantly, though, the flow speed remains below 4 m/s in all modules for both linac configurations. Measurements with He II have identified this value as being the threshold to unstable (non-stratified) two-phase flow [24]. Thus, even for a total cryogenic load of $18 \cdot 250 \text{ W} = 4.5 \text{ kW}$, the linac could still be operated stably, providing an ample safety margin for the planned 3 kW BESSY FEL operation.

Clearly, the main benefit of using configuration b) in figure 6.14 lies not in the improved pressure drop along the GRP but in the significantly lower vapor speed (2.6 m/s at its maximum) compared to 3.6 m/s for configuration a). In this case, even for 400 W operation of a module the vapor speed does not exceed 4 m/s and stratified flow is maintained. To take advantage of this additional safety factor and the improved operational flexibility, the BESSY FEL cryogenic system will therefore be based on layout b).

A more rigorous analysis of the flow pattern is provided in [25], in terms of the two dimensionless parameters F and K , which are defined as

$$F = \sqrt{\frac{\rho_g}{\rho_l - \rho_g}} \frac{U_{gs}}{\sqrt{Dg}} \quad (6.1)$$

$$K = \sqrt{\frac{\rho_l \rho_g U_{gs}^2 U_{ls}}{(\rho_l - \rho_g) g \mu_l}} . \quad (6.2)$$

Here ρ_l and ρ_g are the liquid and vapor density of the helium, D is the diameter of the two-phase tube, g the gravitational acceleration, μ_l the viscosity of He II, and U_l and U_{gs} are the superficial velocities of the helium liquid and vapor.

These parameters are used to distinguish between stratified and non-stratified flow (F) and between stratified-smooth and stratified-wavy flow (K). Figure 6.17 depicts the results for the most critical module of layout (b) in figure 6.14. The plot of the F parameter clearly demonstrates that the flow pattern should be stratified, in agreement with the conclusions in [24]. The parameter K , however, indicates that some waves may still form. Still, it is unlikely that the cavity performance will be impacted by light waves. For reference, simulations of the two-cavity CW ELBE module [26] were also performed. The cryogenic and operational aspects of this module are very similar to the BESSY FEL modules (1.8 K CW operation with a heat load of $\approx 50 \text{ W}$ per cavity). The results depicted in figure 6.17 illustrate that the flow pattern in the ELBE module is similar to that expected in the BESSY FEL. It has been operated stably for some time now at a cavity bandwidth of 70 Hz, without adverse microphonic detuning being detected, and it is reasonable to expect similar conditions in the BESSY FEL modules.

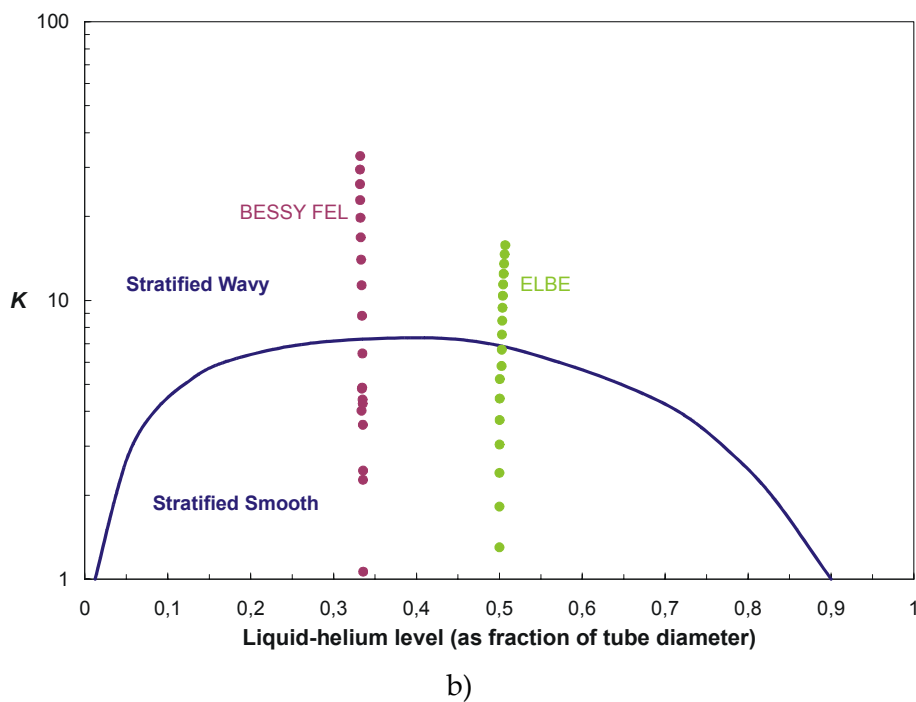
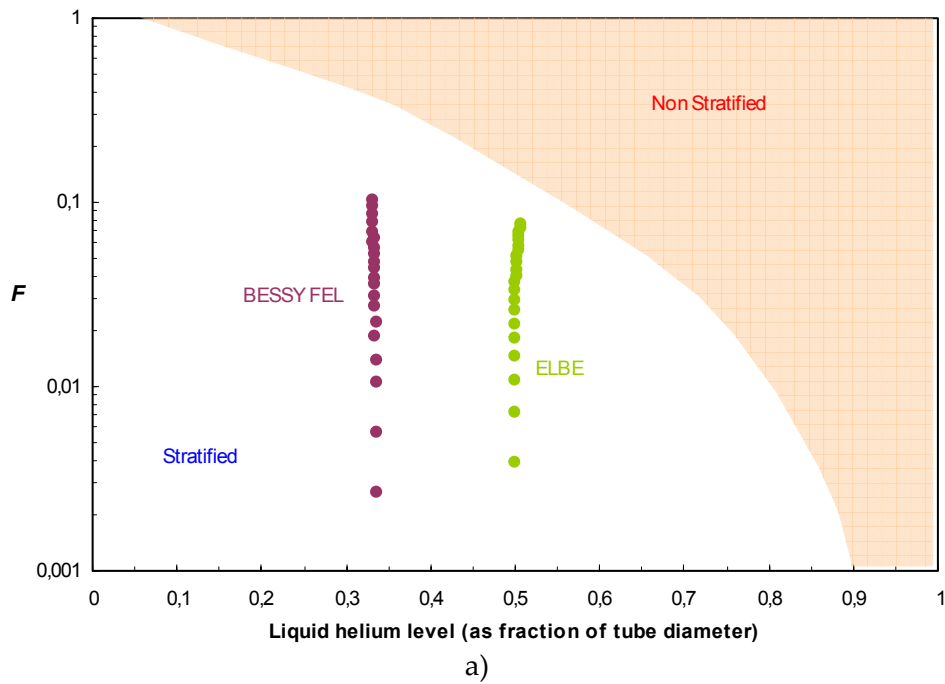


Fig. 6.17: Two-phase-flow pattern in the most critical module of layout (b) at various points in the two-phase line. Also included are simulation results for the two-cavity CW module in operation at ELBE which is also based on TESLA cavities. In the ELBE case the two-phase line is half filled during normal operation. a) Dimensionless parameter F versus liquid level, and b) dimensionless parameter K versus liquid level.

6.3.5 Impact of Microphonics on CW Operation

Any mechanical vibrations transmitted through connections to the cavity will cause the resonance frequency to shift. Similarly, bath-pressure fluctuations will shift the frequency by 20 Hz/mbar [3]. Figure 6.18 depicts two examples of detuning measurements in a TTF module. The root-mean-square (rms) values were in the range 2 - 7 Hz. Slow variations (< 1 Hz) can be compensated by a mechanical tuner and are therefore not included in figure 6.18. But rapid changes must be compensated by applying additional RF power to maintain a constant voltage.

The required power reserve is dependent on the level of microphonics and the bandwidth of the cavity, the latter being determined by the coupling strength of the input coupler.

In the absence of microphonics, a cavity can be operated without power reflection if

$$Q_{\text{ext}} = \frac{V_{\text{acc}}}{\frac{R}{Q} I_b}; \quad (6.3)$$

that is, all power is transferred to the beam. Here V_{acc} is the cavity voltage, I_b the beam current, and R/Q is the geometric shunt impedance (the definition $R = V_{\text{acc}}^2/P_{\text{diss}}$ being used). If the cavity then is detuned by an amount δf , the required power to maintain a constant voltage is given by

$$P_g = P_b \left(1 + \frac{(\delta f)^2}{\Delta f^2} \right), \quad (6.4)$$

Δf and P_b being the fwhm bandwidth ($\approx \omega/Q_{\text{ext}}$) and beam power, respectively.

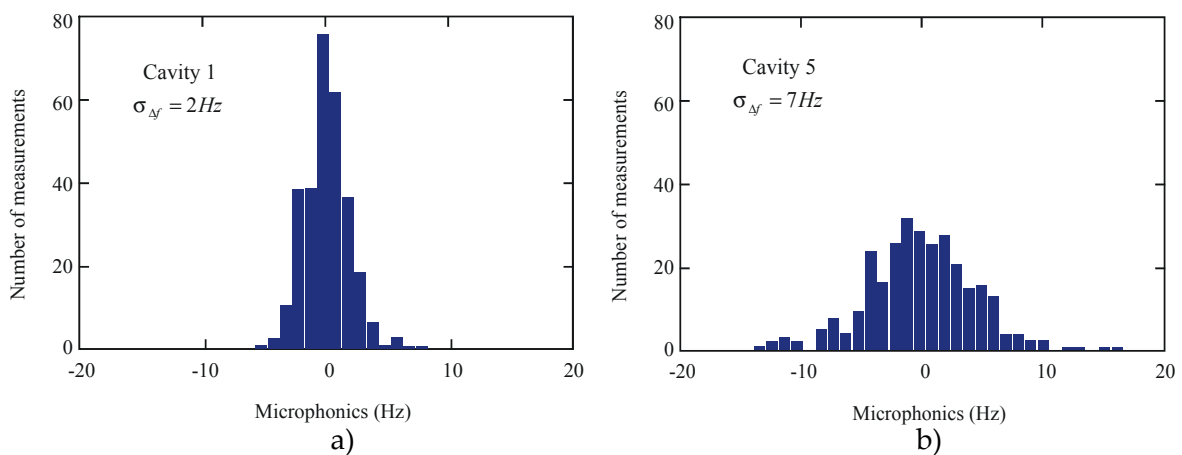


Fig. 6.18: Distribution of detuning of two cavities in a TTF module due to microphonics. Slow drifts below 1 Hz were filtered out [27].

In the BESSY FEL, beam-dump considerations dictate that the average current may not exceed $75 \mu\text{A}$. In the absence of microphonics the optimum bandwidth therefore is of order 5 Hz, as given by equation (6.3). Detuning by the same amount would therefore double the required generator power. Given the peak detuning in figure 6.18, the required power reserve would be even greater. To avoid this situation, the cavity must be overcoupled to increase the bandwidth which therefore is determined by the microphonics rather than the beam loading.

Figure 6.19 graphs the required RF power versus bandwidth in a cavity operating at 20 MV for different values of detuning [19]. The beam loading is included in this calculation and amounts to 1.5 kW. Clearly a significant power reserve is needed to compensate the microphonics, even for small detuning values.

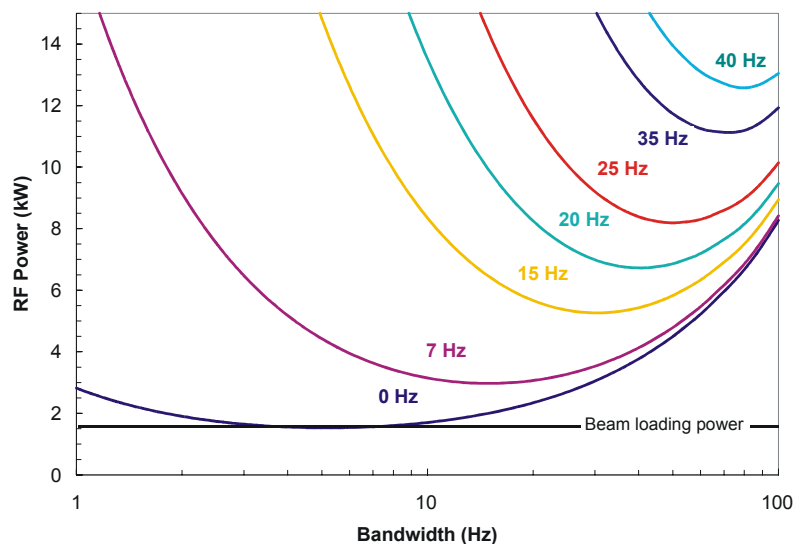


Fig. 6.19: Required RF power versus bandwidth for a number of different values of detuning. The cavity voltage is 20 MV and the average beam current is $75 \mu\text{A}$.

If insufficient power is available during a detuning spike, the cavity may trip and the beam is lost. This situation is illustrated in figure 6.20 which depicts simulation results of the feedback control of a single 9-cell cavity. For the simulation, microphonic detuning with a peak excursion of 27 Hz, as well as Lorentz force detuning was also included. To minimize the required peak RF power, the cavity bandwidth was set to 54 Hz (equation (6.6) below). Nevertheless, 8 kW peak power is required to maintain 20 MV even though beam loading was not included in the simulation.

The red curves represent the results if a 6 Hz offset is included in the detuning (for example, if the bath pressure rises by 0.3 mbar) and the klystron power is capped at 8 kW. Clearly, the power demand exceeds this level several times during the simulation. The first two times the field recovers once the detuning decreased again, but the third time it

rapidly drops to a small value. Even if the field does not collapse completely, there is a danger that the beam energy drops below the energy acceptance of a downstream device, leading to a trip by the machine-protection system.

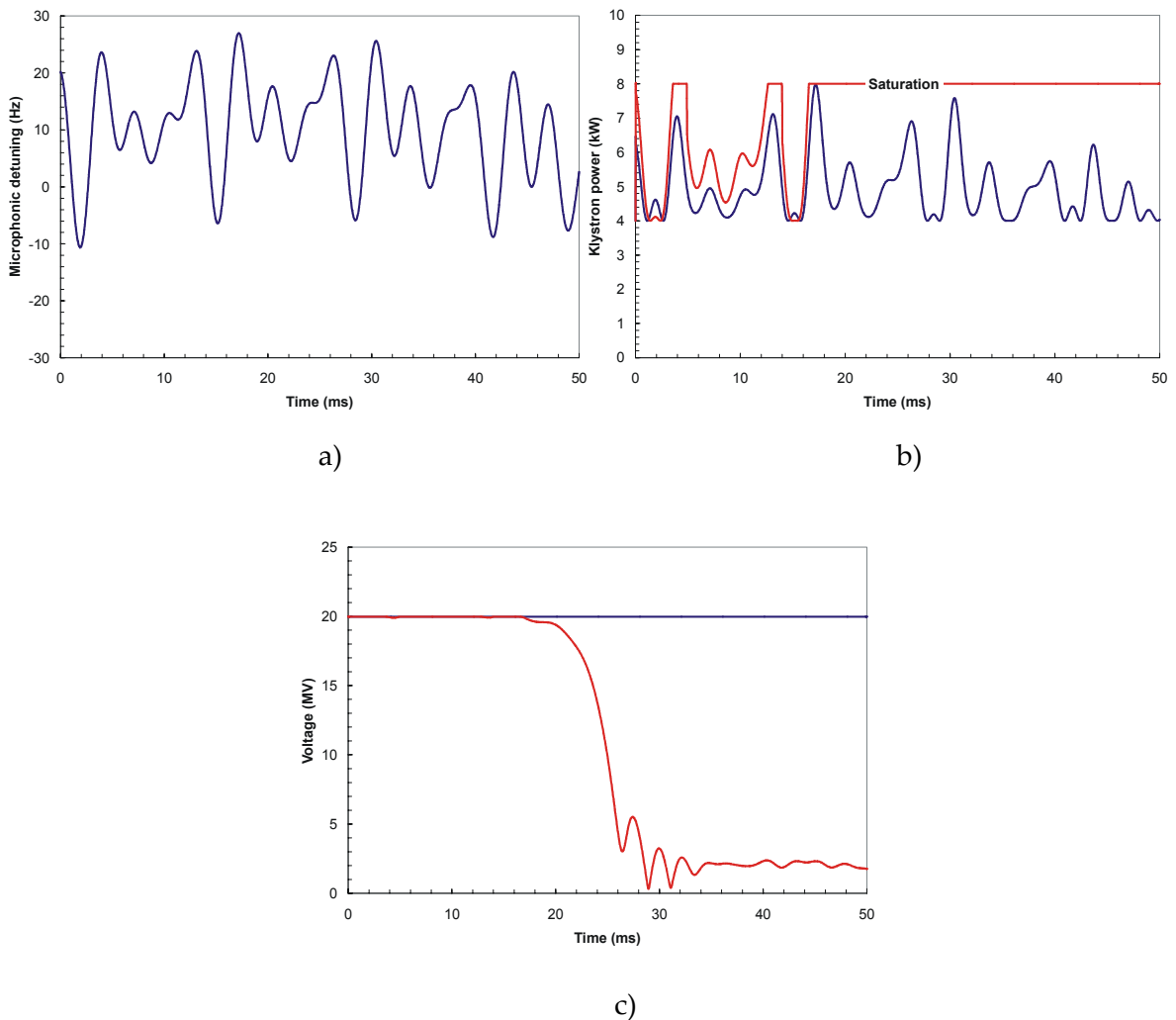


Fig. 6.20: Simulation of feedback control of a 9-cell cavity as a function of time in the presence of microphonic and Lorentz force detuning. The set value was 20 MV, the cavity bandwidth was 54 Hz ($Q_{\text{ext}} = 2.4 \cdot 10^7$), the available klystron power was 8 kW and beam loading was not included. Shown as a function of time are a) microphonic detuning, b) RF power supplied, c) cavity voltage. Blue curves depict simulation results obtained with the microphonic detuning in a) whereas the red curves were obtained when a 6 Hz offset was added to the detuning.

Lorentz force detuning is responsible for the collapse of the field as shown in figure 6.20. When insufficient power is available, the cavity field reduces, thereby diminishing the magnitude of the Lorentz force detuning. This shifts the resonance towards higher

frequencies and increases the power demand further. Since this no longer can be met by the saturated klystron, the field continues to drop.

The trip rate per cavity must be low enough so that for 144 cavities it does not exceed a few per 24-hour day. Given that the vibration spectrum extends up to a few hundred Hz, the power budget has to be sufficient to compensate excursions up to about $6 \sigma_{mic}$, σ_{mic} being the rms value of the microphonic detuning. A more rigorous analysis in [28] confirms this estimate.

Only few measurements of microphonics have been performed in TESLA modules, as in figure 6.18. In those cases rms values were in the range 2 - 7 Hz. Thus the *peak* RF power must be able to handle excursions up to ± 40 Hz. Future measurements should, however, yield more reliable values and the installed RF power will be adjusted accordingly. Also, techniques to reduce the microphonics are being investigated, which potentially can yield a large RF power savings (section 6.6).

6.3.5.1 Optimum Input Coupling

As can be seen in figure 6.19, for a given amount of detuning, there exists an optimum bandwidth at which the RF power is minimized. The bandwidth in turn, is determined by the input coupling (Q_{ext}), where

$$\Delta f \approx \frac{f_0}{Q_{ext}}. \quad (6.5)$$

If beam loading and cavity power dissipation are negligible, the optimum (FWHM) bandwidth is given by

$$\Delta f^{opt} = 2\delta f_{mic}. \quad (6.6)$$

Figure 6.21 depicts the required RF power as a function of detuning provided the bandwidth is always adjusted to the value given by equation (6.6). For a peak detuning of 40 Hz, the RF system must be able to deliver nearly 13 kW *peak power* if the cavity bandwidth is 80 Hz ($Q_{ext} = 1.6 \cdot 10^7$). However, given that the rms detuning is of order 7 Hz, clearly one cannot operate the cavity in a manner that minimizes both the required peak power and rms power.

For example, if the bandwidth is optimized for a peak detuning of 40 Hz and the rms value is 7 Hz then the average RF power will be of order 7 kW (figure 6.19). Depending on the CW operating limit of the coupler, this value can be reduced. For example, a smaller bandwidth of 50 Hz will lower the required CW power to 5 kW, but then 14 kW of peak power are needed. The BESSY FEL RF system therefore will deliver up to 15 kW at each cavity to have sufficient overhead to handle all anticipated microphonics.

This example also illustrates one of the reasons why the input coupling has to be adjustable. Since the level of microphonics is expected to vary from cavity to cavity, the coupling can then be optimized in each case, either by changing the penetration depth of the antenna, or by means of a three-stub tuner in the waveguide. An added benefit lies in the fact that strong coupling (at the 10^6 level) will also enable high-power processing [9] of cavities in case of excessive field emission.

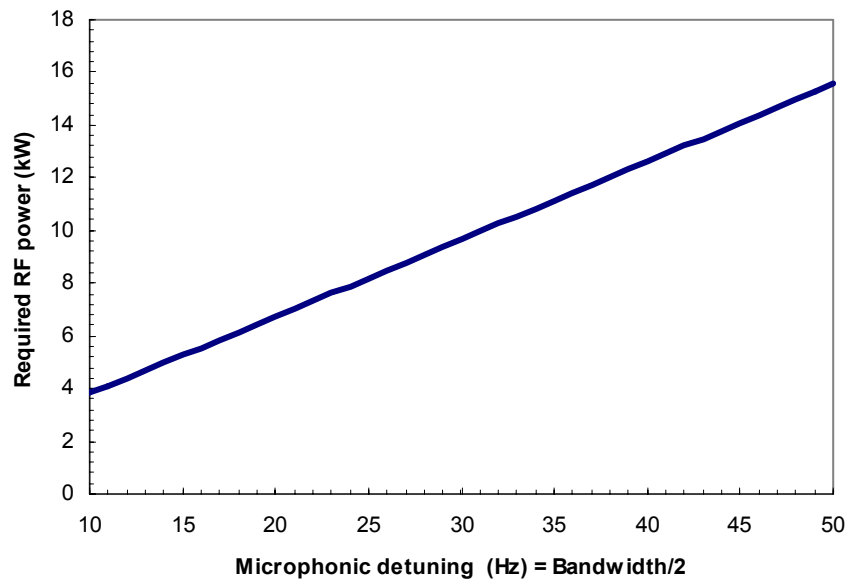


Fig. 6.21: Required RF power for cavity operation at a voltage of 20 MV as a function of microphonic detuning, assuming that the input coupling is adjusted to meet the condition in equation (6.6). The beam current is 75 μ A.

Clearly the microphonics are the dominant driving factor in dimensioning the RF system. This is in contrast with pulsed systems such as TTF and TESLA, where the beam power is two orders of magnitude greater and therefore microphonics play only a small role.

For that reason the ongoing HoBiCaT test program at BESSY [29] will focus to a large extent on

- a) Measuring the level of microphonic detuning.
- b) Determining the sources of the microphonics.
- c) Exploring passive means of mitigating the microphonics.
- d) Exploring active means of compensating the microphonics.

For d), piezo stacks integrated in the cavity tuner system may be used in conjunction with a feedback system to cancel out the detuning effect of mechanical cavity vibrations.

The TTF tuner system can be adapted to accommodate a piezo stack by substituting it for one of the links in Figure 6.8 a) [30]. Details are given in section 6.6.

Microphonic compensation using a piezo tuner has already been demonstrated to be feasible for two different cavity systems [31, 32]. Figure 6.22 depicts an example of these measurements, the reduction of the microphonics by a factor of three clearly being demonstrated. If such levels of suppression can also be achieved with the BESSY FEL cavities, the required peak RF power would be reduced to less than 5 kW and the average power to less than 3 kW. Clearly this would have a dramatic impact on the layout of the RF system.

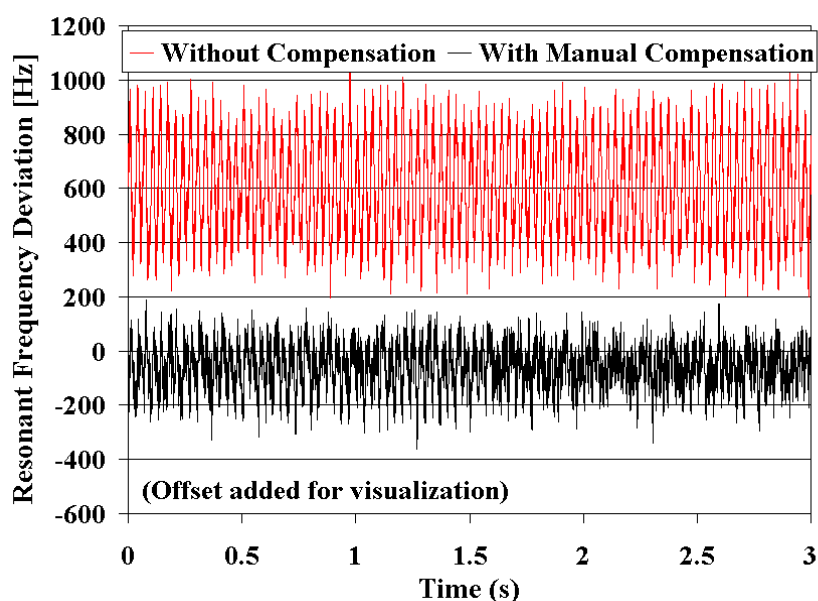


Fig. 6.22: Measured microphonics in a 3-cell, 3.9 GHz prototype at 1.8 K with and without piezo-tuner compensation of microphonic detuning. An improvement by a factor of three was recorded after the piezo compensation was engaged [32].

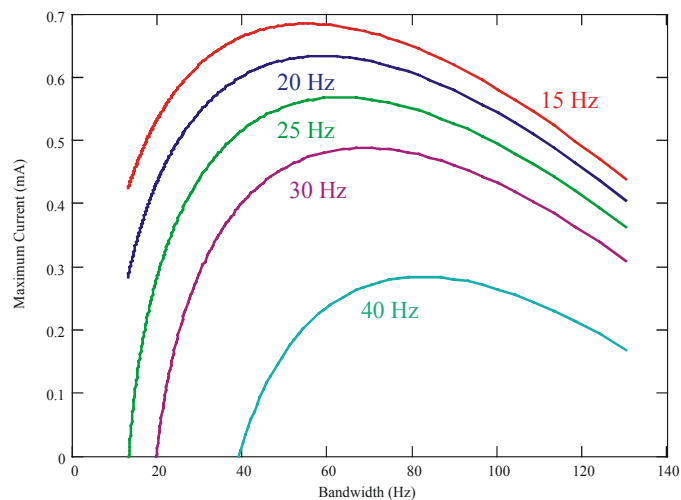
6.3.6 Beam Loading

Initially, the BESSY FEL will run with a normal-conducting RF photoinjector. Power-dissipation constraints limit operation to a repetition rate of 1 kHz. Given a bunch charge of 2.5 nC, the average current thus is 2.5 μ A. Later, an upgrade to a superconducting photoinjector is planned and significantly higher repetition rates are possible. In that case beam-dump considerations might limit the current to about 75 μ A (30 kHz at 2.5 nC) on average.

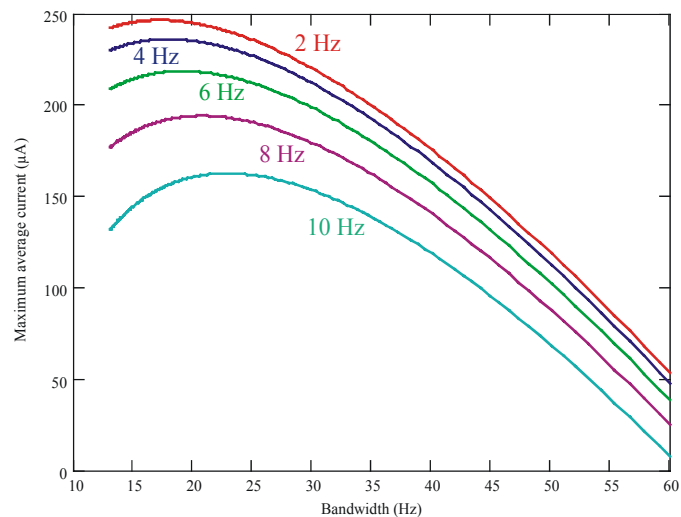
However, the user community has expressed a strong interest in operation with variable bunch spacing and bunch trains, so that high *peak* currents may be accelerated. Several factors impact how much current can be accelerated by the cavity units.

For the average current, the CW power handling capability of the input coupler is the limitation. Here one must not only include the CW beam loading but also the rms microphonic detuning, as discussed in section 6.3.5. The coupler is expected to handle at least 5 kW CW power, although the actual limit still needs to be determined in tests.

Regarding the peak loading, the coupler is not a limitation, as it is designed to handle up to 230 kW for 1.3 ms for TESLA. Rather, the available peak RF power (15 kW being planned) limits the peak current that can be accelerated. Again, not only does this power budget have to cover the peak beam loading, but also the peak microphonic detuning.



a)



b)

Fig. 6.23: a) Maximum peak current that can be accelerated given that 15 kW peak klystron power is available, for various peak values of detuning. b) Maximum average current that can be accelerated given a 5 kW CW standing-wave power limit, for various rms values of detuning. In both cases the cavity voltage is 20 MV.

Figure 6.23 depicts the maximum peak and average current that can be accelerated given the 15 kW and 5 kW power constraints, respectively. For the anticipated 40 Hz peak detuning, up to 0.3 mA peak current can be accelerated within a bunch train provided that the cavity bandwidth is 80 Hz. Given a bunch charge of 2.5 nC the bunch spacing must therefore be greater than 8.3 μ s.

However, figure 6.23 b) illustrates that the average current constrains the cavity bandwidth. Operating at an average current of 75 μ A and given rms microphonics on the order 7 Hz, the bandwidth has to be about 53 Hz or less ($Q_{\text{ext}} > 2.5 \cdot 10^7$) for the average RF power to stay below the 5-kW coupler limit. In that case the peak current that can be accelerated with 15 kW drops to about 0.19 mA with a bunch spacing of 13.2 μ s.

If the peak and rms microphonics can be decreased, the current improves dramatically. For example, a factor of 3 reduction as in figure 6.22, increases the peak current by nearly a factor of five to 0.7 mA while still being able to accelerate an average current of 76 μ A.

One should note, though, that small-gap bunch train operation as opposed to equal bunch spacing, may require the implementation of feed forward in the low-level RF control system to avoid large bunch-to-bunch energy jitter (section 6.5).

6.3.7 Higher-Order-Mode Power

A benefit of superconducting cavity technology lies in the fact that low-frequency structures with large irises can be used. As a result, the wakefield generation is reduced, thereby minimizing the power lost to monopole modes and kicks due to dipole modes. In fact, higher-order mode (HOM) excitation is not expected to be a critical issue in the BESSY FEL because both the peak and average currents (< 0.7 mA and 75 μ A, respectively) are less than those in the TESLA collider/XFEL combination (11 mA and 102.5 mA), while the bunch charge is the same. The values quoted here are from the TESLA TDR [1]. Since its publication, some parameters have changed.

The short-range monopole wakefield function for a point charge traversing a periodic array of TESLA cavities per meter has been calculated in [33]. Assuming that the bunch distribution can be approximated by a Gaussian, the monopole loss factor per cavity evaluates to

$$k_{\text{loss}} = 15.4 \frac{\text{V}}{\text{pC}} . \quad (6.7)$$

About 90% of the generated HOM power is above the cutoff frequency of the beam pipe (2.94 GHz) and is thus heavily damped by the HOM couplers and the beam-tube HOM load at the end of the cryomodule. Resonant excitation of these modes therefore does not have to be considered. In that case the expected HOM power is of order 2.4 W/cavity.

Even if a significant fraction of this HOM power is dissipated in the cavity walls, it does not represent a dramatic increase of the cryogenic load. In any case, most of this power is expected to be absorbed by the two HOM couplers, which are anticipated to be able to handle up to 10 W each. The power limit of the couplers is set by the feedthrough and cables.

The first and second monopole bands are below cutoff and resonant excitation is possible. Table 6.5 lists the modes with the highest R/Q values. In the case of the two TM_{010} modes ($7\pi/9$ and $8\pi/9$), loading is due to the input coupler. For these modes the field distribution peaks in the last cell (or is close to the maximum), so that the external coupling is at least as strong as that to the accelerating (π) mode, which is expected to be around $3 \cdot 10^7$. For the TM_{011} modes, the Q_{ext} values were measured at TTF [34]. Also listed in table 6.5 is the power dissipation in those monopole modes, given the worst-case of resonant beam excitation. Even in this case, the HOM power is negligible.

Apart from the power dissipation in monopole modes, the impact of HOM excitation on both the longitudinal and transverse beam profile (single-bunch and multi-bunch) must be investigated. This is discussed in Chapter 8.

Table 6.5: Electrical parameters of the worst HOMs in the first and second pass-band. Also listed is the power dissipation per cavity if the modes are resonantly excited [35].

Mode	Frequency (GHz)	R/Q(Ω)	Q_{ext}	P_{HOM} (W)
$TM_{010}^{(7)}$	1.2955	0.068	$3 \cdot 10^7$	0.008
$TM_{010}^{(8)}$	1.2976	0.033	$3 \cdot 10^7$	0.004
$TM_{011}^{(8)}$	2.4499	155.3	$1.3 \cdot 10^5$	0.113
$TM_{011}^{(9)}$	2.4539	148.7	$2.5 \cdot 10^5$	0.163

6.4 High-Power RF System

The RF system for the BESSY CW linac will consist of 144 individual transmitters supplying each cavity with up to 16 kW. This power level is sufficient for 20 MV/m operation given the anticipated beam loading and microphonic detuning (section 6.3.5). To account for distribution-line losses, the transmitters must provide 20 kW. The RF-system concept allows for maximum flexibility and reliability. For example, cavities that do not achieve the required gradient can be set to a lower gradient while others are run at a higher gradient so that the final beam energy is unchanged.

An alternative approach that powers eight cavities from a single transmitter has been investigated. In this case, a power divider distributes the RF power to the individual cavities. Each power line has to be equipped with a ferrite high-power device for amplitude and phase control. Issues such as cross talk, bandwidth of the ferrites and also costs, however, do not favor this solution.

The main components of the RF system are the RF-power amplifier, the DC-power supplies for the amplifier, the RF power cables, waveguides and circulator, the interlock system, and the low-level RF-control system providing the required stability. Figure 6.24 shows the schematic layout of the cryomodules in the tunnel. The transition to waveguide occurs at the circulator protecting the power tube from reflections. A waveguide 3-stub tuner between the circulator and the cavity can be used to extend the input coupling range.

6.4.1 RF-Power Tubes

Three different transmitters have been considered:

Klystron amplifier: Klystron amplifiers operate in class-A mode at a bandwidth of some MHz. However when they are modulated, their efficiency is poor. The DC power supply has to provide the maximum power at all times. A failure of a single klystron results in the switching off of the whole transmitter.

Solid-state amplifier: Solid-state amplifiers run at a low supply voltage and are class-B devices. Nevertheless their efficiency at 1.3 GHz is poor. Solid-state amplifiers use a large number of power transistors, each delivering about 100 W. In case of a failure, normally only a few transistors fail and the amplifier will still run at a reduced power level.

IOT amplifier: The Input-Output Tube (IOT, figure 6.25) is a grided tube with an output resonator. It can be operated in class-B mode and has a good efficiency. A high voltage is needed to operate the tube and a failure results in the switching off of the whole transmitter. IOTs have become the standard tube for TV transmitters and are as reliable as klystrons.

The major advantages and disadvantages of the different systems are listed in table 6.6. In case of a linac with high-Q superconducting cavities, IOT tubes are the best choice and suppliers of RF tubes are intending to build 1.3-GHz prototype IOTs in 2004. It is planned to test one of these tubes in the HoBiCat facility (section 6.6). Until then HoBiCaT will be equipped with a klystron and a solid-state amplifier. In table 6.7 the preliminary data for the IOTs are listed and contrasted with those of a klystron.

For 1.3 GHz, 20 kW operation only one klystron is currently available (CPI VKL7811). This klystron is a scaled version of the CEBAF 1.5 GHz tube.

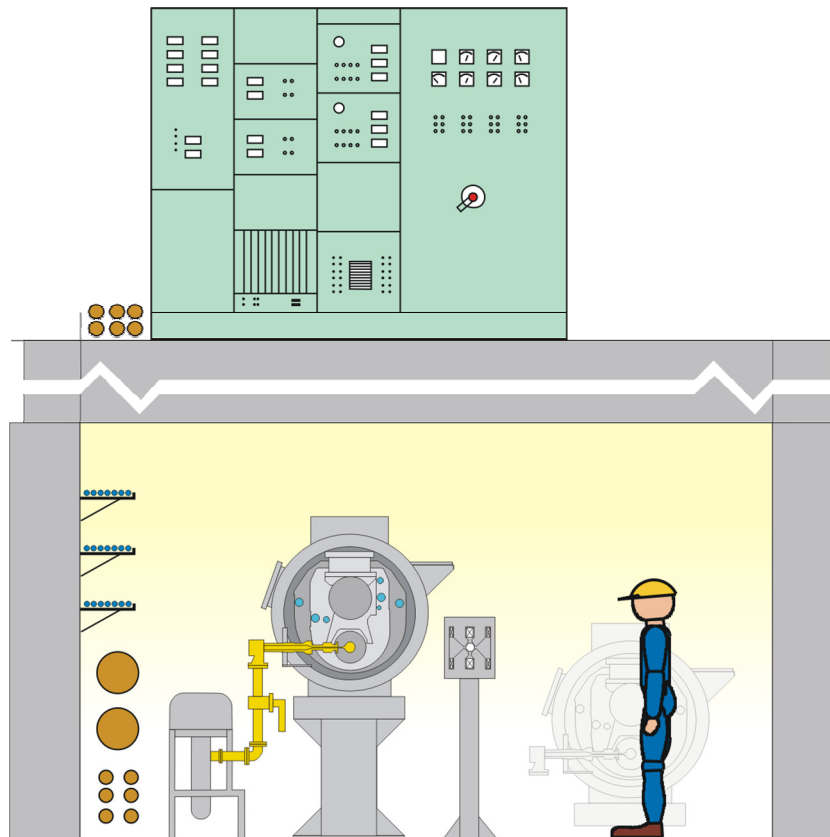


Fig. 6.24: Cross section of the linac illustrating the layout of the cryomodules in the tunnel.

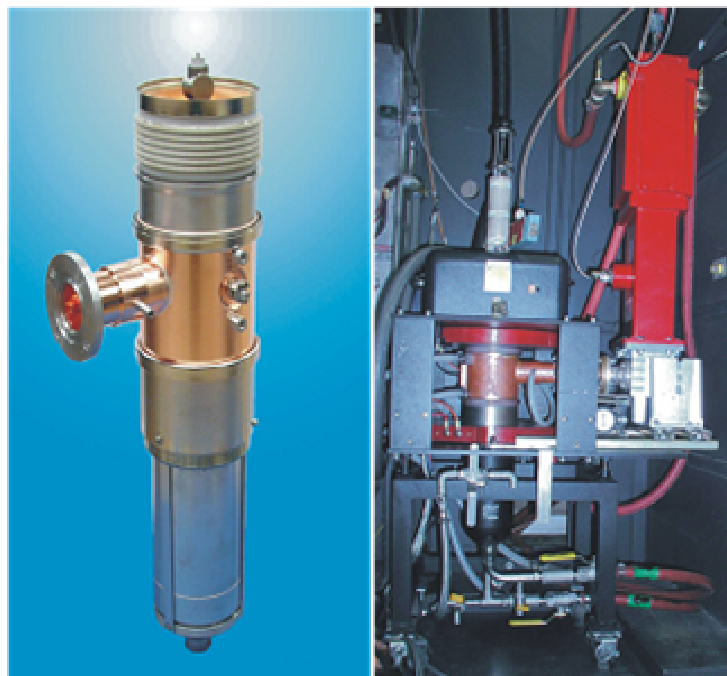
Given that the beam loading is at most 1.5 kW, one finds that the microphonics dominate the RF budget and the RF source has to cope with a varying power demand determined by the instantaneous cavity detuning. The bandwidth for the microphonics is expected to be less than 1 kHz.

Table 6.6: Advantages and disadvantages of various power amplifiers operating at 1.3 GHz.

Parameter	Klystron	IOT	Solid State
Operating mode	Class A	Class B	Class B
Efficiency at full power	50%	60%	30%
Efficiency (modulated power)	12%	60%	30%
Failure mode	Switch-off	Switch-off	Red. power
Power supply	15 kV	25 kV	33 V
Lifetime	30 000 hr	30 000 hr	Cont. decline

Table 6.7: Data of proposed IOT power tubes compared with those of a klystron.

	IOT			Klystron	Unit
	CPI (preliminary)	E2V (preliminary)	Thales (preliminary)	CPI VKL7811	
Frequency	1.3	1.3	1.3	1.3	GHz
CW power	16/26	16/20	20	12	kW
Bandwidth	6/8	4	1	3	MHz
Efficiency	62/60	60	> 60	38	%
Gain	22.5	> 20	> 19	36.5	dB
Drive power	90/145	< 200	< 200	2.7	W
Collector voltage	24/28	25	25	15.5	kV
Collector current	1.1/1.55	1.07/1.33	1.5 - 2	2.1	A
Bias voltage	-50/-58	-70 - -150	-100	N/A	V
Heater voltage	9	8 - 10	N/A	6.9	V
Heater current	8.5	8 - 10	N/A	4.25	A

**Fig. 6.25: CPI IOT prototype. Left: tube, right: test stand.**

6.4.2 RF Transmitter Power Supplies.

For operation of an IOT tube, several DC power supplies are needed. These include the main collector power supply and power supplies for the grid bias, heater, getter pump and focusing magnet (figure 6.26). Special focus is on the main collector power supply because any noise on the collector or bias power supply will cause amplitude and phase noise on the RF output signal. A switched power supply, with a noise specification of 10^{-4} peak-to-peak, has been chosen. To avoid aliasing, the internal clock of the switching devices will be synchronized with the linac repetition rate. Auxiliary power supplies are modules integrated in the main power supply and controlled via fiber optic links. The interlock connections will be done locally for each power supply. A prototype of the power supplies will be tested in the HoBiCaT facility.

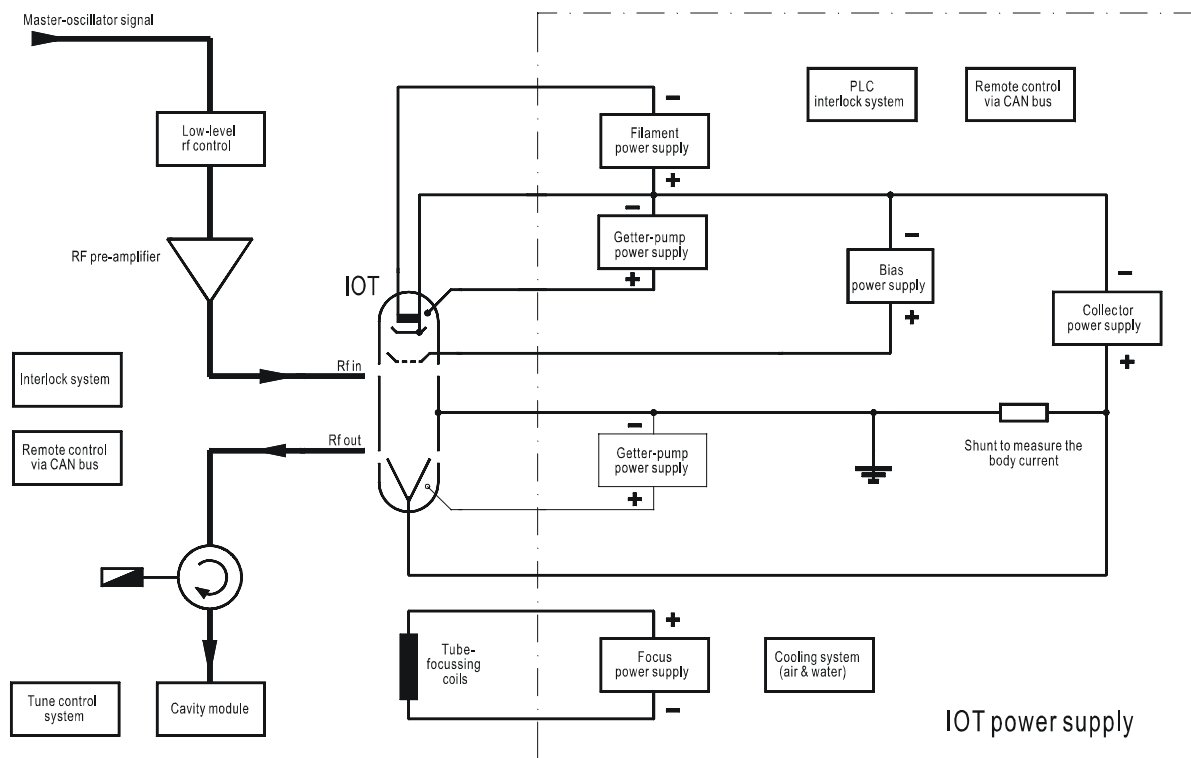


Fig. 6.26: Layout of the transmitter.

6.5 Low-Level RF Control

6.5.1 Motivation for Low-Level RF Control

RF feedback control of the cavity voltage is required to maintain a constant voltage and phase in the cavities and hence to minimize the bunch-to-bunch energy spread (jitter). This is critical for three reasons:

1. The energy jitter at the end of the linac should be less than the bandwidth of the FELs so that the FEL light output is not affected by the energy jitter.
2. Any energy jitter produced by the cavities is translated by the bunch compressors into timing jitter (and vice versa). Thus, even if the injection is perfectly synchronized with the master clock, the bunches arriving at the FELs will jitter in time.
3. In theory, the bunch compressors decrease the time jitter from the photoinjector by nearly the same factor as that for the bunch length, provided the uncorrelated energy jitter due to the cavities is small. For effective time-jitter compression the field fluctuations (amplitude and phase) must therefore be kept to a minimum.

6.5.2 Layout of the Low-Level Control System

Low-level RF control will be achieved with a combination of feedback and feedforward, supplemented by a two-component tuning system consisting of a slow mechanical tuner and a fast piezo tuner (section 6.2.3). These compensate, at least partially, for cavity detuning due to slow bath pressure variations (mechanical tuner) and fast vibrations as well as Lorentz-force detuning during cavity turn-on (piezo tuner). The remaining “noise” on the cavity voltage will be reduced by the feedback controller. Each cavity will be regulated by its own feedback loop, so that the systems can be optimized for each cavity’s performance.

Presently, the feedback system is based on a simple proportional digital controller which will be replaced by a more sophisticated algorithm once results of the studies of the cavities in the HoBiCaT test facility are available. A feed-forward system to compensate for repetitive perturbations due to, for example, beam loading may be used to further improve the cavity performance.

There are two ways to represent and measure the cavity voltage: amplitude/phase determination of the in-phase/quadrature (I/Q) components. In the early linac sections, acceleration is off-crest and a high gain is necessary to minimize the impact of microphonics on the energy jitter. In this situation, amplitude/phase control is susceptible to producing

a correction in the wrong quadrant leading to unstable performance. This problem does not exist for I/Q control, which thus has been adopted for the BESSY FEL.

Recent improvements in the digital hardware have increased the speed of digital controllers to levels competitive with analog systems and they have been adopted for a number of accelerators such as CESR-c [36], the 400-MeV proton linac of the JAERI/KEK joint project [37], APT [38] and both TTF I and II [39].

Digital systems offer a number of advantages which make them well-suited for the BESSY FEL. They include:

- Flexibility in designing complex controllers adapted to the transfer function of the system being controlled.
- Programmability to handle the control of large systems, as for example during the start-up of the linac. This is especially important for the narrow-bandwidth cavities of the BESSY FEL because little RF power is available to compensate for the large amount of Lorentz-force detuning that occurs in ramping the field from 0 to 15 MV/m.
- Implementation of adaptive feed forward and feedback via lookup tables.
- Flexibility in data analysis.
- Availability of complex filters (e.g., Kalman filters for white noise).

A digital I-Q feedback system with a latency of less than 1 μ s was recently developed at Cornell University for the proposed Energy-Recovery Linac (ERL) [36]. It will control TESLA cavities operating under conditions that are very similar to those of the BESSY FEL (little beam loading and a small bandwidth). Under a BESSY-Cornell collaboration, this system is also planned for the BESSY FEL.

The basic configuration of the system is shown in figure 6.27. A probe on the cavity beam tube provides a signal proportional to the cavity field. It is mixed with a reference signal from the master oscillator (1300 GHz + 11.9 MHz) to down-convert the probe signal to an 11.9 MHz intermediate frequency (IF). This signal carries the amplitude and phase information. A fast analog-to-digital converter (ADC) samples this signal at four times the IF frequency, whereby subsequent samples provide the I and Q components, respectively. A digital low-pass filter then removes high-frequency noise. Corrections for systematic errors can also be added computationally.

The digitized cavity voltage is compared with the set-point table to produce the error signal, which is amplified by values from the gain table (P controller) and added to values from the feed forward table. Following conversion back to an analog signal, the I and Q values control the low-level input to the klystron's pre-amplifier via a vector modulator.

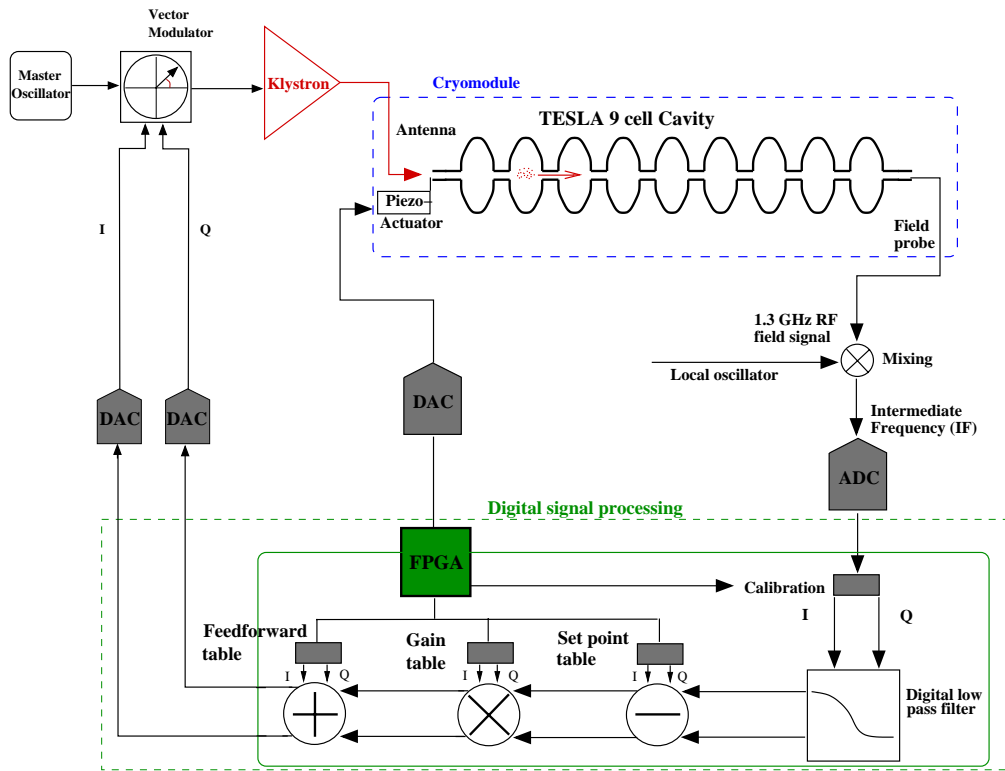


Fig. 6.27: General layout of the BESSY FEL low-level RF control system, based on the Cornell ERL design.

6.5.3 Energy- and Time-Jitter Requirements.

The bunch-to-bunch energy and timing stability (jitter) must be better than 10^{-3} and 50 fs, respectively.

Simulations of the HGHG cascades have shown that the laser power changes little if the relative energy jitter remains below 10^{-3} , the bandwidth of the final amplifier. Two different constraints potentially impact the timing-stability requirement. First, the seed laser for the HGHG scheme must overlap the bunch in a manner that leaves a sufficiently long part of the bunch untouched for fresh-bunch operation in subsequent sections of the FEL. The more stages used in the HGHG scheme, the smaller the required time jitter. Second, the energy of the individual bunches is chirped. Hence any timing jitter will shift the central energy of the fresh-bunch slices used in the HGHG scheme. The jitter must be small enough so that the shifted energy remains within the bandwidth of the undulator. The larger the chirp, the more tightly the jitter must be constrained.

6.5.4 Error Sources

Numerous “noise” sources impact the voltage regulation. The following are among the most common:

Microphonics: Microphonic detuning shifts the resonant frequency and thus changes both the voltage amplitude and phase. Due to the narrow bandwidth of the BESSY-FEL cavities this effect is large even for a detuning of only a few Hz (see section 6.3.5 for details).

Lorentz-force detuning: The radiation pressure of the stored energy deforms the cavity and hence also changes its frequency, similar to the microphonics. This effect increases quadratically with voltage and complicates matters, especially for pulsed operation as with TESLA. But even for CW operation voltage fluctuations can excite mechanical oscillations, thereby increasing the energy jitter.

Beam loading: Varying beam-loading conditions change the voltage amplitude and, if acceleration is off-crest, phase. This includes injection timing jitter and charge jitter. If an irregular bunch pattern is injected intentionally, a feed forward system can be used to compensate for this.

Measurement noise: Noise on the pickup signal, which is used to generate the error signal for feedback, is amplified by the gain and acts back on the cavity voltage.

Klystron noise/non-linearity: Noise in the high-voltage supply of the klystron changes both gain and phase of the klystron and thus that of the feedback loop. Nonlinearities in the klystron gain result in a power-dependent feedback gain which, in turn, affects the steady-state cavity voltage.

Feedback noise: Noise within the feedback controller (such as conversion noise in a digital system or amplifier noise) is added to the measurement noise and is also amplified.

How much each of these noise sources affect the total bunch-to-bunch energy distribution depends on whether these errors are correlated or uncorrelated from cavity to cavity. Uncorrelated errors are less critical since they are reduced by a factor of \sqrt{N} , N being the number of cavities used for acceleration.

Obvious correlated noise sources are the beam loading, master-clock jitter and klystron-gain non-linearities. In other cases it is not clear whether a noise source is correlated or not. An important example is the microphonic detuning. All cavities are connected to the same helium plant and slow helium pressure fluctuations will affect each by approximately the same amount. These will be tuned out by the mechanical tuner. But other, higher-frequency vibrations, such as from turbo pumps will only impact nearby cavities so it is likely that the dominant microphonics will be largely uncorrelated.

6.5.5 RF Control Simulations

To better understand the expected performance of the BESSY FEL, simulations of digital RF control were performed. For such simulations the cavity voltage is evolved in time in the presence of beam loading, microphonics and the other noise terms in section 6.5.4. Feedback is applied by a proportional controller, sampling the I and Q components of the cavity field at 1 MHz and filtering them with a first-order, 50-kHz, low-pass filter. The model for this system is described in detail in [40]. A second-order model of the cavity's mechanical modes is used to simulate dynamic Lorentz-force detuning [41], whereby ten modes, as given in [30], are included.

These simulations are repeated for all 144 cavities, and the beam is tracked from one cavity to the next. Included in the calculations are the bunch compressors, the arc, and third harmonic cavities so that the time-jitter compression can be estimated.

6.5.5.1 Choice of Gain

An analysis of the stability limit for the controller was done in [27]. The TESLA system becomes unstable at a gain of 210, given a cavity bandwidth of 430 Hz, a sampling frequency of 1 MHz, and a latency of 5 samples (no filter). If a 110 kHz filter is used, the critical gain drops to 190. The instability onset at these values was also confirmed with the simulation program.

For the BESSY FEL, the cavity bandwidth will be approximately 10 times smaller. Since the magnitude of the cavity transfer function scales inversely with frequency at high frequencies, it drops by 20 dB per decade. Thus the critical gain should increase by approximately a factor of 10 to 2000 (66 dB), although a 50 kHz filter reduces this to about 1745. Even higher gains are possible because present-day digital feedback systems based on field-programmable gated arrays (FPGAs) achieve a latency of less than 1 μ s [36].

Noise on the pickup signal will, though, limit the usable gain. The output noise of the klystron power is given by twice the gain times the relative measurement noise (σ_v/V). A gain equal to $V/2\sigma_v$ will produce about 100% noise at the klystron output. For a noise level of 0.05% a gain limit of 1000 thus applies, especially if the klystron is operated close to saturation.

6.5.5.2 Simulation Results

Figures 6.28 and 6.29 depict an example of the simulations. Shown in figure 6.28 are a) the amplitude and b) phase for one of the 144 cavities versus time, given the beam loading and microphonic detuning in c) and d), respectively. Other noise terms such as measurement noise and klystron noise were also included in these simulations.

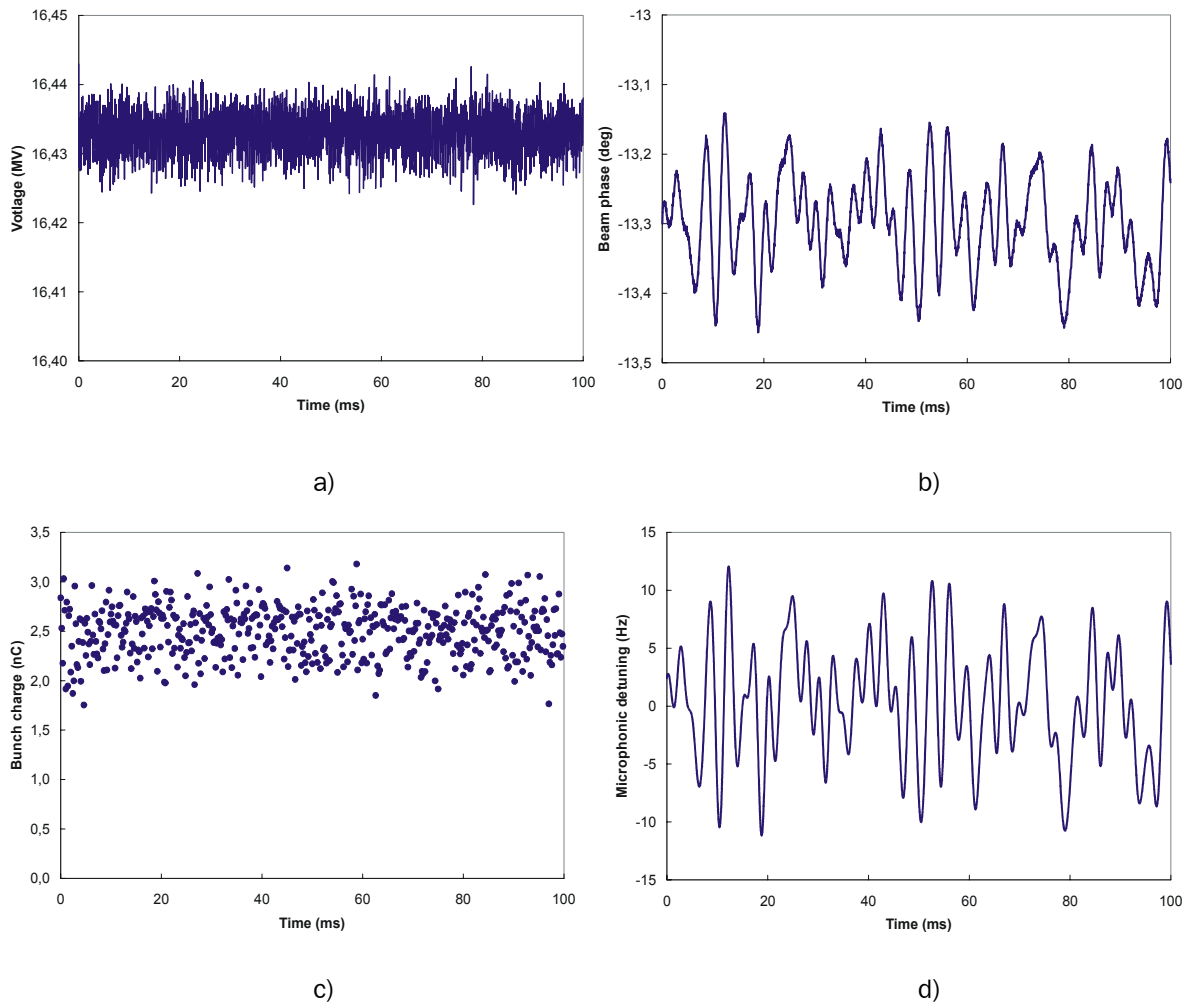


Fig. 6.28: a) Amplitude and b) phase of the cavity voltage, given a bunch-charge jitter as shown in c) and microphonic detuning as in d). A number of other noise source, not shown, were also included in the simulation. For clarity, not all bunches used in the simulation are shown in c).

Shown in Figure 6.29 is the energy-time distribution of the bunches before and after the two bunch compressors, at the extraction point for the low-energy FEL and at the end of the linac. The energy and time jitter at the linac exit was $1.3 \cdot 10^{-4}$ and 42 fs, respectively, better than the requirements discussed earlier.

The correlated energy jitter results from the fact that the injection-time jitter (500 fs rms in this case) is translated into an energy jitter by the off-crest acceleration in the first six modules. The uncorrelated energy spread results from the imperfect control of the RF

voltage and limits the amount of jitter compression in the bunch compressors. This is clearly visible after the second bunch compressor, where the bunch length is reduced from 152 fs to 42 fs. In this case, the final bunch length is determined almost entirely by the uncorrelated energy jitter prior to the compression. In fact, the bunch-length compression ratio for all the dispersive sections in the linac is about 30, but the time jitter is only reduced by a factor of 12.

This illustrates that good RF control is especially critical in the early modules, prior to the dispersive sections. Here acceleration is off-crest and microphonics dominate the energy jitter and a large gain must be used to minimize their impact. This, however, is only possible if the measurement noise is small as this is amplified by the gain. In this particular simulation the gain in the first six modules was 200.

Also visible in figure 6.29 is the damping of the relative energy jitter as the beam energy increases. For this simulation, the microphonics were taken to be largely uncorrelated from cavity to cavity. If this is not the case, the damping is much less pronounced and a large energy jitter results.

Measurement data of the various noise sources are still lacking and a number of assumptions must be made for the simulation parameters. Table 6.8 summarizes some results for various input parameters.

Microphonics dominate the performance and a high gain should be used in the early linac sections where acceleration is off-crest. The measurements of the detuning in a TTF module in [27] yield an average value of 4.3 Hz (rms) for all cavities. For the simulations this value was increased to 5 Hz. Injection and charge jitter are determined by the laser for the RF injector. For the simulations very conservative values of 250 – 500 fs and 5 – 10 % were used for the time and charge jitter, respectively. As is discussed below, even in that case the energy and time jitter requirements at the FELs are satisfied.

Assuming, as in case A, little noise and injection jitter as well as high-gain operation (60 dB), the jitter at the undulators will be reduced to 26 fs with an energy jitter of order $6 \cdot 10^{-5}$ ($1.4 \cdot 10^{-4}$ at the low-energy FEL) which is significantly better than the requirements discussed earlier.

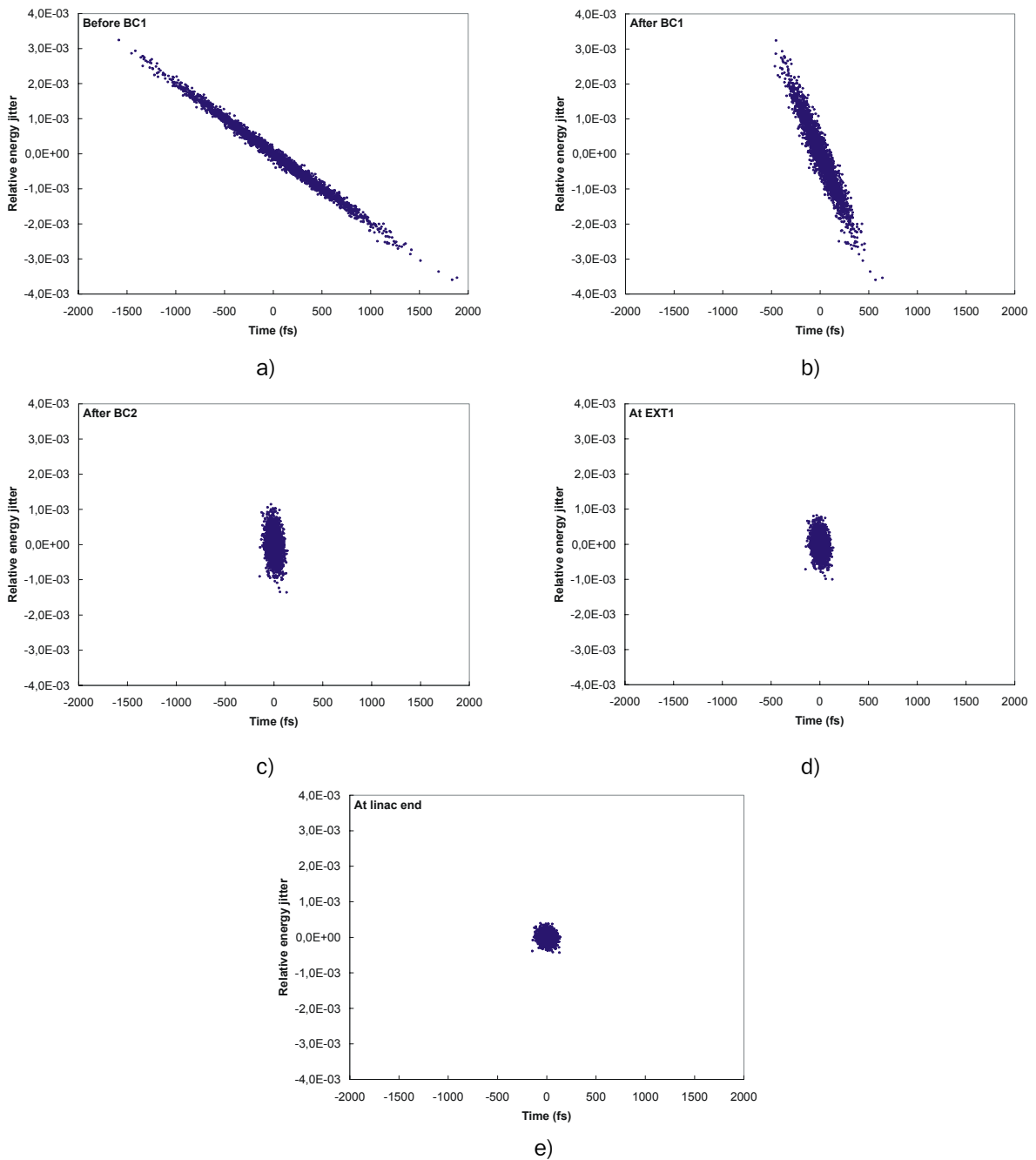


Fig. 6.29: Distribution of the relative bunch energy (σ_E/E) versus time a) before BC1 and b) immediately after BC1 illustrating the jitter compression, c) after a further jitter compression in BC2 and the arc, d) at the extraction for the low-energy FEL and e) at the end of the linac. The initial injection jitter was 500 fs rms. This was reduced to 152 fs after the first bunch compressor, and further to 42 fs by the arc and second compressor.

Table 6.8: Energy- and time-jitter simulation results for various input parameters. Note that the energy jitter includes correlated jitter due to the off-crest acceleration in the early linac sections.

A. Measurement noise = 0.05% Injection jitter = 250 fs			
Charge jitter = 5%		Microphonics 5 Hz (rms, uncorr.)	
Position	σ_t (fs)	σ_E/E	Gain in prec. section
Entrance L1	250	$5.5 \cdot 10^{-4}$	1000
After BC1	80	$5.2 \cdot 10^{-4}$	1000
After arc + BC2	21	$1.9 \cdot 10^{-4}$	500
EXT1	21	$1.4 \cdot 10^{-4}$	100
End	21	$6.5 \cdot 10^{-5}$	100
B. Measurement noise = 0.1% Injection jitter = 500 fs			
Charge jitter = 10%		Microphonics 5 Hz (rms, uncorr.)	
Position	σ_t (fs)	σ_E/E	Gain in prec. section
Entrance L1	500	$1.1 \cdot 10^{-3}$	200
After BC1	152	$1.0 \cdot 10^{-3}$	200
After arc + BC2	42	$3.7 \cdot 10^{-4}$	200
EXT1	42	$2.7 \cdot 10^{-4}$	100
End	42	$1.3 \cdot 10^{-4}$	100
C. Measurement noise = 0.1% Injection jitter = 500 fs			
Charge jitter = 10%		Microphonics 5 Hz (rms, corr.)	
Position	σ_t (fs)	σ_E/E	Gain in prec. section
Entrance L1	500	$1.1 \cdot 10^{-3}$	200
After BC1	180	$1.0 \cdot 10^{-3}$	200
After arc + BC2	146	$3.8 \cdot 10^{-4}$	200
EXT1	146	$2.8 \cdot 10^{-4}$	100
End	146	$1.3 \cdot 10^{-4}$	100
D. Measurement noise = 0.1% Injection jitter = 500 fs			
Charge jitter = 10%		Microphonics 1.7 Hz (rms, corr.)	
Position	σ_t (fs)	σ_E/E	Gain in prec. section
Entrance L1	500	$1.1 \cdot 10^{-3}$	200
After BC1	157	$1.0 \cdot 10^{-4}$	200
After arc + BC2	49	$3.8 \cdot 10^{-4}$	200
EXT1	49	$2.8 \cdot 10^{-4}$	100
End	49	$1.3 \cdot 10^{-4}$	100

Even for very conservative values (case B), where only a maximum gain of 200 (46 dB) is used, and the injection jitter is increased to 500 fs, the requirements are satisfied as the final energy and time jitter are $1.3 \cdot 10^{-4}$ and 42 fs, respectively.

In fact, the magnitude of the injection jitter has fairly little bearing on the timing jitter at the end of the linac. Simulations for case B were repeated with the injection jitter halved and although the jitter after BC1 was nearly halved, the final jitter (after the arc and BC2) was essentially unchanged. Thus, the time jitter of the photoinjector laser is not critical, rather it is important that the microphonics and other noise terms are reduced for effective beam time-jitter control.

However, it is important that the microphonics are uncorrelated. It is very unlikely that the microphonics of all cavities in the linac are the same because many source terms (such as pumps) will only act locally on the cavities. This statement is supported by the measurements in [27], where even for cavities within a single module the microphonic excitation varied dramatically. Should the microphonics, nevertheless, be correlated in the BESSY FEL, then the time jitter is expected to increase to 146 fs (case C), thereby exceeding the timing requirements. In this case noise-suppression measures, as discussed below, will need to be implemented.

6.5.6 Piezo Compensation

The possibility of using piezo stacks with feedback to actively compensate for microphonic detuning was already discussed in section 6.3.5. Due to the narrow bandwidth of the cavities, any reduction of the microphonics results in a significant RF power savings (installed and operating). Their reduction has the added benefit that the uncorrelated energy jitter of the beam, and hence the time-jitter compression, is also improved.

The operation of a piezo feedback loop has also been integrated in the simulation program. However, its performance depends critically on the transfer function of the piezo tuner/cavity system and the location of the mechanical resonances. These parameters must still be determined experimentally in the HoBiCaT test program before an appropriate controller can be designed, so that simulations including the piezo system have not yet been performed.

Assuming that a factor of three reduction of the microphonics can be achieved, as in figure 6.22, then Case D represents a worst-case situation where the microphonics are correlated in all cavities. In this case the jitter requirements are again satisfied.

6.6 HoBiCaT—a Test Facility for Superconducting Cavities

The development of the TESLA technology has been aimed at high-power pulsed operation. Although, in general, this technology is also well suited for low-power CW operation, a number of issues, as discussed in the previous sections, need to be addressed. These include:

1. CW measurement of the Q of a complete cavity unit (including all ancillary devices) as a function of voltage and temperature to optimize the bath temperature.
2. Improvements of the cavity quality—for example by improving the magnetic shielding to reduce the dynamic losses.
3. Determination of the CW power limit of the (cold) TTF III input coupler under standing-wave conditions.
4. The gain limit for feedback voltage control and the attainable cavity-voltage stability, in the presence of microphonics and other noise sources must be measured.
5. Reduction of microphonic detuning by passive means.
6. Characterization of the TTF and blade tuners. Integration of piezo elements and their use to actively damp the microphonic detuning.
7. Steady CW cryogenic operation and attainable pressure stability with dynamic cavity losses of up to 40 W per cavity.

Based on theoretical analyses, a number of modifications of the TESLA technology necessary for CW operation have already been identified (e.g., the size of the two-phase line). However, measurements that complement these studies are also needed to confirm the conclusions.

To this end, BESSY constructed a horizontal test facility name HoBiCaT (**H**orizontal **Bi**-Cavity Test facility). Details are given in [29]. HoBiCaT's purpose is to permit rapid-turnaround testing of TESLA equipment in a two-cavity “module” under conditions that are close to that of the BESSY FEL.

The HoBiCaT system includes a cryostat, feedbox, helium refrigeration plant, RF power supply and two TESLA cavities as well as associated ancillary equipment (input coupler, tuner, HOM loads). The main system parameters are summarized in Table 6.9.

Table 6.9: Parameters for the HoBiCaT test facility.

Parameter	Value	Unit
<i>Mechanical</i>		
Interior length	3.5	m
Interior diameter	1.1	m
Number of cavities	Two 9-cell cavities	
<i>Main cryogenics</i>		
Temperature	1.5-2.2 , 4.5	K
Capacity at 1.8 K	80	W
Pressure stability	± 0.1	mbar
Static losses at 1.8 K	3	W
<i>Secondary loops</i>		
Table cooling	4.5	K
Cavity fill	4.5	K
Coupler cooling	4.5-20	K
Radiation shield	77	K
<i>RF power</i>		
Frequency	1.3	GHz
Power	10	kW

6.6.1 HoBiCaT Cryostat and Refrigeration

6.6.1.1 Cryostat

Shown in figure 6.30 are the cryostat and feedbox. The horizontal vacuum tank has interior dimensions of 1.1 m (dia.) and 3.5 m (length). These are sufficient to accommodate 2 complete TESLA 9-cell cavities with RF couplers, tuners, and helium tanks. The cavity units slide into HoBiCaT on a rolling table. Power couplers penetrate the vacuum vessel via two of the four large feedthroughs on the side, their arrangement being the same as on TESLA modules. Numerous diagnostic ports are provided for additional instrumentation. Doors at either end allow for quick access to the unit so that rapid testing is possible.

The feedbox sits on the main vessel. It receives 4.5 K liquid helium (LHe) from the BESSY cryoplant and supplies the cavities with 1.8 – 2.2 K or 4.5 K LHe. The layout of the cavity helium supply was designed to be the same as in the modules for the BESSY FEL.

Thus helium is expanded into a two-phase line (dia. 94 mm) which feeds both cavities via chimneys to the helium tanks. A reservoir with heater and level meter at the end of the two-phase line is used for level control and to balance the dynamic heat load of the cavities.

HoBiCaT is designed to handle a heat load up to 80 W at 1.8 K, or 40 W per cavity—the absolute maximum expected in BESSY FEL modules. Pressure regulation is possible in the temperature range 1.5 - 2.2 K with a pressure stability of ± 0.1 mbar. Thus Q_0 measurements as a function of temperature are possible. Additional cryogenic loops cool the coupler (4.5 - 20 K), the support table (4.5 K) and the radiation shield (77 K). Another 4.5 K line is used to fill the cavities during cooldown.



Fig. 6.30: Cryostat and feedbox for the HoBiCaT test facility.

6.6.1.2 Refrigeration

A medium-size cryogenic plant has been installed to supply liquid Helium (LHe) to a number of superconducting devices in the BESSY II storage ring. This plant will also supply HoBiCaT. Figure 6.31 depicts the layout of the system, the main parameters being listed in table 6.10.

A standard Linde TCF-50 helium liquefier supplies LHe at a rate of 85 l/h (180 l/h with LN₂ precooling), using a 220 kW frequency controlled helium compressor. Liquid helium is stored in a 2000 l dewar, and gas is stored at a maximum pressure of 12 bar in a 74 m³ gas tank. A 13000 l dewar provides storage for liquid nitrogen. Figure 6.32 shows a photo of the cold box and dewar after installation in autumn 2003. Liquid helium is distributed in flexible vacuum-shielded cryogenic lines, with additional LN₂ shielding provided for the line to HoBiCaT. The 14 mbar HoBiCaT return gas is warmed to room temperature and pumped by two sets vacuum pumps with a total pumping speed of 6400 m³/hr. A bypass, combined with pump-frequency control, provides the required ± 0.1 mbar pressure stability.

Table 6.10: Main parameters of the BESSY cryoplant.

Parameter	Unit	
Refrigerator	TCF-50	
LHe temperature	4.4	K
Liquefaction rate without LN ₂ precooling	85	l/h
Liquefaction rate with LN ₂ precooling	180	l/h
He-gas storage	74	m ³
LHe storage	2000	l
N ₂ liquid storage	13000	l
Mains power of compressor	220	kW
Vacuum pumps suction pressure	14	mbar
Vacuum pumps, speed	6400	m ³ /hr

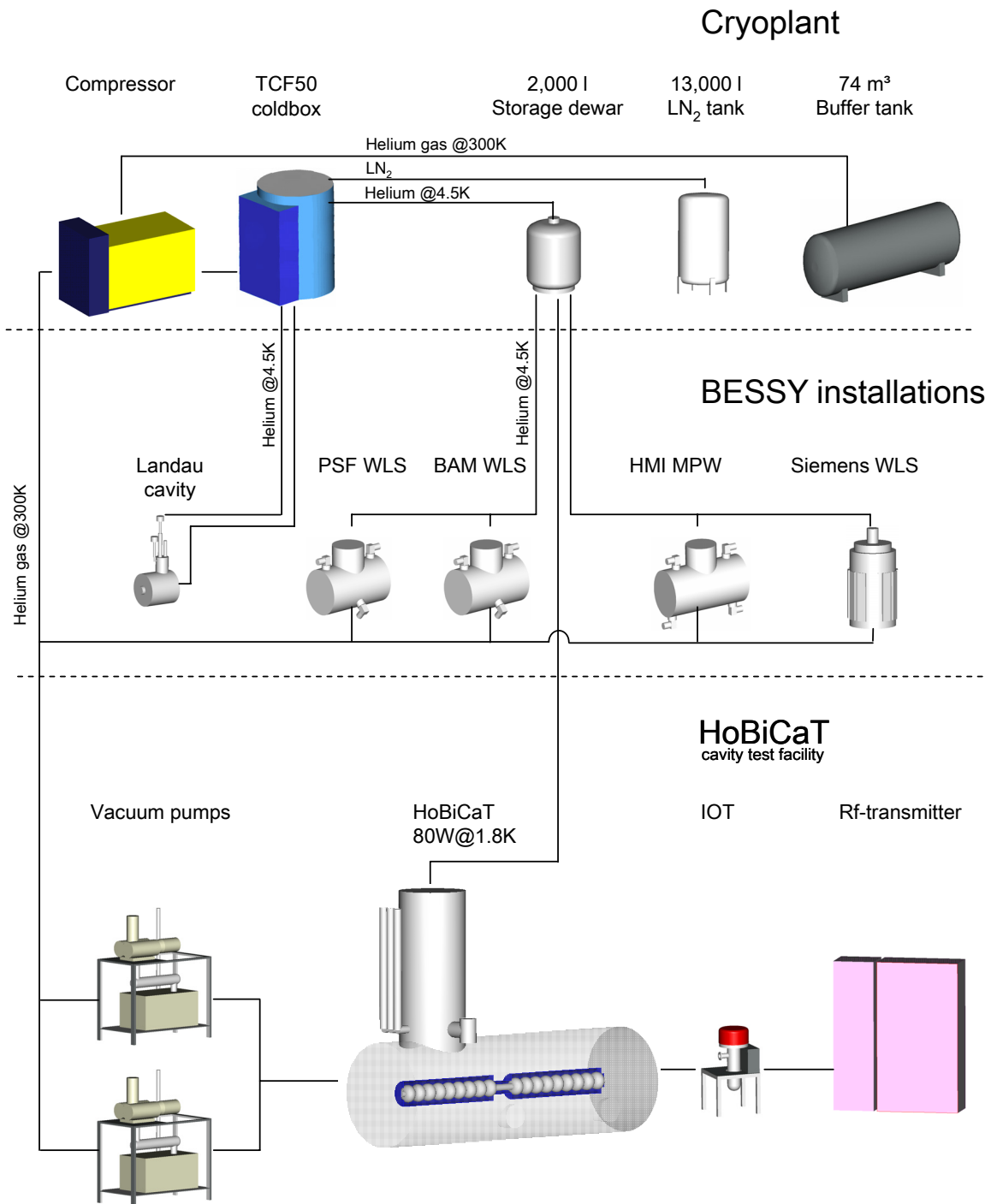


Fig. 6.31: Schematics of the cryogenic plant for HoBiCaT and the supply of superconducting devices in the BESSY II storage ring.



Fig. 6.32: TCF-50 cold box and 2000 l LHe dewar installed at BESSY in autumn 2003.

6.6.2 RF Transmitter for HoBiCaT

A prototype of the linac RF transmitter will be installed at HoBiCaT. This includes a 3" coaxial cable, the circulator, and the 3-stub tuner to be used in the final configuration. Initially, a 12 kW CPI klystron will provide the RF power. It will be replaced by an IOT as soon as 1.3 GHz tubes become available, the transmitter being designed to accommodate such a tube if minor modifications are made. An additional 1 kW solid-state amplifier is available for cavity-Q measurements with a phase-locked loop and weak input coupling.

6.6.3 HoBiCaT Cavity Units

Two complete cavity units have been produced for tests in HoBiCaT. Each unit includes

- A TESLA 9-cell cavity,

- A helium tank,
- A TTF III input coupler,
- A tuner (TTF-style or blade tuner).

The TTF III coupler was modified slightly to enhance its coupling range, thereby spanning Q_{ext} values from $2 \cdot 10^6$ - $2 \cdot 10^8$. An additional 3-stub tuner in the waveguide feed permits that range to be extended further into the 10^9 range [42] so that accurate Q measurements by power decay curves are possible with the 1 kW amplifier. These results are also used to calibrate alternative Q measurements via helium boil-off, which are used whenever the cavity is greatly overcoupled.

Two different tuner systems are being investigated; the traditional TTF-style system that mounts at the end of the helium tank, and the blade tuner [13] which mounts coaxially in the middle of the helium tank (figure 6.8). Their impact on the mechanical properties of the cavity units, in particular the frequency spectrum of mechanical modes, is being investigated to identify the system that will minimize the coupling of microphonics to the cavity resonance. Furthermore, the integration of piezo stacks in the tuners for fast tuning is progressing. Of particular importance is the measurement of the transfer function (piezo-actuation voltage to cavity detuning), which will allow the design of a suitable feedback controller to actively suppress microphonics.

References

- [1] R. Brinkmann, K. Flöttmann, J. Roßbach, P. Schmüser, N. Walker, H. Weise, (editors), TESLA Technical Design Report, Part II - The Accelerator, DESY-2001-011 (2001).
- [2] D. A. Edwards (editor), TESLA Test Facility Linac Design Report, TESLA Collaboration Report, TESLA-1995-01 (1995).
- [3] B. Aune, R. Bandelmann, D. Bloess, B. Bonin, A. Bosotti, M. Champion, C. Crawford, G. Deppe, B. Dwersteg, D. A. Edwards, H. T. Edwards, M. Ferrario, M. Fouaidy, P.-D. Gall, A. Gamp, A. Gössel, J. Graber, D. Hubert, M. Hüning, M. Juillard, T. Junquera, H. Kaiser, G. Kreps, M. Kuchnir, R. Lange, M. Leenen, M. Liepe, L. Lilje, A. Matheisen, W.-D. Möller, A. Mosnier, H. Padamsee, C. Pagani, M. Pekeler, H.-B. Peters, O. Peters, D. Proch, K. Rehlich, D. Reschke, H. Safa, T. Schilcher, P. Schmüser, J. Sekutowicz, S. Simrock, W. Singer, M. Tigner, D. Trines, K. Twarowski, G. Weichert, J. Weisend, J. Wojtkiewicz, S. Wolff, K. Zapfe, *Phys. Rev. ST Accel. Beams* **3** (2000) 092001.
- [4] J. G. Weisend, C. Pagani, R. Bandelmann, D. Barni, A. Bosotti, G. Grygiel, R. Lange, P. Pierini, B. Petersen, D. Sellmann, S. Wolff, *Adv. Cryog. Eng.* **45A** (2000) 825.
- [5] C. Pagani, D. Barni, M. Bonezzi, J. G. Weisend, *Adv. Cryog. Eng.* **45A** (2000) 939.
- [6] C. Pagani, D. Barni, M. Bonezzi, P. Pierini, R. Bandelmann, G. Grygiel, K. Jensch, R. Lange, A. Matheisen, W.-D. Möller, H. Peters, B. Petersen, J. Sekutowicz, D. Sellmann, S. Wolff, K. Zapfe, TESLA Report DESY-TESLA-2001-36 (2001).
- [7] S. Wolff, H. Lierl, B. Petersen, H. Quack, TESLA Report DESY-TESLA-2001-37 (2001).
- [8] W.-D. Möller for the TESLA Collaboration, *Proc. 9th Workshop on RF Superconductivity* (1999) 53.
- [9] C. Crawford, J. Graber, T. Hays, J. Kirchgessner, A. Matheissen, W.-D. Möller, H. Padamsee, M. Pekeler, P. Schmüser, M. Tigner, *Part. Accel.* **49** (1995) 1.
- [10] B. Dwersteg, D. Kostin, M. Layalan, C. Martens, W.-D. Möller, *Proc. of the 10th Workshop on RF Superconductivity* (2001).
- [11] D. Kostin, DESY, private communication.
- [12] S. Belomestnykh, Cornell University, private communication.
- [13] D. Barni, A. Bosotti, C. Pagani, R. Lange, H.-B. Peters, *Proc. of the 8th EPAC* (2002) 2205.

- [14] L. Lilje for the TESLA Collaboration, *Proc. of the 10th Workshop on RF Superconductivity* (2001) 287.
- [15] W.-D. Möller for the TESLA Collaboration, *Proc. of the 10th Workshop on RF Superconductivity* (2001) 212.
- [16] P. Kneisel, *Proc. of the 1980 Workshop on RF Superconductivity* (1980) 27, also published as internal Kernforschungszentrum Karlsruhe Report KFK-3019.
- [17] P. Kneisel, B. Lewis, L. Turlington, *Proc. 6th Workshop on RF Superconductivity* (1993) 628.
- [18] J. Knobloch, *AIP Conf. Proc.* **671**/1 (2003) 133.
- [19] H. Padamsee, J. Knobloch, T. Hays, *RF Superconductivity for Accelerators*, Wiley and Sons, New York (1998).
- [20] V. Arp, *Cryogenics* **10** (1970) 96.
- [21] T. Peterson, TESLA Technical Report 1994-18 (1994).
- [22] Y. Xiang, J. W. II, M. Smith, B. Petersen, D. Sellmann, H. Lierl, S. van Sciver, S. Wolff, *Cryogenics* **42**/11 (2002) 719.
- [23] Y. Xiang, N. Filina, S. W. van Sciver, J. Weisend II, S. Wolff, *Advances in Cryogenic Engineering* **45** (2000) 1001.
- [24] B. Rousset, L. Grimaud, A. Gauthier, *Cryogenics* **37**/11 (1997) 733.
- [25] Y. Taitel, *Encyclopedia of Fluid Mechanics* **3** (1986) 403.
- [26] A. Büchner, F. Gabriel, E. Grosse, P. Michel, W. Seidel, J. Voigtländer and the Elbecrew, *Proc. of the 7th EPAC* (2000) 732.
- [27] T. Schilcher, PhD thesis, Universität Hamburg, DESY Report TESLA 98-20 (1998).
- [28] J. Delayen, L. Harwood, *Proc. of the 2003 PAC* (2003) 992.
- [29] J. Knobloch, W. Anders, D. Pflückhahn, M. Schuster, *Proc. 11th Workshop on RF Superconductivity* (2003).
- [30] L. Lilje, S. Simrock, D. Kostin, *Proc. of the 8th EPAC* (2002) 2256.
- [31] S. Simrock, G. Petrosian, A. Facco, V. Zviagintsev, S. Andreoli, R. Paparella, *Proc. of the 2003 PAC* (2003) 470.
- [32] R. Carcagno, L. Bellantoni, T. Berenc, H. Edwards, D. Orris, A. Rowe, FERMILAB-CONF-03-315-E (2003).
- [33] A. Novokhatski, M. Timm, T. Weiland, TESLA Technical Report TESLA 1999-16 (1999).

- [34] G. Devanz, M. Jablonka, C. Magne, O. Napoly, M. Huening, M. Wendt, *Proc. of the 8th EPAC* (2002) 230.
- [35] R. Wanzenberg, TESLA Technical Report TESLA 2001-33 (2001).
- [36] M. Liepe, S. Belomestnykh, J. Dobbins, R. Kaplan, C. Strohman, *Proc. of the 2003 PAC* (2003) 3347.
- [37] S. Michizono, S. Anami, M. Kawamura, S. Yamaguchi, T. Kobayashi, *Proc. of the LINAC 2002 Conf.* (2002) 185.
- [38] Y. Wang, A. Regan, S. Kwon, C. Ziomek, *Proc. of the 1999 PAC* (1999) 1070.
- [39] S. Simrock, *Proc. of the 2001 PAC* (2001) 473.
- [40] M. Liepe, PhD thesis, Universität Hamburg (1998).
- [41] G. Devanz, M. Luong, A. Mosnier, *Proc. of the 8th EPAC* (2002) 2220.
- [42] M. Hüning, PhD thesis, RWTH Aachen PITHA 98/8 (1998).

7 Bunch Compression

To operate free electron lasers, high brilliance electron beams are required with an extremely high peak current, e.g. high electron density with a low transverse emittance and a small energy spread. The requirements on the electron beam increase with increasing FEL photon output energy. The FEL projects proposed, working in the VUV and X-ray spectral range, set highest demands on the electron beam quality. Present day electron source technology is able to deliver these high brilliance beams which are reduced further in emittance by adiabatic damping while being accelerated to sufficiently high electron energies. The required peak currents are achieved by reducing the bunch length in several magnetic chicanes called bunch compressors. Thus, there is a clear way to realize FELs at photon wavelengths of nm and even to the Å regime.

7.1 Principle of Bunch Compression

According to Liouville's theorem on conservation of phase space volume, a reduction of bunch length is feasible but only with a corresponding increase either in transverse emittance or energy spread. For short wavelength FELs the transverse emittance is a sensitive parameter that should be as small as possible to avoid performance loss in the FEL output. Energy spread is the remaining phase space dimension that potentially has to compensate for bunch length reduction. Redistribution of longitudinal phase space is done in two steps:

- **Redistributing the longitudinal phase space** by off-crest RF acceleration of the electron bunch, resulting in an energy modulation respectively. This process, called chirping, correlates the energy distribution dE_c/E_0 of the electrons with their longitudinal position z inside the bunch. In linear approximation the chirped energy distribution can be written as

$$dE_c(z) = e \cdot dV_{rf} / dz \cdot z, \quad (7.1)$$

with dV_{rf}/dz as the gradient of the local acceleration field the electrons experience in the center of the bunch.

- **Redistributing the longitudinal bunch density** by passing a non-isochronous section, making use of the different path lengths of electrons depending on their energy. The path length deviation dL can be expressed in linear approximation by

$dL = R_{56} \cdot dE_c / E$, where $R_{56} = \int \eta(s)/\rho ds$ is the first order momentum compaction factor depending on the bending radius ρ of the dipole magnets and the (first order) dispersion function η . With a negative momentum compaction in a conventional chicane $R_{56} < 0$ and a positive chirp $dE_c / E_0 > 0$, a resulting longitudinal density distribution is derived, where the electrons in the head of the bunch (in the tail) which are of lower (higher) energy, travel a longer (shorter) path. The final bunch length σ_{zf} can be reduced ideally (no higher order effects, wakefields etc. considered) to a minimum value determined only by the initial energy spread σ_{pi} :

$$\begin{aligned}\sigma_{zf} &= \sqrt{(1 + kR_{56})^2 \sigma_{zi}^2 + R_{56}^2 \sigma_{pi}^2} \\ &= R_{56} \sigma_{pi} \quad \text{for } R_{56} = -1/k,\end{aligned}\tag{7.2}$$

where $k = \delta(dE_c/E_0)/\delta z$ is the linear correlation constant and σ_{zi} the initial bunch length. In this case the final energy spread results to

$$\sigma_{pf} = \sqrt{k^2 \sigma_{zi}^2 + \sigma_{pi}^2} .\tag{7.3}$$

Although the scheme looks simple in principle, non-linear chirp, space charge effects, wakefields and the emission of coherent synchrotron radiation (CSR) set constraints in reaching the desired current density.

For small deviations from the reference phase ψ_0 the RF-voltage

$$V_{rf} = V_0 \cdot \cos(\psi_0 + \phi)\tag{7.4}$$

can be expanded showing higher order components and

$$V_{rf} = V_0 \left[\cos(\psi_0)(1 - \phi^2/2) - \sin(\psi_0)(\phi - \phi^3/6) \right].\tag{7.5}$$

Usually the quadratic ϕ -term of the reference phase dominates distortions of the energy position correlation, limiting the maximum compression and therefore the final bunch length. An elegant way to reduce this effect is the use of accelerating cavities operating on

a higher harmonic frequency, mostly third harmonic, $\omega_h = h\omega_0$ of the main RF system (see also chapter 5). In this case the total acceleration voltage is

$$V_{rf} = V_0 \cdot \cos(\omega_0 t + \psi_0) + V_h \cdot \cos(\omega_h t + \Phi_0). \quad (7.6)$$

The distortion can be compensated at a harmonic accelerating voltage of

$$V_h = -V_0 / h^2 \cdot \cos(\phi_0) / \cos(\phi_h). \quad (7.7)$$

To minimize the required voltage the harmonic phase should be $\phi_h = 0$ or π , causing a reduction of the electron energy in both cases. For the BESSY FEL, a 3rd harmonic cavity system will be installed immediately after the first acceleration module.

Taking into account contributions from higher order momentum compaction the path length variation in the bunch compressors can be written as

$$dL = R_{56} dp / p + T_{566} (dp / p)^2 + \dots \quad (7.8)$$

The second order momentum compaction T_{566} can be controlled by multipole magnets in the bunch compressor. However, these multipoles have a deleterious effect on the inherent perfect achromaticity for most simple rectangular bend types of chicanes and require a sophisticated chicane layout.

Space-charge effects need to be considered due to the high electron density since the repulsive Coulomb force between electrons inside the bunch tends to increase the longitudinal and the transverse emittance. This is the case especially at low beam energies. With increasing electron energy, the influence of the space-charge forces decreases drastically.

Electron beams generate **wakefields** due to their interaction with the vacuum chamber (geometric wakes) and chamber material (resistive wall wakes) that cause energy modulation along the bunch. The effects strongly depend on the beam pipe dimensions. For the superconducting accelerating structures operating at L-band frequencies there is no significant influence to the beam since the geometrical apertures are large (40 mm). However, the narrow undulator vacuum chambers will have to be designed minimizing both types of wakes (see also chapter 9).

In the bends of the bunch compressors the extremely short bunches emit long wavelength synchrotron radiation, which coherently superimposes when the wavelength exceeds the bunch length. The radiated power of this coherent synchrotron radiation (CSR) scales with the square of the number of electrons in the bunch. Thus an infra-red (IR) radiation field is built up in the dipole magnets, traveling faster than the electrons. As a consequence the IR radiation overtakes the previous bunch and interacts with the electrons, inducing a position dependent momentum modulation. In a 1-dimensional approximation, neglecting the transverse bunch size, this momentum modulation scales as [1]

$$dp_{csr}(s)/ds \approx \int_{s-\rho\phi^3/24}^s w_{csr}(s-s')\lambda(s')ds' \quad (7.9)$$

$$\text{with} \quad w_{csr}(s-s') = -\frac{2}{(3\rho^2)^{1/3}} \frac{\partial}{\partial s'} \frac{1}{(s-s')^{1/3}}, \quad (7.10)$$

where ρ is the dipole bending radius, ϕ the passed angle in the dipole magnet and w_{csr} the CSR wake-function. With decreasing bunch length the derivatives of the longitudinal charge density $\partial\lambda(s)/\partial s$ and hence the CSR induced momentum modulation increases. The interaction with the CSR field, however, not only increases the momentum spread in the electron bunch but also its horizontal emittance when horizontally bending compressor magnets are used. As the momentum modulation occurs in a dispersive section, the reference trajectory of the electron beam changes instantaneously and the electron starts to perform betatron oscillations equivalent to an increase in the single particle emittance. With the optical functions in the bunch compressor the resulting CSR induced emittance growth can be estimated from

$$d\mathcal{E}(s)_{csr} = H(s)(dp(s)/p)_{csr} \quad (7.11)$$

$$\Delta\mathcal{E}_{csr} = \int^{Komp.} H(s)(dp(s)/p)_{csr} ds \quad (7.12)$$

$$H(s) = \gamma(s)\eta(s)^2 + 2\alpha(s)\eta(s)\eta'(s) + \beta(s)\eta'(s)^2 \quad (7.13)$$

where α , β , γ are the Twiss parameters, and η and η' are the dispersion function and their derivative, respectively.

In case of strong CSR effects the deformed longitudinal phase space limits the shortest achievable bunch length. Besides this, the deformation in phase space can develop spikes in the local density which again increases the CSR effects. An instability may grow which finally dilutes emittance, leaving a beam which is no longer suited to drive a short wavelength FEL.

For the simulation of CSR effects and the optimization of the bunch compressors the simulation code ELEGANT [2] was used, which takes into account the effects within the 1-D model introduced above. Due to its extensive capabilities to calculate linear and higher order beam optics, wakefields, incoherent synchrotron radiation etc., the code is most suitable for deriving a most realistic simulation of linac beam optical properties.

7.2 Bunch Compression Scheme for the BESSY FEL

Designing an optimized bunch compression scheme for the BESSY FEL, one has to take into account that the multi-stage HGHG-FELs require long flat-top pulses of typically 290 μm in length with moderate peak current of $I_p \cong 1.8$ kA.

To leave space for future upgrades and expansions on the BESSY site, the FEL scheme uses a 180 degree arc, i.e. folding the linac. Due to the finite momentum compaction of the arc its influence for the bunch compression has to be considered. Effects disturbing the emittance (mainly due to CSR) have been carefully investigated and have been successfully reduced to acceptable values.

In principle, any bunch compression could be done within one step. In reality, the nonlinearities arising from wakefields, CSR, and space-charge effects and their energy dependence, prevent a one step compression. Therefore a two stage compression scheme was adopted for the BESSY FEL. Energy momentum compaction and optical functions in the two bunch compressors and in the 180 degree arc as well as the size of the momentum chirp have been optimized. Optimization goals were the beam parameters at the end of the linac satisfying the FEL requirements with respect to energy, emittance, peak current, and energy spread.

7.2.1 Basic Layout Considerations

The **momentum chirp** in general should be as large as possible to reduce bunch compressor strengths, momentum compaction, and thus CSR effects. The upper limit arises from the momentum acceptance of the linac and from higher order effects in transverse and longitudinal transformation through the magnet optics of the entire linac.

The **first compression stage** (BC1) should be placed at the lowest possible energy. Since the HGHG-FEL needs long bunches, they strongly scan the nonlinearities of the RF potential independently of the chosen accelerating reference phase. The lower energy

limit is set by space charge effects which arise when the compression and thus the electron density is too high.

Strength and momentum compaction need to be adjusted with respect to the 180 degree arc. An excellent compromise was found for the arc with the dipole magnet fields less than 1 T at a bending radius of 2.55 m. Because the bunches are long, the CSR effects are small, causing non-severe influence to beam emittance.

For the second compression stage a chirp in the longitudinal phase space distribution is needed. The momentum compaction of the arc has to be taken into account as it modifies the bunch length similar to a compressor stage. However, the sign of the momentum compaction of a “normally” tuned arc is reversed compared to that of the magnetic chicane bunch compressors, and the compression of the first stage would be partly cancelled. Using adequate multipole magnets, the arc can be made isochronous ($R_{56}=0$), or even set such that the momentum compaction has the same sign as in the bunch compressors. The effect of these strong multipoles on the transverse nonlinear transformation properties had to be carefully optimized to avoid emittance dilutions. The energy of the electrons passing the arc should be as high as possible; the increasing magnetic rigidity making the electron beam less sensitive for any kind of disturbing effects. The maximum energy is limited by CSR effects in the second bunch compressor. Due to adiabatic damping the relative momentum chirp dp_c/p decreases with increasing energy. To reach the same compression, the momentum compaction has to be adjusted.

The **second compression stage** (BC2) is placed directly after the 180 degree arc to avoid further adiabatic damping of the momentum chirp, keeping the momentum compaction of the second bunch compressor as small as it is. To reduce CSR effects during the final compression, the dipole strength was reduced by increasing the number of magnets from four bends (the most simple chicane type) to six and finally to eight in the course of the optimization procedure. Quadrupole magnets were implemented to better control the beta-functions in the last compressor dipoles.

The location of the **extraction sections**, where the bunches are deflected into the FEL lines, is defined by FEL requirements and is not an object of the bunch compression optimization. The extraction section should be transparent for both, the extracted and the non-extracted beam. The extraction optics should have a small or vanishing momentum compaction to keep the bunch length and peak current unchanged. Since the extraction sections are passed by very short bunches with high peak currents, only weak dipole magnets are used to avoid strong CSR induced emittance dilutions.

7.2.2 Injector Beam Parameters

To deliver high density electron bunches to the individual FEL lines, the bunch compression scheme was optimized with regard to the input beam parameters from the injector. The basic injector beam parameters just before entering the first bunch compressor are summarized in table 7.1.

Table 7.1: Injector beam parameters.

Parameter		Unit
Bunch charge	2.5	nC
Bunch length σ_1	8.6 (fwhm)	mm
Peak current I_p	65	A
Norm. emittance ϵ_n	1.38	π mm mrad
Energy spread σ_E (%)	15	keV
Momentum chirp	1.4	$d(dp_c/p)/dz$ (MeV/mm)

Table 7.2: Parameters of the first bunch compressor.

Parameter		Unit
Energy E	219	MeV
Momentum compaction R_{56}	-10.5	cm
2 nd order momentum compaction T_{566}	16.4	cm
Dipole length L_B	0.4	m
Dipole bending radius ρ	BB1, BB2	1.80 m
	BB3, BB4	2.25 m
	BB5, BB6	4.50 m
Dipole bending angle α	BB1, BB2	222 mrad
	BB3, BB4	178 mrad
	BB5, BB6	89 mrad
Quadrupole length L_Q	0.2	m
Quadrupole strength k	< 3.0	m^{-2}

7.2.3 Layout of BC1

A schematic drawing of the first compressor stage is shown in Figure 7.1. To reduce CSR effects a six instead of a four magnet chicane is used. The bending radius of the otherwise identical dipole magnets increases to the end of the chicane with decreasing bunch length. Together with the other main parameters of the first bunch compressor they can be extracted from table 7.2. The optical functions have been optimized to reduce CSR induced emittance dilution in the last two bending magnets of the chicane where the shortest bunch lengths are reached. Low values of the horizontal beta function with small derivative $d\beta/ds$ have been adjusted. Figure 7.2 shows the optical functions in the first bunch compressor.

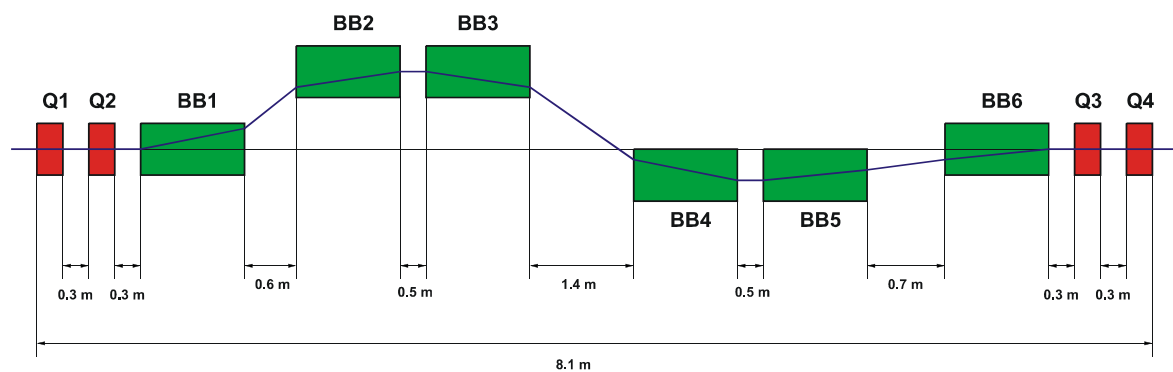


Fig. 7.1: Layout of the first bunch compressor, showing the dipole magnets (green), and the quadrupole magnets (red).

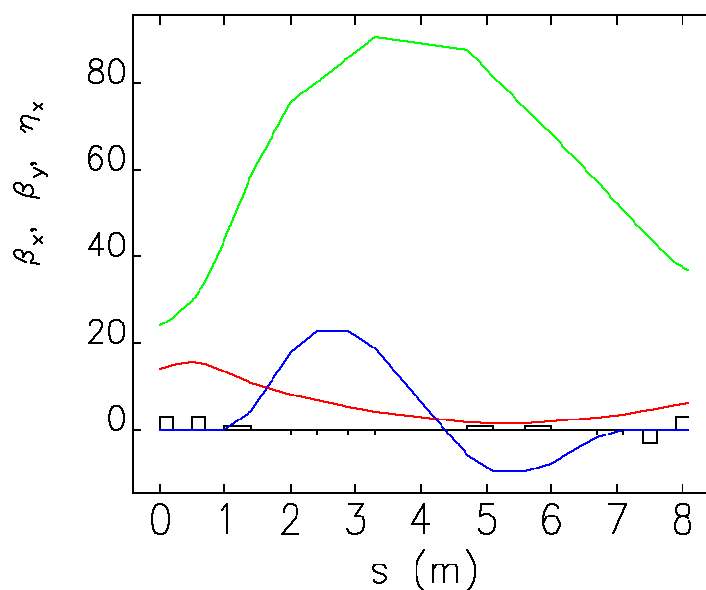


Fig. 7.2: Optical functions of the first bunch compressor: horizontal (red) and vertical (green) beta function in meters and dispersion (blue) in centimeters.

7.2.4 Layout of BC2

Figure 7.3 shows the schematic drawing of the second bunch compressor stage. To avoid strong CSR effects the number of dipole magnets has been increased to eight, again the bending radii increase with decreasing bunch length. The main parameters of the second bunch compressor stage are collected in table 7.3.

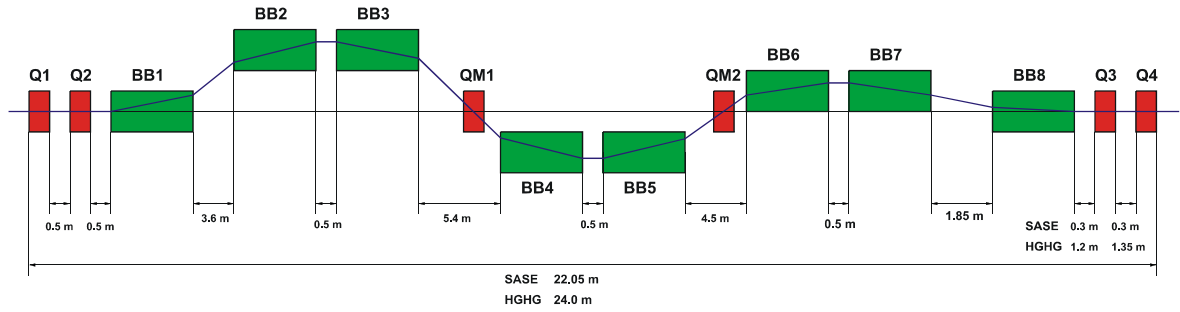


Fig. 7.3: Layout of the second bunch compressor, showing the dipole magnets (green), and the quadrupole magnets (red).

Table 7.3: Parameters of the second bunch compressor.

Parameter		Unit
Energy E	753	MeV
Momentum compaction R_{56}	-9.29	cm
2 nd order momentum comp. T_{566}	14.04	cm
Dipole length L_B	0.4	m
Dipole bending radius ρ	BB1, BB2, BB3, BB4	4.36 m
	BB5, BB6	8.50
	BB7, BB8	13.89
Dipole bending angle α	BB1, BB2, BB3, BB4	92 mrad
	BB5, BB6	47
	BB7, BB8	29
Quadrupole length L_Q	0.2	m
Max. quadrupole strength $ k $	< 5.0	m ⁻²

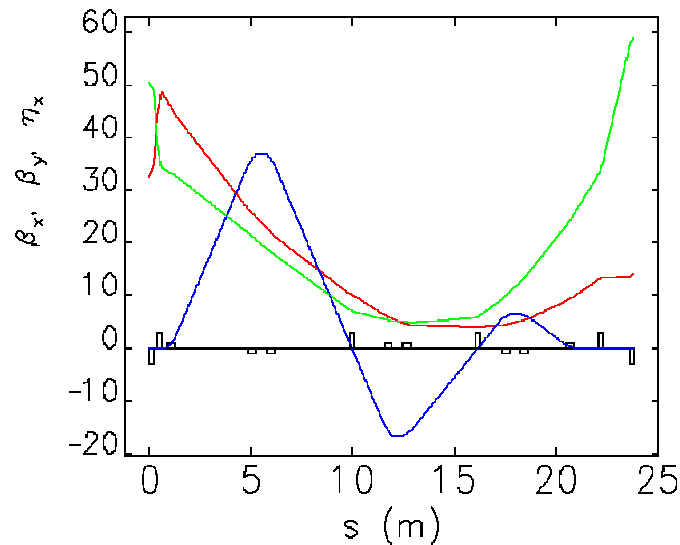


Fig. 7.4: Optical function of the second bunch compressor: horizontal (red) and vertical (green) beta function in meters and dispersion (blue) in centimeters.

According to the same principles already used for the optimization of the first compressor stage, the optical functions have been optimized to reduce CSR induced energy modulation and emittance dilution. Due to the increased compressor length two quadrupole magnets have been inserted in the compressor to have better control of the beta functions. These magnets QM1 and QM2 have been placed at the zero crossing positions of the dispersion function to keep the dispersion and thus the compressors' momentum compaction independent from the setting of these quadrupoles. Figure 7.4 shows the optical functions.

7.3 The 180 Degree Arc

The 180 degree arc consists of four Triple Bend Achromat (TBA) structures, each bending the beam by 45 degrees. Figure 7.5 shows a schematic drawing of one TBA unit cell. The middle achromat dipole is twice as long as the outer dipoles. Two quadrupole families inside the achromat are used to bring the dispersion to zero and to control the momentum compaction R_{56} , enabling the tuning of the arc to an isochronous or even slightly compressing structure. By means of two sextupole families, placed inside the achromat, chromaticity is corrected.

The main parameters of the arc are listed in table 7.4. The optical functions for one half of the 180 degree arc are plotted in figure 7.8. Again low values of the horizontal beta function have been adjusted in the achromat, minimizing CSR effects.

Table 7.4: Parameters of the 180 degree arc.

Parameter		Unit
Energy E	753	MeV
Total length	48.4	m
Distance incoming to outgoing beam	28.83	m
Momentum compaction R_{56}	-1.87	cm
2 nd order momentum compaction T_{566}	110	cm
Dipole length L_B	BB1, BB3	0.50 m
	BB2	1.00
Dipole bending radius ρ		2.55 mrad
Dipole bending angle α	BB1, BB3	196.3 mrad
	BB2	392.7
Number of quadrupole families	achromat	2
	for matching	6
Number of sextupole families		2

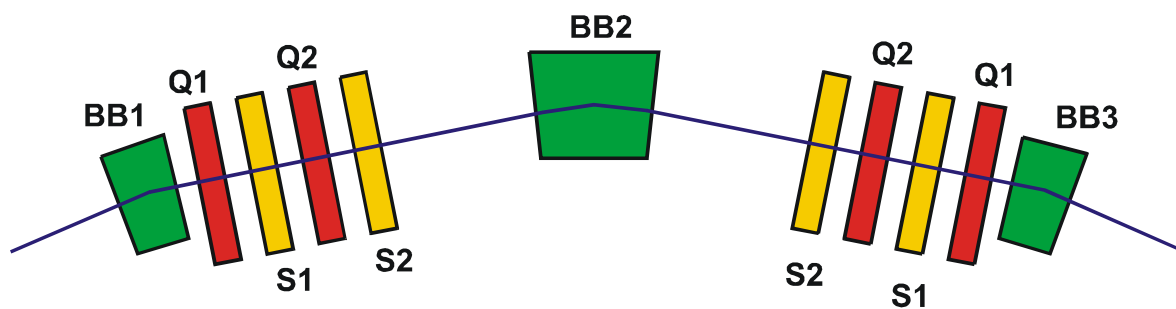


Fig. 7.5: Layout of the 180 degree arc, showing the dipole magnets (green), the quadrupole magnets (red), and the sextupole magnets (yellow).

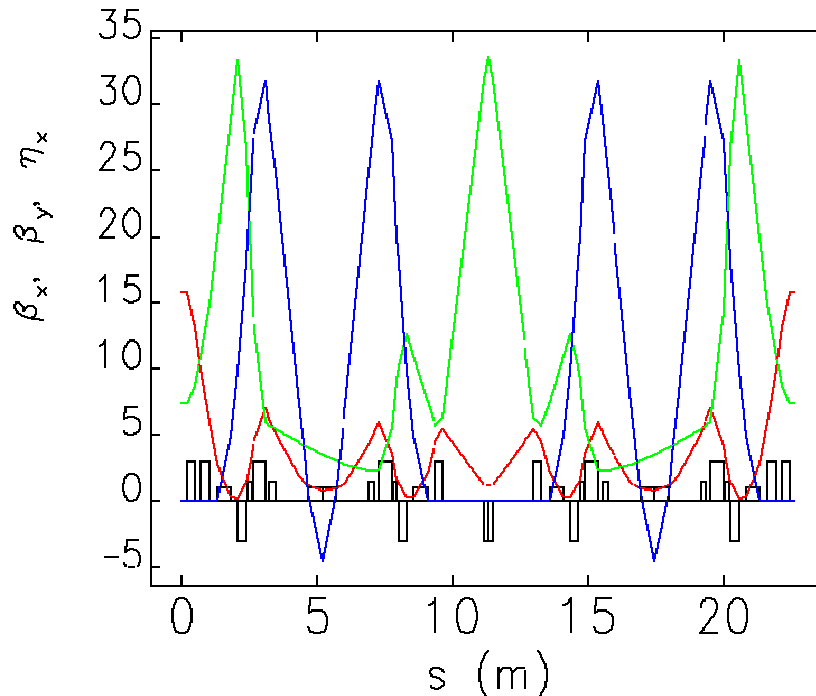


Fig. 7.6: Optical functions for one half of the 180 degree arc: horizontal (red) and vertical (green) beta function in meters and dispersion (blue) in centimeters.

7.4 Electron Beam Extraction

Two extraction sections serve to distribute the electron bunches between the three individual FEL lines. A schematic is shown in figure 7.7. A fast magnetic sine-half-wave kicker with time constants in the microsecond range gives a 5 mrad kick to the bunch to be extracted. After a drift space sufficiently long to achieve clearance to non-deflected bunches, a septum magnet gives a second kick to the extracted bunch. After another drift space a quadrupole triplet follows, which is tuned to set the dispersion at the section end to zero. The last dipole bends the bunches to obtain clearance from the next acceleration section and leaves the extracted beam with an angle of 5.66 degrees to the non-extracted beam direction. After passing the final matching quadrupole doublet the extracted beam has reached a transverse separation of more than 70 cm, sufficient to be guided to the FEL line without colliding with the cryo-tanks of the superconducting cavity modules.

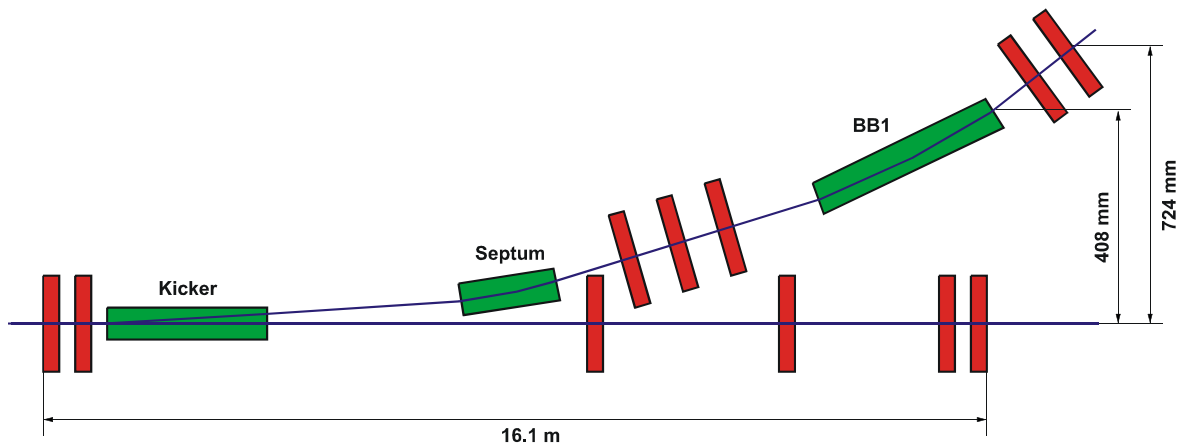


Fig. 7.7.: Layout of the extraction section: dipole magnets (green), and quadrupole magnets (red).

Since the extraction sections do not require special values for the initial beta functions, the same lattice can be used in all three cases, independent of the extraction energy. The main parameters are summarized in table 7.5

The optical functions for the extracted and the non-extracted beam are shown in figure 7.8.

Table 7.5: Parameters of the extraction section.

Parameter			Unit
Total length	non-extracted beam	16.10	m
	extracted beam	18.55	m
Total bending angle		98	mrad
Momentum compaction R_{56}		0.3	cm
2 nd order momentum compaction T_{566}		4.3	cm
Dipole length	Kicker	2.50	m
	Septum	1.50	m
	BB1	3.00	m
Dipole radius	Kicker	500	m
	Septum	48	m
	BB1	48	m
Dipole angle	Kicker	5.00	mrad
	Septum	31.25	mrad
	BB1	62.50	mrad

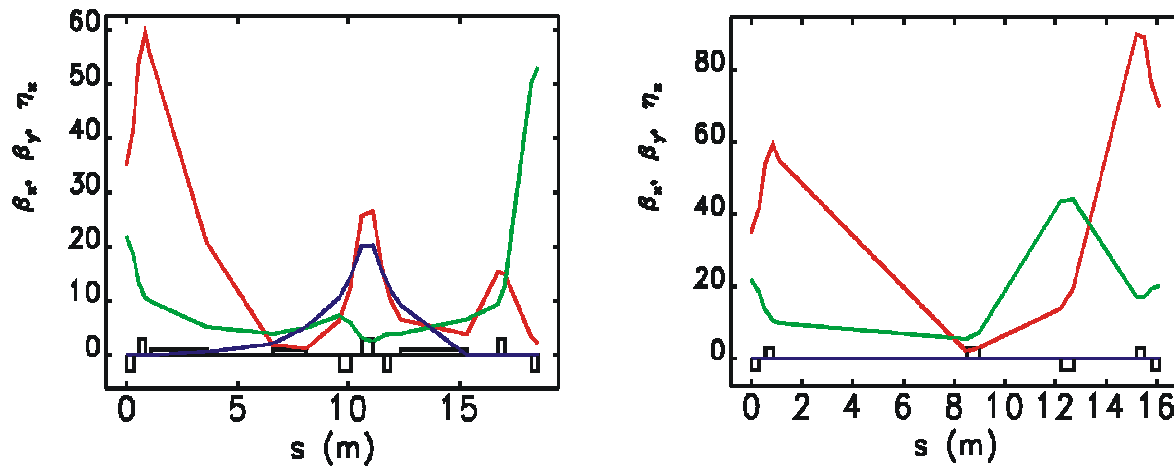


Fig. 7.8: Optical functions of the extraction section: horizontal (red) and vertical (green) beta functions in meters and dispersion (blue) in centimeters. Left: extraction on; right: extraction off.

7.5 Start-to-End Simulations

Several programs are used to simulate a full FEL device from the injector cathode to the undulator end. The different input requests of the code often make a parameterization of the electron bunch necessary, calculating projected mean and rms values. Because of the non-standard particle distributions, varying sliced values over the bunch length, and correlations in the 6-D phase space, this parameterization is usually connected with a loss of information. To avoid this for start-to-end simulations, any parameterization was abandoned and the 6-D phase space was passed directly between the programs. For the injector part simulations with usually 100,000 particles were tracked with ASTRA [3] up to the first bunch compressor. The ASTRA output is then converted and passed onto ELEGANT. The calculated phase space distribution at the linac's end can be analyzed and transformed to the sliced input format of GENESIS [4].

The results of the start-to-end simulations (S2E) are summarized in table 7.6 and figures 7.9 to 7.12. Although the required peak current is easily reached, the projected emittance grows in the vertical and in the horizontal plane. The reason for this is the longitudinal variation of the transverse beam center. In the longitudinal projection this converts to an increased emittance. The sliced emittance is mainly conserved as is seen in figure 7.11 and is well suited as input beam for the HGHG cascade.

Table 7.6: Results of start-to-end simulations: bunch charge, $Q = 2.5$ nC, emittances, and energy spread are projected values.

	E (MeV)	σ_l (fwhm) (mm)	I_p (A)	$\epsilon_{x,n}$ (π mm mrad)	$\epsilon_{y,n}$ (π mm mrad)	σ_p/p (x 1000)
Before BC1	219	8.6	65	2.12	2.12	24.1
After BC1	219	2.7	200	2.14	2.20	24.1
After arc	753	2.3	240	2.82	2.14	9.3
After BC2	753	0.29	2000	2.82	2.40	8.9
End of linac	2300	0.29	2000	3.95	2.59	3.7

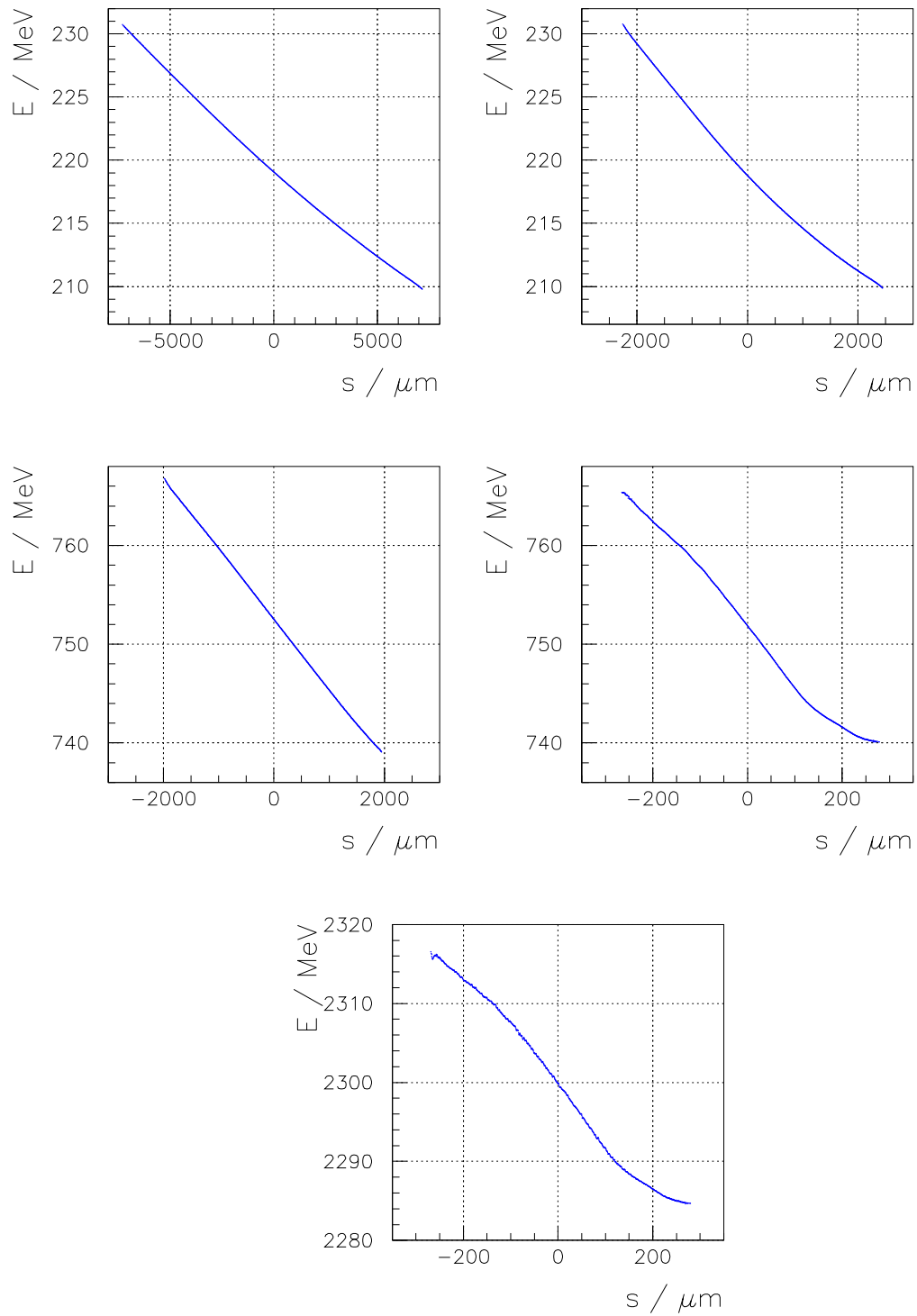


Fig. 7.9: Slice analysis of the S2E simulation results: mean slice energy before BC1 (top left), after BC1 (top right), before BC2 (mid left), after BC2 (mid right) and at the linac end (bottom).

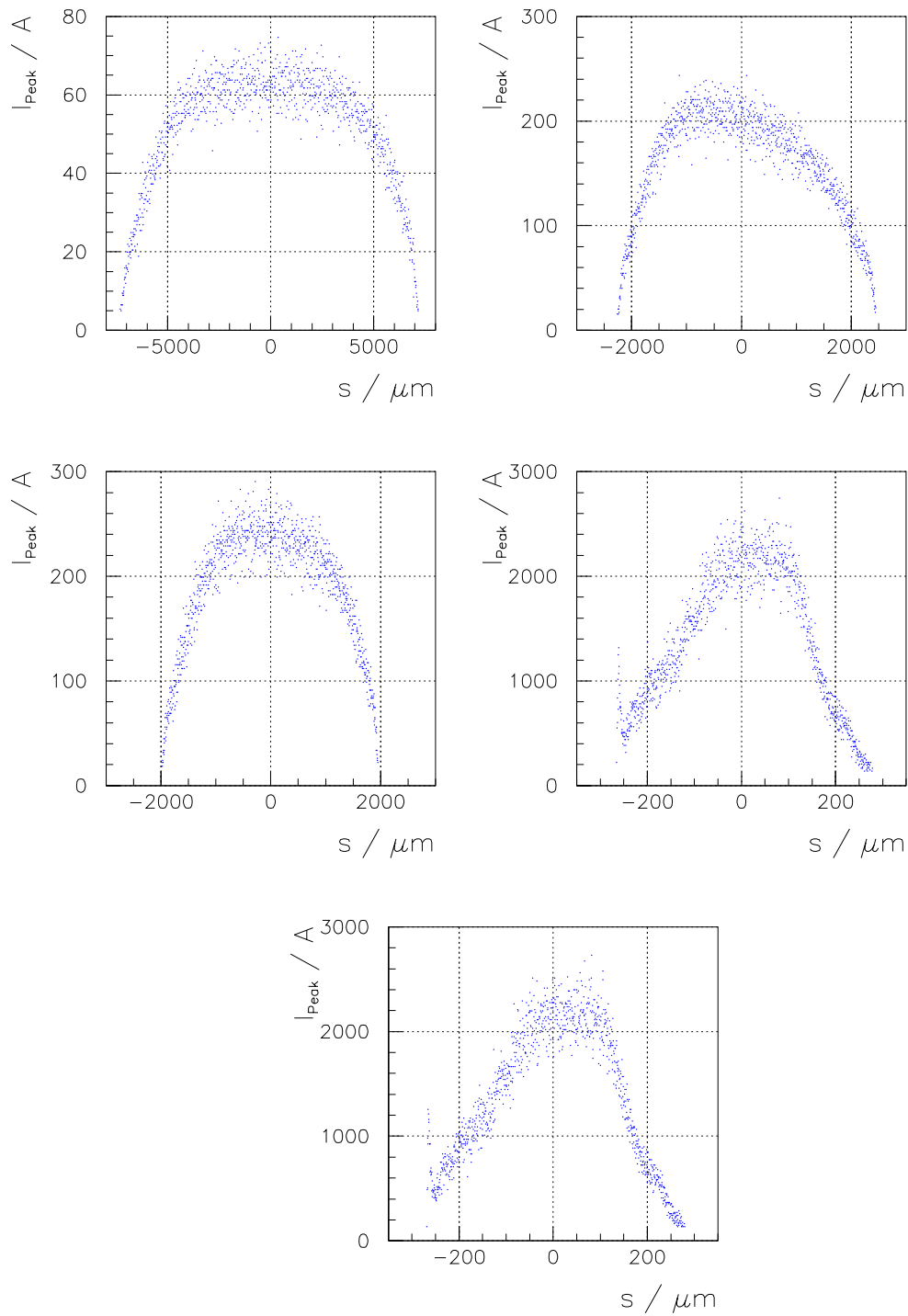


Fig. 7.10: Slice analysis of the S2E simulation results: mean slice current before BC1 (top left), after BC1 (top right), before BC2 (mid left), after BC2 (mid right) and at the linac end (bottom).

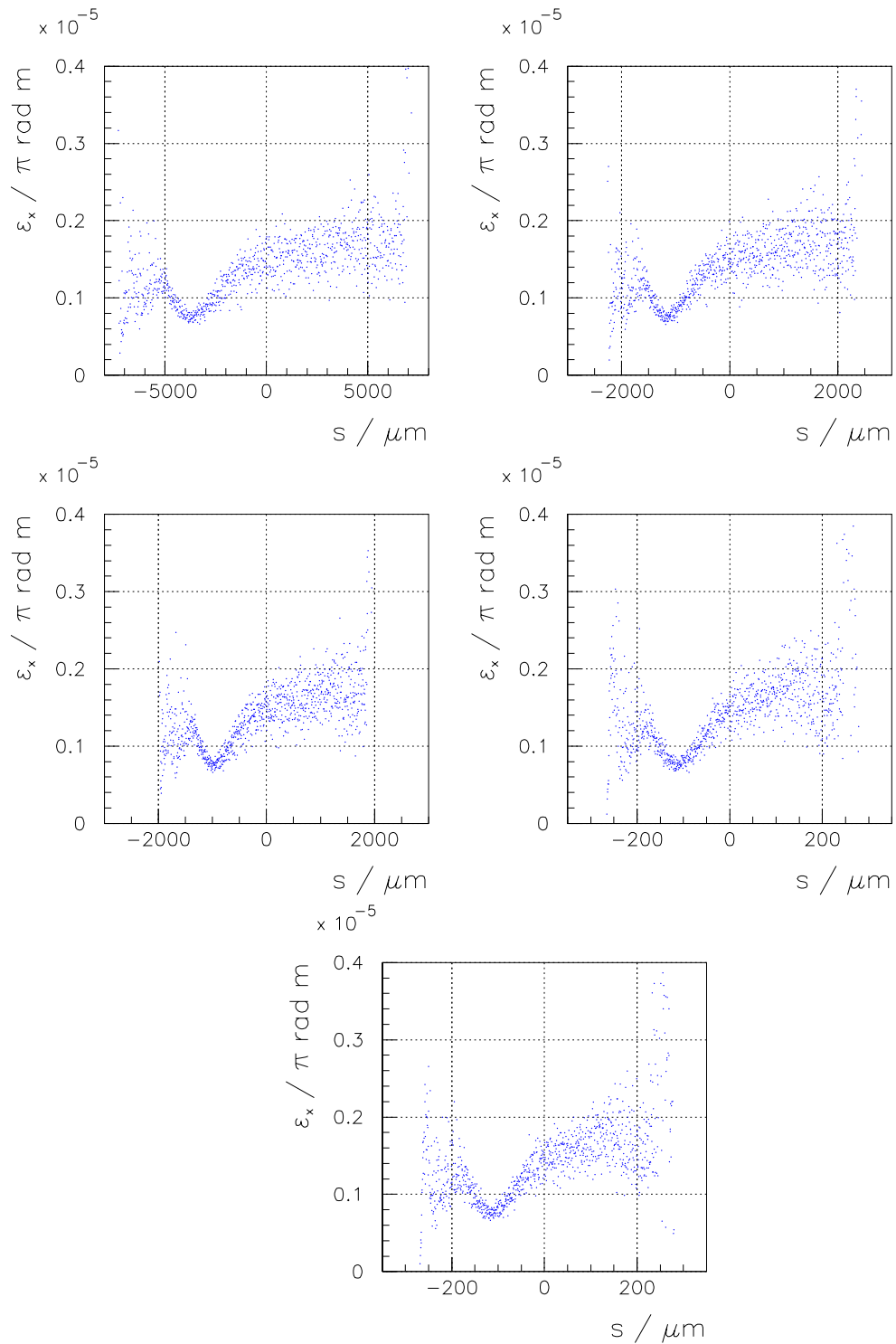


Fig. 7.11: Slice analysis of the S2E simulation results: mean horizontal slice emittance before BC1 (top left), after BC1 (top right), before BC2 (mid left), after BC2 (mid right) and at the linac end (bottom).

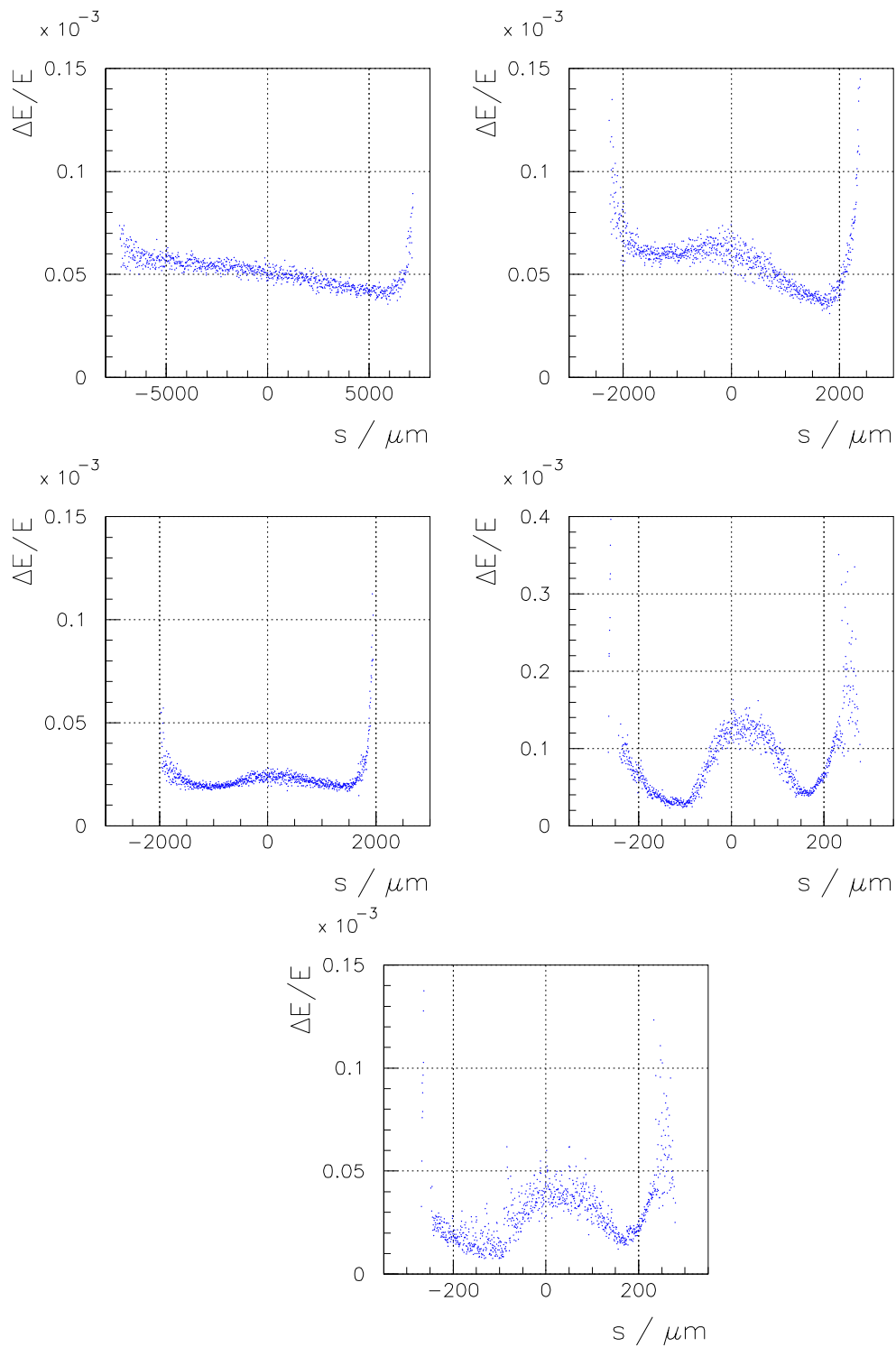


Fig. 7.12: Slice analysis of the S2E simulation results: mean (uncorrelated) slice energy spread before BC1 (top left), after BC1 (top right), before BC2 (mid left), after BC2 (mid right) and at the linac end (bottom).

References

- [1] E. Saldin, E.A. Schneidmiller, M.V. Yurkov, TESLA Technical Report TESLA-FEL 96-14 (1996).
- [2] M. Borland, *Elegant: A Flexible SDDS Compliant Code for Accelerator Simulation*, Advanced Photon Source LS-287, Sep. 2000.
- [3] K. Flöttmann, “ASTRA, A Space Charge Tracking Algorithm“:
<http://www.desy.de/~mpyflo>.
- [4] S. Reiche, *Nucl. Instrum. and Meth. A* **429** (1999), 243.

8 Beam Distribution System

8.1 The Linac Optics

To accelerate the electrons to their nominal energy of up to 2.3 GeV, 18 superconducting (s.c.) modules are used for operation in CW mode at an average field of 16.0 MeV/m. Each module is equipped with eight s.c. 9-cell cavities. Furthermore, the modules contain a superconducting quadrupole magnet for beam focusing and combined vertical and horizontal steering dipole magnets as well as a beam position monitor of RF cavity type. Several modules are linked up to a longer string and the quadrupole magnets are used to realize a FODO channel. The quadrupole strength was chosen for a phase advance of about 90 degrees per cell. This gives the smallest average transverse beta function and beam size respectively, reducing transverse higher order effects in the magnet lattice and particle losses at the mechanical aperture. Besides this, the 90 degree phase advance is well suited for orbit diagnostics and correction. Parameters of the FODO lattice and optical functions are given in table 8.1 and figure 8.1 respectively.

Table 8.1: FODO lattice parameters.

Parameter		Unit
Phase advance	0.248	rad/2 π
Av. beta function	20	m
Min./max. beta function	7.2/41.1	m
Quadrupole length	0.5	m
Quadrupole strength	± 0.235	m ⁻²
Unit cell length	24.4	m

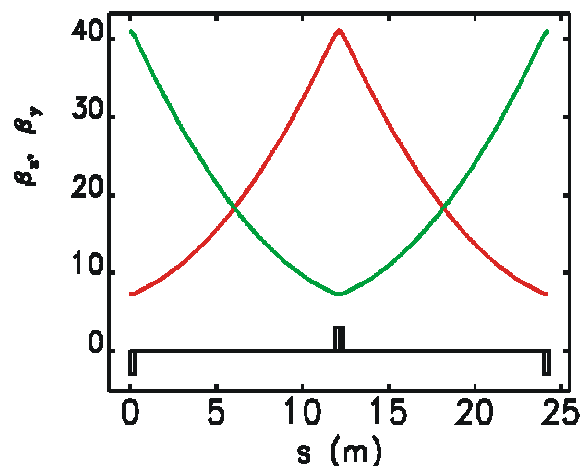


Fig. 8.1: Optical functions of the FODO cell: horizontal (red) and vertical (green) beta function in meters.

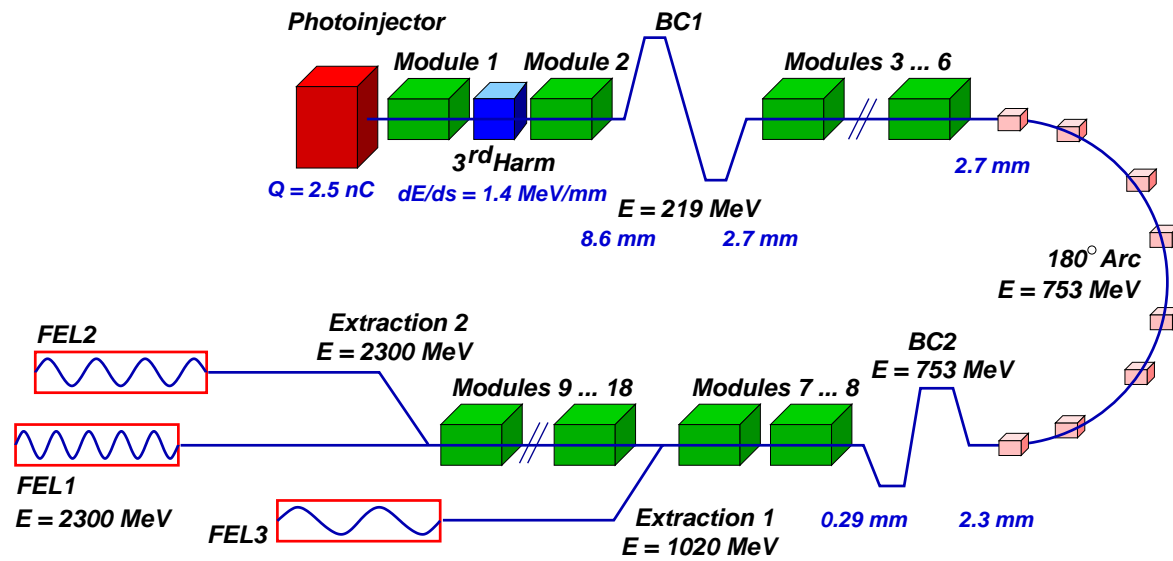


Fig. 8.2: Schematic layout for the BESSY Soft X-ray FEL. Bunch length decreases from 8.6 mm to 0.29 mm.

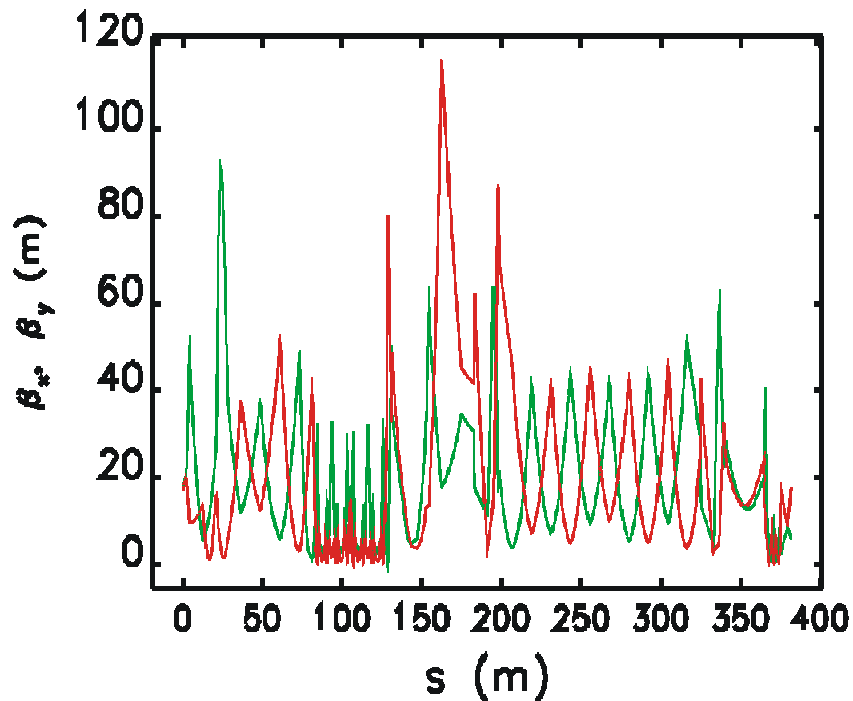


Fig. 8.3: Optical functions of the linac: horizontal (red) and vertical (green) beta function in meters.

Table 8.2: Linac acceleration parameters.

Device	Acc. Field (MV/m)	Energy (MeV)
Start		
Gun	40	4
Module 1	15.8	131
Harm. Module		96
Module 2	16.7	219
BC1		219
Module 3	16.7	353
Module 4	16.7	486
Module 5	16.7	620
Module 6	16.7	753
Arc		753
BC2		753
Module 7	16.7	886
Module 8	16.7	1020
FEL 3 extr.		1020
Module 9	15.8	1148
Module 10	15.8	1276
Module 11	15.8	1404
Module 12	15.8	1532
Module 13	15.8	1660
Module 14	15.8	1788
Module 15	15.8	1916
Module 16	15.8	2044
Module 17	15.8	2172
Module 18	15.8	2300
FEL 2 extr.		2300
FEL 1		2300

The linac is interrupted by two bunch compressors, the arc and the extraction sections. Each of these elements has optimized beta functions which have to be matched to the linac optics by quadrupole doublets or triplets before and after the bunch compressors, arc, and extraction regions. To reduce the number of matching quadrupoles, the linac quadrupoles are used for matching the beta functions as well. As a consequence the FODO lattice in the linac is somewhat irregular and the beta functions reach larger values at

some points in the linac as compared to a symmetric FODO lattice. Since the increased transverse beam size does not lead to strong non-linearities this is tolerable.

Nonlinear effects have been investigated in tracking simulations for the bunch compression (chapter 7). Simulations show no significant disturbances either for the transverse or for the longitudinal phase space. Figure 8.2 shows the schematics of the entire electron path starting at the injector up to the end of the cascaded HGHG-FEL.

Beam energies at the location of major components are summarized in table 8.2. The optical functions in the linac are plotted in figure 8.3. As there is hardly space for focusing quadrupoles in the injector part and due to the large distance from the injector to the first quadrupoles in accelerating modules #1 and #2, the beta functions are not easy to control. To avoid large excursions of the beta functions in this area, and to ensure low values in the bunch compressor BC1, a quadrupole triplet between the first and second accelerating module has to be inserted.

8.2 Beam Distribution Kickers and Pulsers

8.2.1 Stability Requirements for the Kickers

A kicker system is used to extract bunches from the main linac into the low-energy and medium-energy FEL lines at beam energies of 1.02 and 2.3 GeV, respectively. The main parameters of the extraction system result from constraining the physical needs with the available space, geometry considerations to the optics, and the linac timing structure.

Two different kicker coil designs have been investigated: a single coil ferrite kicker with a low gap height and a modest pulse current and a slotted pipe kicker [1] with higher pulse currents avoiding the ferrites. The later one was selected, its parameters are listed in table 8.3.

To achieve optimum FEL gain, it is crucial that the beam is well centered in the undulator sections. The limit for horizontal beam position off-set was found to be $\Delta x \leq 5 \mu\text{m}$ at the undulator entrance. With a mean beta function of 16 m at extraction and at the undulator entrance, this translates into a requirement for the relative stability of the extraction angle θ of $\Delta\theta/\theta \leq 5 \cdot 10^{-5}$. This requirement for the stability of pulsed elements is demanding. The BESSY II storage ring extraction and injection kickers, achieve a relative shot-to-shot stability of 10^{-3} (long term drifts not included) using established technology such as RC circuits with thyatron switches. This seems to be the stability limit of a non-feedback, free-running design, and is at least one and a half orders in magnitude away from the requirements for the FEL. Evidently a new concept had to be developed.

Table 8.3: Parameters of the kicker-system for the low-energy and medium-energy FEL lines.

Parameter		Unit
Kick amplitude	5	mrاد
Relative deflection stability	$\leq 5 \cdot 10^{-5}$	
Repetition frequency	1000	Hz
Pulse form	sine half wave	
Pulse duration (fwhm)	< 2	μs
Number of magnets	5	
Number of windings	1	
Total length of magnets	2.5	m
Gap height of kicker magnet	12	mm
Max. load current	120	A
Inductance incl. connectors	1	μH
Circuit capacitance	200	nF

8.2.2 A Semiconductor-Based Pulser for the Kicker

The stability of the extraction system is determined primarily by the reproducibility and the long-term stability of the pulser.

There are two different causes of magnetic field variations: Amplitude noise and phase jitter. The phase jitter is generated by small temporal fluctuations of the actual time the pulse is fired with respect to the ideal time. It is caused by thermal noise in the pulser electronics and cross-talk. Amplitude noise is due to ripple of the charging power supply and by thermal drift effects.

In order to avoid thermal noise and cross-talk, a new design for the pulser was developed based on power semiconductor technology (IGBT). A test pulser was built and successfully tested at BESSY. Figure 8.4 shows the pulser prototype. Major improvements in this concept are:

- Optimized geometry of the power stack to minimize intrinsic inductance,
- Optimization of the power stack and the gate drive with respect to power requirements and stability,
- Careful design of the grounding geometry,
- Gate drive of the semiconductor switches hardened against cross-talk,
- Accurate pulse forming by electronic decoupling of stray capacitance from, for example, cables from power supplies,
- Solid layout and air-temperature control of the whole circuit.

To monitor the pulse current to high precision ($\Delta I/I \cong 10^{-5}$) specially designed and manufactured low-noise pulse transformers were used.

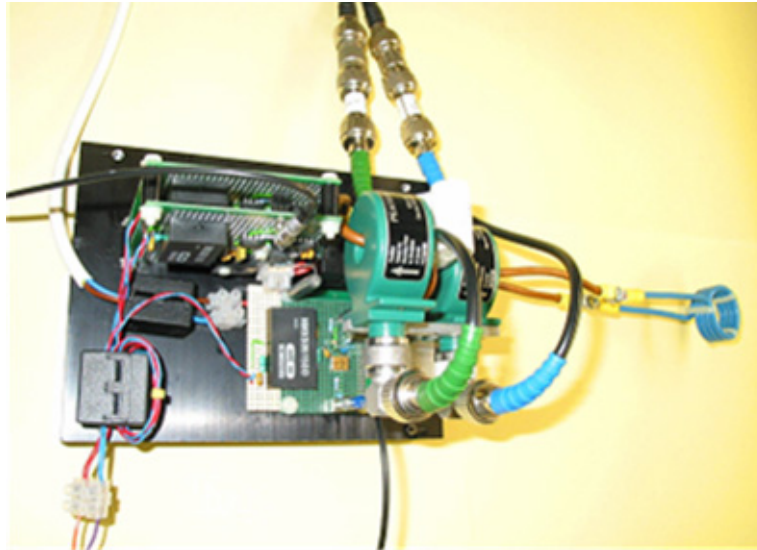


Fig. 8.4: Photo of the pulser test setup.

8.2.3 First Results from the Test Pulser

The pulser prototype was tested at nominal currents of up to 120 A and at repetition frequencies ranging from 10 to 1000 Hz. A simple solenoid of appropriate inductance was used as magnet coil.

Figure 8.5 (right) depicts a measured kicker pulse. No transient oscillations could be detected - an essential point for operation of the system. Pulse length and width are in accordance with the theoretically expected values. The signal of the current monitor - some hundred consecutive pulses accumulated on top of each other - is shown in figure 8.5 (left). These measurements showed no significant difference between the first pulse and the last one within the resolution limit of the analyzer. With the present measurement system it is not possible to discriminate signal jitter originating from the pulser within the resolution of the analyzer. Therefore, at the time of writing, an upper limit to the pulser stability corresponds to a kick-angle spread of the electron beam smaller than $\Delta\theta/\theta \leq 3 \cdot 10^{-4}$.

In order to be able to further optimize the system stability, measurements of the field jitter have to be improved. The main difficulty arises from the large dynamic range needed for proper measurements of the signal.

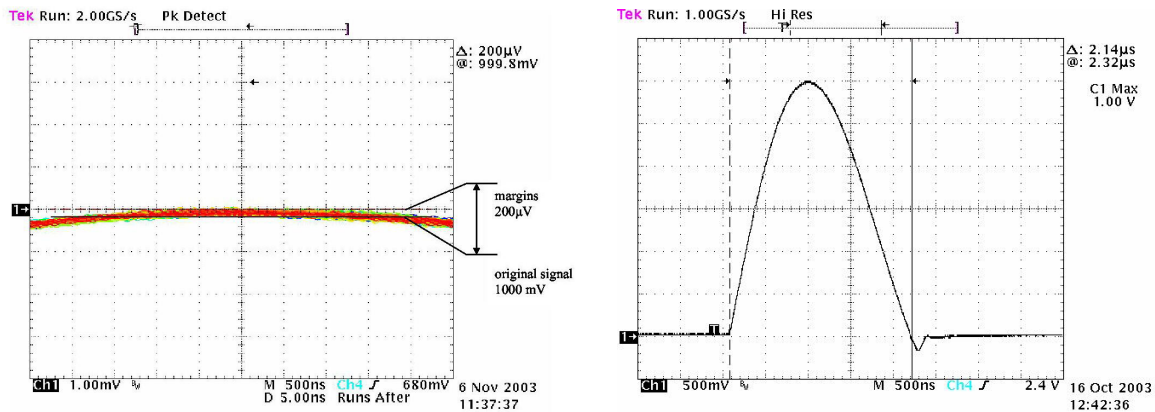


Fig. 8.5: Left: Accumulated pulses showing a system stability of better $3 \cdot 10^{-4}$. Right: Single kicker pulse.

Inspired by the ideas proposed in [2], an electro-optical set-up is realized to measure the magnetic field by means of the Faraday effect (figure 8.6). A Terbium-Gallium-Garnet (TGG) crystal with high Verdet constant is positioned inside the kicker coil. A polarized laser pulse generated from a He-Ne laser is sent through the crystal, passing a polarimeter downstream with a high-sensitive avalanche diode as detector. The TGG crystal rotates the polarization plane of the laser pulse according to the coil's magnetic field. The polarizer position is rotated to maximum flux extinction if the magnetic field is exactly at its nominal value. Small fluctuations around the nominal field show up as light flux variations at the photodiode. Thus, highly accurate difference measurements enable a high precision determination of the field deviation to be made. The measurement set-up has been installed and is being commissioned.

Further commissioning work of the test kicker system is in progress and will give an improved understanding of factors that may influence the magnetic field stability such as:

- Long-term performance of the semiconductors,
- Influence of temperature on the stability of the kickers,
- Grounding,
- Cross-talk on the electronic boards,
- Trigger concepts.

However, the stability of the charging power supply is crucial for the magnitude of the amplitude jitter. So far power supplies not optimized for small high voltage ripple were used. Power supplies with a relative stability of 10^{-5} are feasible which will further considerably decrease the present amplitude jitter.

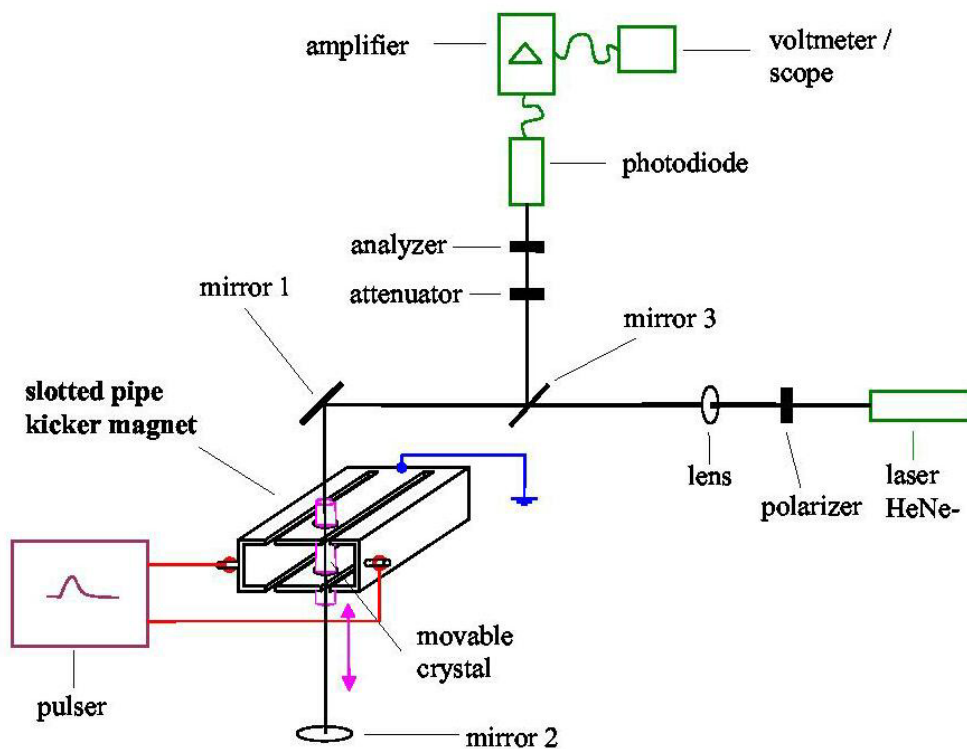


Fig. 8.6: Schematics of the electro-optical measurement set-up to determine the stability of the kicker system.

8.3 Standard ‘Warm’ Vacuum System

The vacuum system for the BESSY FEL is separated into “cold sections” of the superconducting cryomodules and “warm sections” equipped with standard room-temperature vacuum chambers. In the following only these standard vacuum sections are considered. For the “cold vacuum sections” see chapter 6.

The requirements for the vacuum pressure in the presence of beam, as well as without beam, are determined more by technical aspects such as “poisoning” the cathode in the injector region and degradation of the superconducting Niobium cavities, than by the interaction of the electrons with residual gas molecules. The gas flux from the “warm vacuum sections” needs to be limited by differential pumping to reduce build-up of one monolayer on the critical surfaces to a time scale of at least 10 days. This is equivalent to a pressure of $\leq 10^{-10}$ mbar in the injector and s.c. cavity areas, whereas for the conventional chambers an average pressure of 10^{-8} mbar N_2 equivalent is sufficient.

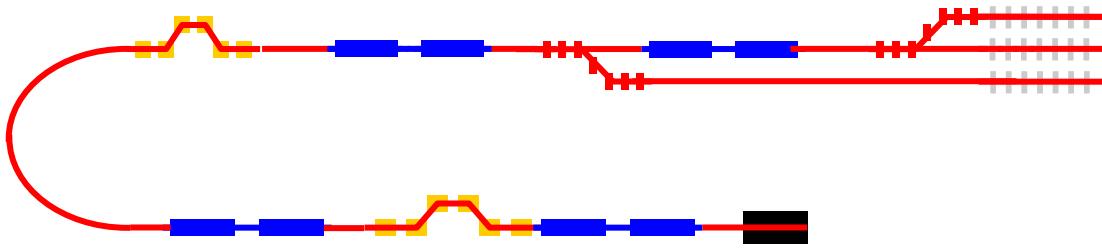


Fig. 8.7: Schematics of room temperature vacuum system indicated in red and s.c. structures (blue).

Figure 8.7 shows a schematic overview on the cold and warm vacuum section. The total lengths of warm sections add up to 235 m.

8.3.1 Materials

The selection of materials for the vacuum system, especially for the undulator region, is challenging since a low resistive wall impedance is required with an extremely smooth surface finish, to avoid wakefields deteriorating the electron beam. From this point, copper seems to be the material of choice. Wherever possible copper chambers or stainless steel bodies, e.g. SS 316 LN, with a $\geq 5 \mu\text{m}$ thin copper layer, e.g. using “Chemical Vapor Deposition” (CVD) on an electro-polished body, will be used in the machine where required, due to the short bunch length.

Special attention needs to be paid to locations with shielded bellows, VAT[®]-seal flange connections, diagnostic or pumping ports and gate valves, to avoid changes in the chamber cross section. Proper RF shielding using copper-beryllium contacts has to be employed in order to minimize heating of the elements and deterioration of the electron bunch phase space by wakes due to the high average peak current of up to 1.8 kA.

Since the wakefields are influenced by the material conductivity as well as by the surface roughness, the latter can be reduced to a level of a few percent compared to the resistive wakefield effect by a surface smoothed to the level of $R_a = 100 \text{ nm}$.

8.3.2 Vacuum Pressure

For pumping, oil-free turbo-molecular roughing stations are used until the mid- 10^{-6} mbar pressure is reached, then ion getter pumps will bring down and keep the vacuum pressure at the required level of 10^{-8} mbar. Due to the small physical dimensions of the

chambers of typically 30 mm x 20 mm (horizontal x vertical), the system is totally conductance-limited. Thus, the effective pumping speed S_{eff} of a pump with a nominal pumping speed S_0 in a tube of length L is small. Figure 8.8 gives the calculated effective pumping speed as a function of the recipient length for various values of S_0 . As soon as the distance between neighboring pumps exceeds 0.5 m, the pumping speed drops down to less than 1 l/s independent of the nominal pumping speeds. This demands a large number of low-pumping speed pumps.

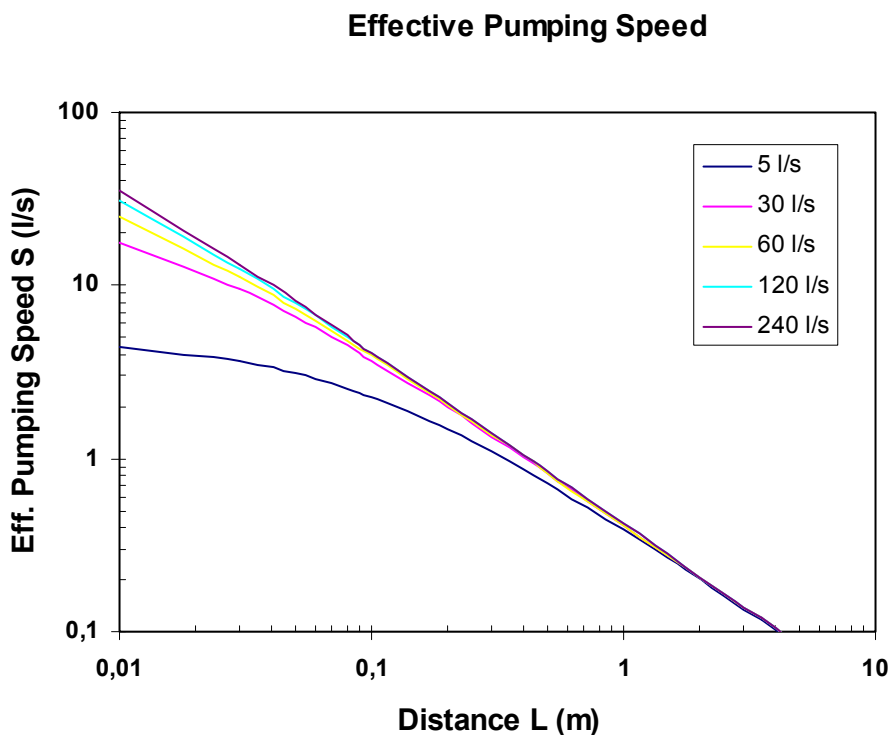


Fig. 8.8: Calculated effective pumping speed for various pump sizes at a conductance of $c = 0.14$ l/s.

In the undulator sections with a circular vacuum chamber of 9 mm diameter the situation is even worse, since the distance between 2 pumps is set by the length of the undulator modules of typically 3.5 m. With suitable pumps in the 'intersections', e.g. the 0.92 m long section for beam manipulation, diagnostics and pumping, the pressure distribution inside the undulator chamber is depicted in figure 8.9. The conductance assumed is 0.04 l/s. Even with a desorption rate of $1 \cdot 10^{-12}$ mbar l/s cm^2 from the chamber walls the mean gas pressure - no stimulated desorption from beam loss or synchrotron radiation assumed - is hardly below $5 \cdot 10^{-9}$ mbar N_2 equivalent, however, sufficient not to cause harm to the superconducting acceleration structures nearby.

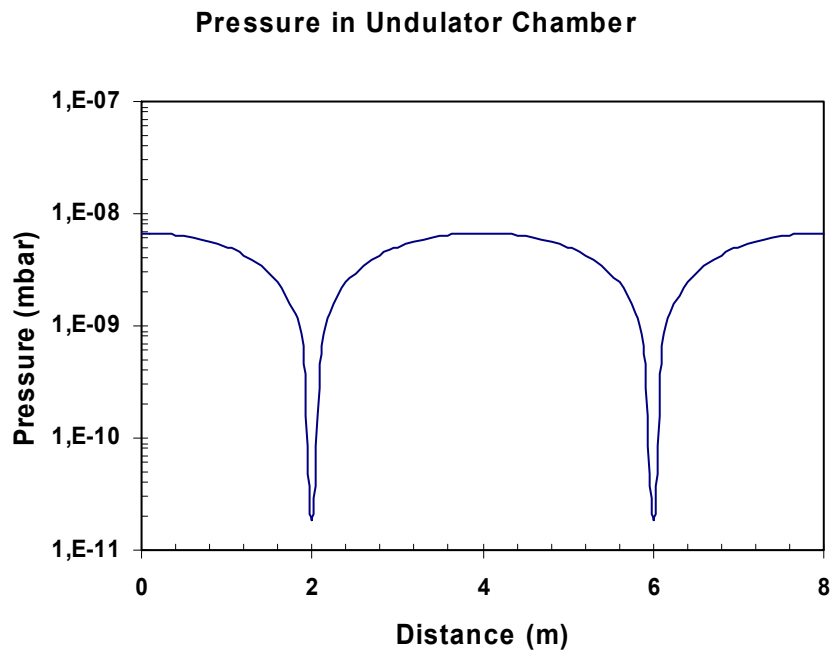


Fig. 8.9: Pressure distribution inside the undulator vacuum chamber. The desorption rate used for the calculation is $1 \cdot 10^{-12}$ mbar l/s.

8.4 Beam-Transport Elements

Beam transport between the s.c. linac structures and the undulator section is provided by room temperature bending and multipole magnets. From electron-optical considerations, a 20 to 25 mm diameter aperture is sufficient to guide the beam to the undulators. This gives the possibility for a technical and cost saving solution of identical cross sections for the laminated bending and multipole magnets. Thus a 25 mm good field radius in all beam transport elements is adopted. Table 8.4 gives a list of elements needed for beam transport.

Table 8.4: List of beam transport elements in the linac. The locations refer to BC - bunch compressor, ARC - 180-degree bending section, EXTRACT - beam extraction, and COL - collimation section. The beam energy at these positions is listed as well as the element's length, vertical aperture, and field strength.

Location	Energy (GeV)	Type	No.	Length (m)	Full gap, aperture dia. (mm)	B (T), k (1/m) or k_2 (1/m ²)
BC1	0.22	RBend	2	0.4	30	0.55
		Rbend	2	0.4	30	0.275
		Rbend	2	0.4	30	0.165
		Quad	4	0.2	40	5
BC2	0.75	Rbend	4	0.4	30	1.0
		Rbend	2	0.4	30	0.5
		Rbend	2	0.4	30	0.3
		Quad	6	0.2	40	4
ARC	0.75	Rbend	8	0.5	30	1.3
		Rbend	4	1.0	30	1.3
		Quad	30	0.3	40	6
		Sextup	16	0.2	40	250
EXTRACT1	1.02	Rbend	1	1.5	30	0.08
		Rbend	1	2.5	30	0.008
		Rbend	1	3.0	30	0.08
		Quad	11	0.3	40	3
COL 1	1.02	Rbend	2	0.4	30	0.4
		Quad	13	0.3	40	5
EXTRACT 2	2.3	Rbend	1	1.5	30	0.16
		Rbend	1	2.5	30	0.016
		Rbend	1	3.0	30	0.16
		Quad	11	0.3	40	3
COL 2	2.3	Rbend	2	0.4	30	0.85
		Quad	13	0.2	40	5
COL 3	2.3	Rbend	2	0.4	30	0.85
		Quad	13	0.2	40	5

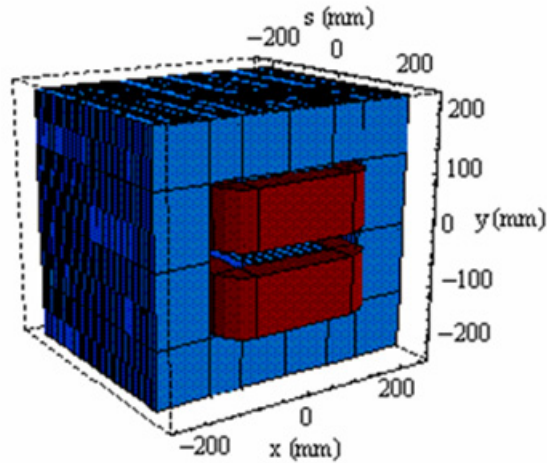
8.4.1 Conventional Magnet Designs

For beam transport in the linac 155 laminated magnets are required. The different elements are listed in table 8.5. All magnet types are of the same cross section but of different length. Thus nine individual magnet types are to be produced. All elements are laminated for economical reasons. The laminations will be backlack-isolated which has the advantage that the yokes are glued, minimizing geometrical distortions as there are no welds needed for clamping and fixing the iron. Dipole magnets are of straight box-type H-configuration while the quadrupoles are of the “figure 8 type”. There will be exchangeable spacers in the vertical dimension to allow for diagnostics ports to be installed wherever necessary avoiding collisions with the vacuum installations and with a fixed return yoke. In the arc no lumped steering coils will be installed, x- and y-steering action will be integrated into the sextupoles which are equipped with two additional coils per pole. These coils can be connected to produce a horizontal, a vertical or a skew quadrupole field as needed. In tables 8.6 to 8.8 the main layout parameters of (one of each length) the bending, the quadrupole, and the sextupole magnets are listed together with a 3-D plot of the model as was used in the RADIA code [3].

Table 8.5: Magnet types to be used for beam transport in the linac.

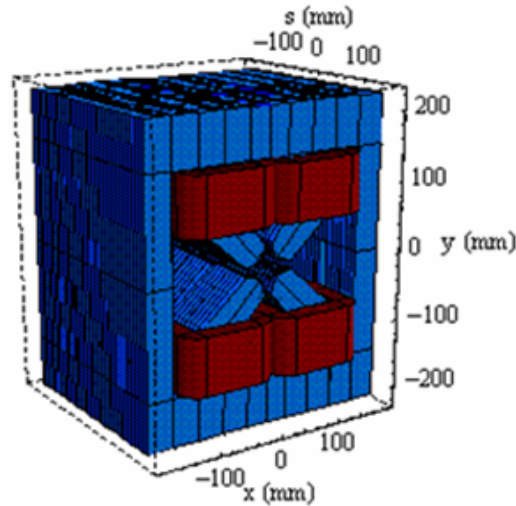
	Length (m)	No. of magnets
Dipole	0.4	20
	0.5	8
	1.0	4
	1.5	2
	2.5	2
	3.0	2
Quadrupole	0.2	36
	0.3	65
Sextupole	0.2	16

Table 8.6: Geometry and parameters of the generic layout of the FEL bending magnets. Data refer to the 0.5 m long-box-type bends in the arc.



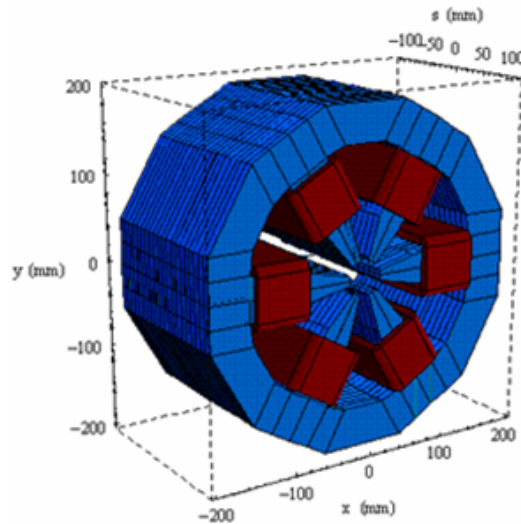
Dipole short	Symbol	Value	Unit	Remark
Field	B	1.3000	T	
Mech. length	L	0.500	m	
Eff. mag. Length	l	0.524	m	
Gapheight	g	0.030	m	
Ampere-Wdgs	I·N	15518	A Wdgs	
No. of windings	N	80		
Current	I	194	A	
Current density	j	6.8	A/mm ²	
Conductor dimension		7 x 7, Ø 5	mm	
Cooling requirement		4.2	l/min.	per magnet
Conductor cross section		29	mm ²	
Temperature increase	ΔT	25	K	
Water pressure	p	7.1	bar	
Cooling circuits		8		
Mean conductor length		1.50	m	per coil
Total conductor length		124	m	all coils
Resistance	R	0.154	Ω	per magnet
Voltage	U	30	V	per magnet
Power	P	5790	W	per magnet
Inductance	L	90	mH	per magnet

Table 8.7: Geometry and parameters of the generic layout of the FEL quadrupole magnets.



Quadrupole FEL	Symbol	Value	Unit	Remark
$k \cdot L$	$k \cdot L$	1.5	1/m	
k	k	5.000	1/m ²	
Gradient	g	38	T/m	
Mech. length	L	0.3	m	
Eff. mag. length	l	0.32	m	
Aperture radius	r	0.02	m	
Ampere*Windings	$N \cdot I$	6101	A Wdgs	
No of windings	N	60		per coil
Current	I	102	A	
Current density	j	5.2	A/mm ²	
Poletip field	B_0	0.767	T]	
Conductor dimension		5.5 x 5.5, \varnothing 3.5	mm	
Cooling requirement		1.4	l/min.	per magnet
Conductor cross section		20	mm ²	rectangular wire
Temperature increase	ΔT	20	K	
Water pressure	p	7.1	bar	
No. of cooling circuits	n	8		
Pressure per circuit	p	7.15	bar	
Mean conductor length		0.82	m	per winding
Conductor length		52	m	per coil
Resistance	R	0.188	Ω	per magnet
Voltage	U	19	V	per magnet
Power	P	1944	W	per magnet
Inductance	L	2.08	mH	per magnet

Table 8.8: Geometry and parameters of the generic layout of the FEL sextupole magnets.



Sextupole FEL	Symbol	Value	Unit	Remark
Gradient	S	250	T/m ²	
Mech. length	l	0.20	m	
Eff. mag. length	l	0.21	m	
Aperture radius	r	0.020	m	
Ampere*Windings	N·I	265	A Wdgs	
No. of windings	N	60	per coil	
Current	I	4.0	A	
Current density	j	0.8	A/mm ²	
Poletip field	B _o	0.05	T	
Conductor dimension		2.5 x 2.5	mm	massive conductor
Cooling requirements				indirect cooling
Conductor cross section		5.0	mm ²	
Temperature increase	ΔT	10	K	
Mean conductor length		0.62	m	per coil
Total conductor length		40	m	per coil
Resistance	R	814	mΩ	per magnet
Voltage	U	3.60	V	per magnet
Power	P	16	W	per magnet
Inductance	L	32	MH	per magnet

8.4.2 Power Converters

Most magnets are powered by high-stability DC-switch-mode power converters. Their ratings and number are listed in table 8.9.

The requirements for the magnet power supplies are moderate. All technical characteristics such as current, voltage, accuracy, and ramp characteristics are within the usual requirements of accelerator facilities. No technological limits are surpassed, and there is no need for new developments and no risk. Standard techniques will be used with an analogue interface for set-point and read-backs and digital interface for command settings and status information. There will be only one type for analogue and digital interface, identical for all power supplies. The high bandwidth-regulation loop is an integral part of each power supply. If necessary an external digital regulation loop can be added with a lower bandwidth via interface card. This concept reduces the costs of signal-processing components to a minimum.

For power supplies with a rated power in excess to 1000 W a switch mode circuitry will be the best technical and economical solution. Most bipolar steerer power supplies (less than 100 W) can be realized with linear series transistors.

Table 8.9: Power supplies for beam transport elements.

Magnet type	I (A)	U (V)	L (mH)	P (kW)	No of. PS
Triplett	100	20	2	2	3
ARC_Rbend short	200	240.0	720	48.0	1
ARC_Rbend long	200	200.0	704	40.0	1
ARC_Quad	55	80.0	16.6	4.4	2
ARC_Quad	55	40.0	8.3	2.2	1
ARC_Quad	55	20.0	4.2	1.1	3
ARC_Quad	55	10.0	2.1	0.5	4
ARC_Sextupol	4	30.0	2040	0.1	2
ARC_Steerer horiz.	4	2.5		0.01	16
ARC_Steerer vertical	8	2.5		0.02	16
BC1_Rbend	100	25.0	146	2.5	3
BC1_Quad	15	2.0	1.4	0.03	4
BC2_Rbend	150	20.0	73	3.0	4
BC2_Quad	35	7.5	1.4	0.2	6
EX1_Bend 1	15	7.5	262	0.1	1
EX1_Bend 2	15	10.0	433	0.1	1

Power Supplies for Beam Transport Elements (continued)					
Magnet type	I (A)	U (V)	L (mH)	P (kW)	No of. PS
EX1_Bend 3	15	10.0	520	0.2	1
EX1_Quad	30	5.0	2.0	0.2	11
EX2_Bend 1	30	12.5	262	0.3	1
EX2_Bend 2	30	17.5	433	0.5	1
EX2_Bend 3	30	20.0	520	0.6	1
EX2_Quad	60	12.0	2.0	0.7	11
COL1_Rbend	60	10.0	73	0.6	1
COL1_Quad	50	10.0	2.0	0.5	13
COL2_Rbend	150	20.0	73	3.0	1
COL2_Quad	100	15.0	1.5	1.5	13
COL3_Rbend	150	20.0	73	3.0	1
COL3_Quad	100	15.0	1.4	1.5	13
LE_Steerer	4	2.5	-	0.01	18
LE_Quad	50	5.0	1.0	1.5	4
LE_D_Bend	60	10	2.0	0.6	6
LE_FA_Quad	50	5.0	1.0	0.3	3
ME_Steerer	4	2.5	-	0.01	24
ME_Quad	50	5.0	1.0	0.3	6
ME_D_Bend	120	20	2.0	2.4	9
ME_FA_Quad	50	5.0	1.0	0.3	6
HE_Steerer	4	2.5	-	0.01	36
HE_Quad	50	5.0	1.0	0.3	8
HE_D_Bend	120	20	2.0	2.4	12
HE_FA_Quad	50	5.0	1.0	0.3	7
Linac sc Quads	50	1.0	360	0.05	18
Linac sc Steerer	100	1.0	15	0.1	18

References

- [1] G. Blokesch, M. Negrazus, K. Wille, *Nucl. Instrum. and Meth. A* **338**/2-3 (1994) 151.
- [2] E. Efstathiadis, Y. Y. Lee, J.-L. Mi, C. Pai, J. M. Paley, B. L. Roberts, R. T. Sanders, Y. K. Semertzidis, D. S. Warburton, *Nucl. Instrum. and Meth. A* **496** (2003) 8.
- [3] O. Chubar, P. Elleaume, J. Chavanne, *J. Synchrotron Rad.* **5** (1998) 481.

9 Undulators for the BESSY Soft X-Ray FEL

The BESSY Soft X-ray FEL user facility will provide light in the energy range from 24 to 1000 eV. Variable polarization of the light will be a key issue that can be controlled by the user according to their experimental needs. Right and left handed circular as well as linear polarization at arbitrary angles will be produced by the undulators.

For the three FEL lines making use of the cascaded HGHG-FEL schemes, different undulators (modulators, radiators and final amplifiers) are needed (table 9.1). The FEL lines are labeled according to the photon energy range they are designed for: Low-Energy, Medium-Energy and High-Energy-FEL (LE-, ME-, HE-FEL).

The gap of the undulators will be variable in order to tune the photon energy. This requires a separated function scheme for focusing. A FODO lattice is superimposed onto the undulator structure with the quadrupole magnets located at the intersections between the undulator modules.

The modulators and radiators of the first stages are realized as planar pure permanent magnet undulators. The polarization is controlled in the last radiator and the final amplifier. A new magnetic design (modified APPLE II) has been chosen for these sections.

The requirements for FEL undulators are slightly different from the requirements for undulators at third generation light sources. Small phase errors, essential for a high brightness at high undulator harmonics are less important since harmonics higher than $n = 5$ will not be used. On the other hand for an FEL undulator the tolerances on trajectory errors within each segment and between segments are very tight as sufficient overlap between the electron and the photon beam has to be ensured.

The technique to optimize fields of planar undulators (shimming) has been developed over the last ten years and these devices now operate close to the performance of an ideal undulator. Their spectral output in storage rings is limited only by beam emittance and energy spread. The field optimization of APPLE II devices, however, is more challenging but special shimming techniques guarantee excellent field quality for these devices as well.

Each undulator is composed of modules with lengths ranging from 1.6 m to 3.9 m. The phase between electron and photon beam has to be matched between the modules with a phase shifter.

Because the planar undulators are short and nearly ideal, focus is on the last radiators and the long final amplifier in the rest of this chapter. These are elliptical devices.

Table 9.1: Undulator parameters for the BESSY FELs. The undulator lengths do not include the intersections.

FEL		LE-FEL	ME-FEL	HE-FEL	Unit
Photon energy range		24 - 120	100 - 600	500 - 1000	eV
1. Stage	Modulator λ_u	80	122	122	mm
	Modular length	1.600	2.196	2.196	m
	Radiator λ_u	62	92	92	mm
	Radiator length	3.472	3.680	3.680	m
2. Stage	Modulator λ_u	62	92	92	mm
	Modular length	1.612	2.024	2.024	m
	Radiator λ_u	50	70	70	mm
	Radiator length	3.450	2 x 3.360	2 x 2.730	m
3. Stage	Modulator λ_u		70	70	mm
	Modular length		2.100	2.100	m
	Radiator λ_u		50	50	mm
	Radiator length		3 x 3.40	3 x 2.8	m
4. Stage	Modulator λ_u			50	mm
	Modular length			3.450	m
	Radiator λ_u			28.5	mm
	Radiator length			2 x 3.135	m
Fin. of Amp.	Fin. of amp. λ_u	50	50	28.5	mm
	Fin. of amp. length	3 x 2.80	5 x 3.450	5 x 3.135	m

9.1 Magnetic Design

9.1.1 Choice of the Undulator Design

The magnetic structure of undulators can be divided into three categories: electromagnets, superconducting magnets and permanent magnet devices. Electromagnets are mechanically simple and the price is relatively low. They offer the possibility of fast field variation and are suitable for rapid helicity switching. Electromagnetic elliptical devices are operated successfully in many laboratories [1 - 4]. The achievable fields are, however, rather low, in particular for small period lengths and, therefore, they are not usable for the BESSY Soft X-Ray FEL.

The superconducting technology is well developed for static devices like wavelength shifters or multipole wigglers [5 - 7]. Short period superconducting undulators have been

built [8, 9]. The technology is promising since the fields are expected to be a factor of 2 higher compared to permanent magnet devices using NbTi at 4 K. The use of the more complicated NbSn technology increases the achievable field by another factor of 1.5 - 2.

However, the superconducting technology for undulators is not yet mature and many questions are still open like hysteresis effects, persistent currents etc. which are of utmost importance for devices with variable fields. In undulators for an FEL it is essential that the field integrals stay constant for variable gap or polarization. This has not yet been achieved in superconducting devices where the field integrals are dependent on the history of the current settings. Development is, however, closely viewed for possible future upgrade possibilities.

The only alternative for the BESSY undulators are permanent magnet devices. Planar devices can be built as pure permanent magnets [10] or as hybrids including iron poles [11]. The modulators and radiators (excluding the last radiator) will be planar pure permanent magnet devices. Linearly polarized light can in principle be converted to circularly polarized light using quarter wave plates. However, in the energy regime covered with the three BESSY FELs no quarter wave plates are available and therefore, the desired polarization has to be produced within the last radiator and the final amplifier.

Various types of planar helical / elliptical permanent magnet devices have been built [12 - 14]. The APPLE II design [15] provides the highest magnetic fields and has become the standard device in many laboratories. BESSY has built and already installed five of these devices with a total magnetic length of 19 m [16] in the 3rd generation storage ring light source BESSY II. This design provides a flexible polarization as demanded for the FELs.

The principle of their magnetic structure is sketched in figure 9.1. The device consists of four rows of magnets. By moving two diagonal rows, the ratio between horizontal and vertical fields can be varied and thus the polarization can be controlled. The relative phase between the horizontal and vertical fields for various row positions is drawn in figure 9.2a. For a parallel motion the phase is 90° and for antiparallel motion the phase is 0° resulting in helical / elliptical and linear polarization, respectively. In the latter case the tilt angle of the linear polarization can be varied continuously with an appropriate row phase setting (figure 9.2b).

The field of a conventional APPLE II undulator is too low to cover the demanded energy range of the BESSY Soft X-ray FEL. An in-vacuum APPLE II device provides higher fields. However, at the time of writing there is no mature design for an in-vacuum APPLE II undulator.

Therefore, the last radiators and the final amplifier of the three FEL undulators (LE-, ME- and HE-FEL) will be realized in a new (in air) magnetic design (modified APPLE II design) which provides higher fields at the expense of a reduced access from the side.

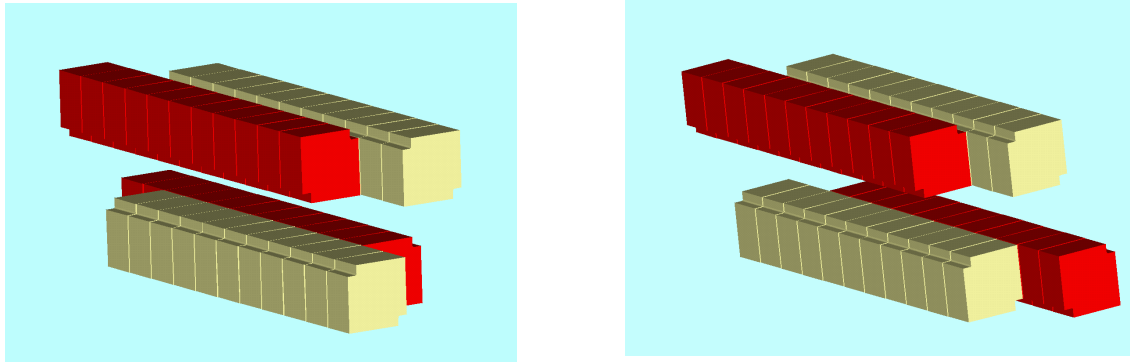


Fig. 9.1: APPLE II structure: Parallel mode (left) and antiparallel mode (right).

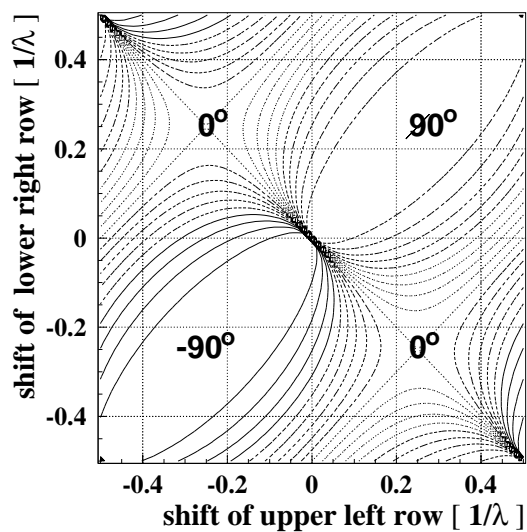


Fig. 9.2a: Relative phase of horizontal and vertical magnetic fields for various shifts of the magnet rows.

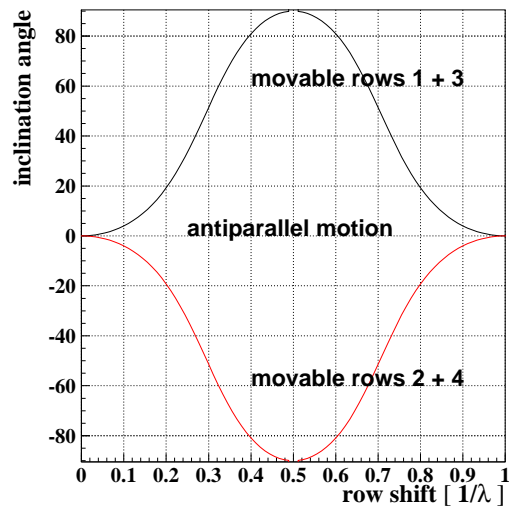


Fig. 9.2b: Inclination angle of the polarization vector in the antiparallel mode.

9.1.2 The Modified APPLE II Design

Whereas the electron beam requires a large horizontal aperture in a storage-ring undulator, in an FEL undulator a circular vacuum chamber can be used. This provides the flexibility to fill part of the horizontally available space with magnetic material [17].

Figure 9.3 shows the new magnetic structure in comparison with an APPLE II device. Both designs provide the same space for a circular vacuum pipe. In the context of the new design the terminus gap for the smallest vertical distance between the upper and lower beam will be used in the following. In this sense a gap of 5.4 mm is compatible with a beam pipe of 10 mm diameter. Three constraints determine the minimum gap of 5.4 mm: i) The magnetic field will be measured from the side. The minimum gap provides enough space for a commercial probe with a height of 2.4 mm. ii) The vacuum chamber has to be supported from the side. iii) Thermoluminescent detectors for radiation detection with dimensions of $3 \times 3 \times 1 \text{ mm}^3$ will be placed close to the vacuum chamber. Two types of magnets are used in the magnetic design: longitudinally magnetized blocks, A – magnets, and vertically magnetized blocks, B – magnets.

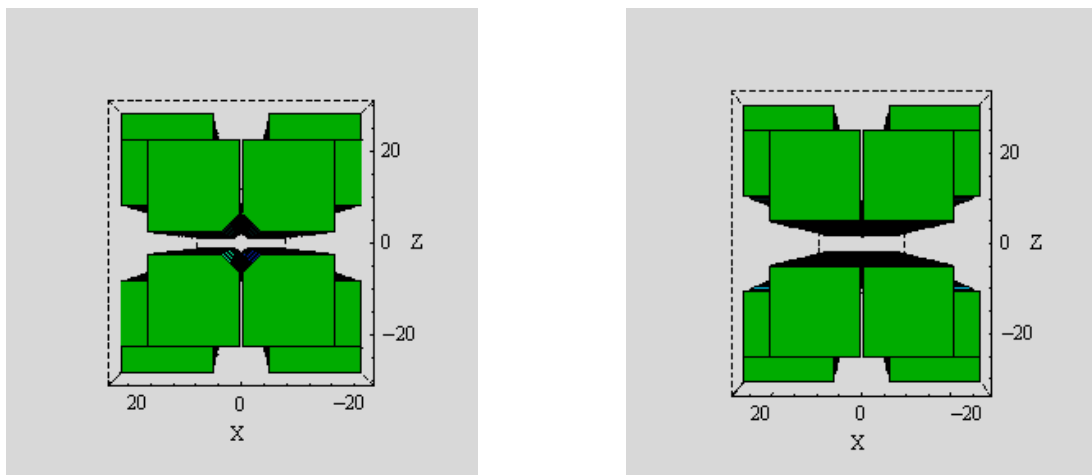


Fig. 9.3: New magnet design (left) and APPLE II design (right), units in mm. The segmentation of the magnets in the figures is required for the simulations. In reality the magnet blocks are produced as single pieces.

The magnetic field of the new design is significantly higher as compared to the APPLE II design. It can be further enhanced if the magnetization direction of the B-magnets is tilted. The fields of the new and the APPLE II design are plotted in figure 9.4. Data are given for tilt angles of the magnetization of 0° , 15° , 30° , 45° , 60° , 75° , 90° . The abscissa represents the shift at which the device delivers circularly polarized light.

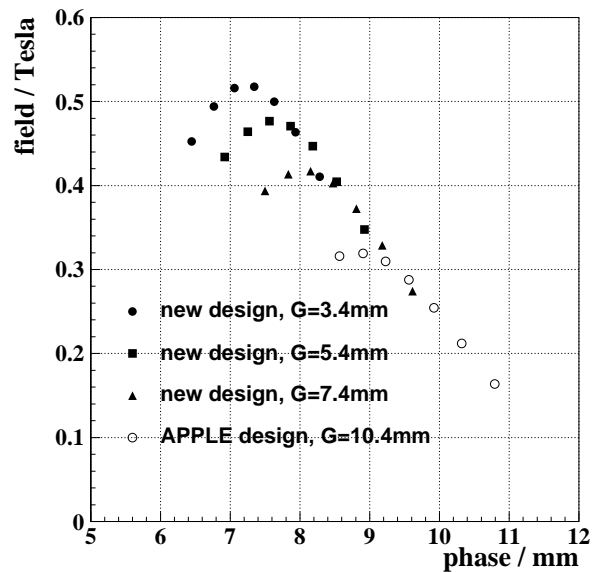


Fig. 9.4: Fields of the new undulator design as compared to the field of an APPLE II. The data are given for tilt angles of 0° , 15° , 30° , 45° , 60° , 75° , 90° respectively.

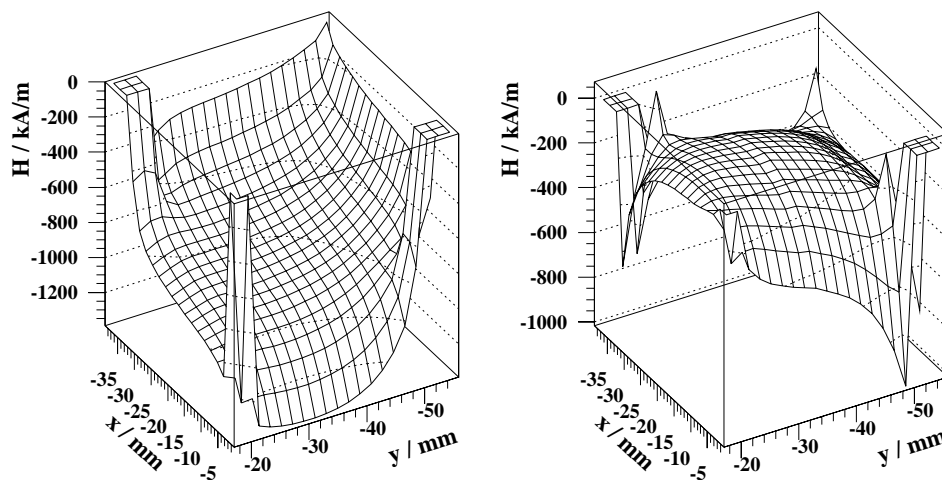


Fig. 9.5: Maximum magnetic field H in A-magnets (left) and B-magnets (right) for the ME- and LE-FEL. The absolute values for the HE-FEL are lower. The fields have been set to zero at the cutouts and the chamfer.

Obviously, the new design provides the highest fields at a tilt angle of about 45° whereas the APPLE II has its optimum close to 0° . It is interesting to note that the tilt angle of the APPLE I [18], the predecessor of the APPLE II, was 45° .

The curves in figure 9.4 have been calculated for the same magnetic material. The demagnetizing fields (figure 9.5) are higher in the new design by about 3 KGauss. This requires more stable material. A higher coercive force is combined with a lower remanent field and about 6% in remanence compared to the APPLE II is sacrificed. Taking this difference into account a gain of about a factor of 1.4 (circular mode) is reached with the new design using a gap of $g = 5.4$ mm.

9.1.3 Selection of Magnetic Material for the Undulators

Several authors have reported radiation damage of permanent magnet materials used in undulators at synchrotron radiation facilities [19, 20]. Due to the large number of accelerated particles of the FEL linac and the delivered high beam power - up to 50 kW in our case - it is essential to study loss scenarios and radiation damage for the FEL undulators. Although permanent magnets from SmCo show a significantly better resistance against radiation damage, it has been decided to use NdFeB magnets for the undulators of the BESSY FEL. The reason is the higher remanence of the NdFeB-magnets that is needed for the desired deflection parameter K of the undulators. Systematic studies for different grades and geometries of NdFeB magnets and for different beam qualities have been carried out at the European Synchrotron Radiation Facility (ESRF) [21] and at the Pohang Accelerator Laboratory (POSTECH) [22]. A detailed analysis of the results can be found in [23]. From these findings one can conclude that for most magnet types the radiation damage depends mainly on the reduced dose deposited by high-energy electrons (> 20 MeV). The effects of photons and electrons with lower energies seem to be significantly smaller. This means that not only the measured dose characterizes the demagnetization but also the beam quality.

In order to derive limits for the acceptable number of electrons that hit the undulator chamber, Monte-Carlo-simulations using GEANT3 [24] have been done for the geometry considered for the BESSY FEL. Figure 9.6a shows the undulator magnets and the surrounding vacuum chamber schematically. The magnets are divided into cells for the dose scoring. Figure 9.6b shows the dose profile. The dose is averaged over the magnet volume, the error bars correspond to the spread of the dose in the scoring cells. The simulation assumes a Gaussian beam that hits the chamber at an angle of 1 mrad. The first magnets receive a lower dose due to the still developing shower. The highest dose is found in the fifth magnet, where the shower is fully developed. The peak value of the dose is about 7000 mGy per nC beam charge. This scenario reflects the worst case. For a more realistic case, where the beam is smeared over the chamber wall, the dose values are more than an order of magnitude lower. From these simulations and assuming a linear demagnetization with the dose, we derive a limit for the maximum tolerable beam losses in the vacuum chamber of the undulator. With an accepted demagnetization of 10^{-4} and an assumed

reduced dose of 70 kGy [23] for a 1% demagnetization (figure 9.7) the acceptable beam loss is 300 nC.

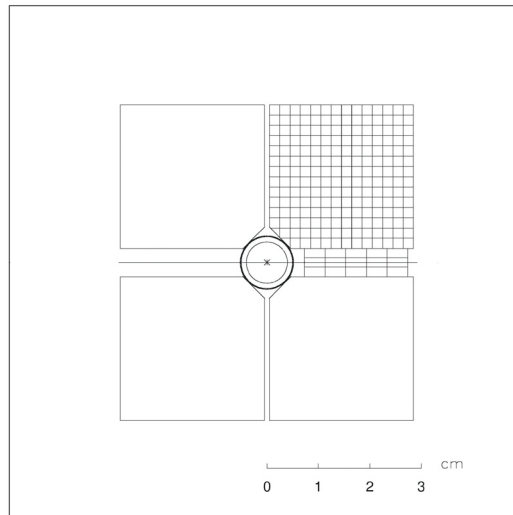


Fig. 9.6a: Schematic view of the undulator for the LE-FEL. The upper right magnet is divided into cells for the dose scoring. The volume in the gap to the right of the chamber is a scoring phantom to monitor the dose that can be measured with dosimeters.

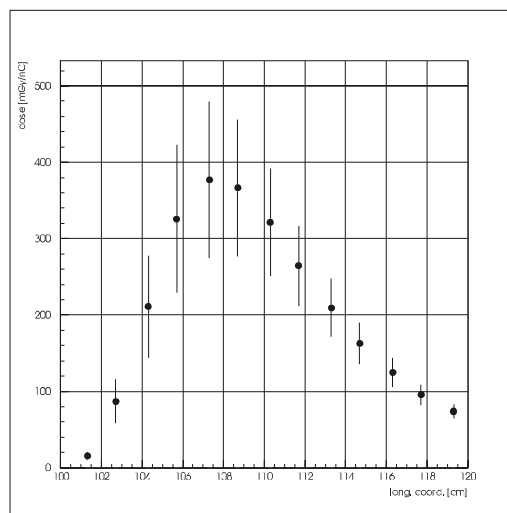


Fig. 9.6b: The average dose in mGy/nC received by each magnet.

As a result of these considerations it is evident that a collimator system to protect the undulator magnets must be included in the FEL design.

The 1%-demagnetization dose of 70 kGy (reduced dose) corresponds to the magnet material VACODYM396 (Nd-Dy-Fe-B) with a remanence of $B_r = 1.15$ T and a coercivity of $H_c = 2150$ kA/m. For the BESSY FELs the following grades for the magnets were chosen: i) planar devices: $B_r = 1.20 - 1.26$ T, $H_{cj} = 1910$ kA/m; ii) elliptical devices: $B_r = 1.13-1.18$ T, $H_{cj} = 2565$ kA/m. Since these parameters are similar to VACODYM396 a value of 700 Gy for the critical dose was adopted.

At TTF an undulator module has been remeasured after three years of operation [25]. An accumulated dose of 12 kGy did not demagnetize the structure within the measurement accuracy of $2 \cdot 10^{-4}$. The reduced dose is at least a factor of three lower and is of the same order of magnitude as the critical dose of 700 Gray.

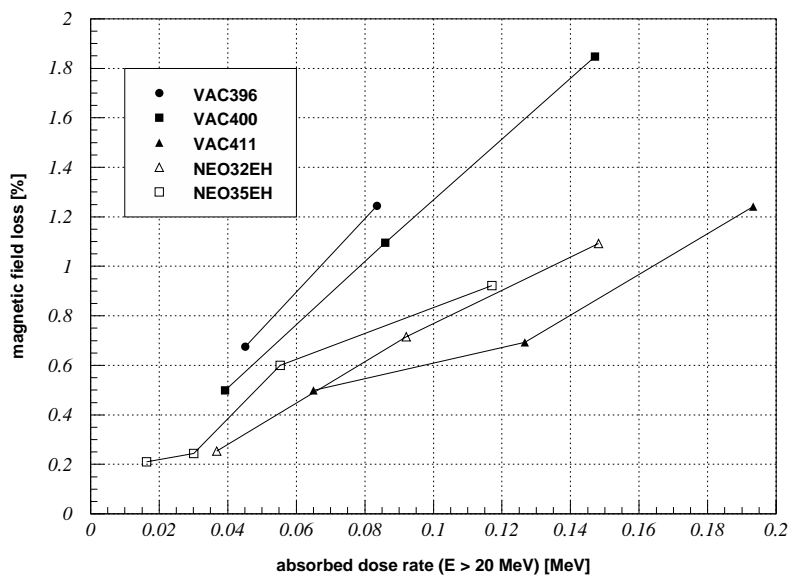


Fig. 9.7: The effect of radiation as a function of the reduced dose on different magnetic materials, taken from reference [23].

9.1.4 Parameters of the Undulators

The fields of permanent magnet undulators can be parameterized with the following equation:

$$B = a \exp(b (\text{gap} / \lambda_u) + c (\text{gap} / \lambda_u)^2) \quad (9.1)$$

Elleau [26] gives numbers for the variables a , b , c for various planar and helical undulator designs. For the modified APPLE II design the constants a , b , c for the different

modes of polarization were evaluated using the 3D code RADIA [27]. The following parameters have been used: remanence = 1.13 and 1.19 Tesla for the A- and B-magnets, respectively; block dimensions = $40 \times 40 \text{ mm}^2$; minimum vertical distance = 5.4 mm. The constants a,b,c have been fitted within a region of $20 \text{ mm} < \lambda_u < 50 \text{ mm}$ for a constant gap of 5.4 mm (table 9.2).

Table 9.2: Parametrization of the magnetic field of the new design.

	Hor. lin. pol.	Vert. lin pol.	Circ. pol.	Lin. pol. tilted
a	2.481	2.035	2.209	1.569
b	-6.258	-6.576	-6.400	-6.392
c	0.112	0.602	0.285	0.231

The basic parameter for the undulator design is the magnetic gap. The minimum vacuum aperture on the other hand was selected as a compromise from beam stability (wake-fields) and practical considerations (vacuum pressure) etc. A beam stay clear aperture of 8 mm diameter has been adopted for the vacuum chamber with a total vertical height of the chamber of 9 mm. This number defines the minimum magnetic gap between the 45° chamfers to be ≥ 10 mm. The shimming of the undulators will be done by transverse movement of the magnets. This requires additional space of 0.2 mm at both sides which results in a minimum nominal gap between the diagonal magnets of 10.4 mm.

The nominal horizontal gap between the magnet rows has been chosen to be 1.0 mm. Two rectangular cutouts per block for clamping are arranged for.

The two types of magnets used in the magnetic design: (A- and B – magnets) will be formed under high pressure in a die in order to control the field inhomogeneities. The A-magnets can not be pressed transversely due to the high aspect ratio. This results in a lower remanence compared to the B-magnets. For the BESSY APPLE II devices remanence values of 1.20 T and 1.26 T have been chosen for the A- and B-magnets, respectively. The corresponding coercive force of $H_{cj} = -1910 \text{ kA/m}$ is safe for a maximum magnetic field of $H = -1300 \text{ kA/m}$.

For the new design a higher coercive force is required which implies smaller remanences ($H_{cj} = -2465 \text{ kA/m}$ and $B_r = 1.13 \text{ T}$ (1.18 T) for A- (B-) magnets). This magnet grade guarantees that all parts of the A-magnets are well above the demagnetization knee. The B-magnets are exposed to smaller demagnetizing fields and this grade provides even higher safety for them. This is important because a local demagnetization of B-magnets would immediately cause trajectory errors.

The transverse block dimensions of 27.5 mm (HE-FEL) and 37.9 mm (ME- and LE-FEL) provide 98% of the maximum achievable field. For mechanical simplicity square magnet blocks have been chosen. In the case of the A-magnets this doubles the number of potential block orientations during assembly.

Figure 9.8 shows the fields of the devices. The vertical fields (blue) are maximum at shift=0 and decrease for larger shifts. At the same time the horizontal fields (red) increase. In the parallel mode the effective field decreases continuously for shift = 0 to shift = $\lambda_u/2$. For the antiparallel mode a pronounced minimum of the effective field shows up at an inclination angle of about 45°.

The effective fields (table 9.3) define the tuning ranges of the photon energy. They are related to the Fourier components B_n of the field via

$$\tilde{B} = \sqrt{\sum_{n=1} \frac{B_n^2}{n^2}} . \quad (9.2)$$

Table 9.3: Effective fields of the FEL undulators. The values of the new design are based on 6% less remanent material compared to the old design to account for stronger reversing fields. B-anti is the minimum field in the antiparallel mode.

	HE-FEL new design	HE-FEL APPLE II	ME-,LE-FEL new design	ME-, LE-FEL APPLE II
B-hor (T)	0.5891	0.4027	1.0015	0.8146
B-circ (T)	0.6544	0.4715	1.1046	0.8942
B-vert (T)	0.7530	0.5988	1.2586	1.0106
B-anti (T)	0.4647	0.3349	0.7847	0.6347

The energy ranges of the three devices overlap except for a small regime between 120 and 132 eV in the tilted linear polarization mode for the ME-FEL (table 9.4).

Table 9.4: Tuning ranges of the three final amplifier undulators via gap motion.

Polarization	LE-FEL	ME-FEL	HE-FEL
	energy range / eV		
Horizontal linear	11-120	56-600	591-1000
Circular	14-120	71-600	705-1000
Vertical linear	16-120	85-600	795-1000
Linear with variable angle	25-120	132-600	1000

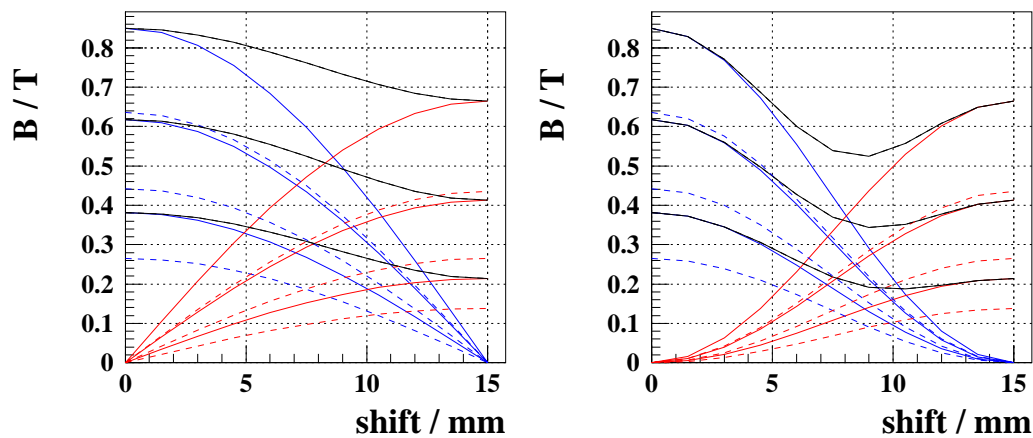


Fig. 9.8a: Vertical (blue), horizontal (red), and effective (black) fields of the HE-FEL undulator. Left: Parallel mode. Right: Antiparallel mode. The data are plotted for gaps of 5.4, 9.4, 14 mm (new design, solid line) and for gaps of 10.4, 14, 19 mm (APPLE II design, dashed line).

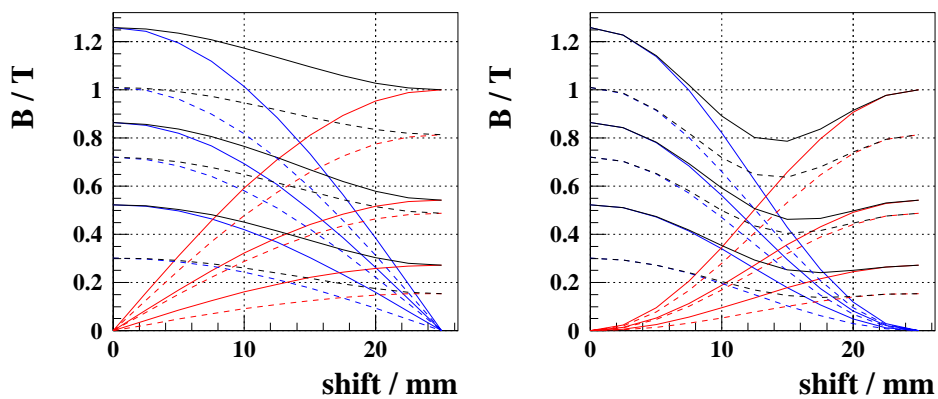


Fig. 9.8b: Vertical (blue), horizontal (red), and effective (black) fields of the ME-FEL and LE-FEL. Left: parallel mode, right: antiparallel mode. The data are plotted for gaps of 5.4, 12, 20 mm (new design, solid line) and for gaps of 10.4, 16, 30 mm (APPLE II design, dashed line).

9.1.5 The Endpole Structure

The undulator ends have to be designed such that the first and second field integrals are small for all gap and row shifts. Assuming a magnet block permeability of $\mu=1$ a kick

and displacement free trajectory in a pure permanent magnet undulator can be achieved with an endpole excitation pattern of $1/4, 3/4, 1$ [28]. The permeability of rare earth cobalt magnets is typically 1.06 and 1.17 parallel and perpendicular to the easy axis. This leads to gap and row shift dependent field integrals. Within a period the terms cancel for an ideal undulator and only the endpoles contribute.

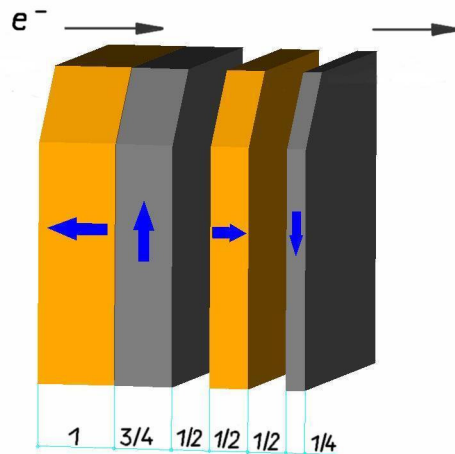


Fig. 9.9: Endpole design of the modified APPLE II devices. The end of one row is drawn. The magnetization direction of the thin magnet is identical for the upstream and downstream endpoles (symmetric design).

From symmetry considerations it can be shown that the symmetric field component produces residual field integrals [29]. The field integral of the perpendicular component is zero. Appropriate endpole designs can minimize the effects of the symmetric component [16, 30].

The FEL undulators will have a symmetric magnet structure. Scaling the BESSY endpole design (figure 9.9) to the dimensions of the FEL undulators we obtain row shift dependent vertical field integral variations of 0.01 Tmm for the HE-FEL and 0.03 Tmm for the ME- and LE-FEL (figure 9.10). Additional shift dependent terms originating from the geometric tolerances of the periodic part are of the same order of magnitude and further optimization of the end structure is not necessary. The compensation of the shift dependent terms is described in chapter 9.4.

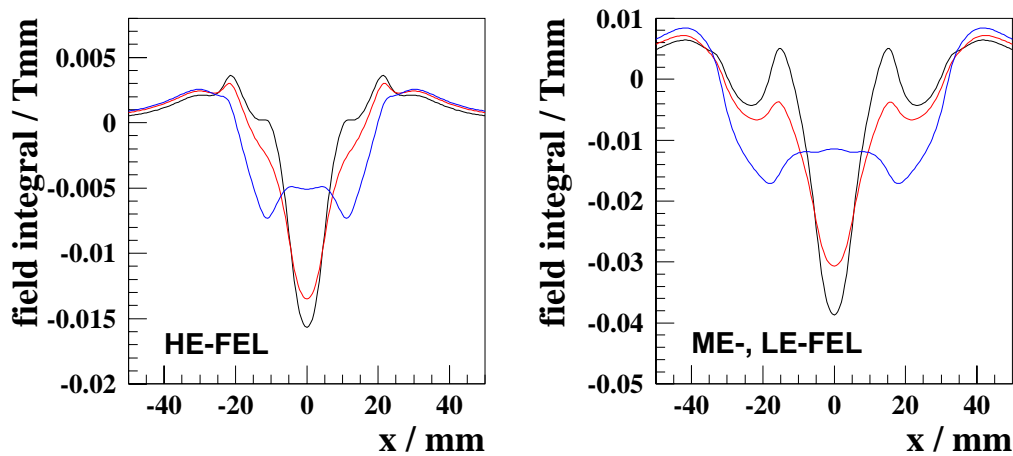


Fig. 9.10: Field integrals at lowest gap for various row shifts: shift = 0 (black), $\lambda_u/4$ (red) and $\lambda_u/2$ (blue) for the three undulators.

9.2. Transverse Field Distribution and Focusing

The transverse field distribution is important in two aspects:

- 1) The effective fields have to be homogeneous within the width of the electron beam in order to fulfill the resonance condition for the FEL process.
- 2) The transverse roll-off defines the focusing properties of the device.

The transverse field distribution of the helical devices deviates significantly from that of a planar device. In a planar device with wide poles the horizontal roll-off is negligible and the vertical distribution is described by $k_y = \lambda_u/2\pi$. Figure 9.11 shows the transverse field distribution of an APPLE II and of the new design. The vertical field has a minimum on the central axis which is due to a 1 mm slit between neighboring magnet rows. The horizontal field has a sharply peaked maximum.

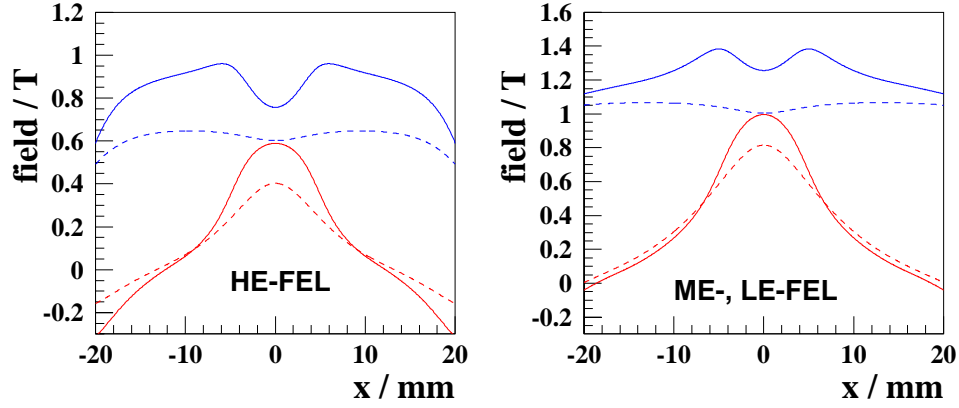


Fig. 9.11: Transverse field profiles for the HE-FEL evaluated for an APPLE II design (dashed line) and the new design (solid line). The vertical field (blue) is calculated at row shift = 0 and the horizontal field (red) at row shift = $\lambda_u/2$.

The transverse field distribution can be parameterized as follows:

$$k_{x\text{-eff}}^2 = -\frac{\partial^2 B_{\text{eff}}}{\partial x^2} / B_{\text{eff}} \quad (9.3)$$

$$B_{\text{eff}} = \sqrt{\tilde{B}_{x\text{-eff}}^2 + \tilde{B}_{y\text{-eff}}^2} \quad (9.4)$$

and similar by for the vertical plane. For Halbach fields the natural focusing is given by:

$$K_x = k_{x\text{-eff}}^2 / (2 \cdot k^2 \cdot \rho_{\text{eff}}^2) \quad (9.5)$$

$$k_{x\text{-eff}}^2 = \sum_{n=1}^{\infty} \frac{(B_{xn}^2 \cdot k_{xxn}^2)/n! + (B_{yn}^2 \cdot k_{xyn}^2)/n!}{B_{xn}^2/n! + B_{yn}^2/n!} \quad (9.6)$$

$$1/\rho_{\text{eff}} = (eB_{\text{eff}})/(\gamma mc) \quad (9.7)$$

and the effective k-values are related via

$$k_{x\text{-eff}}^2 + k_{y\text{-eff}}^2 = k^2. \quad (9.8)$$

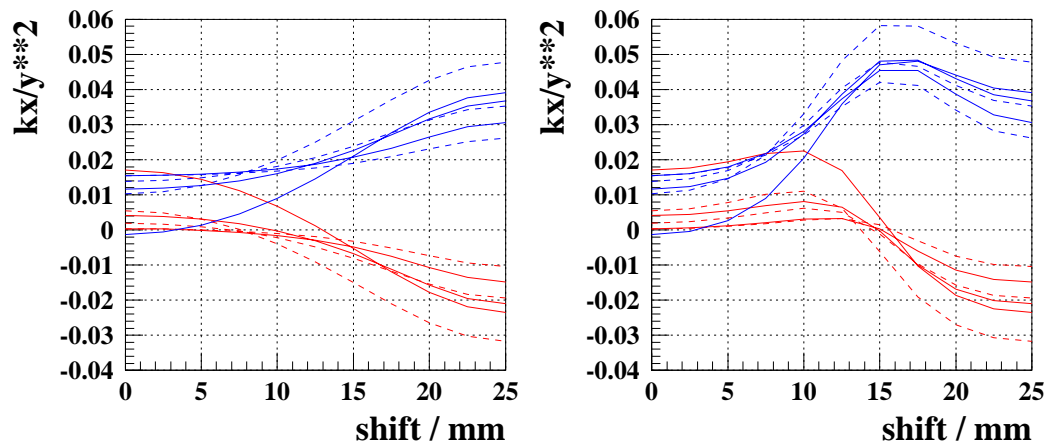


Fig. 9.12a: Horizontal (red) and vertical (blue) variation of the effective field of the HE-FEL operating in parallel (left) and antiparallel (right) mode. The data are plotted for the gaps of 5.4, 9, 14, 26 mm (new design, solid line) and 10.4, 14, 19, 31 mm (APPLE II design, dashed line).

The term k_{xyn} characterizes the horizontal variation of the n^{th} Fourier component of the vertical field (B_{yn}). In the parallel mode the fields can be expressed as Halbach fields and the equations apply. In case of antiparallel motion the vertical fields are horizontally non-symmetric and the focusing properties have to be deduced from numerical tracking.

The values $k_{x\text{-eff}}$ and $k_{y\text{-eff}}$ have been derived from RADIA simulations and are plotted in figure 9.12. The transverse roll-off of the effective field is smallest at shift = 0 mm which corresponds to a planar undulator. The roll-off in the vertical direction dominates.

For finite shift the roll-off in the horizontal as well as in the vertical direction increases. The maximum field variations within a width of ± 0.1 mm (corresponding to 2σ of the electron beam) are summarized in table 9.5.

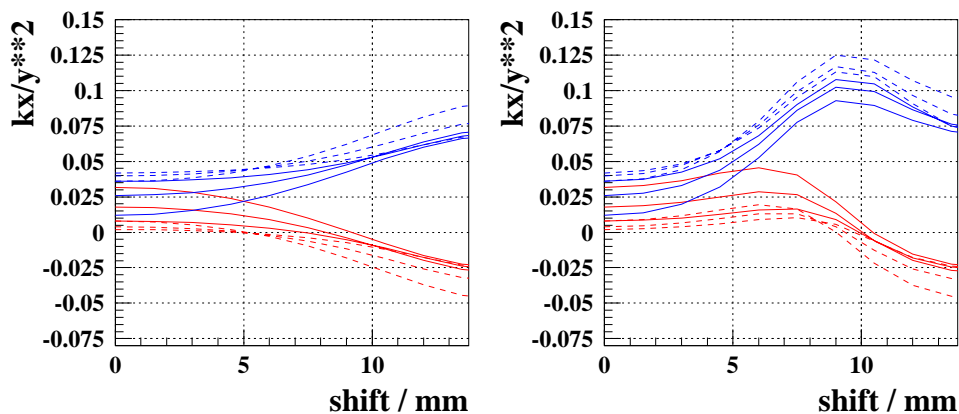


Fig. 9.12b: Horizontal (red) and vertical (blue) variation of the effective field of the ME- and LE-FEL operating in parallel (left) and antiparallel (right) mode. The data are plotted for the gaps of 5.4, 12, 20, 35 mm (new design, solid line) and 10.4, 16, 30, 50 mm (APPLE II design, dashed line).

Table 9.5: Transverse field variations.

	ME-, LE-FEL new design	HE-FEL APPLE II	ME-, LE-FEL new design	HE-FEL APPLE II
Parallel mode				
$\Delta B_{\text{eff}} / B_{\text{eff}}$ (hor.)	$-1.4 \cdot 10^{-4}$	$-2.4 \cdot 10^{-4}$	$-1.1 \cdot 10^{-4}$	$-1.6 \cdot 10^{-4}$
$\Delta B_{\text{eff}} / B_{\text{eff}}$ (vert.)	$3.8 \cdot 10^{-4}$	$4.9 \cdot 10^{-4}$	$2.0 \cdot 10^{-4}$	$2.4 \cdot 10^{-4}$
Antiparallel mode				
$\Delta B_{\text{eff}} / B_{\text{eff}}$ (hor.)	$-1.4 \cdot 10^{-4}$	$-2.4 \cdot 10^{-4}$	$-1.1 \cdot 10^{-4}$	$-1.6 \cdot 10^{-4}$
$\Delta B_{\text{eff}} / B_{\text{eff}}$ (vert.)	$5.9 \cdot 10^{-4}$	$6.9 \cdot 10^{-4}$	$2.5 \cdot 10^{-4}$	$2.9 \cdot 10^{-4}$

The strongest variations are observed for the HE-FEL in the antiparallel mode. The field homogeneity is better for the new design than for the APPLE II.

The focusing properties depend strongly on the row shift. At shift = 0 mm the devices focus mainly in the vertical direction and only to a small amount horizontally. For larger shifts a horizontal defocusing occurs whereas the vertical focusing increases.

Figure 9.13 shows the focusing properties of the undulators at smallest gap. The data for the parallel mode have been derived analytically using the equations above. For the antiparallel mode, trajectories with various initial conditions have been tracked through the undulators and a linear transfer matrix has been fitted to the results. The focusing properties are deduced from this matrix.

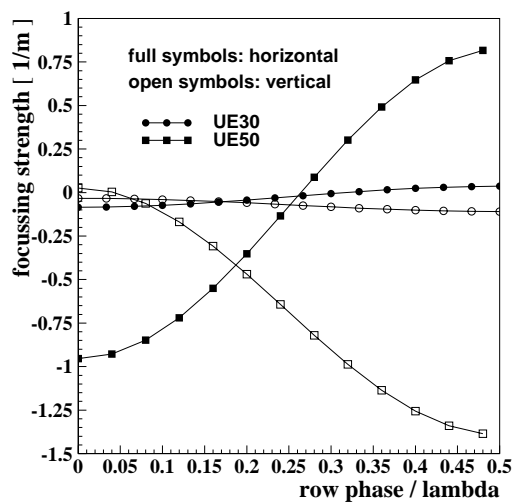


Fig. 9.13a: Focusing in the parallel mode.

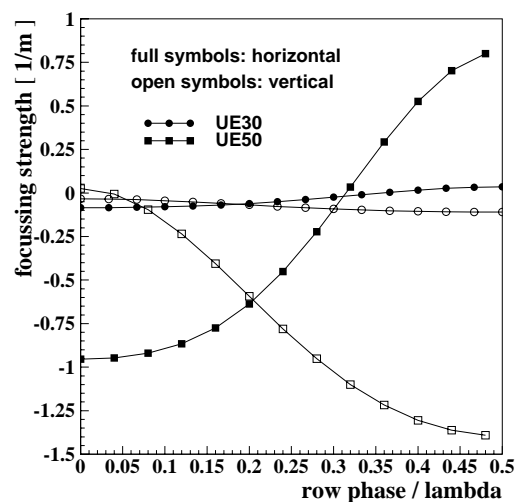


Fig. 9.13b: Focusing in the anti-parallel mode.

9.3 Undulator Tolerances

9.3.1 Tolerance Estimates from 1-D Theory

The error sources leading to degradation of the FEL performance can be divided into four classes.

- Trajectory errors
- Systematic field errors
- Phase errors
- Multipole errors

1. The **trajectory errors** have to be smaller than the natural width of the photon beam. GENESIS simulations on SASE undulators show that the errors must not exceed one wiggle amplitude [31]. Similar values are valid for the HGHG scheme. These tolerances can be achieved with elaborate shimming techniques which will be described in section 9.5.

2. **Systematic field errors** e.g. caused by gap errors, produce a shift of the resonance energy. The line width of the radiation (fwhm) is given by $\Delta\lambda / \lambda = 2\rho\Delta c$ [32] with the Pierce parameter [33], ρ , and the amplification bandwidth of Δc . The value of Δc is of the

order of 1.5. For small K we have $\Delta\lambda / \lambda \approx \Delta K / K$. The wavelength variation due to systematic field errors has to be smaller than one third of half the bandwidth and for small K $\Delta K / K \leq 0.33 \times 1.5 \rho = \rho/2$ is obtained.

For the HE-FEL the Pierce parameter is approximately 10^{-3} and the field variations have to stay within $\Delta K / K \leq \pm 5 \cdot 10^{-4}$. This limit defines the accuracy of the support and drive system, the tolerances for the specifications for the temperature variations and tolerances for the module alignment.

The **field variations with gap** of the HE-FEL are for vertical linear polarization and smallest gap: $\Delta B / B = 1.4 \cdot 10^{-4} \Delta \text{gap} / \mu\text{m}$. A gap positioning accuracy of $\pm 2 \mu\text{m}$ produces field errors of $\Delta B/B = \pm 3 \cdot 10^{-4}$.

The magnets are mounted on four movable aluminum bars which are elongated or compressed due to the longitudinal forces. The corresponding field variations (figure 9.14) of the individual components are a factor of six above the limit. The effective field, however, which enters into the resonance condition is within tolerance. The longitudinal forces of the ME- and LE-FEL are a factor of two higher. For these devices the longitudinal drive system is coupled at two locations to the movable rows, thus keeping the averaged field variation low.

The temperature coefficient of the magnet material is on the order of $10^{-4} / ^\circ\text{C}$. Temperature variations within $\pm 0.2 ^\circ\text{C}$ contribute to the field variations with $\pm 2 \cdot 10^{-4}$.

The data of table 9.5 show that the field variations within $100 \mu\text{m}$ are below the limit of $\pm 5 \cdot 10^{-4}$ except for the HE-FEL in antiparallel mode where the values are 18% higher (new design). The alignment tolerances must not increase the field variations by more than 50%. For the HE-FEL this requires an alignment accuracy in the transverse direction of $\pm 20 \mu\text{m}$.

3. The **phase errors** due to energy spread dominate over phase errors from field imperfections for the following condition [34]: $\Delta\Phi_{\text{rms}} \leq \sigma_\gamma / \gamma\rho \sqrt{3} \approx 4^\circ$ for the HE-FEL at shortest wavelength. The phase errors of the BESSY APPLE II devices are typically $\Delta\Phi_{\text{rms}} \approx 3.5^\circ$ without explicit phase shimming. The tolerances on phase errors are therefore non-critical.

4. **Multipole errors** are less critical for single pass devices. However, a flat field integral distribution is required if the gap dependence of the field integrals is to be small. Field integral variations below $\pm 0.01 \text{ Tmm}$ within a transverse range of $\pm 20 \text{ mm}$ can easily be achieved with the techniques described in section 9.4.

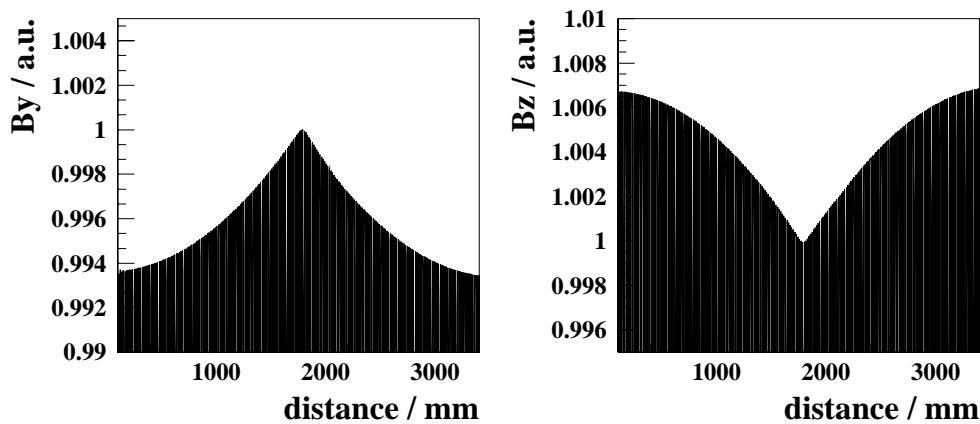


Fig. 9.14: Vertical (left) and horizontal (right) field variation due to the elongation and compression of the magnet rows. The data are calculated for the smallest gap and largest forces (antiparallel mode, shift = $\lambda_w/2$) of the HE-FEL. The fields are normalized.

9.4 Field Optimization

9.4.1 Characterization of Magnets

At the time of writing the magnetic material commercially available does not offer the quality necessary to build high performance undulators without any magnet sorting or shimming. Typical dipole errors of die-pressed magnets from one production charge with sizes comparable to the dimensions used in the BESSY undulators are below 0.3% rms for the magnitude and 0.3° rms for the easy axis orientation error. The dipole errors are partly due to geometric tolerances of the blocks.

Furthermore, the material is not magnetized homogeneously. As a consequence field integrals of typically ± 0.05 Tmm peak-to-peak at a distance of 8 mm to the surface of the blocks are observed.

The dipole errors and the inhomogeneities can be divided into systematic and non-systematic errors. Systematic errors are introduced by an inhomogeneous external field during pressing. Another potential source is a misalignment of the blocks during final machining. The systematic errors can easily be cancelled by an appropriate pairing [16, 35]. The remaining errors, non-systematic, have to be reduced by sorting and shimming. The effectiveness of the sorting depends strongly on the quality of the magnet block characterization.

At BESSY two experimental stations have been developed for a precise characterization of the blocks:

1) An automated Helmholtz coil system is employed to determine the dipole errors. The repeatability of the system is 0.05% rms for the magnitude and 0.06° rms for the orientation of the blocks.

2) A stretched wire system is used for the characterization of the inhomogeneities. The repeatability of this system is 0.0004 Tmm rms for the easy axis of the magnets parallel to the wire and 0.002 Tmm rms for blocks with the easy axis perpendicular to the wire.

9.4.2 Sorting

The dipole and inhomogeneity data of the individual magnetic blocks are used in a simulated annealing code [36] in order to minimize the field errors of the completed undulator by a suitable arrangement of the blocks.

Figure 9.15a compares the predicted local field distribution with measurements. In figure 9.15b predicted and measured field integrals at various transverse locations are compared. An excellent agreement within ± 0.15 Tmm is observed.

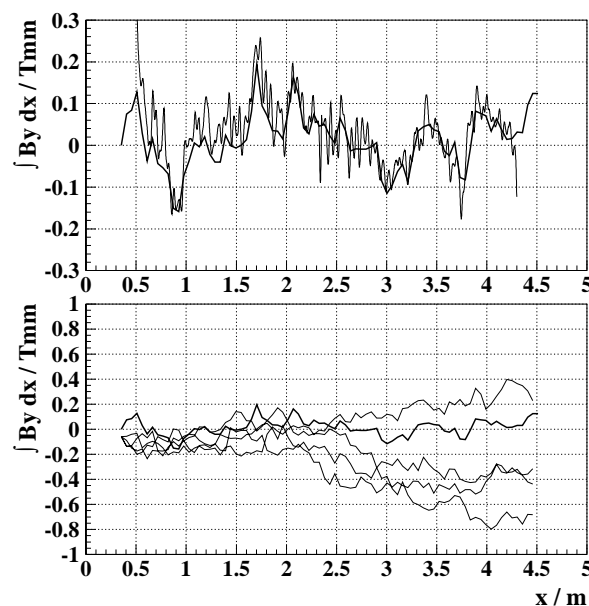


Fig. 9.15a Top: Predicted vertical field integrals (thick line) at $z = 20$ mm are compared to Hall probe data (the periodic part is filtered out). Bottom: Predicted field integrals for the sorted and several unsorted configurations.

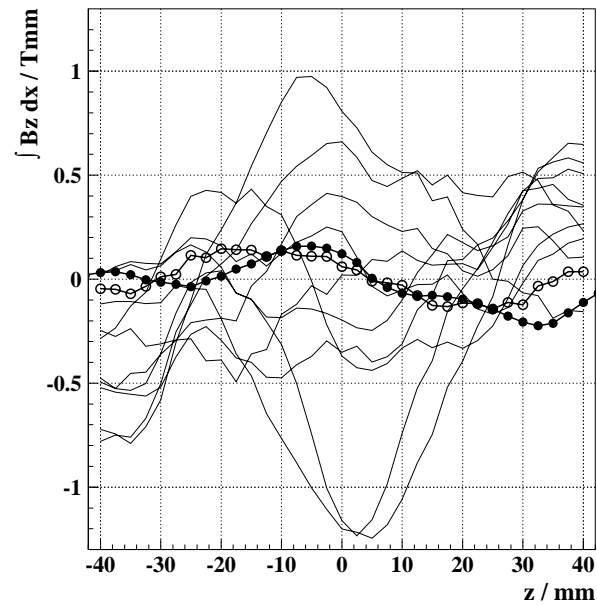


Fig. 9.15b: Transverse distribution of the horizontal field integrals. Open circles: Prediction. Full circles: Measurement. Predicted data for several unsorted configurations are given as well.

Both graphs contain predicted field distributions for several unsorted configurations. For these arrangements the field errors are significantly larger which demonstrates the effectiveness of the sorting algorithm.

9.4.3 Shimming

After sorting, the remaining field errors have to be reduced with shimming techniques. Conventional shimming with iron shims as used for planar devices [37] is not applicable. Other shimming techniques have been developed for APPLE II devices which can be used also for the new magnetic design. A field quality similar to the results for planar devices is achievable.

The shimming has to be done in three steps:

- 1) Trajectory shimming.
- 2) Shimming of shift-dependent field integrals.
- 3) Shimming of shift-independent field integrals.

1) Trajectory Shimming

The trajectory shimming, and to a certain extent also multipole shimming, is usually done via so-called virtual shimming [38]. The magnets or larger magnet units are moved transversely in a horizontal or vertical direction introducing vertical or horizontal field integral changes at the undulator axis. For an APPLE II device the shimming of horizontal

and vertical trajectories is decoupled, whereas for the new magnet design a certain crosstalk is observed (figure 9.16). Nevertheless, virtual shimming is possible also in this case. Multipoles are less important for single-pass FELs. However, gap-dependent field integral variations can be reduced by flattening the transverse distribution.

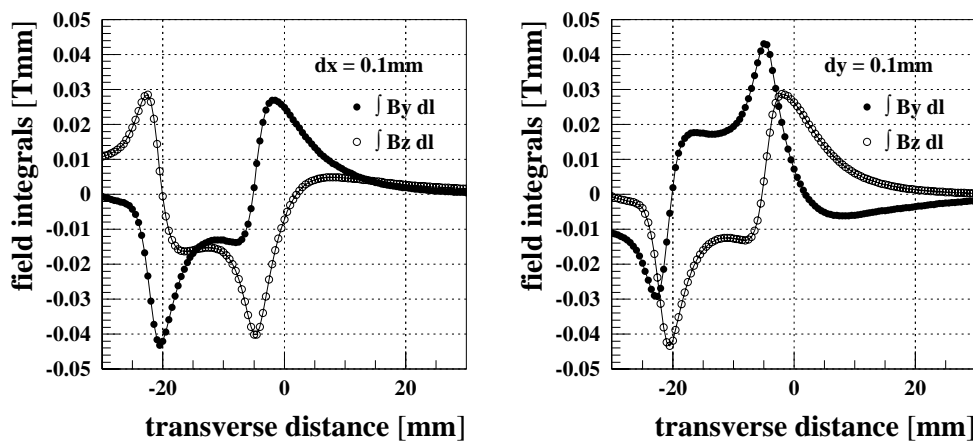


Fig. 9.16: Response function for a horizontal (left) and vertical (right) keeper movement of the HE-FEL (new design).

2) Shimming of Shift-Dependent Field Integrals

The field integral distribution changes when the magnet rows are shifted. Typical values for the BESSY devices are 0.03 - 0.06 Tmm. This effect is due to the permeability of the magnets. The end-poles have to be designed such that their contribution is low (see section 9.1.5). Additionally, shift-dependent terms are observed which originate from the periodic part of the undulator. Geometric tolerances contribute partly to these numbers. Virtual shimming increases the shift-dependent terms as well. The shift-dependent terms can be minimized using iron shims which are glued onto the magnets as has been demonstrated for the BESSY UE52 APPLE II undulator [35].

3) Shift-Independent Field Integrals

a) In-situ sorting

Based on the inhomogeneity information of the individual magnet blocks these blocks or larger units can be flipped or exchanged in order to improve the field integral distribution. This technique has been developed at SPring8 [39] and is now successfully applied to in-vacuum undulators where conventional shimming is not possible. This technique is slightly more time consuming compared to the use of the magnet array, the resulting dis-

tribution, however, is smoother. The undulators will be subject to an *in-situ* sorting procedure prior to final shimming.

b) Permanent magnet arrays at either end of the undulator

Appropriate permanent magnet arrays can be arranged at the undulator ends which compensate for 1st and 2nd field integrals on and off-axis [35]. The measured field integral distribution, as well as the signature of the shim magnets, are used to set up a family of linear equations. The solution of these equations is the thickness distribution of the trim magnets.

9.5 The Phase Shifters

Segmentation of the undulator requires an adjustment of the phase i.e. of the longitudinal position of the micro-bunched electron beam with respect to the optical wave. This is achieved by deflecting the electrons away from and back onto the axis, thus increasing the path length of the electrons with respect to the straight line taken by the light. In the following a phase shifter based on permanent magnets and incorporating air coils for steering purposes is proposed for the BESSY FEL.

It turns out that only one type of phase shifter is needed. The layout is shown in figure 9.17. The electron beam passes through the center along the y-axis. The pair of coils generating a vertical field is separated by 20 mm leaving ample room for the beam pipe.

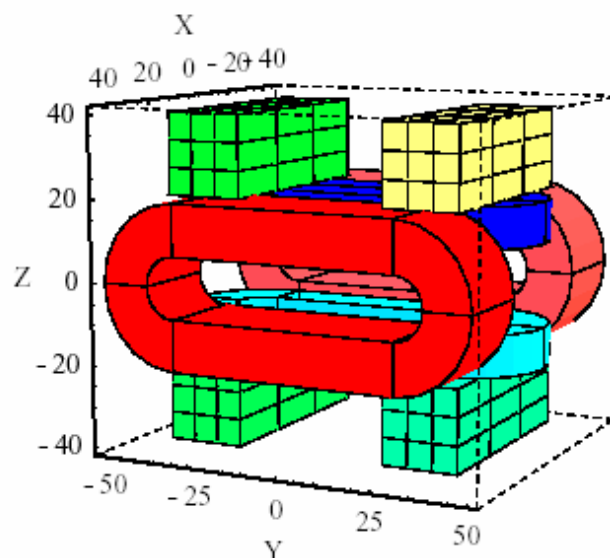


Fig 9.17: RADIA input geometry for the phase shifter with longitudinally magnetized permanent magnets and vertical and horizontal steering coils, units in mm. The overall length is 100 mm. Forces are calculated for the yellow magnet (see below).

The permanent magnets are located above and below the horizontal plane. They are longitudinally magnetized, i.e. parallel to the electron beam axis. The blocks upstream and downstream are magnetized in opposite directions. Also the blocks above and below the mid-plane are magnetized in opposite directions. The dimensions of the magnets are given in table 9.6.

Table 9.6: Dimension of the phase shifter.

Magnet dimensions (mm)	27 x 27 x 60
Air space (mm)	23
Gap (mm)	40 - 100

The vertical separation of the magnets, i.e. the gap g is mechanically changed between $g = 40$ mm and $g = 100$ mm like in an undulator. The drive system is vertically oriented (along the z -axis). A single guide system with two slides and a common spindle with a right-and-left screw driven by a single motor located at the side of the beam pipe will be used. Measurement of the actual gap is done using a linear encoder.

The gap dependences of the shift of the electrons with respect to the co-propagating light wave are shown in figure 9.18a and 9.18b. The maximum available shift is larger than the maximum wavelength by a sufficient margin.

The maximum forces and torques (with respect to the center of each magnetic bloc) together with the field amplitude at the midpoint at minimum gap are given in table 9.7. The forces are such that the magnets repel each other in the longitudinal direction and attract each other vertically. There is a torque around the horizontal axis perpendicular to the beam (x -axis in figure 9.17). Forces are calculated for the yellow magnet in figure 9.17.

Table 9.7: Central field amplitude, forces, and torque on permanent magnets at minimum gap.

Parameter		Unit
Central field	0.16	T
Vertical force	-25	N
Longitudinal force	26	N
Torque around transverse axis	230	N·mm

The reproducibility of the gap setting should be ± 25 μm to set the optical phase within $\pm 1^\circ$ of the wavelength at the high-energy end of the tuning range. This assumes that when

the FEL is operating near the high energy end of its tuning range a large gap is used in the phase shifter. The actual tolerance on the phase shift is to be determined by simulations of the HGHG process and is expected to be larger than $\pm 1^\circ$.

The optimum setting of the gap of the phase shifter is allowed to be different from segment to segment relaxing the requirements on the tolerance of the absolute gap value, the magnetization strength of the magnets, etc.

All tolerances on the geometry are easy to meet except for the orientation of the magnetization. The magnetization must be parallel to the electron beam within ± 3 mrad = $\pm 0.2^\circ$ to keep the angular kick below ± 1 μ rad $\cong \pm 0.06$ Tmm. This requires magnetic measurements, shimming, and/or modifications of the geometry to compensate for magnetic errors, and iteration.

The steering coils are designed to provide integrated fields on-axis of 0.25 Tmm at a current density of 1.0 A/mm².

The coil design assumes self supporting, air-cooled iron-free coils of race track shape made of copper wire (cf. figure 9.17). The bi-polar power supply of 50 W is rated at a maximum current of ± 3 A. Parameters are collected in table 9.8.

Table 9.8: Steering-coil parameters.

Steering coils	Vertical coil	Horizontal coil	Unit
Field direction	x	z	
Field integral	0.25	0.28	Tmm
Field	0.0036	0.0033	T
Length	100	100	m
Width	40	40	mm
Height	10	25	mm
Coil cross section	12.5 x 10	12.5 x 25	mm
Current density	1.0	1.0	A/mm ²
No. of windings	42	105	
Wire diameter	1.6	1.6	
Current	3.0	3.0	A
Power per coil	1.0	2.5	W

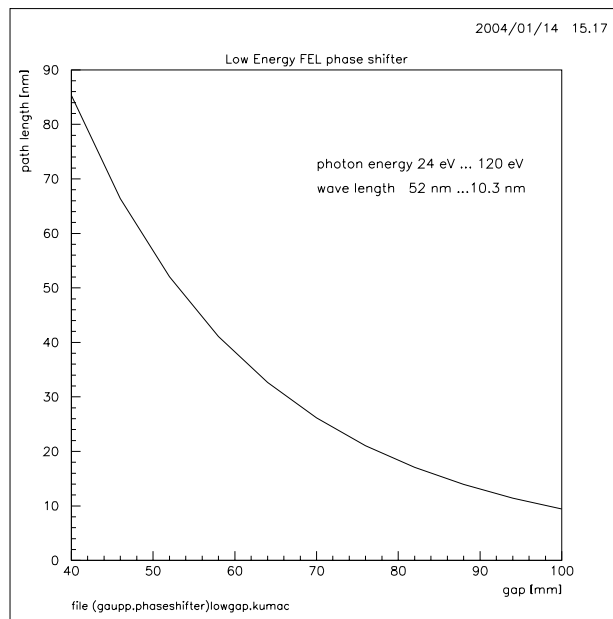


Fig. 9.18a: Path length difference versus gap for the phase shifter for the low-energy FEL.

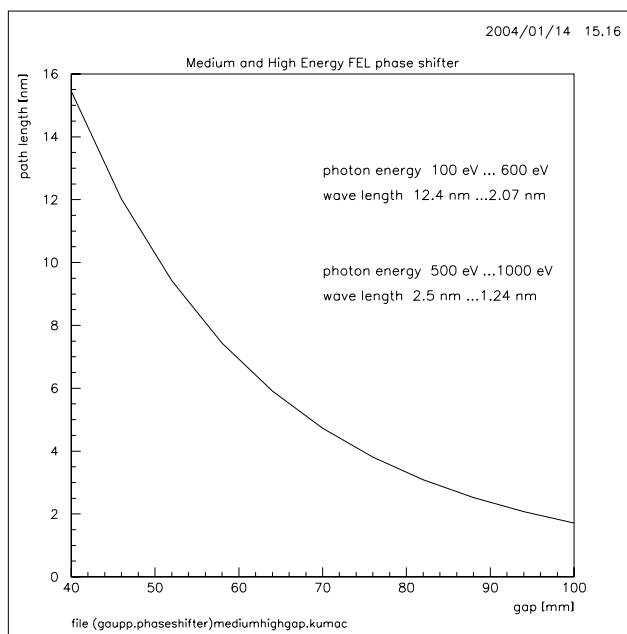


Fig. 9.18b: Path length difference versus gap for the phase shifter for the medium energy FEL and high-energy FEL.

A field integral up to about 3 times higher may be achievable by choosing a higher current density. The higher current density requires active cooling which can be done inserting water pipes “from the side” through the opening in the horizontal coil.

The magnetic field of the phase shifter does not interfere with the undulator performance. To verify this, the magnetic code RADIA was used to obtain on-axis fields for the undulator and the phase shifter. Using the code ANALYZE, the spontaneous spectrum at the first and fifth harmonic was investigated under various conditions. No effect longer than $\pm 2 \cdot 10^{-3}$ was observed between the two cases and without phase shifter adjacent to one end of the undulator.

9.6 The Mechanical Layout

9.6.1 The Magnetic Structure

The topology of the magnetic structure is similar to the one of the BESSY UE49 insertion device. Two magnets are mounted into one holder which can be assembled on either one of the four magnetic rows. This flexibility is needed for the in-situ sorting (see 9.4.3). Adjustable spacers between the magnet holder and the girders provide the possibility for virtual shimming (see 9.4.3).

The magnet forces bend the girders causing a systematic fluctuation of the undulator field. To minimize this effect the girders are supported at four locations using two cross-bars which are located inside the girders.

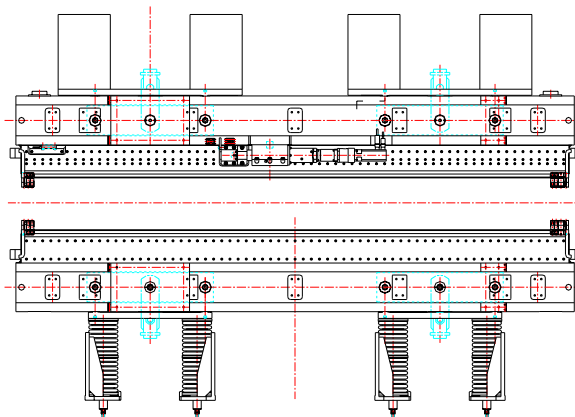


Fig. 9.19a: Technical drawing of the magnetic system of the BESSY UE46 (left).



Fig. 9.19b: Magnetic girders before installation into the support structure. The longitudinal drive system is already mounted.

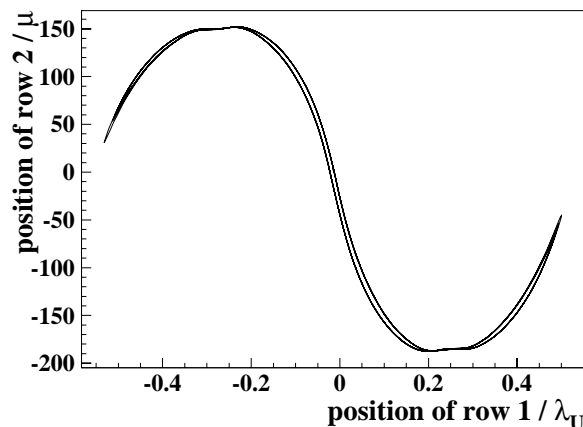


Fig. 9.20: Elastic deformation of the drive system of magnet row 2 during movement of the neighboring row 1. Data are taken from the BESSY UE49 APPLE II.

The magnet girders experience varying forces which change sign during gap and shift movement. Therefore, the upper girder is preloaded with blocks of lead whereas the lower girder is preloaded with springs (figure 9.19a).

Two longitudinal drive systems will be mounted onto each girder. They are coupled at the center of each magnet row in order to minimize the shift-dependent elongation and contraction of the rows. The backlash of the drive system produces a parasitic movement of the fixed row of less than 20 μm during the movement of the neighboring row. Elastic deformations of the drive system and the magnet row are responsible for additional movements on the order of 200 μm (figure 9.20). A closed loop servo-system for all magnet rows minimizes this effect.

9.6.2 The Support and Drive System

The standard BESSY structures can be easily adapted to the needs of the FEL undulators.

The support and drive system has to adjust the gap between the magnet girders with an accuracy better than $\pm 2 \mu\text{m}$. This number has to be achieved in the presence of strong magnetic forces (figure 9.21). The forces vary with gap and reverse sign with shift. In the parallel mode longitudinal and transverse forces compensate within each girder. In the antiparallel mode longitudinal and transverse forces between the magnet girders show up.

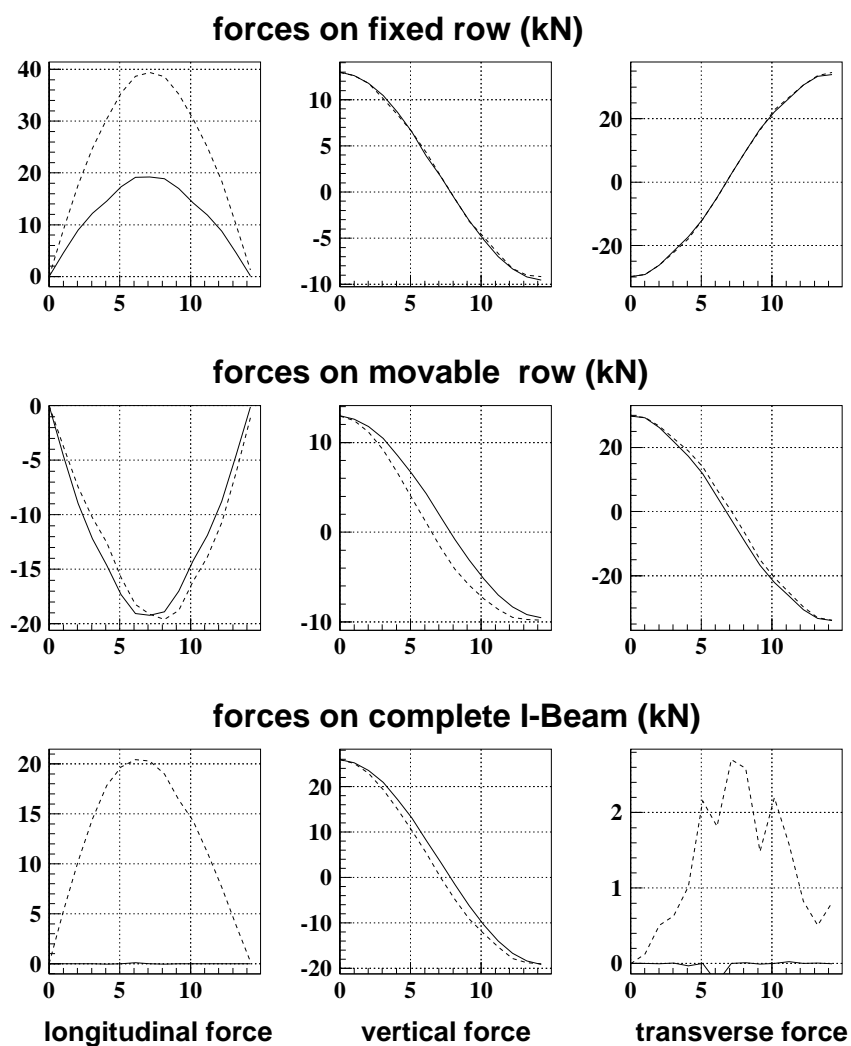


Figure 9.21: Forces of the HE-FEL in the parallel mode (solid line) and antiparallel mode (dashed line). The forces of the ME- and LE-FEL are roughly a factor of two larger. Abscissas are in mm.

The servo-motors are used in a feedback mode. Each axis has its own linear encoder which measures the gap. The positioning accuracy with respect to the linear encoder with a resolution of $0.1 \mu\text{m}$ is better than $0.5 \mu\text{m}$ as demonstrated for the BESSY system [40]. The encoder has to be located directly above the electron beam in order to exclude the Abbe comparator error (figure 9.22). Measurements demonstrate that the gap can be adjusted with an accuracy of better than $2 \mu\text{m}$ (figure 9.22).

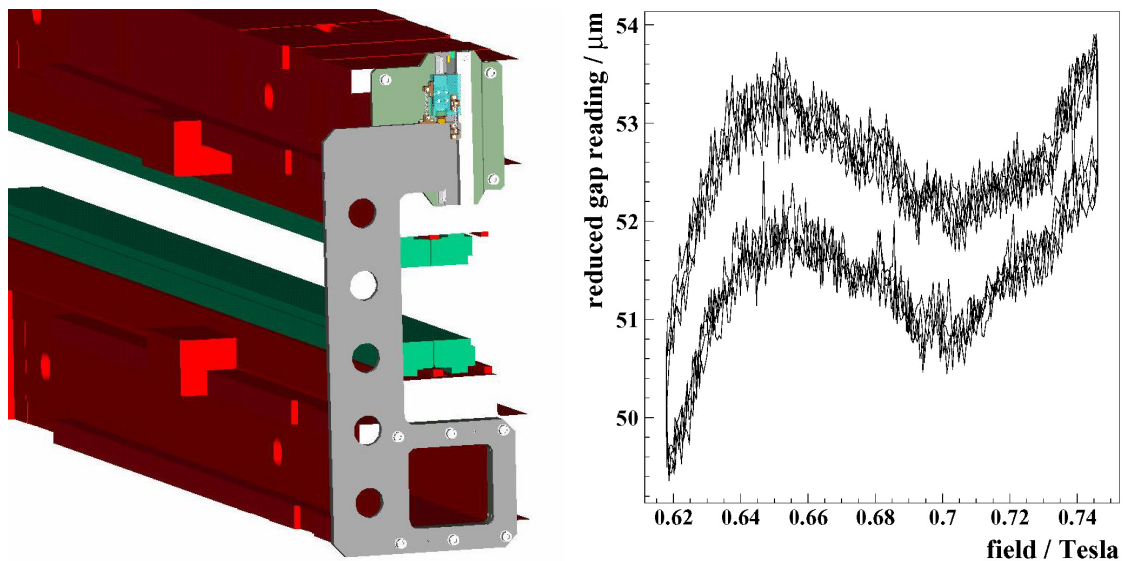


Figure 9.22: Left: Schematic drawing of the gap measurement at the BESSY undulator UE49. Right: Measurement of the correlation of gap and field for several opening and closing cycles. A third-order polynomial has been subtracted from the measured gap.

9.7 Manufacturing of the Undulator Modules

9.7.1 R & D Studies

The undulator system can be built with the required accuracy using the technology developed for the undulators at the BESSY II storage ring. The HE-FEL undulators produce moderate magnetic forces which can already be handled with the existing BESSY support and drive system. The forces of the LE-FEL and ME-FEL are larger and making a mechanical adaptation necessary.

Modules have to be built within a time frame of 2-3 years. In view of the number of modules and the variety of magnetic structures that must be built and tested, an R&D and prototyping phase is necessary to simplify the production process and to assure the quality in preparation for out-of-house manufacturing.

9.7.2 Fabrication and Logistics

During the production phase the following working packages will be treated in close cooperation between BESSY and industry:

1. Fabrication of the I-beams.
2. Fabrication of the support and drive system.
3. Fabrication of the electrical cabinet.
4. Magnet production.
5. Magnet characterization.
6. Magnet assembly onto the magnet girder.
7. Assembling of the magnet girder into the support structure.
8. Installation of the electrical and pneumatic components and the central lubrication system.
9. Final magnetic shimming.

The working packages include in detail:

1: The fabrication of the magnet girders includes the assembly and the test of the linear bearings.

2: The support and drive system will be completely assembled and tested prior to delivery. The testing includes mechanical as well as electrical tests on the actual electrical components to be used for these modules. The motor resolvers (rotary encoders mounted on the motor axis) will be used during the checkout of the drive system.

3: One electrical cabinet will be delivered to the manufacturer of the support and drive system for testing.

4-6: The magnet supplier will characterize the magnet units. The data will be sent to BESSY where the sorting is done. According to the sorting results the magnet supplier assembles the magnet units onto the magnet girders. A final magnetic check will be done at the magnet supplier to assure the expected magnetic field quality before shimming.

7-8: The magnet girders will be assembled into the support structures. This can be done either by the manufacturer of the support structure or by the magnet supplier or by a third company. At this place the final electrical installation will be done. The encoders will be installed and tested. The pneumatic installations for the brakes will be done and the central lubrication system will be assembled. The complete device will be delivered to BESSY turnkey ready.

9: At BESSY the relative alignment of the magnet girders in the support system as well as the calibration of the linear encoders will be done.

In the next step the devices will be shimmed as described in section 9.4. Local measurements will be done with a 2-axis Hall probe mounted on a 5 m long precision guide system already in use at BESSY. These measurements provide the information on the horizontal and vertical trajectories. Integrated measurements are done with a stretched moving wire. These data provide the transverse distribution of the field integrals. Furthermore, the stretched wire data are compared to the Hall probe data in order to check for a DC offset of the Hall probe.

Finally, the magnetic center of the undulators will be transferred to the alignment fiducials which are located at either end of the upper magnetic girder (Taylor Hobson Balls).

9.8 Drive and Control System

9.8.1 Specifications

The FEL undulators consist of a variable number of modules. Each of these modules controls seven axes. Four motors are needed for the longitudinal motion, and two motors for the vertical motion. The phase shifter which is a pure permanent magnet design needs an additional motor. When the undulator is moved, all axes of all modules have to start simultaneously within 1 msec. The deviations from the predefined position must not exceed $\pm 2 \mu\text{m}$ during the movement. Each girder can be tapered by an amount of 1.5 mm.

Due to production tolerances the gap settings of the individual modules as well as the phase shifters will be slightly different from each other in order to achieve equal fields and path length delays, respectively.

The last radiator and final amplifier modules have to be aligned remotely in the horizontal and vertical directions. The adjustment will be done by means of beam based alignment. Three motors are needed for the vertical and two motors for the horizontal motion.

Each module is equipped with horizontal and vertical steering coils at each end. Furthermore, two long correction coils for horizontal and vertical fields are installed. The

currents of these six correction coils are set with a rate of 10 Hz. The settings depend on the actual gap and row shift.

9.8.2 The Axis Controller and Interfaces

Each axis (horizontal and vertical) is equipped with an absolute linear encoder, a servo-motor and an individual axis controller for feedback positioning and speed control. The position and speed are downloaded via a CAN-bus. An Ethernet interface is needed for program development, status inquiry, remote reset, remote maintenance, local operation and PID loop tuning.

An SPS controls the limit switches and the brakes. This device can also be used for local operation.

9.8.3 Computer Hard- and Software

The selection of the computer-hardware is based on the positive experiences gathered with the BESSY II undulator control system. A VME-Bus based computer system is selected. This system has proven to be reliable, and a large number of interface cards exist.

The external axis controllers are controlled via the CAN bus. VME Interface cards for this bus exist, and software drivers have already been developed for the BESSY II undulator control system. One master IOC for each of the three FELs controls the synchronous start of the movement of all axes by a dedicated digital signal line. The slave-IOCs control 4 modules each. The slave-IOCs also control the settings of the correction-coil currents. Figure 9.23 shows a general layout of the control system.

EPICS is selected as the framework for the development of the control software. EPICS is a joint software project for control-systems. It provides a large set of hardware drivers, a protocol for reliable transmission of process variables across the ethernet, and a graphical user-interface-builder tool among others.

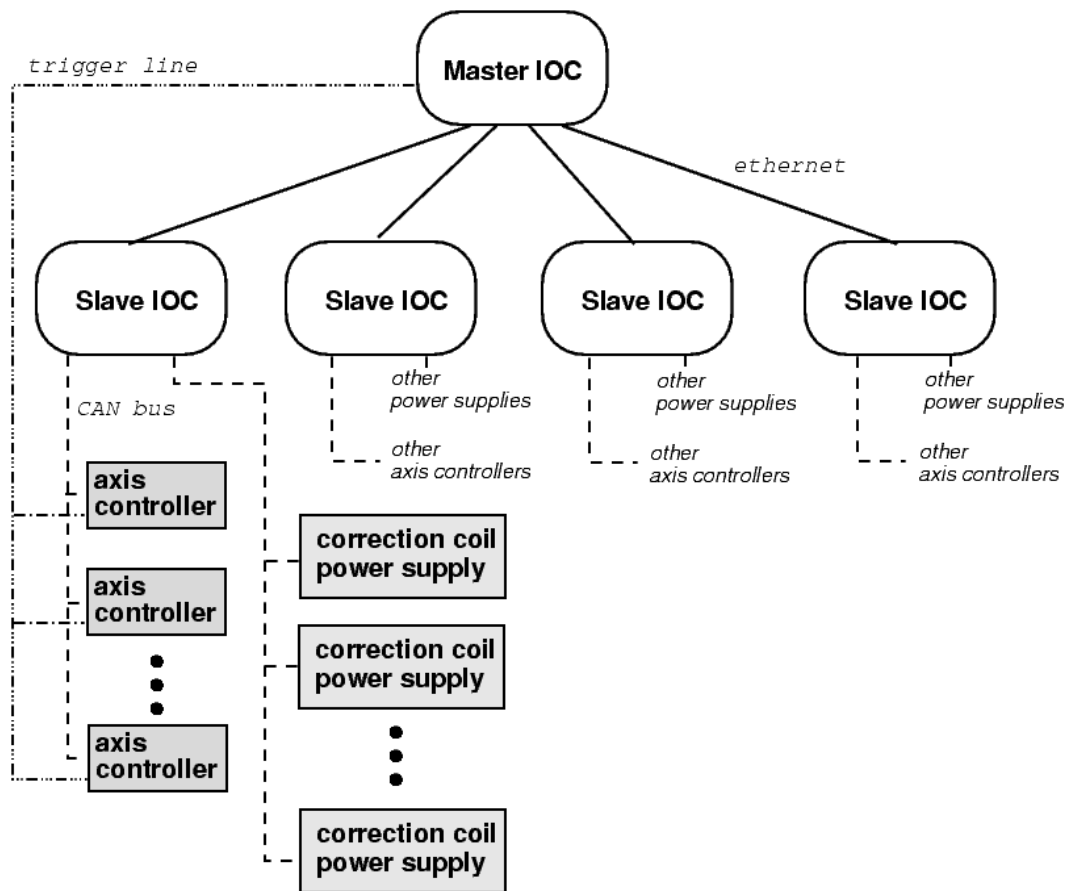


Fig. 9.23: Layout of the control system for one FEL undulator.

9.9 Beam Collimation at the Undulator Sections

Experiences from linac operation for example at SLC [41] at TTF I [42] indicate that beam collimation is essential for the successful running of an FEL at a linear accelerator. Recent experiments carried out at the TTF I show that complete undulator protection and dark current collimation is necessary to avoid degeneration of the undulator magnets. In the following the design of the BESSY FEL collimator section is described.

The collimator section serves as a transverse and longitudinal phase-space filter. In the transverse plane the undulator downstream of the collimator has to be protected against a missteered beam. This is achieved by a set of apertures limiting the downstream transverse phase space volume. In addition, the collimator is designed to remove halo and dark current created and transported through the linac upstream. The various halo sources include the bunch compressor, wakefield-generated beam tails, a mismatched and/or missteered beam. In the longitudinal plane off-energy particles are dark current

electrons and energy tails produced in the bunch compressors. Dark current is mainly created in the gun and through field emission in the super-conducting cavities [43] and can pose a serious risk for successful FEL operation.

9.9.1 Boundary Conditions

For undulator protection the collimator must completely shadow the undulator beam pipe with a beam stay clear distance of at least 20% of the undulator beam pipe radius ($r = 4.5$ mm). For halo removal the collimation cut is set to 30σ horizontally and vertically. Initially the energy cut is set to 5%. It is planned to combine the primary energy collimator with a system for initial dark current removal at 10 % energy offset. All collimators should be able to withstand the event of a complete bunch train of up to three particle bunches hitting the collimator directly. Monitoring of the charge transmission through the collimator together with an adequate machine protection system can disable linac operation within a few microseconds, i.e. from one pulse to another.

9.9.2 General Layout of the Collimator

In figure 9.24 the general layout of the collimator section is depicted. After the last accelerating module the beam first enters the transverse collimation section containing a matching quadrupole triplet and the two transverse collimators CT1 and CT2.

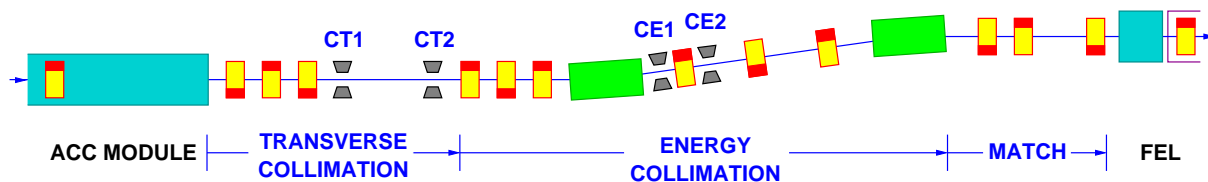


Figure 9.24: Collimator beamline including the last accelerating module, the energy variation cavity and the beginning of undulator.

Then the beam passes another matching section before traveling through a dogleg structure made up by two dipole magnets separated by a drift region with a quadrupole triplet. Before and after the first quadrupole magnet of this triplet two apertures, named CE1 and CE2, are located. While CE1 serves as dark current collimator the task of CE2 is to remove all further off-energy electrons. In order to minimize the flux of photons escaping the transverse collimation section, the dogleg is placed between the undulator and the transverse collimation section. The collimator beamline ends with the last matching section preparing the Twiss parameters according to the specification of the undulator lattice.

Directly in front of the undulator, space is provided for an optional energy modulation cavity. With this cavity the beam energy can be modified by about 10^{-3} without re-tuning the linac. The Twiss parameters for the collimator section are plotted in figure 9.25.

The first triplet focuses a round beam with a waist in a drift space of length equal to two times the amplitude of the beta function in the center between the apertures CT1 and CT2. The dogleg section produces a closed dispersion bump. After the dogleg the Twiss parameters are matched to the undulator entrance. The collimator beamline is 40 m long. The last part of the accelerating sections adds 8 m to that.

9.9.3 Transverse Collimation

Because of the length of the 2.3 GeV linac, a collimator scheme with two spoiler-absorber pairs was dropped in favor of a more compact setup with two absorbers. Recent studies for the TTF II [44] show that with this scheme a high collimation efficiency can be achieved for FEL operation.

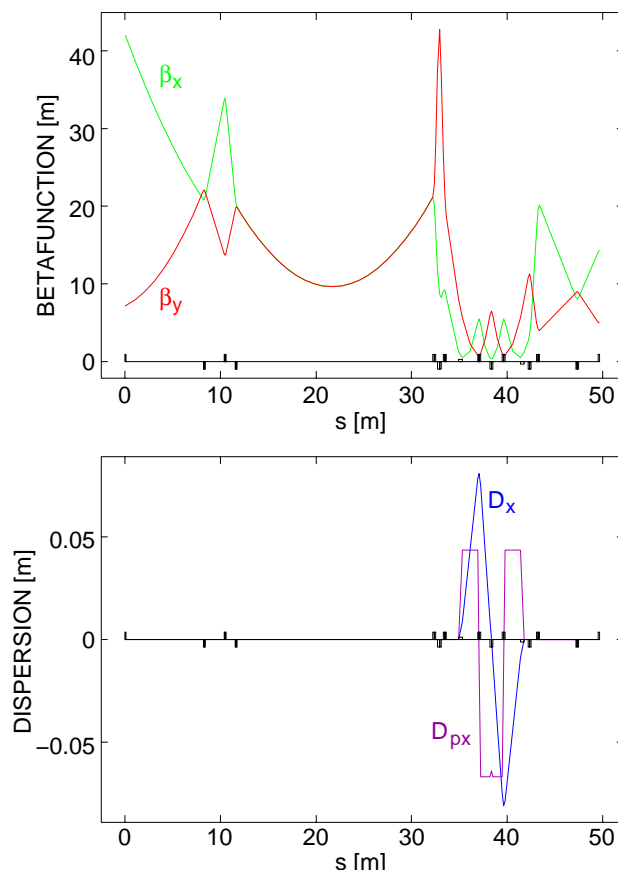


Fig. 9.25: Twiss parameters for the collimator beamline.

The transverse collimation section contains two absorber blocks separated by $\pi/2$ phase advance. The task of these absorber blocks is to completely shadow the undulator vacuum pipe region in phase space, so that no particle can hit the undulator vacuum chamber. Furthermore, the transverse collimator should provide halo removal. The upper limit for the collimator acceptance is given by the beam stay-clear distance Δx_{clear} and the maximum beta function in the undulator β_{max} according to

$$a_{coll} \leq \frac{(r_{pipe} - \Delta x_{clear})^2}{2\beta_{max}} \quad (9.9).$$

For the given case the collimator acceptance is $a_{coll} = 0.3575 \mu\text{m}$. From this the absorber radius can be calculated with

$$g_{coll} = \sqrt{a_{coll} \cdot L_{coll}} \quad (9.10)$$

where the transverse collimator length, L_{coll} , is the distance between the two apertures CT1 and CT2.

For the given scenario with a central waist between the two apertures and no magnets in between this is equal to the beta function at the absorber locations. The collimator gap radius is then 2.6 mm. Copper absorbers were used for the calculations. More studies are underway to compare the performance for copper and titanium. The length of the absorber is around 10 radiation lengths and thus 140 mm for copper. In figure 9.26 the geometry of the collimator blocks is shown. In order to minimize wakefield effects and to keep the total block length within limits, a step plus taper combination was chosen for the transition between gap radius and beam pipe radius. The taper length is 200 mm and the taper radius is 5 mm, resulting in a total collimator block length of 540 mm. The taper radius has been chosen to minimize the transverse wakefield kick.

In figure 9.27 the phase-space portrait of the undulator vacuum chamber at the center of the transverse collimator is shown. The apertures CT1 and CT2 cut out the phase space allowed for particles in the undulator. The undulator beam chamber is completely in the shadow of these two apertures.

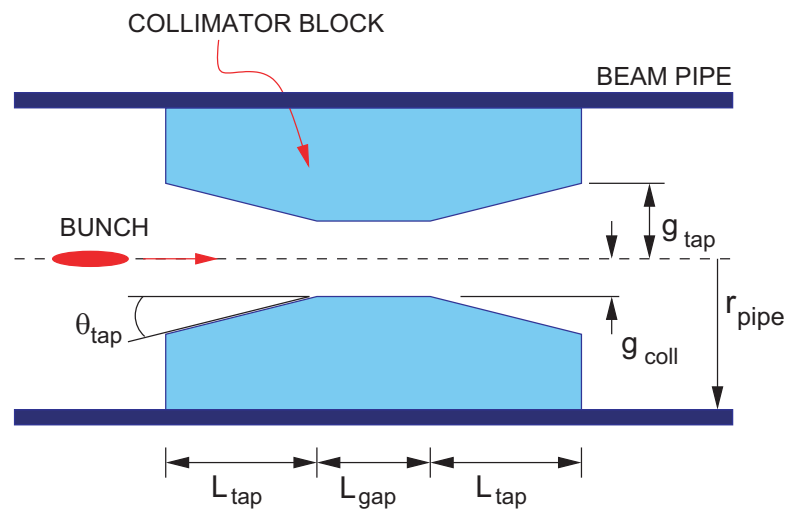


Fig. 9.26: Geometry of collimator block.

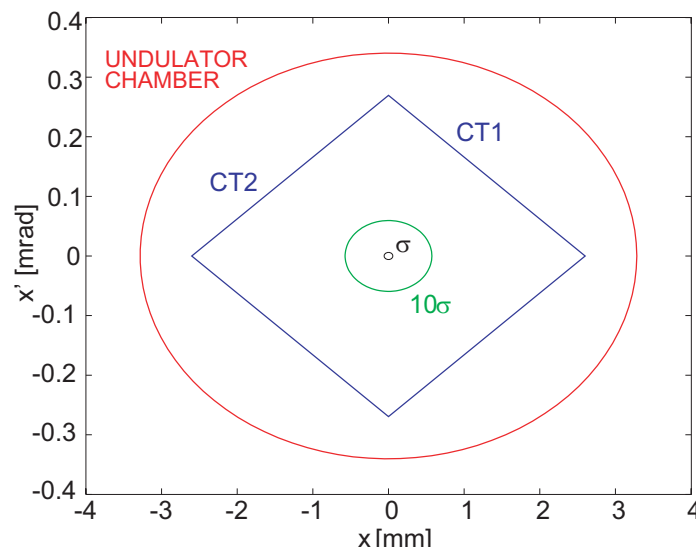


Fig. 9.27: Phase-space portrait of the back-transformed undulator aperture, CT1 and CT2 at the center of the transverse collimator. Also shown are the one-sigma (black) and ten-sigma (green) beam radius.

9.9.4 Energy Collimation

Energy collimation and passive protection against off-energy particles is achieved in the dogleg section with horizontal dispersion. The dipole angle is 2.5 degrees. Together with the dogleg length of 6.5 m a beam path off-set of roughly 30 cm results. According to

simulations using ELEGANT [45], the energy acceptance of the second energy collimator is 5%.

9.9.5 Diagnostics

The collimator section is a key component in the linac beamline since it is positioned directly in front of the FEL undulator. All phase-space parameters like emittance, bunch length, and energy spread, can be measured here. For orbit steering, some quadrupoles in the beamline will be equipped with stripline beam-position monitors (BPMs). For tuning of the transverse collimator an Optical Transition Radiation station (OTR) is planned for the location of the beam waist between CT1 and CT2. The energy spread can be measured with another OTR station in the dispersive arm. To study the efficiency of the dark current suppression, current transformers are located in front of and after the dogleg. More current transforms will be put at the beginning and the end of the collimator section to monitor overall transmission through the system. The dipole chambers will all have exit windows to enable detection of the synchrotron radiation for beam profile measurements.

9.9.6 Further Studies

Further studies are under way to study the effect of the collimator on the beam emittance due to wakefields and coherent synchrotron radiation. First estimates show that the combined effect on the emittance is less than 10% keeping the slice emittance well within the limits required for the FEL process. Surface roughness may cause considerable problems in terms of wakefields if not tackled early in the production process of the spoilers. This can be done by polishing the inner surface of the aperture. To enable such a procedure it is planned to produce the collimators in two halves which can be joined with a precision of several ten micrometers.

The final decision on the best collimator material must still be made since the collimator has to survive two scenarios. Direct impact of missteered or sudden off-energy beam, i.e. due to klystron failure and slow 2% average beam loss. Simulations using the code GEANT [46] are in preparation to study the energy deposition of a bunch train hitting the collimator blocks head on. The average loss of 2% percent leads to an average power of 400 W (at 1 nC bunch charge) dumped in the collimators which is no problem for standard cooling techniques.

9.10 Wakefield Effects in the Undulator Section

The highly charged electron bunch generates electric fields, which depend on the electrical shielding of the bunch environment, i.e. the vacuum chamber, RF cavities, diagnostic and pumping ports etc. These wakefields will act back onto the bunch and thus can deteriorate its longitudinal and transverse phase-space distribution and finally may lower the efficiency of the FEL process. The energy change of the bunch distribution by these fields is estimated in this paper. Much work has been published on the subject discussing wakefield effects for FEL and linear collider design work, see for example. [47, 48].

The modulation of the longitudinal and transverse wake along the bunch produces nonlinear distortions to the bunch phase space distribution. Directly at the source point the longitudinal wake starts with a final value similar to a cosine-like function. The wakefields become stronger the shorter the bunches are. The effect on the bunch is an additional nonlinear energy modulation. The transverse wake leads to different transverse kicks along the bunch, enlarging the bunch emittance. It shows a sine-like dependency: fields are zero at the chamber axis and increase in strength for off-axis positions. For well centered bunches these fields are less critically.

The wakefield $W(s)$ generated by a bunch can be calculated by folding the wakefield $w(s)$ of a point charge (Green's function) with the bunch charge distribution $\lambda(s)$

$$W(s) = \int_0^{\infty} ds' \lambda(s-s')w(s') \quad (9.10)$$

where $\int_0^{\infty} ds' \lambda(s-s') = Ne$ is the bunch charge. The total energy loss ΔU of the bunch in the structure is given by the integral

$$\Delta U = \int_{-\infty}^{\infty} ds \lambda(s)W(s). \quad (9.11)$$

The wakefield can be separated with respect to different sources.

The **resistive wakefields** are the dominating part of the fields. They are excited due to the finite conductivity of the wall materials. The Green's function of the wakefield is given by [49]

$$w(s) = -\frac{4ceZ_0}{\pi a^2} \left(\frac{1}{3} e^{-\zeta} \cos(\sqrt{3}\zeta) - \frac{\sqrt{2}}{\pi} \int_0^{\infty} \frac{x^2}{x^6 + 8} e^{-x^2\zeta} dx \right) \quad (9.12)$$

where $s = \zeta \cdot s_0$, s_0 is the characteristic length given by $s_0^3 = 2a^2/Z_0\sigma$ with σ the conductivity of the beam tube, $Z_0 = 120 \cdot \pi \cdot \Omega$ is the free space impedance and a the beam tube radius. For the present parameters s_0 is typically 12 μm . This function describes the dc part of the wake and is valid for short bunches, the ac-component can be neglected for our parameters. To keep these fields small for a fixed radius, the conductivity of the vacuum chamber should be large.

Geometric wakefields are excited by sudden geometric changes of the vacuum chamber, such as aperture jumps or cavities. The Green's function is given by ref. [50]:

$$w(s) = -\frac{Z_0 ec}{3\pi a L_{per}} \sqrt{\frac{g}{2s}} \quad (9.13)$$

where g is the longitudinal length of the aperture opening. For each periodic distance L_{per} of our beam transport an aperture change is assumed, like a small cavity in a diagnostics section. A smooth step-less beam pipe will lower these wakes.

Surface-roughness wakefields are excited by the interaction of the bunch charge with the roughness of the surface, e.g. see the review article [51]. To model these wakes the roughness is described by bumps on the surface, which are characterized by an amplitude h , a size g and a periodicity p . In the synchronous wave model the effect of the surface bumps are summarized to an effective dielectric layer, described by a wave vector k_0 . The Green's function is given by [52]

$$w(s) = -\frac{Z_0 ec}{\pi a^2} \cos(k_0 s). \quad (9.14)$$

In this model the synchronous modes travel with a phase velocity smaller than the speed of the light and can be excited and propagated synchronously with the bunch. Due to recent experiments [53] there should be only minor effects as long as the bumps are randomly distributed. Also, if the aspect ratio g/h is greater 1 the synchronous mode can be neglected [51, 54]. For realistic smooth beam pipes we have h less than 1 μm and g larger than several tens of μm , leading to an aspect ratio $\gg 1$.

An additional model which needs to be considered for the surface roughness is the inductive model [55, 56]. This model superimposes individual bump contributions. If the aspect ratio is much greater 1, no strong resulting field is excited [51].

The Green's function for this model is given as [51]

$$w(s) = -\frac{cZ_0eh^2\kappa^3}{2\sqrt{\pi}a} \frac{\partial}{\partial\zeta} \frac{1}{\sqrt{\zeta}} \left(\cos \frac{\zeta}{2} + \sin \frac{\zeta}{2} \right) \quad (9.15)$$

where $\zeta = \kappa s$ and $\kappa = 2\pi/g$. The impedance in the model is purely inductive i.e. the bunch does not lose energy, but the energy is redistributed in the head and the tail of the bunch. The resulting energy spread can be calculated [53]

$$\delta E_{rms} = 0.175Ne^2L_{ind}Lc^2 \frac{1}{\sigma_z^2} \quad (9.16)$$

where L_{ind} describes the inductance of the surface[51], L the beam pipe length and σ_z the rms bunch length. For realistic values of tube radius time inductance $a \cdot L_{ind} = 8 \cdot 10^{-4}$ pH/m [51] an additional relative energy spread of $2.5 \cdot 10^{-5}$ at 2 GeV occurs which is tolerable. If for the undulator beam tube the applied surface inductance L_{ind} and an aspect ratio $\gg 1$ are achievable, only minor effects from the surface roughness on the beam are expected [57].

The final amplifier undulator sections of the HGHG-FELs consist of up to 8 modules, each of 3.5 m in length, followed by a 0.92 m long intersection for phase shifters, orbit correction, diagnostics and pumping. The vacuum chamber inside the undulator has an inner radius of 4.5 mm. Wakefield related effects grow with the bunch charge and the length of the undulator sections and are weaker for longer bunches. Therefore only the high-energy beam line is considered.

To minimize the resistive wakefields the wall surface will consist of a high conductivity material such as copper. Stainless steel would generate seven times stronger fields. A stainless-steel tube with a thin copper layer has a higher surface roughness than pure copper which is therefore being considered for the mechanical layout of the chamber.

The geometric wake model is used to estimate wakes excited in the diagnostic sections between the undulator modules. These intersections of 0.92 m in length include a more complicated electrical environment for the wakefields. It is assumed that the vacuum chamber cross section stays basically unchanged with comparable conductivity and smoothness. This structure is interrupted by two flanges, one pumping slot and a strip-line, which will excite mostly geometric wakefields. For bellows we assume no effect as they are screened by an RF shielding.

Wakefields for the HGHG-FELs with $\sigma_G = 140 \mu\text{m}$ and $q = 2.5 \text{ nC}$ are estimated. These bunch length values σ_G are a result of a Gaussian fit to the ‘center part’ of the charge distribution.

Table 9.9: Parameters and peak wakepotentials excited in the diagnostic section.

Bunch length σ_G	Bunch charge	Wakepotentials				Sum	Effective. Gap length
		Flange	Pump	Stripline			
140 μm	2.5 nC	-3.3 kV	-8.5 kV	-7.2 kV	-27 kV	0.44 cm	

A small change of chamber aperture over a length of $g = 1 \text{ mm}$ in the beam direction is used to characterize each of the two flanges. This leads to peak geometric wakes of -3.3 kV. To estimate the effects of pumping slots MAFIA-based results [58] were scaled to the BESSY FEL values, by applying the Green’s function of the geometric wakefield. The bunch-length dependency is scaled $\sim \sigma_G^{-1.4}$ as suggested in [58]. For this scaling a Gaussian σ_G fit to the bunch shape is required. There are eight pumping slots per 360° of about 2 mm width and 18 mm length. The scaling leads to wakefields of -8.5 kV.

Due to its non-rotation-symmetrical geometry striplines are difficult to scale. The stripline has four slots in the azimuthal direction which are partially filled with the pick-up electrode leaving an isolating space of nearly 1 mm between the electrodes and the wall. If we use a cavity-like object of $g = 12 \text{ cm}$ gap length to estimate the excited wakefield we compute a value of -36 kV. Assuming that the field is excited in linear proportion to the azimuthal filling factor of 20% we get a reduced field of -7.2 kV/m.

The peak values of the wakefields in the intersection regions are summarized in table 9.9. The wakefield contributions are added linearly and an effective gap length g_{eff} , is adjusted to achieve the same peak wakefield. This g_{eff} value is used for the calculations shown in figure 9.29.

The wakefield examples of figure 9.28 and 9.29 were calculated using a code from [13]. In this code the Greens functions are folded with the charge distribution. For a Gaussian and a trapezoidal idealized bunch shape the resulting longitudinal wake is given in figure 9.28. Fields of up to -30 kV/m are excited. The trapezoidal bunch shows a very smooth behavior for the induced wakefields. For a short bunch the resistive wake is dominating, it is stronger but faster decays faster ($\sim \sigma_{\text{rms}}^{-1.5}$) than the geometric wake ($\sim \sigma_{\text{rms}}^{-0.5}$). For a long bunch the geometric wake gains relatively in strength.

For a realistic bunch of the HGHG-FEL the resulting longitudinal wakes are given in figure 9.29. These fields are the accumulated values after the beam has passed the first

undulator module of 3.5 m length and the intersection region. For a 2.4 nC bunch charge, wakepotentials up to -150 kV are excited.

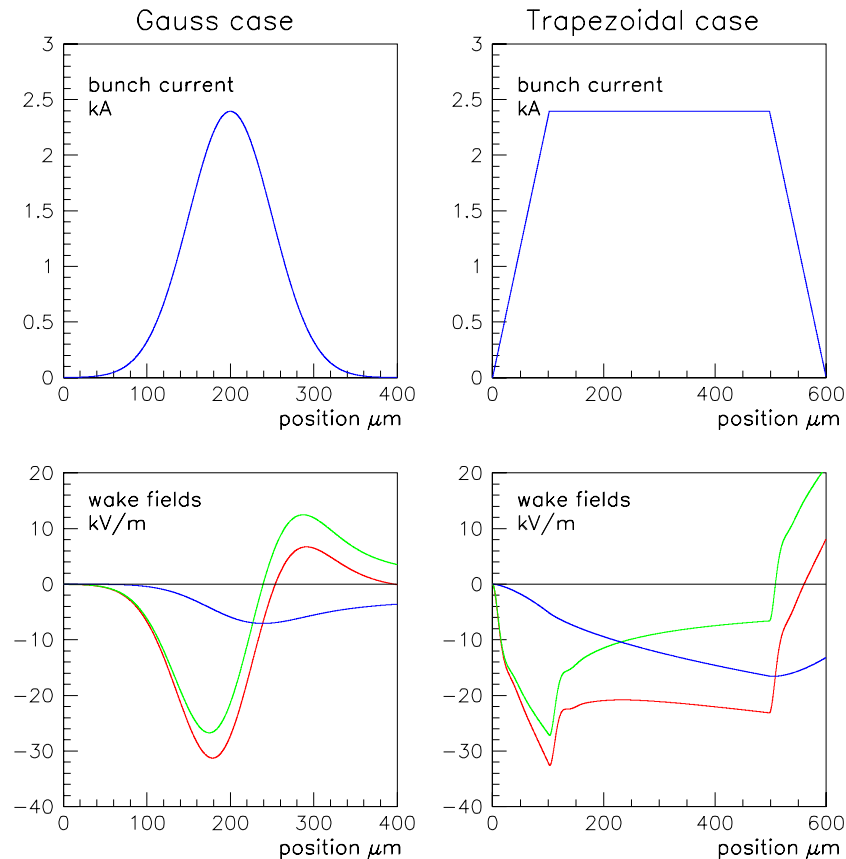


Figure 9.28: The upper part shows a Gaussian (1 nC) and a trapezoidal (4 nC) charge distribution of equal peak current. The lower part shows the total induced wake (blue line) with up to -30kV/m field strength, the resistive wake (red), and the geometric wake (green).

The average energy loss of the bunch by the longitudinal wakefields can be compensated by a tapered undulator gap along the beam path. For the HGHG bunch 18 keV/m is expected in this case.

The full length of the undulator section will be nearly 55 m. The integrated wakepotentials will be 20 times stronger than the 100 kV per 4 m-module, yielding 2 MV and leading to a coherent energy loss of max. 2 MeV. The average energy loss per bunch of 18 keV/m accumulates to 1.4 MeV for the full length. Both numbers are tolerable for the FEL operation.

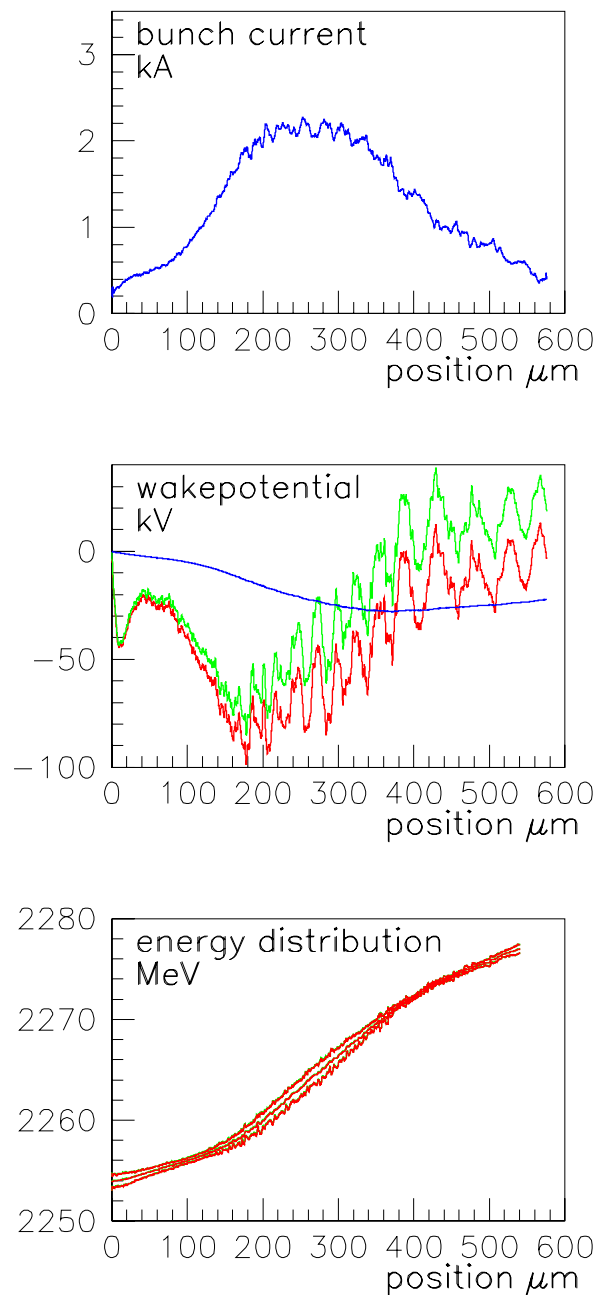


Fig. 9.29: The upper part shows simulated charge distributions, for a trapezoidal HGHG bunch with 2.4 nC. The next row shows the wakepotentials of these distributions (red = total field, green = resistive and blue = geometric wake). The field values are accumulated from the entrance of the first undulator module to the entrance of the next one including the intersection region. The last row shows the energy distribution of the bunch before it enters the first and second undulator module (green, respectively red line). The energy distribution is characterized by three lines, the average energy and the $\pm 10_{\text{rms}}$ values.

9.11 The Intersection Regions

The undulator modules of the final amplifiers are separated by the so-called “intersection region”, which incorporates all necessary equipment for beam transport and diagnostics. The total length of the intersection will be 920 mm. The elements are listed in table 9.10.

Table 9.10: Elements and their total length in the intersection region.

Item	Function	Total length (mm)
1	Space for longitudinal shift of undulator rows	2 x 90
2	Flange connections	2 x 45
3	Phase shifter	100
4	Undulator 1 st and 2 nd field integral correction	100
5	Quadruple magnet	150
6	Stripline BPM (integrated in quad)	
7	x-y steering magnet	100
8	Bellows	100
9	Destructive beam monitor	50
10	Pumping ports	50
Sum		920

Figure 9.30 depicts the technical details of the intersection region which requires a 90 mm drift space at the ends for the longitudinal motion of the undulator rows when varying photon beam polarization. To correct for gap-dependent changes of the undulator first and second-field integral, two x and y correctors are planned, one realized as lumped element, the second integrated into the phase shifter which allows for proper adjustment of the bunch position with respect to the phase of the photon beam. A quadrupole singlet in the middle of the intersection defines the electron beam optics. A stripline for beam position measurements fits into the magnet bore. A special chamber with well shielded ports to install destructive beam sensors as simple viewing screens, OTR foils or a wire scanner is located next to the quadrupole. A pinhole monitor will be mountable in the chamber which will provide a port for vacuum pumping.

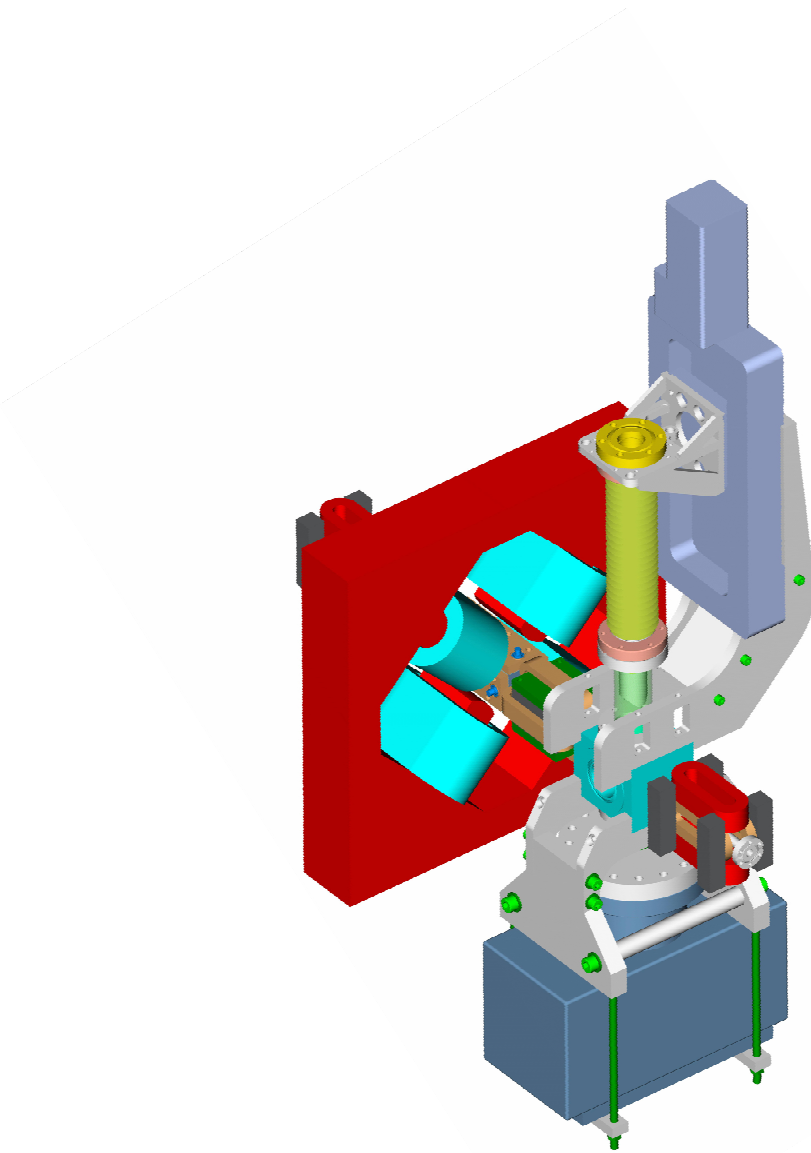


Fig. 9.30: 3-D model of the intersection region between two undulator modules.

9.12 The Undulator Vacuum Chamber

The present design of the undulator vacuum chamber is determined by the geometry of magnet segments of the new elliptical undulator design (section 9.1.2) which is consistent with a round cross section of < 10 mm. On the other hand the chamber inner cross section should provide a circular beam stay clear aperture of diameter 8.5 mm. Thermal RF aspects demand a high conductivity material and it has been shown that a copper clad surface is sufficiently smooth and mechanically stable for this purpose. A cross section of the undulator chamber is depicted in figure 9.31. The massive “wings” in the midplane of the construction are for stabilization and mounting the chamber.

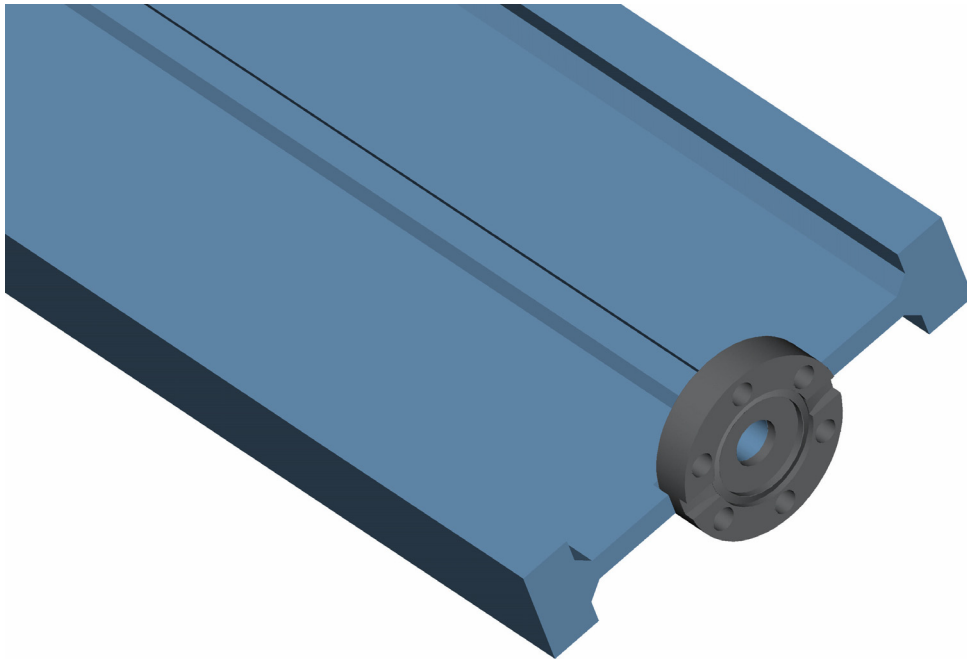


Fig. 9.31: Cross section of the extruded copper chamber of the undulators.

To control the resistive wall effect the surface roughness of $R_a = 100$ nm is expected to be achieved with an extruded hollow copper conductor profile with a bore of 8.5 mm. This technique results in $R_a = 1000$ nm surface roughness that can be processed further, i.e. by electropolishing or other means reducing the roughness by another factor of 10.

References

- [1] J. Chavanne, P. Elleaume, P. Van Vaerenbergh, *Proc. of the 6th EPAC* (1998) 317.
- [2] R. Walker, D. Bulfone, B. Diviacco, W. Jark, P. Michelini, L. Tosi, R. Visintini, G. Ingold, F. Schäfers, M. Scheer, G. Wüstefeld, M. Eriksson, S. Werin, *Proc. of the 1997 PAC* (1997) 3527;
R.P. Walker, R. Bracco, D. Bulfone, B. Diviacco, P. Michelini, N. Pangos, M. Vento, R. Visintini, D. Zangrando, *Proc. of the 6th EPAC* (1998) 2255.
- [3] T. Schmidt, R. Abela, G. Heidenreich, A. Imhof, G. Ingold, B. Jakob, B. Kalantari, A. Keller, T. Korhonen, L. Patthey, M. Rohrer, L. Schulz, M. Shi, C. Vollenweider, P. Wiegand, E. J. Antokhin, A. V. Utkin, P. D. Voblyi, N. I. Zubkov, *Proc. of the 8th EPAC* (2002) 2631.
- [4] E. Gluskin, N. Vinokurov, V. Tcheskidov, A. Medvedko, Yu. Evtushenko, V. Kolmogorov, P. Vobly, E. Antokhin, P. Ivanov, I. B. Vassermann, E. M. Trakhtenberg, P. K. Den Hartog, B. Deriy, M. Erdmann, O. Makarov, E.R. Moog, *AIP Conf. Proc.* **521** (2000) 344.
- [5] *Proc. of the "Workshop on superconducting undulators and wigglers"*, Grenoble, France (2003): http://www.esrf.fr/Accelerators/Conferences/ID_Workshop .
- [6] G. LeBlanc, E. Wallen, M. Eriksson, "The MAX wiggler", *Proc. of the 7th EPAC* (2000) 2334; G. LeBlanc, E. Wallen, *Proc. of the 8th EPAC* (2002) 2622.
- [7] D. Berger, H. Krauser, M. Rose, V. Dürr, E. Weihreter, S. Reul, *Proc. of the 8th EPAC* (2002) 2598.
- [8] G. Ingold, I. Ben-Zvi, L. Solomon, M. Woodle, *Nucl. Instrum. and Meth. A* **375** (1996) 451.
- [9] R. Rossmannith, H. O. Moser, A. Geisler, A. Hoble, D. Krischel, M. Schillo, *Proc. of the 8th EPAC* (2002) 2628.
- [10] K. Halbach, *Nucl. Instrum. and Meth. A* **187** (1981) 109.
- [11] K. Halbach, *J. Phys.* (1983) C1-211.
- [12] P. Elleaume, *Nucl. Instrum. and Meth. A* **291** (1990) 371.
- [13] B. Diviacco, R. P. Walker, *Nucl. Instrum. and Meth. A* **292/2** (1990) 517.
- [14] T. Hara, T. Tanaka, T. Tanabe, X.-M. Marechal, K. Kumagai, H. Kitamura, *J. Synchr. Rad.* **5** (1998) 426.
- [15] S. Sasaki, *Nucl. Instrum. and Meth. A* **347** (1994) 83.
- [16] J. Bahrtdt, W. Frentrup, A. Gaupp, M. Scheer, W. Gudat, G. Ingold, S. Sasaki, *Nucl. Instrum. and Meth. A* **467-468** (2001) 21.

- [17] J. Bahrddt, W. Frentrup, A. Gaupp, B. Kuske, A. Meseck, M. Scheer, SRI 2003 (2003), to be published in *AIP*.
- [18] S. Sasaki, K. Kakuno, T. Takada, T. Shimada, K. Yanagida, Y. Miyahara, *Nucl. Instrum. and Meth. A* **331** (1993) 763.
- [19] J. Chavanne, P. Elleaume, P. Van Vaerenbergh, ESRF Machine Technical Note 1-1996/ID (1996).
- [20] M. Petra, P. K. Den Hartog, E. R. Moog, S. Sasaki, N. Sereno, I. B. Vasserman, *Nucl. Instrum. and Meth. A* **507** (2003) 422.
- [21] P. Colomp, T. Oddolaye, P. Elleaume, Technical Report ESRF/MARCH-ID/93-09 (1993).
- [22] T. Bizen, T. Tanaka, Y. Asano, D.E. Kim, J.S. Bak, H.S. Lee, H. Kitamaru, *Nucl. Instrum. and Meth. A* **467-468** (2001) 185.
- [23] H. Schlarb, Dissertation Universität Hamburg, DESY-THESIS-2001-055 (2001).
- [24] GEANT - Detector Description and Simulation Tool, CERN Program Library Long Writeup W5013.
- [25] J. Pflüger, B. Faatz, M. Tischer, T. Vielitz, *Nucl. Instrum. and Meth. A* **507** (2003) 186.
- [26] P. Elleaume, J. Chavanne, B. Faatz, *Nucl. Instrum. and Meth. A* **455/3** (2000) 503.
- [27] P. Elleaume, O. Chubar, J. Chavanne, *Proc. of the 1997 PAC* (1997) 3509; O. Chubar, P. Elleaume, J. Chavanne, *J. Synchr. Rad.* **5** (1998) 481.
- [28] K. Halbach, *Nucl. Instrum. and Meth. A* **250** (1986) 95.
- [29] Ch. Wang, L.H. Chang, C.H. Chang, M.C. Lin, C.-S. Hwang, J.-R. Chen, *J. Synchr. Rad.* **5** (1998) 478.
- [30] J. Chavanne, P. Elleaume, P. Van Vaerenbergh, *Proc. of the 1999 PAC* (1999) 2665.
- [31] B. Kuske, M. Abo-Bakr, J. Bahrddt, A. Meseck, G. Mishra, M. Scheer, *Proc. of the 24th FEL conf.* (2002), to be published in *Nucl. Instrum. and Meth. A*.
- [32] E. L. Saldin, E. A. Schneidmiller, M. V. Yurkov, "The Physics of Free Electron Lasers", (Advanced Texts in Physics), Springer-Verlag Berlin Heidelberg (2000).
- [33] J. B. Murphy, C. Pelegrini, R. Bonifacio., *Opt. Commun.* **53/3** (1985) 197.
- [34] B. Faatz, J. Pflüger, Y. M. Nikitina, *Nucl. Instrum. and Meth. A* **393** (1997) 380.
- [35] J. Bahrddt, W. Frentrup, A. Gaupp, M. Scheer, U. Englisch, *Nucl. Instrum. and Meth. A* **516/2-3** (2004) 575.

- [36] N. Metropolis, A.W. Rosenbluth, M.N. Rosenbluth, A.H. Teller, E. Teller, *J. Chem. Phys.* **21** (1953) 1087; S. Kirkpatrick C. D. Gelatt, Jr. M. P. Vecchi, *Science* **220** (1983) 671; A. D. Cox, B. P. Youngman, *SPIE* **582** (1985) 91.
- [37] D. C. Quimby, S. C. Gottschalk, F. E. James, K. E. Robinson, J. M. Slater, A. S. Valla, *Nucl. Instrum. and Meth. A* **285** (1989) 281; S. C. Gottschalk, D. C. Quimby, K. E. Robinson, J. M. Slater, *Nucl. Instrum. and Meth. A* **296** (1990) 579; B. Diviacco, R.P. Walker, *Nucl. Instrum. and Meth. A* **368/2** (1996) 522; J. Chavanne, P. Elleaume, *Synchr. Rad. News* **8/1** (1995) 18.
- [38] S. Marks, J. DeVries, E. Hoyer, B. M. Kincaid, D. Plate, P. Pipersky, R. D. Schlueter, A. Young, *Proc. of the 1999 PAC* (1999) 162.
- [39] T. Tanaka, T. Seike, H. Kitamura, *Nucl. Instrum. and Meth. A* **465/2-3** (2001) 600.
- [40] J. Bahrtdt, A. Gaupp, G. Ingold, M. Scheer, *Proc. of the 5th EPAC* (1996) 2535.
- [41] D. R. Walz, E. Lewandowski, A. McFarlane, J. Zabdyr, *Proc. of the 1989 PAC* (1989) 553.
- [42] H. Schlarb, *Proc. of the 8th EPAC* (2002) 2706.
- [43] H. Schlarb, *Proc. of the 8th EPAC* (2002) 1190.
- [44] V. Balandin, K. Flöttmann, N. Golubeva, M. Körfer, DESY-TESLA-2003-17 (2003).
- [45] M. Borland, Advanced Photon Source, ANL APS Report LS-287.
- [46] R. Brun, F. Bruyant, M. Maire, A. C. McPherson, P. Zancarini, CERN-DD/EE/84-1.
- [47] R. Brinkmann, K. Flöttmann, J. Rossbach, P. Schmüser, N. Walker, H. Weise, (editors) TESLA-Technical Design Report Part II -The Accelerator, TESLA Report 2001-23 (2001); G. Materlik, Th. Tschentscher, (editors) TESLA-Technical Design Report Part V - The X-Ray Free Electron Laser, TESLA Report 2001-23 (2001).
- [48] Linac Coherent Light Source (LCLS), Conceptual Design Report, SLAC-R-593 (2002).
- [49] K. L. F. Bane, M. Sands, *AIP Conf. Proc.* **367** (1995).
- [50] K. Bane and M. Sands, SLAC-PUB-4441 (1987).
- [51] G.V. Stupakov, SLAC-PUB-8743 (2000).
- [52] A. Novokhatski, A. Mosnier, *Proc. of the 1997 PAC* (1997) 467.
- [53] F. Zhou, J. H. Wu, M. Babzien, I. Ben-Zvi, R. Malone, J. B. Murphy, X. J. Wang, M. H. Woodle, V. Yakimenko, *Phys. Rev. Lett.* **89** (2002) 174801.
- [54] K. L. F. Bane, A. Novokhatski, SLAC-AP-117 (1999).
- [55] G. V. Stupakov, *PRST-AB* **1** (1998) 064401.

- [56] K. L. F. Bane, C. K. Ng, A. W. Chao, *Proc. of the 1997 PAC* (1997) 1738.
- [57] S.-H. Lee, P. Den Hartog, E. Trakhtenberg, *Proc. of the 2003 PAC* (2003) 824.
- [58] M. Dohlus, R. Lorenz, Th. Kamps, H. Schlarb, R. Wanzenberg, TESLA-FEL 98-02 (1998).
- [59] S. Reiche, UCLA, private comm. (2003).

10 Beamlines for the BESSY FEL

10.1 Introduction

Three free electron lasers will be employed to deliver light between 24 eV and 1000 eV with bandwidths between 0.1% and 0.2%. For many experiments, a higher degree of monochromatization or an increase in spectral purity is necessary and beamlines have to reduce the bandwidth to a level of 10^{-4} - 10^{-5} . But due to the short pulses of an FEL an unprecedented high peak power of up to several gigawatt imposes severe constraints on the beamline design. As a consequence special attention was set on prevention of photon induced damage on the optical elements. Another consequence of the short pulses is a fundamental conflict between a beamline design for high-energy resolution, and simultaneously for short pulses. At the BESSY FEL facility we therefore plan to have at least two different beamlines at each FEL. One type of beamline will be optimized for high-energy resolution, the other for short-pulse conservation. Design studies for the latter type of beamline have shown that the pulse prolongation by the beamline can be kept to below 10 femtoseconds. For the high-energy resolution beamlines resolving powers of up to 270000 can be achieved.

These two types of beamlines have been designed and optimized for the energy ranges of the three FELs: LE-FEL: 24 - 120 eV; ME-FEL: 100 - 600 eV; HE-FEL: 500 - 1000 eV. Only one beamline at each FEL will be used at a time, and switching between both is accomplished by means of a moveable mirror. This concept has been already realized very successfully at the insertion device beamlines of the storage ring BESSY II.

10.2 General Considerations

For a successful design of FEL beamlines a thorough consideration of the power impact on the optical elements is unavoidable. Solutions have to be found for the short time regime (10 femtoseconds) to avoid ablation as well as for the long time regime (seconds) to prevent a macroscopic distortion of the optics. In the standard operation mode of the FEL facility, the bunches accelerated by the LINAC are distributed among the three FELs. For the long time regime the worst case would happen — as seen from the beamline — if all pulses are directed into the same FEL and hence one beamline. In particular the optical element upstream of the gratings would then have to handle the corresponding power load. Typical values of the power load together with other photon-beam related parameters of the FEL are shown in table 10.1. They are compared to corresponding values of a typical undulator operating at the storage ring BESSY II. The U41 undulator is listed as a typical example. The numbers for the FEL assume (after a start-up phase with a 1 kHz pulse repetition rate) a repetition rate of 25 kHz using a superconducting injector. De-

pending on energy range and type of the FEL, the total power incident on the first mirror varies from 0.4 to 8 W. Thus, even for the 25 kHz operation of the FEL, the power to be removed is not critical. Conventional cooling schemes like side cooling are sufficient to remove the average heat load from the mirrors. In addition the absorbed power can be easily distributed amongst all optical elements.

The situation is completely different in the short-time regime, i.e. when peak photon densities are considered. Even in a highly diluted FEL beam, the energy and photon densities are 4 - 5 orders of magnitude higher than in undulator beams at 3rd-generation storage rings. This, together with the very short pulse length of about 10 - 30 femtoseconds, leads to a high number of ionized surface atoms on the optical elements before de-excitation processes can take place. If the distance between ionized atoms then falls below a certain value desorption (ablation) of surface atoms will occur. However, the order of the critical distance (or photon density) is not yet known for the X-ray energy range of the planned FEL. Only for silicon, carbon and gold coated mirror surfaces first experiments at 12 eV at the TTF-FEL at DESY showed that ablation already occurs up to a factor 100 "earlier" than expected. For the design of the BESSY FEL beamlines a 10 times lower photon density was taken as a safety margin to observed limits. For the same reason focusing of the undispersed FEL beam onto optical elements - including slits - has been avoided. As far as possible, only surface materials with low ionization cross sections have been taken for the specific energy ranges of the FELs. An issue to be considered in detail is the temperature development of the surface within a bunch train. This is addressed in section 10.2. Hence, above all, the beamline design has to account for the high peak photon density and avoid any degradation of or damage to the optical elements.

Up to now, there are some uncertainties concerning the source sizes relevant for optical imaging. Within GENESIS [1] a source size is computed for the region where the laser field strongly couples to the electron beam. On the other hand, beamline design deals with the free propagating wave field, which is known to consist of one transverse fully coherent mode. First calculations, where the wave field generated by GENESIS is treated with wave optical methods indicate that the free propagating light field is indeed diffraction limited. As a starting point for the beamline design the FEL beam is assumed to be diffraction limited with a source size calculated from the divergence, given by GENESIS, according to equation 10.8 (below). These diffraction-limited source sizes are also listed in table 10.1.

Table 10.1: Parameters of the FELs and comparison to the existing U41 undulator at BESSY II. Source size, divergence, bandwidth, pulse length, and beam width are given as fwhm-values.

	U41	LE-FEL	ME-FEL	HE-FEL	Unit			
Photon energy	160	24	120	100	600	500	1000	eV
Repetition rate	$5 \cdot 10^5$	25	25	25	25	25	25	kHz
Pulse energy	0.001	320	36	160	30	20	15	μJ
Pulse length	50000	22	30	25	20	21	7	fs
Source divergence	200	160	35	45	16	21	14	μrad
Source size [†]	30	140	130	52	24	52	37	μm
Bandwidth	5.4	0.1	0.18	0.16	0.23	1.5	2	eV
Total power	14^*	8	0.9	4	0.75	0.5	0.38	W
Ang. flux density	400^*	300	700	2000	3000	1100	2000	W/mrad ²
Photon number [§]	$2.5 \cdot 10^{16}$	$2 \cdot 10^{18}$	$4.5 \cdot 10^{16}$	$2.5 \cdot 10^{17}$	$7.8 \cdot 10^{15}$	$6.2 \cdot 10^{15}$	$2.3 \cdot 10^{15}$	1/s
Photons per pulse [§]	$5 \cdot 10^8$	$8 \cdot 10^{13}$	$1.7 \cdot 10^{12}$	$1 \cdot 10^{13}$	$3.1 \cdot 10^{11}$	$2.5 \cdot 10^{11}$	$9.4 \cdot 10^{10}$	
Typ. first mirror position	17	40	40	40	40	50	50	m
Beam width	2	6.4	1.4	1.8	0.64	1.0	0.7	mm
Area	9	32	1.5	2.5	0.32	0.79	0.38	mm ²
Flux density	4.5^*	0.25	0.6	1.6	2.3	0.6	1.0	W/mm ²
Energy density	$1 \cdot 10^{-5}$	1	2.4	6.4	9.4	2.5	4.0	mJ/cm ² /pulse
Photon density [§]	$6 \cdot 10^{-5}$	2.5	1.2	4	1	0.3	0.25	1/nm ² /pulse

* Integrated over the full spectrum § In the first harmonic

† Diffraction limited size, see text

10.2.1 Photon-Induced Damages

Well established continuous wave and nanosecond laser ablation is used in many fields, such as materials processing and medicine. In these regimes the dominant process involved is the heating of the target material through the liquid phase to the vapor phase, resulting in expansion and expulsion of the desired target material. This is accompanied by heating and collateral damage to the surrounding area, the degree of which is determined by the rate of energy absorption and the rate of energy loss through thermal conduction in the material.

On the other hand, due to their high-peak intensities and short-pulse duration, picosecond and femtosecond pulses ablate material via the rapid creation of plasma that absorbs the incident energy resulting in direct vaporization from the target surface. This avoids collateral heating and shock-wave damage. With energy densities of several J/cm²

it is possible to drill holes in metals and to machine features with high precision [2], but for the components of the FEL such results are very undesirable.

In recent experiments at the TTF free electron laser (pulse length of 100 fs, pulse energy 40 μJ), damage thresholds for the following materials were reported for 98 nm wavelength [3, 4]:

Carbon	60	mJ/cm^2
Silicon	30	mJ/cm^2
Gold	40	mJ/cm^2

The corresponding power density of the FELs at the location of the first optical elements is at least a factor of 4 lower than these values (see table 10.1). In addition, as explained below, geometric factors and the high reflectivity reduce the surface load by further 2 - 3 orders of magnitude. This is sufficiently low for a safe and reliable operation of the beamline components.

10.2.2 Mirrors

10.2.2.1 Total External Reflection

Generally, the reflectance of optical surfaces increases with smaller grazing incidence angle θ and the footprint of the incident beam is distributed over a larger area proportional to $1/\sin\theta$. At first sight it seems that a reduction of the incidence angle always reduces the load on the optical surfaces. However, a careful inspection of the Fresnel formulas [5, 6] shows that the corresponding decrease of the penetration depth reduces the geometrical dilution effect and even increases the load on the very first layers.

Fortunately, in the VUV and X-ray region the index of refraction of matter is smaller than its vacuum value – the vacuum is optically denser than matter – and total external reflection occurs on surfaces for incident angles smaller than the critical angle θ_c .

In the regime of total external reflection the penetration depth d_e is nearly independent of the incident angle while the dilution effect is still proportional to $1/\sin\theta$.

For a given reflectance R , the intensity in the material decreases exponentially along the depth z , perpendicular to the surface

$$I(z) = I_0 \sin \theta (1 - R) e^{-z/d_e}, \quad (10.1)$$

where I_0 is the intensity of the incident radiation. Based on this (phenomenological) description, the power P_a absorbed by atoms (with atomic volume V_A) in the uppermost layer can be written as

$$P_a = I_0 \sin \theta (1 - R) V_A / d_e = \sigma_a \cdot I_0. \quad (10.2)$$

The last equation defines a phenomenological cross section σ_a for surface atoms with respect to the incident beam. Due to the exponential decrease of the wave field, lower lying atoms absorb less power. The numbers calculated by this formula give therefore an upper limit of the power absorbed by the constituent materials.

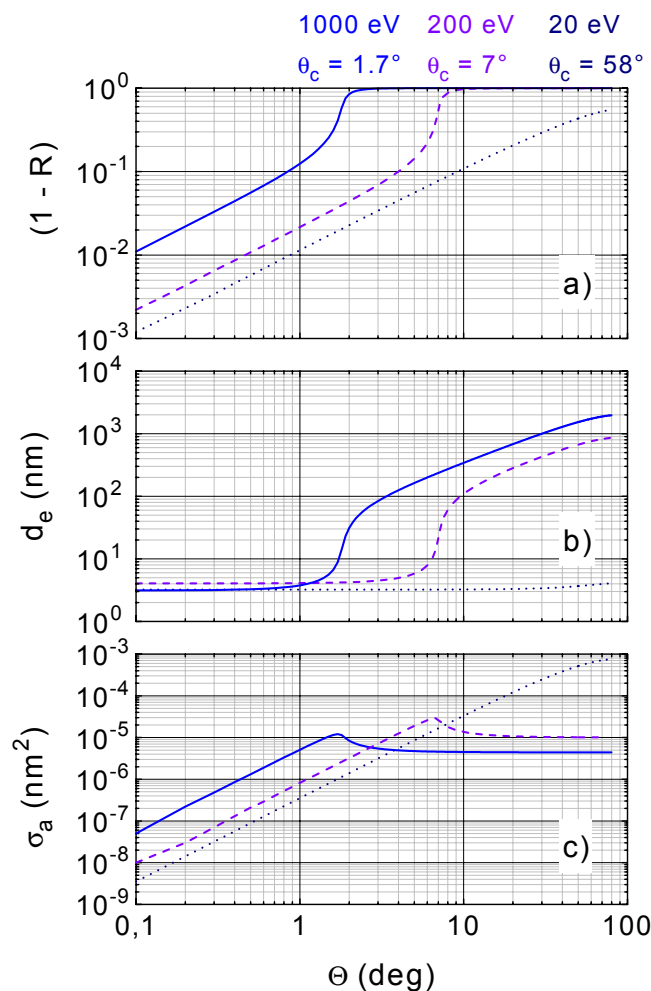


Fig. 10.1: a) Absorption $(1-R)$ as a function of the incident angle on a silicon mirror for photons of 20 eV, 200 eV and 1000 eV, respectively. b) Penetration depth of the exponentially damped beam. c) Phenomenological cross section of surface atoms according to equation (10.2) is shown.

Figure 10.2 shows the dependence of absorption, penetration depth and cross section for surface atoms with respect to the incident angle. From this it is apparent, that the cross section of the surface atoms increases while the incident angle is reduced and a maximum occurs at the critical angle, but below the critical angle the cross section decreases according to θ^2 . Besides the dilution effect, which accounts for a factor θ , the absorption $(1-R)$ also decreases proportionally to θ . This is shown in figure 10.2 for silicon at three photon energies.

10.2.2.2 Coatings

Optical elements in the VUV and soft X-ray regime are in general coated with material different from the substrate to enhance the reflectance in a specific spectral range. The phenomenological absorption cross section of the surface atoms with respect to the incident beam intensity according to equation (10.2) is used as a figure of merit to compare different materials. Figure 10.3 shows the cross section with respect to the photon energy of some commonly used coating materials for soft X-ray optics.

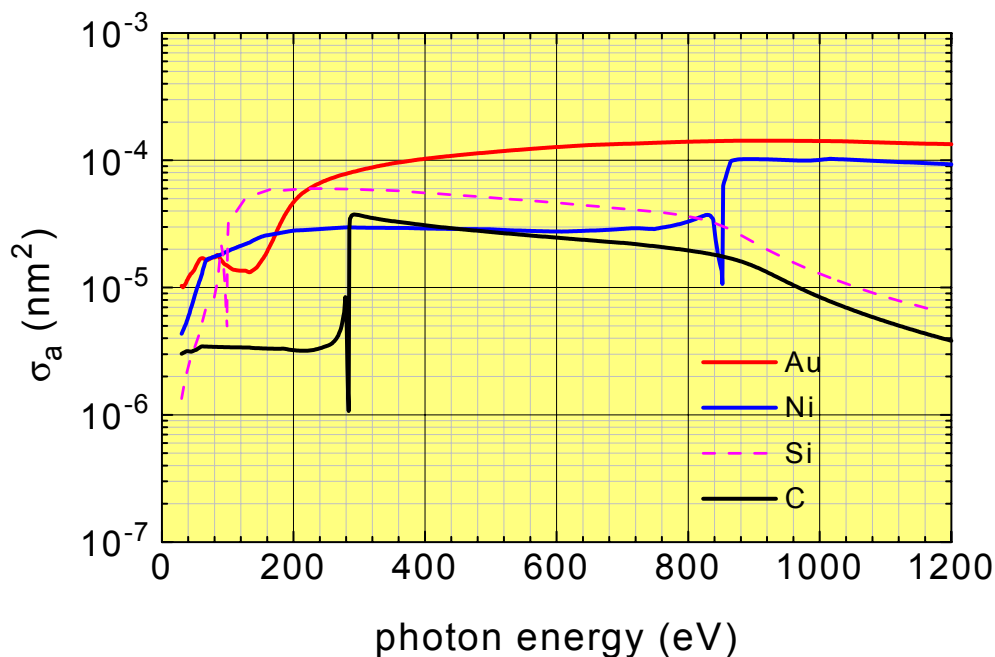


Fig. 10.2: Absorption cross section for atoms of different coatings. The cross sections increase strongly above the absorption edges.

The first experimental results about ablation on surfaces at the TTF free electron laser at 98 nm have been recorded at relatively low photon energies, where the cross sections defined by equation (10.2) are low. But, for excitation energies at the K- and L-edge, the cross section increases by up to one order of magnitude.

Besides the risk of damage due to strongly enhanced absorption the reduced reflectance also precludes their use. Hence, coatings should have no absorption edges within the photon-energy range of the beamline. Generally coating materials with small atomic numbers are more able to withstand the intense FEL beam.

Figure 10.3 shows the values for gold, nickel, silicon, and carbon for the two extreme photon energies of 24 eV and 1000 eV far away from absorption edges with respect to the angle of incidence. The cross section of the low Z elements carbon and silicon are up to two orders of magnitude lower than, for example, the high Z element gold. For the beamlines attached to the low- and the high-energy FELs, carbon is therefore used as coating material. For the beamlines at the medium-energy FEL it cannot be used due to its K-absorption edge. For this beamline nickel is a possible candidate for a coating material. Its L-edge at 853 eV is well above the energy range of the ME-FEL.

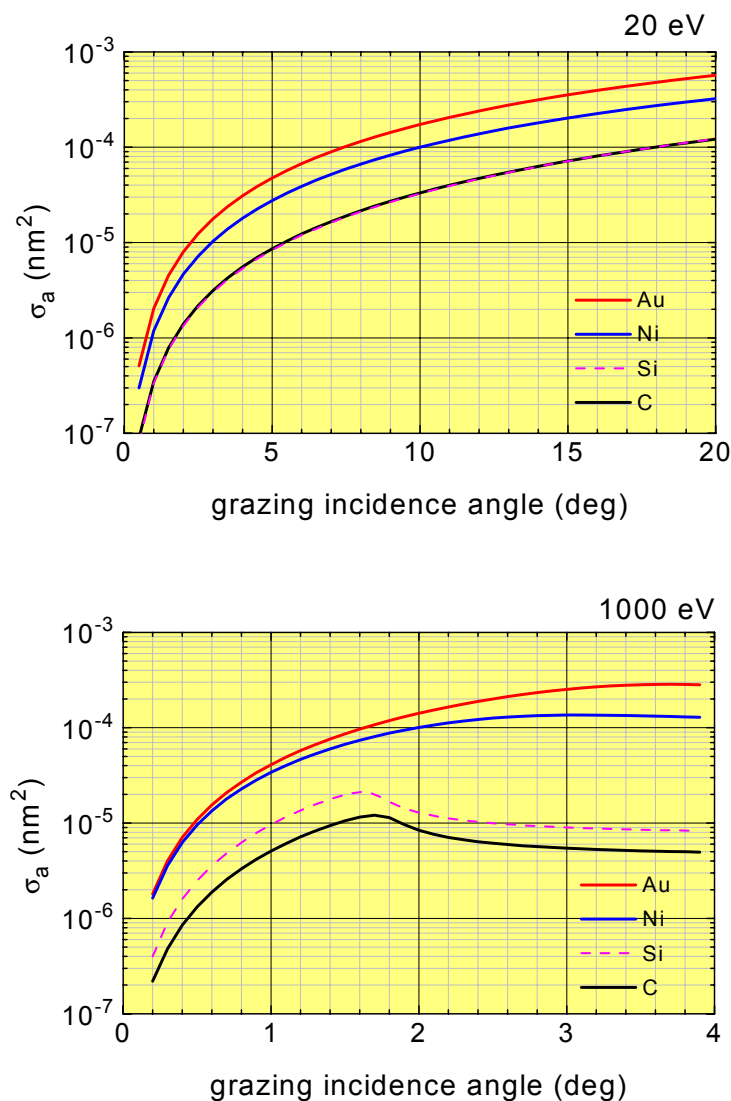


Fig. 10.3: Absorption cross section for atoms of different coatings. At 20 eV the critical angles (grazing) are 58° (C), 55° (Si) and 27° (Ni). For gold the index of refraction is larger than one and no total external reflection occurs. At 1000 eV the critical angles are 1.8° (C), 1.7° (Si), 2.7° (Ni) and 3.71° (Au). The optical constants are taken from [7].

10.2.2.3 Thermal Properties

The warming of the mirror surface after the reflection of an FEL pulse can be estimated with some assumptions. During reflection, a fraction of its energy is absorbed and deposited in the electronic system of the surface. Subsequently, this energy is transferred to the crystal lattice with a typical time constant of a few picoseconds. The thermal deformation of the surface, that accompanies the temperature rise of the lattice, takes place after the pulse has already been reflected. A short FEL pulse will therefore not see the thermal deformation induced by itself.

The volume in which the absorption takes place can be approximated by the illuminated area A , multiplied by the penetration depth d_e . Assuming that the absorbed fraction of the FEL pulse Q heats only this volume $A \cdot d_e$ the increase in temperature ΔT can be approximated by means of

$$\Delta T = \frac{Q}{c \cdot m} \quad \text{with } m = \rho \cdot A \cdot d_e, \quad (10.3)$$

where ρ and c are the density and the specific heat of the material, respectively. A deposited pulse energy of $60 \mu\text{J}/\text{cm}^2$ increases the temperature at a silicon surface, for example, by 80 K.

For a more detailed estimation of the temperature profile in the mirror the process of power absorption and heat conduction was modelled with the computer code MECHANICA (PTC, Needham, MA, USA). Time dependent temperatures calculated at selected distances to the surface are shown in figure 10.4. For the calculation with MECHANICA a cylindrical rod of silicon with 200 nm diameter and 20 μm depth was considered. The heat could only be conducted along the depth of the cylinder, no heat transfer through the wall was allowed.

In the calculation it was assumed that the absorbed fraction of the pulse energy is transferred with a constant rate over one picosecond to the lattice. For a metallic coating this is a reasonable realistic assumption. For silicon the energy transfer from electronic excitation to the lattice should be a factor of 10 to 100 slower. The accompanying temperature rise at the surface from 20° C to 80° C is in good agreement with the rough estimation made above.

Heat conduction into the volume lowers the surface temperatures to the initial values after some nanoseconds. This time constant is much smaller than the shortest planned bunch separation of 2 μs . Crystal deformation can therefore be abated before the subsequent pulse arrives and no melting is expected. On the other hand, optical elements usu-

ally have coatings with a thickness of 20 nm to 30 nm. As can be seen from figure 10.4 the coating will experience a larger temperature variation than the bulk below.

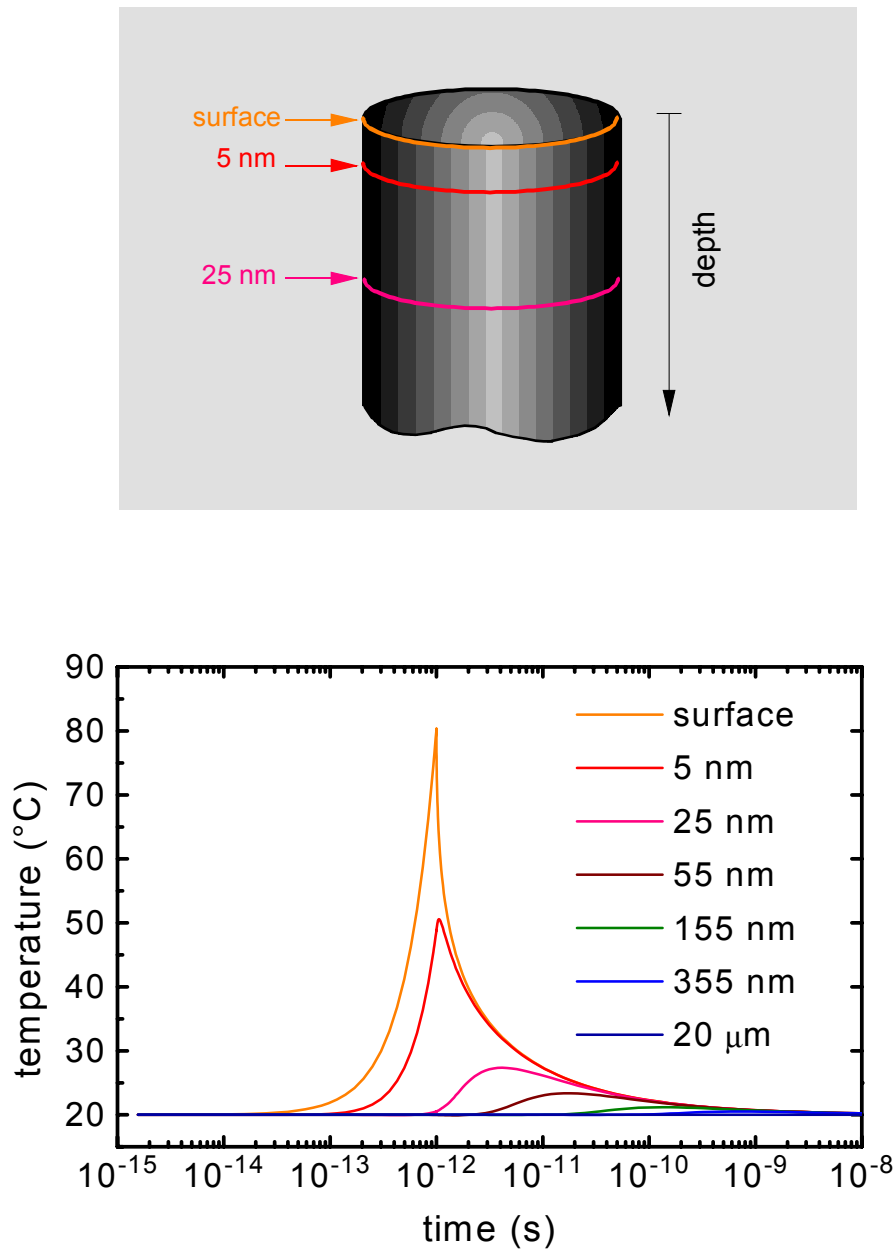


Fig. 10.4: Heat-load calculation for silicon. The figure shows the temperature profile at selected depths below the surface.

Not included in the MECHANICA calculations is the thermal contact resistance between coating and bulk, which could lead to a somewhat higher temperature in the coating than estimated with the simple monolithic model.

10.2.2.4 Surface Quality

Surface quality is treated in terms of slope errors and surface roughness. Slope errors describe deviations of a real macroscopic surface from the ideal one on spatial frequencies smaller than $\approx 1/\text{mm}$, whereas surface roughness deals with deviations in the micrometer-down to the atomic-nm-scale.

Surface roughness σ reduces the specular reflectance R_0 of a surface and increases the amount of non-specularly reflected light, i.e. stray light. The reduction of specular reflectance is described by a Debye-Waller formula

$$R = R_0 \exp \left[- \left(\frac{4\pi\sigma \sin \phi}{\lambda} \right)^2 \right] \quad (10.4)$$

where ϕ is the grazing angle of incidence. The reduction becomes more important for steep incident angles. The small incidence angles of the FEL-beamline designs allow for relatively large surface roughness values. Even for 1000 eV light incident under 2° on a mirror, a surface roughness of 0.5 nm diminishes the reflectance by only 3%. If small amounts of stray light do not spoil experiments, state-of-the-art optics with roughness of 0.5 nm are tolerable.

Slope errors are treated in geometrical optics as local deviations of the surface slope that change the angular direction of reflected beams. Their most significant effect is the broadening of focal spots. State-of-the-art rms values for optics used in third-generation storage-ring instrumentation are 0.1 arcsec (rms) for plane and spherical elements and 0.5 arcsec / 1 arcsec (rms) for toroidal and cylindrical elements in meridional / sagittal direction. Beamlines for ultrahigh energy resolution at FELs (see for example table 10.2) require much better surfaces.

A national project (NOK-Verbundprojekt) has already made significant improvements in manufacturing and measuring techniques. As a part of this project, and for the above mentioned purpose, the world's most precise measuring machine has been developed at BESSY. In the course of the improved diagnostics, optical elements with five to ten times lower slope errors will become available in the near future. Currently the best values for plane surfaces manufactured in the NOK-Verbundprojekt are 0.05 arcsec and 0.03 arcsec for plane elements with a length of 600 mm and 100 mm, respectively.

10.3 Diffractive X-Ray Optics

In hard X-ray monochromators crystals with bandwidths significantly smaller than the bandwidth of the incident light are used to select a specific wavelength. Because of this mismatch, most of the incoming radiation does not fulfill the Bragg equation and is not diffracted. Instead, it penetrates through the surface and is absorbed in the crystal. In addition the much steeper incidence angles in crystal monochromators lead to smaller footprints and to higher power densities compared to gratings. Crystal monochromators suffer therefore to a higher extent from the average power than gratings, and therefore need a better cooling. On the other hand, the penetration depth for hard X-rays is larger than for VUV and soft X-ray radiation, and the energy absorbed in the topmost layers does not increase to the same extent. The larger penetration depth may also reduce the strain due to the high-peak photon density. Since the lowest energy of a crystal monochromator is around 800 eV, this kind of monochromator would not cover the full range of the high energy FEL and will not be further considered.

Because of their limited usable photon-energy-range zone plates as well as Bragg-Fresnel zone plates cannot be considered as general optical elements for tuneable FEL beamlines. In the VUV- and soft X-ray regime usually different kinds of reflection gratings are used to disperse the light. Light with wavelength λ illuminating a grating with line density N under a grazing incidence angle α is diffracted into the angle β of k^{th} order according to the grating equation

$$Nk\lambda = \cos \alpha - \cos \beta. \quad (10.5)$$

Different wavelengths, incident with the same angle, are diffracted into different diffraction angles. In almost all cases the grating is operated in a mode where all light within the bandwidth of the incident FEL beam is diffracted into different diffraction orders including the specular reflection into zero order. Therefore the grating does not suffer from a bandwidth mismatch as discussed for crystals. Losses occur only due to the incomplete reflectance of the coating. Grating monochromators with reflection gratings are employable from visible light up to more than 2000 eV. Hence, all proposed BESSY FEL monochromators are based on reflection gratings.

In grating monochromator designs with variable deflection angle $2\theta = \alpha + \beta$ the grating equation can be fulfilled for a variety of incident and diffracted angles. The magnification, c , of the grating

$$c = \frac{\sin \beta}{\sin \alpha} \quad (10.6)$$

is used to refer to a specific choice of the angles α and β [8].

Because of the increasing absorption at large angles of incidence the grazing incidence angle should be kept low, e.g. $\alpha = 2.3 - 0.5^\circ$ and $\theta = 3.4 - 1.8^\circ$ for a beamline from 500 eV - 1000 eV. This implies a large magnification factor which yields a high-energy resolution but also causes a significant time stretching of the pulses. On the other hand, decreasing c for maintaining the short pulses of the FEL after the monochromator would bring up again the absorption problem with the risk of ablation. A high power density may partly be diluted by diverging the beam in the direction parallel to the grating profile, where it does not affect pulse length and resolving power. A further consideration is the grating efficiency, which depends on the magnification factor. A value of $c = 2.2$ gives good efficiency in many cases. Thus, the requirement for good efficiency and high throughput may collide with requests for high-energy resolution and/or pulse dilatation.

As can be seen in later sections it is not possible to fulfill all conditions with one beamline. Instead, two beamlines with different optimisation goals have been designed. In order to maintain the short pulses for experiments at the FELs it was necessary to split the FEL beam into two branches: the high-energy resolution branch and the short-pulse branch. In general short pulses require narrow beams in dispersive direction whereas high energy resolution calls for a longer illumination of the grating.

The energy bandwidth and temporal length of a pulse are mutually dependent. The rms values of the pulse length ΔT and bandwidth ΔE are related by the Fourier-transform limit

$$\Delta E \cdot \Delta T \geq \frac{h}{4\pi}, \quad (10.7)$$

which is an inherent relation independent of the type of source or monochromator. The actual time-bandwidth product of an initially transform limited pulse after transmission through a monochromator can be related to the phase space volume of the incident beam

$$\sigma\sigma' = F \cdot \frac{\lambda}{4\pi}. \quad (10.8)$$

Here σ and σ' are the rms size and the beam divergence of the source. The factor F equals one for diffraction-limited beams and is larger for all other beams. For monochromators with source size-limited resolution it can be shown that the bandwidth and pulse prolongation are related by the same factor

$$\Delta E \cdot \Delta T = F \cdot \frac{h}{4\pi}. \quad (10.9)$$

The performance of a monochromator in terms of energy resolution and pulse dilatation therefore is strongly related to the phase-space volume of the incident radiation. This must be kept in mind during the optimization process of the FEL source.

10.3.1 Beam Shaping

As shown in the last section, the performance of a beamline depends on the quality of the FEL photon beam. In experiments with lasers, spatial filtering is commonly used to improve the quality of the beam, if necessary. For beamlines in the VUV and soft X-ray range similar techniques exist. However, the low reflectivity of mirrors in this spectral regime forbids the use of too many optical elements.

Entrance slits offer the possibility to decrease the phase space volume of a given beam down to the diffraction limit [9]. By closing the slit to a size where the divergence of the transmitted beam is dominated by diffraction, the effective source size can be decreased. In this regime the bandwidth of the monochromator can be diminished without increasing the pulse length more than given by equation (10.7). Of course, this works only because portions of the beam outside of the minimum phase-space volume are discarded.

In FEL beamlines the use of slits in the focused undispersed beam is not safe with respect to ablation on the jaws, and beam shaping with entrance slits is not possible. To some extent baffling of the grating offers a comfortable and, in terms of damage, safe method to improve the pulse length without deteriorating the resolving power too much. As baffling reduces the divergence of the beam, the pulse length can be reduced, but it does not affect the source size as an entrance slit would do. Baffling can improve the energy resolution in beamlines with aberration-limited energy resolution but cannot improve the energy resolution if the beamline is limited by a large source size.

In any case, the improvement of the beam quality in the beamline is paid for by a corresponding loss of intensity. Hence, the parameter F in equations (10.8) and (10.9) can be also called the loss factor and stands for losses in the FEL/monochromator system.

10.3.2 Timing

In pump-probe experiments a potential timing jitter of the FEL beam imposes severe problems in determining the interval between the FEL beam and a second short-pulse laser beam, usually a laser in the visible regime.

The interval between the laser pulses could be measured if small fractions of the beams are extracted near the experiment and are used in a coincidence experiment to obtain the

actual time shift. Experiments could use this information to sort their results post mortem according to the actual offset.

As in the visible regime the grating can be used as a beam splitter. It can be shown that in the on-blaze mode the angular separation of first and zero diffraction order remains constant. If the optical design of the beamline ensures that the focusing of both orders is unchanged while scanning the energy, both beams can be used simultaneously.

Using the first order diffracted light at the experiment behind the exit slit, the zero order remains spatially fixed even if the monochromator pass energy is altered. If, on the other hand, experiments in the zero diffraction order are performed, the energy distribution of the actual pulse could be determined by a detector in the exit slit plane.

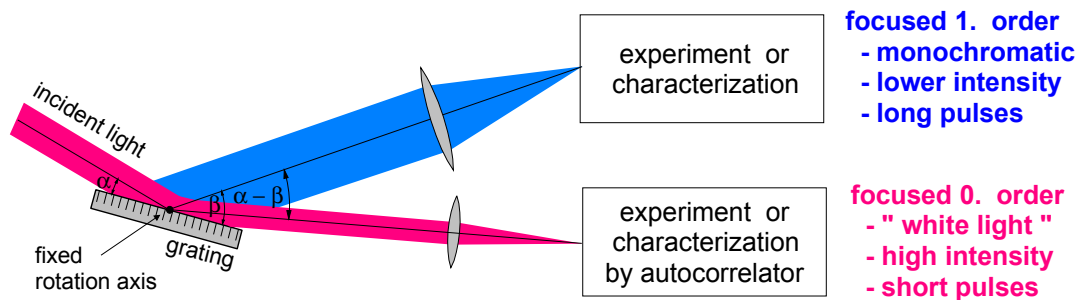


Fig. 10.5: Fixed angular deviation between zero and first diffraction order.

This detector can also be used as a diagnostic tool to characterize the FEL beam in the commissioning period. The constant resolving power in the on-blaze mode [10] facilitates the design of the detector in the exit slit plane.

The on-blaze mode requires an additional plane mirror to set in the appropriate deflection angle at the grating. This is the so-called SX-700 concept [11] and is included in the designs proposed here. An unwanted side effect of the variable deflection angle is a systematic variation of the path length in the monochromator. Because this variation occurs between the pre-mirror and the grating, it affects both diffraction orders in the same manner and their relative offset remains unchanged. The absolute value of the path length depends on the energy and the c-value setting of the monochromator and can be calculated analytically. The variation at the experimental station of the high-energy-resolution beamline of the HE-FEL is for example shown in figure 10.17 (see below).

10.3.3 Raytracing

The raytrace calculations were performed with the BESSY code RAY [12]. Since it is a geometric raytracing program it cannot *ab initio* account for diffraction effects. Yet in order to account for finite grating and mirror apertures as well as small slits, diffraction at apertures was implemented in the code in a phenomenological way. The diffraction pattern of the aperture was used as probability distribution according to which any beam passing through the aperture is deflected in a stochastic manner.

The various FEL sources were modelled as Gaussian beams with parameters given in table 10.1. Calculations with GENESIS and PHASE [13] indicate that the source point of the FEL beam is near the saturation point in the final amplifier which may vary with photon energy. But with the ability to operate the various segments independently, it becomes possible to keep the saturation point always near the end of the final amplifier. For the raytrace calculations a fixed source point at the end of the final amplifier was assumed. The time structure of the FEL pulse was assumed to be of Gaussian shape and the spectral distribution was assumed to be either Gaussian or rectangular.

10.4 General Layout

The general layout of the beamlines in the experimental hall is shown in figure 10.6. The electron bunches for the low-energy FEL beam are extracted and deflected before the medium- and high-energy FELs. The low-energy FEL is mounted at an angle of 5° with respect to the previous accelerator and directs its light through the radiation safety wall to the beamlines in the front part of the experimental hall. Behind the extraction point, a further accelerator section accelerates the electron bunches from 1 GeV to 2.3 GeV, the energy required for the two other FELs. They diverge from each other to obtain lateral floor space for the beamlines and the experiments. At each FEL beam a retractable first mirror will be used to extract the beam for a white-light beamline (figure 10.6). In these white-light beamlines the undispersed FEL beam is focused down to micrometer scale foci and peak-power densities of up to $3 \cdot 10^{14}$ W/mm²/s, which corresponds to 200,000 photons/nm²/pulse, are achieved.

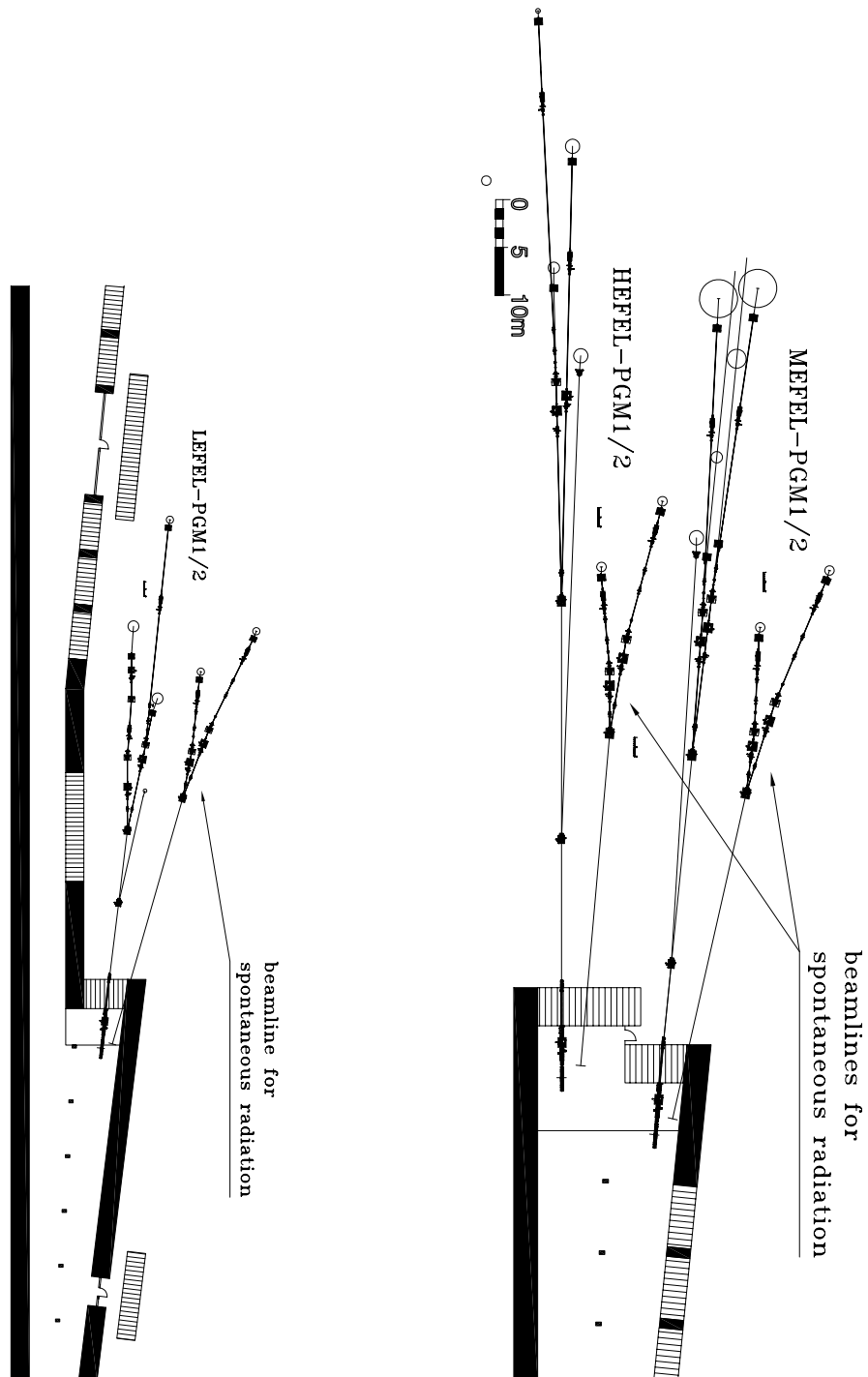


Fig. 10.6: General layout of the user facility. The left figure shows the LE-FEL before the last acceleration stage with the beamlines for the LE-FEL. The right figure shows the end of the accelerator building with the beamlines for the HE-FEL and LE-FEL. The radiation shielding outside the main accelerator section are not shown.

Alternatively, two interchangeable mirrors guide the beam either to a dedicated short-pulse beamline or to a beamline for highest energy resolution. The beamlines for highest energy resolution achieve resolving powers of up to 270,000. Due to their narrow energy bandwidth the pulses are stretched to 80 picoseconds (section 10.6.1).

Dedicated beamlines for conservation of the pulse lengths are used to separate the FEL pulse from background radiation. These beamlines should not stretch the pulse significantly, so emphasis is put on a design that intrinsically allows for wide spectral bandwidths. Ideally these beamlines enable the users to manipulate the spectral bandwidth while keeping the pulse length transform limited (section 10.6.2).

In the regular operation of a beamline the dispersed light is guided through the exit slit and subsequently directed to the experiment. Due to the limited diffraction efficiency of the grating, only a small fraction of the incident light is utilized in this way whereas most of the light remains unaffected in the zero order and is captured by baffles. Operating the grating as a beam splitter and using both beams opens up new opportunities as described in section 10.3.5. This concept is planned for all high energy resolution beamlines but described only once, in section 10.7.1.

By deflecting the dispersed light with a plane mirror in front of the exit slit as indicated in figure 10.8 it is possible to use the monochromator as spectrograph. A fluorescence screen placed in the focal plane of a lens-CCD-camera system enables one to detect a complete single-shot spectrum at once. This setup is required by the two-beams mode described in section 10.3.5 but is also extremely helpful for commissioning and optimizing the FEL operation. Again the scheme is depicted only once in figure 10.8 but will be installed at all beamlines for high-energy resolution.

After the electron beam has passed the FEL undulator, the electron bunches are still of high enough quality to generate short pulses of spontaneous radiation in additionally installed undulators. The pulse lengths of this radiation are expected to be in the low picosecond range and offer additional experimental opportunities. Such undulators are equipped with two undulator beamlines (section 10.8).

In the following, different types of beamlines for the FELs are presented. They address issues on high-energy resolution and short-pulse operation at the extreme photon energies.

10.5 Frontends

The frontend is the interface between photon source and the user beamline. It serves to separate the two from each other in terms of vacuum and radiation safety. It is the last group of components in the radiation tunnel before the FEL radiation enters the experimental hall and the beam line.

Although the frontends at the BESSY FEL must fulfill the same function as at BESSY II, the user operation with the BESSY FEL is very different from that at the BESSY II storage ring. For each FEL line there is only one user at a given time and the FEL can be switched off without affecting the operation of the other two. In addition to that it is possible to switch off any one of the three FELs very quickly both at the seeding laser and at the injector itself. Even with a 25 kHz repetition rate the FEL can be stopped from one pulse to the next. This makes for a simple logic for the radiation safety and vacuum interlock systems and for a safe operation of the facility.

A front-end (figure 10.7) must fulfill the following explicit functions:

1. Vacuum separation of the machine from the following components (valve 1), and in turn those from the beamline (valve 4).
2. Vacuum interlock system to regulate the manual opening and manual/automatic closing of valves 1 through 4.
3. Vacuum protection of the machine from sudden ventings somewhere in the beamline (fast closing valve).
4. Radiation separation of the machine area from the experimental hall and the beamline (beamshutter).
5. Definition of the optical path and suppression of scattered light between the machine and the beamline (precision moveable apertures).
6. Diagnostics for determining the position and the emission angle of the radiation source or of the center of gravity of the FEL radiation in the front-end.
7. Suitable vacuum housing, frames, interlocks, and controls for the above functions.

In the design of the front-ends, the following items must be taken into account:

- a) The radiative power, in particular the peak-power density of the FEL radiation that may impinge on the components of the front-end.
- b) Bremsstrahlung that may impinge on the components of the front-end.
- c) The acceptance or opening angle required to permit the desired radiation to pass through.
- d) The quality of vacuum that should optimally be maintained in the machine.

a) Peak-power density

For a rough estimate we refer here to the ME-FEL, where the largest energy density per pulse is expected (table 10.1). At 600 eV an energy-density normal to the beam of 38 mJ/cm² is expected at a distance of 20 m from the source. By using a grazing angle of incidence of $\approx 6^\circ$ the primary fluence can be reduced by a factor of ten to ≈ 3.8 mJ/cm². Since

only a fraction of about 40% is absorbed and the rest specularly reflected or scattered, a fluence of about 1.5 mJ/cm^2 in the surface may be expected.

Despite the uncertainties in the experimental data concerning ablation under high-power femtosecond pulses (section 10.2.1), it would appear that the power levels we can expect at the BESSY FELs are on the safe side. Thus, all surfaces lying within the direct FEL beam should work at a grazing angle of typically 6° to avoid the problem of ablation. Furthermore, the radiation which is reflected and scattered from these surfaces must be directed onto a well-defined surface where it is finally absorbed.

Where materials and/or grazing angles are not practicable, and the possibility that the laser for some reason does not shut off, a component can be protected by another component which can be allowed to suffer ablation without losing its functionality. For the most critical safety element of the front-ends, the protective shutter just in front of the fast closing valve, a combination of all three approaches, is taken: material, angle, and allowable ablation. For these reasons, it appears that the various aspects of handling the very high peak powers of the FELs can be dealt with directly and safely.

b) Bremsstrahlung

Because of the very high degree of collimation of the radiation, the front-end can be designed with a very small aperture. The collimation along with the low gas load in the machine and the low current densities in the electron beam lead to levels of bremsstrahlung which are of no consequence for the metallic components of the frontend.

As far as radiation safety is concerned, a beam shutter made of a tungsten alloy (Hevimet, Densimet, etc.) with a length of 350 mm and a diameter of 100 mm fulfills the necessary safety conditions. This cylinder will be located directly in front of the radiation safety wall. In order to be able to test the FEL with the beam shutter closed, the precision vertical apertures, which are generally used to define the optical path vertically, are so designed to be able to withstand the high repetition rate of FEL pulses indefinitely.

c) Acceptance, FEL beam cross section

For a front-end starting about 17 meters from the end of the final amplifier and with a length of 6.2 meters, the parameters of the beam can easily be calculated from the numbers given in table 10.1.

The maximum diameter of the LE-FEL beam in the front-end is about 10 mm (6 sigma) while for the other FELs it is significantly smaller. Hence, standard vacuum components can be used in the front-end, depending upon the function required of the particular component.

d) Quality of the vacuum

The superconducting technology of the linac requires that fast closing valves must respond to a vacuum alarm as fast as possible. For NW35 such valves are available with a closing time of about 10 ms. These valves have a viton seal which enables them to close completely with a leak rate $<1 \cdot 10^{-10} \frac{\text{mbar} \cdot \text{l}}{\text{s}}$. It is the only component in the front-end which at all costs must be shielded from the FEL radiation. This is accomplished by a shield shutter placed directly in front of the valve and which closes somewhat faster, within about 5 ms. Besides the shielding function it has no vacuum-sealing function. In this way, the viton-sealed fast-closing valve will always be shielded from the FEL radiation, even if the "turning off" of the laser should fail. However, the pulsed laser will always be "turned off" in the event of some beamline accident. Since nothing else in the front-end or the beamline behind it moves anywhere near as fast, this shutter will protect the entire front-end and beamline in case of some mishap.

If there is a catastrophic venting of the beamline somewhere and no small apertures are incorporated in it, the air/gas will travel with a speed of 500 -1000 m/s. Only hydrogen and helium are significantly faster. Thus, any venting which lies more than 10 meters behind the first fast closing valve will have no significant effect on the vacuum in the machine. In order to reduce the danger of a partial machine venting, which is extremely critical because the superconducting linac components should remain clean and at a vacuum in the 10^{-10} mbar range, further fast closing valves should be incorporated both upstream of that in the front-end (with a shield shutter) and in the beamlines.

10.5.1 Diagnostics

The SR-Diagnostics will take advantage of the long path of the FEL radiation through the radiation-shield wall by employing a pinhole monitor just behind the valve 1 in the tunnel and a second pinhole monitor just behind valve 4 outside the tunnel. These two monitors enable SR-beam based alignment to be performed on the beamline.

In addition an X-ray beam position monitor (XBPM) is included in the front-end design. This monitor is capable of shot-by-shot position diagnostics. These elements are described in more detail in chapter 12.

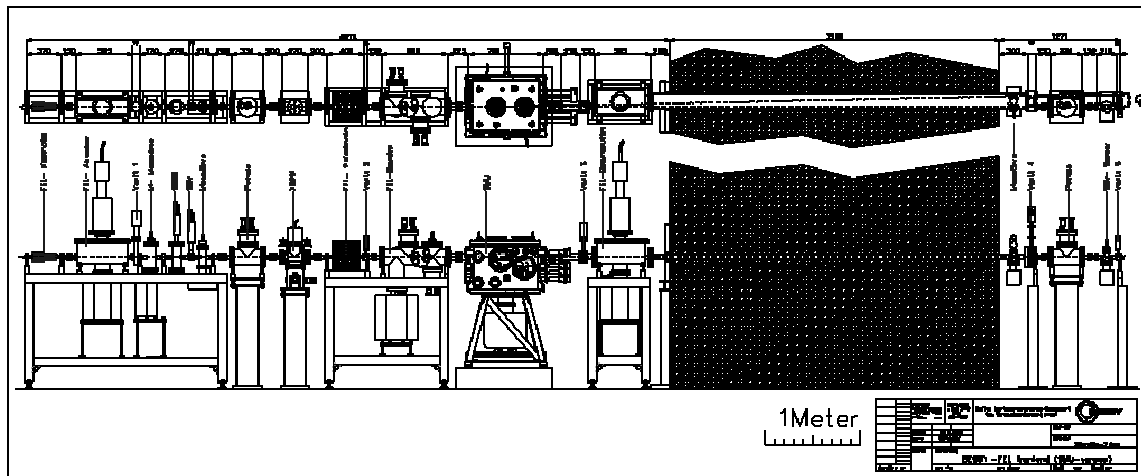


Fig. 10.7: Sketch of the front-end.

10.6 Beamlines for the Low-Energy FEL

10.6.1 Beamline for High-Energy Resolution

The beamline for the low-energy FEL is based on the collimated plane-grating monochromator design developed for BESSY II [14]. In this design the operation of the grating in collimated light offers a free selection of the grating magnification factor as defined in equation 10.6 and allows for a very flexible usage of the beamline. Its optical layout is shown in figure 10.8.

A beam defining aperture at 20 m is used to separate the FEL beam from the background and to reduce the level of stray light. Mirror M_1 is located in a distance of 40 m from the end of the FEL. The beam diameter at this position is approximately 6.4 mm (fwhm). The high reflectances of the mirror coatings in this energy range allow for quite large deflection angles, so the mirror dimensions listed in table 10.2 are still reasonable. For the mirrors with fixed deviation angle, M_1 , M_2 , and M_3 , incidence angles of 3° were chosen.

Mirror M_1 collimates the beam in the vertical dispersive plane while it focuses it horizontally onto the exit slit. This minimizes optical aberrations and is an essential requirement for ultrahigh-energy resolution. Horizontal focusing is performed by means of M_1 due to the high angular divergence and limits the size of M_3 . The demagnification ratio of 1 : 0.8 allows for an almost aberration-free horizontal image.

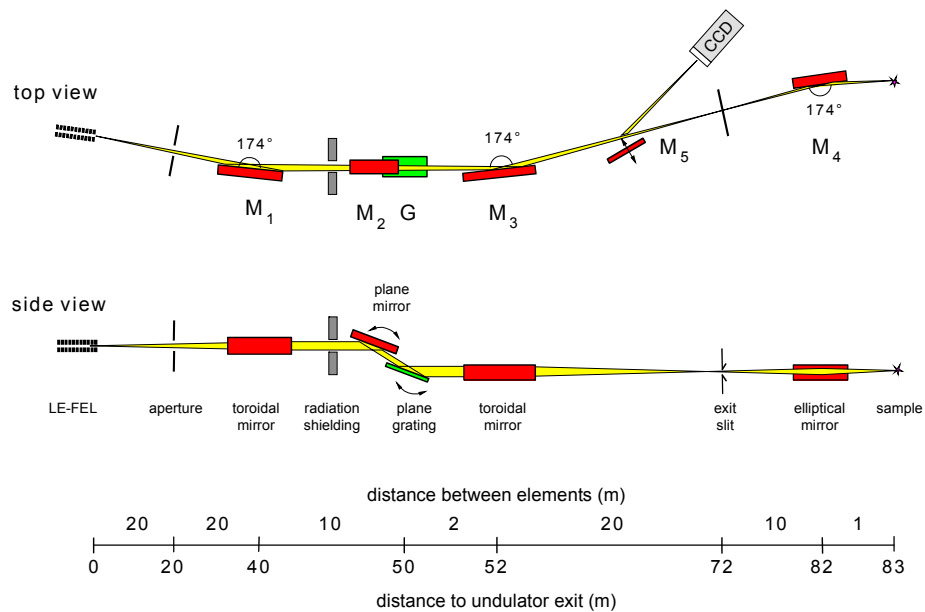


Fig. 10.8: Optical design of the beamline for high-energy resolution at the LE-FEL.

The collimated light is dispersed by a grating with line density of 2400 lines/mm operating at $c = 10$. The diffracted light is subsequently focused by M_3 onto the exit slit. Sagittal focusing [15], exploited at mirrors M_1 and M_3 , reduces the effects of surface imperfections and distortions. A horizontally deflecting elliptical mirror is used to refocus the intermediate focus at the exit slit onto the sample position with a demagnification ratio of 10 : 1. The horizontal focus size of approximately $60 \mu\text{m}$ at 24 eV is quite large but results in the low demagnification ratio of 1 : 0.8 of M_1 necessary to obtain ultrahigh resolution. Here the request for ultrahigh-energy resolution collides with the demands for a smaller focus.

Mirror M_2 is used to set the appropriate deflection angle at the grating. It varies between 16° at 24 eV and 7° at 120 eV. This element has the steepest incidence angle of all elements in the beamline and suffers most from the intense FEL beam. But due to the large distance of 50 m, the footprint on the surface is spread over an area of 2 cm^2 and the peak-energy density of the incident beam is diluted to 0.3 mJ/cm^2 . This is two orders of magnitude below the ablation thresholds as listed in section 10.2.1 and damage to the optical elements should not occur in this beamline.

Between mirror M_3 and the exit slit a retractable plane mirror is mounted to switch the beamline into the spectrograph mode. In this mode the dispersed light is deflected horizontally to a fluorescent screen located in the focal plane of M_3 . The screen is viewed by a CCD-camera with integrated objective lens. This setup showed a spatial resolution of $1 \mu\text{m}$ at BESSY II undulator beamlines [16]. As listed in table 10.3 the highest resolving power is obtained with a $10 \mu\text{m}$ slit size, an interval which is well resolved by the CCD-

camera. The dispersion in the focal plane is between 150 $\mu\text{m}/\text{meV}$ at 24 eV and 12 $\mu\text{m}/\text{meV}$ at 120 eV. The entire bandwidth of the FEL beam thus extends over 1.2 mm (fwhm at 24 eV) and is well within the field of view. Hence, the diagnostic station allows one to record the entire spectrum of a single FEL pulse at once.

Table 10.2: Parameters of the optical elements of the high-energy-resolution beamline at the LE-FEL. The silicon substrates are coated with carbon with a roughness specified to 0.5 nm (rms) for all elements. The slope errors (m/s = meridional/sagittal) are given as rms-values. R and ρ denominate the meridional and sagittal radii of the toroidal mirrors, a and b being the long and short half axis of the ellipse, respectively.

Optical element	M_1	M_2	M_3	M_4	G_1	Unit
Shape	toroid	plane	cylinder	elliptical	plane	
Geom. surface size	600·80	350·30	350·120	320·120	200·50	mm ²
Opt. surface size	580·40	340·20	330·100	300·100	190·40	mm ²
Slope error (m/s)	0.5''	0.1''	0.25''	5''/2''	0.02''	
Source dist. (m/s)	40	-	∞	10	-	m
Image dist. (m/s)	32/ ∞	-	20	1	-	m
Mirr. parameter	R=679371	-	-	a=5500	-	mm
	ρ =4187	-	ρ =2093	b=165.5	-	mm
Grazing incidence angle	3°	-	3°	3°	-	
Line density	-	-	-	-	2400	l/mm
Blaze angle	-	-	-	-	8°	

To obtain ultrahigh-energy resolution, the optical surfaces, especially that of the grating, have to be significantly better than in currently installed beamlines at third generation storage rings. The parameters of the optical elements are summarized in table 10.2. From these values their relative contributions to the total energy resolution are calculated according to [14] and shown in figure 10.9. Although limitations in resolving power due to aberrations and finite apertures of the optical element are not accounted for in this simple estimation, it gives an instructive overview of the expected performance. More accurate results are obtained by the raytrace calculations described below. The chosen grating length of 200 mm sets a fundamental limit of the resolving power to 480.000. At $c = 10$ this corresponds to the limitation of a 10 μm exit slit size. Below $c = 7$ the resolving power is determined by the diffraction-limited source size. Although operation in collimated light allows for a free choice of the c -value, a detailed investigation is only done for $c = 10$. Higher c -values are necessary if the source size is larger than expected, but as the grating

efficiency decreases with increasing c-value, and the grating will be overfilled, the throughput will be reduced.

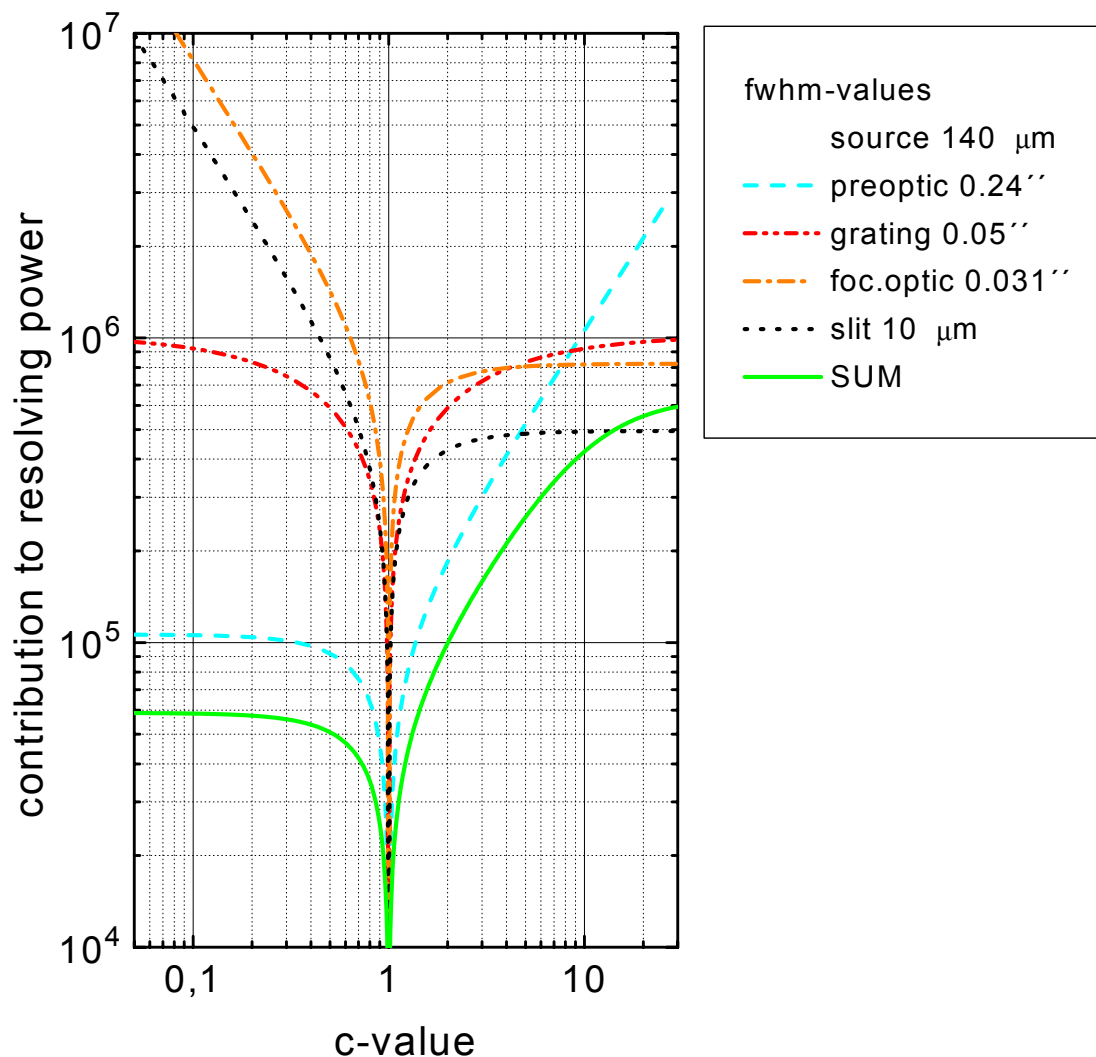


Fig. 10.9: Contributions of slope errors and source size to the resolving power at 24.3 eV. The values are taken from table 10.2 and converted to fwhm values. The values for the pre-optics include mirrors M_1 and M_2 . The forgiveness factor due to the sagittal focusing geometry is also taken into account for mirrors M_1 and M_3 . The contribution of a $10 \mu\text{m}$ exit slit is shown to relate the curves to the dispersion of the grating. It is not included in the SUM curve.

The total beamline transmission for $c = 10$ including grating efficiency is shown in figure 10.10. The transmission at low energies is approximately 5% and drops between 50 eV and 90 eV to 2%. The obvious discontinuity at 30 eV is due to the two different sets of op-

tical constants used in the calculations. Below 30 eV the data of Palik [17] are used, above 30 eV the data of Henke [7]. The size of the discontinuity may also give an estimate of the accuracy of the calculation.

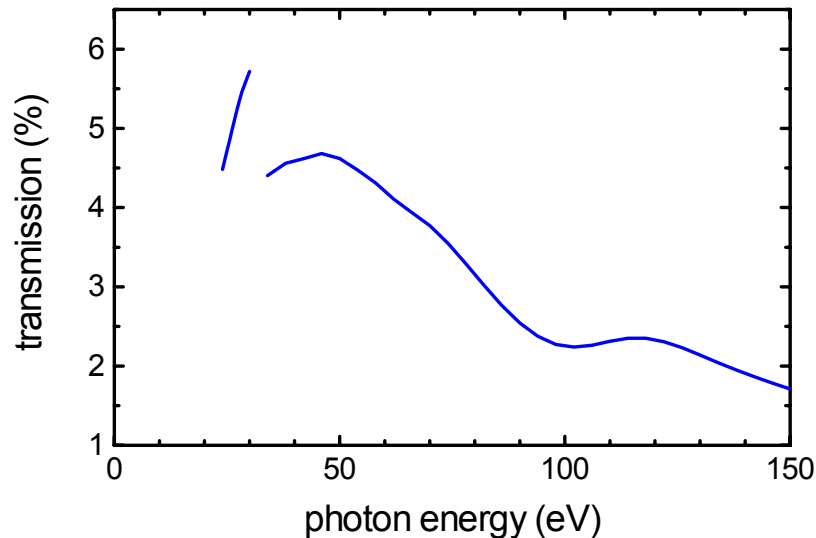


Fig. 10.10: Beamline transmission for $c=10$ and a blaze angle of 8° .

Detailed raytrace calculations are performed for the lowest and highest photon energy. The results for small and medium-sized exit slits are summarized in table 10.3. As an example, figure 10.11 shows the spectral and temporal power distribution of the light at the sample position for 24.3 eV and $10\ \mu\text{m}$ exit-slit setting. With these settings an energy resolution of $90\ \mu\text{eV}$ can be achieved. The photon flux of $1.6 \cdot 10^9$ photons per pulse is concentrated in a $60 \cdot 12\ \mu\text{m}^2$ wide spot. Due to the low-energy bandwidth the initially 22 fs long pulse extends now over 80 ps. This is comparable to pulse lengths at third generation storage rings. The peak-power level behind the beamline is correspondingly reduced to 100 W.

The pulse length itself is defined by the illuminated grating length; it cannot be reduced by increasing the energy bandwidth due to an increased slit width. Opening the slit increases merely the energy bandwidth and transmitted photon flux while the pulse length is unaffected. The power level after a $100\ \mu\text{m}$ exit slit for example is raised by a factor of 10 compared to figure 10.11.

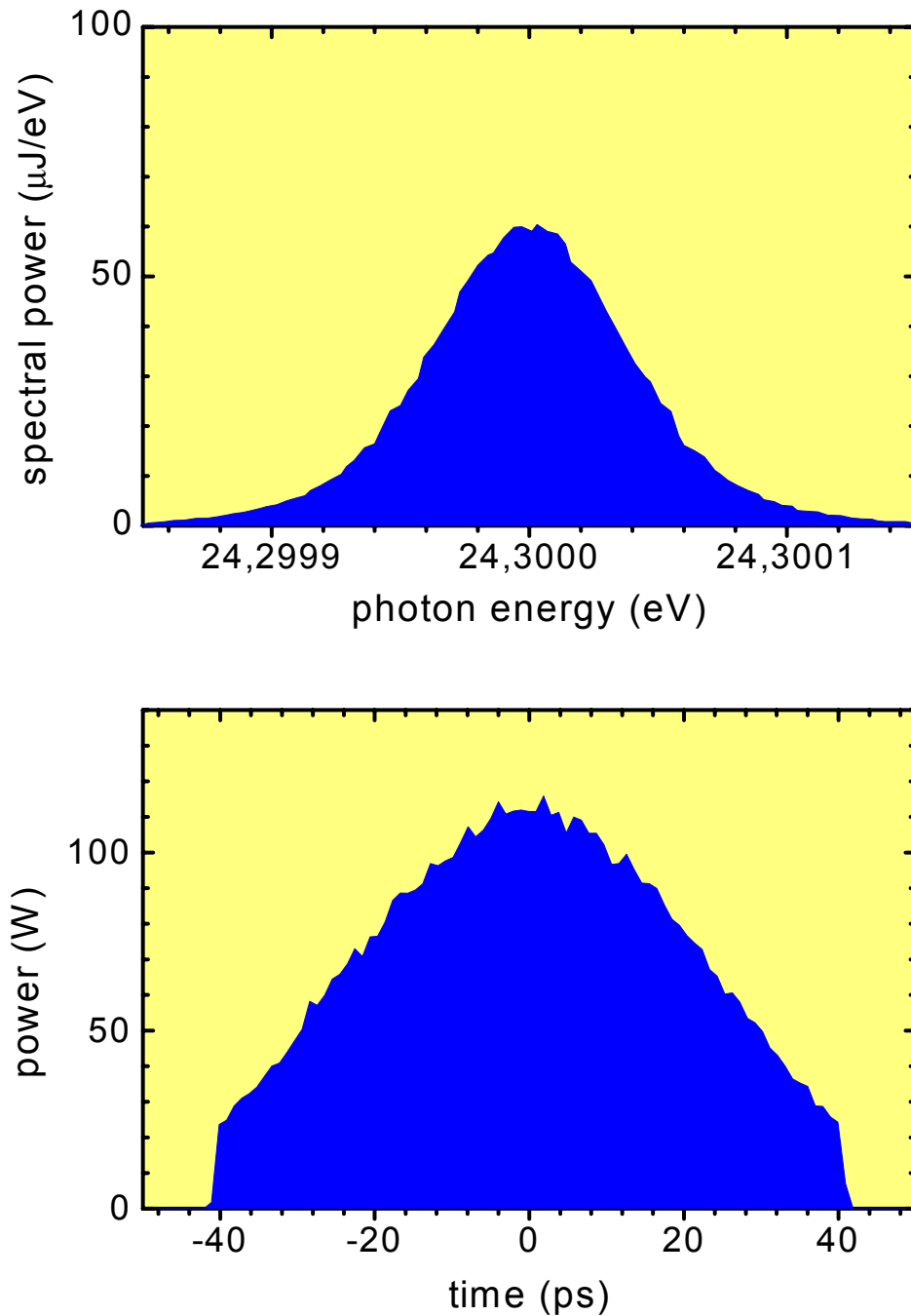


Fig. 10.11: Bandwidth and pulse shape for 10 μm slit setting of the high-energy resolution beamline at the LE-FEL. The bandwidth corresponds to a resolving power of 270,000. This is close to the diffraction limit due to the illuminated grating length (336,000).

Table 10.3: The performance of the high-energy-resolution beamline on the LE-FEL. The values for bandwidth, pulse length, and spot size are given as fwhm numbers.

Parameter					Unit
Photon energy	24		120		eV
Exit slit size	10	100	10	100	μm
Bandwidth	90	470	800	6000	μeV
Photons per pulse	$1.6 \cdot 10^9$	$1.6 \cdot 10^{10}$	$1.2 \cdot 10^8$	$1.2 \cdot 10^9$	
Pulse length	80	80	5	5	ps
Spot size (hor. \times vert.)	60×16	60×13	60×7	60×9	μm^2

10.6.2 Beamline for Short Pulses

The beamline for short pulses has to separate the FEL pulse from background radiation while their length has to be conserved. The background radiation consists of stray light generated in the previous seeding stages, spontaneous radiation of the undulator, and radiation generated in bunch compressors or other magnets within the accelerator structure. Its bandwidth and pulse length is large, compared to the FEL pulse, and the photon energies of the previous seeding stages differ by several electron volts from the FEL pulse. The bandwidth of the beamline should therefore be comparable to the FEL pulse and considerably larger than in the high-energy resolution beamline described above.

In low-energy beamlines with only one dispersive element the pulse prolongation cannot be kept in the order of 10 fs. A grating with a line density of 100 l/mm illuminated with 50 nm radiation over a length of only 10 mm for example adds a pulse length of 160 fs to the incident pulse duration. If the pulse length within a beamline has to be conserved at a 10 - 20 fs level, a second dispersive element has to reverse the dispersion and compensate the lengthening introduced by the first dispersive element. A possible design of such a beamline is shown in figure 10.12.

The first part from the source to the slit position is a collimated plane grating monochromator with a low-line density grating operated in outside-diffraction order and a demagnification ratio of $c = 0.7$. This allows for a rather steep incident angle on the grating ($3.5^\circ - 8^\circ$ in the present design) and reduces the number of illuminated lines. As an additional advantage the cross section of the diffracted beam after the grating and the illuminated area of M_3 are reduced according to the c -value. Therefore the focal length of M_3 can be as short as 4 m without introducing significant aberrations to the monochromatic image at the slit.

In outside diffraction order it is advantageous to place the plane mirror M_2 downstream of the grating, otherwise the influence of its surface errors on the energy resolution would be increased. A similar beamline design has been implemented at the U41-PGM beamline at BESSY [18] and is in successful operation since 2000. In the focal plane of M_3 the entire bandwidth of the FEL beam is focused to a spot of 1 mm size.

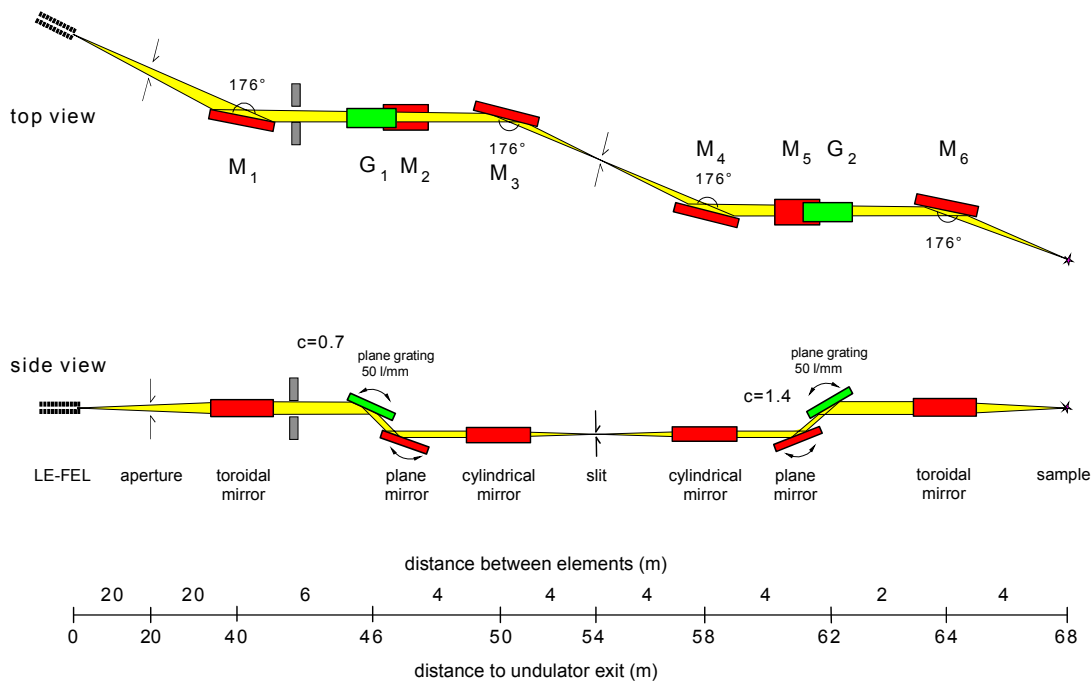


Fig. 10.12: Optical design of the beamline for short pulses at the LE-FEL.

The second part of the beamline is a mirror image of the first part. The only difference occurs in the focal length of M_6 . It is reduced to 4 m to obtain a small spot on the sample. The second grating is operated at $c = 1.4$ which is the reciprocal value of the c -value of the first grating and reflects the reversed beam direction. The dispersion in the slit plane is completely cancelled by the second part of the beamline and the bandwidth and length of the pulse can be controlled by choosing an appropriate slit size. A pulse length of about 30 fs can be maintained with a 1 mm slit width at the lowest photon energy of 24 eV, while the bandwidth of the monochromator is about the same as that of the FEL (figure 10.13).

The gratings together with mirrors M_3 and M_4 establish a so-called $4f$ setup (f is the focal length of the mirrors), where the two gratings and the slit are in the corresponding focal planes. Grating G_1 disperses the spectral components of the pulse and mirror M_3 performs the Fourier transform. The Fourier spectrum appears in the slit plane, where the

amplitudes and the phases of the spectrum can be manipulated by appropriated masks [19]. Mirror M_4 performs the inverse Fourier transformation and grating G_2 merges the spectral components back to a pulse, which is focused by M_6 .

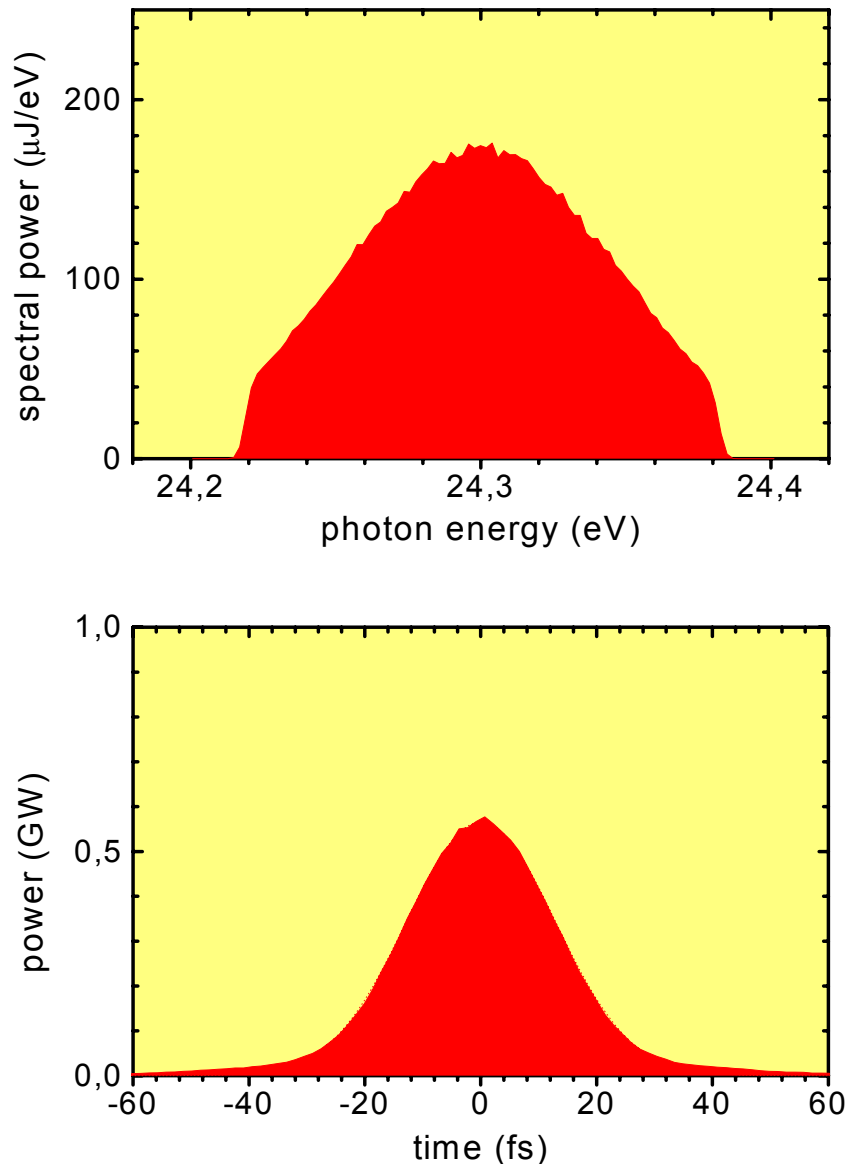


Fig. 10.13: Bandwidth and pulse shape for 1 mm slit setting. The Gaussian shape of the energy distribution reflects the spectral distribution of the incident light, which is assumed to be Gaussian with a width given in table 10.1. With this slit setting almost the complete bandwidth of the FEL beam is transmitted through the beamline.

Although the slit between both parts of the beamline decouples their operation, care has to be taken that the angular settings of both grating-mirror combinations are exactly

the same. An offset would cause the focus at the sample position to move in vertical direction. For most experiments this would be unacceptable. Unfortunately the vertical beam position and direction behind the second grating cannot be detected without a disturbance of the experimental conditions. A possible solution (not shown in figure 10.12) is the installation of an aperture at the focal point at 68 m and an additional refocusing mirror to image this aperture to a new sample position. The photocurrent signals of the vertical blades could be used to establish a feedback system for the grating rotations.

Table 10.4: Performance of the short-pulse beamline on the LE-FEL. Bandwidth, pulse length and spot size are given as fwhm values.

Parameter					Unit
Photon energy	24		120		eV
Exit slit size	100	1000	10	100	μm
Bandwidth	16	160	50	160	meV
Photons per pulse	$7.2 \cdot 10^{11}$	$4.9 \cdot 10^{12}$	$1.3 \cdot 10^9$	$1.1 \cdot 10^{10}$	
Pulse length	210	30	170	35	fs
Spot size (hor. \times vert.)	120 \times 55	110 \times 50	85 \times 21	80 \times 20	μm^2

Figure 10.14 shows the effect of the slit width at 24 eV on the pulse characteristics. The bandwidth is proportional to the slit width, whereas the pulse length is inversely proportional to it. Because the transmitted flux is also proportional to the opening, the power level of the pulse at the end of the beamline is proportional to the square of the slit size. Some examples are shown in figure 10.14. Closing the slit decreases the bandwidth and increases the pulse length considerably. With a 10 μm slit width the energy resolution is 4 meV and the pulse length is increased to 1300 fs.

The 200 μm curve shows secondary maxima which are due to the diffraction pattern of the light behind the slit. This occurs for all slit settings that are smaller than the corresponding bandwidth of the incoming FEL beam. After passing through the slit, the rays in the first secondary maxima of the 200 μm curve show an angular displacement of ± 380 μrad with respect to rays in the central beam. Subsequently the intersection with the grating surface outside the center causes a temporal shift with respect to the central beam which is conserved in the pulse structure.

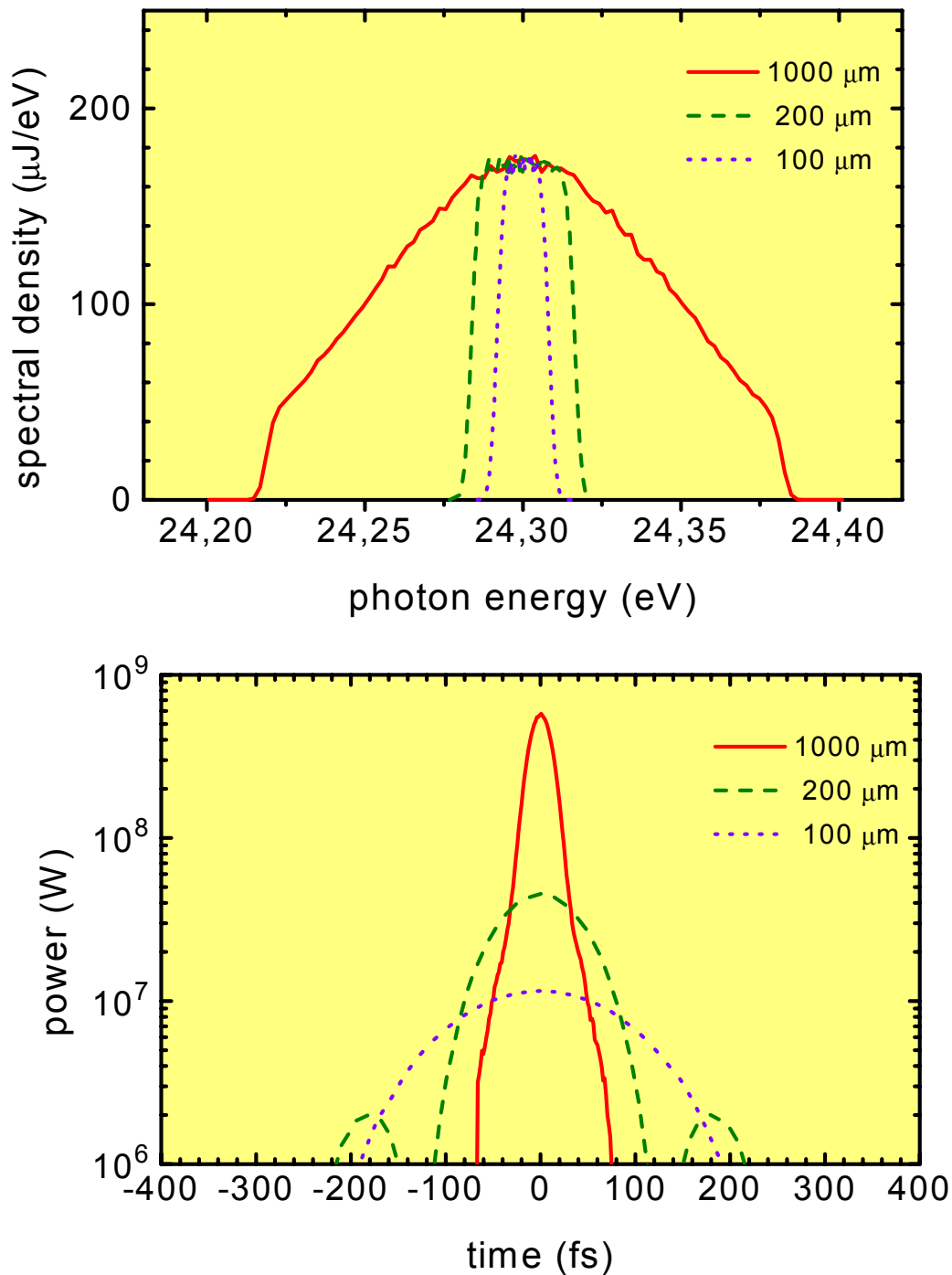


Fig. 10.14: Variation of the transmitted bandwidth and power by opening the slit to 1000 μm , 200 μm , and 100 μm . The secondary maxima of the 100 μm curve are outside of the scaling.

10.6.3 Focused Direct Beam

For experiments that do not need any spectral filtering of the radiation the undispersed FEL beam is focused to a small spot in a separate beamline. Its optical layout is depicted in figure 10.16. A plane mirror M_1 deflects the beam horizontally to obtain floorspace for the experimental station. Subsequently an elliptical mirror M_2 is used to focus the beam with a strong demagnification ratio of 56 : 1. The last mirror has a total length of 600 mm and slope errors of 0.5 arcsec in the meridional and 2 arcsec in the sagittal direction. Its sagittal radius of curvature is $\rho = 82$ mm. These values are similar to presently available elliptical mirrors.

The distance to the end of the mirror has been chosen to be 500 mm to give reasonable space for experimental equipment. Smaller foci are possible but need smaller distances and require a detailed investigation of the specific experimental environment.

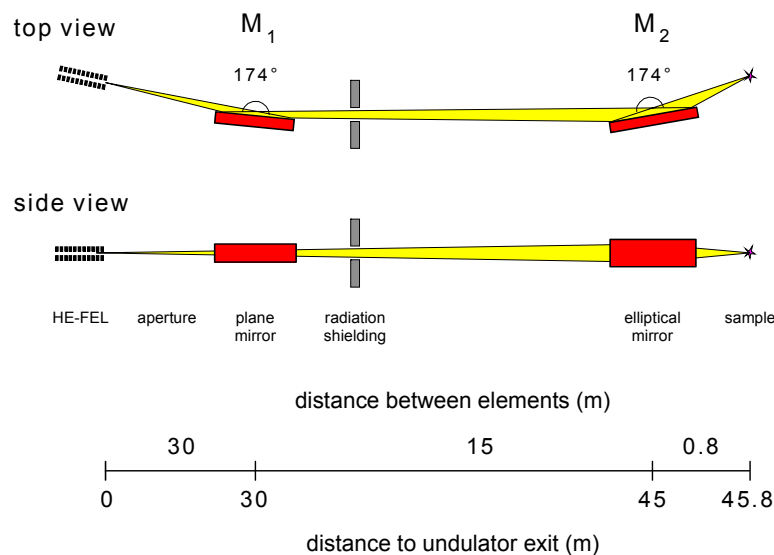


Fig. 10.15: Optical design of the beamline for focused direct light at the LE-FEL.

Focusing by conventional zone plates or reflecting Bragg-Fresnel lenses is an alternative method to form small foci. With this method even sub-micrometer foci are achievable. The variation of the focal length with respect to the photon energy and the transmission losses are some obstacles that would have to be kept in mind in their application. Due to the already small spectral bandwidth of the FEL beam the chromatic errors are small. Applications that aim for extremely small foci and high spatial resolution would benefit from these optical elements.

Table 10.5. Performance of the beamline for direct light at the LE-FEL. The spot size is given as fwhm-value.

Parameter			Unit
Photon energy	24	120	eV
Photons per pulse	$6 \cdot 10^{13}$	$1.5 \cdot 10^{12}$	
Spot size (hor. \times vert.)	10×3	10×3	μm^2
Pulse energy density	$8 \cdot 10^5$	$1 \cdot 10^5$	$\text{mJ}/\text{cm}^2/\text{pulse}$
Photon density	$2 \cdot 10^6$	$5 \cdot 10^4$	$1/\text{nm}^2/\text{pulse}$
Peak power density	$3 \cdot 10^{16}$	$3 \cdot 10^{15}$	W/cm^2
Avg. power density	$2 \cdot 10^7$	$3 \cdot 10^6$	W/cm^2

10.7 Beamlines for the Medium-Energy and High-Energy FELs

The beamlines for the mid-energy-range FEL are similar in design and performance to the high-energy beamlines and are therefore not separately described in this report. The most significant difference is the use of an alternative coating because carbon shows a strong absorption edge at 280 eV in the middle of the energy range. Nickel is a possible choice as coating material without absorption edges in this energy range.

10.7.1 Beamline for High-Energy Resolution

The high-energy resolution beamline for the high-energy FEL is a stigmatic, collimated PGM similar to the low-energy high-resolution beamline. Its optical design is shown in figure 10.16. It is optimized to the source properties of the high-energy FEL. The source parameters differ mainly in terms of divergence, size and pulse energy. The divergence is decreased from 160 μrad at 24 eV to 60 μrad at 1000 eV and the diffraction-limited size from 140 μm at 24 eV to 37 μm at 1000 eV. In the higher photon energy range the seeding is less efficient and the pulse energy is reduced to 15 μJ .

Although the pulse energy is considerably smaller than in the low-energy FEL, the smaller divergence leads to a higher angular power density which exacerbates the conditions on the optical elements.

A toroidal mirror M_1 deflects the beam horizontally by 1.4° and collimates it in both directions. Since the HE-FEL energy range is well above all absorption edges of carbon all optical elements are coated with this material.

After diffraction at the grating the beam rises with 2° relative to the horizontal plane. This reduces the deflection angle at the mirror necessary for a given c-value by 1° , results

in a lower power density and, even more important, in a higher reflectance. As shown in figure 10.18 the incidence angle at the plane mirror remains below the critical angle in the regime of total external reflection.

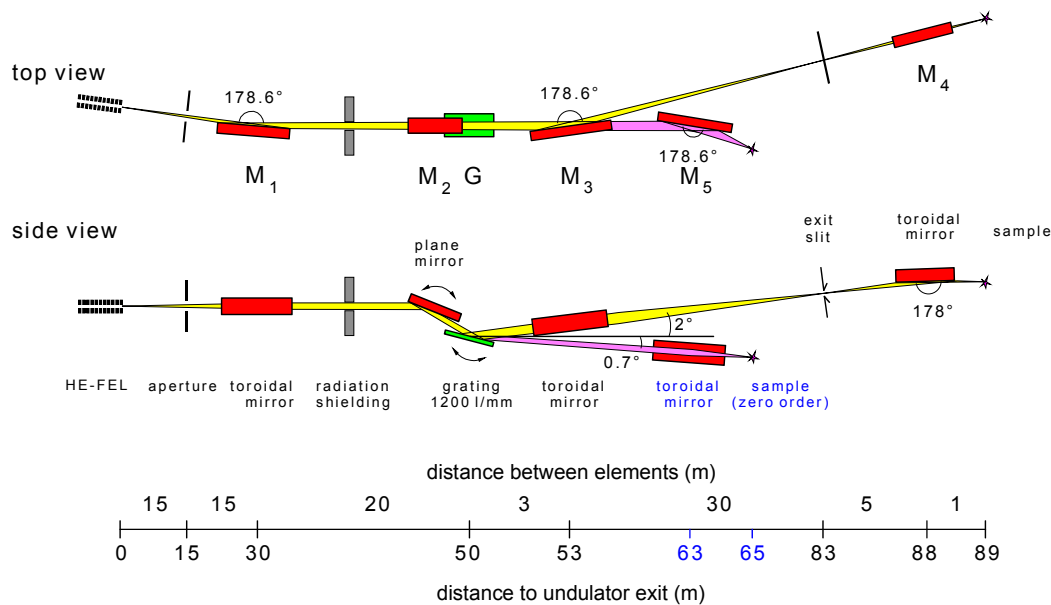


Figure 10.16: Optical design of the high-energy-resolution beamline at the HE-FEL.

Mirror M_3 focuses the diffracted beam in both directions onto the exit slit. Focusing should now be safe with respect to power density considerations because the beam is dispersed and the diffracted pulse energy is vertically distributed over a large area at the exit slit. Nevertheless, care must be taken when focusing the zero order on the slit as the energy density becomes higher than the ablation threshold. The exit slit is demagnified by the vertically deflecting refocusing mirror M_4 and the beam leaves the beamline in horizontal direction. For an exit slit setting of $100 \mu\text{m}$ and $c=10$ the focus size is $40 \cdot 30 \mu\text{m}^2$ (vertical \cdot horizontal). The transmission as shown in figure 10.17 is about 1%.

The focus position is 1000 mm downstream of the center of the last mirror. This seems to be a comfortable distance for most experiments and decouples the beamline from the experimental systems. Smaller foci can be achieved if the distance is shortened but then the refocusing mirror becomes part of the experimental environment. The design of the refocusing optics for smallest foci should therefore be postponed to the time when experimental chambers are designed.

As mentioned above, the ascending beam after the grating allows for a smaller grazing incidence angle at the plane pre-mirror, keeping the deflection angle at the grating fixed.

Figure 10.18 shows the working curve for the plane mirror M_2 when operated in the on-blaze and constant c mode.

The incident angle at the plane mirror changes while scanning the energies as shown in the lower part of the figure. The reflectance in the fix-focus mode with $c = 10$ is significantly higher than in the on-blaze mode, which is due to the smaller grazing incidence angles.

As in the beamline at the LE-FEL the angle at the plane mirror is the steepest of all mirrors in the beamline and the mirror becomes the most sensitive element concerning damage by the high peak photon density. With a cross section of $\sigma_a = 3.3 \cdot 10^{-6} \text{ nm}^2$ as defined by equation (10.2) and a peak photon density of $I_0 \approx 1 \cdot 10^{11} \text{ 1/mm}^2$ only one out of $2 \cdot 10^6$ surface atoms absorbs a photon. The absorbed energy density of 0.003 mJ/cm^2 should not cause damage to the mirror surface.

The beamline was designed for $c = 10$, where the grating accepts 1.5 times the fwhm of the incident beam. This yields the highest resolving power for this beamline. The performance of the beamline in the time and spectral domain is shown in figure 10.19 for 1000 eV. With a $10 \text{ }\mu\text{m}$ slit resolving powers of 50,000 are expected.

Table 10.6: Parameters of the optical elements of the high-resolution HE-FEL. The substrates are silicon coated with a carbon layer with a roughness specified to 0.5 nm (rms). The slope errors (m/s = meridional/sagittal) are given as rms-values. R and ρ denominate the meridional and sagittal radii of the toroidal mirrors.

Optical element	M_1	M_2	M_3	M_4	M_5	G_1	Unit
Shape	toroid	plane	toroid	toroid	toroid	plane	
Geom. surface size	330×25	410×30	500×50	500×50	500×50	200×50	mm ²
Opt. surface size	300×20	400×20	480×40	480×50	480×50	190×40	mm ²
Slope error (m/s),	1"	0.05"	1"	1"/2"	1"/2"	0.02"	
Source dist. (m/s)	50	-	∞	5	∞	-	m
Image dist. (m/s)	∞	-	30	1	2	-	m
Mirror parameter:	8185315	plane	491118	95498	327413	-	R mm
	1222	-	733	29.1	48.9		ρ mm
Grazing incidence angle	0.7°		0.7°	1°	0.7°		
Line density	-	-	-	-		1200	1/mm
Blaze angle	-	-	-	-		1.35°	

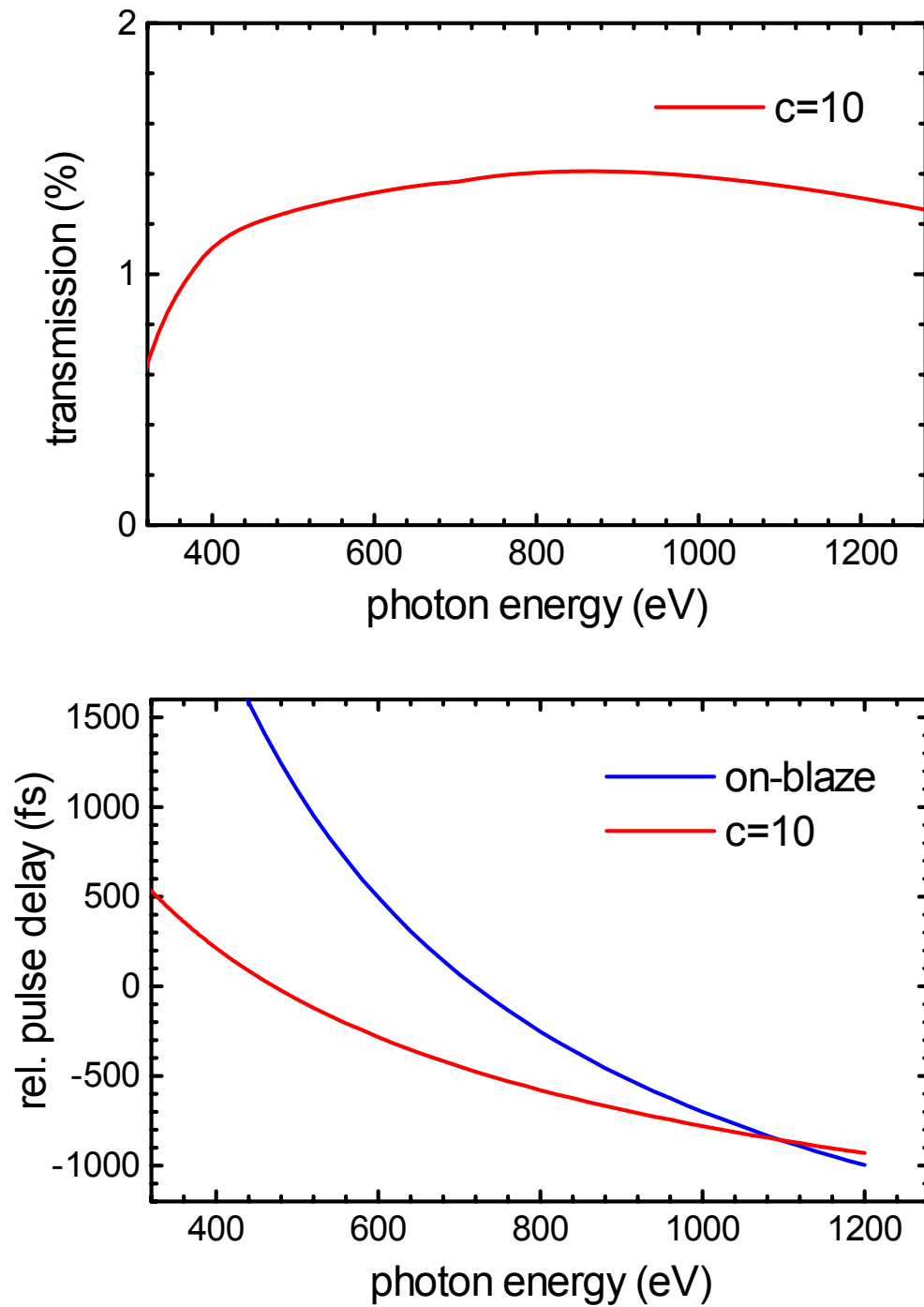


Fig. 10.17: Transmission and path length variation in the high-resolution beamline at the HE-FEL. $N = 1200$ l/mm.

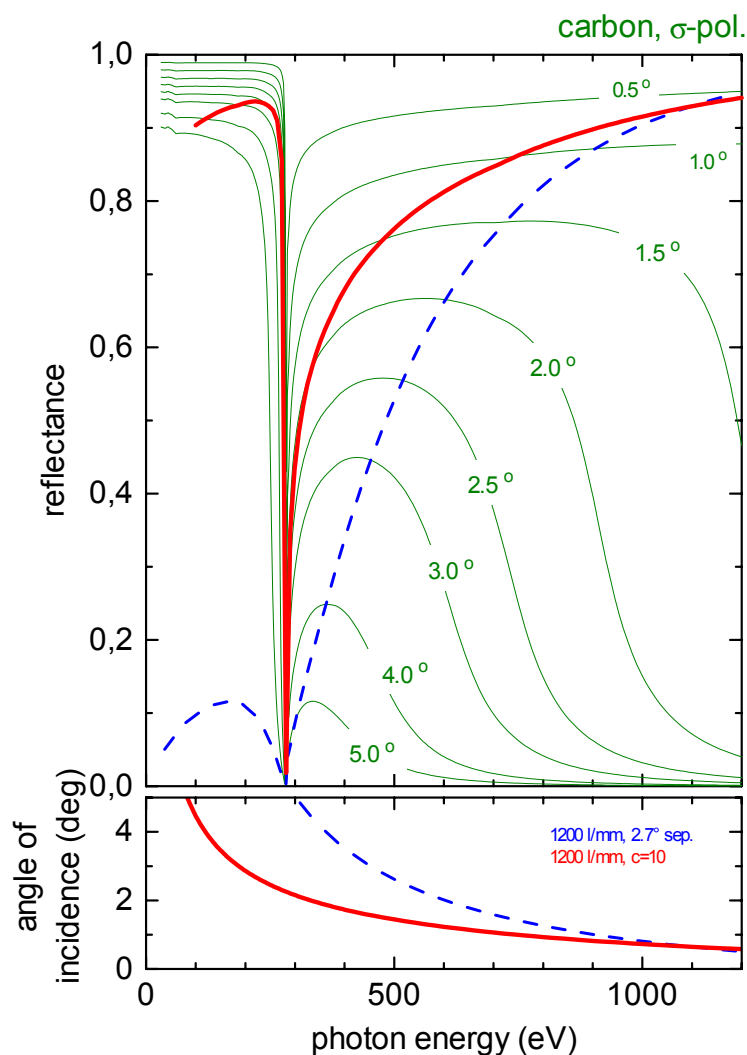


Fig. 10.18: Working curve of the plane pre-mirror for a carbon coating. The thin green lines show the reflectances of the carbon-coated pre-mirror at fixed angles of incidence. The blue dashed line shows the reflectance when operated in the on-blaze mode where first and zero order are separated by 2.7°. The red curve represents the constant c-mode for $c = 10$. The lower part of the figure depicts the angle of incidence for the corresponding working curves.

A very comfortable way to manipulate the time-bandwidth product of the output of the beamline is to utilize the variation of the incidence angle at the grating. This is accomplished by operating the beamline with a smaller c-value. The corresponding reduction of resolving power is only noticeable for smaller slits (10 μm). For wider slits (100 μm) the difference as shown in table 10.7 is quite small. Figure 10.19 shows the power distribution for $c = 2.2$ compared to the high resolution mode with $c = 10$. A slit setting of 10 μm was chosen to make the reduction in bandwidth visible. The figure clearly shows the merits of a reduced c-value. With $c = 2.2$ four times the flux is concentrated in a shorter time inter-

val and results in a 20 times higher peak power, while the bandwidth is increased by only 65%. Opening the slits will increase the power level but not alter the pulse length. For a slit width of 100 μm or larger even, the bandwidths differ by less than 20%. A moderate resolution ($E/\Delta E \leq 7000$) is therefore accomplished by opening the slit and making a corresponding reduction of the c -value.

Although the pulse length could be reduced by a factor of five, both modes still stretch the initial pulse length of 7 fs significantly. Reducing the number of illuminated lines by an aperture before the grating could reduce the pulse length at the expense of less total flux — yet nearly the same peak power — to values of 50 – 100 fs. A further reduction requires a grating with lower line density. Calculations for a grating with a line density of 100 l/mm operated at $c=1.1$ show that the pulse length can probably be limited to values below 20 fs. A drawback of the operation with such a small c -value is the increased amount of stray light from the zero order, which is separated from the first order by only 0.1° or 52 mm at the exit slit.

The spectral density behind the beamline is 0.7 $\mu\text{J}/\text{eV}$ for $c=2.2$ and 0.2 $\mu\text{J}/\text{eV}$ for $c=10$ at 1000 eV. For a 100 μm exit slit setting and $c=2.2$ the total pulse energy is 100 nJ, resulting in an energy density at the sample position of 20 mJ/cm^2 within a bandwidth of 140 meV. Closing the slits reduces not only the total transmitted power but also the spectral peak pulse density.

As described above, the beamline can be operated in the on-blaze mode where the zero order remains at a fixed angle while in the first order the dispersed light is scanned through the exit slit. The operation with collimated light decouples the dispersive and focusing properties of the grating and both beams can be focused with conventional mirrors independent of the chosen energy. The zero order is then focused by M_5 in a fixed distance of 2 m to a spot with $60 \cdot 5 \mu\text{m}^2$ size.

Table 10.7. Performance of the high-energy-resolution beamline at the HE-FEL. Bandwidth and pulse length are given as fwhm values.

Parameter					Unit
Photon energy		1000			eV
c		10		2.2	
Exit slit size	10	100	10	100	μm
Bandwidth	20	120	33	140	meV
Photons per pulse	$1.5 \cdot 10^7$	$1.5 \cdot 10^8$	$6 \cdot 10^7$	$6 \cdot 10^8$	
Pulse energy	2.4	24	10	100	nJ
Pulse length	650	650	120	120	fs

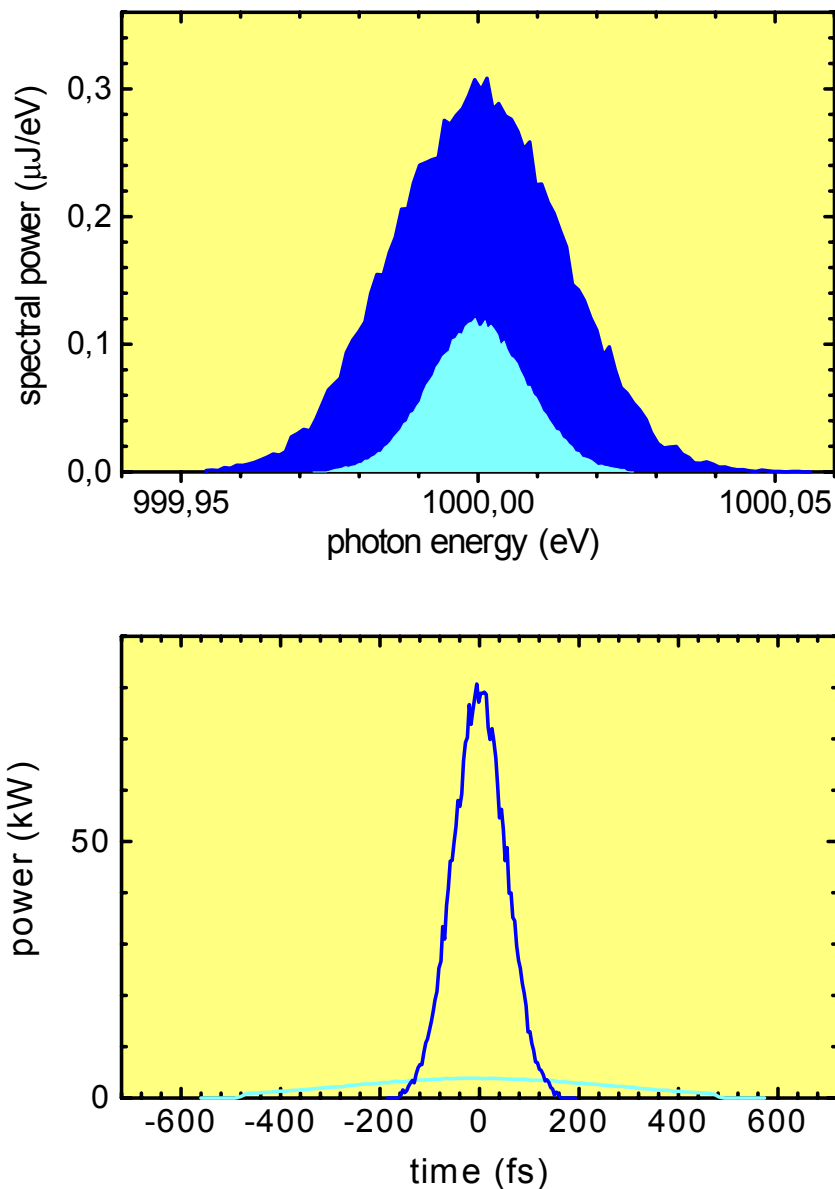


Fig. 10.19: High-energy-resolution beamline at the HE-FEL: Power and spectral power distributions for $c=2.2$ (blue) and $c=10$ (light blue) with an exit slit setting of $10\ \mu\text{m}$. See also table 10.7. With the high c -value setting the pulse length is limited by the determined grating length.

10.7.2 Beamline for Short Pulses

In beamlines for high-energy resolution the grating is operated in a photon beam of large diameter to illuminate as many lines as possible, and in the beamline described above, approximately 200.000 lines are within the diameter of the beam. A beamline design that preserves pulse length should illuminate as few lines as possible. This is

achieved by using gratings with low line densities and with steep incident angles in photon beams with narrow cross sections.

In contrast to the short-pulse beamline for the LE-FEL described above (section 10.6), the shorter wavelengths permit now a beamline design that can operate without a second grating to reverse the dispersion.

The principle of the short-pulse beamline is to vertically concentrate the beam on the grating in order to illuminate only as many lines on the grating as one can afford for certain pulse lengths. In the horizontal direction the beam is collimated. Figure 10.20 shows the optical design of the proposed beamline.

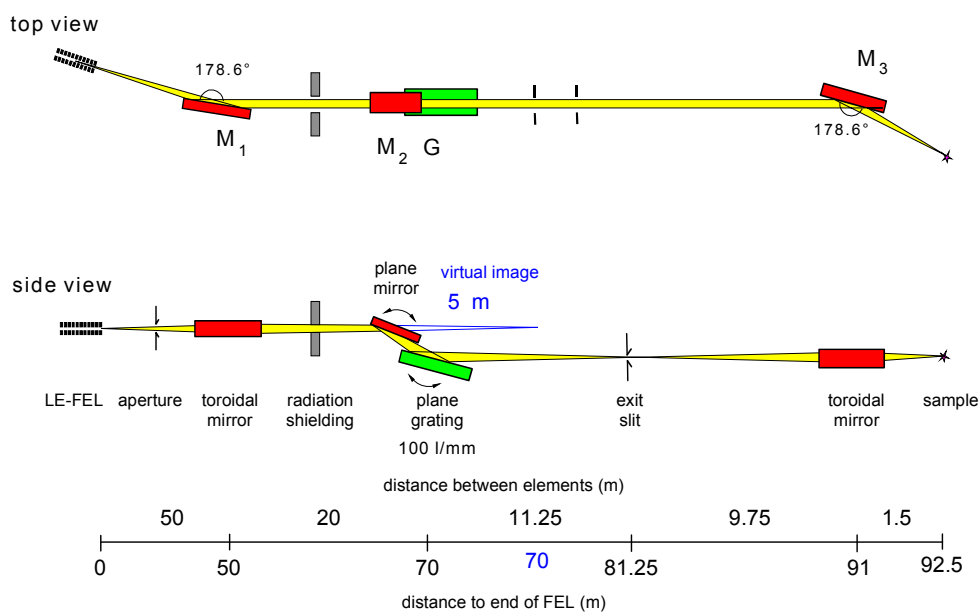


Fig.: 10.20: Optical design of the short pulse beamline at the HE-FEL.

Mirror M_1 images the source vertically with a demagnification ratio of 2 : 1 to a virtual image $r = 5$ m downstream of the grating. Horizontally the beam is collimated.

In the dispersion plane the grating is illuminated with convergent light and has to be operated with a constant c -value (fix-focus-mode). For this design $c = 1.5$ has been chosen. Due to the focusing properties of the grating a real image is formed at the position of the exit slit at a distance r' behind the grating

$$r' = c^2 r . \quad (10.10)$$

The variable deflection angle required is accomplished by means of M_2 . The toroidal mirror M_3 demagnifies the slit vertically 6.5 times. In conjunction with M_1 the source is demagnified horizontally by a factor of 20.

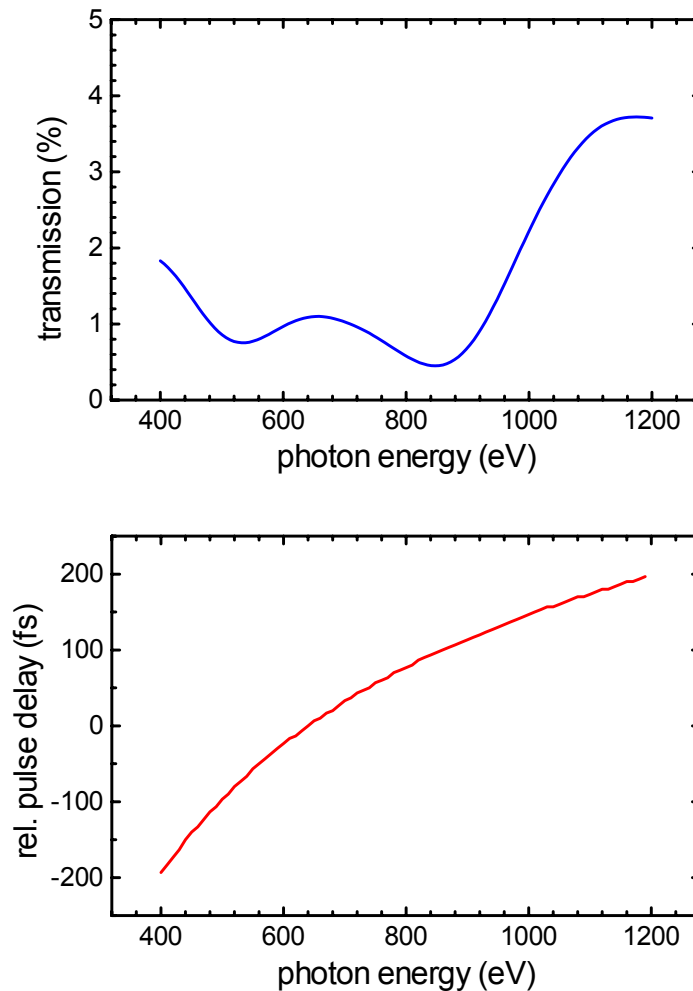


Fig. 10.21: Transmission of the beamline operated at $c = 1.5$ and time delay introduced by the variable deflection angle at the grating.

The transmission of the beamline is shown in figure 10.21. It starts with 2% at 400 eV, shows a decrease to 1% at 500 eV and 900 eV and ends with 2% at 1000 eV. This behavior is mainly due to the grating efficiency as defined by the grating profile parameters. Using a second interchangeable grating with a different profile will improve the performance at 500 eV and 900 eV.

The energy-dependent pulse delay in the beamline is shown in figure 10.21 and is in the order of ± 200 fs. The pulse length is not deteriorated by the beamline. It ranges from 22 fs at 500 eV to 8 fs at 1000 eV.

The performance of the beamline has been calculated with RAY [12] at 1000 eV for slit settings of 20 μm and 50 μm . The results are summarized in table 10.8. The temporal and spectral power densities for both settings are illustrated in figure 10.22. Due to the low line density of the grating the bandwidth for small slit width is well adapted to the intrinsic bandwidth of the FEL beam of 2 eV. It can be transmitted through a slit width of only 150 μm and is concentrated at the sample position in a focus of 20-50 μm^2 size. The horizontal focus size of 50 μm is caused by the slope errors of M_1 and M_3 . Better surfaces could reduce the horizontal focus size to below 10 μm .

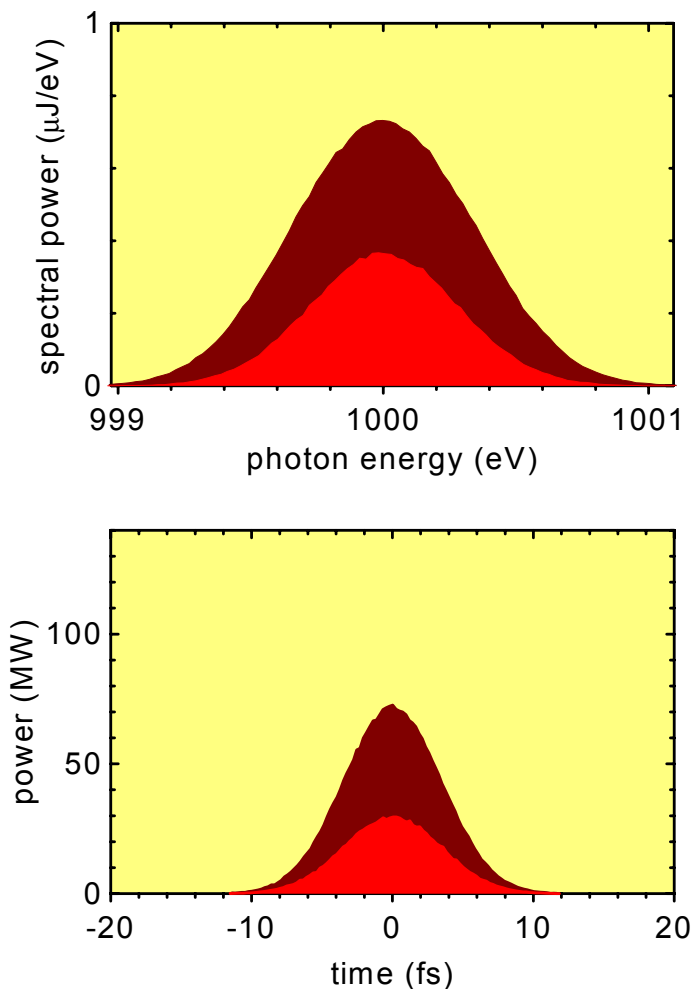


Fig. 10.22: Bandwidth and pulse shape in the short-pulse beamline at the HE-FEL for 20 μm (light red) and 50 μm (dark red) slit setting.

Table 10.8: Performance of the short pulse beamline at the HE-FEL. Bandwidth, pulse length and spot size are given as fwhm values.

Parameter			Unit
Photon energy	1000		eV
Exit slit size	20	50	μm
Bandwidth	650	794	meV
Photons per pulse	$16 \cdot 10^9$	$3.8 \cdot 10^9$	
Pulse energy	254	620	nJ
Pulse length	8	8	fs
Spot size (hor. \times vert.)	30×4	30×8	μm^2

Table 10.9: Parameters of the optical elements for the short pulse high energy beamline at the HE-FEL. The substrates are silicon coated with a carbon layer with a roughness specified to 0.5 nm (rms). The slope errors (m/s = meridional/sagittal) are given as rms-values. R and ρ denominate the meridional and sagittal radii of the toroidal mirrors.

Optical element	M_1	M_2	M_3	G_1	Unit
Shape	toroid	plane	toroidal	plane	
Geom. surface size	900×100	310×30	360×80	100×20	mm^2
Opt. surface size	850×40	300×20	380×20	90×15	mm^2
Slope error (m/s),	0.5"/1"	0.1"	0.5"/1"	0.1"	
Source dist. (m/s)	50	-	$\infty/9.75$	-	m
Image dist. (m/s)	$\infty/25$	-	1.5	-	m
Mirror parameter	R=8185315	-	R=245559	-	mm
	$\rho=407.2$	-	$\rho=31.8$	-	mm
Grazing incidence angle	0.7°		0.7°		
Line density	-	-	-	100	1/mm
Blaze angle	-	-	-	0.8°	

10.7.3 Focused Direct Beam

Similarly to the LE-FEL beamline described above, a beamline for undispersed focused light is proposed for the HE-FEL. The proposed design is sketched in figure 10.24.

The plane mirror M_1 deflects the beam horizontally at 25 m. Focusing is done by the elliptical mirror M_2 at 74 m with a demagnification ratio of 90:1. The mirror has a total length of 800 mm and slope errors of 0.5 arcsec in the meridional and 2 arcsec in the sagittal direction. Its sagittal radius of curvature is $\rho = 33.1$ mm. In a distance of 400 mm from

the end of the last mirror a focus size of $9.1 \mu\text{m}^2$ is achievable. This size is directly related to the meridional slope errors and the distance between mirror and focus. Smaller foci could be obtained by a Kirkpatrick-Baez system of two plane elliptical mirrors, but then the additional reflecting surface would reduce the transmitted power. With two reflections of 177.8° and 177.6° as in the current scheme more than 70% of the input pulse power is transmitted.

In the focus the peak power density is $2 \cdot 10^{14} \text{ W/mm}^2$ and the average power density at a full repetition rate of 25 kHz is as high as 30 kW/mm^2 .

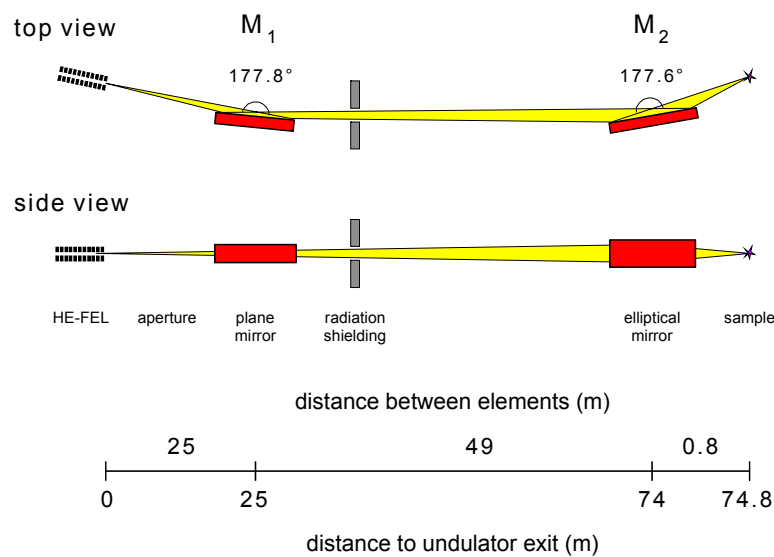


Fig. 10.23: Optical design of the beamline for focused direct light at the HE-FEL.

The high beam divergence of 4 mrad facilitates an easy adjustment of the power density on the sample by moving the sample along the beam direction out of the focal plane.

Table 10.10. Performance of the beamline for direct light at the HE-FEL. The spot size is given as fwhm value.

Parameter	Unit	
Photon energy	1000	eV
Photons per pulse	$6.6 \cdot 10^{10}$	
Spot size (hor. \times vert.)	9×1	μm^2
Energy density	$1.2 \cdot 10^5$	$\text{mJ/cm}^2/\text{pulse}$
Photon density	7000	$1/\text{nm}^2/\text{pulse}$
Peak power density	$2 \cdot 10^{16}$	W/cm^2
Average power density	3000	kW/cm^2

10.8 Beamlines for Spontaneous Radiation

After the electron beam has passed the FEL undulator, the bunch quality is no longer good enough to generate FEL radiation in an additional FEL undulator. Nevertheless it is still possible to produce short pulses of spontaneous radiation in a conventional undulator.

The pulse length of this radiation is expected to be 2 - 3 picoseconds with peak powers two or three orders of magnitude higher than in the low-alpha mode of BESSY II. This will offer additional experimental opportunities.

The beamlines for the additional undulators are patterned on the existing undulator beamlines at BESSY II. A possible design is sketched in figure 10.24. By adapting the deflection angles of the mirrors and the line densities of the gratings, this beamline design can cover the energy range from 5 eV to 2000 eV.

For high photon energies the pulse length conservation at a picosecond level is even possible for high-energy-resolution beamlines, whereas at lower energies care has to be taken not to exceed the intrinsic pulse length given by the electron bunch length.

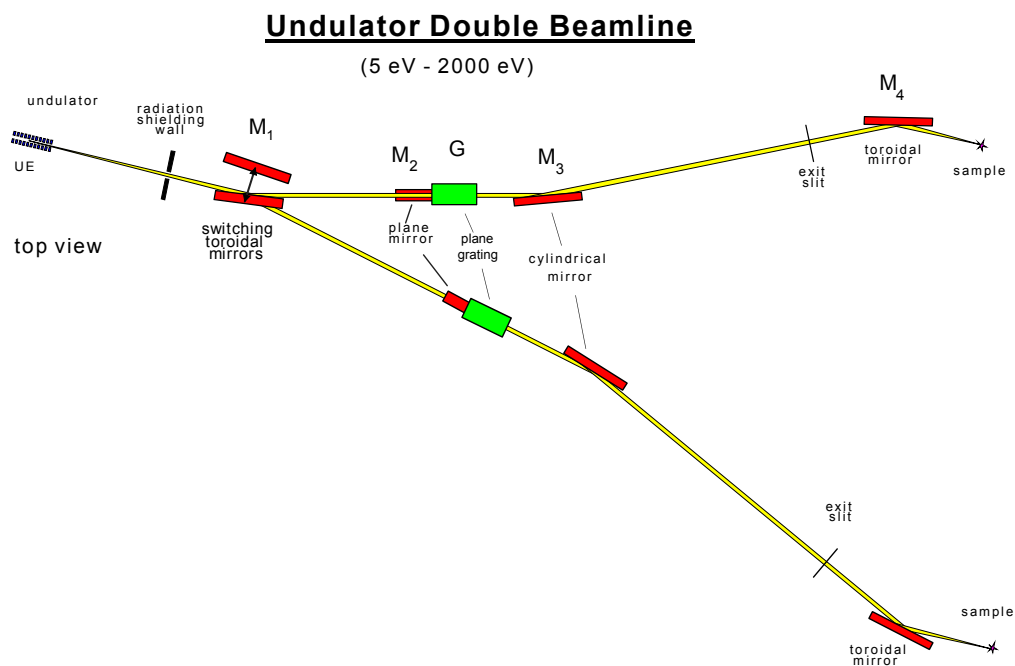


Fig. 10.24: Optical design of a double beamline to exploit the spontaneous radiation of additional undulators.

References

- [1] S. Reiche, *Nucl. Instrum. and Meth. A* **429** (1999) 243.
- [2] C. Momma, S. Nolte, B. N. Chichkov, F. von Alvensleben, A. Tunnermann, *Appl. Surf. Sci.* **109-110** (1997) 15.
- [3] B. Steeg, S. Jacobi, R. Sobierajski, C. Michaelsen, J. Feldhaus, *Proc. of the 24th FEL conf.* (2002), to be published in *Nucl. Instrum. and Meth. A, Technical Report TESLA-FEL 2002-06 DESY* (2002).
- [4] A. Andrejczuk, U. Hahn, J. Krzywinski, J. Pelka, H. Reniewicz, E. A. Schneidmiller, W. Sobala, R. Sobierajski, M. V. Yurkov and TTF FEL team, *HASYLAB Annual Report, Part I*, (2001) 117.
- [5] E. M. Gullikson, Academic press: *Experimental Methods in the Physical Sciences 31:Vacuum ultraviolet spectroscopy*, (2000) 257.
- [6] R. Tatchyn, *SLAC-PUB* 6064 (1993).
- [7] B. L. Henke, E. M. Gullikson, J. C. Davis *At. Data Nucl. Data Tables* **54** (1993) 181.
- [8] H. Petersen, C. Jung, C. Hellwig, W.B. Peatman, W. Gudat, *Rev. Sci. Instrum.* **66** (1995) 1.
- [9] T. Miyahara, *Rev. Sci. Instrum.* **60/7** (1989) 2068.
- [10] K. J. S. Sawhney, F. Senf, W. Gudat, *Nucl. Instrum. and Meth. A* **467-468/1** (2001) 466.
- [11] H. Petersen, *Opt. Commun.* **40/6** (1982) 402.
- [12] F. Schäfers, *BESSY Technical report* 202/96 (1996).
- [13] J. Bahrtdt, *Appl. Opt.* **36/19** (1997) 4367.
- [14] R. Follath, F. Senf, *Nucl. Instrum. and Meth. A* **390/3** (1997) 388.
- [15] W. Cash, *Appl. Opt.* **26/14** (1987) 2915.
- [16] K. Holldack, T. Zeschke, F. Senf, C. Jung, R. Follath, D. Ponwitz, *BESSY annual report* (2000) 336.
- [17] E. D. Palik, *Handbook of Optical Constants of Solids*, Academic Press (1985).
- [18] M. R. Weiss, R. Follath, F. Senf, W. Gudat, *J. Electron. Spectrosc. Relat. Phenom.* **101-103** (1999) 1003.
- [19] D. Goswami, *Phys. Rep.* **374/6** (2003) 385.

11 Experiments and End-Stations

The following key scientific areas have been identified in the “Visions of Science” for the BESSY FEL. Here we outline the experimental facilities needed to perform these investigations. The plan is to provide a common base for experiments which will be installed ready to use for external groups in pursuit of their scientific programs. These instruments will be designed for easy installation at all three FEL lines.

A. Femtochemistry – The Dynamics and Formation of Chemical Bonds

Atom specific femtochemistry in a gas phase molecular beam, on surfaces and in liquids in general requires access to valence and core electronic levels over the whole energy range of 20-1000 eV. However, a clear preference can be given to the medium energy FEL were the edges from carbon to oxygen are covered. Both photon-in/photon-out (resonant inelastic X-ray scattering) and photon-in/electron-out (high-temporal-resolution photoemission, photoemission electron microscopy) will be used.

B. Magnetization Dynamics of Nanostructures on the fs Time Scale

Exploring the ultimate time scale of magnetization dynamics requires access to resonant excitation of $3d$ and $4f$ valence shells in transition metals and rare earth systems. Experimental facilities for photoemission electron microscopy, resonant X-ray scattering and coherent X-ray scattering at the low-energy and the high-energy FEL lines are needed for these experiments.

C. Atoms and Molecules – New Fundamental Limits

The photoionization of atoms and molecules exploiting the high FEL brilliance, and the high temporal resolution in FEL-pump/optical-probe experiments is proposed. The variety of available atomic and molecular systems to be studied requires that facilities (cluster and atomic/molecular beam instrumentation including atomic traps) can be installed at all three FEL lines

D. The Nature of Complex Solids

Understanding the structure-function relationship in complex materials requires ultra-high resolution photoemission and photon-in/photon-out resonant inelastic/coherent X-ray scattering facilities to be installed at both the low-energy and the high-energy FEL lines.

E. Dynamics of Biological Systems

Biological investigations using Soft X-ray FEL radiation proceeds mainly via single shot X-ray microscopy and holography experiments at the medium-energy FEL line.

F. Chemistry of Radicals

These studies will utilize the cluster and atomic/molecular beam instrumentation at all three FEL lines to access the entire photon energy range.

G. Clusters as New Materials

Clusters will be studied with a cluster beam setup in photon-in/electron-out experiments at all three FEL lines.

H. Ultra – High Resolution Spectroscopy

Very high energy resolution photoemission spectroscopy becomes feasible due to the dramatic increase in brightness offered by FEL sources. Ultra high absolute energy resolution can be utilized especially at the corresponding beamline at the low-energy FEL line.

I. New Perspectives on Catalysis

Research on catalysis is based on optical-FEL sum frequency generation utilizing an inelastic scattering setup for the medium energy and high energy FEL lines.

J. Materials and Processes Observed under Technologically Relevant Conditions

Elementary processes at solid/electrolyte interfaces will be studied using inelastic X-ray scattering instrumentation at the medium energy and high energy FEL lines.

K. Characterization of Fusion Plasmas

Atomic data of highly ionized species found in fusion plasmas will be obtained by single and multi-photon excitation spectroscopy using focused FEL radiation. In addition the FEL pulses themselves can be used to generate plasmas from solid targets. These studies will be performed mainly at the medium energy and the high energy FEL lines with user supplied plasma sources and focused FEL radiation using X-ray microscopy techniques.

L. Time Resolved Spectroscopy – Reaching the "as" Range

Coherent two-photon-photoemission of core-electrons at surfaces can be performed using an FEL pulse splitter. FEL wavefront correction should enable one to perform interferometrical measurements at the low- and medium energy FEL line.

M. New Frontiers in Photon-related Spectroscopies and Coherence

Resonant inelastic/coherent X-ray scattering at the medium energy and high energy FEL lines will make possible critical investigations both on novel materials and on important chemical and physical phenomena including process monitoring.

In the following, some experiments and setups will be described with the goal to have generic experimental setups available for certain classes of experiments. The intent here is to standardize certain experimental environments for easy and fast access of user groups who come with specific scientific projects. Of course, there will always be the possibility to carry out totally different experiments and to install the necessary equipment for these.

11.1 X-Ray Microscopy and Holography – Single-Shot Experiments

X-ray microscopy at 3rd generation synchrotron sources like BESSY II is a powerful imaging method for life, materials and environmental sciences [1, 2]. The penetration power of X-rays through matter permits studies on entire biological cells, on fully passivated electronic devices or on metal layers in an applied magnetic field [3 - 10]. Many different contrast mechanisms such as phase contrast imaging, exploitation of dichroic effects, chemical contrast imaging and X-ray fluorescence have been used to demonstrate the potential of X-ray microscopy techniques. The time resolution achievable is given by the required exposure times - a few seconds at state-of-the-art X-ray microscopes. The exciting prospects are that, with the FEL snapshot-like images of the same quality but with much higher time resolution can be obtained with only a single fs-FEL-pulse. This is important for many scientific applications such as *Dynamics in Biological Systems* and *Characterization of Fusion Plasmas* as described in the scientific case of the BESSY FEL.

For example, biological pore structures in cells can rapidly expand to diameters of 20 - 120 nm in the first 20 ms after exposing them to an electric field. Electrochemical processes in nerve cells take place also within this time range. Vastly faster processes – from fs to ns - occur in chromophores after electronic excitation in an optical laser beam. With current X-ray microscopes at existing synchrotrons such studies are impossible because of the inherently long exposure time. In addition, biological systems can be investigated with X-ray microscopy methods only if they are protected against radiation damage. For this purpose biological cells are cooled to cryogenic temperatures, which make dynamical studies impossible. For studying living biological cells the image recording has to be much faster than structural changes induced by the radiation. Model calculations show that snapshot-like X-ray images of natural, unaltered objects can be recorded in the fs-time domain without introducing artifacts by the imaging process itself [10]. Experience from 3rd generation synchrotron radiation sources shows that an integral photon density on the order of several 10^8 photons/ μm^2 is needed to obtain images with 20 nm resolution [3]. At the BESSY FEL about 10^{11} photons/pulse in an energy bandwidth of 0.1% such images can be obtained with a single X-ray pulse, thus opening up the possibility of observing *Dynamics in Biological Systems* on ultrafast time scales.

Another exciting field for X-ray imaging techniques with the BESSY FEL is the *Characterization of Fusion Plasmas*. X-rays are ideally suited to penetrate plasmas which are dense in the optical wavelength range. A target like a liquid jet of only a few microns diameter can easily be heated up to several million degrees Kelvin forming a plasma. The dynamics of the plasma formation can be measured by X-ray imaging with fs time resolution. The ion population can be studied by imaging the plasma at different wavelengths. Due to the unique nature of X-rays, no other imaging technique can provide such data for understanding plasma dynamics. Such experiments on the 20 fs time scale require the planned BESSY HGHG-FEL. Especially its well-defined pulse structure and its much easier synchronization with external optical lasers make pump-probe experiments with nm spatial resolution possible. In the following, two different optical setups for X-ray imaging with a HGHG-FEL source are described.

For the medium-energy FEL beamline, it is planned to develop:

1. A transmission X-ray microscope for direct imaging without the need for image processing and
2. A novel holography end-station for three-dimensional imaging allowing for the reconstruction of a complex object from a Gabor in-line hologram.

Full-field X-ray microscopy will be used for time resolved studies for biological and plasma formation studies. Both applications require special setups for the object region, e.g., cells in their native wet environment or liquid jets in vacuum heated to million degrees forming a plasma. Therefore, it is planned to develop different microscopy sample environments optimized for the application fields. The holography setup will be optimized to obtain 3-D information from samples. Due to the coherence length of the FEL beam, the dimensions of the samples are limited to a few micrometers. The three systems will be designed as end-station modules for the medium energy FEL beamline which can be interchanged

11.1.1 Transmission X-Ray Optics for nm Focusing of FEL Radiation

In the last decade advances in nanostructuring technology have led to rapid improvements in the quality of diffractive X-ray optics. Such optical elements are the key to high spatial and energy resolution X-ray imaging techniques performed at current 3rd generation synchrotron sources [11-13]. This is expected to be the case at the future FEL sources as well. However, for high intensity FEL beams the problem of the thermal stability of the X-ray optics is critical. State-of-the-art transmission zone plates provide about 25 nm resolution below 1 keV photon energy [3]. Their diffraction efficiency is 10 - 20% depending on the geometry of the zone structures, the material and the photon energy. Such optics are manufactured on thin silicon membranes with about 100 nm thickness. An integral

FEL flux of 10^{11} photons/pulse at 0.5 keV photon energy through an aperture of 0.1 and 1mm diameter would cause a temperature rise of the zone plates of about 1000 and 10 K, respectively. Accordingly the illumination has to be chosen such that the maximum temperature rise is less than 100 K. It is known from X-ray microscopy experiments at the BESSY II undulator U41 that transmission zone plates made from silicon (figure 11.1) under continuous X-ray irradiation for many months can withstand a temperature increase of 10 – 100°C without damage to optical elements. At repetition frequencies of 1 – 10 kHz, the optics can be expected to have cooled down by the time the next pulse arrives.

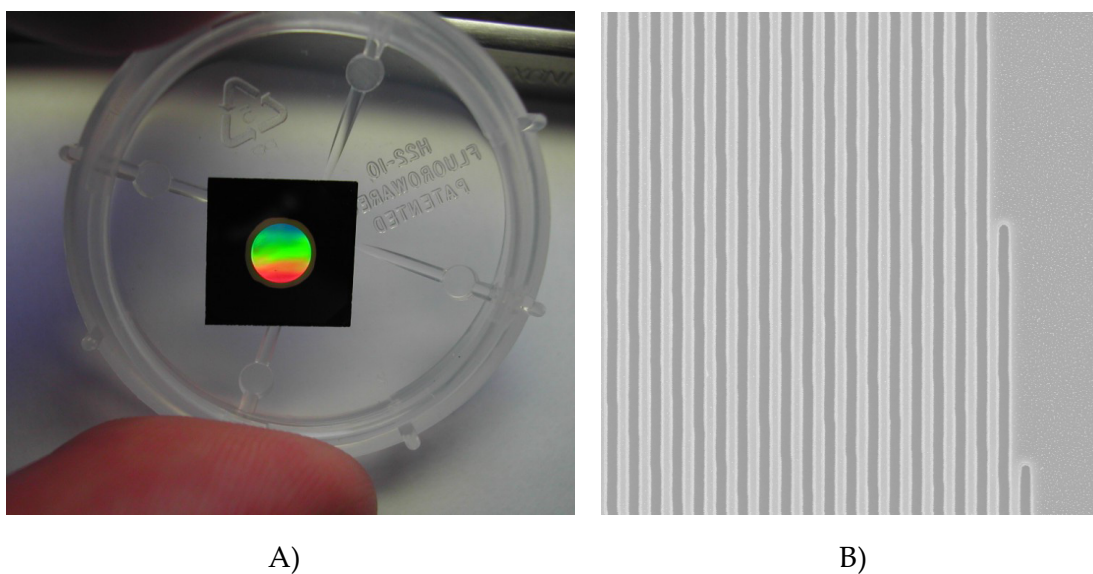


Fig. 11.1. A) Photograph of a silicon off-axis transmission zone plate with a circular shape of 4 mm diameter. B) SEM-micrograph of the 260 nm wide silicon zones of an off-axis transmission zone plate as currently used in the full-field X-ray microscope at the BESSY II undulator U41 [14].

11.1.2 Full-Field Microscope for fs X-Ray Imaging

In figure 11.2 the planned X-ray optical setup of the full-field X-ray microscope in amplitude contrast mode is shown. Basically only the source itself and the condenser are different from an X-ray microscope at a 3rd generation synchrotron source. Analogous to previous experiments at synchrotron sources it is also possible to implement phase contrast imaging in full-field X-ray microscopes at FEL sources. In this case a phase ring has to be mounted in the back-focal plane and the hollow-cone illumination of the beam-shaper has to be modified to geometrically match the phase ring for phase shifting of the undiffracted light of the object by 90° or 270° (figure 11.3).

For single shot experiments it is essential to collect as many photons as possible. Therefore, the diameter of the X-ray condenser has to be matched to the FEL beam diameter and the number of X-ray optical elements in the optical setup has to be minimized (figure 11.2). The optical setup of a full-field X-ray microscope requires a condenser which produces a nearly homogeneous illumination of the object field. A zone plate 1 mm in diameter focuses a parallel beam onto the object, but at the cost that only a tiny object field of less than 1 μm in diameter is illuminated. To overcome this problem, special X-ray optical devices which influence the wave-field by diffraction can be employed. A specified illumination wave – in this case the FEL beam – can be converted to a diffracted wave with a desired distribution of its amplitude or phase by a computer generated hologram acting as an X-ray beam shaper. If the incoming wave field is known, the beam shaper can generate nearly any illumination distribution such as a homogeneously illuminated object field with a few μm in diameter. With such a beam shaper as a condenser the aperture of the X-ray objective further downstream can be nearly matched and the required hollow cone illumination of the object can be generated by a single X-ray optical element. At the same time these conditions optimize the spatial-frequency transfer of the microscope towards high spatial resolution.

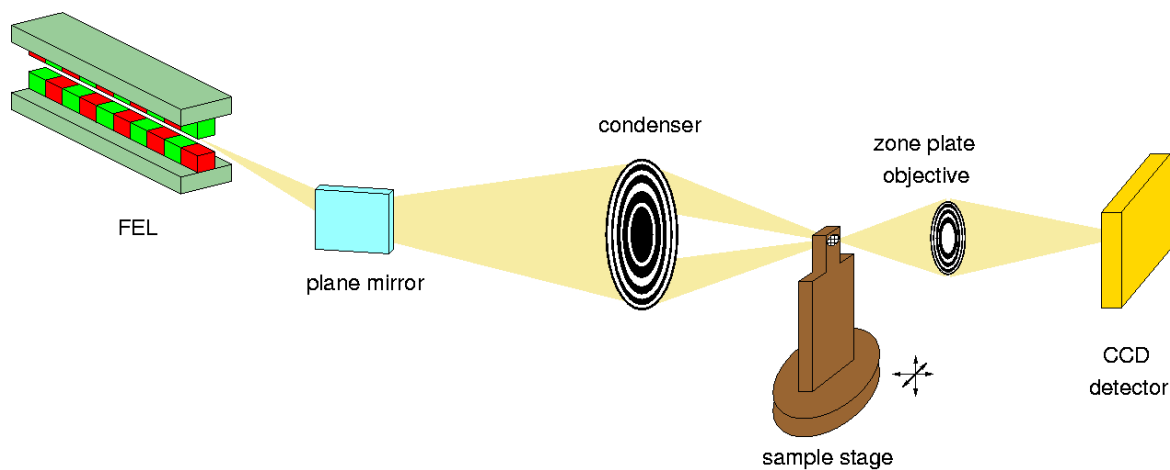


Fig. 11.2: X-ray optical setup of the full-field microscope in the amplitude contrast mode at the BESSY FEL. Radiation safety requires a mirror in front of the microscope. It is planned to use a nickel coated plane mirror under 1.5° incidence angle with a reflectivity of about 80%. The FEL radiation is then collected by a special condenser - a beam shaping diffractive optics of about 1 mm in diameter - which forms a nearly homogeneous hollow-cone illumination onto the object field.

However, the short-pulse duration of only 20 fs and the coherence of the beam have to be taken into account. The beam diameter at the beam shaper is required to be about 1 mm to prevent damage of the optical elements. The optical path difference between the center and the outer diameter of the beam shaper to a point at the sample plane is then about 15 μm which corresponds to a 50 fs propagation time difference of the X-rays. Therefore, the HGHG-FEL offers two major advantages over a SASE-FEL for single shot X-ray imaging:

1. The short-pulse duration of 20 fs makes the illumination more incoherent. The wave-field generated by the inner and outer part of the beam-shaping condenser cannot interfere in the object plane since it arrives at time delays longer than the intrinsic FEL pulse duration and

2. No monochromator is required in front of the condenser since the monochromaticity of the HGHG FEL-beam is already about $\lambda/\Delta\lambda = 1000$.

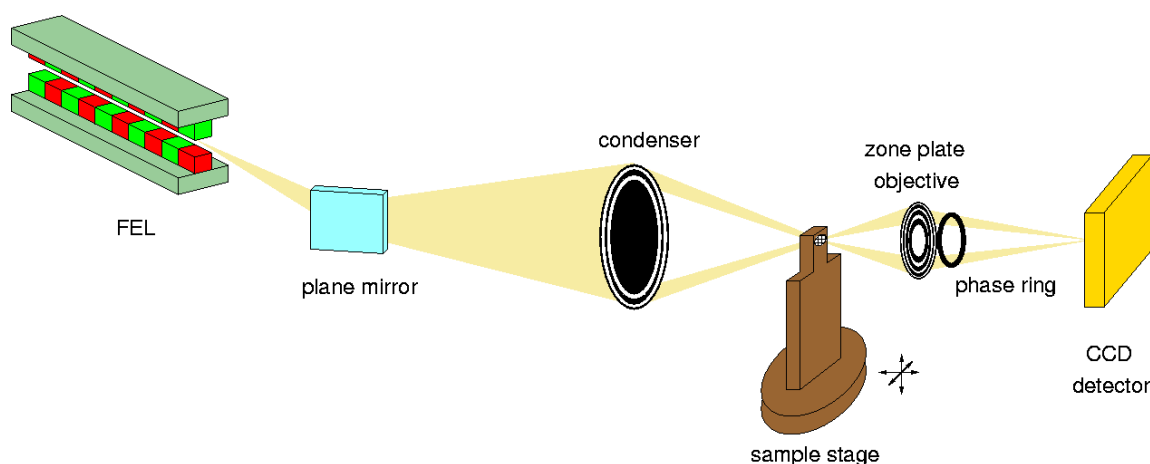


Fig. 11.3: X-ray optical setup of the full-field microscope in the phase contrast mode. The direct light passing the object is phase-shifted in the back-focal plane by a phase plate with ring-shaped geometry [15]. Note that the diameter of the central stop in the condenser has to be larger than in the amplitude contrast mode in order to shrink the width of the phase rings. A small ring width of about 1 μm or less is required for generating phase contrast images of small and medium size object details (high and medium spatial frequencies). Low spatial frequencies are not affected by the phase plate. If the ring width is too large, only very high-spatial frequencies generate phase contrast and the so-called halo-effect with large intensity modulations at edges is enhanced, giving rise to artefacts.

To obtain an X-ray image with 20 – 30 nm resolution and a signal-to-noise ratio of 3, at least 10^8 photons/ μm^2 are necessary for object illumination assuming a perfect X-ray objec-

tive with 100% efficiency [3]. As mentioned above, the integral photon flux of the ME-FEL is 10^{11} photons/pulse. A realistic diffraction efficiency is 10% for the condenser element. Therefore, about 10^{10} photons/pulse will be focused onto the sample. The X-ray objective will be a conventional Fresnel transmission zone-plate with about 20 nm resolution and about 10% efficiency. This means that about 10^9 photons/pulse can be used to form an X-ray image with a single pulse exposure of an FEL. Under these conditions the size of the object field will be about $3 \times 3 \mu\text{m}^2$ which should be sufficient for many applications. In case a larger object field is required, a beam shaper illuminating a bigger field has to be used at the cost of a slightly reduced spatial resolution as limited by the decreased signal-to-noise ratio in the image.

The FEL monochromaticity makes it possible to perform X-ray imaging free of chromatic aberration with transmission microzone plate condensers of 1 mm diameter and objectives which are typically 100 μm in diameter. From their diameter and the expected transmitted flux we can estimate that the temperature rise from a single FEL shot in the beam-shaping condenser element will be about 10 K and in the much smaller X-ray objective zone plate will be below 100 K if both elements are made out of silicon. As discussed above, this temperature rise will not be critical for either X-ray optical element.

However, the photon density in the object plane is so high that the sample is likely to be destroyed after a single image in a FEL full-field microscope. This is different from existing full-field microscopes and makes it necessary to precisely align the object with visible light, e.g. an optical microscope, before the X-ray imaging takes place. In practice, it means that not only the object specimen has to be very well-characterized before X-ray imaging is attempted but also that high-resolution optical diagnostic tools have to be incorporated into the FEL X-ray microscope for the required highly precise alignment of the object and all of its optical components. Sub- μm precision is required in all dimensions. It is, therefore, planned to use a high-resolution optical microscope for alignment purposes. Switching between the light microscope and the beam-shaper condenser can be done by precisely moving both components in and out of the X-ray beam path.

11.1.3 Single Shot X-Ray Holography with Coherent FEL Radiation

Full-field X-ray microscopy can provide 3D-information only by multiple exposures of the same object under various viewing angles. This tomographic approach becomes impractical when a single FEL pulse can already damage the object. An alternative method for obtaining 3D-information is holography originally proposed by Gabor [16]. X-ray holography has long been discussed as a method for high-resolution X-ray imaging. So far experimental work on X-ray holography has been carried out only at synchrotron sources. The different X-ray optical setups which have been tested in the past can be divided into two groups:

1. Gabor in-line holograms: The origin of the reference wave and the object wave are placed behind each other and both waves propagate in nearly the same direction to the hologram plane where the superposition of both waves is recorded. The hologram consists of a system of circular fringes, and the smallest object point that can be reconstructed corresponds to the smallest fringe width. The reconstructed conjugated image ("twin image") is superposed onto the real image but is focused in a plane farther away. It can be eliminated by mathematical phase retrieval algorithms. Radiation with small coherence length requirements can be used. If the reference wave and the object are at large distances from each other the twin image will be reconstructed far away from the real image and only minor blurring occurs. In any case, a high resolution hologram recording material is required to record the fine fringes generated in the hologram plane. If sub-optical resolution must be achieved in the reconstructed real image, X-ray resists can be used as a recording material. After development the resist shows a surface profile which has to be digitized with a surface sensitive nanoprobe, e.g. with an AFM.

If the reference and the object wave originate at a small distance from each other the twin image will be reconstructed close to the real image. Phase retrieval algorithms have to be applied to eliminate blurred twin image which is superimposed onto the real reconstructed image. Image recording can be done with CCD cameras of low resolution compared to the resolution to be achieved in the reconstructed image.

The reason for this behavior is simple: As both types of waves originate at nearly the same distance from the hologram plane an object point will generate only a very small number of fringes in the hologram plane, which can easily be recorded with a CCD of standard pixel size. The reconstruction algorithm "illuminates" the hologram with a wave converging in the reference point - only minimal diffraction of this converging wave is necessary to "refocus" it in the object point located close to the reference point.

2. Fourier transform holograms: The origin of the reference wave is placed in the same plane as the object, separated only by a short distance which has to be smaller than the coherence length of the beam. Reference wave and object waves propagate with a small inclination, θ , to the hologram plane, where the superposition of both waves is recorded. A system of straight or slightly curved fringes results with a period of $d = \lambda/\theta$. The information on the object is stored in the hologram as a locally modulated displacement of the fringes. The reconstructed conjugated image is located in the same plane as the real image but strictly separated from it by a certain displacement. Radiation with a large coherence length has to be used. Recording of the fringes and their positional modulation can be done using a CCD camera, if the object reference wave and the object points are very close to each other.

For the BESSY HGHG-FEL the Gabor in-line holography approach is favored. The proposed setup is shown in figure 11.4. The advantage of this setup with a spherical reference wave close to the object is that the cumbersome use of photo-resist detectors can be avoided. CCD cameras offer the advantage of being linear detectors with a relatively high dynamic range and, in the soft X-ray region, with a high quantum detection efficiency of up to 70% at 500 eV photon energy. The sample is illuminated with the coherent wave-field generated by focusing the coherent FEL beam with a transmission zone plate. The focused X-rays pass through a pinhole which serves as a spatial filter and generates a well-defined spherical wave-field.

The spatial resolution that can be obtained in this holography setup is mainly determined by the numerical aperture of the zone plate which forms the focal spot. The spatial filter which is a small pinhole made from a highly X-ray absorbing material such as gold will not influence the source size. Very similar to an X-ray microscope, the outermost zone width of the zone plate determines the numerical aperture and the size of its focal point and, therefore, the ultimate instrumental resolution. With present day diffractive transmission zone plates one can expect to obtain a resolution of about 20 nm in the reconstructed hologram. Progress in nanotechnology might lead to sub-10 nm resolution as predicted by electro-dynamical calculations [17, 18].

The resolution of the reconstructed images depends on the information recorded in the hologram which is limited by the size of the detector and its resolution (section 11.2). For a digitally recorded hologram this resolution is given by the number of pixels, their size, spacing and the dynamic range of the recorded signals. Two points close together in the object can be reconstructed from the hologram if the fringes they generate in the hologram plane are out of phase by π at the rim of the recording CCD detector and can be resolved by it.

From a single hologram a series of selected object depths can be reconstructed two-dimensionally. Such a stack of two-dimensional images will then allow one to reconstruct the object in all the three dimensions. However, the 3-D resolution that holography really provides must be evaluated in more detail. The depth resolution obtainable in a holographic reconstruction is about $4 \lambda/\theta^2$ (θ = effective numerical aperture) and is, thus, generally much smaller than the transverse resolution. This behavior is equivalent to optical lenses and zone plates of numerical aperture θ . In practice a transverse resolution of 10 – 20 nm depending on the outermost zone width of the zone plate creating the point source can be expected. The focus depth should be between 100 – 500 nm when extracting the 3-D information from a single hologram. We conclude that holography is especially suited for flash imaging using an intense coherent FEL X-ray source as the BESSY Soft X-ray FEL.

In order to form a diffraction-limited focal spot a fully spatially coherent beam is required. The optical path difference from the outer part of the zone plate and its center to

the focus has to be smaller than the FEL pulse length. This is the case for zone plates up to a size of about $300 \times 300 \mu\text{m}^2$. A zone plate with 60 nm outermost zone width and 300 μm in diameter has about 1000 zones. Therefore, the maximum path length difference produced by this zone plate (in first order) is 500λ . At a wavelength $\lambda = 2.48 \text{ nm}$ corresponding to 500 eV photon energy the optical path length difference is compatible with the longitudinal coherence length generated by the medium energy HGFG-FEL. If the resolution of the holographic setup has to be increased, a zone plate with a smaller outermost zone width has to be used. Since the number of zones has to be kept constant such a zone plate has a smaller diameter. In practice the coherent flux utilized will be an order of magnitude lower than the integral FEL photon flux. This implies that in single shot experiments the temperature increase of the zone plate will remain in the acceptable range below 100 K.

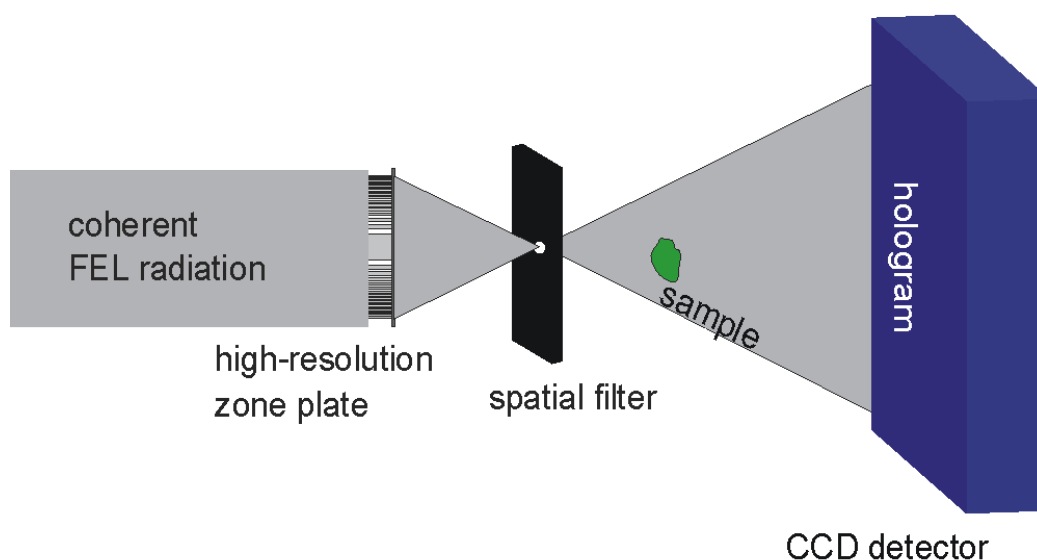


Fig. 11.4: Proposed X-ray optical setup of the holography end-station. The coherent FEL radiation is focused by a high-resolution zone plate into a small pinhole acting as a spatial filter to provide a well-defined wave-field as a reference wave and for sample illumination. The Gabor type in-line hologram is recorded by a slow-scan CCD camera with 2024x2024 pixels. Note that no further monochromator is required which means the time-structure of the FEL pulse is nearly maintained. The diameter or the number of zones of the focusing device are adapted to the monochromaticity of the FEL pulse, which is about $E/\Delta E=1000$ at 500 eV photon energy.

11.2 Coherent X-Ray Scattering

If an X-ray scattering experiment is performed coherently, i.e. such that all X-rays collected at the detector can interfere, a fine structure called *speckle* develops. This fine structure reflects the *individual* sample structure beyond statistical averages. This is illustrated in figure 11.5.

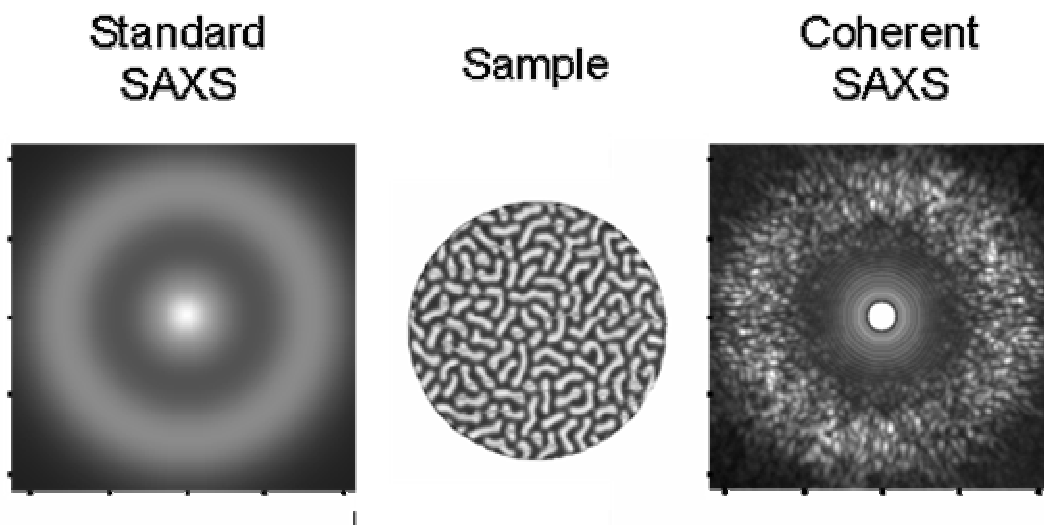


Fig. 11.5: Coherent vs. incoherent small angle X-ray scattering (SAXS). The sample has an in-plane domain structure which gives rise to SAXS. A 2D map of the in-plane momentum transfer is shown. Statistical properties such as the in-plane correlation length can be extracted from standard SAXS. When the entire sample is illuminated by a transversely and longitudinally coherent X-ray beam, speckle fine structure develops due to interference of the scattered X-rays. This fine structure is generated by the specific arrangement of individual domains in the sample.

The existence of speckle fine structure can be exploited in different experimental techniques. These techniques are related by the underlying mechanism of coherent scattering but focus on different scientific problems and have slightly different experimental requirements. Nevertheless, they can be performed in a single suitably equipped experimental station. The instrument can be used at the fs beamlines at all FEL branches, *i.e.* over the entire FEL energy range. It is also possible to use the instrument without a monochromator.

11.2.1 Experimental Techniques

The different experimental techniques and their requirements are briefly outlined below:

Speckle as a fingerprint of the individual sample configuration: Different configurations of a sample can be distinguished by the coherent scattering pattern. This has been demonstrated *e.g.* for magnetic materials in [19], where the microscopic origins of magnetic return point memory are being investigated. This technique requires the detection of the coherent scattering pattern with an angular resolution that is sufficient to resolve individual speckles. Parallel detection of a 2-D region of reciprocal space will yield a scattering pattern in a single shot. (An example discussing the scattering intensities is given in section 11.2.2). Apart from the need to resolve the speckle, the experimental boundary conditions are as in a standard scattering experiment with parallel detection of a 2-D region of reciprocal space. The spatial resolution is determined by the maximum momentum transfer recorded. For a given detector area and pixel size, the maximum momentum transfer can be traded for angular resolution by varying the sample-detector separation.

Lensless Imaging: If the scattering pattern is measured with sufficient oversampling and the sample is spatially confined to a predefined region, the real space structure of the sample can be reconstructed by iterative retrieval of the phase [20-22]. Recent progress in this field includes spatial resolution below 10 nm [23], three dimensional imaging [24] and phase retrieval using exclusively X-ray diffraction data [25, 26]. In comparison to the speckle fingerprint technique, lensless imaging has the additional requirement that the scattering pattern has to be detected with sufficient spatial oversampling in order to solve the phase problem [21]. As compared to a 2-D diffraction pattern sampled at the Nyquist frequency, the number of pixels per detector axis has to be increased by the square root of the oversampling factor. At the same time, the transverse coherence length has to be increased by the same amount for the oversampled pattern to be meaningful. While it is sufficient to probe only a part of the reciprocal space for fingerprinting (*e.g.* a part of the scattering ring in figure 11.5), missing parts of reciprocal space can affect the image reconstruction in a more severe way. A well defined intensity response function of the detector over the dynamic range of the scattering pattern is important for the imaging process. Again, 2-D detection makes single-shot experiments possible.

X-Ray Photon Correlation Spectroscopy (XPCS) requires the detection of a change in the coherent scattering pattern after a delay time τ in order to probe the dynamics of the sample [27-32]. With 2-D detection of the scattered intensity several length scales and directions can be probed simultaneously. With a continuous radiation source (such as a cw laser in the visible spectral range) or a quasi-continuous radiation source (with a time structure below the detector temporal resolution) the delay times can be probed in a (quasi-)continuous way in order to obtain the temporal correlation function. The time

resolution is then set by the time resolution of the detector. Recently, a time resolution of 50 ns has been achieved in XPCS using a fast avalanche photodiode [29]. Significantly shorter time scales can be accessed by pump-probe techniques, where the delay time, τ , is defined by the time interval between pump and probe pulses. This allows one to probe the sample dynamics on the time scale τ without being limited by the detector readout time. With a beam splitter for the FEL, X-ray pulse delay times in the fs regime can be realized. (See chapter 12 for a discussion of FEL beam splitters.)

11.2.2 Experimental Setup

A schematic layout of the ultra-high vacuum experimental station is shown in figure 11.6. Sample and detectors are mounted on goniometers in order to define the scattering geometry (Θ , 2Θ). Both reflection and transmission geometries can be realized. The spatially resolving detectors can be translated along the beam direction in order to vary the oversampling rate (Ω) and the maximum momentum transfer (q_{max}). In the following, we discuss the experimental setup with respect to the different types of experiments. The signal intensity in single shot experiments and detector technology are discussed below. The design of the experimental setup is based on a currently available soft X-ray CCD as a detector and will be functional with existing detector technology, although the duty cycle will be reduced. The detector can be upgraded independently from the remainder of the experimental setup as soon as a better suited detector becomes available (see 11.2.4).

Figure 11.6a shows the setup for static coherent scattering experiments such as lensless imaging and speckle fingerprinting. In order to extend the dynamic range in the detection channel, three separate 2-D position sensitive detectors (D) are used for high- q and low- q regions of reciprocal space. In addition, laterally microstructured absorbers (A) can be placed in the central beam to further extend the dynamic range. With this setup a large region of reciprocal space can be covered in a parallel way, *i.e.* in a setup suitable for single shot experiments. Pinholes can be introduced in front of the sample to restrict the illuminated area, which is important in order to achieve an appropriate oversampling. Alternatively, microstructured samples can be used. An example is shown in figure 11.7, where the coherent resonant scattering pattern from a CoPt multilayer sample is presented. This sample has magnetic domains similar to those shown in figure 11.5, which give rise to small angle scattering when magnetic dichroism at the Co $2p_{3/2}$ resonance is exploited as a contrast mechanism. With lithographic techniques the sample has been patterned into an equilateral triangle with sides of 7.5 μm length. Such sample patterning approaches are important as they allow one to increase the oversampling and to separate scattering from internal structure and from the overall shape of the object.

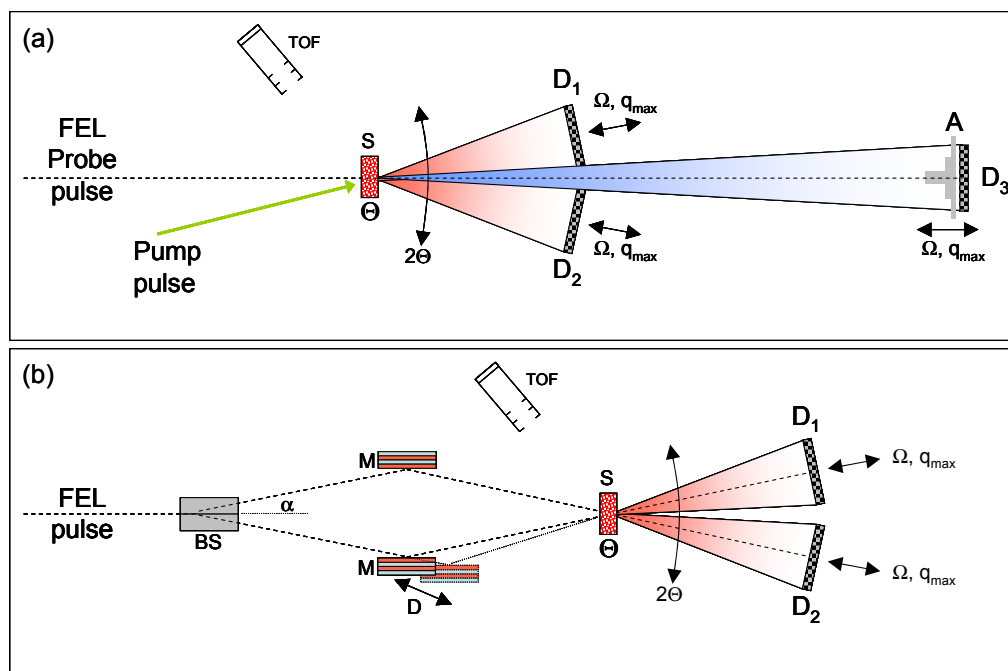


Fig. 11.6: Scheme of the experimental setup. (a) Setup for static experiments and pump-probe experiments. Three 2D spatially resolving detectors detect the scattering from the sample (S) at high (D_1, D_2) and low (D_3) momentum transfer. Microstructured absorbers (A) can be used to extend the dynamic range of the multi-detector setup. The scattering geometry and oversampling rate can be varied by the overall geometry. Different types of pump pulses can be coupled in. A photoelectron spectrometer (TOF) is available to characterize the temporal overlap of pump and probe pulses. (b) Setup for X-ray photon correlation spectroscopy. A multilayer mirror (M) beam splitter is moved into the beam in order to produce an initial x-ray pulse and a delayed x-ray pulse at 10° off the optical axis. D_1 and D_2 now serve to measure the initial and the delayed scattering pattern. In this way, the dynamics of the sample and, in particular, the intensity fluctuation auto-correlation function $g_2(\tau)$ are accessible.

Dynamic information on the sample (S) can be obtained combining coherent scattering experiments with pump-probe techniques, exploiting the fs time structure of the FEL X-ray pulses. Typically, the coherent scattering generated by the FEL pulse will probe the system. The X-ray tuneability will enable one to exploit scattering resonances and, thus, provides various contrast mechanisms for scattering, such as elemental, chemical, magnetic or orientational sensitivity.

Two “standard” pump pulses can be delivered:

- (a) An optical laser, synchronized with the FEL.
- (b) An FEL X-ray pulse. The X-ray pulse will be split and delayed by a beam splitter as described in chapter 12. The beam splitter can be a part of the beamline optics upstream of the experimental station.

Other probe pulses depend on the system under investigation. For studies on magnetic materials, a magnetic field pulse can be delivered by a micro-coil or strip line [33].

The time zero in X-ray-pump, X-ray-probe experiments will be determined at the sample position employing *two-photon photoemission* as described in section 11.3. For this purpose an electron spectrometer (TOF) is integrated into the experimental chamber.

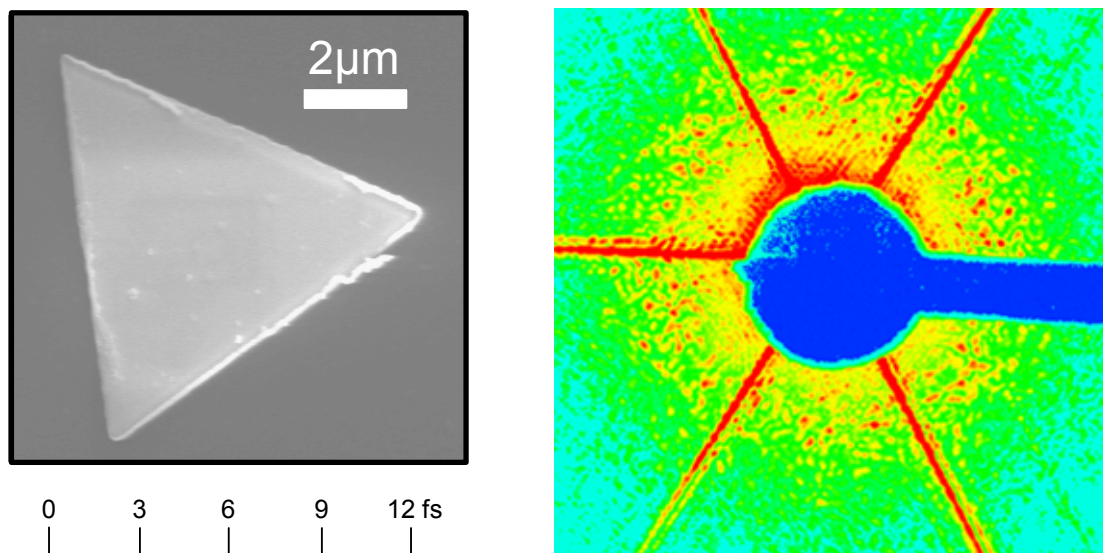


Fig. 11.7. Left: Magnetic multilayer sample, lithographically patterned into a triangle. The time axis indicates the lateral timing gradient for two beams impinging under $\pm 10^\circ$ off-normal on the sample (see text). Right: Coherent scattering pattern exploiting magnetic dichroism at the Co $2p_{3/2}$ resonance. A ring of speckle due to scattering at magnetic domains is visible and separated from the diffraction from the equilateral triangle. A beam stop (blue) blocks the center beam.

Dynamic experiments such as fluctuations in a sample can be studied by x-ray photon correlation spectroscopy (XPCS). A suitable setup for this type of measurement at the FEL is sketched in figure 11.6b. The X-ray beam is split into an initial and a delayed pulse. The delay time, τ , can be varied by changing the optical path length of one beam (D). In contrast to a “standard” X-ray beam splitter, the two beams impinge on the sample each with an angle of 10° off the optical axis. As a result, two separate scattering patterns can be re-

corded with a maximum deflection angle of 10° . At a photon energy of 707 eV (Fe $2p_{3/2}$ resonance), this corresponds to $q_{\max} = 0.63$ nm, allowing one to probe lateral structures down to the 10 nm length scale. From the change of the scattering patterns during the delay time, τ , the intensity fluctuation autocorrelation function, $g_2(\tau)$, can be determined as a function of momentum transfer. Two experimental issues arise from the 10° off-axis soft X-ray beams:

(a) Glancing reflection angles of 10° on the optical elements of the beam splitter at photon energies above 500 eV imply low reflectivities. For example, the reflectivity of a gold mirror under 10° glancing angle at 707 eV is $5 \cdot 10^{-3}$, i.e. after two reflections the intensity is reduced by five orders of magnitude. In order to reduce this loss while being able to operate at 10° , a beam splitter based on multilayers is incorporated into the experimental chamber. In multilayers, the reflectivity can be significantly enhanced in a certain photon energy band pass. With a $[\text{W}(2 \text{ nm}) / \text{B}_4\text{C}(3 \text{ nm})]_{100}$ multilayer on a Si substrate, a reflectivity of 0.23 can be achieved at the Fe $2p_{3/2}$ resonance in the vicinity of 707 eV [34]. As a result, the photon flux is reduced only by a factor of 20 in the multilayer beam splitter.

(b) 10° off normal incidence on the sample implies a timing gradient over the sample, as the wavefront reaches different parts of the sample surface at different times. This gradient within each beam amounts to 1.7 fs per 1 μm lateral distance on the sample, which has to be multiplied by 2 in order to obtain the gradient in the pump-probe delay time, τ . As an example, this timing gradient is shown for the sample in figure 11.7 at the bottom. As the lateral dimension (or illumination) of the specimen will be typically 10 μm or less in order to achieve high oversampling, the maximum delay time shift over the sample is 34 fs. This magnitude is comparable to the intrinsic pulse length delivered by the short-pulse beamlines and represents the short-time limit for XPCS with this setup. It might turn out that in some cases this gradient can be turned into an experimental advantage. For example, when a large sample is imaged by lensless imaging, the image will contain a lateral delay time ramp.

The experimental chamber will be set up for the investigation of solid samples. For studies on magnetic materials, a magnetic field up to 6 T field strength can be applied. The sample will be mounted on a He cryostat cold finger, allowing for operation down to 20 K.

11.2.3 Single-Shot Experiments: Intensity Considerations

What can be expected for FEL single-shot measurements can be deduced on the basis of multi-shot experiments performed at BESSY II. In figure 11.8, results for a lensless imaging experiment at 3.1 nm wavelength (400 eV photon energy) are reproduced [26]. The experiment was performed at the UE56-1/SGM beamline, operating in the unfocused beam with an energy resolution of $E/\Delta E = 5000$.

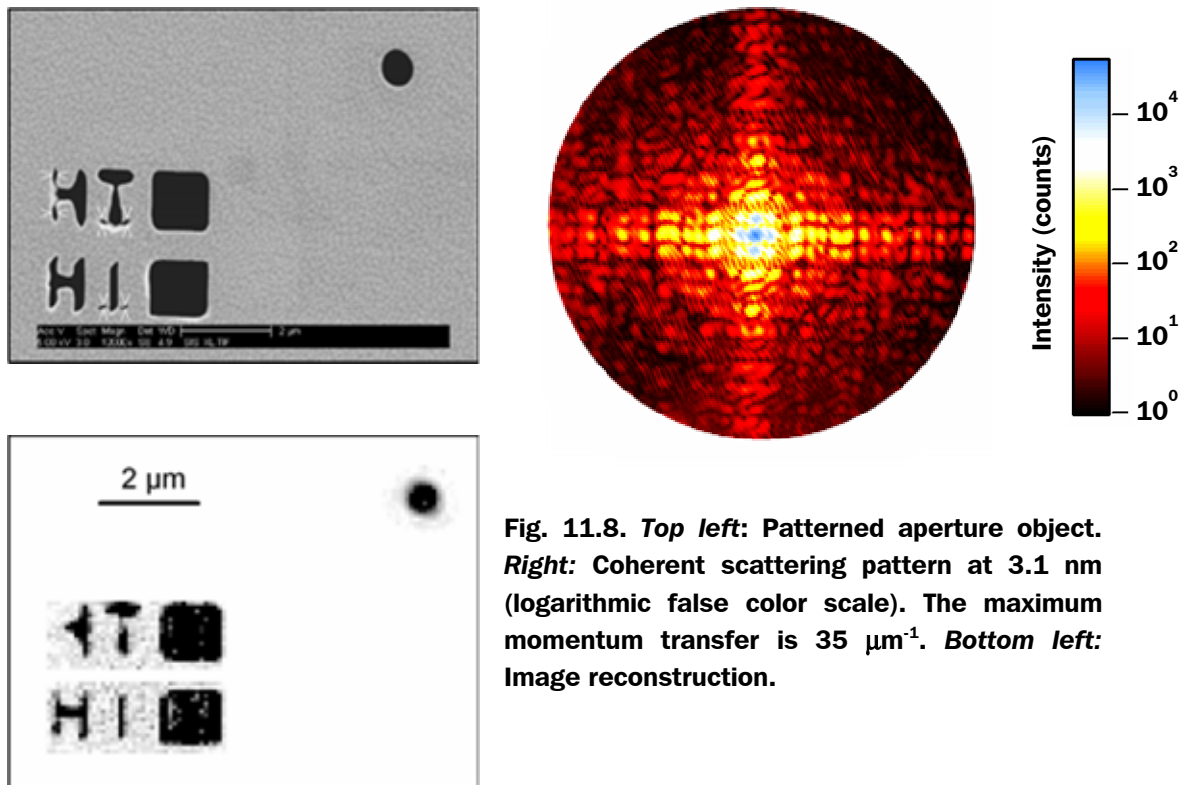


Fig. 11.8. *Top left: Patterned aperture object. Right: Coherent scattering pattern at 3.1 nm (logarithmic false color scale). The maximum momentum transfer is $35 \mu\text{m}^{-1}$. Bottom left: Image reconstruction.*

The sample consisted of letters and holes (“HI ■”) cut through a $2 \mu\text{m}$ gold film. The contrast in a transmission experiment is thus 100%. The coherent scattering pattern was measured up to a maximum momentum transfer of $35 \mu\text{m}^{-1}$ (detector cut-off), corresponding to a spatial resolution of 180 nm. An exposure of 30 minutes was required to record the image. The average count rate on the detector was 2700 counts/s which translates into a total incident coherent photon flux of $2 \cdot 10^5$ photons/s at the sample position, when the sample geometry and detector quantum efficiency are taken into account. The dynamic range in the recorded scattering pattern is 10^4 , the oversampling factor is 16. The image of the test object could be retrieved from the scattering pattern without further input by iterative phase retrieval on the basis of a Gerchberg-Saxton algorithm [21]. Features below 180 nm cannot be resolved. At an energy resolution of $E/\Delta E = 1000$, a single FEL pulse will contain 10^{11} photons with full transverse coherence in a $50 \mu\text{m} \times 10 \mu\text{m}$ focus. The available incident photon flux from a single FEL pulse of 20 fs duration would thus generate a 2500 times more intense scattering pattern as the one observed here. If we approximate the intensity dependence in the scattering as a function of momentum transfer q as $I \propto q^{-4}$, we would expect to be able to resolve 25 nm structures in a single-shot coherent scattering experiment using a FEL X-ray pulse.

11.2.4 Single-Shot Experiments: Signal Detection

A single shot experiment requires 2-D detection of the scattered intensity. As the entire signal is generated within a few tens of fs, typical single-photon-counting approaches for position determination such as resistive anodes or delay lines will not be applicable. Pixel based detectors which integrate the signal in each pixel over the duration of the X-ray pulse will have to be used. The dynamic range encountered in such an experiment is on the order of 10^6 , which is beyond the capabilities of any currently commercially available pixel based detector such as a CCD. As the overall intensity dependence has a strong q -dependence, this problem can be solved with suitably structured attenuators in front of the detector and/or by dividing up reciprocal space on several detectors operating in parallel. In this way, back illuminated CCD detectors can be used in the soft X-ray range to provide the spatial resolution needed in a parallel detection mode. A 2048x2048 pixel CCD with a clock speed of 1 MHz, as is currently available at BESSY, has a frame transfer rate of four seconds. CCDs with 20 MHz clock speed are currently available, bringing the readout time down to 200 ms [35, 36]. In this way the proposed experiments are possible but would not take full advantage of the 1 kHz repetition rate of the FEL. For *XPCS* and *speckle fingerprinting* experiments, where it is sufficient to probe a small part of reciprocal space, correspondingly higher readout rates can be realized with CCD detectors. A very promising alternative technology for faster readout times are DEPFET active pixel sensors for soft X-ray applications, which are currently being developed at the Semiconductor Laboratory of the Max-Planck-Institut for Extraterrestrial Physics [37]. Here, individual amplifiers are combined with each pixel. As a result, pixels can be addressed individually and high frame transfer rates can be realized [38], and a 1024 x 1024 active pixel sensor with a frame readout time of 1 ms is currently under development. For high energy physics applications at TESLA a fast readout concept with 50 μ s frame transfer rate for a 520 x 4000 active pixel sensor array has been developed [39, 40]. We anticipate that a 1024 x 1024 CCD or active pixel detector with a spatial resolution below 10 μ m and a frame transfer rate of 1 ms will be available five years from now.

11.3 Resonant Inelastic X-Ray Scattering

Resonant inelastic X-ray scattering (RIXS) provides information about the electronic structure of materials, allowing one to probe both occupied and unoccupied electronic states. In broadband materials one obtains the local partial density of electronic states via soft X-ray emission and fluorescence-yield soft X-ray absorption. In addition, it is possible to preferentially probe specific parts of the Brillouin zone. In narrow band materials electron correlation effects can be observed in the RIXS spectra. In a scattering experiment, contrast due to locally different electronic structures, *e.g.* for different atomic species, can be exploited.

These techniques are applicable to a wide variety of samples, as RIXS is a bulk probe with an analytically predictable information depth. In combination with the inherent atomic and chemical selectivity, this allows one to probe buried structures, such as solids covered by liquids. In contrast to photoemission based techniques, sample charging or the presence of either electric or magnetic fields does not affect RIXS, which is solely based on photon-in photon-out processes. As a consequence a wide variety of materials can be investigated and very diverse scientific and technological questions can be studied. In the scientific case RIXS experiments have been identified as relevant in the areas of femto-chemistry, the nature of complex solids, new perspectives on catalysis, materials and processes observed under technologically relevant conditions, and new frontiers in photon-related spectroscopies.

In a RIXS experiment inelastically scattered X-rays are analyzed with respect to their energy and scattering angle. The core part of the experimental setup is thus a soft X-ray spectrometer. All currently operational RIXS systems for the soft X-ray regime rely on reflection gratings in grazing incidence as dispersive elements. The vast majority of RIXS experiments today are signal intensity limited, due to (a) inherently low fluorescence yield for many chemical elements and (b) the low solid angle coverable by a grazing incidence grating spectrometer. As a result 2-D area detectors are generally employed to collect as much of the dispersed radiation as possible in order to obtain a spectrum. Most existing instruments and the only commercially available instrument [41] rely on a channel plate and resistive anode readout detector (MCP-RAE) [42]. This is a single-photon counting system and is, thus, well adapted to low count rates typically encountered today. Due to its operation principle the spatial resolution breaks down completely for events occurring within 400 ns of each other.

Hence, such a detector can not be employed at an FEL source where all events are produced within a short time window in the fs range. A suitable spatially resolving detector has to accumulate all events during an FEL pulse and, ideally, can be read out before the advent of the next pulse, *i.e.* within 1 ms. Back illuminated CCD detectors can be used in the soft X-ray range to provide the spatial resolution needed in the spectrometer. They have been successfully integrated in spectrometers based on varied line spacing (VLS) gratings, where they can be used in normal incidence with high quantum efficiency [43]. This design allows a 1-D resolved readout of the CCD, as the aberrations perpendicular to the dispersion direction are low. A 2048x2048 Pixel CCD with a clock speed of 1 MHz, can be read out in 100 ms in 1-D line binning mode. CCDs with 20 MHz clock speed are currently available, bringing the readout time down to 5 ms [35, 36]. The requirements regarding readout times are thus significantly reduced compared to 2-D single-shot experiments.

The optical design is based on a currently available soft X-ray CCD as the detector and will be functional with existing detector technology although the duty cycle will be reduced. The experimental setup can be upgraded as soon as a more suitable detector becomes available.

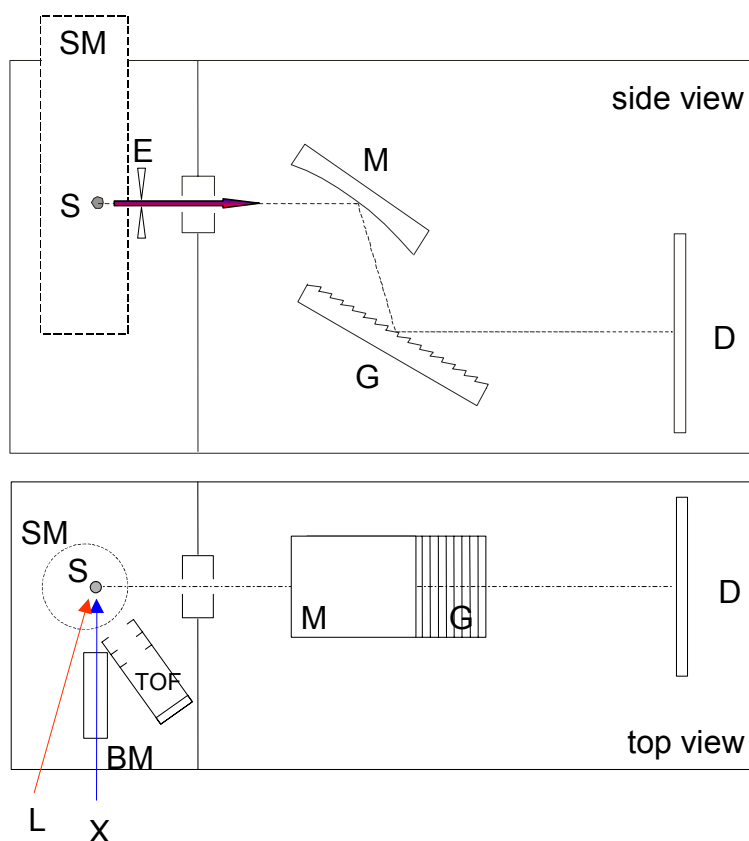


Fig. 11.9: Scheme of the main components and optical layout of the RIXS spectrometer. The optical design is based on a varied line spacing (VLS) grating (G) in conjunction with a spherical mirror (M), focusing the radiation from the source (S) onto the detector (D). An entrance slit (E) can be closed for calibration purposes. The sample, which is contained in the sample module (SM) is excited by X-ray (X) and/or laser (L) pulses. The X-ray beam is refocused on the sample by a bendable mirror (BM). Temporal correlation in “laser pump – X-ray probe” operation can be determined by sideband generation using the spectrometer itself. In “X-ray pump – X-ray probe” operation, temporal overlap is detected by two-photon photoemission using an electron spectrometer (TOF). For clarity, not all components are shown in both views.

The layout of the instrument is shown in figure 11.9. The X-ray beam (X) is refocused on the sample by a plane-elliptical bendable mirror (BM), which is integrated in the experimental chamber because of its short focal length. The mirror enables one to match the X-ray spot on the sample to the acceptance of the spectrometer which is 5 mm (horizontal)

$\times 2 \mu\text{m}$ (vertical) in the high-resolution mode. The vertical size of the focus can be varied in order to prevent radiation damage, depending on the sample properties. Variation of the focus size is also important to avoid space charge problems when determining the temporal overlap in “X-ray pump – X-ray probe” mode by photoemission (see below). The spectrometer consists of an entrance slit (E), a spherical focusing mirror (M), a plane, varied line spacing grating (G) and a back illuminated CCD detector (D). This VLS-type optical layout [43] is currently operational in several soft X-ray spectrometers. It can be chosen such that an energy resolution $E/\Delta E > 1000$ is obtained over the entire photon energy range.

Since solid, liquid, and gaseous samples are to be investigated, a separate sample chamber module (SM) has to be inserted for the different types of samples. These modules allow one to couple X-ray (X) and laser (L) beams in and out, provide differential pumping and sample transfer. Solids will be introduced on a manipulator which provides sample positioning and scanning as well as liquid helium cooling and resistive heating. Liquids are introduced into the experimental chamber in the form of a jet or as a liquid film on a solid surface. Gaseous materials will be contained in a small, differentially pumped volume. Studies on *The Nature of Complex Solids* require low temperatures (20 K) and high magnetic fields (6 T). *Femtochemistry, New Perspectives on Catalysis and Materials and Processes Observed under Technologically Relevant Conditions* require a temperature variable between 120 K and 800 K.

For the experiments outlined in the scientific case, the instrument will be used in the following modes:

- *Standard FEL pulses*

Requires no further hardware

- *X-ray pump – X-ray probe*

Requires a VUV/X-ray beam splitter, as described in chapter 12, installed in front of the RIXS spectrometer.

Due to the HGHG-FEL scheme, the pulses do not have to be characterized on a shot-to-shot basis. It is sufficient to determine the time zero *e.g.* once per hour in order to compensate for thermal drift. The time zero will be determined at the sample position employing *two-photon photoemission* as described in chapter 12, *i.e.* an electron spectrometer (TOF) has to be integrated in the experimental chamber.

- *Laser-pump – X-ray probe*

This requires synchronization between the laser and the FEL pulses (chapter 4). Again, it is sufficient to determine the time zero once per hour to compensate for slow drift. The time zero can be determined at the sample position on the basis of

pulse cross correlation by sum frequency generation (chapter 12). It is especially advantageous that the RIXS spectrometer itself can be used to determine the temporal overlap. If the 1.5 eV (3 eV) laser pulse has temporal overlap with the X-ray pulse, a sideband separated by 1.5 eV (3 eV) is generated which can be detected in the spectrometer. An energy resolution of 1000 is necessary in order to detect the low-intensity sideband next to the main line.

11.4 Cluster and Atomic/Molecular Beam Instrumentation

The fundamental process for all FEL experiments is the interaction of light with matter. Gas phase studies will give the most sophisticated insight into the interaction of photons with atoms. Therefore, different types of gas phase experiments are planned at the BESSY FEL such as photoionization experiments on atoms and molecules, the chemistry of radicals, and clusters as new materials.

The BESSY FEL will provide the opportunity to explore dilute systems (target density $<10^7/\text{cm}^3$) as well as atomic and molecular beams ($\sim 10^{11}/\text{cm}^3$) by site- and atom-specific X-ray absorption and X-ray photoemission spectroscopy beyond the linear optical regime at high and tunable photon energies. In addition, the study of molecular reaction dynamics by time-resolved core-level spectroscopy (e.g. $\Delta t \sim 30$ fs at 130 eV) will become feasible. This is particularly important for catalytic processes on chemically reactive nanoclusters. Determination of essential parameters such as the total valence electron structure and core electron binding energies, single and multiple inner shell photoionization cross sections, geometries, binding sites, short-lived intermediate states, transition states, and transition rates, is of importance to help develop a fundamental understanding of these nanostructures and improved theoretical models. In general, such data will be essential when FEL radiation is used to gain information about more complex and technologically important systems such as nanoparticles, proteins, surfaces, and bulk solids.

Gas-phase experiments of atoms, molecules, and clusters, deliver information on the free undisturbed system. Therefore, certain information of the explored particle itself is gained which is not modified by the environment, e.g. a supporting substrate or solvent molecules. In addition, gas phase experiments can take full advantage of the extreme FEL peak power in the GW range because the targets do not suffer from any beam damage. Space charge effects can be avoided by a reduction of the target density.

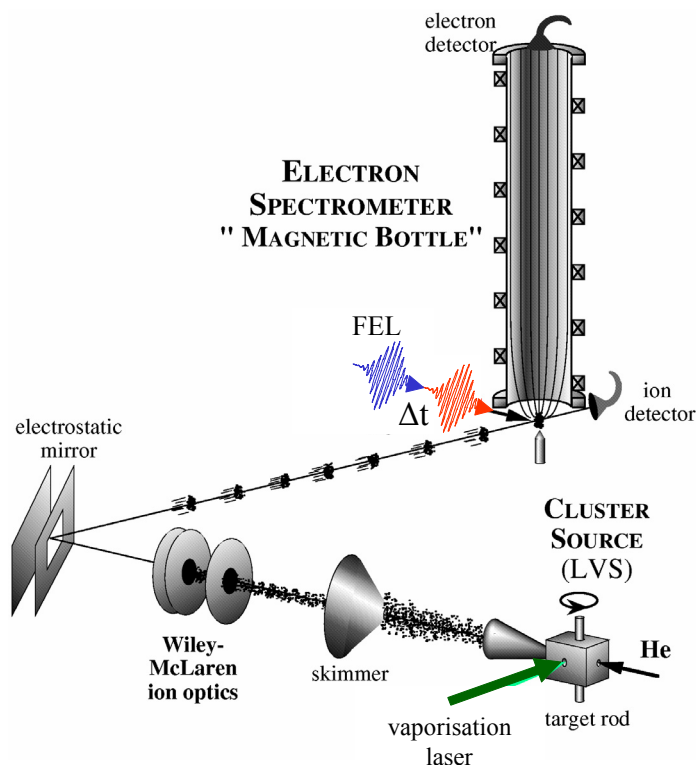


Fig. 11.10: Setup for photoionization experiments on a mass-selected cluster beam. A single FEL pulse is used for static core-level spectroscopy. Time-resolved measurements are indicated using an fs-laser pump (red) and an FEL probe (blue) pulse. The spatial overlap of the fs-laser and FEL beams is monitored by a CCD camera on a fluorescent screen which can be moved into the beam at the interaction point. The photoelectrons emitted can be analyzed by a magnetic-bottle time-of-flight spectrometer (shown) or by some other kind of electron spectrometer on the same port.

Common to all gas phase experiments is a photoionization ultrahigh vacuum chamber in which free particles interact with the FEL beam (figure 11.10). The experimental chamber must be equipped with an electron spectrometer which could either be a magnetic-bottle time-of-flight spectrometer, a cylindrical mirror analyzer or a spherical deflecting analyzer. While the magnetic-bottle time-of-flight spectrometer is suitable for the analysis of slow photoelectrons (< 15 eV) at full solid angle, the dispersive analyzers are useful to analyze higher electron kinetic energies such as Auger electrons. For compatibility reasons with other gas phase experiments the same port should also be able to accommodate an ion-electron imaging coincidence spectrometer (COLTRIMS) [44] to study ultra-cold ion beams as well as a fluorescence spectrometer for X-ray spectroscopy on gas phase particles. Using COLTRIMS technology adapted to a pulsed cluster source, coincidence

measurements of angle-resolved, imaged spectra of ions and electrons will become feasible. Those measurements will soon be tested at the UV-FEL in Hamburg [45].

Conventional photoelectron experiments will be performed by intersecting a gas phase beam with the FEL beam. For laser-pump/FEL-probe experiments, a laser pulse and the FEL beam must overlap temporally and spatially at the object point of the electron spectrometer, the interaction point. The geometrical overlap between the X-ray pulse and a synchronized optical laser pulse will be checked by a scintillation plate which converts the X-ray pulse into visible light. A CCD camera will be used to monitor the *spatial* overlap of the X-ray and optical pulse through a vacuum window. The *temporal* overlap will be measured by photoelectron sideband generation (chapter 12) on noble atoms [46]. For well-defined time information, the FEL and the optical beam should enter the interaction zone as plane waves. Therefore, the laterally incident laser beam will be focused onto the interaction point by an elliptical mirror which ensures that the laser enters at the interaction point with a planar wavefront. The laser mirror is mounted on the main axis of the experimental chamber, along which the FEL beam is introduced through a hole of the focusing laser mirror, similar to the arrangement used in recent laser-HHG cross correlation experiments on atoms [47]. The FEL beam is focused by a grazing incidence X-ray mirror.

For time-resolved experiments using two time-correlated FEL pulses, i.e. an X-ray pump and a probe pulse, respectively, a grazing incidence delay stage has been constructed [48]. This optomechanical device uses a sharp mirror edge ($<50\ \mu\text{m}$ edge radius) as beam splitter. At an incident angle of 3° a maximum delay of $\sim 25\ \text{ps}$ is feasible. The split X-ray pulses will be joined on the same axis as the incoming beam which allows one to move the delay stage into the beamline without changing the beam direction relative to the experimental chamber. This ensures that experiments can be carried out either with or without the delay stage in order to do pump-probe experiments or not. The delay stage will also be used as X-ray autocorrelator to measure the temporal width of the FEL pulses.

Beam experiments require a preparation chamber where the gaseous beam is formed by supersonic expansion (figure 11.10). For the formation of atomic or molecular beams the targets can be injected at high pressure directly from a compressed gas bottle. Alternatively a liquid jet setup can be used. Clusters from solid targets are formed by vaporization of the material and cooling in a pulsed helium seed gas. A metal cluster source can be either a continuously working magnetron plasma sputter source or a pulsed Smalley-type [49] laser vaporization source. High power YAG-lasers with $> 20\ \text{mJ/pulse}$ and a $M^2 < 1.5$ are well suited to vaporize high melting materials, e.g. platinum, where M^2 is the beam quality factor with respect to a perfect Gaussian beam ($M^2=1$). Such diode pumped lasers are already commercially available even at 1 kHz repetition rate [50]. The clusters are formed upon multiple collisions of the vaporized atoms with a pulsed high-pressure helium seed gas. At 1 kHz repetition rate the high pressure seeding pulse can be delivered

by a pulsed piezoelectric gas injector. The clusters generated expand supersonically into the vacuum through a nozzle (1 - 3 mm). In order to achieve the necessary conditions for a supersonic beam and to reach low UHV conditions at the final experimental chamber the high seed-gas flow (1 - 10 mbar·l/s) must be efficiently pumped down by a powerful pumping stage consisting of a sequential combination of turbomolecular pumps and roots pumps. After the supersonic expansion and after passing a small skimmer orifice (~ 5 mm), the charged clusters are accelerated by a pulsed electric field to ~1 keV kinetic energy. Clusters from different longitudinal starting points are temporally focused at the interaction point by a two-stage Wiley-McLaren spectrometer. Using a reflectron time-of-flight spectrometer, different expansion velocities can additionally be compensated for to reach a mass resolution of $m/\Delta m > 1000$. After a field-free drift length (1 – 2 m) different cluster sizes are mass-separated owing to their different flight times. Thus, each cluster mass can be individually explored by triggering the time of cluster extraction relative to the static arrival time of the FEL pulse.

At a low cluster density of $10^6/\text{cm}^3$, an absorption length of 0.5 cm, a typical photoabsorption cross section $\sigma = 10 \text{ Mb}$, and 10^{11} photons per FEL pulse, a photoelectron rate of 0.5/pulse is expected. This makes a high detection efficiency necessary which is provided by a magnetic-bottle time-of-flight electron spectrometer (4π solid angle) having an energy resolution of ~1% (1.5 m drift tube). To increase the target density and to minimize the Doppler broadening of the photoelectron lines, the ions are both decelerated and spatially focused by a pulsed electrostatic lens immediately in front of the entrance to the magnetic bottle spectrometer [51]. Electrons are detected at the end of the magnetic flight tube by a channel plate detector. The signals are amplified and converted by a single channel time-to-digital converter with $> 1 \text{ GHz}$ resolution. Such a resolution is sufficient to count photoelectrons within an arrival time window of 1-10 μs at a nominal kinetic energy resolution of 1%. For dilute systems a high signal-to-noise ratio is crucial. Therefore, a low background pressure is essential (10^{-11} mbar corresponds to $\sim 10^5$ particles/ cm^3) which is best achieved by additional cryostatic cooling of the interaction region and a collimation of the FEL beam to avoid scattered electrons in the experimental surrounding [45].

Intensity-dependent non-linear processes such as two-photon photoemission using two photons from the same FEL pulse (10^{11} photons, $\Delta t = 30 \text{ fs}$) need a target density of $\sim 10^{11}/\text{cm}^3$ at a focus size of $100 \times 100 \mu\text{m}^2$ to accumulate a count rate of 10^4 per second ($\sigma^{(2)} = 10^{-54} \text{ cm}^4\text{s}$ for Ne 1s at 430 eV [52]). Such a particle density is easily reached in neutral atomic or molecular beams.

For laser-pump/FEL-probe experiments, the total count rate depends on the intensity product of the two subsequent photon pulses. However, if a Ti:Sa laser in the visible photon energy range is used for excitation, the target can be saturated as our experience shows [53]. Under those conditions similar count rates comparable to single-photon FEL

experiments can be realized also for pump-probe experiments. In purely Ti:Sa based two-photon photoionization experiments with slightly focused (ca. 1 mm^2) red (10^{14} photons/pulse) and blue (10^{13} photons/pulse) beams respectively, a count rate of $\sim 100/\text{s}$ at 50 Hz has been reached [53]. Thus, using a focused FEL beam, we expect a similar count rate for laser-pump/FEL-probe experiments as for pure two-photon photoemission laser experiments which makes time-resolved XPS on monodispersed clusters possible the first time. This opens the door for an element-specific spectroscopic investigation of the core orbitals of heteronuclear clusters which is of high current interest in nanocatalysis, for the study of nanoalloys and metal-doped endohedral fullerenes. While photoionization experiments on mass-selected cluster anions are just feasible with the predicted Soft X-ray FEL intensity, the improvement of the cluster density down to the space charge limit, the vacuum technology to cope with a 1 kHz high-pressure injection, and the reduction of the background pressure will further increase the scientific opportunities on low-density targets such as size-selected cluster ions, isotope-selected ions [54] and highly-charged ions in a trap.

In figure 11.11 a possible experiment is shown where a delayed FEL pulse is used to follow a catalytic reaction over the activation barrier. The reaction is triggered by a laser pulse. The progress of the reaction is probed by a time-correlated X-ray pulse. New information on the core electron structure and thus about the geometry, as well as on the active sites and atoms of the transition state and intermediates will be obtained by this kind of experiment. The transformation of a chemical bond from a bonding into a non-bonding orbital can be directly followed by probing a photochemical dissociation reaction.

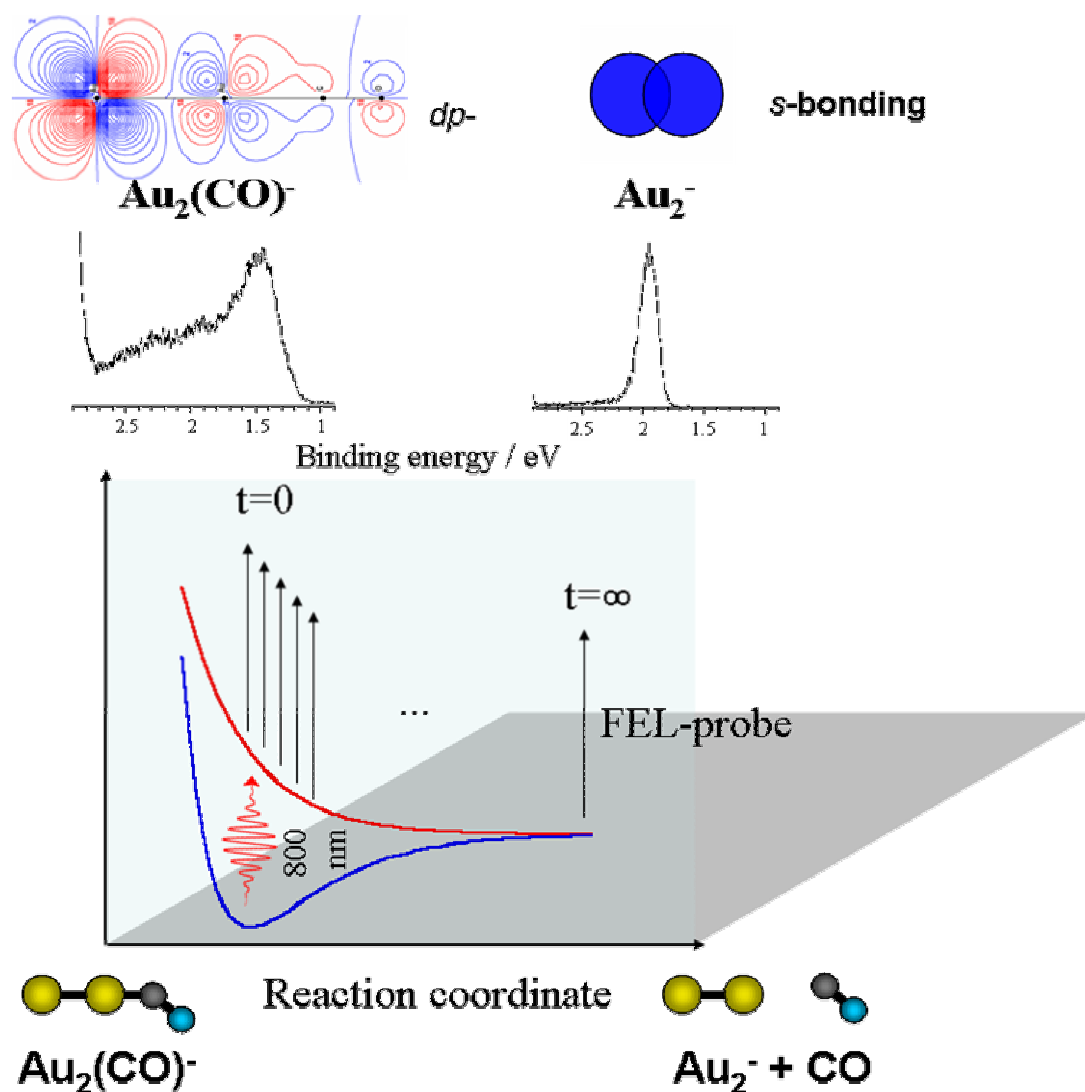


Fig. 11.11: Laser-pump FEL-probe spectroscopy on heteronuclear clusters will give element-specific insight into the transformation of a chemical bond during a chemical reaction, e.g. photo-dissociation or a catalytic cycle. The contour-plots at top show the electron density for the metal-ligand bond (dp-hybrid) and the pure metal-metal bond (s-like) after dissociation which can be probed by the FEL.

11.5 Very High-Energy-Resolution Photoemission

Photoemission with a resolution larger than $E/\Delta E = 50000$ has been identified in the scientific case (ultra-high-resolution spectroscopy) as a tool with large impact on the understanding of the structure/function relationship and the nature of complex materials. The idea is to reduce the influence of thermal excitations to an energy scale below 0.1 meV corresponding to sample temperatures of about 1K and to probe the electronic structure with a comparable energy resolution. Several attempts towards this goal are underway worldwide.

An experimental setup based on commercially available electrostatic electron energy analyzer (Scienta R4000) is shown schematically in figure 11.12. With such an analyzer ($E/\Delta E = 4000$) an energy resolution of 0.6 meV photon energy has recently been demonstrated using 7 eV laser radiation. However, electrostatic analyzers are reaching their technological resolution limit. To achieve even higher resolving powers it will be necessary to resort to time-of-flight techniques. Such techniques are already in use with photoelectron energy resolution down to 0.1 meV [55]. This is usually done by having electron kinetic energies below 1eV along a time-of-flight drift path of typically 1m length resulting in flight times ranging between 1 - 100 μ sec. With an electronic timing resolution as good as 100 ps, values of $\Delta E = 0.06$ meV or better can be achieved. This example shows that inherently pulsed photon sources such as FELs operated in a CW mode, which can produce almost freely selectable pulse patterns, are essential to achieve ultra-high resolution. (Note: the pulse spacing at synchrotron sources is typically several ns and, therefore, too short for high-resolution time-of-flight spectroscopy).

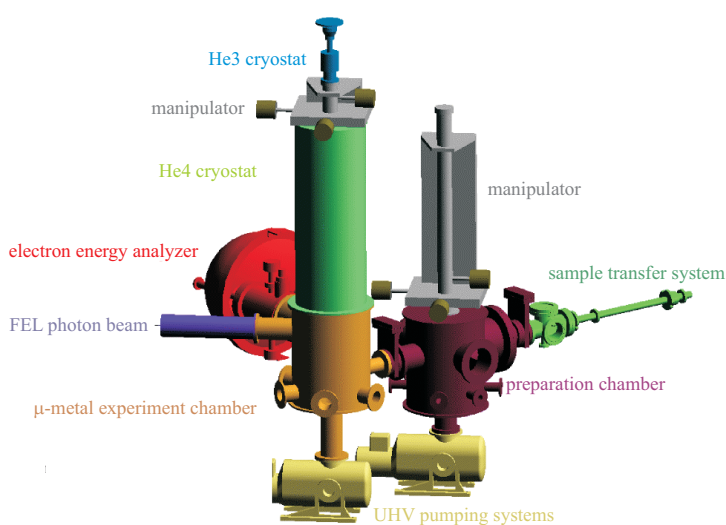


Fig. 11.12a: Schematic layout of the high-resolution photoemission experiment. Even higher resolution will be reached by replacing the electrostatic electron energy analyzer by time-of-flight detection using pulsed FEL radiation.

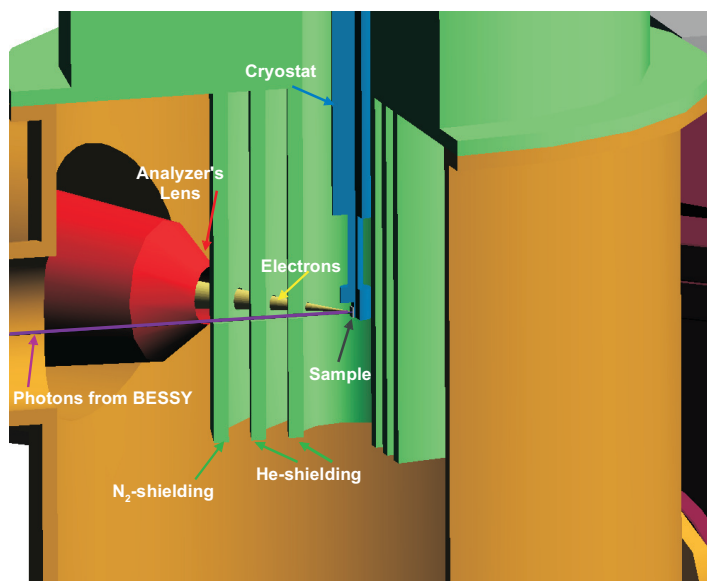


Fig. 11.12b: Details near the sample position.

The photoemission setup in figure 11.12 can be adapted to very high energy resolution FEL operation. In principle, only the energy analyzer will have to be replaced by a time-of-flight detector. At the entrance of the analyzer (figure 11.12b) photoelectrons will have to be decelerated with suitable lenses or grids to the drift energy of 1 eV and below. Behind the time-of-flight path the photoelectrons and their flight times will be measured with an array of two-dimensional detectors. It is extremely helpful to extrapolate from existing experiments with optical fs-lasers. Space charge effects which can change the photoelectron energy have to be avoided. From experiments with 6 eV laser radiation of 100 fs duration [56] it is known that more than one photoelectron/pulse in a time-of-flight spectrometer with 2° acceptance angle will cause space charge distortion of the photoelectron distribution. The strength of electron-electron repulsions causing space charge effects should scale with the time two electrons spend in proximity to each other, i.e. it should decrease both with $E_{\text{kin}}^{-1/2}$, where E_{kin} is the electron kinetic energy, and with the laser pulse length during which photoelectrons are generated. Taking into account typical FEL photon energies above 20 eV and pulse lengths of about 100 ps for the high photon energy resolution beamline, we can estimate that space charge will be avoided for $10^6 - 10^7$ electrons/(100 ps 2π rad). With typical cross sections for valence level photoemission from $3d$ transition metals and O ions FEL pulses of $10^8 - 10^{10}$ photons/(100 ps 0.001% bw) can be utilized for very high-resolution experiments. This matches very well the output obtained for the high-energy-resolution beamline of the low-energy FEL.

The previous example illustrates that $10^6 - 10^7$ electrons/(100 ps 2π rad) should be detected covering preferably a large solid angle. This could be achieved by dividing up the full solid angle into smaller parts covered by two-dimensional time-of-flight detectors. Such detectors already exist and consist of a multi-channel plate amplifier/detector com-

bination. The x,y -coordinates of the photoelectrons are determined by measuring the difference in arrival time of the amplified current pulses through two perpendicular sets of wires. Such delay line detectors are commercially available and capable of an overall temporal resolution of about 100 ps. The maximum count rate is given by the pulse propagation time in the delay lines. At the time of writing this is about 1 MHz and limited by the readout electronics. An increase to 15 MHz has been announced with a fundamental limit due to the wire length being about 1 GHz [57]. This translates into about 10^4 events that can presently be detected during each 100 μ s interval. Such count rates are expected in solid angles of about 5° , a value that is easily achievable with a standard active detector diameter of 80 mm [57, 58] at a distance of 1 m to the sample. A row of 10 of these detectors would give an accessible solid angle similar to present-day electrostatic analyzers (Scienta R4000) although with a significantly superior angular resolution ($< 0.02^\circ$).

11.6 High Temporal Resolution Photoemission: Spectroscopy and Microscopy

Time resolved photon-in/electron-out experiments with fs or even as resolution is one of the main areas where ultra-short FEL pulses will be applied to solid surfaces, thin films and nanostructures to probe femtochemistry and magnetization dynamics in real time via optical-pump/FEL-probe experiments. The studies of magnetization dynamics explicitly require nm lateral resolution. This can be achieved by using photoemission electron microscopy. Even if lateral resolution is not mandatory for femtochemistry studies it will prove extremely helpful to characterize the FEL spot at the sample and to check the spatial overlap between optical-pump and FEL-probe beams.

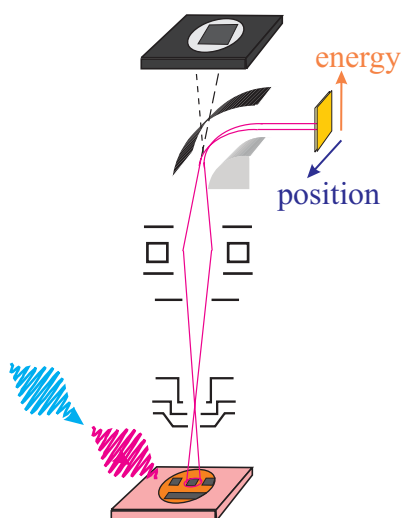


Fig. 11.13. Layout of a time-resolved photoemission experiment. Using a photoemission electron microscope results in nm spatial resolution. The setup can also be used as an in-situ diagnostic tool to characterize the spatial overlap between optical-pump (red) and FEL-probe (blue) pulses.

Photoemission electron microscopy using synchrotron radiation [59] of fs-laser sources [60] is by now a well established technique. The photoelectron distribution at the sample surface can be imaged onto a screen providing topological, work function, chemical or magnetic contrast. It is also possible to image the dispersive plane of a hemispherical energy analyzer and to obtain photoelectron spectra along a line on the sample surface (figure 11.13) [59]. Using pulsed photon sources and time-of-flight detection techniques it is possible to measure photoelectron spectra for each point on the sample surface [61]. This latter option seems to be the most promising for CW FEL sources.

Photoemission electron microscopes that accelerate the photoelectrons up to 20 keV away from the sample surface and use the same kinetic energy for their transmission through the electron optics are proposed. This should significantly reduce space charge effects inside the microscope. After the final magnification stage when the electrons are furthest separated from each other they will be decelerated to several eV kinetic energy and enter the time-of-flight drift tube. Using a delay-line detector about 10^4 electrons can be detected for each FEL pulse. We expect that this value can be increased by a factor of 10 - 100 by faster readout electronics and partitioning the detector area into regions which are read out independently from each other [57]. It is estimated that the resulting maximum count rates are comparable to the values where space charge effects at the sample might be expected to set in (chapter 12). These values translate into a maximum acceptable photon flux of about 10^9 photons/pulse.

One of the key aspects of the proposed experiments is the chemical sensitivity gained by tuning the FEL photon energy on to the absorption edges of the elements studied. For investigations of magnetization dynamics, the relevant absorption edges are the transition metal L-edges covered by the high-energy FEL and the rare earth M-edges in the medium-energy FEL region. Also for femtochemistry, access to both FEL branches is required.

11.7 Summary

In this chapter several generic experiments have been described that will cover the basic experimental requirements for the many scientific applications of the BESSY FEL as described in the scientific case. These experiments will be installed at the FEL beamlines as shown in Table 11.1.

Table 11.1: Distribution of the different experimental systems over the three BESSY FEL lines.

	LE-FEL 24-120eV	ME-FEL 100-600eV	HE-FEL 500-1000eV
X-Ray Microscopy		X	
Coherent X-Ray Scattering			X
Inelastic X-Ray Scattering		X	
Cluster and Beam Instrumentation	X	X	X
Very High Res. Photoemission	X		
Pump-Probe Spectromicroscopy		X	X

References

- [1] J. Kirz, C. Jacobsen, M. Howells, *Q. Rev. Biophys.* **28** (1995) 33.
- [2] J. Susini, D. Joyeux, F. Polck (Eds.), Proceedings „X-Ray Microscopy 2002“, 7th Int. Conf. on X-Ray Microscopy, *J. Phys. IV* **104** (2003)
- [3] G. Schneider, *Ultramicroscopy* **75/2** (1998) 85.
- [4] D. Weiß, G. Schneider, B. Niemann, P. Guttmann, D. Rudolph, G. Schmahl, *Ultramicroscopy* **84/3-4** (2000) 185.
- [5] G. Schneider, E. Anderson, S. Vogt, C. Knöchel, D. Weiss, M. LeGros, C. Larabell, *Surf. Rev. Lett.* **9/1** (2002) 177.
- [6] S. Vogt, G. Schneider, A. Steuernagel, J. Lucchesi, E. Schulze, D. Rudolph, G. Schmahl, *Journal of Structural Biology* **132** (2000) 123.
- [7] G. Schneider, G. Denbeaux, E. H. Anderson, B. Bates, A. Pearson, M. A. Meyer, E. Zschech, D. Hambach, E.A. Stach, *Appl. Phys. Lett.* **81/14** (2002) 2535.
- [8] D. Scherfeld, G. Schneider, P. Guttmann, M. Osborn, *Journal of Structural Biology* **123** (1998) 72.
- [9] P. Fischer, T. Eimüller, G. Schütz, P. Guttmann, G. Schmahl, K. Pruegl, G. Bayreuther, *J. Phys. D: Appl. Phys* **316/6** (1998) 649.
- [10] J. C. Solem, *J. Opt. Soc. Am. B* **3/11** (1986) 1551.
- [11] G. Schneider, T. Schliebe, H. Aschoff, *J. Vac. Sci. Technol. B* **13/6** (1995) 2809.
- [12] D. Hambach, G. Schneider, *J. Vac. Sci. Technol. B* **17/6** (1999) 3212.
- [13] D. Hambach, M. Peuker, G. Schneider, *Nucl. Instrum. and Meth. A* **467/2** (2001) 877.
- [14] S. Rehbein, *J. Phys. IV France* **104** (2003) 207.
- [15] G. Schmahl, D. Rudolph, G. Schneider, P. Guttmann, B. Niemann, *Optik* **97 4** (1994) 181.
- [16] D. Gabor, *Nature* **161** (1948) 777.
- [17] D. Hambach, G. Schneider, E. Gullikson, *Opt. Lett.* **26/15** (2001) 1200.
- [18] G. Schneider, *Appl. Phys. Lett.* **71/16** (1997) 2242.
- [19] A. C. Price, L. B. Sorensen, S. D. Kevan, J. Toner, A. Poniewierski, R. Holyst, *Phys. Rev. Lett.* **82/4** (1999) 755.
- [20] J. R. Fienup, *Appl. Opt.* **21/15** (1982) 2758.
- [21] J. R. Fienup, *J. Opt. Soc. Am. A* **4/1** (1987) 118.

- [22] J. W. Miao, P. Charalambous, J. Kirz, D. Sayre, *Nature* **400** (1999) 342.
- [23] J. Miao, J. E. Amonette, Y. Nishino, T. Ishikawa, K. O. Hodgson, *Phys. Rev. B* **68**/1 (2003) 012201.
- [24] J. W. Miao, T. Ishikawa, B. Johnson, E. H. Anderson, B. Lai, K. O. Hodgson, *Phys. Rev. Lett.* **89**/8 (2002) 088303.
- [25] H. He, S. Marchesini, M. Howells, U. Weierstall, H. Chapman, S. Hau-Riege, A. Noy, J. C. H. Spence, *Phys. Rev. B* **67**/17 (2003) 174114.
- [26] S. Eisebitt, M. Lörngen, W. Eberhardt, J. Lüning, S. Andrews, J. Stöhr, *Appl. Phys. Lett.*, in press (2004).
- [27] R. Pecora, *Dynamic Light Scattering: Applications of Photon Correlation Spectroscopy*, Plenum Pub. Corp., (1985).
- [28] D. O. Riese, W. L. Vos, G. H. Wegdam, F. J. Poelwijk, D. L. Abernathy, G. Grübel, *Phys. Rev. E* **61**/2 (2000) 1676.
- [29] W. H. de Jeu, B. I. Ostrovskii, A. N. Shalaginov, *Rev. Mod. Phys.* **75**/1 (2003) 181.
- [30] M. S. Pierce, R. G. Moore, L. B. Sorensen, S. D. Kevan, O. Hellwig, E. E. Fullerton, J. B. Kortright, *Phys. Rev. Lett.* **90**/17 (2003) 175502.
- [31] I. Sikharulidze, I. P. Dolbnya, A. Fera, A. Madsen, B. I. Ostrovskii, W. H. de Jeu, *Phys. Rev. Lett.* **88**/11 (2002) 115503.
- [32] C. Gutt, T. Ghaderi, V. Chamard, A. Madsen, T. Seydel, M. Tolan, M. Sprung, G. Grübel, S. K. Sinha, *Phys. Rev. Lett.* **91**/7 (2003) 076104.
- [33] S. B. Choe, Y. Acremann, A. Bauer, A. Scholl, A. Doran, J. Stöhr, H. A. Padmore, *Rev Sci Instrum.*, accepted (2003).
- [34] REFLEC simulation including 0.3 nm rms surface roughness.
- [35] E.g. Dalstar 1M60: <http://www.dalsa.com>.
- [36] A. Bargigia, E. Emolumento, C. Liguori, E. Paganini, U. Perini, V. Piemontese, G. Tondello, *Meas. Sci. Technol.* **3**/10 (1992) 992.
- [37] <http://www.hll.mpg.de> .
- [38] R. H. Richter, L. Andricek, P. Fischer, K. Heinzinger, P. Lechner, G. Lutz, I. Peric, M. Reiche, G. Schaller, M. Schnecke, F. Schopper, H. Soltau, L. Strüder, J. Treis, M. Trimpl, J. Ulrici, N. Wermes, *Nucl. Instrum. and Meth. A* **511** (2003)250.
- [39] L. Strüder, MPI für Physik, Halbleiterlabor, private communication.
- [40] M. Trimpl, L. Andricek, P. Fischer, G. Lutz, R. H. Richter, L. Strüder, J. Ulrici N. Wermes, *Nucl. Instrum. and Meth. A* **511** (2003) 257.

- [41] Gammadata/Scienta XES300: <http://www.gammadata.se> .
- [42] Quantar Technology MCP-RAE open face sensor: <http://www.quantar.com> .
- [43] J. H. Underwood, in: J. A. Samson and D. L. Ederer: *Vacuum Ultraviolet Spectroscopy*, Academic, San Diego, (2000).
- [44] R. Dörner, V. Mergel, O. Jagutzki, L. Spielberger, J. Ullrich, R. Moshammer, H. Schmidt-Böcking, *Phys. Rep.* **330**/2-3 (2000) 95.
O. Jagutzki, V. Mergel, K. Ullmann-Pfleger, L. Spielberger, U. Spillmann, R. Dörner, H. Schmidt-Böcking, *Nucl. Instrum. and Meth. A* **477** (2002) 244.
- [45] Project: BMBF05 KS1HR1/9: „Aufbau und Charakterisierung eines Experimentes am Freie-Elektronen-Laser zur Untersuchung größenabhängiger Eigenschaften von massenselektierten Clusterionen“, Uni Rostock, Uni Konstanz, Uni Hamburg, Uni Würzburg, Hasylab/DESY, BESSY mbH, coordinator: K. H. Meiwes-Broer, Universität Rostock
- [46] T. E. Glover, R. W. Schönlein, A. H. Chin, C. V. Shank, *Phys. Rev. Lett.* **76**/14 (1996) 2468.
- [47] P. O’Keeffe, M. Meyer, L. Nahon, in 3rd Annual Report (p.10 – 11, 3/2003) of the “XRAY FEL PUMP-PROBE” project (HPRI-CT-1999-50009, coordinator: J. Feldhaus), 5th EU – Framework program:
<http://www-hasylab.desy.de/facility/fel/vuv/projects/pump.htm> .
- [48] R. Mitzner, N. Pontius, M. Neeb, W. Eberhardt in 3rd Annual Report (p.16 – 18, 3/2003) of the “XRAY FEL PUMP-PROBE” project (HPRI-CT-1999-50009, coordinator: J. Feldhaus), 5th EU – Framework program.
<http://www-hasylab.desy.de/facility/fel/vuv/projects/pump.htm> .
- [49] N. Pontius, P. S. Bechthold, M. Neeb, W. Eberhardt, *Appl. Phys. B* **71**/3 (2000) 351.
- [50] Spectra Physics Corp.: <http://www.spectraphysics.com> ;
Quantronix Corp. : <http://www.quantron.com> ;
Coherent Corp.: <http://www.coherent.com> .
- [51] C. Y. Cha, G. Ganteför, W. Eberhardt, *Rev. Sci. Instrum.* **63**/12 (1992) 5661.
- [52] S. A. Novikov, A. N. Hopersky, *J. Phys. B: At. Mol. Opt. Phys.* **33**/12 (2000) 2287.
- [53] G. Lüttgens, N. Pontius, P. S. Bechthold, M. Neeb, W. Eberhardt, *Phys. Rev. Lett.* **88**/7 (2002) 076102.
- [54] R. Fromherz, G. Ganteför, A. A. Shvartsburg, *Phys. Rev. Lett.* **89**/8 (2002) 083001.
- [55] K. Kimura, *J. Electron. Spectrosc. Relat. Phenom.* **100**/1-3 (1999) 273.
- [56] H.-S. Rhie, H. A. Dürr, W. Eberhardt, *Phys. Rev. Lett.* **90**/24 (2003) 247201.

- [57] http://www.surface-concept.de/html/roadmap_delayline.html .
- [58] <http://www.roentdek.de> .
- [59] E. Bauer, *J. Phys.: Condens. Matter* **13/49** (2001) 11391.
- [60] H. A. Dürr, F. Kronast, W. Eberhardt, *Adv. in Solid State Phys.* **41** (2001) 557.
- [61] A. Krasnyuk, A. Oelsner, S.A. Nepijko, A. Kuksov, C.M. Schneider, G. Schönhense, *Appl. Phys. A* **76/6** (2003) 863.

12 Electron and Photon Beam Diagnostics

Beam parameters have to be observed and controlled along the linac with high precision in order to guarantee a high performance level of the BESSY FEL. Since the photon beam properties are directly linked to the electron beam parameters, it is essential to map the six-dimensional phase space at strategic locations in the linac and bunch compressors and especially directly in front of the undulator sections. The electron beam parameters determine the type and design of the diagnostics tools. In table 12.1 the main beam parameters of the linac are listed.

Table 12.1: Electron beam parameters utilizing an n.c. injector.

Parameter	Unit	
Number of electrons per bunch	1.9	10^{10}
Number of bunches per train	3	
Train length	≤ 10	μs
Repetition rate for trains	1	kHz
Normalized emittance	1.5	π mm mrad

To optimize FEL operation, all beam parameters have to be observed for each individual bunch, a challenge since the electron bunch length is 45 ps after the gun and is shortened to about 900 fs after the second bunch compressor BC2. Furthermore the overlap between electron beam and photon beam has to be ensured throughout all FEL cascades at a mean position deviation between photon and electron beam of less than 5 μm .

Further downstream for the experiments detailed information has to be acquired about the lateral position, the spectral content of the FEL pulse, its temporal profile, and also the synchronization for pump-probe experiments on a shot-to-shot basis.

12.1 Distribution of Diagnostics

In figure 12.1 the distribution of diagnostic components along the linac is shown. The distribution enables the measurement of the complete six-dimensional phase space at important locations at the beginning and end of each warm section, bunch compressor, and collimator. Redundancy was folded into the layout to improve the reliability of the diagnostics.

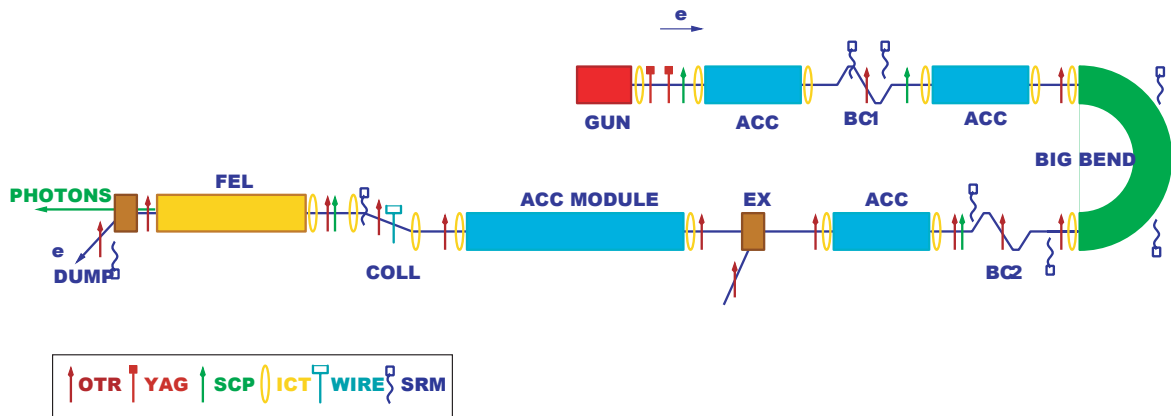


Fig. 12.1: Distribution of linac diagnostic components: Optical Transition Radiation stations (OTR), Viewscreens (YAG), Streak Camera Ports (SCP), Integrating Current Transformer (ICT), Wire scanner (WIRE), Synchrotron Radiation Monitor (SRM).

To ensure that the beam overlap in the individual modulators is optimal it is crucial that diagnostic tools are located along the HGHG cascades to determine:

- Electron beam emittance, position, and angle.
- Overlap of seed laser and electron beam in the 1st modulator.
- Overlap of amplified VUV pulse from radiators and subsequent modulators.
- Final photon beam position and angle.

The location of the diagnostic tools in the undulator section and beamlines downstream the HGHG cascade are shown in figure 12.2. The details of the different diagnostic tools in figures 12.1 and 12.2, their purpose and technical implementation are described in the following sections.

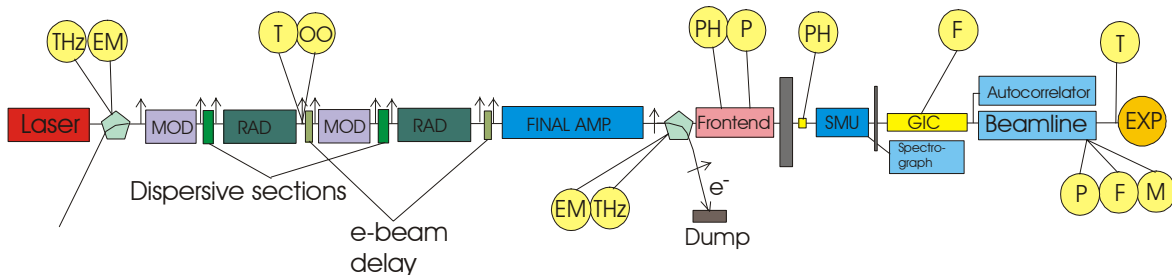


Fig.12.2: Distribution of diagnostic components in the undulator and beamline section: Coherent synchrotron radiation bunch diagnostics (THz), Optical Overlap detectors (OO), Position detectors (P), Flux detectors (F), Microfocus detectors (M), Transverse emittance detectors (EM), Time domain detection (T), Pinhole detectors (PH), Giant Ionization Chambers / Gas attenuators (GIC), Modified Optical Transition Radiation Screens (MOTR, arrows).

12.2 Electron Beam Diagnostics in the Accelerator

The requirements for the electron beam diagnostics of the BESSY FEL are listed in table 12.2.

Table 12.2: Electron beam diagnostics

Beam parameter	Technique	Achievable accuracy
Bunch charge	Current transformer	$\leq 10^{-3}$ in 5 nC range
	Faraday cups and BPM sum signals	
Bunch length	Streak camera	≈ 200 fs
	RF techniques	50 – 100 GHz, relative measurement
	(cavity and waveguide pickups)	
	Spectra of coherent radiation (synchrotron or transition rad.)	better than 100 fs
Beam position	Cavity BPMs	≤ 10 μm
	Button pickups	≤ 20 μm
	Stripline electrodes	≈ 1 μm
Transverse emittance	Imaging with Optical Transition and Synchrotron Radiation (OTR and SR), Viewscreens, Wire scanner	$\approx 3 - 10$ % of the emittance
Dark current, halo	Wire scanner	Single particles
	Si APD (avalanche photodiode)	
	Loss monitoring	
Energy and energy spread	Beam position measurements and beam imaging at dispersive sections	$\leq 10^{-4}$ $\sim 1 - 2\%$ of the energy spread

12.2.1 Energy and Energy Spread

In dispersive sections the radial position of the beam centroid is a measure of the average energy of the bunch. There is a large energy variation of the electrons along the bunch linearly correlated with their longitudinal position. Actual numbers can be found in table 12.3.

Table 12.3: Energy Spread along the linac

Location	Beam energy	Energy spread (fwhm)	Dispersive beam size (fwhm)
BC1	218 MeV	9 %	21 mm
ARC	753 MeV	2.4 %	11 mm
BC2	753 MeV	2.4 %	6.1 mm

The energy spread leads to very large horizontal beam sizes at locations where the dispersion function is large: At bunch compressor 1 the horizontal fwhm approaches 21 mm, in the ARC 11 mm, and in bunch compressor 2 the size reaches 6.1 mm. The measurement of the horizontal beam position in case of such broad distributions is difficult although possible with arrays of button pickup electrodes.

12.2.2 Charge

Traditionally *beam current transformers* are used in linear accelerators to measure the bunch intensity. A current transformer produces a signal that is a scaled replica of the beam current which passes through the monitor. It is planned to install up to 20 current transformers along the machine.

If properly designed, Faraday cups can be used as total current monitors and simultaneously as beam dumps for low-power beams. Two of these devices are provided right after the gun and at the end of the tune-up bump following the gun.

In the beam position measurement of each bunch the difference-over-sum (Δ/Σ) signal-processing technique will be employed. Therefore, to first order, position-independent sum signals proportional to the charge of individual bunches are available. In order to test the quality of the sum signals as a means to determine the bunch intensity, experiments were performed at the BESSY II storage ring operating with single bunches of up to 4 nC total charge corresponding to the intensity range of the HGHG-FEL.

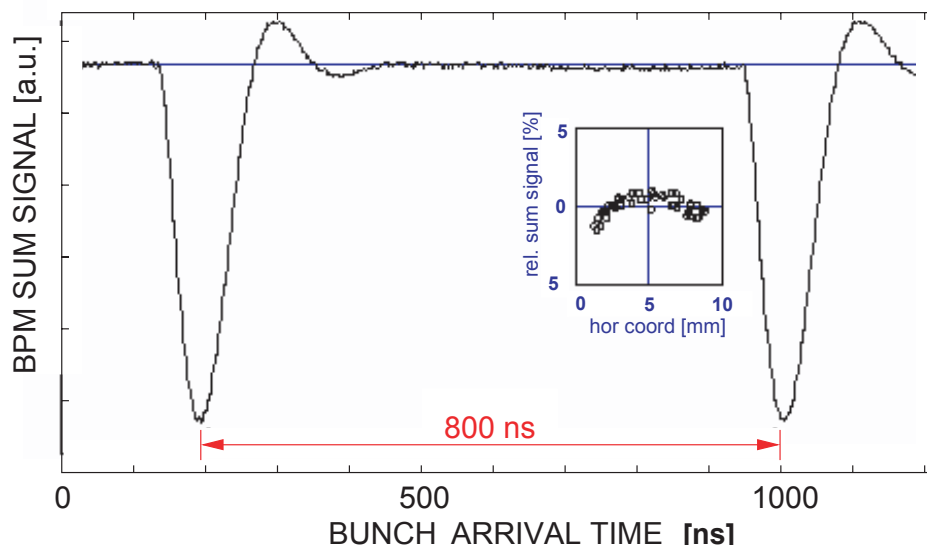


Fig. 12.3: BPM sum signal for two consecutive passages of the same bunch measured at the BESSY II storage ring. In the insert the measured dependence of the sum signal on the horizontal position of the beam is shown.

In this experiment four bandpass filtered stripline signals were sampled with a fast digital oscilloscope at a rate corresponding to the centre frequency of the filter (500 MHz). However, at this high speed the resolution is only 8 bit. The analog-to-digital conversion was locked to the accelerating cavity RF of the ring and thus to the revolution time of 800 ns. The data collected for two passages of the same bunch are shown in figure 12.3. The integrated intensity distribution can be determined and reproduced with an accuracy of $5 \cdot 10^{-4}$ for each passage of the bunch. This is related to the resolution limitation of the ADC employed. The observed resolution compares well with standard current transformers.

In the insert of figure 12.3 the observed dependence of the integrated sum signal on the horizontal beam position is depicted. The beam was kicked transversely and the beam motion was observed turn-by-turn. The quadratic dependence is expected and can be corrected for by including this well known geometric effect numerically in the data analysis.

The linearity of the signal was checked against a high precision current transformer. The result is shown in figure 12.4. In the required small dynamic range the linearity is better than 0.1 %. Thus it is possible to use these sum signals after a proper calibration against the current transformers as additional inputs to the fast machine protection system.

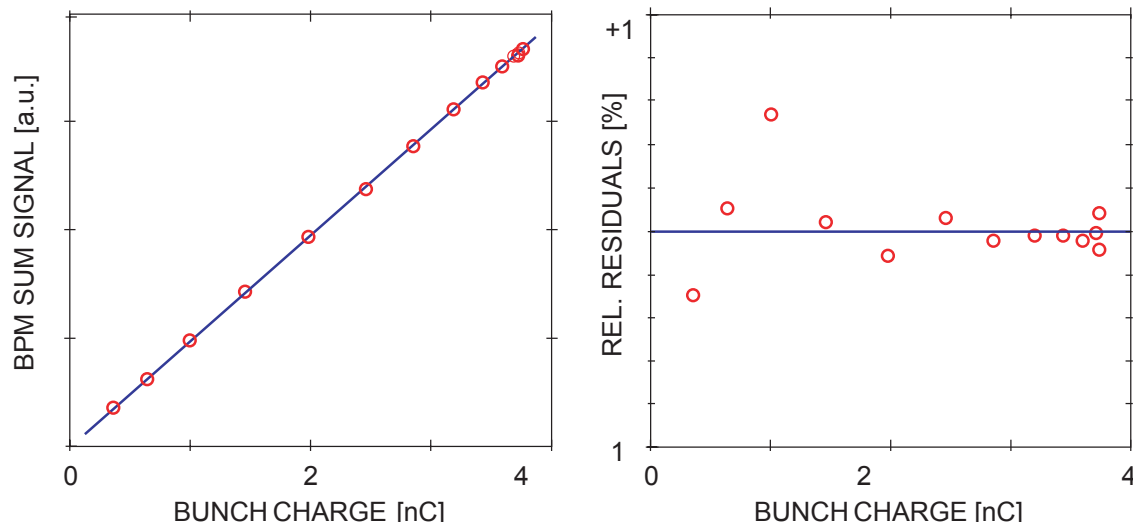


Fig. 12.4: Test of the linearity of the single passage, single-bunch integrated BPM sum signal in comparison with the high-resolution parametric current transformer installed in the BESSY II storage ring.

12.2.3 Bunch length

12.2.3.1 Cavity Bunch-Length Monitor

The longitudinal particle distributions together with their corresponding spectral power density as calculated for the BESSY FEL linac are shown in figure 12.5. Up to the beginning of the second bunch compressor the spectrum extends to regions where conventional microwave technologies are available and power measurements up to 100 GHz immediately allow one to assess the shape of the particle distribution. These measurements are non-destructive. At SLAC a two-cavity system was developed operating at 25 and 36 GHz [1]. The cavities are located behind a ceramic vacuum break and are excited by the beam spectrum. The deposited power is measured and allows one to make relative comparisons of the length of different bunches. At CLIC a bunch-length monitor for bunches with an rms length ≤ 1 ps has been implemented working with rectangular waveguides connected to the vacuum chamber, coupling out the spectral information of the bunches in the K_{α} (26.5 – 40 GHz) and the E band (60 – 90 GHz) [2]. The detailed analysis of the spectral power distribution to be expected at the end of the waveguides has been performed by [3].

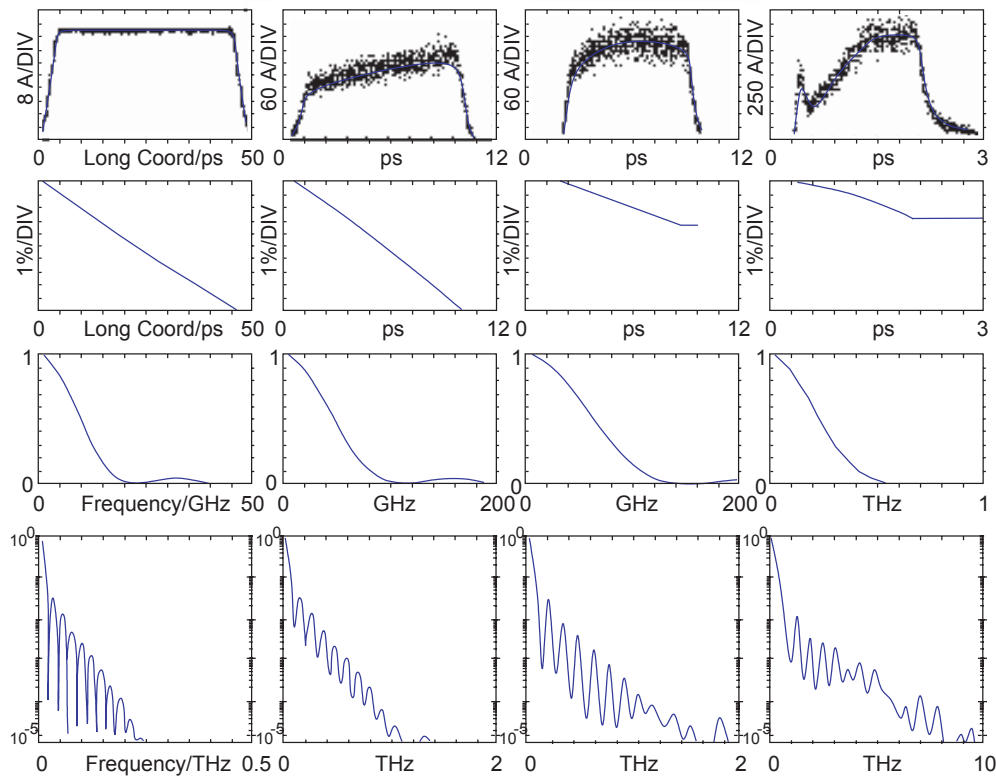


Fig. 12.5: Top row: Longitudinal particle distributions for an HGHG-FEL scheme at 3 nC bunch charge. Second row: correlation between longitudinal position and energy. Third and fourth row: spectral power density of the bunches in linear and logarithmic scale respectively. First and second columns: before and after the first bunch compressor (BC1); third and fourth columns: before and after the second bunch compressor (BC2).

In the HGHG-fresh-bunch scheme a flat-top longitudinal particle distribution is required with rise and fall times as short as possible. Up to the second bunch compressor the flat top of the bunch shapes can be observed with a streak camera having ps-resolution. Rise and fall time measurements require faster diagnostics like streak cameras with 100 – 200 fs resolution or other techniques like the observation and analysis of coherent radiation. The light emitting process in the visible or far infrared region of the spectrum can be either synchrotron radiation or transition radiation. In both cases radiation at wavelengths shorter than the bunch length is emitted coherently and the spectral distribution of the coherent radiation is related to the bunch shape. The square of the form factor of the longitudinal particle distribution is the spectral power density of the coherently emitted radiation and can be found in the two bottom rows of figure 12.5.

12.2.3.2 Zero-Phasing Technique

An energy variation along the bunch can be created by the zero phasing of some of the accelerating cavities. If the resulting energy chirp on to the electron bunch is much larger than the initial uncorrelated energy spread and if the resolution is not spoiled by a too large transverse emittance, the longitudinal particle distribution can be observed in the dispersive plane behind a spectrometer dipole. The resolution of the zero-phasing technique approaches 50 fs [4]. Whenever applicable this technique is the obvious choice for the determination of the bunch length in the linac.

12.2.3.3 Streak Camera

For direct bunch-length measurements a fast streak camera will be installed, e.g. Hamamatsu FESCA 200 with 200 fs resolution.

In the design of the imaging optics of the streak-camera setup, care has to be taken not to introduce excessive dispersion in the light path. This requires mirrors for focusing the photon beam onto the pinhole of the streak camera and even a modification of the optics imaging the pinhole onto the photocathode. The wavelength region should be in the red part of the visible spectrum in order to keep the energy spread of the photoelectrons as small as possible. With OTR and Synchrotron Radiation (SR) the photon intensity remains low and space-charge effects of the photoelectron bunch can be neglected. This is no longer the case for the larger intensities available from a laser beam. With a careful selection of the optical components an overall temporal resolution of ≤ 1 ps seems feasible.

12.2.3.4 Coherent Synchrotron Radiation

Diagnostic systems using coherent synchrotron radiation (CSR) at bending magnet sources within the linac are planned, since CSR is emitted when the longitudinal particle distribution in the bunch is shorter than the wavelength [5, 6, 7].

For a given radiation frequency $\nu=1/\lambda$ (wavenumber), the total-emitted spectral power by one bunch, $P(\nu) = P$, can be derived from the incoherent, single-particle power, $p(\nu)=p$:

$$P = Np(1 + Nf_\nu) \quad (12.1)$$

$$P = P_{incoh} + P_{coh} \quad (12.2)$$

$$\frac{P_{coh}}{P_{incoh}} = Nf_\nu \quad (12.3)$$

where f_v is a form factor, which is the square of the Fourier transform of the longitudinal electron density $S(z) = dN/dz$:

$$f_v = \left| \int S(z) e^{i(2\pi z\nu)} dz \right|^2 \quad (12.4)$$

and $N \gg 1$ is the total number of electrons in the bunch. An impressive gain in emission up to the number of particles N in the bunch (N at 3 nC $\approx 2 \cdot 10^{10}$ electrons) can be achieved. For the BESSY HGHG-FEL the spectral power gain distribution as expected at the bunch compressor BC2 is shown in figure 12.6.

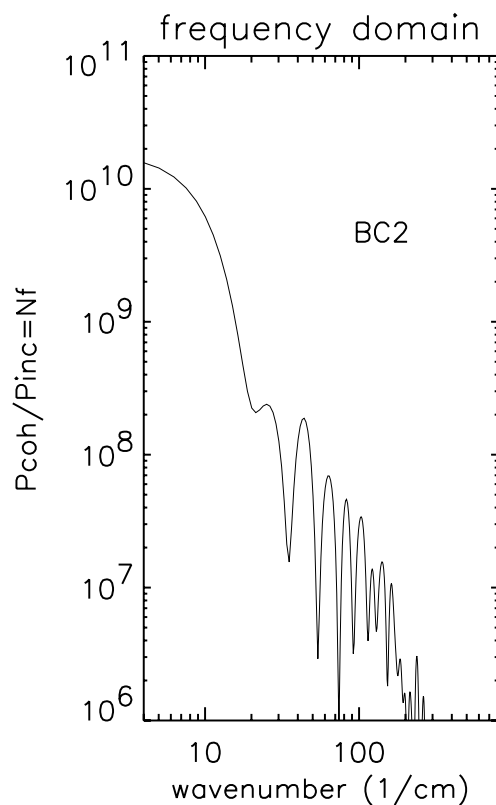


Fig 12.6: Spectral power gain distribution (ratio of coherent to incoherent intensity) as a function of frequency.

The theoretically expected spectral power in the FIR at the second bunch compressor at an acceptance of $60 \times 15 \text{ mrad}^2$ is plotted in figure 12.7. For comparison the incoherent SR spectral power in the BESSY II storage ring at a circulating current of 250 mA is also shown.

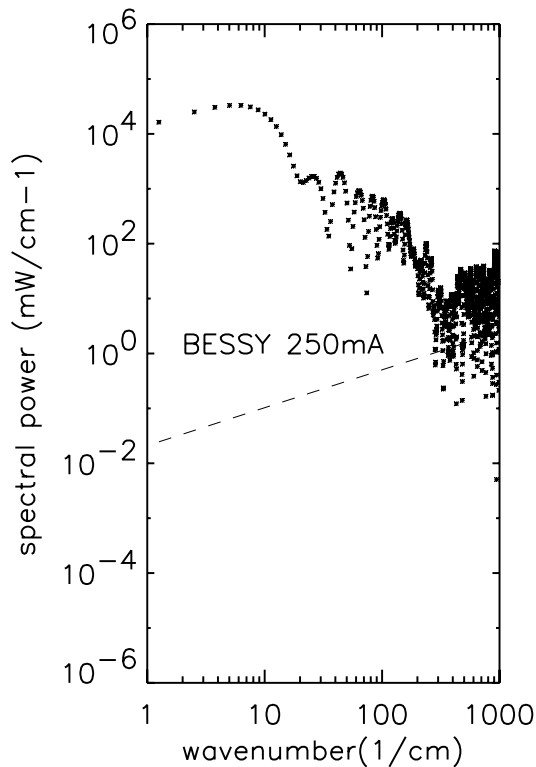


Fig. 12.7 Spectral power expected at bunch compressor BC2. A total power of up to 40 W is expected to be emitted from a 3 bunch multi bunch train at 1 KHz repetition rate between 1 and 1000 wave numbers. The noise above 400 cm^{-1} reflects the numerical jitter.

As expected a gain of more than a factor of 10^{10} can be achieved compared to the incoherent emission at the FEL bunch compressor. However, due to the higher duty cycle of the BESSY II storage ring the spectral gain of the FEL is still $\sim 10^5$.

In reality, the theoretically expected CSR emission is spectrally modified in particular below about 10 cm^{-1} by losses due to different transfer functions:

- The microwave cut-off of the vacuum chamber inside the dipole (2 cm^{-1}).
- The microwave transmission function of the beam pipe (trumpet).
- Fraunhofer diffraction at the first mirror.
- Fresnel diffraction at intermediate apertures, e.g. a diamond window.
- Beam-splitter effects (not important for grid diplexers).
- Dynamic range of the detection system.

These effects reduce the transmission of the setup significantly at energies corresponding to wavenumbers $< 10 \text{ cm}^{-1}$.

12.2.4 Beam Position

The position and angle stability of the electron beam is of significant importance to every linac-based FEL. Table 12.4 lists the electron Beam Position Monitors (BPMs) provided for the BESSY Soft X-ray FEL.

Table 12.4: Beam Position Monitors

Type of Sensor	Location	Operating Frequency	Processing Principle
S.c. cavity type, re-entrant or pill-box	In each accelerating structure	~ 1.3 GHz	Down conversion and digital receiver technique
Button pickups, arrays of button pickups	In bunch compressors and arc	650 MHz	Digital receiver technique (down sampling) of filtered δ -function response
Stripline	In collimators, and between undulator sections	650 MHz	Digital receiver technique (down sampling) of filtered δ -function response

The various types of sensors deliver different kinds of raw signals as the bunch passes by. For maintenance and compatibility reasons it is planned to employ a common digital receiver in order to analyze the signals and to produce beam position as well as charge proportional digital data. This requires sensor-specific RF input stages. For the cavities this includes down conversion to 650 MHz and gain adjustments. For the pickup and stripline sensors only filtering and gain adjustment are needed. A schematic diagram of the RF input stage and the digital receiver unit is shown in figure 12.8.

The signals from the button pickups, stripline, or mixed-down cavity signals are fed into 650 MHz bandpass filters (preferentially Bessel or Gaussian filters) with a bandwidth of 6 MHz. After the filter the signal changes from a large amplitude δ -function spike to a much smaller signal oscillating at 650 MHz ideally with a bell-shaped envelope. After amplification this oscillating RF signal is down-sampled directly with a fast ADC (12 bit, 125 MS/s, analog bandwidth of 750 MHz). Alternatively this signal can be rectified and sampled at a similar rate with 14 bit resolution ADCs. A number of samples (typically 20 – 25) are summed up in order to overcome the limiting ADC digitization error. In both cases analysis of the digitized waveforms either in terms of the in-phase and out of-phase part (I/Q demodulation) or the numerical correction of the rectifier's non-linearity is performed in the field-programmable gate array. In case of the undulator vacuum chambers with a circular ~ 9 mm inner diameter, a 12 bit ADC will limit the resolution of the beam

position determined by the difference-over-sum technique (Δ/Σ) to $\sim 7 \mu\text{m}$ if the signal is sampled only once. With oversampling and by using the full dynamic range of the ADC $1 \mu\text{m}$ resolution is achievable.

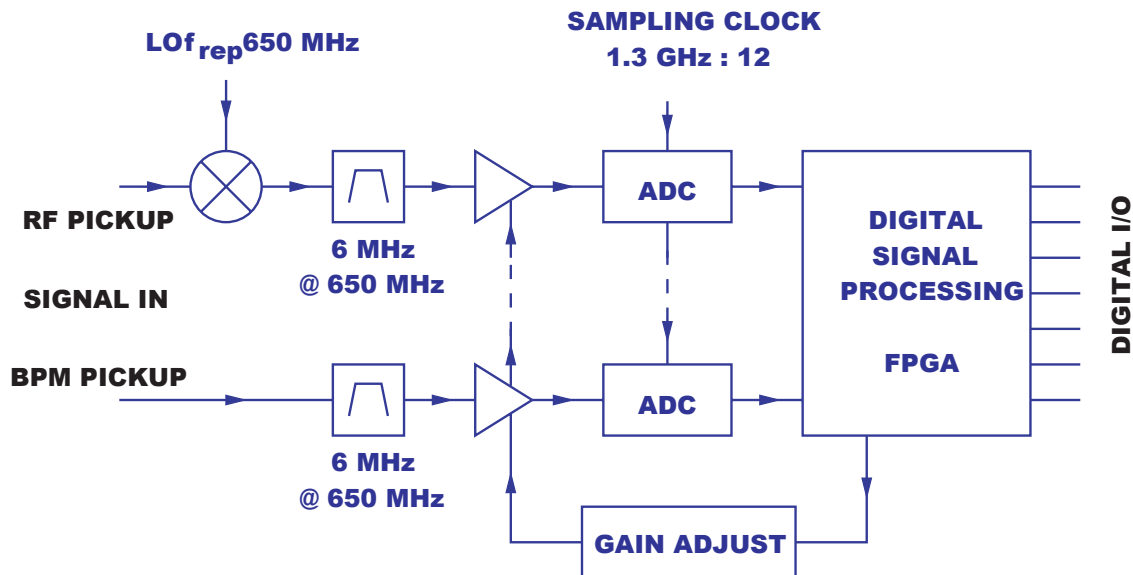


Fig. 12.8: Schematic diagram of the RF input stages and the digital receiver for the measurement of the beam position in the linac.

The vacuum chamber in the warm part of the linac corresponds to a tube of 30 mm inner diameter. In this case the digitization noise from 50 samples leads to an expected combined noise for the beam position of $5 \mu\text{m}$. This value is reached for a bunch charge larger than 1 nC. At lower intensities the resolution will be limited by electronic noise.

12.2.4.1 Pickup BPMs in the Bunch Compressors and the ARC

In the ARC section the horizontal beam size is rather large due to the non-zero dispersion and the correlated energy spread. In addition, the inner diameter of the vacuum chamber is larger in comparison to the undulator sections. This leads to an expected resolution of $\sim 20 \mu\text{m}$ for the BPMs based on arrays of button pickup electrodes. The analysis of the signals from many electrodes requires an adequate algorithm in order to take the horizontal beam size into account. Horizontal size and spacing of the electrodes are of the order of 10 - 20 mm and the analysis requires fast digital data processing. This can be performed in the corresponding field programmable gate arrays as part of the BPM system. At locations with just four button pickup electrodes and smaller horizontal beam size the

resolution will be 5 – 10 μm . The BPM sensors will be rigidly fixed to the massive girders of the magnetic structures and could be similar to those in the BESSY storage ring.

12.2.4.2 Stripline BPMs in the Undulator Intersections

The stripline assembly in the intersection region between the undulators will be similar to the pickup sensors. The striplines are fixed and aligned rigidly to flanges which are fixed to the sensor body. The dimensions have been chosen such that the impedance of the strips is 50 Ohms. It is assumed that the mechanical uncertainty for the center of this assembly is of the order of 25 - 50 μm and remains stable over longer periods of time. With a careful and rigid fixation of the stripline body the long term mechanical stability of this sensor required for beam-based alignment can be achieved.

12.2.4.3 Cold BPMs

Each acceleration module in the linac is equipped with one cavity-type beam-position monitor. The resolution is about 10 μm for single bunches. A beam-passing offset through the pillbox cavity BPM excites higher-order modes in the cavity with the excitation of the dipole mode proportional to the actual beam offset. Detection of this mode yields a signal proportional to the beam offset.

The dimensions for the cavity BPMs as developed for the TESLA modules are $b_{\text{cav}} = 111$ mm and $l_{\text{cav}} = 18$ mm. The inner surface of the cavity is copper coated for a higher conductivity. The frequency of the dipole mode is thus 1.5 GHz. The signal yield for such a cavity BPM is 6 mV for the given cavity geometry, 10 μm beam offset, and single bunches. The noise level at room temperature is 0.07 mV in a 120 MHz bandwidth circuit.

12.2.5 Phase

In HGHG-FELs the correct timing is important. For example, the 20 fs long seed-laser pulse has to overlap the roughly 1 ps long electron bunch. In addition, the overlap has to be adjustable in the 20 fs range. In an experiment at the BESSY II storage ring a promising approach was tested which allows to determine the electron bunch (or laser pulse) arrival time relative to the RF master oscillator within a resolution of ≤ 100 fs; a 50 fs resolution is expected for an improved arrangement.

The measurement set up is shown in figure 12.9. For the laser pulse a photodiode could be used as signal source instead of the stripline. The high temporal resolution is achieved by the excited and persistent high frequency signal after the bandpass filter: $F_{\text{res}} = \text{RF frequency}$, $Q \sim 100$ depending on the time between bunches or pulses. This signal is rather low in amplitude and has to be amplified by typically 20 dB. In order to determine the phase relative to the RF the amplified signal is fed into a mixer with the RF master oscilla-

tor as local oscillator. By adjusting the phase of the local oscillator with a variable mechanical delay, the base-band output is brought into the most sensitive and linear operating range of the mixer. The low pass-filtered base-band signal is then acquired with a fast analog-to-digital converter preferentially also locked to the RF master oscillator and analyzed on-line with a digital signal processor or by a field programmable gate array.

In case of the BESSY II storage ring the bunch passes by every 800 ns and produces a signal as shown in figure 12.10. The arrival time of the bunches is proportional to the signal integrated over the region displayed in green.

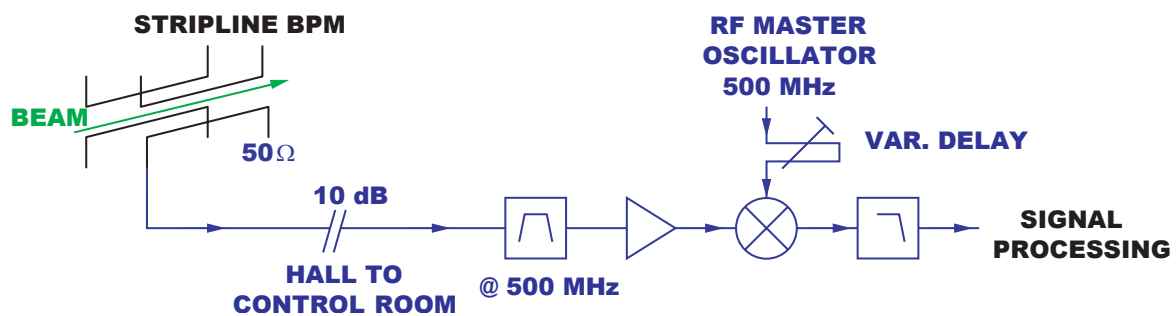


Fig. 12.9: Setup for the measurement of the arrival time of bunches used at the BESSY II storage ring with 100 fs time resolution.

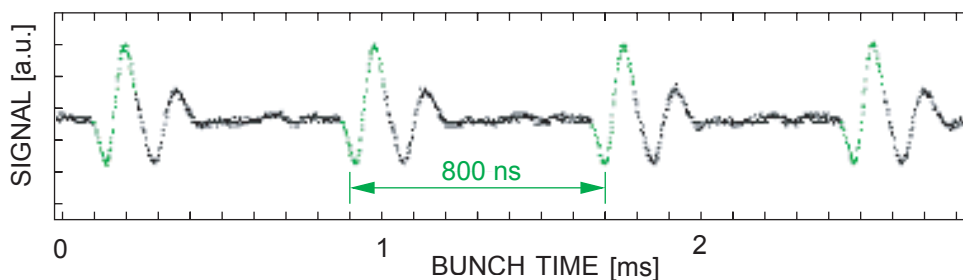


Fig. 12.10: Base band signal behind the mixer with the local oscillator phase adjusted to give maximum time/phase resolution. The colored parts are used for the determination of the exact arrival time of the bunches every 800 ns.

The result of such an analysis over 1200 turns is shown in figure 12.11. The different traces are line triggered and are measured with the local oscillator phase shifted mechanically by 0.6 degrees which corresponds to 3.3 ps at the operating frequency of 500 MHz. As can be seen, a mains ripple excites small 3 ps peak-to-peak synchrotron oscillations of the bunch which are clearly resolved by the measurement on a turn-by-turn basis. The

width of the noise band is approximately 100 fs. With stripline signals delivered from 1 nC bunches the detection scheme is not noise limited. Thus it can be expected that by increasing the observation frequency to 1.3 GHz the resolution will increase correspondingly and reach the 50 fs range. However, within the dynamic range of ~ 100 ps, the response is not necessarily linear and it does depend on the beam position in connection with the chosen sensor. Furthermore, the result has to be corrected for intensity variations or the setup must be recalibrated.

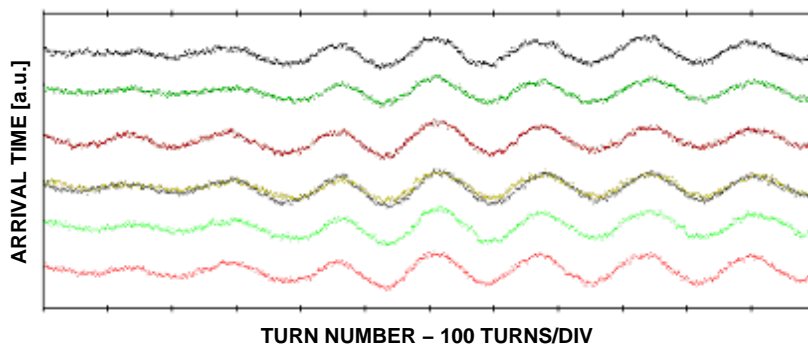


Fig. 12.11: Arrival time of the bunch signal on a ps time scale. The shift between the traces corresponds to 3.3 ps. Small synchrotron oscillations with a 1.5 ps amplitude are excited by a mains ripple. The relative accuracy of the measurement is 100 fs.

12.2.6 Profile and Transverse Emittance

The slice emittance along the bunch is accessible with the zero-phasing technique. In the cavity structure right after the photoinjector an energy chirp is introduced to the electron beam, correlating longitudinal position and energy offset. The bunch then passes through an energy spectrometer where the transverse bunch size, sorted according to its energy, is imaged by means of a screen or OTR monitor. By changing the focusing strength of a quadrupole triplet in between linac and a spectrometer dipole the beam size at the spectrometer screen can be varied, enabling full analysis of the slice emittance via beam size tomography. Such diagnostics will be installed near the gun and in front of BC1.

Measurement of the projected emittance of the high-energy beam along the beamline after the arc and in front of the undulator will be performed using the quadrupole scan method, similar to the slice emittance measurement. The measured beam size then is a quadratic function of the field strength. Using a parabolic fit, the beam matrix elements fully describing the transverse beam phase space can be determined. The accuracy de-

depends on the precision of the beam-size measurement, and on the number of data samples. Assuming 10 μm resolution of the beam-size monitor at least 10 measurements should be performed.

Typical beam sizes along the linac are in the order of 100 μm . Both methods rely on precise measurement of the transverse beam size using screens, OTR stations or wire scanners, which are described in the following sections.

The normalized beam emittance for the FEL is $\epsilon_{x,y} = 1.5 \pi \text{ mm mrad}$. To ensure continuous optimum performance of the FEL, emittance data should be available at a relative error of $\Delta\epsilon/\epsilon = 0.07$. For n beam-size-measurement stations the emittance error is related to the beam-size-measurement error $\Delta\sigma/\sigma$ with $\Delta\epsilon/\epsilon = (2/\sqrt{n}) \cdot \Delta\sigma/\sigma$. Assuming 10 samples for a quadrupole scan, the relative error of the individual beam-size measurement must be less than $\Delta\sigma/\sigma \leq 0.08$. Typical beam sizes to be measured in the linac sections are depicted in figure 12.12.

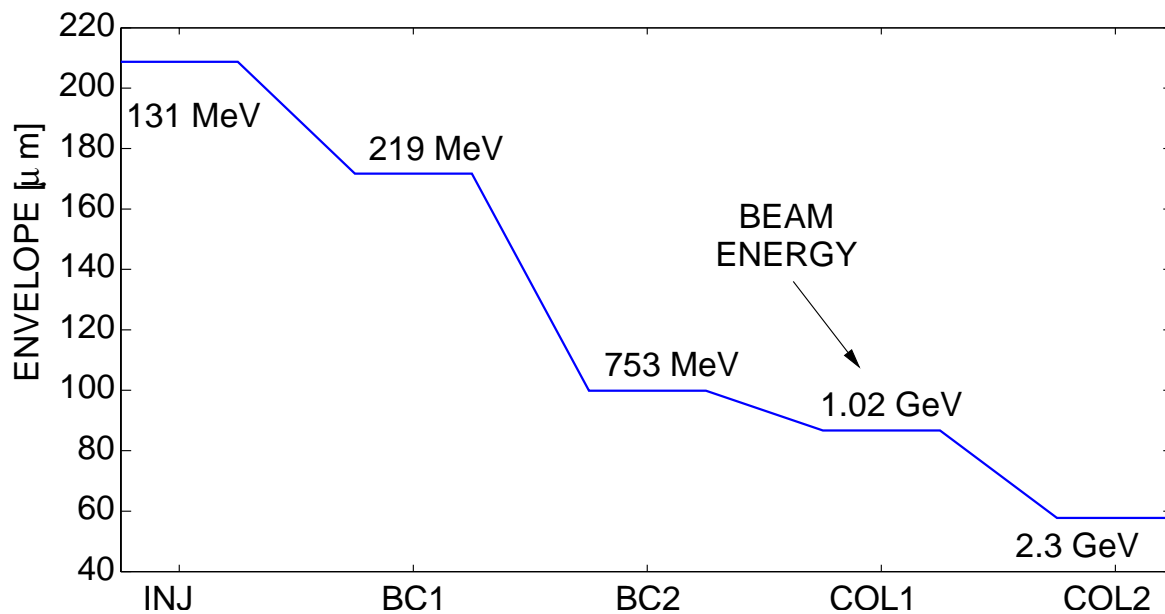


Fig. 12.12: Typical beam sizes (fwhm) along the linac from the gun (GUN) via the two bunch compressors (BC1 and BC2) to the collimators for the two FEL energies (COL1 and COL2). The beam envelope is computed for a beta function of $\beta_{x,y} = 10 \text{ m}$.

12.2.6.1 Viewscreens and Optical Transition Radiation

To measure the beam size in the low energy region of the linac, between the injector and the first accelerating module, intercepting screens are inserted into the beam path.

These viewscreens provide a direct image of the beam profile in transverse space in the linac or transverse-bend space in the dispersive section with single-shot capabilities [8]. Viewscreens are very sensitive, especially at low electron-beam energies in the injector area, but have a poor time response of several ms and can show non-linear behavior at full beam current. The spatial resolution of 20 to 30 μm is given by the grain size and transparency of the fluorescent material.

Transition radiation is emitted when charged particles pass through a thin metallic or dielectric radiator foil (figure 12.13a). At relativistic energies, the radiation is concentrated in cones of small angles in the neighborhood of the particle trajectory (forward radiation) and in the direction of specular reflection (backward radiation).

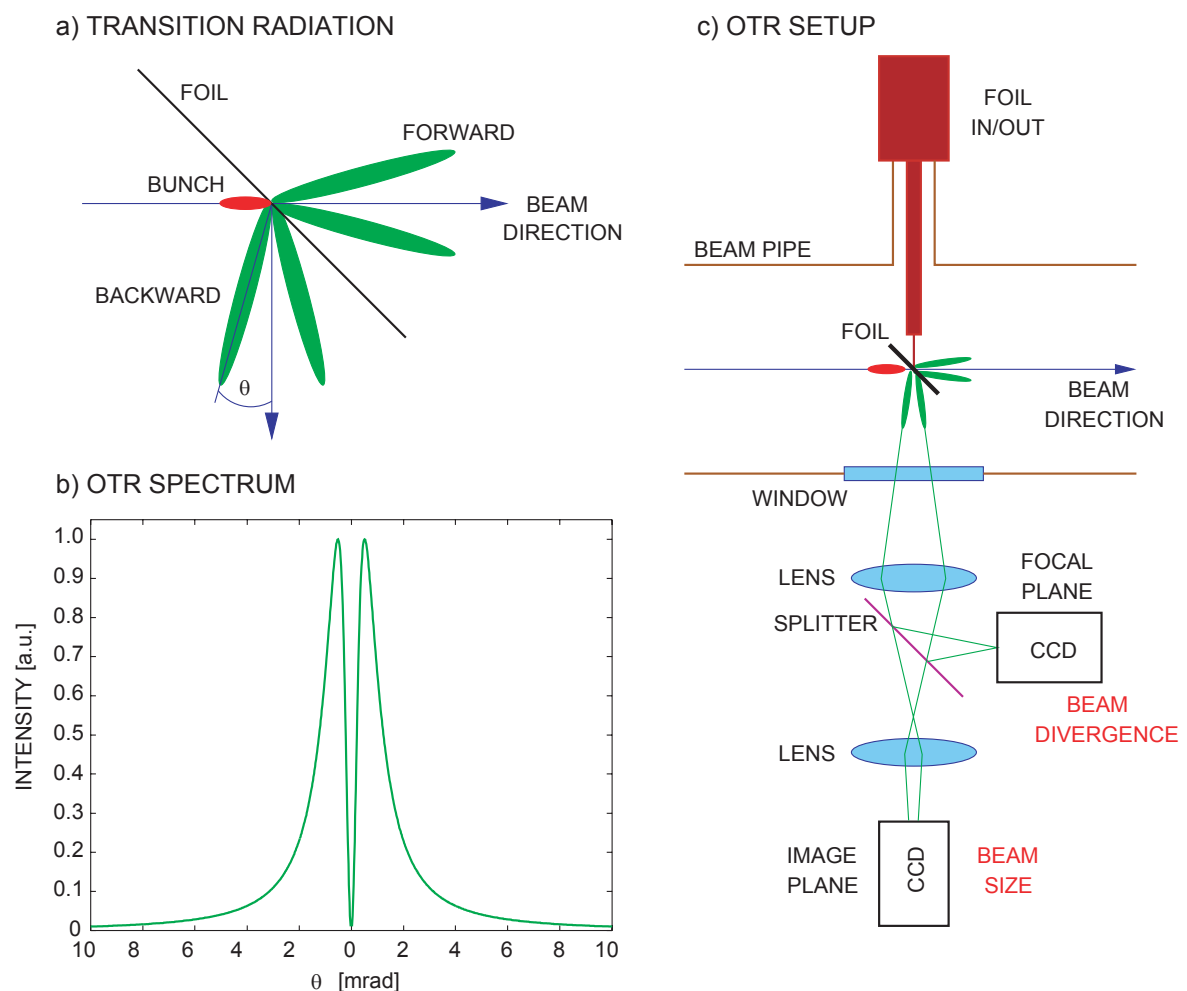


Figure 12.13: a) Principle of optical transition radiation (OTR); b) OTR spectrum and c) setup of a beam size and divergence monitor using OTR screens.

Optical transition radiation (OTR) is the part of the radiation emitted in the optical spectrum between 350 and 750 nm, i.e. it is visible light, and can thus be detected by optical imaging systems. The angular distribution is concentrated into two symmetric lobes with large tails (figure 12.13b). This characteristic pattern is both sensitive to the beam energy, spacing of lobes, and to the energy spread, height of the null between the lobes. Thus, OTR screens can be used to measure not only beam size and divergence but also energy and energy spread [9]. OTR screens are now widely used as a standard tool for beam size diagnostics for linac-based FELs (for example [10]). In figure 12.13c a station is depicted to measure the transverse beam size and divergence using an OTR screen. A CCD camera is located in the image plane of a telescope made up of two lenses providing a geometrical image of the beam. With a second camera located at the focal plane of the first lens, the image detected is not the beam image, but instead an image of the angular distribution of the radiation emitted. Compared to viewscreens, the light output from an OTR radiator is much smaller in intensity but the time response is in the order of ps allowing bunch-to-bunch measurements with gated cameras.

The total number of emitted photons can be computed by integrating over the intensity distribution as a function of frequency and observation angle θ (see figure 12.13):

$$I(\theta, \omega) = \frac{q^2}{\pi^2 c} \left(\frac{\theta^2}{1/\gamma^2 + \theta^2} \right)^2. \quad (12.5)$$

For the wavelength region between λ_1 and λ_2 the photon yield per electron N_γ is:

$$N_\gamma = \frac{\alpha}{\pi} \left[\ln(1 + \theta^2 \gamma^2) - \frac{1}{1 - \theta^{-2} \gamma^{-2}} \right] \ln\left(\frac{\lambda_1}{\lambda_2}\right). \quad (12.6)$$

The number of emitted photons is of the order of the fine structure constant α and scales logarithmically with the beam energy. In figure 12.14 the number of photons per electron is plotted for the energy range of the BESSY FEL. Also shown is the collected intensity for different acceptance angles. With expected bunch charges from 1 nC to 3 nC the photon yield from standard optical channels with 100 mrad acceptance is sufficient to work with standard CCD cameras.

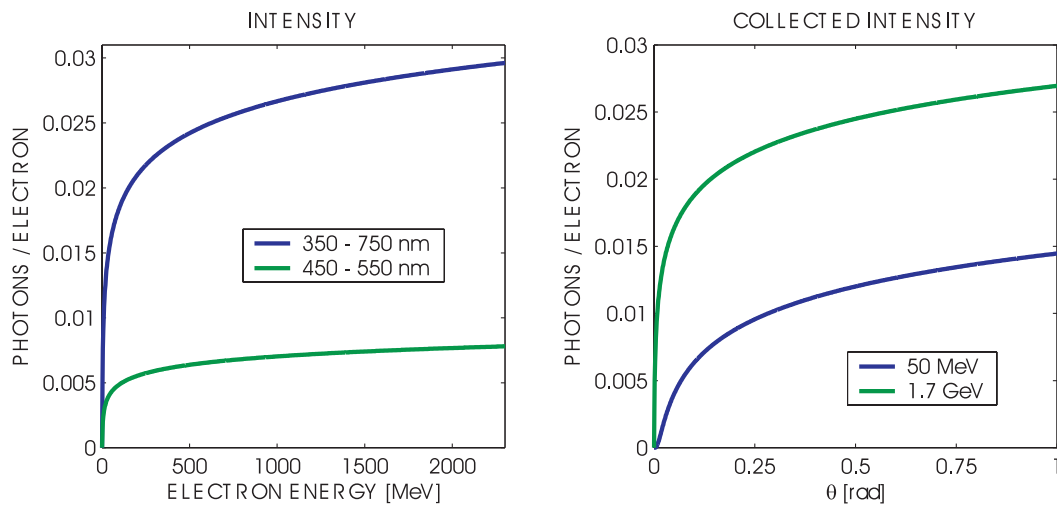


Fig. 12.14: Left: Number of photons per electron for different beam energies. Right: Collected photons for different acceptance angles.

12.3 Electron and Photon Beam Diagnostics in the HGHG Sections

12.3.1 Visible-Light Imaging of Synchrotron Radiation

Live-image optical monitors are an essential diagnostic tool. Any local source of synchrotron radiation (SR) along the entire trajectory is a suitable candidate for beam imaging by this non-intercepting method, allowing one to determine parameters as beam cross section and divergence.

Assuming that the full vertical opening angle of the SR on a dipole is accepted by the optics, the diffraction limited image resolution according to the Rayleigh criterion is given by $\Delta y = (\pi/6)^{1/3} R^{1/3} \lambda^{2/3}$ as long as the vertical opening angle is $\sim (\lambda/\lambda_c)^{1/3}$ for $\lambda \gg \lambda_c$, where $\lambda_c = (4\pi/3)(R/\gamma^3)$ is the critical wavelength. The image is smeared by accepting a finite longitudinal portion of the source to a disk of radius $r_f = (3/4\pi)^{1/3} R^{1/3} \lambda^{2/3}$ being on the same order of magnitude as the diffraction term. The final resolution available at optical systems accepting the entire vertical opening angle is plotted along the linac in figure 12.15.

An optical image of the beam using visible light is diffraction limited in some parts of the trajectory and yields an image blurred by 50 to 200 μm depending on the dipole radius. The expected transverse dimensions of the electron beam at the different sources in the FEL are summarized in table 12.5.

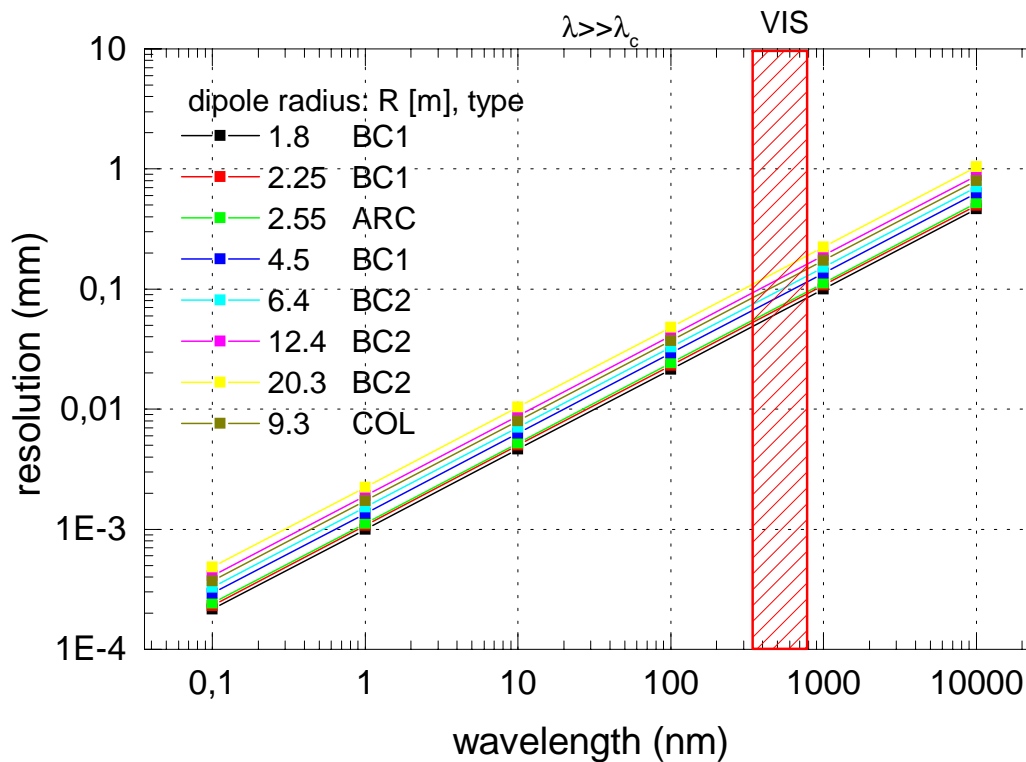


Fig. 12.15: Resolution limit of optical source imaging using dipole sources within the linac.

Comparing the data to the plots in figure 12.15 it can be concluded that visible light imaging before and at BC1 is no problem in terms of resolution. At the arc magnets and at BC2 a resolution of $\sim \sigma_y/3$ is possible. At the collimator magnets X-ray imaging is required. A technical realization of an optical telescope for visible light detection is depicted in figure 12.16.

Table 12.5: Expected source dimensions (rms) along dipole sources along the linac.

Bend type	σ_x (mm)	σ_y (mm)
BC1	5	0.6
ARC	2	0.2
BC2	3	0.5
COL (Dog leg)	0.2	0.15

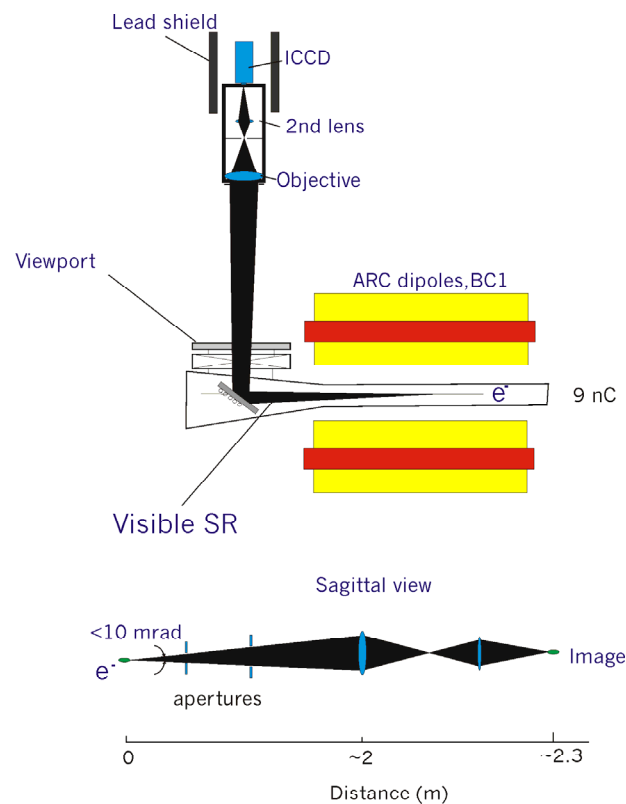


Fig. 12.16: Optics for a bend-magnet source within the linac. A part of the SR fan is reflected into a conventional visible light telescope performing a 1:1 image of the source on an intensified CCD.

12.3.2 X-Ray Imaging of SR

In order to overcome the limit given by Fraunhofer diffraction it is essential to image the beam at short wavelengths to achieve a resolution of $10 \mu\text{m}$ or less. Alternatively, interference methods utilizing the spatial coherence of SR can be used to obtain the beam size indirectly [11]. For fast direct X-ray imaging, however, the quality of the optics (slope errors and aberrations) as well as its mechanical stability has to be high to preserve the diffraction limited resolution.

Several kinds of X-ray and VUV optics have been used for this purpose: Grazing incidence optics in a Kirkpatrick-Baez mirror scheme at the ALS diagnostic beamline [12], crystal based X-ray Bragg-Fresnel lenses at the ESRF [5, 6], X-ray transmission zone plates at the APS [13, 14]. Multilayer Bragg-Fresnel lenses were developed for the diagnostic frontends of the BESSY II storage ring [15].

Another type of X-ray optics is the pinhole array camera developed at BESSY [15]. The pinhole array monitor is extremely robust and reliable and will be used at the collimator magnets and at the dump magnet behind the HGHG section at the final energy of the linac.

12.3.3 Transverse Overlap of the Electron and Photon Beams

Complementary to beam-based alignment techniques using the electron beam, spontaneous photon beams of the different undulator sources also offer the possibility to control the alignment of the whole system. This is provided for X-ray SASE-FELs [16] and can be used for the HGHG-FEL as well to ensure that the radiators and the subsequent modulators overlap on the same axis with the required precision of $< 1 \mu\text{rad}$ and $< 10 \mu\text{m}$. Since the radiation sources are spread longitudinally over a large distance, the photon beam trajectory can be measured by pinholes at staggered locations with $1 \mu\text{m}$ precision. This method can be used to correct deviations caused by dipole errors of undulators and random trajectory offsets. Furthermore, phase slips within segments of the final amplifier can be corrected.

Two movable pinholes, one located within the frontend and one behind the shield wall define an axis behind the final amplifier. Combined with a monochromatic detector (diagnostic spectrograph) further downstream, the central cone radiation is imaged by pinhole maps while the intensity is acquired on the blue edge of one of the harmonics. Monochromatic detection is needed at a spectral resolution $E/dE > 100$ to ensure that the spot sizes are sufficiently sharp in order to achieve a resolution on the micron scale with respect to their center of gravity. The method has already been successfully demonstrated at the BESSY double undulators where the overlap and the phase matching of the two sources were determined (compare also figures 12.20 and 12.21).

Overlap between seed laser pulse and electron beam in the first modulator can be measured and controlled by optical means. Since the wavelength of the seed laser and the modulator radiation is in the visible or near UV range, conventional CCDs can be employed to determine the overlap as well as the angular deviation between both beams using a scheme as depicted in figure 12.17. Although the laser wavelength is fixed, the off-axis modulator radiation is red shifted. Hence the beams can be distinguished by their color using a bandpass filter. The challenge is to extract both the laser as well as the modulator beam from the electron beam path without letting the full electron beam power of up to 150 kW impinge on the mirror. This is possible since the product of the divergence and distance of the laser beam and that of the modulator is large, enabling them to be viewed whereas the electron beam and the amplified photon beam of the radiator have hardly diverged and are small enough to pass through. The former are of lower power and should cause no problems with the mirror. Furthermore the scheme

enables one to extract a part of the laser beam and of the modulator beam for a control over the temporal overlap.

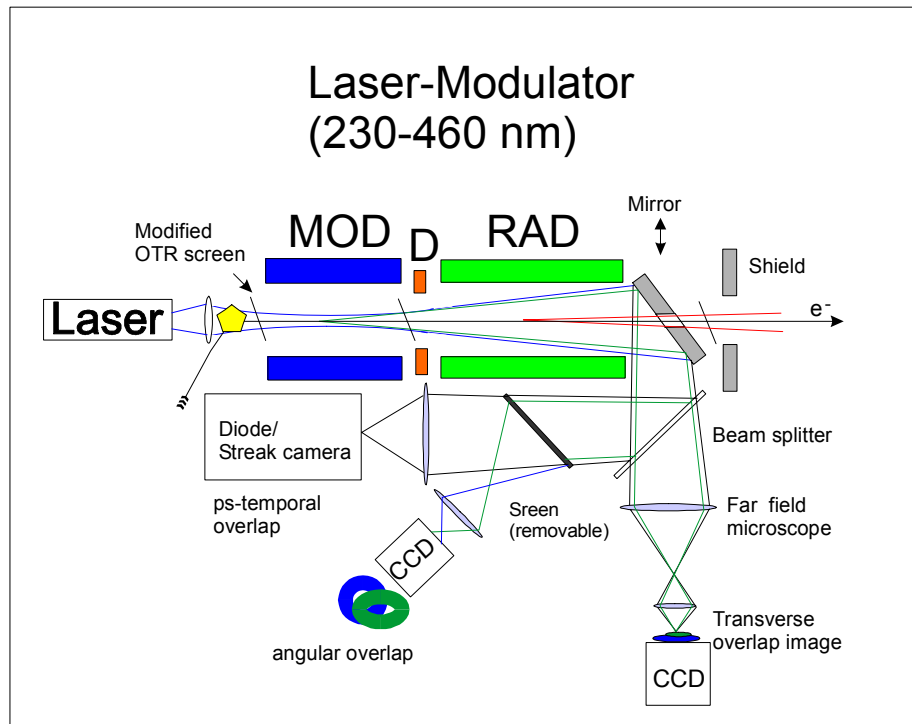


Fig. 12.17: Extraction scheme for transverse and temporal overlap analysis at the first seeding stages.

The image resolution of the scheme with respect to the center of the modulator is diffraction limited by the annular aperture given by the mirror and is of the order of $50\ \mu\text{m}$, i.e. only slightly smaller than the beam size of the laser and the electron beams themselves. However, the determination of the center of gravity of the overlap can be an order of magnitude better.

12.3.4 Longitudinal Overlap of Electron and Photon Beam

Coherent synchrotron radiation (CSR) emitted by the compressed electron bunch gives information on the bunch shape itself. This method has already been successfully demonstrated in the low- α mode of the BESSY II storage ring [5, 6] and can be used to detect density modulation in the seed laser-electron bunch overlap region. Such longitudinal modulation occurs when the bunch passes a dispersive section.

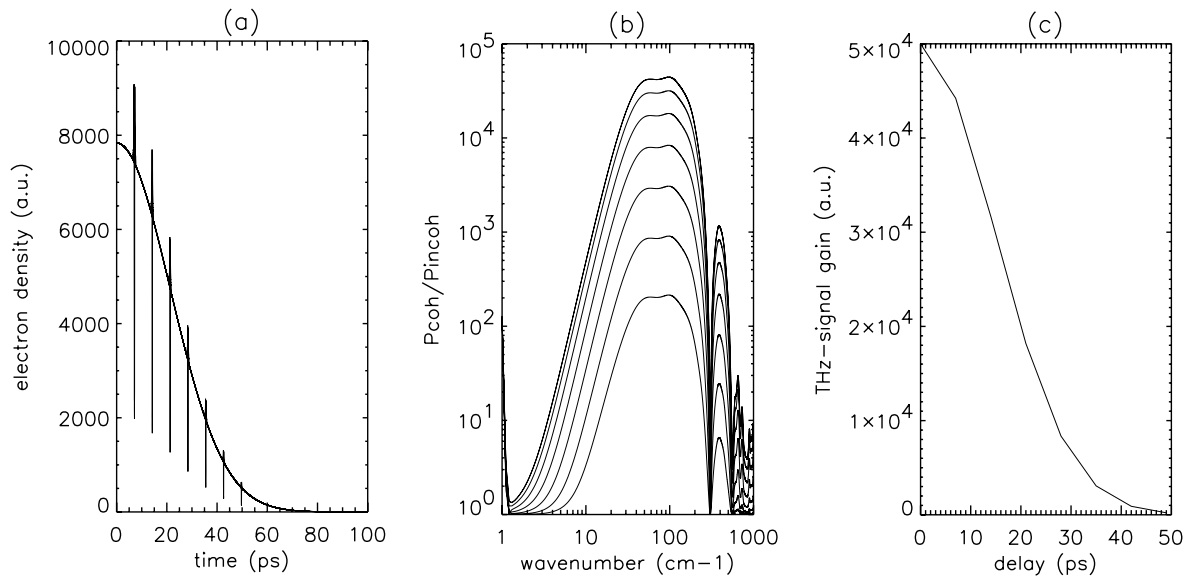


Fig. 12.18: (a) Longitudinal density modulation in a long bunch caused by the interaction with a 30fs Laser pulse after passing a dispersive section (b) Spectral power gain for different delays (1 – 50 ps) between bunch and laser pulse in the THz range (1 to 1000 cm^{-1}); (c) Plot of the THz signal vs. delay which is an image of the bunch shape.

In this measurement applicable for a fixed bunch charge as shown in figure 12.18, the slice itself acts as a probe for the charge density in the bunch. Varying the phase between the laser and the electrons the THz signal will be detected on a dipole magnet after the dispersive section. The signal is proportional to the ratio of electrons in the slice and the number of electrons in the bunch, whereas the total coherent intensity increases proportionally to the square of the total bunch charge. By sweeping the delay electronically, the longitudinal bunch shape will directly appear on an oscilloscope using the infrared detector output. Additional modulations caused by the following seed processes cause characteristic changes in the THz spectra and can be detected at the end of the FEL.

In contrast to the CSR-based bunch shape determination in the linac, a 30 fs-wide longitudinal modulation in charge density causes a broadband spectrum up to the mid-infrared. Here Si-Bolometers are the detectors of choice (operation up to 700 wavenumbers) but the CSR from the flat top bunch itself has to be discriminated against by cut-on filters. If pulses of < 50 fs are achieved, conventional Mercury Cadmium Telluride (MCT) detectors covering the wavelength range down to 400 wavenumbers can be used without liquid helium cooling. The detectors described here are able to detect shot-to-shot intensity variations indicating the longitudinal overlap of laser and electron bunch.

12.3.5 Emittance and Phase Matching in Undulators

Determination of the beam emittance complementary to the above illustrated methods is also possible using the fact that the central radiation cone of the spontaneous emission as well as the FEL radiation contains information on the electron beam emittance if the angular distribution is mapped in the far field using a monochromatic detector. The method [17] is depicted in figure 12.19.

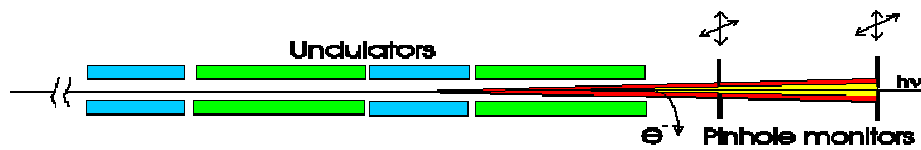


Fig. 12.19: Setup for the determination of the emittance: Two longitudinally staggered pinholes in the frontend and behind the shield wall together with a small bandwidth-detector (diagnostic spectrograph) are used to determine the diameter and the divergence of the undulator radiation.

The intensity measured within a small bandwidth behind a monochromator (diagnostic spectrograph) for different positions of the pinhole aperture yields the distribution of the undulator radiation at the location of the pinhole. The results of such an automatic mapping, stepping over all pinhole positions as is routinely done downstream the undulator source U49/1 at the BESSY II storage ring is depicted in figure 12.20. The bandwidth of the Spherical Grating Monochromator (SGM) at this energy is $< 10^{-4}$.

First, the spectrum is taken with the pinhole on-axis and then the photon energy is set to different photon energies within the harmonic for the mapping.

For the even harmonics, only horizontal off-axis features are observed, while odd harmonics produce vertical spots above and below the ring plane (figure 12.20). In all cases the features are very sharp and on the blue edges the size of the beam is vertically only $400 \mu\text{m}$ fwhm at a distance of 13 m downstream from the source.

The total Gaussian shape of the beam in this blue edge case can be written using equation (12.7) [18], where a is the distance to source and σ_r and σ_r' are the Gaussian diffraction-limited size and divergence, respectively. The second term goes to zero for $\lambda \rightarrow 0$. Hence, one measures the size of the spot for different λ and the beam emittance can be determined from (12.7) in the limit $\lambda \rightarrow 0$.

$$\sigma^2 = \varepsilon \left(\beta + \frac{a^2}{\beta} \right) + \frac{1}{2} \left(\sigma_r^2 + a^2 \sigma_r'^2 \right) \quad (12.7)$$

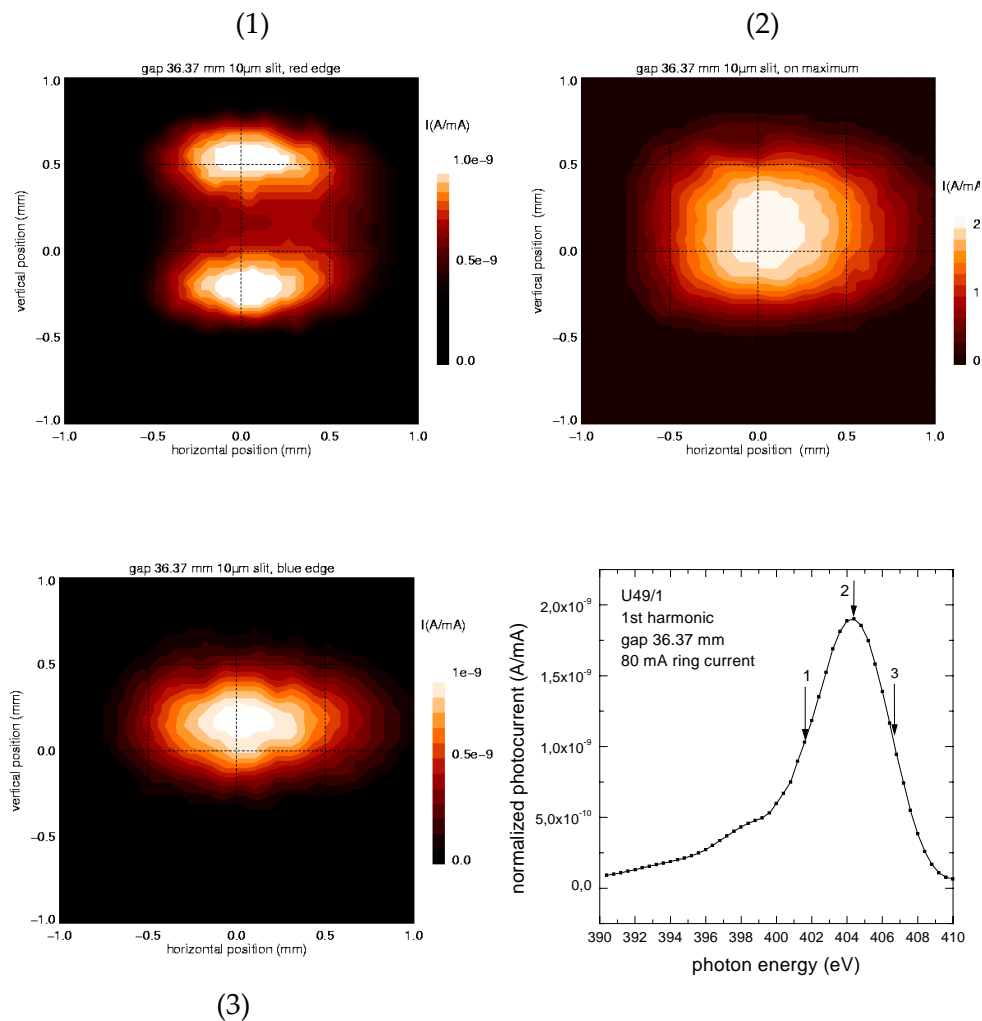


Fig. 12.20: Three intensity maps of the first harmonic using a pinhole ($r = 50 \mu\text{m}$) 13 m downstream the undulator source U49/1 at BESSY II. The three maps were recorded at the three photon energies shown in the plot of the first harmonic of the undulator.

The emittance measurement in the experiment was performed on the blue edges of the first harmonic while the K-value (fundamental wavelength) was varied. Here the spot has a clear 2-D-Gaussian shape.

By using two staggered pinholes the lattice functions can be eliminated since both size and divergence are determined independently. Using stimulated emission the fundamental wavelength of the final amplifier is gained but equation (12.7) is still valid.

The emittance detection scheme can be further extended to control the optimum phase match and overlap of the final amplifier segments.

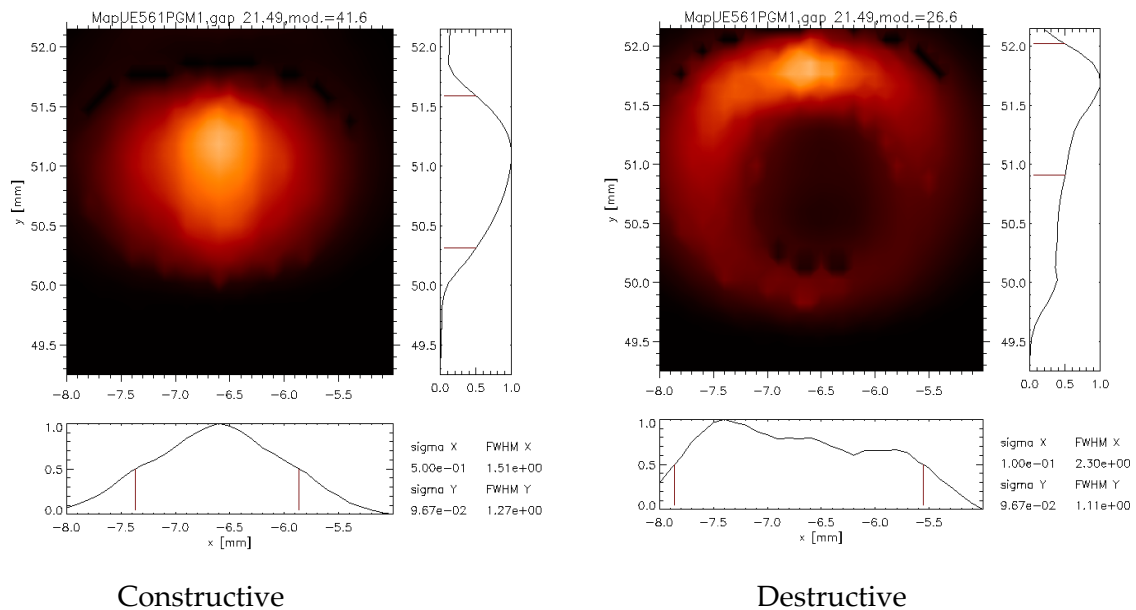


Fig. 12.21: Pinhole maps on the 1st harmonics of two on-axis beams of the UE56/1 double undulator at BESSY II. The asymmetry of both, the constructive overlap, as well as the asymmetric donut for the destructive case, indicate a non-ideal overlap due to a residual vertical kick of the electron beam between both segments.

In measurements made at BESSY II the radiation from two undulators in one straight section separated by a phase varying modulator magnet, is constructively or destructively overlapped in the planar mode (figure 12.21). Optimum phase matching is reached if the on-axis intensity increases proportionally to N^2 , where N is the number of periods involved and if the corresponding image at opposite phase shows an ideal ring shape with minimized on-axis intensity. This can be additionally monitored by leaving the pinhole on axis and measuring the corresponding spectra.

Together with a fit analysis of the projections of the images in figure 12.21 the method is sensitive to $\sim 1 \mu\text{m}$ deviations of the center of gravity and hence of angular deviations of $< 0.1 \mu\text{rad}$ resolution with respect to the overlap of two subsequent undulator beams. By leaving both pinholes on axis, the FEL gain and saturation can be monitored using the same setup.

Since the pinhole/spectrograph method described above detects slow position and angle deviations only, at least one fast photon monitor of the blade type [19] and with shot-to-shot capability is required.

12.4 Photon Beam Diagnostics at the Experiments

Pulse flux, temporal and spatial shape, energy and energy half width/purity and pulse arrival time at the experiment must all be determined in order to perform the experiments. Some of the monitors described above can also be employed here. For some of the parameters, however, different monitors will be required.

12.4.1 Flux Monitors: Giant Ionization Chambers (GIC)

For the detection of the expected peak-power densities conventional solid-state flux monitors are no longer feasible. Either they saturate or they suffer from rapid degradation or destruction. On the other hand gas-phase-ionization detectors, based on atomic photoionization of gases at low particle pressure are indestructible and almost transparent. Tests of such devices at TTF I [20] have demonstrated that at least in the unfocused beam these detectors are suitable flux monitors over a wide range of intensities and wavelengths.

Photoionization chambers are a standard diagnostic tool in all BESSY beamlines [21]. They are installed between the exit slit of the monochromators and the refocusing optics and are separated from the UHV system of the monochromator by thin aluminum or polyimide films. The measured total ion yield of rare gases is commonly used for an absolute spectral calibration of the monochromators rather than flux measurements [22].

In the planned design of the BESSY FEL beamlines, the 10 m long section between the first collimating mirror and the monochromator chamber is a suitable place for installation of an ionization flux monitor. For alignment and optimization of the components for the HGHG process a qualitative flux measurement is adequate. The total photo-ion yield as measured from residual-gas ionization in the 10^{-6} to 10^{-8} hPa range collected over a photon path length of up to 10 m will be extremely useful. For absolute flux measurements calibration of the device, including precise gas composition, pressure and temperature control will be necessary.

A second aspect of having a long gas target at low pressure is the possibility to attenuate the FEL beam easily with a high dynamic range by a gas inlet. Using nitrogen gas single-shot resolution measurements have been performed at BESSY. A slightly modified version of the field-proved cylindrical photoionization chambers [21] can be installed easily in the aforementioned section. The expected photon beam diameter of <6.5 mm (fwhm) is well suited for the existing design. In order to be compatible with the vacuum requirements of the neighboring mirror chambers and optical components a high partial pressure of hydrogen is desirable. This can be realized either by a leak valve or by a palladium diffusion cell. The signal values extrapolated from the measurements in the dispersed photon beam at the BESSY undulator beamlines are in the microampere range and

hence are easily measurable. The electrical readout of the ionization chambers can be optimized either for single-pulse counting measurements or for the time-averaged flux values. Standard low-current measurement electronics are suitable for this purpose.

12.4.2 FEL Pulse-Length Diagnostics

A main advantage of the FEL is the short temporal length of its pulses. The knowledge of the actual pulse length and its temporal profile is crucial not only for time resolved measurements like pump-probe experiments but also for the characterization and optimization of the FEL itself. Additionally, the time-zero or the synchronization with an external laser pulse needs to be established and continuously verified for any pump-probe experiment. Short FEL pulses of some ten fs can only be measured by nonlinear optical methods employing a temporal cross correlation either with itself (autocorrelation) or with a short optical laser pulse. Although cross (auto) correlation is rather straightforward and well established in the spectral region of the UV to the near IR it remains a scientific and technical challenge in the soft X-ray region. Up to now only little work has been done in this field restricted mostly to the VUV with photon energies of only a few tens of eV. This is mainly due to a lack of intense fs sources in the soft X-ray range. In this section approaches for auto correlation as well as cross correlation covering the needs of the different experiments at the BESSY FELs are outlined.

12.4.2.1 FEL Pulse Autocorrelation

In a typical autocorrelation experiment for the determination of the pulse length a replica of the incoming pulse is created by means of a beam splitter. The two identical pulses are delayed against each other and finally spatially and temporally overlapped at the detector. There a nonlinear signal is recorded as a function of the time delay between the two FEL pulses. The pulse length can be derived from this autocorrelation function.

The optical components of an autocorrelator should allow for a high instrumental transmission over the entire energy range of the BESSY FEL. In the VUV/soft X-ray spectral region the limited reflection and the strong absorption of the optical components require an all-reflective geometry with grazing incidence angles at the mirrors. The key element of any autocorrelator, interferometer and/or delay line is a beam splitter. For this purpose gratings [23, 24], geometrical beam splitting [25, 26], and for fixed wavelengths multi-layer beam splitters [27] have been proposed and partially tested in the soft X-ray region. To meet the above stated requirements simple geometrical wave front splitting is the best candidate because its efficiency and broadband capability are only restricted by the reflectivity of the mirrors.

The basis for the planned autocorrelators is a design developed at BESSY for the use at the TTF II in 2004/5. There two half beams are created by geometrical wave front splitting

utilizing a sharp mirror edge which reflects and transmits 50% of the beam, respectively. This concept allows both the handling of high-power pulses as well as a high efficiency (50%) up to 200 eV. A schematic drawing of an autocorrelator is presented in figure 12.22.

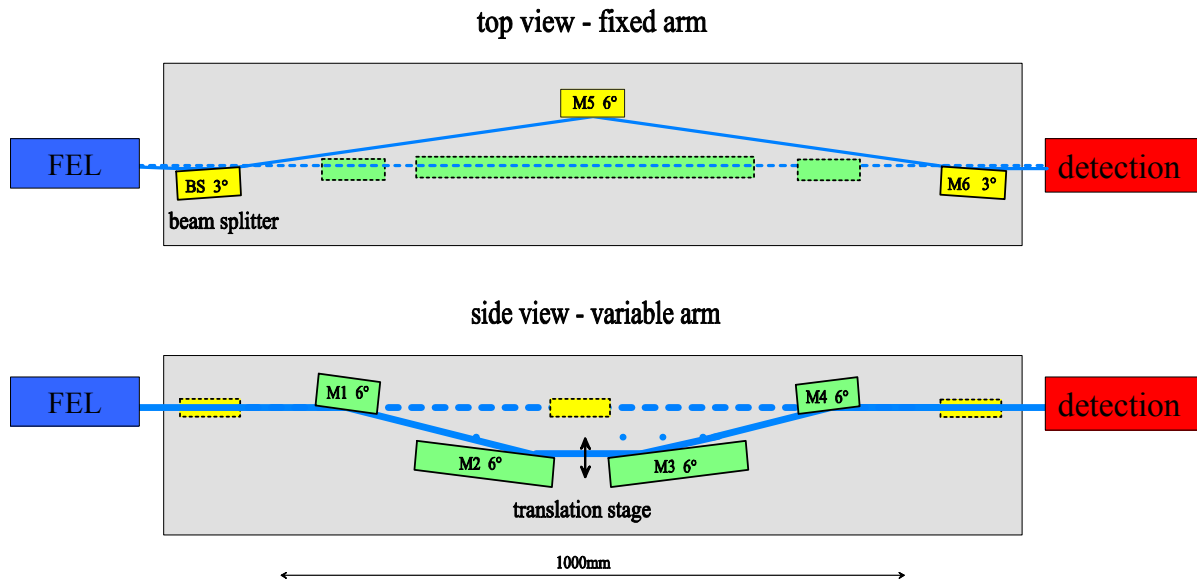


Fig. 12.22: Setup of the FEL autocorrelator developed at BESSY for the TTF II: The lower part of the incoming FEL beam is reflected by the Beam Splitter (BS) into the fixed delay arm (top view). The upper part of the beam propagates unaffected until it is reflected by the Mirror M1 onto the two Mirrors (M2, M3) of the variable delay stage (side view). Mirror M4 in the variable delay arm and mirror M6 in the fixed delay arm reflect the two half beams into their original direction. The split beams fully overlap in the detection chamber.

The angles of incidence chosen are a compromise between reflectivity, delay range and mirror size. For the actual design a total delay of about 25 ps is possible with a resolution of several fs. Due to the high radiation load the mirrors fabricated from silicon will be water cooled. As coating material carbon will be used due to its high reflectivity up to 200 eV. Diffraction analysis demonstrates that the diffraction introduced by the beam splitter can be easily managed allowing versatile time-resolved applications both with focused and unfocused beams.

The requirements for the stability and adjustment resolution are very high: any angle deviation (resolution) must be smaller than $1 \mu\text{rad}$. This will be achieved by combination of passive (extra-stiff tube design) and active measures (online tracking of the tilt, feed-back loop).

An advantage of the autocorrelator design shown in figure 12.22 is the lack of any angle deviation or shift in the direction of the transmitted beam. This permits a simple integration in FEL beam lines as the autocorrelator can easily be retracted vertically out of the beam. Whether or not the autocorrelator is used the location of the experimental chamber behind the refocusing mirror remains the same. This configuration is a kind of all-purpose instrument applicable for pulse characterization as well as for FEL-pump-FEL-probe experiments. For the implementation at the BESSY FEL the photon energy range will be extended to 300 eV using nickel as mirror coating. Above 300 eV the transmission drops dramatically due to the relatively large number of optical elements.

The extension towards higher photon energies is essential and to address this, a second configuration with only one reflection per arm is planned thus being suitable for all three FELs. The setup shown in figure 12.23 based on the concept of the split mirror is already established for the autocorrelation of visible and VUV fs pulses [26]. Whereas this geometry guarantees a mechanically rigid design and thus a very reliable operation, the split mirror introduces a deflection of the beam. Furthermore, the delay range is on the order of only 100 to 200 fs (2 to 3 degree grazing angle). This may limit its applicability for certain FEL-pump-FEL-probe experiments, but it fits perfectly the need for an unambiguous tool for pulse-length monitoring of the 20 to 30 fs FEL pulses. The two proposed configurations using wave-front beam splitting (figures 12.22 and 12.23) complement each other in their scope while covering the entire energy range of the three FELs.

It should be noted that both beam splitters allow for interferometrical autocorrelation measurements provided that the high requirements regarding positioning resolution and stability (step size well in sub-nanometer range) are fulfilled. At the zero delay position these devices can act as classical interferometers utilizing wave-front dividing (figure 12.23b). Without further focusing this results in transversal interference fringes at the overlap. Applications are discussed subsequently.

Detection of the autocorrelation signal requires the use of non-linear processes such as two-photon photoemission or sum-frequency generation. These processes will be described in detail below. In addition it is planned to use the intrinsic interferometric character of the beam splitter for pulse characterization. If the collimated undelayed split beams are spatially overlapped with a small angle (figure 12.23b) lateral fringes from constructive and destructive interference are observed for the spatially coherent FEL beam. Thus the interference pattern and their visibility are a measure of the spatial coherence of the beam. The FEL beam is expected to be fully spatial coherent [28]. Furthermore the interference pattern also reflects the local distortions of the wave front opening up the possibility of wave front characterization.

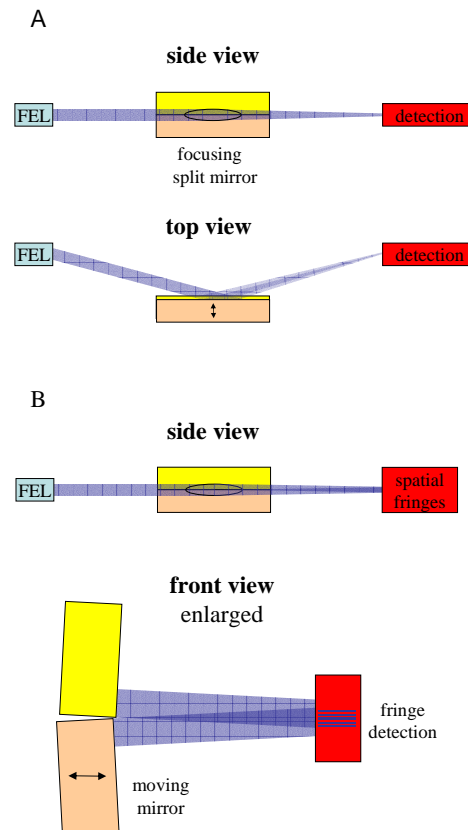


Fig. 12.23: Schematic layout of two “split mirror” configurations: The incident beam is divided into two halves by the split mirror acting as geometric beam splitter and simultaneously as delay line. The delay between the two pulses is introduced by a slight translation of one mirror. (A) Both beams can be refocused to overlap in the focal plane either by means of an additional refocusing mirror or by the split mirrors itself by manufacturing the split mirror from a focusing mirror instead of from a plane mirror. (B) By introducing a small angle between the mirrors (Fresnel bi-mirror) the unfocused beams overlap showing spatial fringes in the detection plane.

When both pulses are delayed relative to each other the interference fringes become less distinct and finally disappear outside the temporal overlay. The observed time constant is a measure of the temporal coherence between the pulses. For temporally fully coherent HGHG-FEL pulses the coherence time is close to the pulse length. The experimental setup is straightforward. The interference pattern can be either recorded on an X-ray camera or after conversion into visible light imaged onto a one- or two-dimensional detector array. It is possible to acquire the pattern from a single FEL pulse. This detection

scheme is applicable to the whole wavelength range of the FELs down to 1 nm using crossing angles from 0.1 to 1 mrad.

12.4.2.2 FEL Optical Sideband Generation

The laser-assisted photoelectric effect [29, 30] known as “sideband” generation is well established in cross-correlation measurements of ultrashort VUV pulses created with the laser driven high-harmonic-generation (HHG) process. The principle is based on the photo-ionization of an atom by the VUV pulse in the presence of a strong infrared laser field. The infrared field “dresses” the atom and increases the ionization potential ponderomotively. This firstly results in an energetic shift of the photoemission peak and secondly in the appearance of sidebands shifted by the photon energy of the infrared. Both the ponderomotive shift and the intensity of the sideband scale linearly with the intensity as well with the temporal overlap of the ionising and the dressing pulse. Due to the high intensities of the infrared laser (10^{14} - 10^{15} Wcm⁻²) the sidebands generated are of considerable strength allowing for sensitive cross correlation measurements with low background signal. Thus, it is planned to monitor the time jitter of the SASE-FEL at TTF II measuring the height of a sideband [31]. The high photon flux at FELs also makes complete single-shot cross correlations feasible [32] if the space-charge effects can be overcome. All those activities at TTF II will further improve this method towards becoming a standard tool in the VUV and soft X-ray range. Even the extension towards higher photon energies, up to 1 keV, appears uncritical since the effect is driven by the dressing IR field.

12.4.2.3 Two-Photon Photoemission

From present experience with fs-laser pulses in the optical [33] and VUV spectral region two-photon photoemission is one of the most widely used techniques to determine the laser pulse shape. If Soft X-ray FEL radiation is being used, the binding energy of the photoemitted electrons has to be larger than the photon energy. This way the simultaneous absorption of two FEL photons is required to generate one photoelectron.

The two-photon ionization of atomic gases has been demonstrated for several noble gases in the VUV: He at 11 eV – 20 eV [34]; Xe, and Kr at 7.7 eV [35] and the He⁺ ion at 42 eV [36]. The estimated cross sections are in the order of 10^{-52} cm⁴s and agree well with theoretical predictions. An examination of the electron binding energies of the noble gases shows the principal possibility to cover the energy range of all three FELs by means of two-photon photoemission. The cross sections determined for the valence electrons are expected to be an upper limit. Cross sections of the two-photon ionization of different core levels have been calculated in [37]. The cross section of the ionization of the neon 1s shell (869.53 eV) by two photons has been determined to about 10^{-54} cm⁴s (photon energy 437 eV) and 10^{-55} cm⁴s (826 eV) respectively. In order to obtain a measure of the sensitivity

the number of ejected electrons has been estimated assuming a pulse energy as low as 1 μJ and a pulse length of 20 fs focused on 30 μm \times 30 μm in 1 torr of neon gas. This results in 100 electrons per second (826 eV) and 3600 electrons per second (437 eV), respectively being sufficient to allow a fast measurement of the pulse length.

In this context the electron yield caused by single-photon ionization from second order FEL radiation has to be considered. The resulting background level should be suppressed below the level of the two-photon electron yield at the fundamental FEL radiation. The cross sections of one photon photoemission processes range from 10^{-18} cm^2 at threshold to below 10^{-20} cm^2 for higher photon energies.

For comparison with two-photon processes the electron yield from single photon ionization was calculated for the Neon 1s shell at 874 eV photon energy [38]. Assuming a pulse energy of the second FEL harmonic of 1 pJ which implies a contrast ratio fundamental/second harmonic of 10^6 , the count rates of the two photon (fundamental) and the single photon signals (second harmonic) are comparable. Even if such a contrast ratio seems high it can be achieved. Presently simulations to estimate the fraction of harmonic radiation for the specific BESSY FELs are being made. However, literature results [39] suggest that a contrast ratio between the fundamental and the second harmonic of 10^3 is realistic. A further suppression of the higher harmonic radiation will be attained by an appropriate configuration of the monochromator [40] an additional filters. Above 100 eV this can result in an improvement of the contrast ratio by a factor of 10^3 .

Still higher sensitivity is expected applying two-photon photoemission from surfaces since in solids the atomic density is significantly higher than in gases. A typical two-color experiment using optical fs lasers that resembles the situation expected for a Soft X-ray FEL is shown in figure 12.24. Optical pump pulses of 1.5 eV photon energy are used to excite electrons in metallic nickel into previously unoccupied states above the Fermi level, E_F . The transient electron population in these states is subsequently probed by pulses of 6 eV photon energy. The photoemission spectra displayed in figure 12.24 show how states above E_F are rapidly depopulated for increasing pump-probe time delay, Δt [41]. The lifetime of the highest excited electrons are known to be only several fs [42]. The photoemission intensity above E_F shown in the inset of figure 12.24 is, therefore, a direct measure of the cross correlation, i.e. the temporal convolution, of pump and probe pulses [41].

This situation can easily be transferred to the case of optical-pump-FEL-probe experiments. Instead of 6 eV, a probe-photon energy up to 1 keV is conceivable without changing the principle of a cross-correlation measurement. In metals the excited electrons and the photo holes dephase within several fs, i.e. they lose memory of the optical excitation [43]. This mechanism is especially pronounced in transition metals at high pump fluencies [44]. As a consequence, the two-photon photoemission cross section can be approximated by the product of the single photon excitation events [42]. As the optical pump excitation

remains the same changes in the FEL-probe cross section with photon energy [43] can easily be compensated for by the available photon flux. This is demonstrated by the example in figure 12.24 where 6 eV pump pulses with approximately $10^3 - 10^4$ photons/pulse were used. These numbers are basically determined by space charge effects of the photoelectrons that start to influence the photoelectron kinetic energy distribution at higher photon flux. This problem is expected to be much reduced for higher kinetic photoelectron energies. The single photon cross section in nickel metal shows some variations but essentially drops by about two orders of magnitude between 10 eV and 1000 eV. This is easily compensated for by the available flux of up to 10^{11} photons/pulse of the BESSY FEL. The process described here is a very sensitive cross correlation mechanism which can be applied universally at all photon energies available at the BESSY FEL.

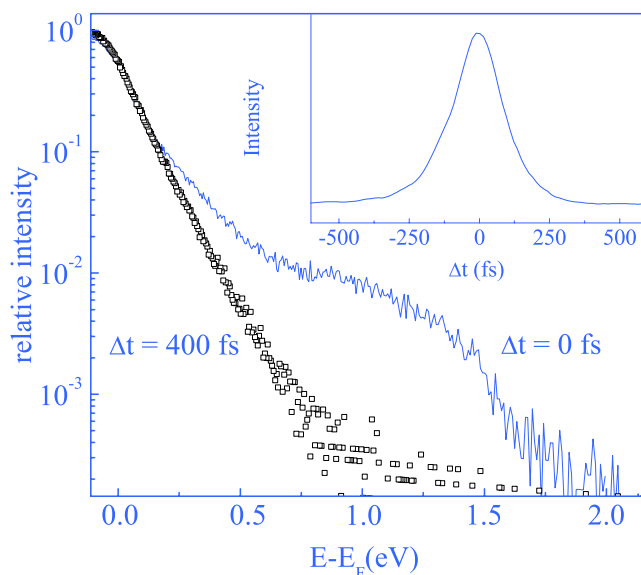


Fig. 12.24 Typical results from a two-photon photoemission spectroscopy experiment from ultra-thin Ni films using 1.5eV pump and 6eV probe photons [41]. Shown are log-plots of the photoelectron intensity vs. binding energy E above the Fermi level E_F for two pump-probe time delays (Δt). Since the pump photons cannot overcome the sample work function only photoemission from probe pulses contribute to the spectra. The spectra represent the relaxation behavior of electrons excited by internal photoemission. The inset shows the pump-probe cross correlation curve obtained as the photoemission intensity measured 1.5eV above E_F vs. time delay.

12.4.2.4 Photon-In Photon-Out Sum-Frequency Generation

The principle of a single-shot cross correlation based on FEL optical pulse sum-frequency generation is shown schematically in figure 12.25. The FEL pulse is mixed with an optical gate laser pulse enclosing an angle α to the sum-frequency-generation signal. The non-collinear propagation of both signals transforms their time delay Δt , into a spatial coordinate Δx , along an optically non-linear medium. The resulting sum-frequency-generation signal can be detected by an imaging detector. Such cross-correlation measurements can be performed in transmission (ultra-thin solid films, fluid and gas samples) or in reflection (solid surfaces).

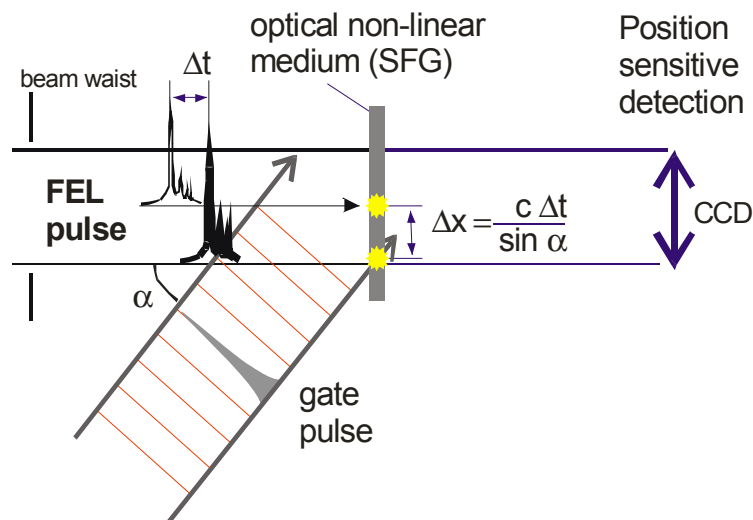


Fig. 12.25: Schematic setup of a single-shot cross correlation based on sum-frequency generation between FEL and optical laser pulses.

For sum-frequency generation at surfaces and in ultra thin films phase matching of the two fundamental signals is not very critical and the enclosing angle α can be chosen arbitrarily. In such a non-collinear setup the resulting sum-frequency signal can be spatially separated from the reflected optical and FEL beams. For an VUV-FEL and for optical frequencies this can be done merely by an aperture (figure 12.26). In the soft X-ray range the angle enclosed by FEL and sum-frequency-generation signals is too small and discrimination will have to be done via the photon energy. It is conceivable that the simple aperture can be replaced by a grating that images the sum-frequency-generation footprint on the sample in the scattering plane. A dispersion perpendicular to the scattering plane can then be measured simultaneously using a two-dimensional detector. Such a setup enables one, in principle, to measure a single-shot cross correlation.

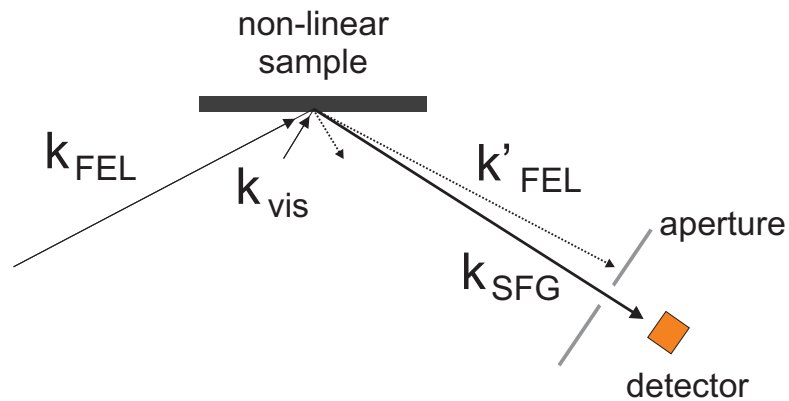


Fig. 12.26: Schematics of a reflection VUV FEL – optical cross correlation. Shown are the wave vectors k , of incident and reflected VUV-FEL and visible optical laser pulses as well as the resulting sum-frequency-generation signal.

So far not much is known about the sum-frequency-generation cross sections that can be expected for VUV-optical and soft X-ray optical frequencies. Experiments to close this gap are planned at the TTF II facility in 2005. It is expected, however, that for a high optical fluence the same arguments as for two-photon photoemission apply. Moreover at FEL frequencies at resonance between core and valence states strong enhancements of the single photon and consequently of the sum-frequency-generation signal can be expected. Systematic studies in the near future especially at the TTF II facility are planned to verify this [45].

References

- [1] E. Babenko, R. K. Jobe, D. McCormick, J. T. Seema, *Proc. of the 1993 PAC* (1993) 2423.
- [2] H. H. Braun, C. Martinez in “Non-Intercepting Bunch Length Monitor for Picosecond Electron Bunches”, 1559.
- [3] J. C. Swartz, B. D. Guenther, F. C. De Lucia, W. Guo, C. R. Jones, H. Kosai, J. M. Dutta, *Phys. Rev. E* **52/5** (1995) 5416.
- [4] D.H. Dowell, P. R. Bolton, J. E. Clendenin, S. M. Gierman, C. G. Limborg, B. F. Murphy, J. F. Schmerge, T. Shaftan, *Nucl. Instrum. and Meth. A* **507/1-2** (2003) 331.
- [5] M. Abo-Bakr, J. Feikes, K. Holldack, G. Wüstefeld, H.-W.Hübers, *Phys.Rev.Lett* **88** (2002) 254801.
- [6] M. Abo-Bakr, J. Feikes, K. Holldack, P. Kuske, W. B. Peatman, U.Schade, G.Wüstefeld, H. W. Hübers, *Phys.Rev.Lett* **90** (2002) 094801.
- [7] H. Wiedemann, „Particle Accelerator Physics I, Basic Principles and Linear Beam Dynamics“, Springer-Verlag Berlin Heidelberg (1999).
- [8] R. Jung, G. Ferioli, S. Hutchins, *Proc. of the 2003 DIPAC* (2003) 10.
- [9] L. Wartski, S. Roland, J. Lasalle, M. Bolore, G. Filippi, *IEEE Trans. Nucl. Sci.* **22/3** (1975) 1552.
- [10] K. Honkavaara, S. Schreiber, C. Gerth, P. Piot, *Proc. of the 2003 PAC* (2003) 911.
- [11] M. Katoh, T. Mitsuhasi, *Proc. of the 1999 PAC* (1999) 2307.
- [12] T. R. Renner, H. A. Padmore, R. Keller, *Rev. Sci. Instrum.* **67/9** (1996) 3368.
- [13] Z. Cai, B. Lai, W. Yun, E. Gluskin, D. Legnini, P. Ilinski, E. Trakhtenberg, S. Xu, W. Rodrigues, H.-R. Lee, *AIP Conf. Proc.* **417** (1997) 101.
- [14] W. Yun, B. Lai, A. A. Krasnoperova, E. Di Fabrizio, Z. Cai, F. Cerrina, Z. Chen, M. Gentili, E. Gluskin, *Rev. Sci. Instrum.* **70/9** (1999) 3537.
- [15] W. B. Peatman, K. Holldack, *J.Synchr.Rad.* **5/3** (1998) 639.
- [16] C. David, V. Schlott, A. Jaggi, *Proc. of the 2001 DIPAC* (2001).
- [17] K. Holldack, W. Frentrup, W. B. Peatman, M. Scheer, F. Senf, *BESSY annual report* (2001) 239.
- [18] H. Wiedemann, „Particle Accelerator Physics I, Basic Principles and Linear Beam Dynamics“, Springer-Verlag Berlin Heidelberg (1999).

- [19] K. Holldack, D. Ponwitz, W. B. Peatman, *Nucl. Instrum. and Meth. A* **467-468** (2001) 905.
- [20] M. Richter, A. Gottwald, U. Kroth, A. A. Sorokin, S. V. Bobashev, L. A. Shmaenok, J. Feldhaus, Ch. Gerth, B. Steeg, K. Tiedtke, R. Treusch, *Appl. Phys. Lett.* **83/14** (2003) 2970.
- [21] G. Reichardt, W. Peatman, *BESSY annual report* (1994) 459.
- [22] J. A. R. Samson, *J. Opt. Soc. Am.* **54** (1964) 6.
- [23] E. J. Moler, R. M. Duarte, M. R. Howells, Z. Hussein, C. Oh, J. Spring, *Proc of SPIE* **3154** (1997) 117.
- [24] J. Filevich, K. Kanizay, M. C. Marconi, J. L. A. Chilla, J. J. Rocca, *Opt. Lett.* **25/5** (2000) 356.
- [25] R. Mitzner, N. Pontius, M. Neeb, W. Eberhardt in 3rd Annual Report (p.16 – 18, 3/2003) of the “XRAY FEL PUMP-PROBE” project (HPRI-CT-1999-50009, coordinator: J. Feldhaus), 5th EU – Framework program:
<http://www-hasylab.desy.de/facility/fel/vuv/projects/pump.htm> .
- [26] H. Mashiko, A. Suda, K. Midorikawa, *Appl. Phys. B* **76** (2003) 525; P. Tzallas, B. Charalambidis, N. A. Papalogiannis, K. Witte, G. D. Tsakiris, *Nature* **426** (2003) 267.
- [27] L. B. Da Silva, T. W. Barbee Jr., R. Cauble, P. Celliers, D. Ciarlo, S. Libby, R. A. London, D. Matthews, S. Mrowka, J. C. Moreno, D. Ress, J. E. Trebes, A. S. Wan, F. Weber, *Phys. Rev. Lett.* **74/20** (1995) 3991.
- [28] V. Ayvazyan, N. Baboi, I. Bohnet, R. Brinkmann, M. Castellano, P. Castro, L. Catani, S. Choroba, A. Cianchi, M. Dohlus, H.T. Edwards, B. Faatz, A.A. Fateev, J. Feldhaus, K. Flöttmann, A. Gamp, T. Garvey, H. Genz, Ch. Gerth, V. Gretchko, B. Grigoryan, U. Hahn, C. Hessler, K. Honkavaara, M. Hüning, R. Ischebeck, M. Jablonka, T. Kamps, M. Körfer, M. Krassilnikov, J. Krzywinski, M. Liepe, A. Liero, T. Limberg, H. Loos, M. Luong, C. Magne, J. Menzel, P. Michelato, M. Minty, U.-C. Müller, D. Nölle, A. Novokhatski, C. Pagani, F. Peters, J. Pflüger, P. Piot, L. Plucinski, K. Rehlich, I. Reyzl, A. Richter, J. Rossbach, E.L. Saldin, W. Sandner, H. Schlarb, G. Schmidt, P. Schmüser, J.R. Schneider, E.A. Schneidmiller, H.-J. Schreiber, S. Schreiber, D. Sertore, S. Setzer, S. Simrock, R. Sobierajski, B. Sonntag, B. Steeg, F. Stephan, K.P. Sytchev, K. Tiedtke, M. Tonutti, R. Treusch, D. Trines, D. Türke, V. Verzilov, R. Wanzenberg, T. Weiland, H. Weise, M. Wendt, T. Wilhein, I. Will, K. Wittenburg, S. Wolff, M.V. Yurkov, K. Zapfe, *Eur. Phys. J. D* **20/1** (2002) 149.
- [29] T. E. Glover, R. W. Schoenlein, A. H. Chin, C. V. Shank, *Phys. Rev. Lett.* **76/14** (1996) 2468.

- [30] E. S. Toma, H. G. Muller, P. M. Paul, P. Breger, M. Cheret, P. Agostini, C. Le Blanc, G. Mullot, G. Cheriaux, *Phys. Rev. A* **62/6** (2000) 061801.
- [31] P. O’Keeffe, M. Meyer, L. Nahon, in 3rd Annual Report (p.10 – 11, 3/2003) of the “XRAY FEL PUMP-PROBE” project (HPRI-CT-1999-50009, coordinator: J. Feldhaus), 5th EU – Framework program:
<http://www-hasylab.desy.de/facility/fel/vuv/projects/pump.htm> .
- [32] M. Drescher, proposal accepted for the TTF2 facility at DESY/Hamburg (2003).
- [33] H. Petek, S. Ogawa, *Prog. Surf. Sci.* **56** (1997) 239.
- [34] N. A. Papadogiannis, L. A. A. Nikolopoulos, D. Charalambidis, G. D. Tsakiris, P. Tzallas, K. Witte, *Phys. Rev. Lett.* **90/13** (2003) 133902.
- [35] D. Descamps, L. Roos, C. Delfin, A. L’Huillier, C.-G. Wahlström, *Phys. Rev. A* **64/3** (2001) 031404(R).
- [36] K. Ishikawa, K. Midorikawa, *Phys. Rev. A* **65/4** (2002) 043405.
- [37] S. A. Novikov, A. N. Hoppersky, *J. Phys. B* **33/12** (2000) 2287.
- [38] J.-J. Yeh, I. Lindau, *At. Data Nucl. Data Tables* **32** (1985) 1.
- [39] A. Doyuran, M. Babzien, T. Shaftan, L. H. Yu, L. F. DiMauro, I. Ben-Zvi, S. G. Biedron, W. Graves, E. Johnson, S. Krinsky, R. Malone, I. Pogorelsky, J. Skaritka, G. Rakowsky, X. J. Wang, M. Woodle, V. Yakimenko, J. Jagger, V. Sajaev, I. Vasserma, *Phys. Rev. Lett.* **86/26** (2001) 5902;
S. G. Biedron, Z. Huang, K.-J. Kim, S. V. Milton, G. Dattoli, A. Renieri, W. M. Fawley, H. P. Freund, H.-D. Nuhn, P. L. Ottaviani, *Phys. Rev. ST Accel. Beams* **5** (2002) 030701.
- [40] R. Follath, *Nucl. Instrum. and Meth. A* **467–468** (2001) 418.
- [41] H.-S. Rhie, H. A. Dürr, W. Eberhardt, *Phys. Rev. Lett.* **90/24** (2003) 247201.
- [42] R. Knorren, K. H. Bennemann, R. Burgermeister, M. Aeschlimann, *Phys. Rev. B* **61/14** (2000) 9427.
- [43] S. Ogawa, H. Nagumo, H. Petek, A. P. Heberle, *Phys. Rev. Lett.* **78/7** (1997) 1339.
- [44] H.-S. Rhie, PhD thesis, Technical University Berlin (2003).
- [45] H. A. Dürr, W. Eberhardt, G. van der Laan, M. Wolf, K. Starke, proposal accepted for the TTF2 facility at DESY/Hamburg (2003).

13 Control System

13.1 Common Controls Environment

The BESSY FEL will be operated as a versatile user facility next to the existing BESSY II storage ring. This synchrotron radiation (SR) facility has been commissioned and is operated with a control system based on the EPICS toolkit [1 - 4].

Experience with EPICS reliability, available functionalities, performance, on-going world-wide developments and in-house expertise suggests EPICS should also be used for the core of the BESSY FEL control system. Since its early days EPICS has been constantly improved with respect to cleaner software interfaces, platform independence and optional functionalities. In addition, the “EPICS 2010” initiative [5] tries to capture upcoming control system requirements to be able to support or steer development efforts towards a long-term sustainable control system environment. At the BESSY II SR facility, installation of new EPICS releases and upgraded packages are part of maintenance procedures needed to keep the high control system quality. Therefore, at BESSY, EPICS is a well understood and sound foundation for FEL controls.

In addition to a common control system for both facilities, a collision-free naming convention [6] has been defined. This will make operation by a common crew from a central control room very convenient. With respect to controls infrastructure, future pump-probe experiments that need to take advantage of certain concerted SR-FEL operation modes become feasible with very moderate effort.

13.2 Architecture

13.2.1 Vertical Structure

For the FEL the (extended) standard model of control system architecture (figure 13.1) will provide an adequate framework: robust and redundant files, data base and application servers in a Linux type environment will be employed for control room services and consoles. Switched GigaBit Ethernet will provide the backbone connectivity. Single board front-end computers (IOC) possibly with power PC CPU in VME or PCI crates will house the I/O boards or connect to robust field buses with real time capabilities. Embedded controllers connected to a field bus segment or Ethernet directly will combine ease of installation with quality capability of signal conditioning wherever possible.

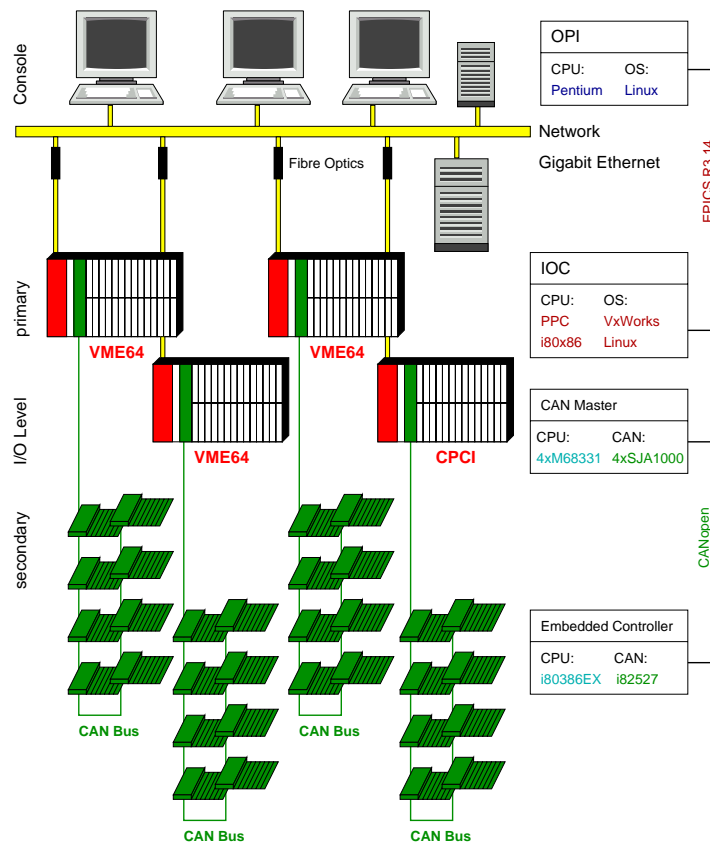


Fig. 13.1: The BESSY “extended” standard model of control-system architecture: Console, network, front-end computers, field bus, embedded controller.

Specific operating systems or hardware platforms that come with dedicated local controls, commercial solutions, unique components or demanding diagnostic requirements will cause no integration problem. Typical examples for smart subsystems are the local controls of the laser systems for the photocathode or the FEL seeding that are expected to be Windows-PC based. Installation and configuration of a *channel access* (CA) server on these systems will be the appropriate integration means and should cause at most minor problems.

According to the excellent experiences at BESSY, *Controller Area Network* (CAN) is the preferred choice for the BESSY FEL field bus. BESSY will also take advantage of EPICS' flexibility and maturity: the vendor supported data exchange network used by the PLC systems controlling the RF IOTs is based on Profibus. In recent developments even simple units (e.g. BPMs) are already directly connected to the Ethernet as network attached devices. Here any solution will be seriously considered that promises simplicity, reliability, enhanced capabilities, or cost savings.

13.2.2 Horizontal Topology

The entire facility consists of a few major functional units: electron injector (domain source S, figure 13.2), linac sectors (A), FEL amplifiers (F), beamlines (L), experimental stations (E) and ancillary systems (C, G, V). These “domains” are relatively independent with respect to basic operational procedures, cabling requirements and supply constraints. They have to be strongly coupled by a fast and reliable backbone connection supporting the rapid flow of diagnostic data and timing relations.

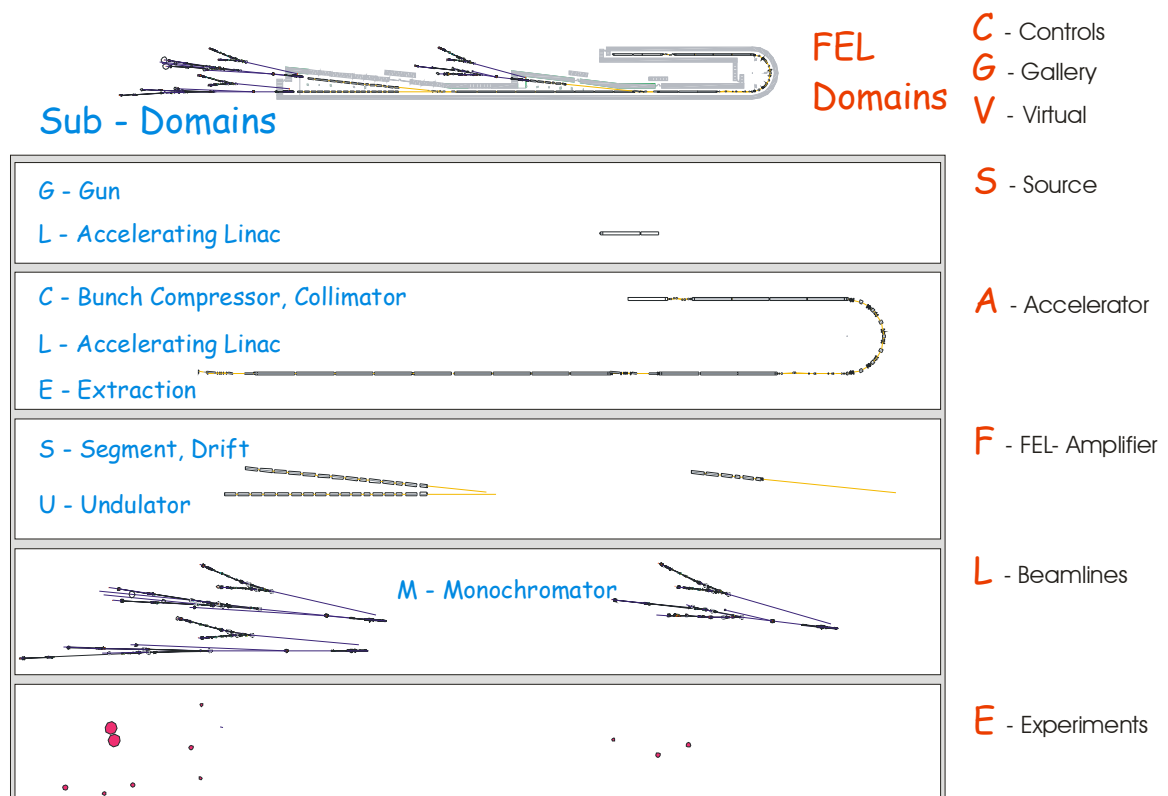


Fig. 13.2: Device grouping according to operational requirements.

For a maximized availability and a minimal crosstalk of perturbances it is helpful to reproduce the facility domains by specific control system areas: dedicated boot, file and application services on dedicated network segments will be assigned to each domain.

For complete transparency to all control system tools the EPICS CA protocol has to be common to all subsystems. Additional network services based on Corba, Java or WEB Services will be provided as needed. For all “intelligent” components, provision for remote configuration, supervision, and maintenance will be incorporated in the system.

Troubleshooting and maintenance in general will be supported by mobile consoles, wireless LAN and PDA integration.

13.3 Data Model: Devices, Device Classes

13.3.1 Goal: Complete Control-System Model

It is commonly agreed that optimal quality assurance for complex control system software requires the application of formal design and verification methodologies. At the beginning of the project general functionality requirements and specific control system use cases should be well captured to be able to model software entities, interfaces, attributes, dependencies, etc., in a consistent way [7]. Within the framework of a control system model appropriate cycles of documentation, implementation, and change requests can be established. A structured construction and test process becomes feasible. The resulting system most probably complies with accepted software quality characteristics standards (such as ISO 9126, figure 13.3).

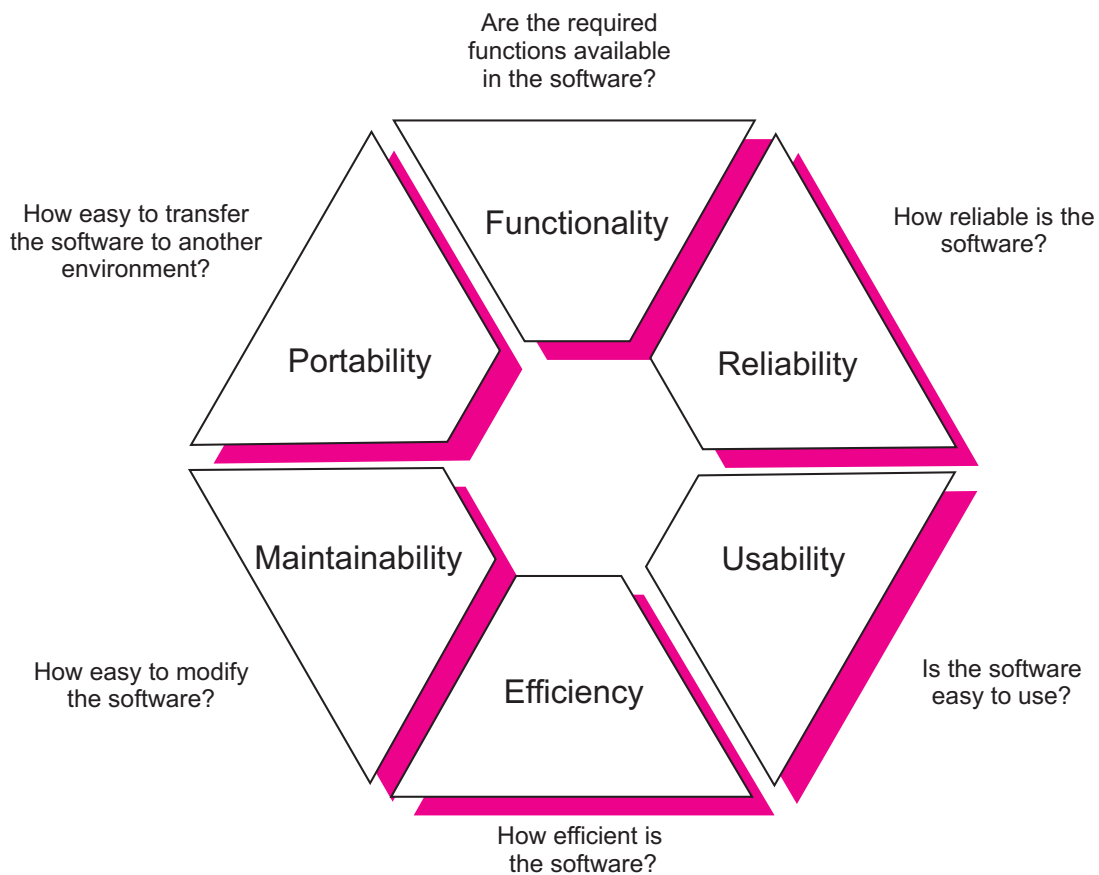


Figure 13.3: ISO/IEC 9126: The six quality characteristics of software.

13.3.2 Starting Point: Consistent Data Model

For accelerator control systems it is frequently not feasible to adhere to such a superior procedure. Despite the lack of a common control system model at least a common *data model* has been well established within the accelerator controls community: Entities to be controlled are “devices”, grouped into “classes” with certain “behavior”, “attributes”, and “events”. Identification of a specific device is mediated by its association to a certain domain, sub-domain, the location, and then by an enumerator.

This core data model is contained in the naming convention. The device names serve as bootstrap information pointing into a fully developed relational database holding all required configuration data. This common data model allows for adopting available generic applications and a base configuration management on a relational data base system (RDBMS). Even integration of specific modules from a different control system is relatively easy as long as the device data model is applied.

13.3.3 I/O Requirements: Device Classes

Hardware specifics of beam accelerating and guiding elements, undulator structures and monochromators at light sources are very similar. Within the EPICS collaboration a huge repository of various hardware drivers exists. The bulk of the devices needed for the FEL are very similar to those already installed at BESSY II or at another light source of the EPICS collaboration:

Even if requirements for control I/O cover literally all levels of equipment complexity or multiplicity: For most of the devices within these different device classes at least a similar sample unit exists at BESSY II or at another EPICS site. Complex device collections such as “perturbation-corrected” undulators are also fully implemented. Virtual “group” devices and state-changing sequences for various operational conditions and procedures exist. For low-level remote control of new (modern or sophisticated) equipment mostly only modification of existing codes is needed instead of new software design and creation.

In addition, there is a change in industry: An increasing number of laboratories already tender equipment with EPICS-ready device specifications (e.g. power supply, klystron) and vendors seem to accept these requirements [9].

Table 13.1: Basic device classes at light sources.

Power supplies	Stability (1ppm), performance (1kHz)
Magnets	Beam guiding elements, kicker, septa
RF system	Amplifier, cavity, circulator, low-level controls
Vacuum	Valves, gauges, pumps
Insertion devices	Movers (motors), encoders,
Beamlines	Front-end, absorber, shutter, valves
Monochromators	Gratings, mirrors, slits
Global timing	Trigger delays, scaler, counter
Feedback systems	Digital loops (FPGA, DSP), coupler, piezo-oscillators, kicker
Diagnostics	Current transformer, BPMs, screens, frame grabber, transient recorder, oscilloscopes, beam loss monitors
Interlocks	Beam permit, device protection, personnel safety
Intelligent subsystems	PLC units, laser systems, cryogenic units
Ancillary systems	Power, water, air conditioning, compressed air

13.3.4 Sub-Systems

Independent of the general control-system design, specific requirements frequently suggest solutions of certain control aspects within more localized and autonomous sub-units. The reason for this may be demands on speed or precision, existing in-house expertise, vendor constraints, savings in implementation effort, pool of spare parts, etc. From the global control system the capability to integrate these complex sub-systems in a transparent and robust way is claimed. For the BESSY FEL some anticipated control sub-systems have already been analyzed and are described within this document: controls of seed lasers (chapter 4), low-level RF (chapter 6), undulators (chapter 9) and instrumentation (chapter 12).

13.4 Control System Applications

13.4.1 Generic Applications

The generic applications available in the EPICS toolkit are well suited to cover all requirements during device test and installation as well as during facility commissioning. A

choice of display managers (*dm2k*, *edm*, *jdm*) will provide engineering screens for low level device control, synoptic views for navigation, status, alarm, and trending for short-term supervisory tasks.

Warnings or faults of major device collections (e.g. power supplies) or complete sub-systems (e.g. cryogenic) can be monitored by the alarm handler application (ALH). Configurations of the ALH can be generated from the central database. Tree-structured navigation guides the operators to the problem (area) and provides the appropriate device control displays.

For “slow” trends and correlations (< 1 Hz) a versatile background archiving and retrieval environment will be available [10]. It is capable of collecting data from several thousand sources and cover years with an average resolution of a few seconds. Complementary instances of a 10 channel strip-tool are available for specific tasks during a shift.

The “application” tools report significant actions, experienced exceptions and monitored events into a database (*CMLOG*) [11]. This is a valuable tool for tracking back to primary sources of malfunctioning and analysis of system functionality.

The powerful *SDDS* toolkit [12] comprises nearly 100 programs with many options and methods for measurement procedures, control and correction tasks, data taking, analysis and display. For commissioning this provides an effective base system for ad-hoc measurement tasks as well as for rapid prototyping and test of control mechanisms.

13.4.2 Beam Steering and Shaping

For high-level software requiring sophisticated online model descriptions like dispersion-free steering there are a number of implementation options. Some laboratories rely on commercial tools (e.g. *Accelerator Toolkit* based on *matlab* [13], SLAC), others embed their favorite modeling engine into their specific environment (BESSY, KEK, SLS). In a more recent approach the concept of a generic application framework is very promising. First implementations are *XAL* [14] at SNS or *Abeans* [15] at CosyLab. The advantage of a common framework is the possibility to exchange and integrate developments carried out at other labs [16].

13.5 New Challenges

In addition to the bread-and-butter requirements of general accelerator slow controls as they are implemented at BESSY II, the FEL requires some specific solutions for very demanding control tasks.

13.5.1 Process Tuning

For FEL tuning and smooth operation, feedback loops of very different scopes will be required. They will range from local beam tweaking to very comprehensive schemes that allow the control system to feedback signal quality and coincidence levels at the experiment to the various sources of drift and jitter.

In this context the low level feedforward and feedback systems needed for the linac cavities to compensate and control jitter and microphonics cover only a specific area. They are very sophisticated as such and crucial for the FEL performance. An existing control hardware [17] will be installed, studied and possibly tuned at the HoBiCaT test facility. For operations these low-level RF control systems have to be integrated into the global EPICS environment to allow for status supervision, parameter adjustment, and external control loops.

As a general framework a powerful infrastructure of generation and distribution of timing fiducials to most technical subsystems is needed. Experience with predecessor timing systems at APS and SLS and the expertise from the event generator manufacturer [18] have been combined for the installation at the Diamond light source [19] which is today's most advanced timing set-up.

13.5.2 Machine Protection

In view of the very high electron and photon beam intensities, thermal susceptibilities of a large 1.8 K cryogenic installation and the complex and ultra-sensitive mechanical and magnetic set-ups, safety control systems play a major role for the FEL: personnel and equipment protection systems have to rule out hazards due to prompt ionizing radiation, oxygen deficiencies, laser radiation or damage of equipment.

The design of the safety systems will be in accordance with the commonly accepted formal standard for Europe (IEC 61508) to ensure the proper implications from the assessment of hazard severity, likelihood, impact and exposure. For each safety system the appropriate Safety Integrity Level (SIL) has to be determined (figure 13.4). A demonstration of the specified protective actions will not be sufficient to accept the proposed engineering design and implementation: The entire hardware and software set-up has to be tested in order to verify that it is suited to fully ensure the required SIL.

DEMAND MODE OF OPERATION		
Safety Integrity Level (SIL)	Average Probability of Failure on Demand	Risk Reduction
4	$\geq 10^{-5}$ to $<10^{-4}$	>10,000 to $\leq 100,000$
3	$\geq 10^{-4}$ to $<10^{-3}$	>1000 to $\leq 10,000$
2	$\geq 10^{-3}$ to $<10^{-2}$	>100 to ≤ 1000
1	$\geq 10^{-2}$ to $<10^{-1}$	>10 to ≤ 100

CONTINUOUS MODE OF OPERATION	
Safety Integrity Level (SIL)	Frequency of Dangerous Failures Per Hour
4	$\geq 10^{-9}$ to $<10^{-8}$
3	$\geq 10^{-8}$ to $<10^{-7}$
2	$\geq 10^{-7}$ to $<10^{-6}$
1	$\geq 10^{-6}$ to $<10^{-5}$

Figure 13.4: Safety Integrity Levels: Metric for risk reduction requirements [20].

13.5.3 Diagnostics

Today, several solutions exist for profile and screen monitors with their specific requirements on data burst transmission or local pre-processing capabilities. For meaningful shot-by-shot analysis and correlations, novel techniques for store and retrieval within huge data sets are needed. For the given high data throughput of the numerous diagnostic units the relational data base (RDB) data store might be an interesting solution. An RDB-based data logging system is presently under study at SLAC and at BESSY and shows promising results [21].

References

- [1] M. E. Thuot, M. Clausen, L. R. Dalesio, T. Katoh, M. E. Kraimer, R. Müller, H. Shoaee, W. A. Watson, *Proc. of the XVIII Int. LINAC Conf.* (1996) 611.
- [2] J. Bergl, B. Kuner, R. Lange, I. Müller, R. Müller, G. Pfeiffer, J. Rahn, H. Rüdiger, *Proc. of the 1997 PAC* (1997) 2493.
- [3] R. J. Bakker, T. Birke, B. Kuske, B. Martin, R. Müller, *Proc. of the 6th ICALEPCS* (1997).
- [4] R. J. Bakker, J. Bergl, T. Birke, B. Kuner, B. Kuske, R. Lange, B. Martin, I. Müller, R. Müller, G. Pfeiffer, J. Rahn, H. Rüdiger, *Proc. of the 6th EPAC* (1998) 1676.
- [5] <http://EPICS-2010.desy.de>.
- [6] http://www-csr.bessy.de/control/Docs/API/nam_conv.html .
- [7] D. Beltran, M. Gonzalez, *Proc. of the 9th ICALEPCS* (2003).
- [8] T. Birke, B. Franksen, R. Lange, P. Laux, R. Müller, *Proc. of the 8th ICALEPCS* (2001) 277.
- [9] S. Hunt, *Proc. of the 8th ICALEPCS* (2001) 41.
- [10] R. J. Bakker, T. Birke, R. Müller, *Proc. of the 8th ICALEPCS* (2001) 662.
- [11] J. Chen, W. Akers, M. Bickley, D. Wu, W. Watson, *Proc. of the 6th ICALEPCS* (1997) 358.
- [12] M. Borland, SDDS (Self-Describing Data Set), User's Guide for SDDS-compliant EPICS Toolkit Version 1.5, Advanced Photon Source, Argonne, IL, USA: <http://www.aps.anl.gov/asd/oag/software.shtml>.
- [13] A. Terebilo, SLAC, Particle Accelerator Modelling Toolkit: <http://www-ssrl.slac.stanford.edu/at>.
- [14] J. Galambos, C. M. Chu, W. D. Klotz, T. Pelaia, A. Shishlo, C. K. Allen, C. McChesney, I. Kriznar, M. Plesko, A. Pucelj, *Proc. of the 9th ICALEPCS* (2003); <http://sns.gov/APGroup/appProg/appProg.htm>.
- [15] <http://www.cosylab.com>.
- [16] Workshop on Automated Beam Steering and Shaping, San Jose, Ca, USA (2001): <http://www-project.slac.stanford.edu/abs2001/Default.htm>.
- [17] M. Liepe, S. Belomestnykh, J. Dobbins, R. Kaplan, C. Strohman, *Proc. of the 2003 PAC* (2003) 3347.
- [18] Micro Research, Finland: <http://www.micro-researchfinland.fi>.

- [19] Y. Chernousko, A. Gonias, M. T. Heron, T. Korhonen, J. Pietarinen, *Proc. of the 9th ICALEPCS* (2003).
- [20] K. L. Mahoney, *Proc. of the 9th ICALEPCS* (2003).
- [21] EPICS Meeting Spring 2002, BESSY, Germany:
<http://www-csr.bessy.de/control/Epics02/Agenda.shtml>.

14 Alignment

14.1 Surveying and Alignment

The consequences of a missteered electron beam on the performance of the FEL, especially regarding the undulator sections has been discussed earlier in this report. However, as at all accelerators it is useful to distinguish effects originating from

- Non-ideal positioning of beam-transport elements on an absolute scale, and
- Time-dependent position drifts of relevant elements.

While the first class of effects can be attacked by conventional alignment tools to a precision in the $1/10$ mm range or better depending on the system involved, the latter is related more to the alignment philosophy during operation of the machine.

State-of-the-art equipment such as a laser tracker in combination with a digital level can assure a proper mechanical positioning. However, the position tolerances of the machine components, accelerator, and undulators, are not achievable with standard procedures alone. With the conventional alignment methods an excellent pre-alignment is possible to achieve a sufficient initial accuracy for the following beam-based alignment.

14.1.1 The Geodetic Reference Frame

Despite the large scale of the project, it is not necessary to project the observed angles and distances into the used local planar system, since the horizontal position differences between the projection of points on the geoid, or a best fitting ellipsoid, and those on a local tangential plane are not significant. In the vertical plane, however, the curvature of the earth needs to be considered. For distances as short as 20m the deviation between a plane and a locally best-fitting sphere is already 0.03 mm.

Due to the global alignment tolerances and the relatively weak links between the machine sections, each machine section can be considered independent, only connected by the attendant network. Using a 3-D free stationing approach, traditionally, forced-centered 2+1-D techniques are no longer necessary and heavy-duty metal tripods or stands are no longer needed. However, the network design must consider other systematic error effects such as lateral refraction. Another aspect is the target reference system. Using free stationing we are dealing only with targets and not with instruments. This approach is centered on a sphere, in which different targets can be incorporated such as theodolite targets as well as glass or air corner cubes for distance measurements. The spheres will be placed in so-called nests mounted on the machine components or fixed at the concrete walls or in the floor.

The geodetic network consists of four subareas: injector, linac, undulators, and transport/experimental area.

Due to the loose positioning tolerance requirements of the injector components, standard networking design and measurement techniques can be used. A horizontal sight through the shielding wall between injector and linac hall must be considered.

Like the injector components the components of the transport line have relaxed positioning tolerance requirements. Hence, standard networking design and measurement techniques can be used. The network for the transport lines will be constructed and established similar to that of the linac and the undulator hall network.

14.1.2 Alignment Coordinate System

The alignment coordinate system will be a right-handed Cartesian system. The origin will be linked to the BESSY II storage ring system, i.e. the injection point of the storage ring is at $x = y = +200.000$ m. This is to avoid negative coordinates for the elements.

The most efficient instrumentation for the network observation will be the combination of a laser tracker with a digital level. Laser trackers will mainly contribute to horizontal position accuracy and digital levels to vertical position accuracy. The laser tracker will be placed successively between adjacent reference-point cross sections of the tunnel network. Nine points in the forward direction and nine points in the backwards direction will be observed from that point. All of these points will also be measured with the digital level in combination with an invar rod.

To reduce the data from the laser tracker measurements, special analysis software, based on the photogrammetric bundle approach, will be used. To reduce errors during the measurements, all data flow must be automated. All instruments have to support direct connection to field computers. All measurements will be guided by software based on rigid procedures running on the field computers. The software will preanalyze the measurements, in an attempt to determine and flag possible outliers before the measurement setup is broken down.

14.1.3 Fiducialization

The affixing of fiducial marks on the individual components is called fiducialization. The fiducialization of the FEL components must be performed with the accuracy required in the position measurements themselves since an error in fiducialization and an error in alignment cannot be distinguished from each other. In particular, the adjustment of the fiducials has to be done very precisely in respect to the magnetic reference features of the magnets and undulators. The most demanding task is the vertical positioning of the undulators. From tolerance studies a precision of 0.05 mm over their total length is required

to avoid orbit corrections. Since the undulators will be aligned relative to their adjacent quadrupoles, both the undulators and the quadrupoles need to be fiducialized to better than 0.05 mm.

A free-standing laser tracker, oriented by means of at least four reference points, will be used for the positioning measurements. The tracking capability of this instrument will significantly aid in facilitating the control of any alignment task, including the moving of components into their positions.

The positioning of the undulators will be carried out in several steps. Beginning with the marking of positions for the component supports on the floor and ending in surveying and adjusting using a laser tracker, an overall absolute position accuracy relative to the reference network of about 0.150 mm can be achieved.

Once the first positioning of all components is completed, they will be mapped as a quality control measure. If any residuals exceed the given tolerances, a second iteration of alignment and quality control survey has to be performed.

14.2 Beam-Based Alignment

With an HGHG-FEL scheme the orbit of the electron beam has to be straight to within $\pm 5 \mu$ all along the sequence of modulators and radiators. This is mandatory in order to have a close to perfect overlap between the light and the electron beam. The requirements cannot be met by conventional survey and alignment techniques alone. With conventional means an accuracy of $\sim 100 \mu\text{m}$ over a distance of ~ 50 m for the absolute positioning of elements is achievable. This is true also for the actual positioning of the BPM stripline sensors. Thus the measured absolute electron beam position will be of similar uncertainty of $\sim 100 \mu\text{m}$. Beam-based alignment is a solution to this problem commonly used in LINAC and in storage ring based light source [1, 2].

The beam-based alignment approach is schematically illustrated in figure 14.1 which shows the setup of the two-stage HGHG-FEL planned as source of low energy photons.

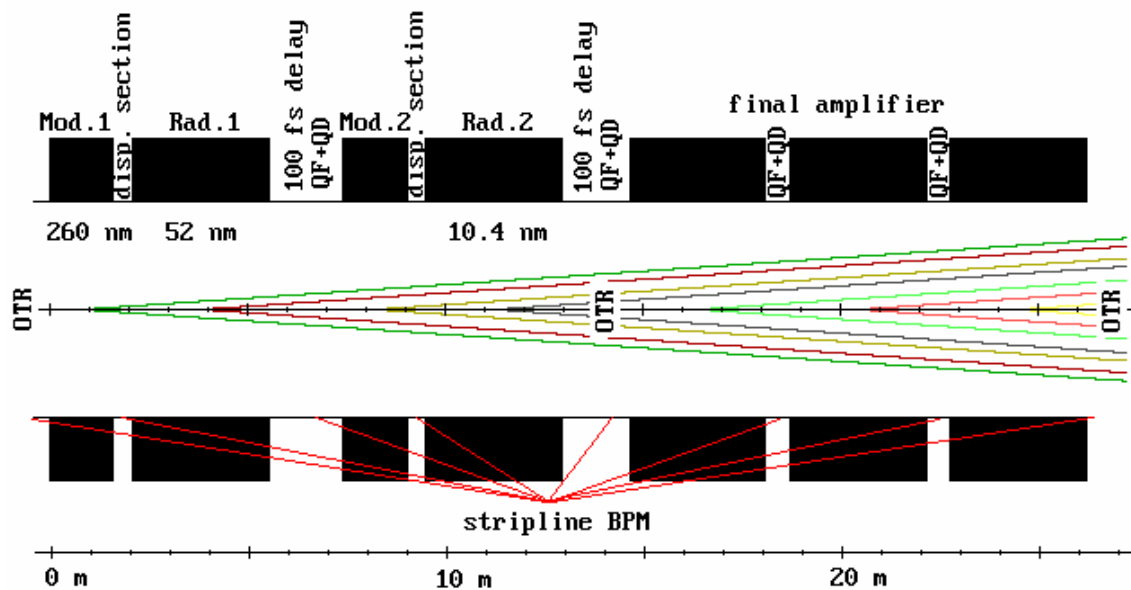


Fig. 14.1: The two stages of the proposed LE-FEL for the creation of radiation at 10.4 nm.

The 260 nm laser beam exchanges energy with the electron beam in the first modulator (Mod. 1) and the energy modulation is turned into a density modulation in the dispersive section. The part of the density modulated electron bunch produces strongly enhanced radiation at 52 nm, the fifth harmonic, in the first radiator (Rad. 1). This first stage is followed by a chicane which delays the bunch by 100 fs such that the 52 nm radiation interacts with a fresh part of the bunch in the second modulator (Mod. 2). Once again the energy modulation is turned into a density modulation in the next dispersive section. Now enhanced radiation in the fifth harmonic is emitted at 10.4 nm in the second radiator (Rad. 2). This is the final wavelength as chosen by the user. The power level is increased with a fresh part of the bunch in the following three modules of the final amplifier. Between all the undulator sections stripline sensors for BPMs are located which are aligned to the above mentioned absolute positioning errors of $\sim 100 \mu\text{m}$. Furthermore, there are correction dipole magnets to steer the beam. At some locations focusing and de-focusing quadrupole magnets are required for controlling the electron beam size. All together three Optical Transition Radiation (OTR) screens can be moved into the path of the electron and the laser beam.

Beam based alignment would proceed in the following way: At first a straight line has to be defined which has to lie within the positioning tolerances of $\sim 100 \mu\text{m}$ for all the undulator segments. This line can be found by one of the two co-propagating beams and with OTR screens carefully aligned relative to the string of undulators. With the OTR

screen mounted under 45 degrees to the nominal beam axis, the reflected laser beam can be viewed by blue sensitive CCD-cameras thereby designing the straight line. In figure 14.1 light beams with 1 mrad divergence are shown. The beam size will be enlarged further due to diffraction effects inside the small beam tube of 8 mm full inner diameter. Similarly by opening all undulator gaps and by turning off all bending and focusing fields along the path of the electrons this beam can be used for the same purpose. The electron beam will also be observed on the OTR screens. With the small transverse emittance of the electron beam its blowup is tolerable. This approach is called ballistic alignment. The OTR screens have the advantage that both the laser and the electron beam can be viewed at the same time. With a blue sensitive streak camera the correct timing at the ps-level and thus the longitudinal overlap can be verified. Once the transverse overlap of the electron and the laser beam has been found, the screens are retracted and the readings of the BPMs are recorded. This is the reference beam. In the next step the focusing elements are set to their nominal values one by one and the initial position of the electron beam is restored with the help of the steering magnets adjacent to the newly set quadrupole magnet. It would be of advantage to include these correctors directly into the quadrupole magnets. Finally the gaps of the undulators are closed one after the other and once again correcting elements located nearby are used to reestablish the reference position of the electron beam as well as possible.

Since the resolution of the BPMs is at the 1 μ -level we can expect that the beam will be straight at the 5-10 μ level after this alignment procedure. This figure is given by the length of the undulator segments and the error distribution inside the undulator. The worst case arises from a kick error located in the middle of the undulator. Since the BPM and the correctors are located outside the undulator i.e. about 1.8 m away from the kick, a perturbation, Θ_{err} , leads to a corresponding orbit distortion after correction which remains at a level of $1.8 \text{ m} \cdot \Theta_{\text{err}}$ inside the undulator. However, kick errors occur most likely at the ends of the undulator segments close to where compensating steering elements are available [3]. Thus, the resulting orbit wander will be smaller than $\pm 5 \mu\text{m}$ over the total length of the HGHG-FEL.

In case OTR screens are intolerable due to the excessive radiation levels produced inside the permanent magnets of the undulators, these screens have to be replaced by pairs of thin wire monitors. The detection of the laser beam would then require higher sensitivity as given for example by micro-channel plates. The overlap between the electron beam and the wires could be detected with beam loss monitors observing the resulting rate of scattered electrons further downstream. Scanning wire monitors and the corresponding data acquisition processes are more complex than the OTR screens. Therefore, these screens are the preferred method for determining the transverse and longitudinal overlap of the light and the electron beam whenever possible.

References

- [1] B. Faatz, Beam Based Alignment of the TESLA X-ray FEL undulators, TESLA FEL Report 2001-04 (2001):
http://tesla.desy.de/new_pages/FEL_Reports/2001/pdf_files/fel2001-04.pdf.
- [2] P. Kuske, H.-G. Hoberg, J. Machado, R. Maier, A. Schiele, *Proc. of the 1st EPAC* (1988) 1214.
- [3] J. Bahrtdt, private communication.

15 Conventional Facilities

15.1 Civil Construction: Site and Buildings

15.1.1 Site Selection

The existing buildings and technical infrastructure on the BESSY site, shown in figure 15.1, were constructed in the 1990's for the synchrotron radiation source BESSY II [1].

The BESSY site forms an isosceles triangle with the circularly shaped experimental hall and storage ring building nearly in the center. The almost 500 m long base line parallel to the Teltow canal offers an ideal site for the FEL [2].



Fig. 15.1: Aerial view of the BESSY site at Berlin-Adlershof.

Geologically, the area is part of the Berlin-Warsaw glacial valley. A two-layer structure characterizes the ground. On top there is a 0.2-2 m thick deposit of replenishment. It consists of sand with inclusions of objects (bricks, concrete, other) resulting from the anthro-

pogenic activities of the last century. Underneath, sands of fine and medium scale granulation have a thickness of 15 m. There is a weak humus layer in the upper region, and a 0.1 m thick interlayer of clay and silt at a depth of 6.5 m. The ground-water level is located between 2.0 and 2.4 m. Thus, no difficult soil and foundation conditions, which otherwise could lead to technical difficulties, are anticipated. Also, sump-pump drainage to lower the ground-water level will be necessary only to a limited degree or not at all. Some soil replacement may be required.

15.1.2 Ground Stability at the BESSY FEL Site

For the FEL a well-aligned and stable electron beam path is essential for optimum performance. Potentially harmful vibrations of the linac components, including bunch compressors, cavities, and undulators need to be considered. The most important sources for vibrations are ground motion due to civil noise and self-made noise from infrastructure on site coupling to various devices via girders, stands, cables, etc. Measurements were performed to quantify the magnitude and spectrum of the ground motion at the BESSY FEL site.

Typical vertical motion as a function of time measured at two different locations on the BESSY FEL site is shown in figure 15.2, the maximum amplitude being up to 250 nm. Similarly, measurements of the horizontal motion yield values up to 200 nm, confirming earlier investigations [3].

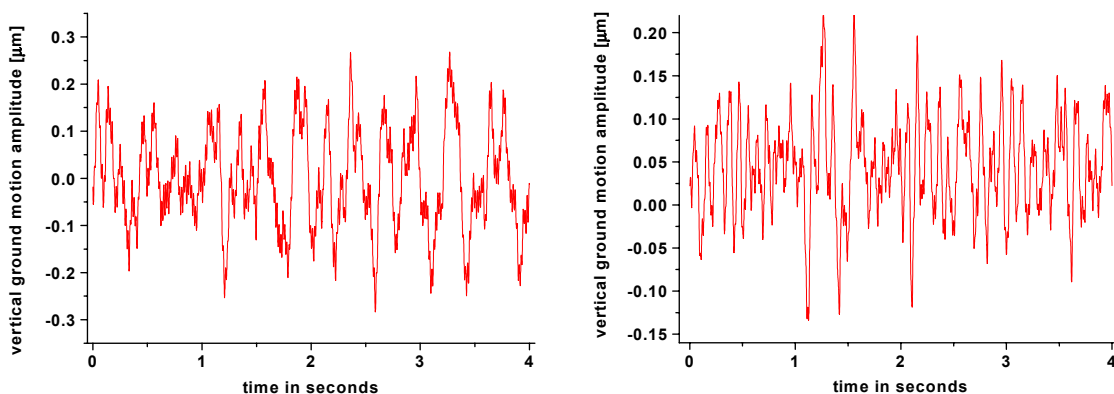


Fig. 15.2: Vertical ground motion measured at two locations on the BESSY FEL site.

A frequency analysis of the data reveals typical civil noise as generated by public traffic. However, a 55 Hz component is recorded in both planes which is the characteristic frequency of the gyrators in the BESSY II uninterruptible power plant. Also the 10 Hz booster repetition frequency is visible in the spectra during injection of the BESSY storage ring. Both sources are controllable by BESSY.

To evaluate the impact of the different excitation sources on the total amplitude, the integrated spectral density, normalized to its value at 60 Hz, as a function of frequency was calculated (figure 15.3). In the worst case the total amplitude reaches 250 nm. While the 55 Hz causes only a tiny increase of the amplitude, civil noise in the frequency range ≤ 10 Hz dominates the ground motion amplitude; the 10 Hz component, however, adds a 25% contribution to the total vertical amplitude. Since the booster typically runs three times a day for about 10 minutes, the overall rms amplitudes are less than 150 nm most of the time. All relevant frequencies could be identified. Work is in progress to reduce the controllable part of the noise level as produced by the BESSY infrastructure on site.

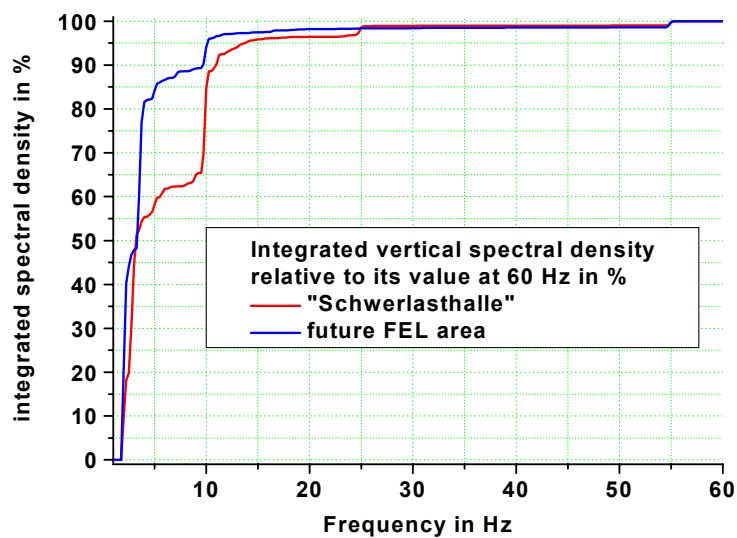


Fig. 15.3: Frequency integrated vertical spectral density relative of its value at 60 Hz.

15.1.3 Buildings for the FEL Facility

Concept

As shown in figure 15.4, nearly all of the BESSY FEL facility will be housed in a single building, whose function is purely that of a protective enclosure and facade. It houses the injector, linac, undulators, beam lines, experiments, the dedicated supply systems, and staging areas for the linac modules. Where necessary, additional enclosures within the main building are adapted to specific needs, e.g. the radiation-shielded linac tunnel, or the clean rooms for handling the linac modules. This “house-in-house” concept provides a cost-effective solution while maintaining the flexibility and upgradeability needed for a research facility [4].

Conventional installations, such as the central electric-power grid, the water-cooling systems, the helium refrigerator, the helium plant, and auxiliary equipment are located in a separate supply building (VT2). An exception is the cold box of the refrigeration system. It will be housed in the existing assembly hall. Annexes, adjacent to the injector and near the experimental area, offer space for laboratories and offices.

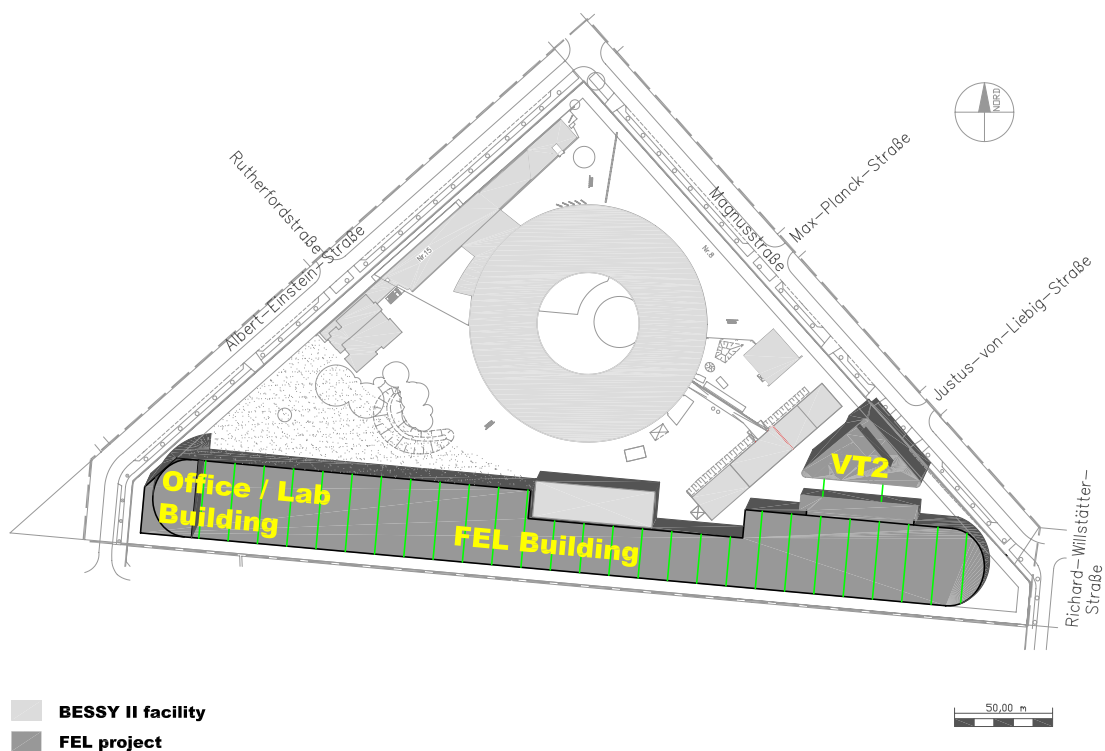


Fig 15.4: Bird's-eye view of the BESSY site.

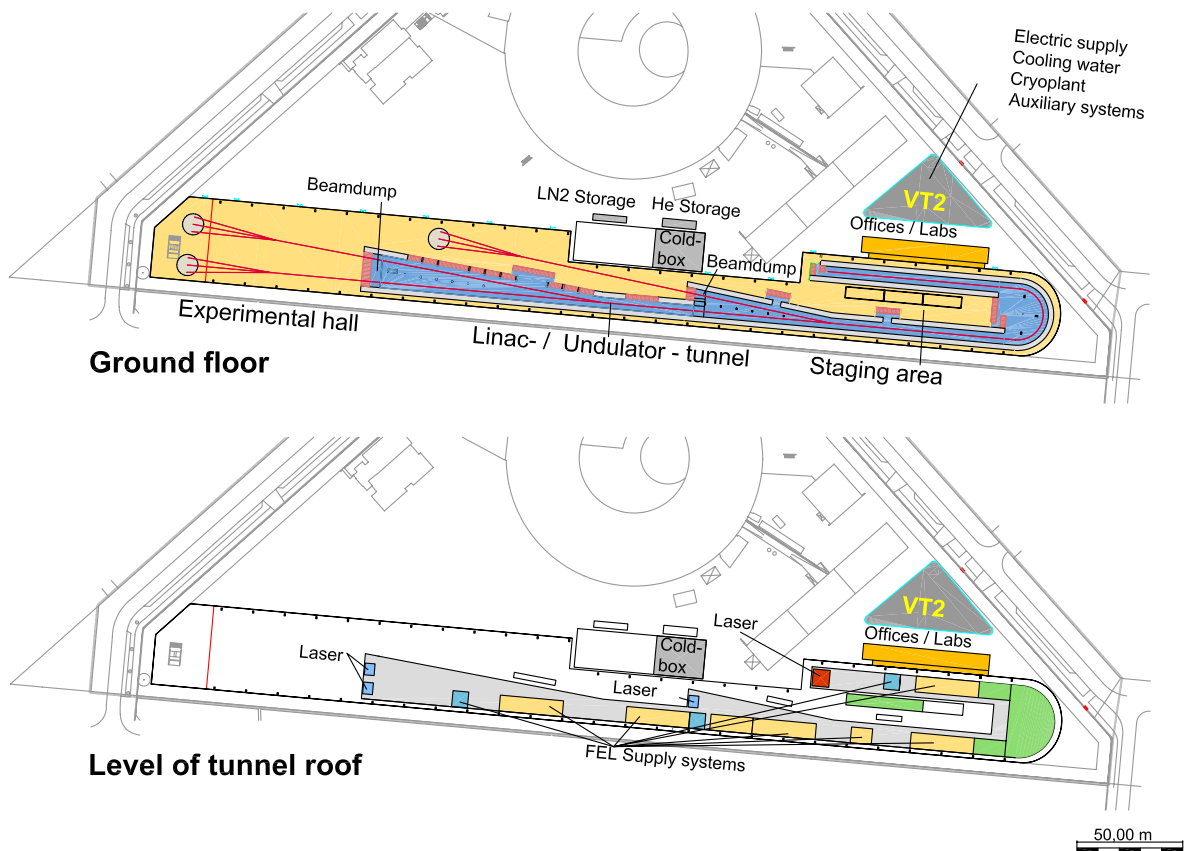


Fig. 15.5: Schematic of functional layout of the FEL building.

FEL Building

Floor plans and sections of the 430 m long, 40 m wide, and 13 m high FEL building are shown in figure 15.5. Its width is reduced to 25 m near the center to accommodate two existing buildings. The plans of the ground floor and the upper level depicted in figure 15.5 indicate their use. By placing the supply units on top of the tunnel, the equipment layout is simplified and cable lengths are minimized.

Different temperature zones with different stability requirements are indicated by the colors in figure 15.6. They are the experimental area, the radiation-shielded tunnel, the house-in-house areas, and the area on top of the tunnel where the supply units for the linac and other machine components will be located.

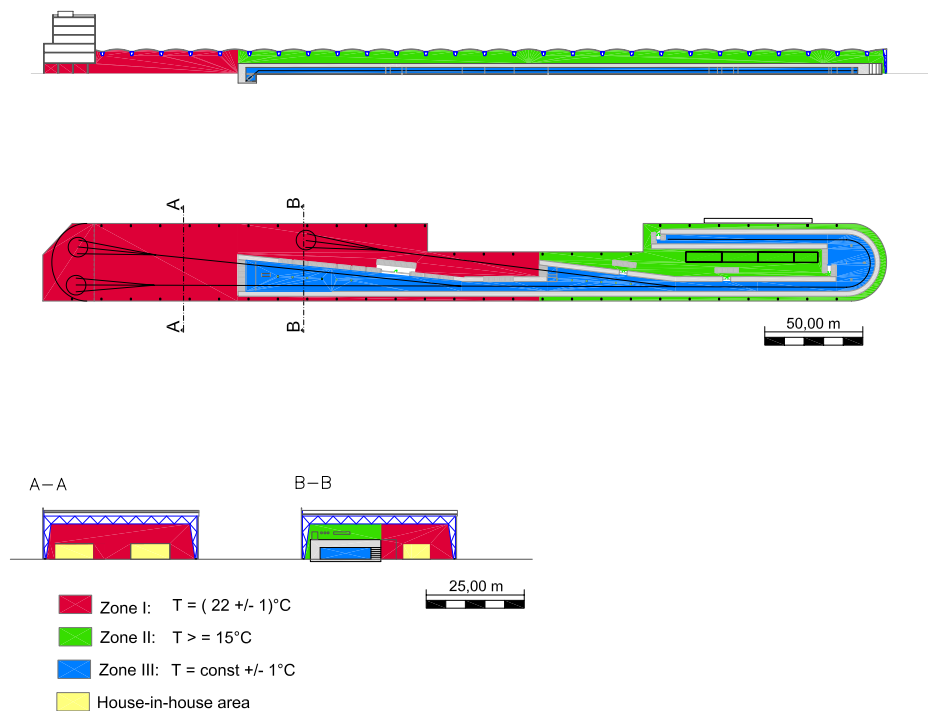


Fig 15.6: Floor plan of the BESSY FEL building. Top: Longitudinal section. Middle: View from above. Bottom: Cross section. The colors represent the different temperature zones.

The staging area for the accelerator modules is located near the return arc between the two electron-beam lines. It consists of three rooms back-to-back, one of them providing a class-100 clean-room environment.

Structural System

As illustrated in figure 15.7, the roof consists of self-supporting shell arch elements of trapezoidal sheet metal with a span of 13 m. These are supported by frame girders 2 m high and 2 m wide, spanning 39 m or two times 19.5 m. The standard distance between girders is 15 m. They bear on 2 x 2 m portal legs that are 10 m high. The latter also support the facade.

The 39 m wide experimental area is spanned completely, whereas pillars in the 39 m wide linac region support the roof at the center. Attractive features of this structure include its low dead load and its convenience to economically install service pipes and cable trays. It also contributes to the longitudinal stiffness of the building and facilitates the use of prefabricated materials. The roof construction will include a 20 centimeter thick thermal insulation from mineral wool.

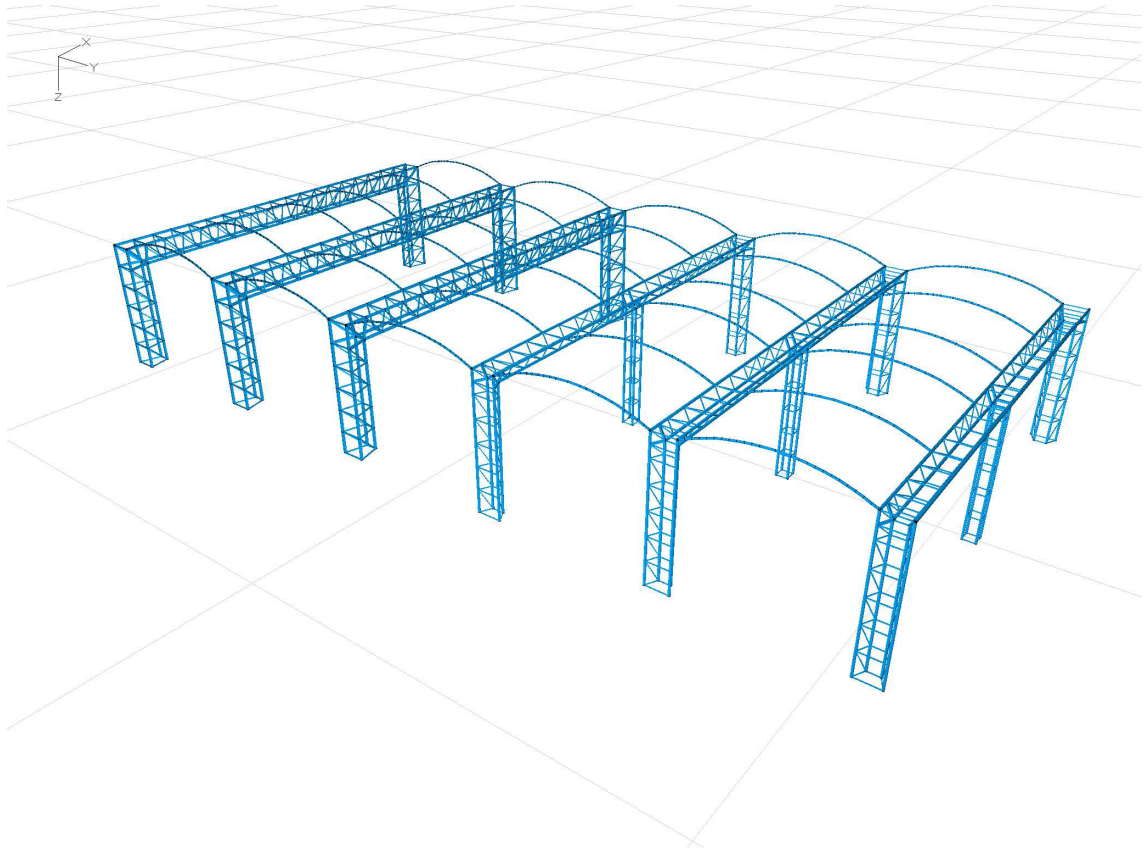


Fig. 15.7: Sketch of the structural system of the main building

Linac and Beam Transport Area

Floor plans and sections of the linac and electron-transport line are shown in figure 15.8. The entire transport line, starting at the electron source up to the beam dumps, will be housed in a common concrete enclosure. The wall thickness varies from 1.5 m at the injector to 4.5 m at the beam dump to satisfy the radiation protection requirements. After passing through the undulators, the electron beam is deflected downwards into a separately shielded cavern below ground and dumped in a water-cooled copper/aluminum cylinder buried in a concrete block. The FEL light generated in the undulators passes through the back of the beam dump shielding to the experimental area. In this region only local shielding will be employed where necessary.

The 5 m wide tunnel fans out to a width of 20 m following the beam extraction points. No ceiling supports are used in the main tunnel but pillars in the funnel-shaped region will reduce the statically relevant ceiling span; the ceiling height is 3 m. To enable openings during the assembly phase or for servicing major components, some sections of the wall will be demountable.

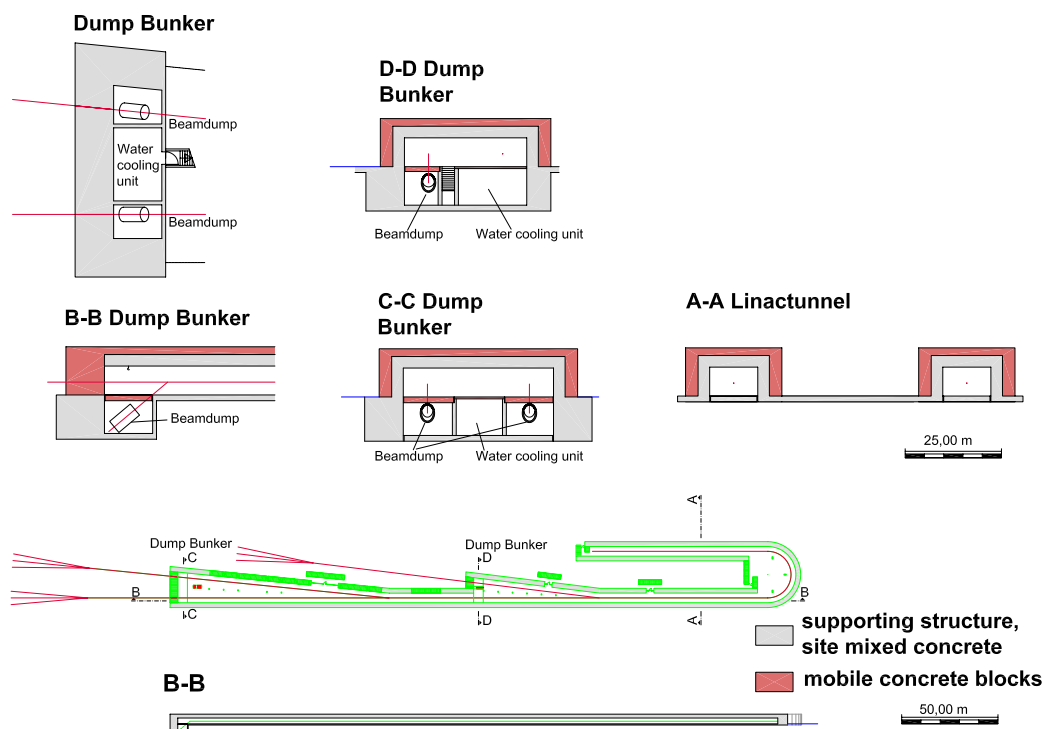


Fig. 15.8: Floor plan, longitudinal and transverse sections of the shielding tunnel.

The tunnel wall consists of 1.5 m thick steel-reinforced concrete with an additional layer of mobile shielding blocks. Further shielding will be added to fulfill the radiation safety requirements wherever necessary. Thus, the wall thickness and/or the material composition can be adapted in a flexible manner to meet the local needs.

15.2 Supply Installations

15.2.1 Electric Power Supply

Primary power for the BESSY facility is provided by the local power company via two 10 kV / 9 MVA cables from a 3 km distant substation. The present power needs of BESSY are about 4 MW. The existing 10 kV switching station on site is working near full capacity and cannot be upgraded - neither in its electric nor in its spatial dimensions. Therefore, new transformers and new switching stations have to be provided and housed. They will be fed by the existing 10 kV cables as shown in figure 15.9.

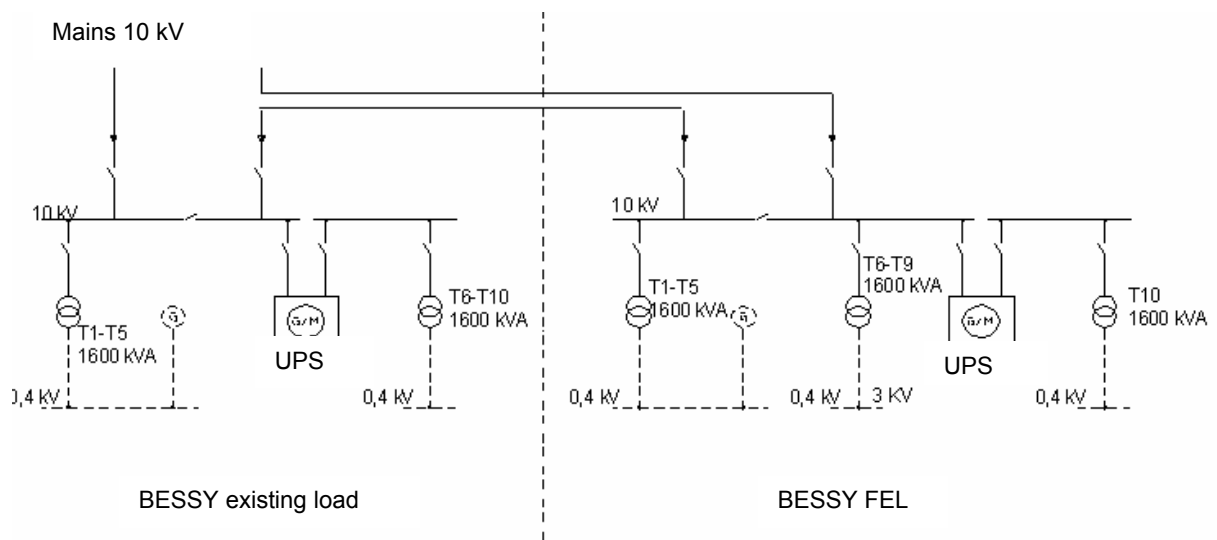


Fig. 15.9: Planned modification of the electricity supply of BESSY.

For the FEL facility the following requirements have to be met:

- Total power requirements 9.2 MW.
- A UPS is needed for a partial load of about 1.5 MW protecting sensitive components against voltage drops.
- A mains backup system for supplying power to some critical electronic components in case of a mains power failure.

An air-insulated switching station is planned for the 10 kV-level, and a structured network will be set up for the lower voltage level, mapping the structure of the FEL complex. It comprises 10 transformers dedicated to the different subsystems. Nine out of these are 10/0.4 kV cast-resin dry-type transformers. As a cost-effective solution a uniformly rated power of 1.6 MVA has been chosen, except for the compressors of the cryoplant which are equipped with high voltage motors and an appended 10/4 kV transformer. A voltage-stabilized, up to 10 seconds interruption-safe network will be installed for sensitive electronic systems like controls, computers, diagnosis, measurement and monitor devices. It is supplied by a 1.6 MVA/1.3 MW - UPS unit with kinetic energy storage.

All components will be housed in the new building VT2 north of the injector [4].

15.2.2 Cooling Installations and Ventilation Equipment

15.2.2.1 Cooling Installation

The existing cooling system, working at its full capacity, requires a new system for lost heat removal. This will be installed in the new supply building (VT2) consisting of 5 hybrid cooling towers of 2 MW cooling power each and 4 secondary cooling circuits. The latter are dedicated to the heat-generating components in the same building (*compressors and vacuum pumps of the cryoplant, refrigerator units*), those in the linac tunnel (*magnets, heat exchangers of the cooling circuits for the beam dumps*), the experimental hall and the technique areas on top of the tunnel roof (*RF installations*).

15.2.2.2 Air Conditioning and Ventilation

Different types of ventilation systems will be provided.

The experimental area has to be temperature controlled demanding partial air-conditioning. Wherever possible the experimental equipment will be housed in individually air-conditioned hutches.

The linac hall will be equipped with simple ventilation units providing recirculation and exchange of exhaust air. In addition locally installed recirculation air coolers will remove lost heat not disposed of by the cooling water.

The tunnel will be ventilated with one air change per hour covering the needs of staff working here during shutdown periods. Distributed overhead coolers equipped with ventilator inserts absorb the energy from internal sources of lost heat. Due to the large thermal mass of the concrete, this configuration guarantees a long-term temperature stability.

Due to air activation in the beam dump a stand-alone system has to be installed for the air-tight sealed dump regions. The German radiation protection law requires one air exchange per hour. The concentration of radioactive nuclei in the outlet air will be kept below the permitted limit (chapter 16). It will be released to the environment together with the exhaust air from the tunnel by one common chimney in which the activation concentration is monitored permanently [4].

15.3 Cryogenics

To reduce development time and costs, and taking advantage of the similarities between TESLA and/or the X-FEL at DESY and the BESSY FEL, BESSY is going to use the proven TESLA cavity and cryomodule technology. Modifications are only necessary to

adapt the BESSY CW system to the higher dynamic load per cavity compared to the pulsed TESLA modules [5].

The active length of the BESSY FEL is only about 300 m compared to the approximately two times 2500 m long double-cryo units of the proposed TESLA collider system, which is cooled by a single refrigerator. Whereas the required refrigeration rate of the BESSY refrigerator will be on the same order of magnitude as for one of the 7 TESLA refrigerators, the associated number of cavities and cryostats as well as the helium inventory is about 15 times smaller.

15.3.1 Cryogenic Supply Network: Cryostats, Modules, Sections

Acceleration is accomplished by using RF cavities cooled with superfluid He II. Eight cavities are grouped in one module and housed in a common cryostat. Between two and ten modules are combined in a section. The active length of the accelerator consists of 4 sections (figure 15.10).



Fig. 15.10: Layout of the BESSY FEL (INJ: injector; BC: bunch compressor; EXT: extraction point)

Between the cold sections the beam has to pass warm sections, which have differing lengths of up to 35 m, used for bunch compression and beam extraction. The cold sections will be supplied by the refrigerator with the cooling agent helium in series or partially in parallel.

Figure 15.11 shows two possible arrangements which are presently under investigation. The decision on the distribution system will be made taking into account the following aspects:

- Flexibility in installation, start-up and/or later modifications
- Available space
- Investment cost
- Cavity temperature. A parallel arrangement would allow for a lower temperature at the cavity furthest away from the refrigerator.

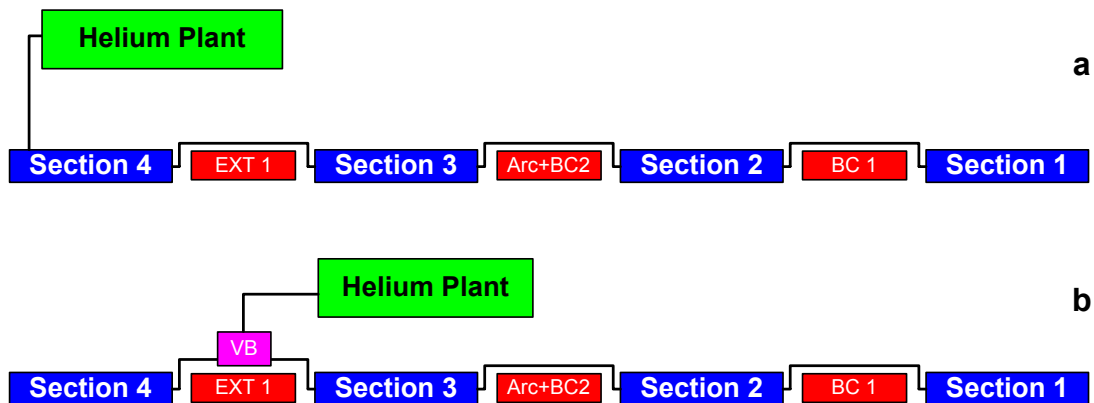


Fig. 15.11: Two options for the cryogenic distribution. Indicated: Helium plant, 4 cold sections, interconnecting transfer lines (including all cryogenic supply and return lines) and valve box (VB).

Figure 15.12 shows the design concept for the modules. The cavities are surrounded by liquid helium tanks, which are connected by a “chimney” to the two-phase line. The liquid-helium level is at 33% in the two-phase line, this being supplied by an LHe supply line via a Joule-Thomson valve. The two-phase line vents at two locations to the gas-return line. Besides the liquid and vapor line, shown in figure 15.12, there are two forward and two return lines for the 5 K and 60 K thermal shields and, in addition, a cool-down/warm-up line. All vacuum-insulated transfer lines that connect the refrigerator to the sections or the cold sections with each other will also contain these seven cold lines.

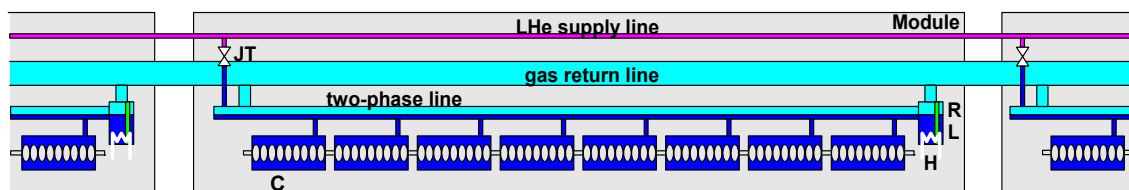


Fig. 15.12: Design concept for the BESSY FEL cryogenic module (C: 9-cell cavity, JT: Joule-Thomson valve, R: reservoir, L: Level sensor, H: heater)

15.3.2 Choice of Refrigerator Size

The design heat loads can be covered by a single large helium refrigerator as it has been built at several other locations: CERN, DESY and CEBAF. Even though there is a

large difference between static and dynamic loads, it would not make sense to split the loads between two refrigerators, because this would not increase the reliability. However, one has to design a system with very good part load efficiency, since it can be expected that the system will run for long periods on reduced loads.

15.3.3 Technology of Large Helium Refrigerators

For the last forty years, accelerator physics has been instrumental in pushing helium refrigerator technology into the direction of higher reliability, better efficiency, and lower cost. All major components of the envisaged BESSY helium refrigerator have been used successfully in similar systems.

While the design of the mechanical components is already fixed, continuous progress is going on concerning quality assurance, instrumentation, diagnostics, and computer simulation of operational conditions.

It is of advantage for BESSY, that the LHC cryogenic system will be in operation a number of years earlier. The BESSY refrigeration system has many similarities with one of the eight LHC systems.

15.3.4 Helium Storage

When in full operation the BESSY cryosystem will contain about 1 t of helium. The commercial value of the helium is about 20 €/kg, i.e. 20.000 € for the total inventory. When the cryostats are warmed up, this helium has to be handled outside the cryostats.

It is proposed to provide gaseous storage at 20 bar. Two cylindrical vessels with a volume of about 300 m³ will be sufficient.

In case of an unplanned refrigerator shutdown and an associated pressure rise in all cold systems, the helium inventory of the portion of the system, which has a high design pressure, will be directed to the 20 bar buffer. This includes the helium in the refrigerator itself and in the 50-80 K shields of the cryostats. The 5-8 K shields will be treated as part of the low pressure system to keep it operational for the purpose described in the next paragraph.

The helium of the part of the system with lower design pressure, i.e. mainly the inventory of the cavity cryostats, will be allowed to rise in pressure and temperature by the 2 K static heat load. Such a warm-up from 2 to 4.4 K will take about 10 to 20 hours. If the pressure in the cryostat exceeds a pressure of about 1.2 bar, vapor is allowed to leave the cryostat, partially also through the 5-8 K shield line. Thus, an additional static heat load to the cryostat is avoided. All emerging vapor will be warmed up to ambient by an air-

heated exchanger and compressed by a compressor, which also works on emergency power, into the 20 bar storage tanks.

The evaporation of all liquid from the cryostats by the static heat load will take about 80 hours.

Table 15.1: Estimated and design heat loads.

	Heat load (W)	COP (W/W)	Input Power (kW)
1.8 K			
Static	95		61,70
Dynamic cavity	2833 (max.)		1841,45
Dynamic supports	46		29,90
Static + dynamic	2975 (max.)		1933,75
Design	3500	650	2275
5-8 K			
Static modules	285		71,25
Static transfer line	130		32,50
Dynamic supports	97		24,25
Static + dynamic	512		128
Design	1000	250	250
40-80 K			
Static modules	1520		30,4
Static transfer line	1300		26,0
Dynamic supports	2140		42,8
Static + dynamic	4960		99,2
design	7500	20	150
Liquification	5 g/s	260	155
Total			2830

15.3.5 Model Refrigerator

A model refrigerator has been designed by the TU Dresden for the TESLA project and it is realistic to propose the same type of plant also for the BESSY FEL project. The model refrigerator allows for:

- Obtaining information on component sizes, number of compressors, flow rates in different loops etc.
- Obtaining provisional data on power consumption for the specification of utility systems and the operating budget.
- Obtaining the approximate size of components for the building layout.

The virtues of the model refrigerator were discussed extensively with experts from industry, confirming that the following important aspects of the model refrigerator are a correct basis for the planning of large systems like the BESSY one:

- The design loads can be covered by a single refrigerator with a single horizontal cold box,
- The number of planned screw compressors is adequate,
- The power consumption estimates (table 15.1) are realistic.

15.3.6 Model Refrigerator Flow Diagram

Helium is compressed at ambient temperature by a two-stage screw compressor group to a pressure in the 20 bar range. After re-cooling to ambient temperature, careful oil removal and removal of residual water vapor, the high pressure helium is cooled in HX 1 to 80 K, where it is purified from residual air in switchable adsorbers.

Then a part of the flow is split off and expanded in turbines T 1, T 2 and T 3 to about atmospheric pressure. After T 1 a part of the stream is split off and cooled in HX 3 to 40 K. Here one part of the flow leaves the cold box and cools the 40/80 K shield in the cryostats. It returns, is cooled in HX 2 and enters T 2. A pressure drop of about 1 bar is envisioned for this shield flow.

One part of the flow, already expanded in T 1 and pre-cooled in HX 3 is further cooled in HX 4 and expanded in T 4 and T 5 to atmospheric pressure. The main high pressure stream leaving the 80 K adsorbers is cooled in HX 2, 3, 4, 5, and 6 and in between purified from neon and hydrogen in the switchable 20 K adsorbers. The high-pressure stream is expanded in two parallel turbines T 6 and T 7 to an intermediate pressure of about 5 bar. The major part is further cooled in exchangers 8, 9, and 10, and is then used for the 5-8 K shield. After returning from this shield, the gas is expanded in T 8 to atmospheric pressure.

Another part of the 5 bar flow is expanded in T 9 and sub-cooled in HX 11 before flowing to the cavity cryostats. After throttling to the 30 mbar pressure level and evaporation in the cryostats, the low pressure helium vapor returns to the refrigerator through the 300 mm line in the cryostats. After superheating in HX 11, the gas is compressed in a three or four-stage cold compression system to a pressure close to atmospheric pressure, but not necessarily to above atmospheric pressure. This stream is separately warmed up to ambient in exchangers HX 4, 3, 2, and 1 and enters its own low pressure screw compressor.

Table 15.2 gives a short summary of the process parameters for the He mass flow, temperatures and pressures of the outlet and return path for the model refrigerator

Table 15.2: Process parameters of the model refrigerator.

	Mass flow (g/s)	Outlet T (K) / p (bar)	Return T (K) / p (bar)
1,8 K load	175	2,34 / 1,3	1,8 / 0,016
5-8 K shield	30	5,1 / 6,0	8,5 / 5,5
40 - 80 K shield	38	40 / 18,5	80 / 13,15
Compressor			
LP I	698	307 / 1,05	310 / 5,2
LP II	170	307 / 0,73	310 / 5,1
HP	868	310 / 5,2	310 / 19,1

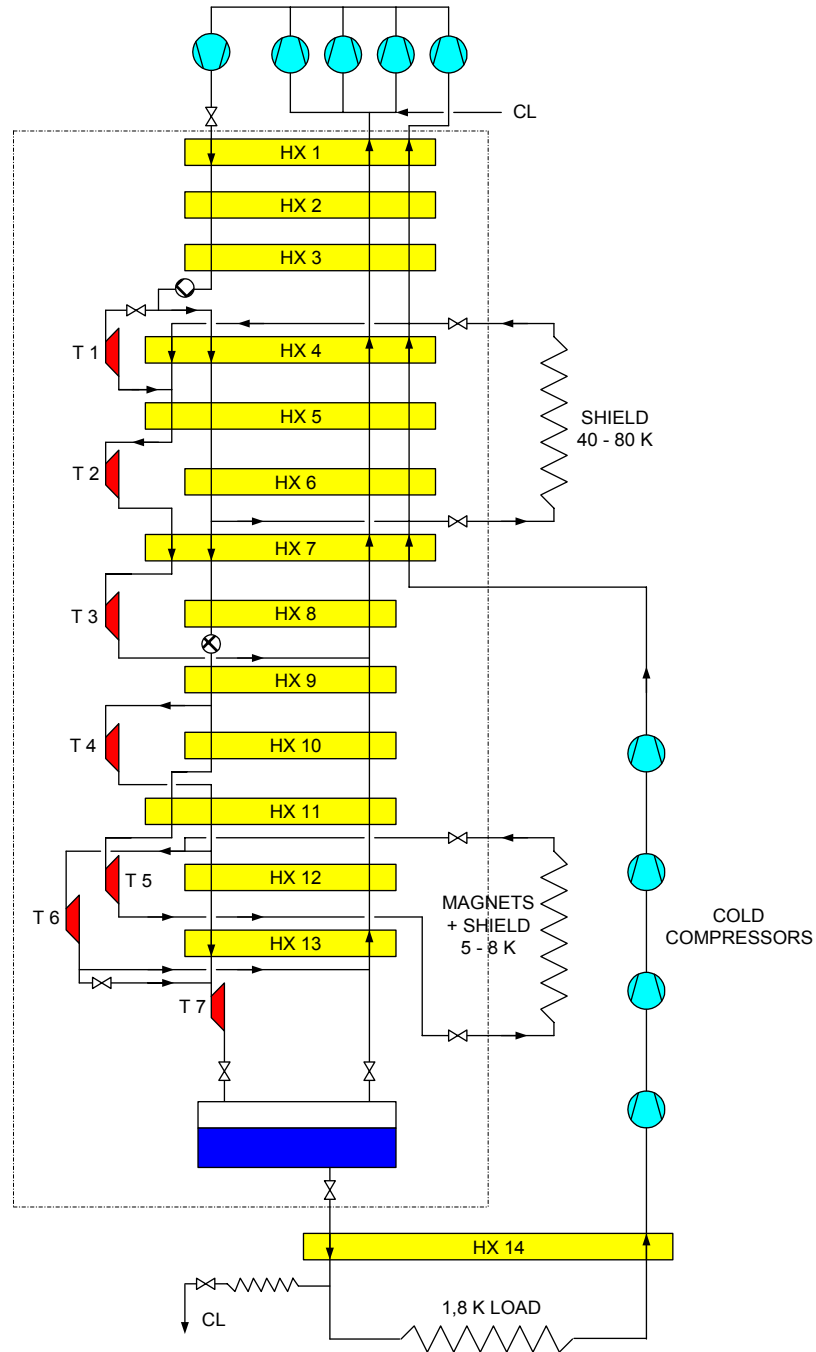


Fig. 15.13: Flow diagram of the model refrigerator.

References

- [1] H. Braun (editor), Bauen für die Wissenschaft: Institute Der Max-Planck-Gesellschaft – Building for Science Architecture of the Max-Planck-Institutes, Basel- Berlin-Boston, Birkhäuser (1999).
- [2] H. Machleidt und M. Krohn / Machleidt + Partner, Studie (2000).
- [3] J. Feikes, *Proc. of the 6th EPAC* (1998) 579.
- [4] Gutachten – Gebäude und haustechnische Ausrüstung des Projekts Freie Elektronen Laser BESSY FEL der Berliner Elektronenspeicherringgesellschaft für Synchrotronstrahlung BESSY G.m.b.H., Bauabteilung der Max-Planck-Gesellschaft z.F.d.W. e.V. in cooperation with H. Machleidt (Machleidt & Partner), C. Huboi (DGI – Bauwerk), M. Hamann (Ing. Büro Krone, Berlin), H. Bleher (Müller & Bleher, Radolfzell), G. Engelbrecht (Ebert Ingenieure, München), (2004).
- [5] H. Quack, Lehrstuhl für Kälte- und Kryotechnik, TU Dresden, private communication.

16 Beam Loss, Radiation Protection, and Environmental Safety Considerations

The BESSY FEL linac will be operated at a maximum energy of 2.3 GeV with an average beam current corresponding to a maximum beam power of the linac of 150 kW and with a superconducting injector in phase II. This beam power is sufficient to destroy the vacuum chamber wall if the beam hits a single spot for a time span ranging from milliseconds to minutes depending on the impinging angle. Thus, an active machine protection system is needed to limit beam losses. Due to electron losses, activation of machine components as well as of air, cooling water, soil, and ground water have to be considered in detail.

16.1 Machine Protection

The three FEL lines will operate initially at a bunch repetition frequency of 1 kHz each. With a bunch charge of 2.5 nC and a beam energy of ≤ 2.3 GeV the beam power is about 3×6 kW. The introduction of a superconducting injector in phase II will increase the total beam power to approximately 150 kW. The stored energy in an individual electron bunch is ≤ 6 J. At no location in the accelerator the structures can withstand this power load for more than 6 successive incidences, e.g. the vacuum chamber wall will be destroyed within 2 ms (250 μ s for the s.c. injector). Figure 16.1 shows the temperature distribution when a single bunch hits a stainless steel surface of 0.5×1000 mm², equivalent to a total beam loss at an angle of 0.1 mrad.

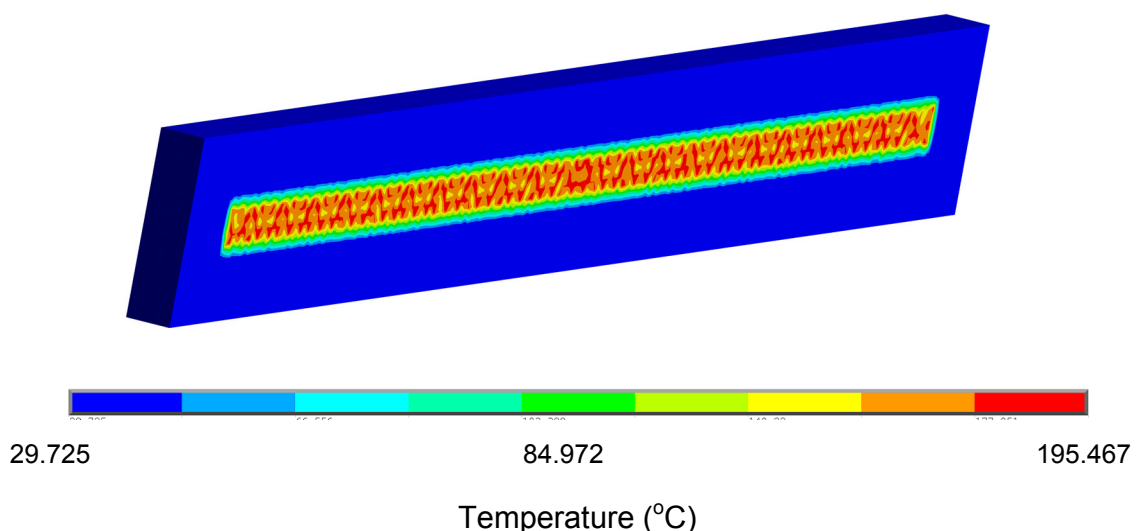


Fig. 16.1: Simulation of the temperature distribution on the vacuum chamber wall assuming the total beam loss of one bunch, and 0.1 mrad angle of incidence.

For the superconducting cavities beam loss is more critical, since in case of a bunch directly impinging on the Niobium surface, the cavity will most likely quench immediately. The goal is to limit the relative beam-power losses to below 10^{-5} , e.g. 1.5 W of the 150 kW as the mean value. This requires an adequate machine protection system (MPS).

The central sensors for the MPS will be a number of fast current monitors that allow one to measure the individual bunch charge at a precision of better than 0.2 pC. Comparing the bunch charge extracted from the injector with that finally entering the beam dump, losses of the order of 0.1% can be registered for every bunch. Fast hardwired electronics, triggering the next bunch train, will intervene if these losses exceed a level of 0.1% and the bunch repetition rate will be immediately decreased from 1000 Hz to 10 Hz. This can be done within a cycle time of less than 5 μ s, i.e. much faster than the 1 ms between two successive bunch trains. In case the losses are just below this first limit the loss power in the accelerator is about 150 W, still enough to heat components and cause desorption resulting in a localized pressure bump. The vacuum pressure readings will indicate the failure. However, the time to obtain reliable signals requires an integration time of seconds. A rough estimate results in a ≤ 10 second response time to detect a 10^{-4} (15 W) mean power loss. As the vacuum pressure signals may strongly depend on the location of the partial beam losses relative to the location of the vacuum sensor a second independent sensor system is provided for redundancy.

This second system consists of about 80 NaI detectors placed along the machine acting as relative beam loss monitors. From their counting rates a signal is derived causing the MPS to reduce the repetition rate also to 10 Hz. From the experience with a similar detector system at the BESSY II storage ring a sensitivity corresponding to a beam loss of about 0.15 W can be safely deduced taking into account that the detection efficiency of the NaI may be only 1% due to a disadvantageous position with respect to the location of the beam loss.

In any of these scenarios this safety chain of triple redundancy will reduce the repetition frequency further from 10 Hz to 0.2 Hz in case the charge losses continue to exceed the 1% level per bunch. Once the repetition rate is 1 per 5 seconds the maximum beam power is 30 W. Although the machine components will be built to withstand these losses the NaI-detectors will further intervene and cause the machine to be operated only in single shot mode. Under no circumstances the mean annual losses can exceed the level of 3 W, i.e. $2 \cdot 10^{-5}$ of the maximum beam power of 150 kW. In fact it is reasonable to assume that the losses will be significantly lower, since the process causing losses of 1% of a bunch do not depend on the repetition rate. In most cases one can assume that on the occasion of a problem the machine is set to single-shot mode until the problem has been solved.

For starting up as well as for commissioning the machine, the single-shot mode will be the only way to operate the machine under non-optimized conditions. This also defines the worst case for continuous beam losses relevant for radiation protection. A schematic of the MPS is shown in figure 16.2.

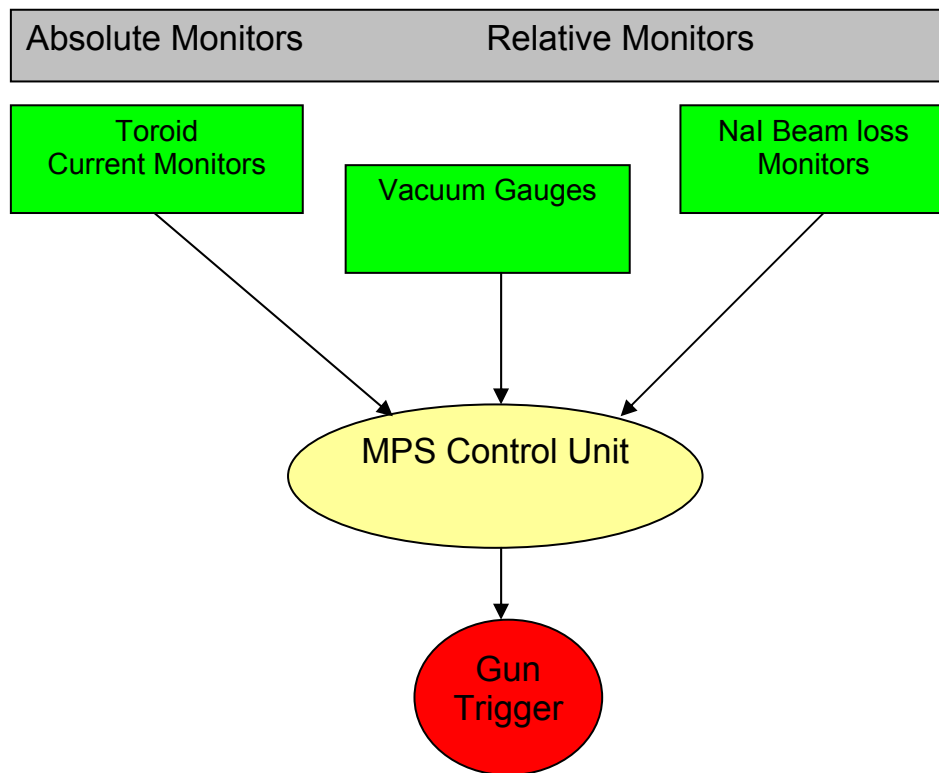


Fig. 16.2: Schematics of the machine protection system. Beam loss is detected by monitors inhibiting the generation of a follow-up bunch train in case the loss limit is exceeded.

16.2 Dose Monitoring in the Undulator Section

16.2.1 Optical Fibers for Cherenkov Radiation

The high sensitivity of the undulator magnets to radiation calls for a dose monitoring in the undulator sections of the FEL. The estimated maximum tolerable dose is 700 Gy for a 10^{-4} demagnetization of the magnet material Nd-Fe-B. Therefore, a fast beam loss and dose monitoring system is required. Optical fibers allow for both, the detection of beam losses, and the monitoring of their location and intensity [1, 2].

When lost electrons hit an optical fiber, Cherenkov radiation is generated, mainly in the near UV, and transported by the fiber to a photomultiplier. From the measured traveling time of the light with respect to the machine trigger or by comparing the signal from both ends of the fiber, the beam loss can be located. Integration of the signal yields the intensity of the radiation.

From a prototype experiment with a single fiber [1], a number of 6000 beam electrons were needed to create one photon that reached the photomultiplier. The typical diameter of the fiber was 100 μm . A time resolution of 1 ns can be realized easily [2]. During tests at the DESY TTF with a bundle of fibers, a beam loss of 0.3% could be detected. The gain can be improved with a larger number of fibers and a closer contact to the undulator vacuum chamber. For the BESSY FEL, Monte-Carlo geometry studies have been performed to determine the expected number of Cherenkov photons and the signal to dose ratio.

Intensive tests of optical fibers for dosimetry have been performed at the TTF for TESLA [3, 4] and for the TTF SASE-FEL [5]. Here germanium-doped Multi-Mode Gradient Index fibers (MM-GI) co-doped with phosphorus were used. When these fibers are exposed to radiation they create color centers which effect the attenuation of light sent through the fiber. With a powermeter and an Optical Time Domain Reflectometer, the dose and the location of the exposure can be determined. The fiber used showed a linear response from 0 - 1000 Gy. The system detects beam losses or radiation within a time scale of a few milliseconds (powermeter) or a few minutes (OTDR), respectively.

In any case, a beam loss at the 0.1% level inside the undulator section is intolerable, since the bunch charge is 2.5 nC; i.e. at a localized loss rate of 0.1% already 120.000 bunches can cause demagnetization of magnet blocks on the 10^{-4} level. Thus, the undulators must be well protected by a collimation system (chapter 9).

16.2.2 Thermo-Luminescence Dosimeters

Thermo-luminescence dosimeters (TLDs) are well-established and commonly used detectors in health physics and radiation protection. They are easy to handle, small, and do not need in-situ electronics. Depending on the material, they recover a dose range from 0.1 mGy to 10^5 Gy. The typical dimensions are on the order of 3 mm x 3 mm x 1 mm, i.e. they fit into the gap of the undulator close to the vacuum chamber. Their disadvantage is that they cannot be read out online but need to be physically removed and replaced for reading and resetting. Assuming a maximum tolerable dose for the undulator magnets of 700 Gy within 10 years, i.e. 6 Gy/month, dose rates should not exceed 1 Gy/month. Based on this number, two types of TLDs will be installed. One for the dose level up to 100 Gy, which will be replaced every month and a high-dose TLD to be read once a year. In the case that the optical fibers show a significant exposure the TLD can be checked at regular intervals.

16.3 Electron Losses, Types of Radiation Produced, Radiation Areas

On the basis of the above mentioned safety measures the electron losses can be limited to 10^{-5} of the total charge on average. Regarding the different reaction products resulting from the electron-nucleus interactions - gamma rays, neutrons, protons, and myons - and the shielding properties of normal concrete it appears that the fast neutrons dominate the radiation field and determine the shielding thickness. For the afore mentioned losses this is calculated to be between 1.5 and 4.5 m of normal concrete depending on the location of loss. It will be realized by an in-situ concrete tunnel construction with walls of about 1.5 m thickness. To obtain the necessary final shielding efficiency adequate to the tolerable electron losses mobile concrete blocks will be added in a flexible manner (chapter 15).

16.3.1 Gamma Radiation

Bremsstrahlung is produced whenever a high energy electron hits a component of the vacuum system or collides with the residual gas nuclei. The energy of the photon may be as high as that of the electrons. However, for energies above 1 MeV the dominating process is pair production, hence $e^- - e^+$ pairs are created which produce further bremsstrahlung and annihilation radiation. While the particles are decreasing their energy, the electromagnetic cascade finally is stopped by ionization processes in the target material.

16.3.2 Neutron Radiation

Photons from bremsstrahlung or from the electromagnetic cascades may create neutrons in nuclear reactions. By the nuclear photo effect γn -reactions create giant resonance neutrons at a threshold energy above 10 MeV for most materials used in the accelerator. The neutrons are emitted isotropically at a maximum energy of approximately 1 MeV. At photon energies above 50 MeV photodisintegration, i.e. quasi-deuteron fission, sets in. Both reaction channels result in neutrons at energies > 20 MeV emitted in the forward direction, rather than in transversal direction. For even more energetic photons exceeding 150 MeV, pion production becomes important.

16.3.3 Proton Radiation

(γ, p) reactions have typically the cross section of photo-disintegration, which is larger than that for the generation of giant resonance neutrons by the γn -channel. So the same number of protons and high energy neutrons are produced approximately. However, due

to their limited range in matter the produced protons will be stopped in the neutron optimized shielding and do not contribute to the dose rate outside.

16.3.4 Myon Radiation

Starting at a photon energy of 212 MeV myons are produced through pair production. Myons lose energy in matter only via ionization making a high Z-material for shielding optimal. At energies of 2.3 GeV the myon production is still negligible in comparison with the other radiation components. Outside the neutron optimized shielding they will contribute less than 1% to the total dose.

For the investigation of the radiation field and dose calculations, semi-empiric formulas as well as the Monte Carlo code FLUKA [6] were used. In the transverse direction, due to the thickness of the concrete wall, only the fast neutrons are relevant outside the shielding as their tenth value length is about a factor of two longer than that for the electromagnetic cascade and the giant resonance neutrons.

16.3.5 The Linac Tunnel

During operation the linac will be an exclusion area. Operation therefore has to be understood as “RF operation enabled”, as dark currents also will cause a γ -dose that is expected to be above the permitted dose rate limits for personal access set by the “Strahlenschutzverordnung”. During periods of no operation the linac tunnel will be a permanent control area due to the possible activation of machine components.

16.3.6 Technical Areas

The roof of the linac tunnel as well as the space within the building along the tunnel walls is designated a surveillance area. Here the technical supply systems will be located.

16.3.7 Experimental Areas

The major part of the experimental area is envisaged to be accessible to the users without restrictions. Only areas close to the front-ends and at the end-stations will be exclusion or control areas, depending on the particular local radiation level.

16.3.8 Beam Dump

The electron beam will be dumped below the floor at the end of the FEL undulators in the linac tunnel. The beam deflection of approximately 40 degrees is effected by an ar-

rangement of electromagnets and for additional safety by a permanent magnet. Thus, the experimental area is protected from any radiation hazard from the primary electron beam.

The layout of the beam dump is shown in figure 16.3. It is a cylinder 2.8 m long with a diameter of 1.5 m made from an onion-like structure of graphite and aluminum, water cooling, copper and concrete. Figure 16.4 depicts the γ - and neutron radiation fields in the environment of the beam dump for a beam power of 50 kW as calculated with the Monte Carlo code FLUKA [7].

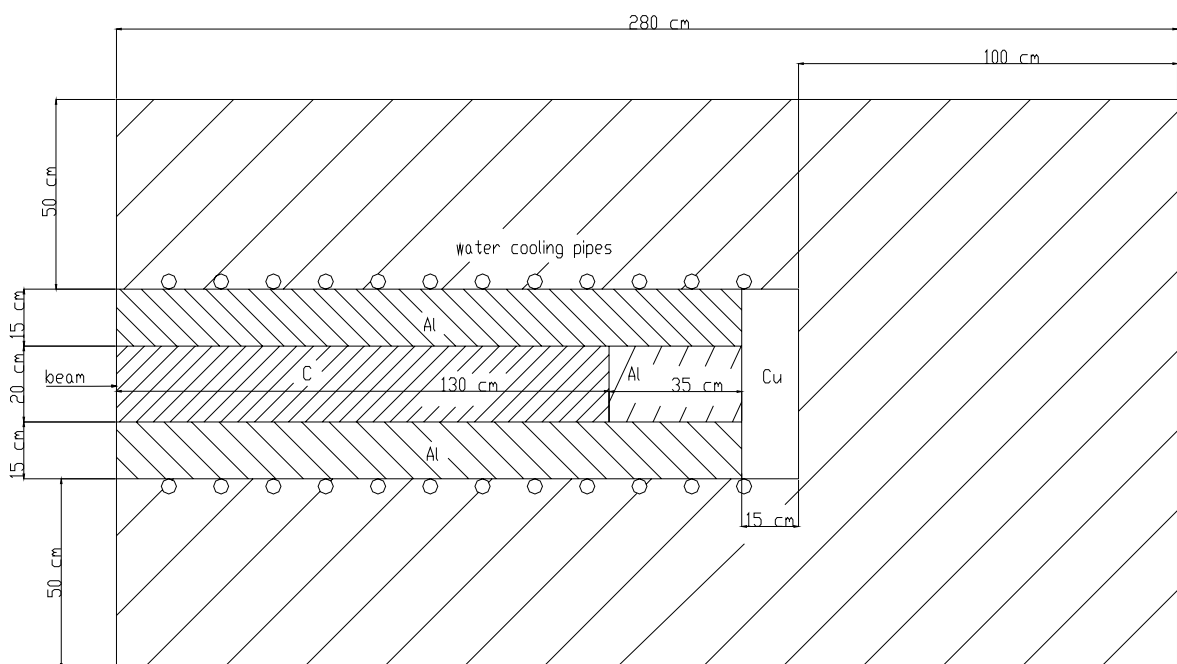


Fig. 16.3: Layout of one of the beam dumps.

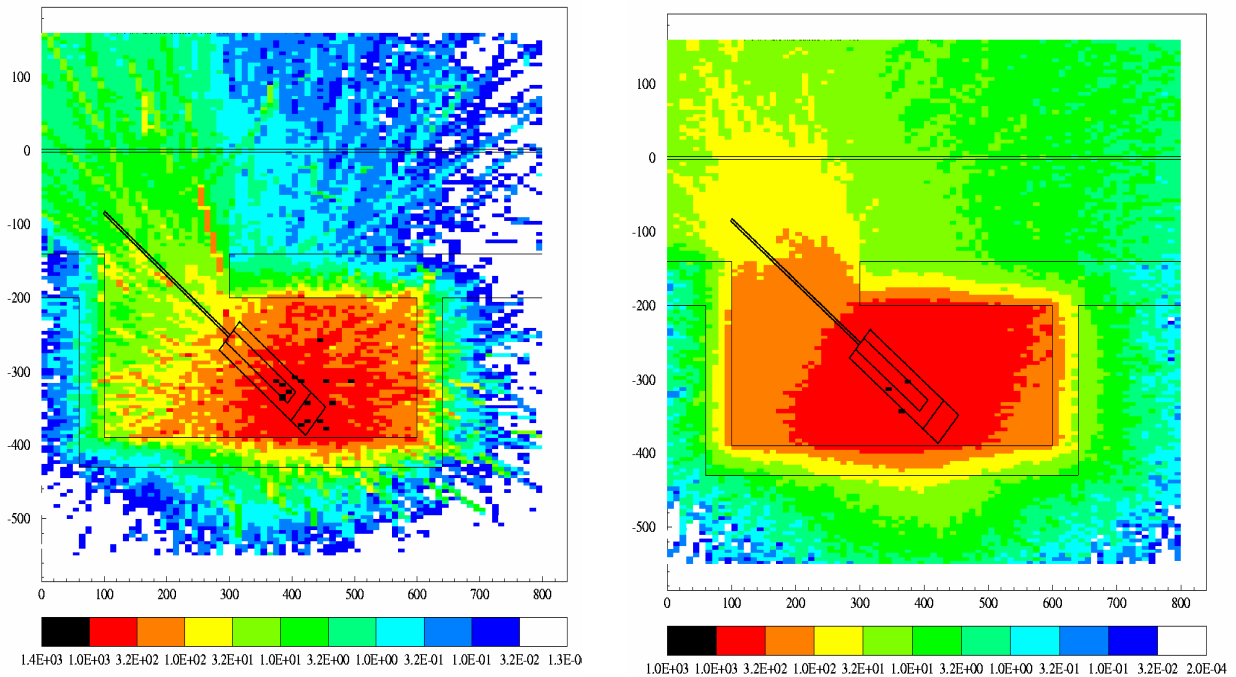


Fig. 16.4: Neutron-dose (left) and γ -dose (right) in the beam dump bunker calculated with the FLUKA code using the shielding as described in the text.

16.4 Activation

16.4.1 Activation of Cooling Water

For the calculation of cooling water activation of the beam dump a 1 cm thick layer of water is assumed enclosing the dump. From the calculations the production rates and the saturation activity of the isotopes involved are derived, leading to a dose rate of 3.8 mSv/h at a distance of 1 m to the cooling water pipe immediately after the end of operation. After two hours the total activity in the water is 3.8 GBq without ^3H and the dose rate has decreased to 114 $\mu\text{Sv/h}$ due to the short lifetime of many of the isotopes, such as ^{10}C , ^{16}N , ^{17}N and ^{14}O .

Thus, for the cooling of the beam dump a closed water circuit with heat exchanger will be provided. The direct neighborhood of the water pipes has to be a permanent control area.

A conservative scaling of the activation in the cooling water circuits of all other machine components leads to a value of 1% at most of that of the dump cooling water. No control areas along these water pipes will be necessary.

16.4.2 Activation of Soil and Ground Water

The results of calculations of the activation of the soil assuming dry sand underneath the 40 cm thick concrete floor of the beam dump are well below any limits. As for the linac itself the production rates will be below 1/100 compared to the dump region, and with a concrete floor shielding even thicker, no activation of the soil is expected. In consideration of ground water direction (to the east and to the north) and velocity (26 m per year) it can be safely assumed that all relevant activity concentrations in the soil and ground water will stay below the relevant limits.

16.4.3 Activation of Air

Activation of the air is dominated by the path length of photons through the surrounding air and the production of ^{11}C along their passage - all other radioactive nuclei being < 1% of ^{11}C . In the beam dump region the calculations assume a 1 cm thick target layer of air between the water cooled dump and its concrete enclosure. Assuming a total air exchange rate once per hour for the dump bunker, the specific activity of the air is calculated to be equal to the protection limit of $3 \cdot 10^6 \text{ Bq/m}^3$. However, since the air from the bunker is released directly to the outside world together with the waste air from the hall, the concentration is diluted by at least three orders in magnitude.

For the air in the linac tunnel a pessimistic permanent 1% loss of electrons was assumed. The air volume is exchanged once per hour for temperature control reasons, leading to activity concentrations dominated by ^{11}C and ^{13}N with 3300 Bq/m^3 and 1630 Bq/m^3 , respectively. This loss scenario is a factor of 100 too pessimistic, and the release will be together with waste air of the total building. The activation concentration of air is therefore kept within the permitted limits with high reliability.

However, in the beam dump bunker the air volume should be as small as possible by proper geometry of the dump and the surrounding concrete base. The dump will be sealed in a concrete block to reduce the exchange of "target" air to less than once per day. To enable a strict surveillance of the activation concentration, all exhaust air from the FEL building will be sent to the environment through one central exhaust.

References

- [1] E. Janata, *Nucl. Instrum. and Meth. A* **493** (2002) 1.
- [2] E. Janata, M. Körfer, H. Schlarb, in press at *Nucl. Instrum. and Meth. A* (2004).
- [3] H. Henschel, O. Köhn, M. Körfer, T. Stegmann, F. Wulf, TESLA Report 2000-25 (2000).
- [4] H. Henschel, M. Körfer, F. Wulf, *Proc. of the 2001 DIPAC* (2001).
- [5] H. Henschel, M. Körfer, J. Kuhnenn, F. Wulf, *Proc. of the 2003 DIPAC* (2003) 248.
- [6] A. Fassó, A. Ferrari, P. R. Sala, *Proc. of the MonteCarlo 2000 Conf* (2000) 159.
- [7] A. Fassó, A. Ferrari, J. Ranft, P. R. Sala, *Proc. of the MonteCarlo 2000 Conf* (2000) 955.

18 Parameter List

The following parameter list gives an overview on the electron and photon beam-parameters and operation parameters for the main hardware components along the linac and FEL lines.

BESSY HGHG-FEL Parameter List

1 General Performance Data						
1.1	<i>Electron Beam Parameters</i>	Applicable to all	HE-FEL	ME-FEL	LE-FEL	Unit
	Electron energy		1.63 - 2.3	2.3	1.02	GeV
	Lorentz factor γ		$3190 < \gamma < 4501$	4501	1996	
	Normalized slice emittance	≤ 1.5				π mm mrad
	Charge per bunch	2.5				nC
	Longitudinal pulse form	“flat top”				
	Transverse pulse form	Gaussian				
	Bunch length (fwhm)	290				μm
	Bunch duration (fwhm)	965				fs
	Peak current	1750				A
	Rel. slice energy spread		$(0.9-1.4) \times 10^{-4}$	9×10^{-5}	2×10^{-4}	
	Repetition Rate		1	1	1	kHz

1.2	FEL Radiation	Applicable to all	HE-FEL	ME-FEL	LE-FEL	Unit
1.2.1	<i>FEL Parameters at Final Amplifier</i>					
	Power gain length		< 3.2	< 3	< 1.8	m
	Saturation length		18	19.7	8.1	m
1.2.2	<i>Output Photon Beam Parameters</i>					
	Peak saturation power P		1.5	1.5 < P < 9	3 < P < 14	GW
	Fundamental radiation wavelength		1.24 < λ < 2.48	2.07 < λ < 12.4	10.4 < λ < 51	nm
	Photon energy		500 - 1000	100 - 600	24 - 120	eV
	Polarization		variable	variable	variable	
	Maximum number of photons per pulse		2×10^{11}	1×10^{13}	7×10^{13}	ph/pulse
	Peak photon flux		1×10^{25}	6×10^{26}	1.6×10^{26}	ph/s
	Peak brightness:		1.3×10^{31}	6×10^{30}	1.6×10^{30}	*
	Photon energy spread $\Delta\lambda/\lambda$		< 0.2	< 0.16	< 0.4	%
	Trans. beam size (rms)		50	< 50	140	μm
	Trans. Beam divergence (rms)		< 20	< 50	< 160	μrad
	Photon pulse length (rms)		20	20	20	fs

* ph/(s mm² mrad² 0.1% bw)

2 Photo-Injector Gun Laser						
2.1	<i>Laser Amplifier</i>	Applicable to all	HE-FEL	ME-FEL	LE-FEL	Unit
	Amplifier	Ti:Sa				
	Output wavelength	263				nm
	Micropulse shape	trapezoidal				
	Pulse repetition rate	1				kHz
	No. of micropulses	3				
	Micropulse energy on cathode	> 10				μJ
	Laser spot on cathode	3				mm
	Micropulse risetime (10-90%)	4				ps
	Flat top duration	20 - 60				ps
2.2	<i>n.c. Gun-Cavity</i>					
	Number of cells	1.5				
	Operation Mode	TM ₀₁₀				
	Operation frequency	1.3				GHz
	Repetition frequency	1				kHz
	Unloaded Q-value	22000				
	Coupling factor	1				
	Field at cathode	40				MV/m
	Peak power in cavity	3				MW
	Average power	75				kW
2.3	<i>Gun RF</i>					
	Power source	Klystron				
	Peak power	10				MW
	Pulse duration	25				μs
	Repetition rate	1				kHz
	Mean drive power	320				W
	Bandwidth	8				MHz

3	Beamtransport and Linac					
3.1	Bunch Compressor BC1	Applicable to all	HE-FEL	ME-FEL	LE-FEL	Unit
	Beam energy	219				MeV
	Bunch length (fwhm), BC1 entrance	8.6				mm
	Bunch length (fwhm), BC1 exit	2.7				mm
	Peak current, BC1 entrance	65				A
	Peak current, BC1 exit	200				A
	Projected horiz. emittance, BC1 entrance	2.12			π	mm mrad
	Projected horiz. emittance, BC1 exit	2.14			π	mm mrad
	Projected vert. emittance, BC1 entrance	2.12			π	mm mrad
	Projected vert. emittance, BC1 exit	2.2			π	mm mrad
	Rel. Energy spread	2.41				%
	Momentum compaction R_{56}	-10.5				cm
	Second order mom. compaction T_{566}	16.4				cm
	No. of bend magnets B_n	6				
	Bending radius B1, B2	1.8				m
	Bending radius B3, B4	2.25				m
	Bending radius B5, B6	4.5				m
	Bend magnet effective magnetic length	0.4				m
	No. of quadrupole magnets	4				
	Quadrupole effective magnetic length	0.2				m
	Max. quadrupole strength	< 3				m^{-2}
	Total length BC1	8.1				m

3.2	180° Bend	Applicable to all	HE-FEL	ME-FEL	LE-FEL	Unit
	Beam energy	753				MeV
	Bunch length (fwhm), arc entrance	2.7				mm
	Bunch length (fwhm) arc exit	2.3				mm
	Peak current, BC2 exit	240				A
	Projected horizontal emittance, BC2 exit	2.82			π mm mrad	
	Projected vert. emittance, BC2 exit	2.14			π mm mrad	
	Rel. Energy spread, BC2 exit	0.93				%
	Momentum compaction R_{56}	-1.87				cm
	Second order momentum compaction T_{566}	110				cm
	Achromat structure	TBA				
	No. of TBA	4				
	No. of bending magnets	12				
	Bending radius	2.55				m
	Bend magnet eff. Mag. length B1, B3	0.5				m
	Bend magnet effective magnet length B2	1				m
	No. of quadrupole magnets per TBA	4				
	Quadrupole effective magnetic length	0.3				m
	Max. quadrupole strength	5				m^{-2}
	No. of sextupole magnets per TBA	4				
	Sextupole effective magnetic length	0.2				m
	Max. sextupole strength	75				m^{-3}
	Total arc length	48.4				m

3.3 Bunch Compressor BC2	Applicable to all	HE-FEL	ME-FEL	LE-FEL	Unit
Beam energy	753				MeV
Bunch length (fwhm), BC2 entrance	2.3				mm
Bunch length (fwhm), BC2 exit	0.29				mm
Peak current, BC2 entrance	240				A
Peak current, BC2 exit	2000				A
Projected horizontal emittance, BC2 entrance	2.82			π mm mrad	
Projected horizontal emittance, BC2 exit	2.82			π mm mrad	
Projected vertical emittance, BC2 entrance	2.14			π mm mrad	
Projected vertical emittance, BC2 exit	2.4			π mm mrad	
Relative energy spread, BC2 entrance	0.93				%
Rel. Energy spread, BC2 exit	0.89				%
Momentum compaction R_{56}	-9.29				cm
Second order momentum compaction, T_{566}	14.04				cm
No. of bend magnets B_n	8				
Bending radius B1, B2B3, B4	4.36				m
Bending radius B5, B6	8.5				m
Bending radius B7, B8	13.89				m
Bend magnet effective magnetic length	0.4				m
No. of quadrupole magnets	6				
Quadrupole effective magnetic length	0.2				m
Max. quadrupole strength	< 5				m^{-2}
Total length BC2	23.0				m

3.4	Collimator (HE-FEL)	Applicable to all	HE-FEL	ME-FEL	LE-FEL	Unit
	No. of dipole magnets	2				
	No. of quadrupole magnets	13				
	Dipole eff. magnet length	0.4				m
	Quadrupole effective magnet length	0.3				m
	Bend magnetic field	< 0.85				T
	Quadrupole strength	< 5				m ⁻²
	Total collimator length	40.65				m
3.5	3rd Harmonic Cavity System					
	Number of cells	9				
	Number of cavities	8				
	Operation mode	TM ₀₁₀				
	Active length	0.346				m
	Resonant frequency	3.9				GHz
	Effective Field gradient	10.2				MV/m
	R _{eff} /Q _o	373				
	B _{pk} /E _{acc}	4.9				mT/MV/m

3.6 Linac						
3.6.1	Optics	Applicable to all	HE-FEL	ME-FEL	LE-FEL	Unit
	Lattice type	FODO				
	Phase advance	0.248				rad/2 π
	Av. Beta function	20				m
	Min./ max. beta function	7.5 / 39.6				m/m
	Quadrupole length	0.5				m
	Quadrupole strength	0.235				m ⁻²
	Unit cell length	23.6				m
3.6.2 Cavity						
	Number of cells per cavity	9				
	Operation mode	TM ₀₁₀				
	Active length	1.038				m
	Resonant frequency	1.3				GHz
	Quality factor (at 1.8 K)	2 x 10 ¹⁰				
	Shunt impedance	1041				Ω
	B _{pk} /E _{acc}	4.26				mT/MV/m
	df/dL	315				kHz/mm
	df/dP	20				Hz/mbar
3.6.3 CW-TESLA Modules						
	Number of cavities	8				
	Number of modules	18				
	Overall module length	12.2				m
	Maximum operating Gradient	16.1				MV/m
	Maximum cavity loss	166				W
	Average Gradient	15.92				MV/m
	Average cavity loss	158				W
	Total cavity losses	2835				W

3.7	RF-System	Applicable to all	HE-FEL	ME-FEL	LE-FEL	Unit
	Tube	IOT				
	Frequency	1.3				GHz
	CW power	< 20				kW
	Bandwidth	< 5				MHz
	Gain	> 20				dB
	Efficiency	> 60				%
	Number of systems	144				
3.8	Cryogenic Parameters					
	1.8K Heat load					
	Static	95				W
	Dynamic	2835				W
	Design	3500				W
	5 - 8K Heat load					
	Static	285				W
	Dynamic	227				W
	Design	1000				W
	40-80K Heat load					
	Static	1520				W
	Dynamic	2140				W
	Design	7500				W

4 HGHG Stages						
4.1	External seed laser	Applicable to all	HE-FEL	ME-FEL	LE-FEL	Unit
	Seed wavelength	$460 < \lambda < 230$	variable	variable	variable	
	Seed power	500				MW
	Seed longitudinal pulse form	Gaussian				
	Seed pulse duration (rms)	15				fs
4.2	Stage 1 undulator Parameters					
	<i>Modulator 1</i>					
	Modulator period length		122	122	80	mm
	Number of periods		18	18	20	m
	Modulator length without intersection		2.196	2.196	1.600	m
	<i>Radiator 1</i>					
	Radiator period length		92	92	62	mm
	Number of periods		40	40	56	
	Radiator length without intersection		3.68	3.68	3.472	m
	Harmonic number		3 / 5	3 / 5	3 / 5	
	Output wavelength		55.9 - 66.96	51.65 - 111.6	51.65 - 153	nm
	Output power		4 - 4.5	1.6 - 5.5	2.5 - 6	GW

4.3	Stage 2	Applicable to all	HE-FEL	ME-FEL	LE-FEL	Unit
	<i>Modulator 2</i>					
	Modulator period length		92	92	62	mm
	Number of periods		22	22	26	
	Modulator length without intersection		2.024	2.024	1.612	m
	<i>Radiator 2</i>					
	Radiator period length		70	70	50	mm
	Number of periods		86	104	69	
	Radiator length including intersection		6.02	7.28	3.45	m
	Harmonic number		5 / 3	5 / 3	5 / 3	
	Output wavelength		11.18 - 22.32	10.33 - 37.2	10.33 - 51	nm
	Output power		1.8 - 4	1 - 2.7	0.6 - 7.5	GW
4.4	Stage 3					
	<i>Modulator 3</i>					
	Modulator period length		70	70		mm
	Number of periods		30	30		
	Modulator length without intersection		2.1	2.1		m
	<i>Radiator 3</i>					
	Radiator period length		50	50		
	Number of periods		180	231		
	Radiator length including intersection		9	11.55		m
	Harmonic number		3	5 / 3		
	Output wavelength		3.73 - 7.44	2.07 - 12.4		nm
	Output power		0.5 - 1.9	0.24 - 1.5		

4.5	Stage 4	Applicable to all	HE-FEL	ME-FEL	LE-FEL	Unit
	<i>Modulator 4</i>					
	Modulator period length		50			mm
	Number of periods		69			
	Modulator length including intersection		3.45			m
	<i>Radiator 4</i>					
	Radiator period length		28.5			mm
	Number of periods		225			
	Radiator length including intersection		6.413			m
	Harmonic number		3			
	Output wavelength		1.24 - 2.48			nm
	Output power		0.13			GW
4.6	Final amplifier					
	Period length		28.5	50	50	mm
	Number of periods		630	393	162	
	Final amplifier length including intersection		17.955	19.65	8.1	m
	Harmonic number		1	1	1	
	Output wavelength		1.24 - 2.48	12.4 - 2.07	10.33 - 51	nm
	Output power		1.5	1.5 - 9	3.5 - 14	GW

5	FEL Beamlines					
5.1	Low energy beamline	applicable to all	HE-FEL	ME-FEL	LE-FEL	Unit
	Photon energy range				24 - 120	eV
5.1.1	<i>High energy resolution beamline</i>					
	Photons per pulse				1.2x10 ⁸ - 1.6x10 ¹⁰	
	Bandwidth				90 - 6000	μeV
	Pulse length (fwhm)				5 - 80	ps
	Exit slit size				10 - 100	μm
5.1.2	<i>Short pulse beamline</i>					
	Photons per pulse				1.3x10 ⁹ - 5x10 ¹²	
	Pulse length (fwhm)				30 - 210	fs
	Bandwidth				16 - 160	meV
	Spot size (horiz. x vertical) (fwhm)				80 x 20 - 120 x 55	μm ²
	Exit slit size				10 - 1000	μm
5.1.3	<i>Direct beam</i>					
	Photons per pulse				1.5x10 ¹² - 6x10 ¹³	
	Spot size (hor.x vert.)(fwhm)				10 x 3	μm ²
	Energy density				(1 - 8)x10 ⁵	mJ/cm ²
	Peak-power density				3x10 ¹⁵ - 3x10 ¹⁶	W/cm ²

5.2	High energy beamline	Applicable to all	HE-FEL	ME-FEL	LE-FEL	Unit
	Photon energy range		500 - 1000			eV
5.2.1	<i>High energy resolution beamline. Data for 1000 eV</i>					
	c- Parameters: c1 (c2)		10 (2.2)			
	Photons per pulse for c1 (c2)		(0.2 - 1.5) × 10 ⁸			
	Bandwidth		(0.6 - 6) × 10 ⁸			meV
	Pulse length (fwhm)		20 - 140			fs
	Exit slit size		650 (120)			μm
	10 - 100					
5.2.2	<i>Short pulse beamline Data for 1000 eV</i>					
	Photons per pulse		1.6 10 ⁹			
			(3.8 × 10 ⁹)			
	Pulselength (fwhm)		8			fs
	Bandwidth		650 (795)			meV
	Spot size (hor. x vert.)(fwhm)		30 × 4 (8)			μm ²
	Exit slit size		20 (50)			μm
5.2.3	<i>Direct beam beamline Data for 1000 eV</i>					
	Photons per pulse		6.6×10 ¹⁰			
	Spot size (hor. x vert.)(fwhm)		9 × 1			μm ²
	Energy density		1.2×10 ⁵			mJ/cm ²
	Peak-power density		2×10 ¹⁶			W/cm ²



In cooperation with:

- Brookhaven National Laboratory, BNL
- Cornell University
- Deutsches Elektronen-Synchrotron, DESY
- Forschungszentrum Rossendorf, FZR
- Max-Born-Institut für Nichtlineare Optik und Kurzzeitspektroskopie, MBI
- Max-Planck Gesellschaft - Bauabteilung
- Technische Universität Dresden
- Technologiestiftung Berlin, TSB

Supported by

Zukunftsfonds des Landes Berlin



**Berliner Elektronenspeicherring-Gesellschaft
für Synchrotronstrahlung (BESSY) m.b.H.**

Albert-Einstein-Straße 15
12489 Berlin
Germany
Tel: +49-(0)30-6392-2999
Fax: +49-(0)30-6392-2990
www.bessy.de
fel@bessy.de

BESSY is a member of the Leibniz Association

Copyright BESSY GmbH, Berlin 2004